Valorisation of Guar (*Cyamopsis tetragonoloba*) straw and Kachri (*Cucumis callosus*) Extract for the development of Biodegradable Packaging Film for selected fruits

Thesis Submitted for the Award of the Degree of

DOCTOR OF PHILOSOPHY

in

Food Science and Technology

By

Ritu Rani

Registration Number: 12208549

Supervised By

Dr. Mukul Kumar (25090)

(Associate Professor)

School of Agriculture

LOVELY PROFESSIONAL UNIVERSITY, PUNJAB
2026

DECLARATION

I, hereby declared that the presented work in the thesis entitled "Valorisation of Guar (*Cyamopsis tetragonoloba*) straw and Kachri (*Cucumis callosus*) Extract for the development of Biodegradable Packaging Film for selected fruits" in fulfilment of degree of **Doctor of Philosophy (Ph. D.)** is outcome of research work carried out by me under the supervision of Dr. Mukul Kumar, working as Associate Professor, in the Department Of Food Technology and Nutrition of Lovely Professional University, Punjab, India. In keeping with general practice of reporting scientific observations, due acknowledgements have been made whenever work described here has been based on findings of other investigator. This work has not been submitted in part or full to any other University or Institute for the award of any degree.

27/6/26

(Signature of Scholar)

Name of the scholar: Ritu Rani

Registration No.: 12208549

Department/school: Food Technology and Nutrition

Lovely Professional University,

Punjab, India

DECLERATION

I, hereby declare that the presented work in the Project entitled **"Valorisation of .Guar (*Cyamopsis tetragonoloba*) straw and Kachri (*Cucumis callosus*) Extract for the development of Biodegradable Packaging Film for selected fruits"** in fulfilment of the degree of Doctor of Philosophy is an outcome of research work carried out by me under the supervision of Dr Mukul Kumar, Associate Professor, Department of Food Technology and Nutrition, School of Agriculture, Lovely Professional University, for the award of degree of Ph.D Food Science and Technology.

Date: 27/6/26

Ritu Rani (12208549)

I certify that the above statement made by the student is correct to the best of my knowledge and belief.

Signature of Supervisor
Dr Mukul Kumar

27/06/2026

Signature of External Examiner

CERTIFICATE

This is to certify that the work reported in the Ph. D. thesis entitled "Valorisation of Guar (*Cyamopsis tetragonoloba*) straw and Kachri (*Cucumis callosus*) Extract for the development of Biodegradable Packaging Film for selected fruits" submitted in fulfillment of the requirement for the award of degree of **Doctor of Philosophy (Ph.D.)** in the Food Technology and Nutriton, is a research work carried out by Ritu Rani, 12208549, is bonafide record of his/her original work carried out under my supervision and that no part of thesis has been submitted for any other degree, diploma or equivalent course.

(Signature of Supervisor)

Name of supervisor: Dr. Mukul Kumar

Designation: Associate Professor

Department/school: Food Technology and Nutrition

University: Lovely Professional University, Punjab, India

Acknowledgement

I would like to express my deepest gratitude to all those who supported and guided me throughout the journey of completing this thesis. The successful completion of this research work would not have been possible without the encouragement, guidance, and blessings of many individuals who have contributed directly and indirectly to my academic and personal growth.

First and foremost, I extend my sincere and heartfelt thanks to my esteemed supervisor, **Dr. Mukul Kumar**, **Associate Professor**, **Department of Food Technology and Nutrition,** his invaluable guidance, constant encouragement, and thoughtful suggestions throughout my Ph.D. journey. His academic excellence, patience, and dedication towards research have been a continuous source of inspiration for me. His constructive criticism, intellectual inputs, and unwavering support have significantly shaped this research work and strengthened my analytical and scientific understanding. I am truly grateful for the trust he placed in me and for providing an environment that encouraged independent thinking and academic growth.

I would like to express my deepest gratitude to **Dr. Sawinder Kaur, Associate Dean, Department of Food Technology and Nutrition**, for her unwavering support and encouragement throughout the course of my research. Her constant motivation, valuable guidance, and commitment to academic excellence created a positive and research-oriented environment that greatly contributed to the successful completion of this work. Her encouragement and administrative support have been truly invaluable during my Ph.D. journey.

I am equally thankful to **Dr. Prasad Rasane, Head of the Department**, for his continuous support, motivation, and valuable guidance throughout the course of my research. His administrative assistance and academic insights were instrumental in facilitating the smooth progress of my work.

I extend my profound gratitude to **Dr. Prince Chawla** and **Dr. Aarti Bains** for their constant guidance, technical expertise, and valuable suggestions during experimentation and data interpretation. Their constructive feedback, encouragement, and willingness to share their knowledge significantly enhanced the quality of this research work. I deeply appreciate their support in refining my experimental approach and strengthening the scientific rigor of my study.

I also express my sincere thanks to **Dr. Manish Bakshi** for his support, encouragement, and guidance during my research tenure. His assistance and motivation contributed positively to the completion of my work.

I would like to acknowledge with sincere appreciation the technical assistance and cooperation of the laboratory staff, **Mr. Om Prakash, Mr. Bansi Lal, Mr. John Masih, and Mr. Devendra Kumar**, for their continuous support during laboratory work. Their readiness to assist, technical expertise, and cooperation ensured the smooth execution of experiments and timely completion of research activities.

My heartfelt appreciation goes to my beloved family, whose unconditional love, patience, and unwavering support have been my greatest strength. I am especially grateful to my husband, **Mr. Sunil Kumar**, for his constant encouragement, understanding, and belief in my abilities. His patience during demanding phases of my Ph.D. journey and his emotional support provided me with the strength to overcome challenges and stay focused on my goals.

I am deeply thankful to my mother, **Mrs. Mona Devi**, for her endless blessings, sacrifices, and emotional support. Her faith in me has always motivated me to strive for excellence. I also sincerely thank my brother, **Mr. Preetam Dhillon**, for his encouragement and constant belief in my capabilities throughout this academic journey.

I would also like to express my sincere gratitude to my in-laws, **Mr. Ishwer Singh** and **Mrs. Sumitra Devi**, for their blessings, understanding, and moral support. Their encouragement and positivity have been a strong pillar of strength throughout this journey.

I extend my heartfelt thanks to my dear friends and colleagues, **Dr. Gaurav Sharma, Shivali Pathania, Vishal Kumar, Pooja Vartia, Puneet Kang, Julia Thakur, Nikhil, Madhu, Ankita, Nidhi Boora, and Pratibha Batra,** for their cooperation, encouragement, and companionship. Their support during discussions, laboratory work, and challenging times made this journey both meaningful and memorable. The camaraderie and shared experiences contributed greatly to maintaining motivation and positivity throughout my research tenure.

I also acknowledge with gratitude all faculty members, staff, and well-wishers who directly or indirectly contributed to the successful completion of this research work. Their support, guidance, and encouragement at various stages of my academic journey have been invaluable.

Finally, I bow in gratitude to everyone who stood by me, motivated me, and believed in my ability to accomplish this milestone. This achievement is a collective outcome of the guidance, blessings, and support of all those who have been part of my journey. I extend my deepest gratitude to all.

Lastly, I would like to acknowledge the resources provided by Lovely Professional University, Phagwara, Punjab, without which this research would not have been possible.

I would like to extend my heartfelt thanks to the **Central Instrumentation Facility (CIF)** for providing access to advanced equipment and technical support, which was crucial for the

successful completion of my research. Their expertise and assistance greatly enhanced the quality of my work.

I am also deeply grateful to the **Department of Microbiology** for their invaluable guidance and support. The knowledge and resources provided by the department were instrumental in the microbiological aspects of my study.

I would also like to acknowledge the **Centre for Research and Development (CRDP)**, especially **Dr. Rajan Miglani**, Coordinator of Division, CRDP, for facilitating a conducive research environment and offering continuous support throughout my PhD journey. Their encouragement and resources played a pivotal role in the progress and completion of this research.

I extend my deepest gratitude to all.

Table of Content

Sr. No.	Content	Page No.
	Abstract	XXXI-XXXIII
1.	Chapter 1- Introduction	1-6
1.1	Chapter 1.1- Research Objective	7
2	Chapter 2- Review of Literature	8-90
2.1	Agricultural Waste Valorisation for Biopolymer Production	8-10
2.1.1	Types of Biopolymers	10-12
2.1.2	Cellulose-Based Biopolymers	12-
2.1.2.1	Extraction Methods for Cellulose from Agricultural Residues	14-15
2.1.2.1.1	Alkaline Treatment	15
2.1.2.1.1	Bleaching	15-16
2.1.2.1.3	Acid Hydrolysis	16-17
2.1.2.1.4	Enzymatic Hydrolysis	17--19
2.1.2.1.5	Ionic Liquid Treatment	19-20
2.1.2.2	Conversion of cellulose into nanocellulose	22
2.1.2.2.1	Acid hydrolysis	22-23
2.1.2.2.2	Alkali hydrolysis	23-24
2.1.2.2.3	Oxidizing agent	24-25
2.1.2.2.4	Organo-solvent	25
2.1.2.2.5	Ionic Liquid	25-26
2.1.2.3	Properties of Cellulose and Nanocellulose	26
2.1.2.3.1	Structural and Chemical Properties of Cellulose	26-27
2.1.2.3.2	Mechanical and Physical Properties	27
2.1.2.3.3	Thermal and Barrier Properties	27-28
2.1.2.3.4	Morphological and Rheological Properties	28
2.1.2.3.5	Hydrophilicity, Hydrophobicity, and Surface Tunability	28-29
2.1.2.3.6	Biodegradability and Environmental Compatibility	29
2.1.3	Preparation Methods of Cellulose-Based Biodegradable film	29
2.1.3.1	Casting method	30

2.1.3.2	Compression molding	30-31
2.1.3.3	Extrusion Methods	31-32
2.1.3.4	Emulsion Based	32-33
2.1.4	Biodegradable films using nano-cellulose from agricultural waste	33-37
2.1.5	Nanoemulsion-based packaging film	38
2.1.5.1	Physicochemical and Functional Characterization of Essential Oil Nanoemulsion-Integrated Packaging Films	41
2.1.5.2	Physical Properties	41
2.1.5.2.1	Colour Attributes	41-42
2.1.5.2.2	Film Thickness	42-43
2.1.5.2.3	Film Solubility	43
2.1.5.3	Physico-Chemical Properties	43
2.1.5.3.1	Water Vapour Permeability	43-44
2.1.5.3.2	Moisture Absorption	44-45
2.1.5.3.3	Mechanical Properties	45
2.1.5.3.4	Tensile Strength	45-46
2.1.5.3.5	Elongation at break	46-47
2.1.5.3.6	Antimicrobial Activity	47-48
2.1.6	Importance of Packaging in Fresh-Cut Fruits and Vegetables	48-49
2.1.7	Starch-based biopolymer	50-51
2.1.8	Protein-Based Biopolymers	51
2.1.9	PHA and PLA	51-52
2.2	*Cyamopsis Tetragonoloba*	52-54
2.2.1	Nutritional Profile of *Cyamopsis tetragonoloba*	54-55
2.2.2	Bioactive Compounds of *Cyamopsis tetragonoloba*	55-58
2.2.2.1	Anticancer	58-59
2.2.2.2	Antioxidant activity	59-60
2.2.2.3	Anti-inflammatory	60-61
2.2.2.4	Antidiabetic	61-62
2.2.3	Utilizations of *Cyamopsis tetragonoloba*	62
2.2.3.1	Food applications of *Cyamopsis tetragonoloba*	62-66
2.2.3.2	Packaging Industries	66-69

2.2.4	Pharmaceutical Industries	69-71
2.2.5	Environmental Impact and Sustainability Considerations	71-72
2.3	*Cucumis callosus*	72-75
2.3.1	Nutritional Profile of *Cucumis Callosus*	75-76
2.3.2	Areas of Distribution and Harvesting of *Cucumis Callosus*	76-77
2.3.3	Bioactivity of *Cucumis callosus*	77
2.3.4	Biological Activities of *Cucumis callosus*	78
2.3.4.1	Anticancer and gastroprotective effects	79
2.3.4.2	Antioxidant and anti-hyperglycemic Activity	79
2.3.4.3	Anti-Inflammatory Activity	80
2.3.4.4	Anti-diabetic activity	81
2.3.4.5	Cardiotoxicity	83
2.3.4.6	Anti-urolithiatic	84-85
2.3.5	Industrial application of *Cucumis callosus* in food	85-86
2.3.6	Non-food applications of *Cucumis callosus*	86
2.4	Chapter-2.4-Hypothesis	87
3	Chapter 3- Materials and Methods	88
3.1	Materials	88
3.2	Methods	88
3.2.1	Preparation of *Cyamopsis tetragonoloba* Straw Sample	88
3.2.2	Proximate analysis of *Cyamopsis tetragonoloba* straw	88
3.3	Functional properties of *Cyamopsis tetragonoloba* straw	88
3.3.1	Bulk Density	88-89
3.3.2	Oil and Water Holding Properties	89
3.3.3	Emulsifying properties	89
3.3.4	Foaming capacity and stability	90
3.4	Characterization of *Cyamopsis tetragonoloba* straw	90
3.4.1	Fourier-transform infrared analysis (FTIR)	90
3.4.2	Scanning electron microscope (SEM)	90
3.4.3	Thermo-gravimetric analysis (TGA)	90-91
3.4.4	X-ray diffraction (XRD)	91
3.5	Ethanolic extraction from *Cyamopsis tetragonoloba* straw	91

3.5.1	Determination of total phenols content	91
3.5.2	Determination of total flavonoid content	91-92
3.5.3	DPPH (2,2-diphenyl picrylhydrazyl) radical-scavenging activity	92
3.5.4	Quantification of polyphenolic compounds	92
3.5.6	Antimicrobial efficacy	92-93
3.5.7	Cytotoxicity	93
3.5.8	Amylase Inhibition Assay	93
3.5.9	Lipase Inhibition Assay	94
3.6	Determination of lignocellulosic material	94
3.6.1	Acid detergent fiber (ADF)	94-95
3.6.2	Acid detergent lignin (ADL)	95
3.6.3	Neutral detergent fiber (NDF)	95
3.7	Extraction of cellulose from guar straw	96
3.7.1	Optimization of the extraction process	97-99
3.7.2	Purity of cellulose	99
3.7.3	Characterization of Cellulose and confirming the conversion of guar straw to nanocellulose	99
3.7.3.1	Particle Size and zeta potential	100
3.7.3.2	Fourier-transform infrared spectroscopy (FTIR)	100
3.7.3.3	Scanning electron microscope (SEM)	100
3.7.3.4	Thermogravimetric analysis (TGA)	100
3.7.3.5	Crystallinity analysis (XRD)	100
3.7.3.6	Differential scanning calorimetry (DSC)	100
3.8	Preparation of *Cucumis callosus* peel, pulp and seed powder	100
3.8.1	Proximate analysis	100
3.8.2	Characterization of different parts of *Cucumis callosus* fruit	101
3.8.2.1	Determination of functional groups	101
3.8.2.2	Phase transition analysis	101
3.8.2.3	Thermal decomposition	101
3.8.2.4	Crystallinity analysis	101
3.8.2.5	Morphological analysis	101
3.9	Preparation of ethanolic extract	101

3.9.1	Biochemical analysis	101
3.9.1.1	Colouring pigment analysis	101
3.9.1.2	Ascorbic acid	102
3.9.1.3	Determination of total phenol content	102
3.9.1.4	Determination of total flavonoid content	102
3.9.7.5	HPLC Analysis	102
3.9.7.6	Antioxidant activity	102
3.9.2	Antinutritional factor	102
3.9.2.1	Phytic acid	102
3.9.2.2	Oxalic acid	102
3.9.2.3	Tannin content	103
3.9.2.4	Antimicrobial activity	103
3.10.1	Formulation of nanocellulose-polyphenolic complex	103
3.10.2	Determination of nanocellulose-polyphenolic complex binding efficiency	103
3.10.3	Determination of functional properties of native nanocellulose and nanocellulose-polyphenolic complex	103
3.10.3.1	Bulk density	104
3.10.3.2	Water absorption and oil absorption capacity	104
3.10.3.3	Foaming properties and stability	104
3.10.4	Physicochemical properties	104
3.10.4.1	Total phenols content	104
3.10.4.2	Total flavonoid content	104
3.10.4.3	Antioxidant activity	104
3.10.5	Quantification of polyphenolic compounds	104
3.10.6	Surface hydrophobicity (SH)	104
3.11	Characterization of nanocellulose-polyphenolic complex	105
3.11.1	Particle size	105
3..11.2	Fourier transform infrared spectroscopy	105
3..11.3	Thermogravimetric analyzer	105
3.11.4	Differential Scanning Calorimetry	105
3.11.5	Scanning electron microscopy	105

3.11.6	X-ray diffraction	105
3.12	Preparation of nanoemulsion	105
3.12.1	Preparation of Nanocellulose-Based Nanoemulsion	105-106
3.12.2	Preparation of Nanoemulsion Incorporated with *Cucumis callosus* Peel Extract	107
3.12.3	Formulation of Sodium Alginate–Based Nanoemulsion	108
3.12.4	Preparation of Guar Gum–Based Nanoemulsions	108
3.12.5	Evaluation of the Physicochemical Stability of the Nanoemulsion	109
3.12.5.1	Creaming index	109
3.12.5.2	Droplet size and zeta potential	109
3.12.5.3	Antimicrobial activity	109
3.12.6	Characterization of nanoemulsion	109
3.12.6.1	Rheology of nanoemulsion	110
3.12.6.2	Scanning electron microscope (SEM) of nanoemulsion	110
3.12.6.3	Fourier Transform Infrared (FTIR) Analysis	110
3.13	Preparation of Ternary Blend and Bioactive Composite Films	110
3.13.1	Optimization of Glycerol Concentration	110
3.13.2	Preparation of functional with *Cucumis callosus* Peel Extract	111
3.13.3	Mechanical and Physicochemical Characterization of Films	112
3.13.3.1	Tensile strength (TS) and elongation at breakage (EB)	112
3.13.3.2	Thickness	112
3.13.3.3	Water Vapor Permeability (WVP)	112
3.13.3.4	Moisture Content and Transparency	113
3.13.3.5	Puncture strength	113
3.13.3.6	Antimicrobial activity	113
3.13.4	Characterization of films	113
3.13.4.1	Morphological Analysis	113
3.13.4.2	Functional Group Analysis (FTIR)	114
3.13.4.3	Thermogravimetric Analysis (TGA)	114
3.13.4.4	X-ray Diffraction (XRD) Analysis	114
3.13.4.5	Differential Scanning Calorimetry (DSC)	114
3.13.5	Biodegradability of packaging film	114

3.13.5.1	Dry method	114
3.13.5.2	Moist soil method	115
3.13.5.3	Oven-Assisted Soil Method	115
3.13.5.4	Enzymatic Degradation	115
3.14	Shelf-life study of cut fruit	116
3.15	Physicochemical Analysis of Fresh-Cut Fruits	116
3.15.1	Proximate of cut fruits	117
3.15.2	Weight Loss and pH Value	117
3.15.3	Total Soluble Solids (TSS) and Titratable Acidity	117
3.15.4	Color Value	117
3.15.5	Firmness	118
3.15.6	Total phenolic content	118
3.15.7	Ascorbic Acid Content	118
3.15.8	Respiration Rate	118
3.16	Statistical Data Analysis	118
4	Chapter-4 Results and Discussion	119
4.1	Proximate analysis	120
4.2	Techno-functional properties	121
4.3	Characterization of Guar Straw	122
4.3.1	Fourier transmission infrared spectroscopy	122-123
4.3.2	Surface morphology	123-124
4.3.3	X-ray diffraction pattern	124-125
4.3.4	Thermogravimetric analysis	125-126
4.4	Ethanolic extraction	126
4.4.1	Phytochemical analysis	126
4.4.2	Quantification of polyphenols through HPLC	127
4.4.3	Antimicrobial efficiency of *Cyamopsis tetragonoloba* straw extract	128-129
4.4.4	Cytotoxicity of guar straw extract	129-130
4.4.5	Amylase inhibition assay	130-131
4.4.6	Lipase inhibition assay	131
4.5	Determination of cellulose, hemicellulose, and lignin	132
4.5.1	Optimization of parameters	132-136

4.5.2	Purity of cellulose	136
4.5.3	Conversion of cellulose to nanocellulose	137-141
4.5.4	Characterization of cellulose and nanocellulose	141
4.5.4.1	Particle size	141-142
4.5.4.2	Determination of functional group	143-146
4.5.4.3	Crystallinity determination using (XRD)	147-148
4.5.4.4	Thermal stability analysis	148-149
4.5.4.5	Surface morphology	150
4.6	Proximate analysis of *Cucumis callosus* (Seed, peel and pulp)	150-151
4.6.1	**Characterization of *Cucumis callosus* (Seed, peel and pulp)**	151
4.6.1.1	**Determination of functional group**	151-153
4.6.1.2	**X-ray differaction**	153-154
4.6.1.3	**Thermogravimetric analysis**	155-156
4.6.1.4	**Differential Scanning Calorimetry**	156-158
4.6.1.5	**Surface morphology**	158-159
4.6.2	**Extraction of *Cucumis callosus* fruit**	160
4.6.2.1	**Physicochemical analysis**	160-161
4.6.2.2	**Biochemical profiling**	161
4.6.2.3	**Chlorophyll and carotenoid content**	161-162
4.6.2.4	**Quantification of polyphenols through HPLC**	162-164
4.6.2.5	**Antinutritional factors**	164
4.6.3	**Antimicrobial efficiency**	164-166
4.6.4	Binding efficiency	166-167
4.6.5	Techno-functional properties of the nanocellulose-polyphenolic complex	167
4.6.6	Quantification of total phenolic content, total flavonoid content and DPPH radical-scavenging activity	168
4.6.7	Determination of polyphenolic compounds	168-169
4.6.8	Hydrophobic characteristics of the surface	169
4.6.9	Characterization of native nanocellulose and nanocellulose-polyphenolic complex	169
4.6.9.1	Fourier Transform Infrared Spectroscopy (FTIR)	169-171

4.6.9.2	X-diffraction analysis	172-173
4.6.9.3	Thermogravimetric analysis	173-174
4.6.9.4	Differential Scanning Calorimetry	174-176
4.6.9.5	Surface morphology examined by FE-SEM	177
4.7	Physical and chemical stability of nanoemulsion	178
4.7.1	Creaming index of nanocellulose-based nanoemulsion	178-180
4.7.1.1	Droplet size and zeta potential of nanocellulose-based nanoemulsion	180-182
4.7.2	Creaming index of nanoemulsion incorporated with *Cucumis callosus* fruit peel extract	182-185
4.7.3	Creaming index of sodium alginate–based nanoemulsion	185-188
4.7.4	Creaming index of guar gum-based nanoemulsion	188-190
4.7.5	Droplet Size and Zeta potential of optimized nanoemulsions	190-192
4.7.6	Rheology of nanoemulsions	192-194
4.7.7	Field emission scanning electron microscopy (FESEM)	194-196
4.7.8	Functional group determination	196-197
4.7.9	Antimicrobial analysis	198-200
4.8	Mechanical and physicochemical properties of glycerol-based packaging films	200
4.8.1	Evaluation of tensile strength (TS) and elongation at break (EB)	200-202
4.8.2	Water vapor transmission rate (WVTR)	203
4.8.3	Thickness	204
4.8.4	Puncher strength	204-205
4.8.5	Toughness	206-207
4.8.6	Moisture Content and Transparency	207-208
4.9	Comparison of mechanical and physicochemical attributes of functional and control films	209
4.9.1	Tensile strength (TS) and elongation at break (EB)	209-211
4.9.2	Water vapor transmission rate (WVTR)	211-212
4.9.3	Thickness	212-213
4.9.4	Puncher strength	213-214
4.9.5	Moisture Content and Transparency	214-217
4.10	Antimicrobial property of packaging films	217-219

4.11	Characterization of packaging films	219
4.11.1	Fourier transform infrared spectroscopy (FTIR)	219-221
4.11.2	Degree of crystallinity (XRD)	221-223
4.11.3	Field emission scanning electron microscopy (FESEM)	223-224
4.11.4	Thermogravimetric analysis (TGA)	224-225
4.11.5	Differential scanning calorimetry (DSC)	226-227
4.12	Biodegradability of packaging films	227
4.12.1	Soil burial method	227-237
4.12.2	Oven-Assisted Soil Method	237-241
4.12.3	Enzymatic degradation	242-244
4.13	Shelf-life study of Control and fresh-cut apple and pear slices in different packaging (Visual Representation)	245-254
4.14	Shelf-Life Study of Control and Fresh-Cut Apple and Pear Slices in Different Packaging	255
4.14.1	Moisture content	255-258
4.14.2	Ash content	259-262
4.14.3	Fat content	262-265
4.14.4	Protein content	266-269
4.14.5	Fiber	269-273
4.15	Physicochemical evaluation of packaged and unpackaged cut apples and pears	273
4.15.1	Color (L value Lightness)	273-277
4.15.2	Color (a value Redness)	277-281
4.15.3	Color (b value yellowness)	281-285
4.15.4	Browning index (%)	285-289
4.15.5	Weight loss (%)	289-293
4.15.6	pH	293-296
4.15.7	Total soluble solids (%)	296-300
4.15.8	Total phenolic content (mg GAE kg^{-1})	300-304
4.15.9	Ascorbic acid (mg/100 g)	304-307
4.15.10	Respiration rate (mg kg^{-1} h^{-1})	307-310
4.15.11	Antioxidant activity (%)	311-313

4.15.12	Firmness (N)	313-316
4.15.13	Titrable acidity (%)	317-320
5	Chapter-5 Summary and Conclusion	321-323
	References	324-359
	Plagiarism Report	360

List of Tables

SI.no.	Content	Page no.
2.1	Biopolymers extracted from various agricultural residues, along with the processing techniques and extraction efficiencies	11
2.2	Comparative Evaluation of Extraction methods of cellulose	21-23
2.3	Extraction methods and application of *Cyamopsis tetragonoloba*	58-59
2.4	Applications of *Cyamopsis tetragonoloba* in the food industries	66-67
2.5	Applications of *Cyamopsis tetragonoloba* in the packaging industries	69-70
2.6	Applications of *Cyamopsis tetragonoloba* in the pharmaceutical industries	71-73
2.7	Nutritional and bioactive composition of *Cucumis callosus*	77
2.8	Highlights of *Cucumis callosus* biological activity and phytochemical	80-82
3.1	Experimental design for optimization cellulose extraction process	97
3.2	Experimental design for optimization nanocellulose extraction process	98
3.3	Experimental design for the preparation of nanocellulose-based nanoemulsions with varying surfactant and oil concentrations	106
3.4	Optimization of *Cucumis callosus* peel extract concentration for nanoemulsion development	107
3.5	Optimization of sodium alginate concentration in nanocellulose-based nanoemulsions incorporated with peel extract	108
3.6	Optimization of guar gum concentration in sodium alginate–nanocellulose nanoemulsions	109
3.7	Glycerol concentrations optimization for ternary blend films	111
3.8	Composition of control and composite films prepared using optimized glycerol concentration	112
4.1	Proximate analysis of Guar (*Cyamopsis tetragonoloba*) straw	120
4.2	Techno-functional properties of Guar (*Cyamopsis tetragonoloba*) straw	121
4.3	Antimicrobial efficiency *of Cyamopsis tetragonoloba* straw extract	128
4.4	Amylase and lipase inhibition assay of different *Cyamopsis tetragonoloba* straw	131

4.5	Ranges of the factors used in central composite design for alkali hydrolysis of cellulose	134
4.6	Model fitness as evaluated through Analysis of Variance (ANOVA), confirming the statistical reliability of the selected models.	134
4.7	Experimental setup and results for the central design matrix for alkali treatment of Cellulose	134
4.8	Ranges of the factors used in central composite design for acid hydrolysis of nanocellulose	138
4.9	Model fitness as evaluated through Analysis of Variance (ANOVA), confirming the statistical reliability of the selected models.	138
4.10	Experimental setup and results for the central design matrix for acid treatment for nanocellulose extraction	139
4.11	Comparison of Functional groups in cellulose and nanocellulose	143
4.12	Proximate composition of *Cucumis callosus* peel	151
4.13	Physicochemical composition of *Cucumis callosus* peel	161
4.14	Photosynthetic pigment content of *Cucumis callosus* peel	162
4.15	Antinutritional Compounds in *Cucumis callosus* Peel	164
4.16	The nanocellulose-phenol interaction efficiency at different polyphenol concentrations	167
4.17	Techno-functional properties of nanocellulose-polyphenolic complex	167
4.18	Phytochemical properties of nanocellulose-polyphenolic complex	168
4.19	Optimisation and different formulation of nanocellulose-based nanoemulsions with varying surfactant and oil concentrations	179
4.20	Optimization of *Cucumis callosus* peel extract concentration for nanoemulsion development	183
4.21	Optimization of sodium alginate concentration in nanocellulose-based nanoemulsions incorporated with peel extract	186
4.22	Optimization of guar gum concentration in nanoemulsions	189
4.23	Effect of glycerol concentration on tensile strength and elongation at break of the films	202
4.24	Effect of glycerol concentration on the mechanical properties of emulsion-templated nanocellulose–sodium alginate–guar gum packaging films	208

4.25	Effect of glycerol concentration on the physicochemical and barrier properties of emulsion-templated nanocellulose–sodium alginate–guar gum packaging films	208
4.26	Mechanical properties of control, composite, and functional emulsion-templated films	215
4.27	Physicochemical and barrier properties of control, composite, and functional emulsion-templated films	216
4.28	Actual Weight of Packaging Films	237
4.29	Weight loss (%) of samples stored under different packaging films in soil degradation process	237
4.30	Changes in moisture content of fresh-cut apple slices as influenced by biodegradable packaging systems during refrigerated storage (0–12 days)	256
4.31	Changes in moisture content of fresh-cut pear slices as influenced by biodegradable packaging systems during refrigerated storage (0–12 days)	257
4.32	Effect of biodegradable packaging films on ash content of fresh-cut apple slices during storage (0–12 days)	260
4.33	Effect of biodegradable packaging films on ash content of fresh-cut pear slices during storage (0–12 days)	261
4.34	Effect of biodegradable packaging films on fat content of fresh-cut apple slices during storage (0–12 days)	263
4.35	Effect of biodegradable packaging films on fat content of fresh-cut pear slices during storage (0–12 days)	264
4.36	Changes in protein content of fresh-cut apple slices as affected by biodegradable packaging and storage duration (0–12 days)	267
4.37	Changes in protein content of fresh-cut pear slices as affected by biodegradable packaging and storage duration (0–12 days)	268
4.38	Evolution of crude fiber content in fresh-cut apple slices packaged using biodegradable films during storage (0–12 days)	270
4.39	Evolution of crude fiber content in fresh-cut pear slices packaged using biodegradable films during storage (0–12 days)	272
4.40	Effect of packaging treatments on L* value (lightness) of fresh-cut	275

	apples during storage (0–12 days)	
4.41	Effect of packaging treatments on L* value (lightness) of fresh-cut pears during storage (0–12 days)	276
4.42	Effect of packaging treatments on a* value (redness) of fresh-cut apples during storage (0–12 days)	279
4.43	Effect of packaging treatments on a* value (redness) of fresh-cut pears during storage (0–12 days)	280
4.44	Color attribute (b* value – yellowness) of packaged and unpackaged fresh-cut apples during storage	283
4.45	Color attribute (b* value – yellowness) of packaged and unpackaged fresh-cut pears during storage	284
4.46	Changes in Browning Index (%) of Packaged and Unpackaged Fresh-Cut Apples	286
4.47	Changes in Browning Index (%) of Packaged and Unpackaged Fresh-Cut Pears	287
4.48	Changes in weight loss (%) of Fresh-Cut Apples Stored under Different Packaging Conditions	290
4.49	Changes in weight loss (%) of Fresh-Cut pears Stored under Different Packaging Conditions	292
4.50	Changes in pH of Fresh-Cut Apples under Different Biodegradable Packaging Films	294
4.51	Changes in pH of Fresh-Cut Pears under Different Biodegradable Packaging Films	295
4.52	Changes in Total Soluble Solids (%) of Fresh-Cut Apples under Different Biodegradable Packaging Films	298
4.53	Changes in Total Soluble Solids (%) of Fresh-Cut pears under Different Biodegradable Packaging Films	299
4.54	Total Phenolic Content (mg GAE/100 g) of Packaged and Unpackaged Fresh-Cut Apples	301
4.55	Total Phenolic Content (mg GAE/100 g) of Packaged and Unpackaged Fresh-Cut pears	303
4.56	Variation in Ascorbic Acid Content (mg/100 g) of Fresh-Cut Apples during Storage	304

4.57	Variation in Ascorbic Acid Content (mg/100 g) of Fresh-Cut pears during Storage	306
4.58	Respiration rate (mg kg^{-1} h^{-1}) of packaged and unpackaged fresh-cut apple slices	308
4.59	Respiration rate (mg kg^{-1} h^{-1}) of packaged and unpackaged fresh-cut pear slices	309
4.60	Antioxidant activity (%) of Fresh-Cut Apples during Storage	311
4.61	Antioxidant activity (%) of Fresh-Cut pears during Storage	312
4.62	Changes in Firmness (N) of Fresh-Cut Apples under Different Biodegradable Packaging Films	314
4.63	Changes in Firmness (N) of Fresh-Cut pears under Different Biodegradable Packaging Films	315
4.64	Changes in Titratable Acidity (%) of Fresh-Cut Apples Stored under Different Packaging Conditions	318
4.65	Changes in Titratable Acidity (%) of Fresh-Cut pears Stored under Different Packaging Conditions	319

List of Figures

Sr. No.	Content	Page No.
2.1	Structure of Cellulose	13
2.2	Production process of *Cyamopsis tetragonoloba* Straw	53
2.3	The chemical structure of Bioactive compounds presents in *Cyamopsis tetragonoloba*	56
2.4	Anticancer mechanism of *Cyamopsis tetragonoloba* seed	59
2.5	Mechanism action of *Cyamopsis tetragonoloba* due to the existence of Epigallocatechin gallate	60
2.6	Mechanism of action of galactomannan shows anti-inflammatory effects of *Cyamopsis tetragonoloba* gum on intestinal epithelial cells	61
2.7	Antidiabetic mechanism of galactomannan *Cyamopsis tetragonoloba*	62
2.8	Alkaloids and other bioactive compounds identified in *Cucumis callosus*	79
2.9	Mechanism of antiulcer with COX-1, COX-2, and prostaglandins	82
2.10	Mechanism of action of *Cucumis callosus* due to the existence of Quercetin-3-rutinoside and Taraxerol	84
2.11	Antidiabetic mechanism of quercetin-3-rutinoside *Cucumis callosus*	87
2.12	Cardiotoxicity mechanism of roemerine of *Cucumis callosus*	88
4.1	Raw biomass materials used in the study: (A) *Cyamopsis tetragonoloba* (guar) straw and (B) *Cucumis callosus* peel	120
4.2	FTIR Spectroscopy spectrum of *Cyamopsis tetragonoloba* straw	123
4.3	Microstructure of Guar straw using Scanning Electron Microscopy (SEM)	124
4.4	X-ray diffraction pattern of *Cyamopsis tetragonoloba* straw	125
4.5	Thermogravimetric analysis of *Cyamopsis tetragonoloba* straw	126
4.6	HPLC Chromatograph of Ethanolic *Cyamopsis tetragonoloba* straw	127
4.7	Cytotoxicity of *Cyamopsis tetragonoloba* straw extract	132
4.8	Yield of lignocellulosic components of *Cyamopsis tetragonoloba* straw	136
4.9	(A) Graphical representation between conc. Of NaOH (%) and Time (h); (B) Contour plot between conc. of NaOH (%) and Temperature (°C); (C)	136

	Contour plot between Temperature (℃) and Time (h).	
4.10	Predicted vs. Actual graph	141
4.11	(A) Graphical representation between conc. of H_2SO_4 (%) and Time (h); (B) Contour plot between conc. of H_2SO_4 (%) and Temperature (℃); (C) Contour plot between Temperature (℃) and Time (h).	140
4.12	Predicted vs. Actual graph	141
4.13	Characterization of guar straw cellulose (A zeta potential and B particle size) and nanocellulose (C zeta potential and D particle size)	142
4.14	FTIR Spectroscopy spectrum of guar straw cellulose (A) and nanocellulose (B)	146
4.15	X-ray diffraction pattern of guar straw cellulose (A) and nanocellulose (B)	148
4.16	Thermogravimetric analysis of guar straw cellulose (A) and nanocellulose (B)	149
4.17	Morphological analysis of guar straw cellulose (A) and nanocellulose (B)	150
4.18	Fourier Transform Infrared Spectroscopy analysis of *Ccucmis callosus* different parts	153
4.19	X-diffraction analysis of *Cucumis callosus* different parts	155
4.20	Thermogravimetric analysis (TGA) of *Cucumis callosus* different parts	156
4.21	Differential Scanning calorimetry (DSC) of *Cucumis callosus* different parts	157-158
4.22	SEM micrograph of *Cucumis callosus* different parts	160
4.23	HPLC Chromatograph of *Cucumis callosus* different parts	163
4.24	Zone of inhibition in *Cucumis callosus* different parts, against *Escherichia coli* and *Staphylococcus aureus*	165
4.25	HPLC Chromatograph of nanocellulose- polyphenolic complex	168
4.26	Fourier Transform Infrared Spectroscopy analysis of guar straw nanocellulose and nanocellulose–polyphenolic complex	170
4.27	X-diffraction analysis guar straw nanocellulose and nanocellulose–polyphenolic complex	172
4.28	Thermogravimetric analysis of guar straw nanocellulose and nanocellulose–polyphenolic complex	173

4.29	Differential Scanning Calorimetry of guar straw nanocellulose and nanocellulose–polyphenolic complex	175
4.30	Surface morphology of guar straw nanocellulose (A,B) and nanocellulose–polyphenolic complex (C,D)	176
4.31	Representative vial image of the nanoemulsion showing a small cream layer formed at the top during storage, indicating minimal creaming behaviour and good physical stability of the formulation	177
4.32	Nanocellulose (NC), Tween 80 (T), Ginger Oil (G), Lecithin (L); NC1 (NC-1, T-0.5, G-1, L-0), NC2 (NC-1, T-0.5, G-2, L-0), NC3 (NC-1, T-0.5, G-3, L-0), NC4 (NC-1, T-0.5, G-4, L-0), NC5 (NC-1, T-1, G-1, L-0), NC6 (NC-1, T-2, G-1, L-0), NC7 (NC-1, T-3, G-1, L-0), NC8 (NC-1, T-4, G-1, L-0), NC9 (NC-1, T-0.5, G-1, L-0.5), NC10 (NC-1, T-0.5, G-1, L-1), NC11 (NC-1, T-0.5, G-1, L-1.5), NC12 (NC-1, T-0.5, G-1, L-2), NC13 (NC-1, T-0.5, G-1, L-0.5), NC14 (NC-1, T-0.5, G-2, L-1), NC15 (NC-1, T-0.5, G-3, L-1.5), NC16 (NC-1, T-0.5, G-4, L-2)	179
4.33	Droplet size of Nanocellulose Nanoemulsion (NC13, NC14, NC15 and NC16)	180
4.34	Zeta potential of Nanocellulose Nanoemulsion (NC13, NC14, NC15 and NC16)	181
4.35	Visual stability assessment of nanoemulsions (NE1–NE10) during storage at 0, 5, 10, 15, 20, 25, and 30 days	184
4.36	Visual stability assessment of nanoemulsions (NSE1–NSE8) during storage at 0, 5, 10, 15, 20, 25, and 30 days	186-187
4.37	Visual stability assessment of nanoemulsions (NG1–NG5) during storage at 0, 5, 10, 15, 20, 25, and 30 days	189
4.38	(a) Droplet size distribution and (b) zeta potential distribution of nanoemulsion formulations NE4, NSE3, and NG3	191
4.39	Rheological behavior of nanoemulsion formulations NG3, NSE3, NE4, and NC14: (a) apparent viscosity as a function of shear rate, (b) shear stress versus shear rate, (c) storage modulus (G′), and (d) loss modulus (G″) as a function of angular frequency	193
4.40	Scanning electron microscopy (SEM) micrographs of nanoemulsion formulations NC14, NE4, NSE3, and NG3	195

4.41	Functional group determination presents in NC14, NE4, NSE3, and NG3 nanoemulsion	196
4.42	Zone of inhibition against *S. aureus* of formulated nanoemulsions	198
4.43	Zone of inhibition against *E. coli* of formulated nanoemulsions	199
4.44	Visual appearance of emulsion-templated nanocellulose–sodium alginate–guar gum packaging films prepared with different glycerol concentrations: G0.1 (0.1 mL/100 mL), G0.2 (0.2 mL/100 mL), G0.3 (0.3 mL/100 mL), G0.4 (0.4 mL/100 mL), G0.5 (0.5 mL/100 mL), and G0.6 (0.6 mL/100 mL)	205
4.45	Visual representation of nanocellulose-based control and emulsion-templated packaging films. (NC) nanocellulose control film, (SA) sodium alginate control film, and (GG) guar gum control film, all plasticized with glycerol	211-212
4.46	Antimicrobial activity of formulated packaging film against *Escherichia coli*	213
4.47	Antimicrobial activity of formulated packaging film against *Staphylococcus aureus*	214
4.48	FTIR spectra of emulsion-based packaging films: (a) nanocellulose emulsion film (NC), (b) sodium alginate emulsion film (SA), (c) guar gum emulsion film (GG), (d) composite emulsion film (NEW), and (e) functional emulsion-templated film (NE)	216
4.49	X-ray diffraction (XRD) patterns of emulsion-based packaging films: (a) nanocellulose emulsion film, (b) sodium alginate emulsion film, (c) guar gum emulsion film, (d) composite emulsion film, and (e) functional emulsion-templated film	218
4.50	FESEM micrographs of emulsion-based packaging films: (NC) nanocellulose emulsion film, (SA) sodium alginate emulsion film, (GG) guar gum emulsion film, (NEW) composite emulsion film, and (NE) functional emulsion-templated film	220
4.51	Thermogravimetric analysis (TGA) curves of emulsion-based packaging films: (NC) nanocellulose emulsion film, (SA) sodium alginate emulsion film, (GG) guar gum emulsion film, (NEW) composite emulsion film, and (NE) functional emulsion-templated film	221

4.52	Differential scanning calorimetry (DSC) thermograms of emulsion-based packaging films: (NC) nanocellulose emulsion film, (SA) sodium alginate emulsion film, (GG) guar gum emulsion film, (NEW) composite emulsion film, and (NE) functional emulsion-templated film	223
4.53	Degradation study of biodegradable film samples during soil burial method on 0 day	225
4.54	Degradation study of biodegradable film samples during soil burial method on the 3rd day	226
4.55	Degradation study of biodegradable film samples during soil burial method on the 6th day	227
4.56	Degradation study of biodegradable film samples during soil burial method on the 9th day	228
4.57	Degradation study of biodegradable film samples during soil burial method on the 12th day	229
4.58	Degradation study of biodegradable film samples during soil burial method on the 15th day	230
4.59	Degradation study of biodegradable film samples during soil burial method on the 18th day	231
4.60	Degradation study of biodegradable film samples during soil burial method on the 21st day	232
4.61	Degradation study of biodegradable film samples during oven-assisted soil burial method on the 0 day	235
4.62	Degradation study of biodegradable film samples during oven-assisted soil burial method on the 2nd day	236
4.63	Degradation study of biodegradable film samples during oven-assisted soil burial method on the 3rd day	237
4.64	Degradation study of biodegradable film samples during enzymatic degradation method on the 0 day	239
4.65	Degradation study of biodegradable film samples during enzymatic degradation method on the 2nd day	240
4.66	Shelf-life study of fresh-cut apple slices in different packaging films at refrigerated temperature (4-7 ℃) at 0 day	241
4.67	Shelf-life study of fresh-cut apple slices in different packaging films at	242

	refrigerated temperature (4-7 ℃) on the 3rd day	
4.68	Shelf-life study of fresh-cut apple slices in different packaging films at refrigerated temperature (4-7 ℃) on the 6th day	243
4.69	Shelf-life study of fresh-cut apple slices in different packaging films at refrigerated temperature (4-7 ℃) on the 9th day	244
4.70	Shelf-life study of fresh-cut apple slices in different packaging films at refrigerated temperature (4-7℃) on the 12th day	245
4.71	Shelf-life study of fresh-cut pear slices in different packaging films at refrigerated temperature (4-7 ℃) on day 0	246
4.72	Shelf-life study of fresh-cut pear slices in different packaging films at refrigerated temperature (4-7 ℃) on the 3rd day	247
4.73	Shelf-life study of fresh-cut pear slices in different packaging films at refrigerated temperature (4-7 ℃) on the 6th day	248
4.74	Shelf-life study of fresh-cut pear slices in different packaging films at refrigerated temperature (4-7 ℃) on the 9th day.	249
4.75	Shelf-life study of fresh-cut pear slices in different packaging films at refrigerated temperature (4-7 ℃) on the 12th day.	250
4.76	Changes in moisture content (%) of fresh-cut apple slices during storage under different packaging materials.	257
4.77	Changes in moisture content (%) of fresh-cut pear slices during storage under different packaging materials.	258
4.78	Changes in ash content (%) of fresh-cut apple slices during storage under different packaging materials.	260
4.79	Changes in ash content (%) of fresh-cut pear slices during storage under different packaging materials.	262
4.80	Changes in fat content (%) of fresh-cut apple slices during storage under different packaging materials.	264
4.81	Changes in fat content (%) of fresh-cut pear slices during storage under different packaging materials.	265
4.82	Changes in protein content (%) of fresh-cut apple slices during storage under different packaging materials.	267
4.83	Changes in protein content (%) of fresh-cut pear slices during storage under different packaging materials	269

4.84	Changes in fiber content (%) of fresh-cut apple slices during storage under different packaging materials	271
4.85	Changes in fiber content (%) of fresh-cut pear slices during storage under different packaging materials	273
4.86	Changes in L value (%) of fresh-cut apple slices during storage under different packaging materials	275
4.87	Changes in L value (%) of fresh-cut pear slices during storage under different packaging materials	277
4.88	Changes in a* value (%) of fresh-cut apple slices during storage under different packaging materials	280
4.89	Changes in a* value (%) of fresh-cut pear slices during storage under different packaging materials	281
4.90	Changes in b value (%) of fresh-cut apple slices during storage under different packaging materials	284
4.91	Changes in b value (%) of fresh-cut pear slices during storage under different packaging materials	285
4.92	Changes in Browning Index (%) of fresh-cut apple slices during storage under different packaging materials	287
4.93	Changes in Browning Index (%) of fresh-cut pear slices during storage under different packaging materials	288
4.94	Changes in Weight loss (%) of fresh-cut apple slices during storage under different packaging materials.	291
4.95	Changes in Weight loss (%) of fresh-cut pear slices during storage under different packaging materials	293
4.96	Changes in pH of fresh-cut apple slices during storage under different packaging materials	295
4.97	Changes in pH of fresh-cut pear slices during storage under different packaging materials	296
4.98	Changes in Total Soluble Solids (%) of fresh-cut apple slices during storage under different packaging materials	298
4.99	Changes in Total Soluble Solids (%) of fresh-cut pear slices during storage under different packaging materials	300
4.100	Changes in Total Phenolic Content (mg GAE/100 g) of fresh-cut apple	302

	slices during storage under different packaging materials	
4.101	Changes in Total Phenolic Content (mg GAE/100 g) of fresh-cut pear slices during storage under different packaging materials	303
4.102	Changes in Ascorbic Acid Content (mg/100 g) of fresh-cut apple slices during storage under different packaging materials	305
4.103	Changes in Ascorbic Acid Content (mg/100 g) of fresh-cut pear slices during storage under different packaging materials	306
4.104	Changes in Respiration rate (mg kg^{-1} h^{-1}) of fresh-cut apple slices during storage under different packaging materials	308
4.105	Changes in Respiration rate (mg kg^{-1} h^{-1}) of fresh-cut pear slices during storage under different packaging materials	309
4.106	Changes in Antioxidant activity (%) of fresh-cut apple slices during storage under different packaging materials.	311
4.107	Changes in Antioxidant activity (%) of fresh-cut pear slices during storage under different packaging materials	313
4.108	Changes in Firmness (N) of fresh-cut apple slices during storage under different packaging materials	315
4.109	Changes in Firmness (N) of fresh-cut pear slices during storage under different packaging materials	316
4.110	Changes in Titratable Acidity (%) of fresh-cut apple slices during storage under different packaging materials	318
4.111	Changes in Titratable Acidity (%) of fresh-cut pear slices during storage under different packaging materials	320

List of Abbreviations

Abbreviation	Full Form
ADF	Acid Detergent Fiber
ADL	Acid Detergent Lignin
ANS	1-Anilino-8-naphthalenesulfonate
AOAC	Association of Official Analytical Chemists
ATR	Attenuated Total Reflectance
BD	Bulk Density
BI	Browning Index
CI	Creaming Index
CTAB	Cetyltrimethylammonium Bromide
DAD	Diode Array Detector
DMEM	Dulbecco's Modified Eagle Medium
DMSO	Dimethyl Sulfoxide
DPPH	2,2-Diphenyl-1-picrylhydrazyl
DSC	Differential Scanning Calorimetry
EAB	Elongation at Break
EAI	Emulsifying Activity Index
EDS	Energy Dispersive Spectroscopy
EDTA	Ethylenediaminetetraacetic Acid
ESI	Emulsifying Stability Index
FC	Folin–Ciocalteu
FESEM	Field Emission Scanning Electron Microscopy
FBS	Fetal Bovine Serum
FTIR	Fourier Transform Infrared Spectroscopy
GG	Guar Gum
HPLC	High-Performance Liquid Chromatography

H_2SO_4	Sulfuric Acid
IC_{50}	Half Maximal Inhibitory Concentration
MHA	Mueller–Hinton Agar
MTT	3-(4,5-Dimethylthiazol-2-yl)-2,5-diphenyltetrazolium Bromide
NaOH	Sodium Hydroxide
NC	Nanocellulose
NDF	Neutral Detergent Fiber
NE	Nanoemulsion / Functional Emulsion Film
NEW	Nanocellulose–Emulsion–Hydrocolloid Composite Film
NPC	Nanocellulose–Polyphenolic Complex
NSE	Sodium Alginate–Based Nanoemulsion
NG	Guar Gum–Fortified Nanoemulsion
OAC	Oil Absorption Capacity
PPO	Polyphenol Oxidase
PS	Puncture Strength
RH	Relative Humidity
RSM	Response Surface Methodology
SA	Sodium Alginate
SDS	Sodium Dodecyl Sulfate
SEM	Scanning Electron Microscopy
SH	Surface Hydrophobicity
TES	N-Tris(hydroxymethyl)methyl-2-aminoethanesulfonic Acid
TFC	Total Flavonoid Content
TGA	Thermogravimetric Analysis
TPC	Total Phenolic Content
TS	Tensile Strength
TSS	Total Soluble Solids
UPLC	Ultra-Performance Liquid Chromatography
UV	Ultraviolet

WAC	Water Absorption Capacity
WHC	Water Holding Capacity
WVTR	Water Vapor Transmission Rate
XRD	X-ray Diffraction
ZP	Zeta Potential
L*, a*, b*	CIELAB Color Parameters

Abstract

Agricultural residues represent an abundant and underutilized biomass resource that can be converted into value-added materials for sustainable food packaging applications. Lignocellulosic wastes such as *Cyamopsis tetragonoloba* (guar) straw and fruit processing by-products such as *Cucumis callosus* peel contain high levels of cellulose, hemicellulose, lignin, and bioactive phytochemicals that can be harnessed for the development of functional biodegradable materials, which are unexplored. Nanocellulose derived from plant biomass has attracted considerable attention due to its high surface area, mechanical reinforcement ability, crystallinity, and excellent barrier properties, making it a promising candidate for advanced bio-based packaging systems. In parallel, plant-derived phenolic compounds exhibit antioxidant and antimicrobial activities, enabling the development of active packaging systems capable of improving food quality and extending shelf life. Recent advances in emulsion-templated film fabrication provide an effective strategy to integrate nanostructured reinforcement with bioactive compounds, generating films with improved mechanical strength, moisture barrier capacity, and functional bioactivity. However, limited studies have explored the simultaneous valorisation of agricultural residues for both nanocellulose extraction and bioactive compound recovery, followed by their integration into functional packaging systems for fresh-cut fruit preservation. Therefore, the present study investigates the valorisation of guar straw and *Cucumis callosus* peel for the production of nanocellulose-reinforced bioactive emulsion-templated biodegradable films and evaluates their effectiveness in enhancing the shelf life and quality retention of fresh-cut apples and pears. The present research focuses on the Valorisation of *Cyamopsis tetragonoloba* (guar) straw and C*ucumis callosus* peel for the development of nanocellulose-reinforced, bioactive, emulsion-templated biodegradable packaging films and their application in extending the shelf life of fresh-cut apples and pears. Guar straw exhibited moisture content of 4.43%, fat 0.30%, protein 4.89%, ash 2.16%, and high total fiber (39.65%). Compositional analysis confirmed cellulose (49.61 ± 0.58%), hemicellulose (20.15 ± 0.74%), and lignin (18.45 ± 0.62%). The material demonstrated strong techno-functional properties, including water-holding capacity (5.08 ± 0.38 g/g), oil absorption capacity (4.85 ± 0.60 g/g), emulsifying activity (41.92 ± 0.56%), and stability (49.99 ± 0.21%). Structural characterization revealed semi-crystalline architecture (73% crystallinity) with thermal stability up to 453.40°C. Optimization using Response Surface Methodology yielded 48.82 ± 0.46% cellulose at 5%

NaOH, 27°C, and 180 min (R^2 = 0.9939), while sulfuric acid hydrolysis (30% H_2SO_4, 27°C, 2 h) produced 70.21 ± 0.89% nanocellulose (R^2 = 0.9976). Particle size reduced from 520.9 nm (cellulose) to 296.0 nm (nanocellulose), with enhanced thermal resistance (onset degradation 311.42°C). Ethanolic extracts (4.50% yield from straw, 7.7% from peel) contained total phenolics (4.15 mg GAE/g) and flavonoids (3.83 mg QE/g), showing 42.06% DPPH scavenging activity. The extract exhibited antimicrobial activity (maximum inhibition zone 10.83 ± 0.31 mm against *Bacillus subtilis*), cytotoxicity against A549 cells (IC_{50} = 43.23%), and enzyme inhibition reaching 90.99% (α-amylase) and 71.86% (lipase). Nanocellulose was further utilized to fabricate control, composite (NEW), and functional emulsion-templated (NE) films. The NE film demonstrated superior mechanical and barrier properties, including tensile strength of 38.71 ± 0.90 MPa, elongation at break 71.3 ± 0.29%, puncture strength 22.1 ± 0.39 N, moisture content 4.91 ± 0.24%, and WVTR 3.18 ± 0.47 g/m²·day, significantly lower than control films (up to 6.35 g/m²·day). Shelf-life evaluation of fresh-cut apples and pears over 12 days demonstrated marked quantitative improvements under NE functional packaging. In apples, weight loss increased to 15.32% in unpackaged samples by day 12, whereas NE-coated samples showed significantly lower weight loss of 8.70%, compared to 9.10% (NEW), 9.50% (GG), 9.90% (SA), and 10.26% (NC). In pears, unpackaged samples exhibited severe dehydration, reaching 29.92% weight loss by day 12, while NE-coated pears showed only 12.55%, compared to 17.45% (NEW), 22.21% (GG), 23.74% (SA), and 27.15% (NC). Browning index values further confirmed the protective effect. By day 12, unpackaged apples reached 81.45 ± 0.33%, whereas NE-coated apples showed only 11.84 ± 0.28%, representing substantial suppression of enzymatic browning. Similarly, pears exhibited browning index of 58.32 ± 0.36% in unpackaged samples, while NE packaging reduced it to 17.60 ± 0.20%. Firmness retention was significantly enhanced under NE treatment. Unpackaged apples declined from 62.39 N (day 0) to 51.08 N (day 12), whereas NE-coated apples retained 59.80 N. Pear firmness decreased from 48.72 N to 42.10 N in unpackaged samples, while NE-coated pears maintained 50.20 N by day 12. Ascorbic acid degradation was also delayed, unpackaged apples declined to 5.30 mg/100 g and pears to 4.65 mg/100 g by day 12, while NE-coated samples consistently retained significantly higher levels throughout storage. Overall, the functional NE film reduced moisture loss by approximately 43% in apples and 58% in pears relative to unpackaged samples, drastically suppressed browning progression, maintained structural firmness, and preserved nutritional antioxidants. The synergistic action of nanocellulose reinforcement, emulsion-templated barrier architecture, and bioactive peel extract contributed to controlled oxygen diffusion, reduced enzymatic oxidation, moderated

moisture transfer, and delayed tissue softening. This research demonstrates a comprehensive circular Valorisation strategy transforming agricultural residues into nanocellulose-reinforced, bioactive, emulsion-templated active packaging systems with quantified improvements in mechanical strength, barrier performance, antioxidant activity, and measurable shelf-life extension of fresh-cut apples and pears, highlighting their strong potential for sustainable and functional biodegradable food packaging applications. The present study demonstrates a comprehensive biomass valorisation strategy for converting guar straw and *Cucumis callosus* peel into functional components for advanced biodegradable food packaging applications. The extracted nanocellulose exhibited desirable structural and thermal characteristics suitable for reinforcement of biodegradable films, while the bioactive peel extracts provided significant antioxidant and antimicrobial functionality. Integration of these components into emulsion-templated films resulted in significant improvements in mechanical strength, moisture barrier properties, and bioactivity. Application of the developed films in fresh-cut fruit packaging effectively reduced moisture loss, suppressed enzymatic browning, preserved firmness, and maintained nutritional quality during storage. These findings highlight the potential of lignocellulosic agricultural residues as sustainable raw materials for the development of nanocellulose-reinforced active packaging systems. The proposed approach contributes to the circular bioeconomy by transforming agricultural waste into high-value biodegradable materials capable of enhancing food preservation while reducing reliance on conventional plastic packaging.

Keywords: *Cyamopsis tetragonoloba* straw, *Cucumis callosus* peel, Nanocellulose, Biodegradable packaging, Agricultural waste, Nanoemulsion, Bioactive extracts, food packaging, Shelf-life extension, Fresh-cut fruits, Valorisation

Chapter 1 Introduction

Packaging for foods is an important part of the food supply chain nowadays because it protects food items from external contamination, extends shelf life, provides information about the products, and allows for safe storage and delivery (Han et al., 2018). Historically, synthetic polymers, glass, metals, and paper-based substrates have been widely used to protect food quality, maintain sanitation, and assure product stability throughout transit and storage. (Shlush and Davidovich-Pinhas, 2022). However, with the rapid growth of population, environmental pollution, and the non-biodegradable nature of synthetic plastics have become a major ecological concern (Etxabide et al., 2022). The persistence of plastic wastes, depletion of non-renewable petroleum resources, and potential migration of toxic additives into food matrices highlight the urgent need for sustainable packaging materials (Eze et al., 2024). Due to these limitations, research worldwide is now focused on creating bio-based packaging solutions that are made from renewable and biodegradable materials and adhere to the concepts of sustainable development and the circular economy. Produced from biological feedstocks, bio-based packaging materials are ecologically friendly substitutes for conventional synthetic polymers due to their degradable nature, lower carbon emissions, and resource recyclability (Huang and Wang, 2025 and Zhao et al., 2023). Biodegradable polymers are generally categorized into two main classes: natural polymeric materials, such as polysaccharides and proteins obtained from plants, animals, and microorganisms and their chemically modified derivatives, and synthetic biodegradable polymers (Mahajan et al., 2023). For a material to function effectively as a food-packaging film, it must possess specific physical attributes like mechanical strength and barrier efficiency to protect food products from external environmental influences. The mechanical characteristics of a film determine its load-bearing capacity, resistance to rupture, and overall durability, while its barrier properties regulate the transfer of gases and water vapour, thereby controlling spoilage and moisture-related deterioration. These performance indicators depend largely on the molecular architecture of the polymer, the cohesive assembly of its matrix, and the processing conditions employed during fabrication. Polysaccharide-based films typically exhibit high tensile strength but limited flexibility, as their extensive network of hydroxyl and carboxyl groups promotes strong intermolecular hydrogen bonding that restricts chain mobility (Liu et al., 2024). Protein-based films, often demonstrate weaker mechanical stability and inferior water-vapour resistance owing to the fragile non-covalent interactions among protein molecules (Mahmood et al., 2023, Spasojević et al., 2019 and Yashwant et al., 2023). Films fabricated from synthetic biodegradable polymers can achieve superior mechanical and barrier

properties (Huang et al., 2023 and Yang et al., 2023), however, even these materials seldom match the performance standards of conventional plastics, necessitating continuous exploration of reinforcement and modification strategies aimed at enhancing strength, flexibility, and permeability resistance (Chang et al., 2023, Méndez et al., 2023 and Xu et al., 2023). Within this framework, the valorisation of agricultural residues into functional biopolymers has emerged as a particularly promising pathway to reconcile performance requirements with environmental sustainability. Valorisation transforms low-value agro-industrial by-products into high-performance biomaterials, thereby supporting waste minimization, resource efficiency, and the circular bio-economy. This approach directly contributes to the reduction of agricultural waste, lowering the carbon footprint of the packaging sector and promoting economic viability and food security consistent with global sustainable-development objectives. *Cyamopsis tetragonoloba* (Guar) (L.) Taub serves as a valuable agricultural crop and a prominent source of lignocellulosic biomass. This annual leguminous species is native to the arid agro-climatic zones of northwestern India and has been traditionally cultivated for its edible pods as well as for industrial gum extraction (Zhang and Li, 2025 and Gautam et al., 2024). Despite its agricultural importance, large volumes of *C. tetragonoloba* residue remain underutilized and are frequently burnt or discarded, contributing to air pollution and the loss of a valuable bioresource. Converting this residue into functional materials such as nanocellulose represents a sustainable route for high-value utilization, simultaneously addressing waste management and material-innovation challenges.

Nanocellulose, a high-value biopolymer derived from cellulose, exhibits exceptional biodegradability, renewability, and mechanical robustness (Thomas et al., 2020). The cellulose molecule, composed of β-(1→4)-linked D-glucopyranose units, forms a crystalline structure stabilized by extensive intra- and intermolecular hydrogen bonding. Conversion of cellulose to nanoscale dimensions produces cellulose nanofibers (CNF) or nanocrystals (CNC) that possess high aspect ratios, outstanding surface area, optical transparency, and excellent reinforcing ability. Extraction of nanocellulose involves an alkaline pretreatment to remove hemicellulose, a bleaching step to eliminate lignin, and subsequent acid hydrolysis or mechanical fibrillation to obtain nanoscale fibrils (Yang et al., 2025). The resulting nanocellulose suspension forms a stable colloidal system capable of self-assembling into thin films during drying, resulting in transparent and mechanically strong materials suitable for use as reinforcement in composites or as stand-alone biodegradable films.

However, the inherent hydrophilicity of cellulose limits its compatibility with hydrophobic polymer systems, necessitating surface modifications or suitable dispersion strategies to

improve interfacial adhesion (Wang et al., 2024 and Kargupta et al., 2023). Nanocellulose aggregation during film formation may create structural discontinuities, reduce transparency, weaken the reinforcing effect, and affect barrier performance. In active food-packaging systems, poor dispersion of nanocellulose may also influence the distribution and controlled release of incorporated bioactive compounds. Therefore, it is necessary to understand not only the extraction of nanocellulose but also its dispersion behaviour, interaction with the film matrix, and influence on functional properties. The use of *C. tetragonoloba* straw as a cellulose source provides an inexpensive, renewable, and regionally abundant alternative to traditional lignocellulosic sources such as wood pulp, cotton linters, or sugarcane bagasse, while also addressing environmental sustainability goals through agro-residue valorisation.

Cucumis callosus (Rottler) Cogn., commonly known as Kachri, represents another promising underutilized bioresource with substantial phytochemical potential. Belonging to the family *Cucurbitaceae*, it is extensively cultivated in semi-arid regions and thrives under drought and low-input conditions (Patel and Panwar, 2022; Deepika et al., 2023). The fruits, roots, leaves, and seeds of C. callosus contain abundant phenolic compounds, flavonoids, and terpenoids (Jailobaeva et al., 2021 and Deepika et al., 2024) responsible for antioxidant, antidiabetic, antihyperlipidemic, and anticancer activities. *C. callosus* offers a low-cost and sustainable source of bioactives that can be harnessed for the formulation of functional foods, nutraceuticals, and biodegradable materials (Swamy et al., 2017). Integrating these natural bioactives into polymeric matrices requires efficient encapsulation and stabilization techniques, among which nanoemulsion technology has recently gained significant attention.

Nanoemulsions are kinetically stable dispersions of immiscible liquids, typically oil and water, containing droplets smaller than 200 nm stabilized by surfactants or solid particles such as nanocellulose (Kanawade et al., 2024). They possess large interfacial areas, transparency, and superior encapsulation efficiency for hydrophobic compounds (Kong et al., 2022). In the present formulation, nanocellulose derived from *C. tetragonoloba straw* acts both as a Pickering stabilizer at the oil–water interface and as a structural reinforcement in the final film, while the *C. callosus* extract contributes phenolic compounds uniformly distributed within the emulsion phase. During drying, the nanoemulsion converts into a cohesive film in which nanocellulose fibrils create a continuous hydrogen-bonded network embedding phenolic molecules. This structure enhances tensile strength, water- and oxygen-barrier efficiency, and allows controlled release of the encapsulated bioactives, converting a passive film into an active food-packaging system (Muhammad et al., 2024). The hydrogen bonding between the phenolic hydroxyls and cellulose surface improves interfacial adhesion and film stability, while

nanoscale droplet entrapment ensures sustained diffusion of antioxidants, delivering prolonged protective effects. Such films provide physical protection along with biochemical defense by combining polysaccharide mechanical strength with the antioxidative and antimicrobial potency of plant-derived bioactives, thereby enhancing food preservation and safety. The synergistic effectiveness of this formulation arises from the complementary functions of both raw materials. *Cyamopsis tetragonoloba*-derived nanocellulose contributes a rigid nanoscale fibrillar framework that strengthens the film matrix and improves structural compactness, whereas *Cucumis callosus* extract enriches the system with phenolic bioactives responsible for antioxidant and antimicrobial activity. Nanoemulsion-assisted incorporation promotes uniform dispersion of these bioactives within the nanocellulose network, improving interfacial compatibility and reducing the limitations commonly observed in single starch- or cellulose-based films, particularly poor active functionality, brittleness, and moisture sensitivity. Therefore, the developed film functions not only as a biodegradable physical barrier but also as an active protective system for fresh-cut fruit preservation.

The developed films are particularly suitable for application in preserving fresh-cut fruits such as pears (*Pyrus communis*) and apples (*Malus domestica Borkh*.), which are highly susceptible to enzymatic browning, dehydration, and microbial spoilage. Upon cutting, cellular compartments rupture, allowing polyphenol oxidase to contact phenolic substrates, which initiates enzymatic oxidation leading to discoloration, quality deterioration, and microbial proliferation. Conventional preservation techniques such as sulphite dips or synthetic coatings can impair flavor, aroma, or consumer safety. In contrast, the biodegradable nanocellulose film incorporating *C. callosus* extract provides a natural and sustainable alternative by functioning as a semipermeable barrier that regulates gaseous exchange, prevents excessive moisture loss, and delivers natural antioxidants to inhibit enzymatic browning. The phenolic constituents simultaneously impart antimicrobial activity, suppressing bacterial and fungal growth and thereby maintaining the sensory and nutritional quality of fresh-cut pears and apples during storage.

Despite many advancements in biodegradable film research, substantial research gaps remain unaddressed. Most studies on nanocellulose extraction have focused on conventional lignocellulosic sources such as wood pulp, sugarcane bagasse, cotton linters, and banana peels, which, although effective, are limited by high processing costs, energy requirements, and environmental issues. The potential of *Cyamopsis tetragonoloba* straw as a novel source of nanocellulose remains largely unexplored despite its high cellulose and hemicellulose content and abundant availability in arid and semi-arid Indian regions. No systematic investigation has

yet reported its efficient extraction, nanoscale characterization, or incorporation into biodegradable or active food-packaging systems. Similarly, while numerous studies have examined polysaccharide-based films for mechanical reinforcement, few have explored the synergistic integration of natural bioactives to create multifunctional active packaging. Existing work has mainly relied on synthetic additives or essential oils, which often exhibit instability, volatility, and incompatibility with hydrophilic matrices, limiting their scalability and reproducibility.

Furthermore, although nanocellulose has been widely used as a reinforcing agent, its application as a Pickering stabilizer in nanoemulsion systems derived directly from agro-waste resources has not been optimized, and the interfacial mechanisms governing droplet stabilization, polymer–bioactive interaction, and controlled release behavior remain poorly elucidated. Importantly, the majority of studies assessing bioactive films have been restricted to in-vitro antioxidant or antimicrobial assays, without validating their functionality in real food models. Very few have evaluated such systems on climacteric fruits like pears and apples, which serve as practical and sensitive models for assessing preservation efficacy.

Therefore, a clear and significant research gap exists in developing an integrated platform that combines low-cost agro-residue valorisation, nanoscale cellulose extraction, and plant-derived bioactive functionalization through nanoemulsion technology to yield high-performance, biodegradable, and multifunctional packaging materials. The current research addresses these deficiencies by systematically investigating *Cyamopsis tetragonoloba* straw as a sustainable nanocellulose source, integrating *Cucumis callosus* extract through nanoemulsion-assisted dispersion, and evaluating the resultant films in terms of their physicochemical, structural, mechanical, barrier, antioxidant, and antimicrobial properties as well as their practical efficacy in extending the shelf life and quality of fresh-cut pears and apples.

This research connects three important scientific areas: agro-waste valorisation, nanocellulose-based biomaterial development, and bioactive encapsulation, creating a sustainable packaging system that adds value to agricultural by-products, reduces plastic waste, and enhances food preservation naturally. It also contributes to the broader goals of sustainable materials research by supporting the transition from petroleum-based packaging to eco-friendly alternatives that are safe, effective, and compatible with environmental conservation.

Chapter 1.1 Research Objective

1. To optimize the extraction of cellulose and nanocellulose from guar (*Cyamopsis tetragonoloba)* straw.

2. To extract and characterize the antimicrobial components from different parts of the kachri (*Cucumis callous*) fruit.

3. To formulate and characterize nanocellulose and fruit extract-based biodegradable packaging film.

4. To assess the potential application of the developed film using a food model system

Chapter 2 Review of Literature

The review of literature provides a comprehensive evaluation of current scientific developments, conceptual frameworks, and technological advancements relevant to the valorisation of agro-industrial residues and the fabrication of biodegradable food-packaging materials. In recent years, the convergence of food safety concerns, environmental sustainability mandates, and circular bioeconomy principles has transformed the research landscape of food packaging. Conventional petroleum-based plastics, despite their cost-effectiveness and functional versatility, are increasingly being replaced by bio-based alternatives derived from renewable biomass owing to their degradability and minimal ecological footprint. Within this context, the exploration of agricultural residues as sustainable feedstocks for functional biopolymers has gained significant importance. Nanocellulose, in particular, has emerged as a promising biopolymer for structural reinforcement due to its exceptional mechanical, barrier, and optical properties. Parallelly, plant-derived extracts rich in polyphenols and flavonoids are being incorporated into polymeric matrices to impart antioxidant and antimicrobial functionalities, leading to the development of "active" packaging films capable of enhancing food quality and shelf life. The literature reviewed in this chapter therefore focuses on the scientific foundation and recent progress in four interconnected domains: the evolution and performance benchmarks of biodegradable food packaging, the role of nanocellulose as a reinforcement agent, the potential of agro-residue valorisation as a sustainable material source, and the functional contribution of bioactive compounds specifically from Kachri (*Cucumis callosus*) in developing active packaging systems. The chapter also highlights existing gaps in knowledge related to guar (*Cyamopsis tetragonoloba*) straw-based nanocellulose extraction, the incorporation of Kachri bioactive, and their synergistic application in nanoemulsion-mediated biodegradable film fabrication.

2.1 Agricultural Waste Valorization for Biopolymer Production

Agricultural residues generated during harvesting and agro-industrial processing represent an abundant and low-cost source of polymer-forming constituents such as cellulose, hemicellulose, lignin, starch, pectin, and proteins. However, a large fraction of these residues is still underutilized or disposed of through burning and landfilling, contributing to environmental pollution and loss of valuable biomass resources (Zalasiewicz et al., 2019; Bangar et al., 2023). Their conversion into biopolymers therefore offers a sustainable route for developing biodegradable packaging materials while reducing dependence on petroleum-derived plastics (Mikus and Galus, 2022). Unlike dedicated biomass crops, agricultural byproducts do not

require additional land, irrigation, or agrochemical inputs, making them economically and environmentally suitable feedstocks for material development (Saleem, 2022).

Among agro-waste-derived biopolymers, cellulose has received particular attention because of its high availability, structural strength, biodegradability, and film-forming ability (Shen et al., 2023). Through suitable chemical, enzymatic, mechanical, or green extraction processes, cellulose-rich residues can be converted into films, coatings, foams, and nanocomposite packaging systems with improved mechanical and barrier properties (Valle et al., 2024; Kumar et al., 2024). However, the performance of such materials depends strongly on feedstock composition, extraction efficiency, and matrix modification. Native biopolymer films often suffer from moisture sensitivity, brittleness, and limited active functionality, which restrict their direct application in food packaging. Therefore, recent studies have focused on reinforcement with nanofillers and incorporation of bioactive compounds to improve strength, barrier performance, antioxidant activity, and antimicrobial protection (Cristofoli et al., 2023; Ahmed et al., 2025). In this context, agro-residue-derived nanocellulose provides a promising platform for active biodegradable packaging, particularly when combined with plant-based bioactives through nanoemulsion-assisted film fabrication.

Table 2.1 Biopolymers extracted from various agricultural residues, along with the processing techniques and extraction efficiencies

Biopolymer	**Agricultural Source**	**Extraction/Recovery Method**	**Yield (%)**	**Reference**
Cellulose	Rice husk	Treatment with sodium hypochlorite followed by ultrasonication	34%	Al-Mofty et al. (2023)
	Corn cobs	Removal of hemicellulose followed by alkaline delignification	77%	Fialho et al. (2024)
Starch	Litchi seed	Extraction using 0.16% sodium bisulfite solution	21.4%	Kaur et al. (2024)
	Mango kernel	Ultrasound-assisted extraction in 1% sodium bisulfite	54%	Mieles-Gómez et al. (2023)

Polyhydroxyalkanoates (PHA)	Molasses–olive oil mixture	Acid pretreatment of substrate for microbial fermentation	2.03 g/L	Razzaq et al. (2024)
Poly Lactic Acid (PLA)	Grape stalk residues	Steam explosion pretreatment	0.98 g	Dambrosio et al. (2023)

2.1.1 Types of Biopolymers

Biopolymers used for biodegradable packaging are mainly classified as polysaccharide-based, protein-based, lipid-based, and microbial or synthetic biodegradable polymers. Among polysaccharides, starch, cellulose, pectin, chitosan, alginate, and hemicellulose are widely studied due to their abundance, biodegradability, and good film-forming ability. Starch-based films are attractive because of their low cost and easy availability; however, their practical use is limited by brittleness, high water sensitivity, and poor dimensional stability under humid conditions. Protein-based films, obtained from sources such as gelatin, soy protein, whey protein, and plant protein isolates, generally show good oxygen-barrier properties but often suffer from weak moisture resistance and structural instability unless crosslinking or blending strategies are applied (Abolore et al., 2024). Lipid-based materials improve water-vapour resistance because of their hydrophobic nature, but their poor mechanical strength restricts their use as independent packaging films.

Microbial and synthetic biodegradable polymers, including polyhydroxyalkanoates (PHA) and polylactic acid (PLA), have also gained attention due to their compostability and relatively better mechanical performance. However, their large-scale application is limited by high production cost, complex processing requirements, and dependence on controlled fermentation or industrial polymerization routes (Naser et al., 2021; Kusuma et al., 2024). In comparison, cellulose-based biopolymers offer a stronger structural framework due to their linear β-(1→4)-linked glucan chains, high crystallinity, and extensive hydrogen bonding. These features make cellulose particularly suitable for developing mechanically reinforced biodegradable films. Nevertheless, native cellulose films remain highly hydrophilic and may show limited active functionality, which reduces their effectiveness for high-moisture food systems. Therefore, conversion of cellulose into nanocellulose and its combination with bioactive compounds or nanoemulsion systems has emerged as a promising approach to improve mechanical strength, barrier performance, and antioxidant–antimicrobial functionality. In the present thesis, this

rationale supports the selection of *Cyamopsis tetragonoloba* straw-derived nanocellulose as the main reinforcing biopolymer for active biodegradable packaging film development.

2.1.2 Cellulose-Based Biopolymers

Cellulose is a linear, naturally occurring polysaccharide composed of repeating D-glucose units linked through β-(1→4) glycosidic bonds (Fig. 2.1). It is the principal structural component of plant cell walls and represents approximately 40–50% of the dry weight of many lignocellulosic materials (Wohlert et al., 2022). Depending on botanical origin and extraction conditions, cellulose exhibits a high degree of polymerization, ranging from several hundred to more than 10,000 anhydroglucose units. The abundance of hydroxyl groups along the cellulose backbone promotes extensive intra- and intermolecular hydrogen bonding, resulting in compact, semi-crystalline microfibrillar structures. This hierarchical organization provides high mechanical strength, rigidity, and thermal stability, making cellulose a suitable precursor for nanocellulose production and reinforced biodegradable packaging films (Selvam et al., 2025).

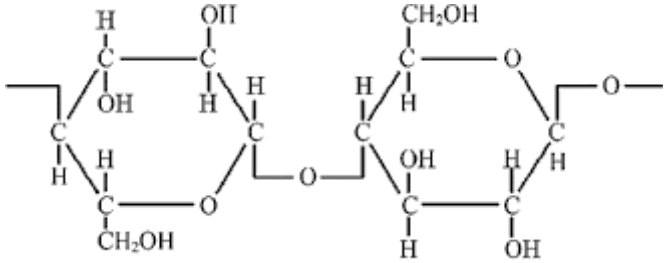

Fig. 2.1 Structure of Cellulose

In recent years, cellulose recovered from renewable lignocellulosic biomass has gained considerable attention as a precursor for biodegradable packaging materials. Agricultural residues such as cereal husks, sugarcane bagasse, wheat straw, fruit peels, maize stalks, and other fibrous by-products contain appreciable cellulose content, generally ranging from 30–50% on a dry-weight basis depending on botanical origin and processing conditions (Nahak et al., 2022). These residues mainly consist of cellulose, hemicellulose, and lignin, where cellulose provides the structural framework, while hemicellulose and lignin contribute to matrix cohesion and rigidity (Pei et al., 2024). Through suitable pretreatment and fractionation, cellulose can be separated from the lignocellulosic matrix and converted into biodegradable films or reinforced composite systems for food packaging applications.

From a materials perspective, cellulose is biodegradable, non-toxic, lightweight, and exhibits good film-forming ability, tensile strength, thermal stability, and oxygen-barrier performance under low-humidity conditions (Kamalesh et al., 2023; Das et al., 2023). However, its abundant hydroxyl groups at the C2, C3, and C6 positions also make cellulose highly hydrophilic, which

limits its moisture-barrier efficiency in high-humidity food systems. Therefore, structural modification, nanoscale conversion, or combination with compatible bioactive compounds is often required to improve hydrophobicity, flexibility, interfacial compatibility, and multifunctional packaging performance (Magalhães et al., 2023). In this context, the use of agricultural residue-derived cellulose, particularly from underutilized sources such as *Cyamopsis tetragonoloba* straw, provides a focused and sustainable route for developing nanocellulose-based packaging films.

2.1.2.1 Extraction Methods for Cellulose from Agricultural Residues

Plant-based agricultural residues, including processing remains from cereals, fruits, and fibrous crops, are largely composed of lignocellulosic biomass. This biomass matrix is formed by three structural polymers: cellulose as the reinforcing framework, hemicellulose as the amorphous polysaccharide component, and lignin as the complex aromatic binder. Cellulose is the preferred material component for its mechanical strength, biodegradability, and renewable nature. However, it is embedded within a matrix of hemicellulose and lignin, which must be removed to expose the cellulose fibers (Sharif et al., 2020). The most commonly used extraction strategy involves an initial alkaline treatment to solubilize hemicellulose and loosen lignin, followed by a bleaching step to eliminate residual lignin and obtain purified cellulose suitable for further processing Shown in Table 2.2 (RazaliI and Kasim, 2022).

2.1.2.1.1 Alkaline Treatment

Alkaline treatment is generally used as the first pretreatment step to disrupt the lignocellulosic matrix and improve cellulose accessibility. During this process, hemicellulose is solubilized and lignin is partially removed, resulting in swelling of fibers, increased porosity, and exposure of cellulose-rich fractions. Sodium hydroxide is commonly applied at concentrations of 2–10% under heating conditions of 60–90 °C, depending on the composition of the biomass (Permata et al., 2024; AL-Rajabi et al., 2024). After treatment, the solid residue is filtered and washed repeatedly until neutral pH is achieved. Although alkaline treatment improves cellulose recovery and facilitates subsequent fibrillation, residual lignin and pigments may still remain in the material, making bleaching necessary for obtaining purified cellulose suitable for nanocellulose production and biodegradable film fabrication (Modenbach and Nokes, 2014; Lu et al., 2021). However, this method is often water-intensive due to repeated washing steps, which should be considered during process optimization.

2.1.2.1.2 Bleaching

Following alkaline pretreatment, a bleaching stage is employed to enhance cellulose purity and optical brightness. Chlorine-based bleaching agents are currently discouraged due to the

formation of chlorinated toxic by-products and the risk of oxidative degradation of the cellulose backbone. Consequently, environmentally benign oxidizing systems such as sodium chlorite ($NaClO_2$) and hydrogen peroxide (H_2O_2), often combined with glacial acetic acid to maintain a mildly acidic reaction environment, are widely adopted for effective delignification and pigment removal (Chik et al., 2024). In a typical bleaching protocol, the alkali-treated cellulose residue is suspended in an oxidizing solution containing approximately 5–10% hydrogen peroxide. The pH of the reaction mixture is adjusted to approximately 4–5 using glacial acetic acid to maintain a stable oxidative environment and facilitate regulated delignification. The suspension is then maintained at a temperature range of 50–80 °C for 1–2 h, with the duration optimized based on the initial lignin concentration and the targeted degree of bleaching. Under these conditions, peracetic acid species and reactive oxygen intermediates are generated in situ. These oxidizing agents cleave aromatic structures within lignin and disrupt chromophoric groups responsible for discolouration (Klunklin et al., 2023). Reactive oxygen species (ROS), such as hydroxyl groups and perhydroxyl anions, selectively interact with electron-dense functional groups present in the lignin network, leading to oxidative cleavage and structural disruption. This oxidative degradation results in fragmentation of lignin macromolecules into low-molecular-weight, water-soluble phenolic compounds that can be removed through subsequent washing. Additionally, conjugated double bonds and unsaturated moieties associated with cellulose discoloration are degraded, producing a significantly whiter cellulose fraction (Li et al., 2025). Bleaching under mildly acidic conditions offers the advantage of preserving cellulose chain integrity. In contrast to highly alkaline bleaching environments, which may induce depolymerization and reduce the degree of polymerization, controlled acidic systems maintain the molecular weight distribution and crystallinity of cellulose (Wang and Zhao, 2021). Preservation of these structural attributes is critical for applications demanding high mechanical strength and thermal resistance, including biodegradable films, membranes, and reinforced composites. Following the bleaching step, the treated material is thoroughly rinsed with distilled water to remove residual oxidizing agents, acidic components, and soluble lignin degradation by-products. The resulting purified cellulose, obtained as a white fibrous mass with substantially reduced non-cellulosic impurities, is then dried at 50–60 °C using a hot-air or vacuum oven before storage or further processing (Tursi and Olivito, 2021).

2.1.2.1.3 Acid Hydrolysis

cid hydrolysis is a widely employed technique for the preparation of cellulose nanocrystals (CNCs) from cellulose derived from agricultural biomass. This process selectively removes the less-ordered amorphous regions of cellulose while preserving the highly crystalline domains,

thereby generating nanoscale crystalline particles (Woldie et al., 2025). Concentrated mineral acids, particularly sulfuric acid (H_2SO_4), are commonly utilized due to their strong hydrolytic capability and ability to infiltrate the cellulose microfibrillar structure. Mechanistically, protonation of the glycosidic oxygen within the β-(1→4) linkage facilitates bond cleavage, preferentially in amorphous regions where molecular packing is less dense. This controlled depolymerization releases rigid, rod-like crystalline fragments corresponding to the intact crystalline segments of cellulose chains. The resulting CNCs typically exhibit lengths in the range of 100–500 nm and diameters of approximately 5–20 nm. These nanostructures possess high crystallinity, superior mechanical properties, and abundant surface hydroxyl groups that enable further chemical functionalization (Saupi et al., 2025).

Careful regulation of key process variables—such as acid concentration, reaction temperature (typically 45–60 °C), hydrolysis duration, and solid-to-liquid ratio—is essential to prevent excessive depolymerization and to maximize CNC yield. Following hydrolysis, the reaction is quenched by dilution with chilled water, and the suspension is subjected to repeated centrifugation and dialysis to remove residual acid and soluble degradation products (Serrano-Martínez et al., 2025). Although sulfuric acid hydrolysis is widely employed due to its efficiency, the use of concentrated acids presents environmental and safety challenges related to corrosiveness and acidic effluent management. Nevertheless, CNCs produced via this method are extensively utilized in biodegradable films, nanocomposite reinforcement, barrier coatings, and pharmaceutical applications owing to their outstanding physicochemical properties. Current investigations are increasingly focused on greener extraction strategies employing milder mineral or organic acids while preserving CNC quality (Chaka, 2022).

In conventional practice, sulfuric acid concentrations of approximately 55–65% (w/w) are employed. When cellulose is exposed to this acidic environment at 40–60 °C, protonation of the glycosidic oxygen occurs, facilitating cleavage of β-(1→4) linkages, particularly within amorphous regions where molecular order and hydrogen bonding are comparatively weaker (Dong et al., 2016). This acid-catalyzed mechanism involves the formation of a transient oxocarbenium ion intermediate, resulting in fragmentation of cellulose chains and liberation of crystalline nanodomains (Olivito et al., 2023, Alhaji et al., 2022). The resulting CNCs generally exhibit lengths ranging from 100–500 nm and widths of 5–20 nm, depending on raw material source and reaction conditions. Excessive temperature or prolonged hydrolysis can induce over-degradation, partial carbonization, or reduction in crystallinity, thereby compromising yield and structural integrity (Almashhadani et al., 2022). Post-reaction purification typically involves dilution, centrifugation, repeated washing, and dialysis to eliminate dissolved sugars, residual

acid, and sulfate ions. The incorporation of sulfate ester groups onto the CNC surface during sulfuric acid treatment imparts negative surface charge, enhancing colloidal stability in aqueous media, however, these sulfate functionalities may also decrease thermal stability due to their acid-sensitive nature (de Farias et al., 2024).

2.1.2.1.4 Enzymatic Hydrolysis

Enzymatic hydrolysis is regarded as a highly selective and eco-friendly approach for transforming purified cellulose derived from agricultural residues into value-added products such as soluble oligomers, glucose, cellulose nanofibers (CNFs), and cellulose nanocrystals (CNCs), depending on the applied process parameters (Banvillet et al., 2021). In contrast to conventional acid or alkali treatments, enzymatic conversion utilizes cellulase enzymes to specifically cleave β-(1→4) glycosidic linkages under relatively mild operating conditions, typically near-neutral pH and temperatures ranging from 40 to 55 °C. Such controlled conditions limit excessive polymer degradation and prevent the generation of harmful by-products, thereby making enzymatic routes particularly suitable for food-contact materials, biomedical systems, and biodegradable packaging applications (Waghmare et al., 2023).

Cellulase complexes consist of synergistic enzyme systems, primarily including endoglucanases (EGs), exoglucanases or cellobiohydrolases (CBHs), and β-glucosidases (BGs). Endoglucanases initiate hydrolysis by randomly cleaving internal β-(1→4) bonds within amorphous regions of cellulose, thereby lowering the degree of polymerization and generating new chain ends (Akram et al., 2021). Subsequently, exoglucanases act on these newly exposed termini to release cellobiose units, particularly from more crystalline domains. Finally, β-glucosidases convert cellobiose and short-chain oligosaccharides into glucose, which can be further utilized in bioethanol production or other biochemical value chains (Amândio et al., 2023). Efficient cellulose depolymerization relies on the coordinated and sequential activity of these enzymes. The catalytic mechanisms of cellulases involve either retention or inversion of glycosidic bond configuration, depending on the architecture of the enzyme's active site. Typically, two catalytic amino acid residues—often carboxylate groups such as glutamate—play a central role, where one residue protonates the glycosidic oxygen while the other acts as a nucleophile or general base. The overall hydrolysis efficiency is influenced by factors such as enzyme loading, substrate concentration, and reaction conditions. Although higher enzyme dosages accelerate hydrolysis rates, they also increase operational costs, highlighting the importance of enzyme immobilization and recycling strategies for industrial-scale processes. Most cellulase systems exhibit optimal activity within a pH range of 4.5–5.5 and temperatures between 45 and 55 °C, however, the precise optimum depends on the microbial source,

including species such as *Trichoderma reesei*, *Aspergillus niger*, and *Thermobifida fusca*. Pretreatment of lignocellulosic biomass—through alkaline processing, steam explosion, or ionic liquid treatment—significantly enhances enzymatic accessibility by removing lignin and hemicellulose and increasing cellulose surface area (Mukherjee et al., 2024). Compared with chemical hydrolysis, enzymatic processing provides higher specificity and reduces the formation of undesirable degradation products. Importantly, it does not introduce sulfate or other chemical groups onto the cellulose surface, thereby preserving native structural integrity and biocompatibility. This feature makes enzymatically produced CNFs and CNCs particularly attractive for applications in pharmaceuticals, food formulations, biomedical scaffolds, and cosmetic systems. Typically, CNFs obtained through enzymatic routes exhibit degrees of polymerization between 100 and 800, whereas CNCs range from 100 to 300, supporting enhanced dispersion stability and functional versatility in aqueous media (Wada et al., 2018). Additionally, the glucose generated during hydrolysis can be valorized for bioethanol production, thereby linking nanocellulose production with sustainable biofuel generation (Afrin and Karim, 2017).

2.1.2.1.5 Ionic Liquid Treatment

Ionic liquid (IL)–assisted processing has increasingly been recognized as an effective strategy for cellulose dissolution and transformation because of its operational efficiency and comparatively lower environmental footprint. Conventional cellulose extraction approaches generally depend on concentrated acids, strong alkaline solutions, or high-temperature treatments to disrupt the lignocellulosic matrix. In contrast, ionic liquids represent an alternative solvent platform characterized by negligible vapor pressure, high thermal stability, non-flammability, and recyclability, making them attractive from a sustainability perspective (Ibrahim et al., 2015). Ionic liquids are typically composed of a bulky organic cation—such as imidazolium, ammonium, or phosphonium—combined with either an organic or inorganic anion, including chloride, acetate, or formate. The structural flexibility of these cation–anion pairs allows precise adjustment of solvent polarity, hydrogen bond basicity, and dissolution behavior. Such tunability enables ILs to effectively disrupt the hydrogen-bonding network that stabilizes cellulose, thereby promoting dissolution and facilitating regeneration into various morphologies (Amini et al., 2021). Cellulose is a semi-crystalline polysaccharide consisting of β-(1→4)-linked glucose units, stabilized by extensive intra- and intermolecular hydrogen bonding among hydroxyl groups. This dense hydrogen-bonding network is responsible for its resistance to dissolution in most conventional solvents (Azimi et al., 2022 and Rahman et al., 2024). The application of ionic liquids offers multiple advantages. Due to their negligible vapor

pressure and potential reusability, ILs reduce volatile organic compound (VOC) emissions and solvent losses. This method eliminates the need for highly corrosive reagents such as concentrated sulfuric acid or sodium hydroxide, thereby decreasing hazardous waste generation and improving process safety. Additionally, several IL systems are capable of dissolving diverse cellulose sources, including untreated lignocellulosic biomass, often minimizing extensive pre-treatment requirements. Regenerated cellulose produced via IL processing generally exhibits desirable crystallinity, mechanical strength, and thermal stability, making it suitable for structural and functional applications (Inman et al., 2022). Moreover, the ability to tailor cation–anion combinations enables optimization of dissolution efficiency, degradation control, and material performance. Acetate-based ILs typically provide efficient dissolution with limited cellulose degradation, whereas chloride-based systems demonstrate enhanced penetration into crystalline domains. Certain ionic liquids have also been engineered to enable simultaneous dissolution and chemical functionalization, allowing in situ modification of cellulose during processing (Ci et al., 2023). Despite these advantages, ionic liquid systems present several limitations that must be considered. The production and purification of high-purity ILs can be expensive, posing economic challenges for industrial-scale implementation. Furthermore, many ILs exhibit high intrinsic viscosity, which may limit mass transfer and require mechanical agitation or co-solvent systems to enhance dissolution kinetics. Although often described as green solvents, some ionic liquids—particularly those containing imidazolium or pyridinium cations, may exhibit environmental persistence or toxicity toward aquatic organisms, raising concerns regarding ecological sustainability. Efficient recovery and recycling of ionic liquids following cellulose regeneration is therefore essential for economic viability, however, separation and purification processes can be technically demanding and energy-intensive (Binnemans and Jones, (2023) and Szabó et al., 2023).

Table 2.2 Comparative Evaluation of Extraction methods of cellulose

Extraction Method	**Experimental Conditions**	**Characteristics of Extracted Cellulose**	**References**
Alkali hydrolysis	Dried straw was soaked in 13% NaOH for 24 h and rinsed, then treated with NaOH + Na_2SO_3 at 100 °C for 3 h, washed, dried, and ground	High crystallinity and enhanced thermal stability.	Bian et al. (2022)

Solvent extraction	Toluene–ethanol extraction (90 °C, 7 h), Sodium hypochlorite/acetic acid treatment (75 °C, 1 h × 3 cycles), 8% NaOH treatment (80 °C, 2 h) , Washing to neutral pH, Drying.	Lower crystallinity compared to alkali hydrolyzed cellulose.	Bian et al. (2022)
Pulping	7% NaOH treatment: Straw soaked in 7% (w/v) NaOH at a solid-to-liquid ratio of 1:10, heated at 100 °C for 150 min.	Yield = 62.7% cellulose.	Morcillo-Martín et al. (2022) and Espinosa et al. (2019)
Two-stage alkaline treatment and enzymatic hydrolysis	Stage 1: WS (0.8 mm) + 2.35% NaOH (1:10), 54 °C, 16 h, centrifuged, dried. Stage 2: Treated powder + 10% NaOH, 121 °C, 1 h, centrifuged, dried.	High yield, ~55% crystallinity, reduced PDI, shorter fiber length	Ceaser and Chimphango, (2021)
Acid hydrolysis	1.5% H_2SO_4 (125 °C, 2 h) → 80% ethanol–water (2 h) → 1% NaOH + H_2O_2 bleaching → washed → dried at 80 °C.	69% crystallinity index, rod-shaped morphology, polymorphic structure, bundle aggregation due to residual hemicellulose/lignin	Li et al. (2019) and Shahbazi et al. (2017)
Two-stage hydrolysis and bleaching	17.5% NaOH (25 °C, 2 h), HCl hydrolysis (121 °C, 30 min), H_2O_2 bleaching (46 °C, 90 min).	High yield, 55% crystallinity, reduced polydispersity index (PDI), shorter fiber length	Ceaser and Chimphango, (2021)
Solvent hydrolysis and bleaching	Toluene–ethanol (RT, 20 h), $NaClO_2$ hydrolysis (70 °C, 5	Yellow fibers, particle size ~40–110 μm, ~60% crystallinity	Oun and Rhim, (2016)

	h), KOH alkaline treatment, water rinse, dried (cellulose)		
Solvent extraction and hydrolysis (organic acids)	85% formic:acetic acid (70:30), 110 °C, 2 h, peroxyformic/peroxyacetic acid (80 °C, 2 h) → 35% H_2O_2 + 4% NaOH (80 °C), washed (white cellulose).	Nanofibers (8–100 nm diameter), high crystallinity, enhanced thermal stability	Nuruddin et al. (2016)
TBAH (tetra-n-butylammonium hydroxide) extraction	Dewaxed straw + 55% aq. TBAH (heated, stirred) → gel formation → centrifuged (5500 rpm) → cellulose precipitate	Good yield, cellulose fibers stable with high crystallinity.	Zhong et al. (2013)
Alkali hydrolysis and bleaching	17.5% NaOH (25 °C, 2 h), H_2O_2 bleaching, 2% NaOH (80 °C, 2 h), $NaClO_2$ bleaching	Removal of phenolics, lignin, and proteins, high cellulose content (84.67%).	Shahbazi et al. (2017)

2.1.2.2 Conversion of cellulose into nanocellulose

Nanocellulose refers to a class of cellulose-derived nanomaterials in which at least one structural dimension falls within the nanometer range. It constitutes the elementary nanoscale unit obtained from naturally occurring cellulose present in diverse biological systems (Abdel-Hakim and Mouradb, 2023). Morphologically, nanocellulose generally displays a stiff, elongated, or rod-like architecture, with diameters typically between 1 and 100 nm and lengths varying from 10 to 100 nm, depending on the origin of the raw material and the extraction technique employed (Xue et al., 2025). Nanocellulose can be derived from numerous renewable sources, including lignocellulosic plant residues, algal biomass, and marine organisms such as tunicates. Additionally, it can be biosynthesized by specific cellulose-producing bacteria, for example, *Acetobacter* species (Catarino et al., 2025). Chemically, it is composed of repeating D-glucopyranose units interconnected through β-(1→4) glycosidic linkages, forming a linear polysaccharide chain. Different classifications are used to describe its structural variations, including cellulose nanocrystals (CNCs), nanofibrillated cellulose (NFCs), microfibrillated cellulose (MFCs), cellulose nanofibers (CNFs), bacterial cellulose (BC), cellulose

nanoparticles, nanowhiskers, and cellulose whiskers (Abdelhamid, 2026). Conversion of bulk cellulose into nanocellulose can be achieved through several approaches, such as acid hydrolysis, alkaline treatment, oxidative processes, organosolv methods, and the use of ionic liquids.

2.1.2.2.1 Acid hydrolysis

Acid pretreatment is a commonly applied strategy for breaking down the compact and structurally complex architecture of lignocellulosic biomass. In acidic environments, hydronium ions diffuse into the biomass matrix and promote the cleavage of inter- and intramolecular linkages among cellulose, hemicellulose, and lignin within the hierarchical cell wall structure. Depending on the concentration of the acid employed, hydrolysis can be conducted under either concentrated or dilute conditions, with treatment severity governing the extent of structural disruption and the composition of the resulting biomass fractions (Hendriks et al., 2009). Strong mineral acids, including H_2SO_4, HCl, H_3PO_4, and HNO_3, are frequently utilized due to their high efficiency in depolymerizing lignocellulosic polymers and enhancing the release of fermentable sugars, particularly in biofuel-oriented processes (Sun et al., 2011 and Zhang et al., 2012). However, in nanocellulose production, complete depolymerization is not desirable, instead, preservation of relatively long cellulose chains is preferred to facilitate effective fibrillation in subsequent mechanical or chemical treatments. Despite their effectiveness, concentrated acids present significant operational and environmental challenges. These reagents are highly corrosive, toxic, and hazardous, requiring specialized corrosion-resistant equipment and strict safety protocols, which substantially elevate processing costs. Moreover, recovery and recycling of the acid are essential to maintain economic feasibility and minimize environmental impact. The overall efficiency of acid hydrolysis depends on parameters such as acid concentration, pH, reaction temperature, and treatment duration, all of which must be carefully optimized to maximize cellulose recovery. Excessive reaction severity can result in uncontrolled depolymerization, leading to excessive monosaccharide release and subsequent acid-catalyzed degradation into secondary products such as organic acids and alcohols (Pedersen et al., 2010). To address these limitations, dilute-acid pretreatment has gained attention as a more practical and cost-effective approach for biomass fractionation. Sulfuric acid solutions with concentrations below 4 wt.% are capable of effectively solubilizing hemicellulose, often converting a large fraction into soluble sugars under relatively mild operational conditions (Mou et al., 2012). After hemicellulose removal, the remaining solid fraction is primarily composed of cellulose and lignin. To isolate a purified cellulose component suitable for nanocellulose production, the material generally undergoes an alkaline treatment

step. During this stage, delignification occurs through the disruption of lignin–carbohydrate complexes, facilitating lignin removal and increasing cellulose accessibility for further hydrolysis or fibrillation processes.

2.1.2.2.2 Alkali hydrolysis

Alkaline pretreatment is widely applied to selectively remove or modify lignin within lignocellulosic biomass, thereby improving the accessibility of cellulose and hemicellulose for subsequent hydrolytic conversion (Lee et al., 2014). In comparison with several alternative pretreatment methods, alkaline processing generally operates under comparatively moderate conditions, often at temperatures below 140 °C and with lower reaction severity. The principal mechanism involves the cleavage of ester linkages that act as cross-bridges between hemicellulosic components, particularly xylan, and the lignin network (Moreira et al., 2016). Disruption of these structural crosslinks enhances biomass porosity and facilitates deeper penetration of chemicals or enzymes during downstream processing. Under alkaline conditions, ester bonds are cleaved via nucleophilic reactions in the presence of alkaline reagents such as NaOH or $Ca(OH)_2$, leading to the formation of soluble carboxylate salts and corresponding alcohol derivatives (Teacă and Tanasă, 2020). This breakdown releases phenolic compounds such as ferulic acid and p-coumaric acid into the reaction medium. Common alkaline agents employed for biomass pretreatment include NaOH, KOH, $Ca(OH)_2$, hydrazine, and ammonium hydroxide (Taherdanak and Zilouei, 2014). Exposure of biomass to alkaline media induces several structural and physicochemical modifications that promote enhanced conversion efficiency: (i) swelling of cellulose fibrils, (ii) expansion of internal surface area, (iii) reduction in cellulose crystallinity and degree of polymerization, (iv) partial solubilization of hemicellulose, (v) saponification and cleavage of lignin–carbohydrate ester bonds, and (vi) fragmentation of the lignin network through disruption of ether linkages. Collectively, these changes improve cellulose accessibility and facilitate subsequent hydrolysis or fibrillation processes.

2.1.2.2.3 Oxidizing agent

Oxidative pretreatment employs strong oxidizing agents, such as hydrogen peroxide (H_2O_2), peracetic acid ($C_2H_4O_3$), ozone (O_3), molecular oxygen, or even air to catalyze the delignification of lignocellulosic biomass through oxidative cleavage and fragmentation of lignin's aromatic ring structures (Abdel-Halim and Al-Deyab, 2011). These oxidants are often used in combination with alkaline pretreatment to enhance delignification efficiency. Under strongly basic conditions (pH > 12), oxygen is reduced to reactive oxygen species, predominantly superoxide radicals (O_2^-), which initiate nucleophilic attack on lignin, leading

to ring-opening reactions and oxidative degradation of phenylpropanoid units (Sánchez et al., 2011). This process effectively converts lignin and portions of hemicellulose into low-molecular-weight carboxylic acids such as formic, oxalic, and acetic acids. Oxidation-based pretreatment is particularly suitable for cellulose extraction because these oxidizing agents preferentially degrade lignin and partially hemicellulose, while cellulose remains relatively resistant to decomposition under such mild conditions (Liu et al., 2019). As a result, oxidative pretreatment significantly improves cellulose purity, enhances fiber accessibility, and facilitates subsequent nanocellulose synthesis.

2.1.2.2.4Organo-solvent

Organosolv pretreatment is a solvent-based fractionation approach designed to extract lignin and partially remove hemicellulose from lignocellulosic biomass through solvolytic and depolymerization reactions (Zhao et al., 2017). In this method, organic solvents or aqueous–organic mixtures serve as reaction media that selectively dissolve lignin fragments and portions of hemicellulose under elevated temperature conditions, while a cellulose-enriched solid fraction remains as residue. Frequently applied low-boiling organic solvents include methanol, ethanol, acetone, ethylene glycol, and ethyl acetate (Zhao et al., 2009). Within organosolv systems, alcohol-derived alkoxide species participate in nucleophilic reactions targeting ester bonds present in lignin–hemicellulose complexes. Concurrently, cleavage of lignin ether linkages and partial hydrolysis of hemicellulosic glycosidic bonds contribute to fragmentation of the aromatic lignin network and associated polysaccharide structures. As a result, lignin is solubilized into the organic phase, facilitating its separation from cellulose. One of the notable benefits of this technique lies in solvent recovery, since volatile alcohol-based solvents can be reclaimed through relatively low-energy distillation processes. These solvents are generally cost-effective, water-miscible, and reusable, which supports their potential application in biorefinery systems. Despite these advantages, economic constraints limit the broader industrial implementation of organosolv pretreatment (Zheng et al., 2009). The process typically requires repeated washing of the treated biomass with organic solvent, followed by extensive water rinsing, to prevent lignin reprecipitation and redeposition onto the cellulose surface. These washing steps increase operational complexity and solvent consumption. Furthermore, although solvent recovery is feasible, the associated distillation processes demand considerable energy input, thereby elevating overall processing costs and restricting large-scale commercialization.

2.1.2.2.5 Ionic Liquids

Ionic liquid (IL) pretreatment represents one of the most recent and promising chemical-based dissolution technologies for lignocellulosic biomass. The high tunability of IL chemistry by the

combinations of organic cations and inorganic or organic anions enables the dissolution of a wide range of biomass types. Unlike conventional heterogeneous systems (e.g., cellulose suspended in water), ILs create a homogeneous reaction environment in which catalytic sites exhibit enhanced accessibility to β-glycosidic bonds. This facilitates efficient biomass fractionation and promotes controlled hydrolysis of cellulose (Xiong et al., 2014). Ionic liquids can dissolve cellulose, hemicellulose, and lignin under relatively mild operating conditions without causing significant degradation of polymer chain integrity. These room-temperature molten salts are typically composed of an inorganic anion paired with an organic cation, and their structural tunability provides selective dissolution capacity for specific biomass components. Overall, among the various chemical pretreatment strategies used for lignocellulosic biomass fractionation, such as dilute- and concentrated-acid hydrolysis, alkaline hydrolysis, oxidative treatments, and organosolv processes, acid hydrolysis remains the most effective and practically favorable method for nanocellulose production. Acid pretreatment provides superior disruption of biomass structure, allowing efficient solubilisation of hemicellulose and enhanced liberation of cellulose fibers under controlled reaction conditions. When optimized for acid type, concentration, temperature, and residence time, this method yields high-purity cellulose with minimal degradation, ensuring the preservation of long-chain cellulose necessary for nanoscale fibrillation. In contrast, other methods, including ionic liquid–based treatments, are associated with higher operational costs, complex solvent recovery, or limited industrial scalability. Therefore, acid hydrolysis offers the best balance of efficiency, process controllability, economic feasibility, and downstream compatibility, making it the most suitable pretreatment technique for achieving high cellulose recovery and producing nanocellulose of desirable quality for advanced applications.

2.1.2.3 Properties of Cellulose and Nanocellulose

2.1.2.3.1 Structural and Chemical Properties

Cellulose is a linear polysaccharide composed of β-(1→4)-linked D-glucose units forming extended chains stabilized through intramolecular and intermolecular hydrogen bonding (Lavoine and Bergström, 2017). This extensive hydrogen-bonding network contributes to its semi-crystalline structure, combining crystalline and amorphous domains, which impart rigidity and mechanical strength (Li, Huber, et al., 2024, Su et al., 2023). The crystalline arrangement governs the stiffness, dimensional stability, and tensile strength, whereas the amorphous regions contribute flexibility and permeability (Ketola et al., 2022). Cellulose's biodegradable nature due to its all-natural composition of polysaccharides, proteins, and fatty acid esters, allowing microbial enzymes to degrade it into glucose derivatives that reintegrate into the carbon cycle

(Shlush and Davidovich-Pinhas, 2022). When used in packaging, this property minimizes environmental impact and post-consumer waste accumulation. However, cellulose's high hydrophilicity, derived from abundant hydroxyl (–OH) groups, limits its barrier performance against moisture and necessitates modification for hydrophobic or mixed-humidity environments (Mokhothu and John, 2015). Surface modifications such as esterification and etherification, or composite blending with hydrophobic polymers, have been used to enhance water resistance and surface energy. For instance, polylactic acid (PLA) coatings increased water contact angles from 94° to 110° (Lujan et al., 2024), while perfluorohexadecyl triethoxysilane (POTS) treatment raised hydrophobicity to 145.5°, maintaining excellent droplet repellency even under immersion and heating (Yu et al., 2024). Thus, cellulose's native polarity can be tuned to design either hydrophilic foams for moisture absorption (fruits, vegetables) or hydrophobic films for dry-food protection (Dinesh et al., 2024).

2.1.2.3.2 Mechanical and Physical Properties

The mechanical properties of cellulose materials depend strongly on pore morphology, polymer orientation, and crystallinity. Small, uniformly distributed pores enhance compressive strength, elasticity, and shock absorption, whereas larger pores lower density but reduce resistance to deformation (Bhagavathula et al., 2021). The crystallinity derived from strong intermolecular hydrogen bonding provides exceptional stiffness and thermal stability (Li, Huber, et al., 2024). Optimization of cellulose solution concentration and foaming parameters can fine-tune tensile and compressive strength while maintaining lightweight structures (Ketola et al., 2022). Chemical modification and ionic crosslinking can further improve strength. For example, metal-ion crosslinked cellulose graphite foams (K^+, Ca^{2+}, Zn^{2+}, Fe^{3+}) achieved higher compressive modulus due to increased molecular chain connectivity (Wang et al., 2022). Such mechanical versatility allows the fabrication of foams suited for protective packaging of fragile foods requiring both cushioning and rigidity. Cellulose nanofibrils (CNFs) and nanocrystals (CNCs), with their nanoscale dimensions and high aspect ratios, reinforce polymer matrices such as PLA and PVA, enhancing tensile strength, Young's modulus, and puncture resistance by over 100% (Bangar et al., 2023, do Lago et al., 2021).

2.1.2.3.3 Thermal and Barrier Properties

The crystalline lattice of cellulose improves thermal stability, with degradation temperatures typically ranging from 320 to 380 °C (Bangar et al., 2023). The strong hydrogen bonding restricts molecular mobility and enhances energy absorption under stress or heat exposure (Li, Huber, et al., 2024). Incorporation of cellulose nanostructures in composite matrices further improves the thermal and barrier performance of films and foams. For example, lignin-

containing nanocellulose–PVA composites exhibited enhanced UV-blocking, increased tensile stress, and reduced water vapor permeability due to the dense packing of nanofibrils and aromatic lignin residues (Punia Bangar et al., 2023).

Cellulose nanofibrils blended with poly (lactic acid) also produce composites of high crystallinity and low WVP, suitable for packaging fresh produce requiring controlled respiration (Alemdar and Sain, 2008). The dense hydrogen-bond network and reduced free volume lower oxygen transmission, making such materials valuable for oxygen-sensitive foods like meats and dairy (Shamsabadi et al., 2015). Thermogravimetric analysis has shown that nanocellulose from wheat straw or rice husk yields higher onset degradation temperatures when neutralized post-acid hydrolysis, owing to reduced sulfate residues (Bangar et al., 2023). These attributes collectively ensure mechanical endurance and safety under variable thermal conditions, critical for microwaveable and hot-food packaging applications (Hou et al., 2023).

2.1.2.3.4 Morphological and Rheological Properties

Morphological analyses reveal that incorporation of cellulose nanocrystals into polymer matrices leads to uniform filamentous dispersion and reduced surface cracking (Pereira et al., 2022). At optimized concentrations (typically 2–5 wt%), CNCs improve homogeneity and interfacial adhesion between fillers and polymer chains, promoting stress transfer and enhancing ductility. However, excessive CNC loading (>5 wt%) can induce agglomeration and microvoid formation, diminishing film strength (Bangar et al., 2023). Scanning electron microscopy (SEM) of nanocellulose-based composites shows smoother, compact surfaces with reduced porosity, indicative of effective filler-matrix bonding. Such morphological refinement directly contributes to improved optical clarity, barrier resistance, and adhesion properties (Bangar et al., 2023). The nanocellulose variants—CNCs, CNFs, and bacterial nanocellulose (BC)—differ in aspect ratio, fibril diameter, and rheological behavior. CNFs provide network-forming capability and shear-thinning viscosity, CNCs impart stiffness and transparency, while BC offers superior purity and water-holding capacity (Huang et al., 2021).

2.1.2.3.5 Hydrophilicity, Hydrophobicity, and Surface Tunability

The hydroxyl-rich surface of cellulose allows strong hydrogen bonding with water, conferring high hydrophilicity and moisture uptake capacity (Mokhothu and John, 2015). This property is advantageous for fresh produce packaging where humidity control prolongs freshness (Wang, He, et al., 2024). In contrast, hydrophobic modifications via polymer coatings or silane treatments create water-repellent surfaces (Yu et al., 2024). For instance, CNF foams treated with POTS achieved contact angles of 145.5°, maintaining repellency under freezing and boiling cycles (Dinesh et al., 2024).

The degree of hydrophilicity/hydrophobicity can be tuned for different food categories: hydrophilic foams for moisture management in fruits and vegetables, and hydrophobic films for dry or oily foods (Cao et al., 2025). Such adaptability ensures controlled water exchange and prevents spoilage or textural degradation in stored products.

2.1.2.3.6 Biodegradability and Environmental Compatibility

The biodegradation behavior of cellulose-based materials depends on polymer composition, crystallinity, and environmental factors such as microbial activity and temperature. Pure cellulose foams degrade completely within 150 days in soil, re-entering the carbon cycle (Sun, Lu, et al., 2024). Composites with synthetic polymers like PLA or polyurethane exhibit slower degradation, as polymer chain structure and hydrophilicity affect enzymatic accessibility (Kwon et al., 2023, Pagar et al., 2022). Surface modifications, while improving hydrophobicity or strength, can alter degradation kinetics. Nonetheless, cellulose's inherent bio-origin and non-toxic degradation byproducts make it an ideal substrate for eco-friendly food packaging, supporting circular economy principles and minimizing landfill accumulation (Shlush and Davidovich-Pinhas, 2022). Cellulose and nanocellulose exhibit a synergistic combination of mechanical strength, thermal resilience, optical clarity, and surface tunability. Nanocellulose variants, due to their nanoscale dimensions, amplify these traits enhancing tensile strength, UV shielding, barrier properties, and thermal stability while remaining fully biodegradable and safe for food-contact applications. These multifunctional attributes position cellulose-derived materials as key enablers of the global transition toward green, intelligent, and high-performance food packaging systems.

2.1.3 Preparation Methods of Cellulose-Based Biodegradable film

The functional performance of cellulose-based biodegradable films and foams is strongly influenced by the processing techniques employed during their fabrication. Film-forming methods govern the molecular arrangement, interfacial interactions, and dispersion of cellulose within the polymer matrix, thereby determining key properties such as mechanical strength, barrier performance, and degradability. Consequently, careful selection and optimization of preparation strategies are critical for tailoring cellulose-based materials for specific packaging applications.

2.1.3.1 Casting method

Solvent casting is widely recognized as one of the simplest and most frequently applied techniques for producing biodegradable and edible films at laboratory and pilot scales. Owing to its operational convenience and adaptability, this method is extensively utilized for fabricating films from plant- and animal-derived biopolymers (Li et al., 2024). In this approach,

a suitable film-forming polymer—such as agar, alginate, casein, cellulose, chitosan, dextran, gelatin, glycerides, various gums, paraffin, pectin, starch, waxes, or whey protein is selected based on the desired mechanical strength, barrier properties, and functional performance of the final material. In the solvent casting approach, the selected polymer is first solubilized or uniformly dispersed in a suitable solvent system, commonly distilled water or a water–alcohol blend, to promote adequate chain mobility and homogeneous film formation. To enhance flexibility and minimize brittleness, plasticizing agents such as glycerol, sorbitol, aloe-based compounds, or natural resins are incorporated into the formulation. The solution is subsequently subjected to thorough mixing or homogenization to obtain a stable and uniform dispersion. At this stage, natural additives and functional modifiers—such as antioxidants, antimicrobial agents, pigments, flavor compounds, emulsifiers, stabilizers, sweeteners, or texture improvers—may be introduced to tailor the desired physicochemical and functional attributes of the final film matrix (Nieto et al., 2023). After homogenization, the film-forming solution is typically degassed, either by vacuum treatment or mild thermal exposure, to eliminate trapped air bubbles that could compromise film uniformity and mechanical strength. The bubble-free solution is then poured onto a smooth, inert surface such as a glass plate, polytetrafluoroethylene (Teflon) sheet, or Petri dish to achieve uniform thickness. Drying is carried out under controlled temperature and relative humidity conditions to ensure gradual solvent evaporation and proper film consolidation. Once fully dried, the films are carefully peeled from the casting surface and conditioned under standardized conditions prior to application or detailed physicochemical evaluation (Sivakumar et al., 2025). The solvent casting technique is widely preferred due to its operational simplicity, minimal equipment requirement, ease of compositional modification, and relatively eco-friendly processing. However, the quality and reproducibility of the produced films are strongly influenced by environmental and processing variables, including drying temperature, drying time, humidity levels, and equipment setup, all of which significantly affect film microstructure, mechanical behavior, and barrier properties (Patwari et al., 2024).

2.1.3.2 Compression molding

Compression molding is a well-established manufacturing technique used to fabricate biodegradable films with precise thickness control and defined geometry. In ultrasonic compression, pre-formed film layers are bonded using an ultrasonic welding system. High-frequency vibrations generate localized heat at the interface of the materials, promoting polymer chain mobility and interdiffusion. This localized thermal effect enables the formation of strong and uniform joints without the need for additional adhesives (Tiwari et al., 2024). In

contrast, thermo-compression molding involves the concurrent application of heat and pressure to soften the polymeric matrix and shape it into the desired configuration. The processing temperature is maintained above the polymer's glass transition or softening temperature to facilitate chain rearrangement and bonding, while the applied pressure ensures consistent thickness and structural compactness (Rech and Daugaard, 2024). After molding or welding, the films are trimmed and cut into specified dimensions for application in sustainable food packaging systems. Various biopolymers can be processed through compression molding to develop nanocomposite films. Starch-based materials, particularly cassava starch, are widely utilized owing to their strong film-forming capability, acceptable mechanical performance, and relative resistance to structural damage under thermal and compressive conditions (Tatara, 2024). Compared with solvent casting, compression molding is considered a faster and more energy-efficient technique with lower solvent-related environmental impact. Nevertheless, its use in edible and biodegradable film production is somewhat restricted due to difficulties in maintaining uniform thickness, managing moisture redistribution during processing, and preventing thermal degradation of sensitive bioactive ingredients incorporated within the polymer network (Olawade et al., 2024).

2.1.3.3 Extrusion Methods

Extrusion is a continuous and scalable processing technique widely employed for the fabrication of biodegradable and edible films, wherein biopolymer-based materials are simultaneously mixed, plasticized, and shaped under controlled conditions of temperature, pressure, and shear (Dutta and Sit, 2024). During extrusion, thermal and mechanical energy supplied by the rotating screw(s) induces polymer melting and molecular rearrangement, resulting in films with tailored structural, mechanical, and functional properties. Owing to its continuous nature and solvent-free operation, extrusion is considered one of the most industrially relevant methods for sustainable packaging applications.

In the context of edible and biodegradable film production, extrusion can be carried out using single-screw, twin-screw, or co-extrusion systems. These configurations allow precise control over processing parameters, enabling the optimization of film characteristics such as tensile strength, flexibility, water vapor permeability, and overall barrier performance (Dutta and Sit, 2024). The incorporation of lipids into polysaccharide-based matrices during extrusion is commonly practiced to enhance hydrophobicity, which contributes to improved mechanical integrity and reduced moisture sensitivity of the films. When multiple biopolymers—most notably starches combined with lipids—and functional additives are processed together, co-extrusion blowing techniques are particularly effective in achieving targeted film performance

and multilayer functionality (Giannakas, 2024). Compared to solvent casting and compression molding, extrusion represents a more dynamic processing approach characterized by intense mixing, high shear forces, and continuous thermal treatment. These conditions promote enhanced dispersion of additives, improved interfacial interactions between polymer components, and greater uniformity in film structure, ultimately leading to superior and more reproducible film properties. The extrusion process typically comprises distinct functional zones within the extruder barrel. In the feeding zone, the biopolymer matrix along with natural additives and modifiers (NAMAs) is introduced into the system, where initial compaction, blending, and partial degassing occur. As the material advances into the kneading or transition zone, both temperature and pressure increase progressively, facilitating improved homogeneity and enhanced film-forming capability (Fig. 3). In the final heating or metering zone, which is subjected to the highest levels of temperature, pressure, and shear, the material undergoes intensive thermal–mechanical processing. This stage plays a critical role in determining the physicochemical properties of the final film, including tensile strength, elongation at break, and barrier functionality against gases and water vapor (Giannakas, 2024).

2.1.3.4 Emulsion-based

A variety of processing technologies are available for the fabrication of biodegradable and edible packaging films, among these, emulsion-based techniques are particularly important when hydrophobic components such as lipids are incorporated into hydrophilic polymer matrices. Before film casting, emulsification of the lipid phase within an aqueous continuous phase is a critical step, as the characteristics of the emulsion strongly influence film-forming behavior and final packaging performance. In emulsion-based packaging films, droplet size plays a decisive role in determining emulsion stability and significantly affects viscosity, flow properties, and the microstructural organization of the dried film. Different homogenization techniques are employed to prepare stable film-forming emulsions. Rotor–stator homogenizers are among the most widely used methods due to their operational simplicity and effectiveness, typically producing emulsions with average droplet sizes of approximately 1 μm (Ma et al., 2012a, Vargas et al., 2011). To achieve finer dispersions, high-pressure homogenization can be applied, resulting in further droplet size reduction through enhanced shear and cavitation forces (Bonilla et al., 2012). Advanced techniques such as microfluidization are capable of generating emulsions with narrow particle size distributions by combining ultrahigh-pressure shear with intense head-on collision stresses (Sherwin et al., 1998). Both microfluidization and ultrasonication have been reported to produce nanoemulsions in the size range of 150–700 nm, with droplet size decreasing as a function of increasing homogenization pressure, processing

time, or sonication duration (Jafari et al., 2006). Among the various emulsification techniques, rotor–stator homogenization remains the most commonly applied approach in packaging film fabrication, primarily due to its versatility and ease of scale-up. However, combined homogenization strategies are frequently adopted to enhance emulsion stability and film quality. For instance, a two-step process involving initial rotor–stator homogenization followed by microfluidization has been successfully used to prepare sodium caseinate-based packaging films containing lipid components such as oleic and stearic acids (Fabra et al., 2011). Intensification of homogenization conditions directly affects the size and spatial distribution of lipid domains in the dried films, leading to improvements in mechanical strength, surface gloss, and optical transparency key attributes for food packaging applications (Fabra et al., 2015).

In the production of emulsion-based packaging films, the film-forming emulsion is typically cast onto a suitable substrate and dried under ambient or controlled environmental conditions to remove the solvent. During drying, polymer chain association occurs concurrently with immobilization of lipid droplets within the continuous polymer network, resulting in a heterogeneous but well-integrated film structure. The processing temperature must be carefully controlled to remain above the melting temperature of the lipid phase, ensuring uniform dispersion, while staying below temperatures that could cause excessive solvent volatilization or disruption of the developing polymer network. Notably, emulsion-based packaging films generally require only a single casting and drying step, making the process relatively simple and energy-efficient.

The emulsion-based approach offers several advantages for biodegradable packaging films, including enhanced water vapour barrier properties due to the presence of dispersed hydrophobic domains and the ability to tailor mechanical and optical characteristics through droplet size control. Moreover, this method enables the efficient incorporation of lipophilic functional additives, making it particularly suitable for active packaging systems. Nevertheless, careful optimization of formulation and processing parameters such as emulsifier type, homogenization intensity, lipid concentration, and drying conditions is essential to avoid phase separation and to maintain adequate film cohesion and mechanical integrity for practical packaging applications.

2.1.4 Biodegradable films using nano-cellulose from agricultural waste

Growing concerns over environmental sustainability have accelerated the search for biodegradable alternatives to conventional packaging materials. In this context, cellulose nanocrystals (CNCs) have emerged as highly attractive candidates for eco-friendly packaging systems owing to their remarkable mechanical robustness, high density of surface hydroxyl

functionalities, excellent biocompatibility, and complete biodegradability (Nguyen and Lee, 2022). Biodegradation of composite polymers predominantly proceeds through enzymatic and non-enzymatic hydrolytic mechanisms initiated by moisture infiltration into the polymer matrix. The ingress of water facilitates scission of polymer chains, progressively reducing molecular weight and ultimately breaking down the material into low-molecular-weight by-products such as carbon dioxide, water, methane, and microbial biomass (Shaikh et al., 2021). In composites incorporating cellulose nanocrystals (CNCs), the high density of surface hydroxyl groups enhances the hydrophilic character of the matrix. This increased affinity for water improves moisture penetration, thereby promoting hydrolytic cleavage and accelerating non-enzymatic degradation under aqueous environments (Pavlatkova et al., 2025). Recent research highlights the valorization of agricultural by-products as renewable sources of nanocellulose for fabricating biodegradable films with improved performance characteristics. For instance, Wu et al. developed polylactic acid (PLA) composite films reinforced with mineralized cellulose nanocrystals (MCNCs). Their biodegradation assessment revealed a substantial increase in degradability following MCNC incorporation. Specifically, mass loss rose from 1.95% in neat PLA to 8.93% in the PLA/MCNC3 formulation, reflecting nearly a 4.6-fold enhancement in degradation rate.

The degradation behavior followed a sequential, three-stage mechanism. Initially, moisture present in soil infiltrates the polymer network, leading to matrix plasticization and relaxation of polymer chains. This is followed by hydrolytic cleavage of aliphatic ester linkages in PLA, wherein water molecules act as nucleophiles, resulting in progressive molecular weight reduction via bulk erosion. In the final stage, the generated low-molecular-weight oligomers and monomers are metabolized by soil microorganisms, completing the degradation process. The presence of MCNCs introduces additional hydrophilic regions within the composite matrix, substantially increasing water absorption and thereby promoting accelerated hydrolytic degradation (Wu et al., 2025). Ilya et al. (2019) conducted a detailed investigation into the effect of varying concentrations of sugar palm nanofibrillated cellulose (SPNFC) on the morphological, structural, and physicomechanical properties of sugar palm starch (SPS)–based bionanocomposite films. Sugar palm fibers, which originate from agricultural waste biomass, were processed using a high-pressure homogenization technique to obtain nanofibrillated cellulose with micrometer-scale lengths and nanoscale diameters of approximately 5.5 ± 0.99 nm. These nanofibrils were subsequently incorporated into the starch matrix using a solution-based film-forming method. Field emission scanning electron microscopy analysis revealed excellent miscibility and homogeneous dispersion of SPNFC within the SPS casting solution,

indicating strong compatibility between the two components. Fourier transform infrared spectroscopy further confirmed the formation of intermolecular hydrogen bonding between starch and nanocellulose, suggesting effective interfacial interactions. As a consequence of nanocellulose reinforcement, the bionanocomposite films exhibited markedly improved physical and mechanical performance compared to the control starch films. The addition of SPNFC restricted the mobility of starch molecular chains, resulting in reduced flexibility and lower elongation at break. However, this reduction in chain mobility led to a significant enhancement in tensile strength and stiffness. Specifically, increasing SPNFC content from 0 to 1.0 wt% resulted in an increase in tensile strength from 6.80 to 10.68 MPa and a rise in Young's modulus from 59.07 to 121.26 MPa, clearly demonstrating the reinforcing efficiency of sugar palm nanofibrillated cellulose.

The utilization of plum shell agricultural waste as a source of nanocellulose reinforcement was explored by Adriana Nicoletta Frone et al. (2019), cellulose nanocrystals (CN) and cellulose nanofibers (CF) were extracted from plum seed shells and employed as reinforcing agents in a polylactic acid/poly(3-hydroxybutyrate) (PLA/PHB) biopolymer blend using a solution-casting technique. This approach was highlighted as a cost-effective and environmentally responsible strategy for converting agricultural waste into high-value biopolymer composites. Comparative morphological analysis revealed that cellulose nanocrystals possessed a more uniform geometry, smoother surface texture, and greater structural regularity compared to cellulose nanofibers. In contrast, cellulose nanofibers exhibited certain limitations in terms of morphological uniformity and thermal behavior. The melting temperature of cellulose nanocrystals was found to be slightly lower than that of cellulose nanofibers, which was attributed to the presence of sulfate ester groups introduced during acid hydrolysis. These sulfate groups promoted dehydration of cellulose chains and contributed to a marginal reduction in thermal stability. Despite this effect, X-ray diffraction and thermal analyses demonstrated that the incorporation of cellulose nanocrystals significantly enhanced the crystallinity and thermal resistance of the PLA/PHB composite films, confirming their superior reinforcing potential.

Reshmy et al (2021) reported the extraction of high-purity nanocellulose from jackfruit (*Artocarpus heterophyllus*) peel waste using hydrolysis-based methods. Thin films were fabricated through solvent evaporation, employing nanocellulose as the primary substrate, Boswellia serrata as a functional bio-based filler, and various plasticizers as activating agents. Structural characterization using FTIR and XRD techniques confirmed strong molecular interactions and improved crystallinity within the film matrix, while FESEM analysis revealed

noticeable modifications in surface morphology following filler incorporation. One of the major advantages of this approach was the environmentally benign bleaching process, wherein the raw fibers were treated with a 4% soapnut solution instead of conventional chlorine-based bleaching agents. The incorporation of Boswellia serrata significantly enhanced the functional properties of the nanocellulose films, making them suitable for future applications. However, nanocellulose-rich films exhibited high water-holding capacity, which led to partial disruption of interactions between nanocellulose and plasticizers during prolonged storage. Despite this limitation, the films showed reduced moisture absorption and swelling behavior compared to other formulations, which is advantageous for food packaging applications.

Sheng Xu et al. (2020) demonstrated the potential of *Artemisia selengensis* stalks as a renewable source of hemicellulose and cellulose nanocrystals for biodegradable film production. Cellulose nanocrystals were isolated from hemicellulose through acid hydrolysis and incorporated into hemicellulose/polyvinyl alcohol (ASH/PVA) composite films. Morphological and structural characterization using SEM, TEM, and FTIR techniques confirmed improved compatibility and uniform dispersion of nanocellulose within the polymer matrix. Compared to the control ASH/PVA films, nanocellulose-reinforced composites exhibited a more compact microstructure with fewer voids. Functional evaluation revealed that these films possessed enhanced tensile strength, improved water vapor barrier properties, and significantly reduced light transmittance. At a nanocellulose loading of 9 wt%, tensile strength increased by 80.1% to 36.21 MPa, while the water vapor transmission rate decreased by 15.45% at a loading of 12 wt%, indicating effective reinforcement and barrier enhancement.

Banana pseudo-stem biomass was investigated by Faradilla et al. (2018) as a sustainable source of nanocellulose for the development of recyclable plastic films. The study examined the combined influence of nanoclay, graphene oxide, and glycerol on the mechanical, thermal, morphological, chemical, and barrier properties of banana pseudo-stem nanocellulose films. Extensive characterization using SEM, TEM, AFM, X-ray diffraction, thermogravimetric analysis, differential scanning calorimetry, ATR-FTIR spectroscopy, and oxygen transmission measurements revealed synergistic interactions when nanofillers were used in combination with glycerol. The presence of glycerol improved tensile modulus and flexibility, while also increasing water vapor permeability due to its hydrophilic nature. In contrast, oxygen permeability decreased with increasing glycerol concentration. Both nanoclay and graphene oxide significantly enhanced tensile strength, although their effect on elasticity was minimal. These findings clearly indicate that the properties of banana pseudo-stem nanocellulose films can be systematically tailored by adjusting the type and concentration of additives.

Didem Sutay Kocabas et al. (2021) proposed the fractionation of bulgur bran into cellulose- and hemicellulose-rich components as a means of valorizing this underutilized agro-industrial residue. To overcome the inherent limitations of hemicellulose-based films, commercial cellulose nanocrystals and cellulose nanofibers were incorporated as reinforcing agents. Structural and thermal analyses using SEM, TGA, DSC, and FTIR revealed the formation of a dense and compact film architecture upon nanocellulose addition. The tensile properties of the hemicellulose films improved significantly, while water vapor permeability, light transmittance, and film solubility decreased. A full-quadratic optimization model demonstrated excellent predictive accuracy ($R^2 = 0.9877$). Films containing 10 wt% CNC and 10 wt% CNF exhibited a 21.3% reduction in film water solubility compared to neat hemicellulose films.

Krishnavani Pavalaydon et al. (2022) extracted micro- and nanocellulose from cassava peel and coconut fiber using sequential mercerization, bleaching, and acid hydrolysis treatments. Optimization of the extraction process was performed using Taguchi experimental design. The extracted nanocellulose was characterized using dynamic light scattering, transmission electron microscopy, and infrared spectroscopy. Bionanocomposite films fabricated using polyvinyl alcohol as the polymer matrix exhibited significant improvements in mechanical performance. Among the tested materials, coir-derived cellulose nanocrystals demonstrated superior reinforcing efficiency, achieving a maximum tensile strength of 38.2 MPa at a low loading of 0.5 wt%, corresponding to a 96.9% improvement over unreinforced PVA films.

Nang et al. (2020) focused on isolating high-crystallinity cellulose nanocrystals from Vietnamese agricultural residues, including *Nypa fruticans* trunk, coconut husk fiber, and rice husk. A three-step extraction process involving organic acid pretreatment, oxidative delignification, and controlled acid hydrolysis effectively removed amorphous cellulose regions while preserving crystalline domains. Structural and thermal characterization using XRD, TGA, TEM, and FTIR confirmed that the resulting nanocrystals possessed crystallinity indices approaching 80% along with enhanced thermal stability. These properties make the nanocellulose suitable for applications in functional papers, filtration membranes, bionanocomposites, and advanced nanomaterial synthesis.

Li et al. (2020) isolated needle-shaped cellulose nanocrystals from pea hull waste through alkali treatment followed by sulfuric acid hydrolysis and evaluated their reinforcing potential in carboxymethyl cellulose films. Detailed characterization demonstrated significant improvements in tensile strength, thermal stability, ultraviolet shielding, and water vapor barrier properties. At a nanocellulose loading of 5 wt%, water vapor absorption decreased by 53.4%, while tensile strength increased by 50.8% compared to neat CMC films. The reduction in

endothermic transition temperature observed with increasing nanocellulose content was attributed to decreased hygroscopicity resulting from sulfate ester groups introduced during hydrolysis. Finally, Jayachandra S. Yaradoddi *et al.* demonstrated the feasibility of converting agricultural waste-derived carboxymethyl cellulose into biodegradable packaging films. Carboxymethyl cellulose extracted primarily from sugarcane waste was blended with gelatin, agar, and varying glycerol concentrations. Physicochemical characterization using thermogravimetric analysis, Fourier transform infrared spectroscopy, and differential scanning calorimetry revealed that glycerol concentration strongly influenced film performance. Among the tested formulations, films containing gelatin, CMC, agar, and 2.0% glycerol exhibited the lowest water vapor permeability and highest recyclability, making them the most suitable for food packaging applications. The use of waste-derived CMC significantly reduced material costs compared to commercial CMC, further enhancing the sustainability and economic feasibility of biodegradable film development.

2.1.5 Nanoemulsion-based packaging film

Microbial contamination occurring throughout packaging, storage, and handling until the point of consumption is a major cause of food spoilage, nutritional loss, quality deterioration, and reduction in market value (Loi et al., 2020). In food packaging applications, various functional compounds such as antimicrobial, antioxidant, anti-browning, flavour-enhancing, texture-stabilizing, and nutraceutical agents can be encapsulated within oil-based nanodroplets. These essential oils (EOs) and bioactive substances can be incorporated directly into foods, placed within a secondary compartment inside the package, or embedded into packaging materials themselves. This approach, known as active packaging, maintains food quality and prolongs shelf life by enabling the controlled absorption or release of functional compounds that suppress microbial growth or delay spoilage (Khaneghah et al., 2018).

When combined with biopolymeric matrices, essential oils have demonstrated strong potential as active functional ingredients in edible coatings and films for food preservation (Ju et al., 2019). Rehman et al. (2020) reported that incorporating EO-loaded nanocarriers into biopolymer coatings significantly improved antimicrobial and antioxidant performance. For example, chitosan coatings infused with Satureja khuzestanica essential oil (SKEO) nanoliposomes effectively preserved the physicochemical quality and microbial safety of lamb meat during 20 days of refrigerated storage (Pabast et al., 2018). Similarly, lemongrass EO-loaded chitosan nanoparticles applied as a coating for bell peppers minimized weight loss, slowed color changes, preserved firmness, and regulated acidity during storage (Ali et al.,

2015). Coating rucola leaves with nano-encapsulated lemon EO also increased shelf life from 3 to 7 days without negatively affecting sensory attributes (Sessa et al., 2015).

In another study, whey protein isolate coatings containing oregano or clove EO nanoemulsions significantly extended the shelf life of chicken breast, with formulations containing 20 g kg^{-1} oregano EO extending storage stability from 6 to 13 days at 4 °C while maintaining desirable appearance and freshness Sessa et al., 2015). Whey protein isolate films incorporating oregano EO or ε-polylysine demonstrated effective inhibition of microbial growth in fresh beef during chilled storage. Likewise, cinnamon EO-loaded alginate coatings exhibited stronger antibacterial action and higher migration of active compounds than oregano or savory EOs when applied to cured meat and beef slices. To achieve optimal performance, the concentration of essential oils in films and coatings must be carefully optimized. While increasing EO content generally enhances antimicrobial activity, excessive levels may impart undesirable flavor or aroma (Chaudhari et al., 2020). For instance, Ribeiro-Santos et al. (2017) reported that whey protein films containing 5% EO blend achieved the highest antimicrobial efficiency without negatively affecting sensory characteristics.

Beyond antimicrobial and antioxidant benefits, EOs can improve the physical, mechanical, and thermal characteristics of packaging films. Cinnamon and clove EO nanoemulsions reduced weight loss and enhanced the functional properties of chitosan films during storage [178]. Carvacrol-loaded chitosan coatings inhibited *E. coli* growth on fresh green beans for up to 11 days (Severino et al., 2014), while incorporating olive, maize, and canola oil nanoemulsions into Plantago major gum films increased film flexibility and decreased water vapor permeability (Xu et al., 2019). Nanoemulsions of geraniol and linalool also inhibited *Listeria innocua*, *E. coli*, and *Pseudomonas lundensis* in meat analog media (Niknam et al., 2019). Additional studies reported delayed protein and lipid oxidation, improved texture, and extended shelf life in coated poultry and pork products (Almaráz-Buendia et al., 2019 and Falguera et al., 2011).

Fruits and vegetables are highly perishable commodities, and their quality rapidly deteriorates due to mechanical injury, moisture evaporation, physiological and metabolic alterations, as well as post-harvest microbial spoilage. These factors collectively contribute to reduced shelf life and significant economic losses. Consequently, the development of protective packaging systems, particularly starch-based biodegradable films—has received considerable research attention as a strategy to minimize quality degradation and extend storage stability. Owing to their rich composition of vitamins, minerals, dietary fibre, and bioactive antioxidants, fruits and vegetables remain essential components of a balanced diet and are consistently prioritized by consumers (Yousuf et al., 2018).

Hadimani et al. (2023) investigated the performance of biopolymer-based films in terms of fruit shelf-life extension, antifungal efficacy, and biodegradability. Grapes wrapped with the developed films exhibited prolonged shelf stability across all storage intervals compared with unwrapped controls. The films also demonstrated significant antifungal activity, effectively inhibiting spore germination of *Fusarium oxysporum* and *Sclerospora graminicola*. Furthermore, the materials showed pronounced biodegradation under soil burial conditions, with substantial degradation occurring within two weeks of incubation. Collectively, these results highlight the multifunctional potential of such biopolymer films as sustainable alternatives to conventional synthetic plastics in fruit packaging.

Oliviero et al. (2023) reported the development of an innovative biodegradable active packaging system based on thermoplastic cellulose acetate (CAT) reinforced with modified layered double hydroxide (LDH) as a functional filler. In this system, potassium sorbate was ionically immobilized within the LDH lamellar structure, enabling a controlled and sustained release mechanism. Thermal and mechanical analyses indicated that incorporation of the LDH–sorbate hybrid filler, up to 5% (wt/wt), had minimal influence on the material's processability. Release kinetics of sorbate from the composite films were evaluated using UV–Vis spectroscopy and interpreted through the Brouers–Sotolongo kinetic model. Application studies demonstrated that the active films effectively preserved the physicochemical quality of pomegranate arils during storage, highlighting their suitability for fresh fruit packaging applications in the food industry.

Similarly, Ramakrishnan et al. (2023) fabricated a functional biodegradable film composed of sodium alginate (SA), carboxymethyl cellulose (CMC), and potato starch (PS), incorporated with grapefruit seed extract (GSE) using the solvent casting technique. Scanning electron microscopy (SEM) analysis revealed homogeneous distribution of GSE within the polymeric matrix, producing a continuous and crack-free surface morphology with uniform thickness. Incorporation of GSE significantly improved ultraviolet barrier performance (>99.9%) while maintaining acceptable transparency. The films exhibited strong antioxidant and antimicrobial activity against Escherichia coli and Staphylococcus aureus. Additionally, GSE inclusion reduced tensile strength and water vapor permeability while enhancing flexibility and thermal stability. Notably, films containing 0.5 g GSE effectively extended the shelf life of green chili by 25 days, demonstrating practical applicability.

Sani et al. (2023) emphasised the growing interest in using agro-industrial by-products as raw materials for biodegradable packaging film production. The valorization of residues from fruit and vegetable processing industries—such as husks, seeds, peels, leaves, and gums—offers

advantages including low cost, availability, environmental sustainability, and functional performance enhancement. These by-products are rich in structural polysaccharides and plant proteins, including starch, cellulose, and pectin, which can be exploited for developing films with improved mechanical, barrier, and functional properties. The integration of such underutilized materials aligns with circular economy principles while addressing food waste management challenges.

2.1.5.1 Physicochemical and Functional Characterization of Essential Oil Nanoemulsion-Integrated Packaging Films

Recent studies indicate that incorporating essential oils (EOs) in nanoemulsion form into film matrices significantly improves both structural integrity and functional performance compared to films containing conventionally emulsified oils. Nanoemulsified EOs not only enhance mechanical strength and uniformity but also demonstrate superior antimicrobial efficacy. For instance, strawberries treated with a pullulan-based film containing cinnamon EO nanoemulsion exhibited markedly lower microbial populations at the end of storage, with bacterial and fungal counts of 2.544 and 1.958 log CFU/g, respectively. In contrast, samples coated with pullulan alone showed substantially higher microbial loads, exceeding 10^3 CFU/g for bacteria and 10^4 CFU/g for moulds (Chu et al., 2020). These findings emphasize the potential of integrating EO nanoemulsions into polysaccharide-based edible films, such as those formulated from pectin or alginate, to create active packaging systems with enhanced antimicrobial functionality. However, to ensure their applicability in food packaging, it is necessary to comprehensively evaluate key film properties, including wettability, physicochemical characteristics, tensile strength, elongation at break, thermal stability, optical parameters (such as brightness and opacity), and surface morphology. The overall effectiveness of such films is influenced by both the type of EO incorporated and its compatibility with the polymer network (Benbettaïeb et al., 2014). Moreover, edible coatings can modify internal gas exchange and restrict volatile compound migration, thereby contributing to a modified atmosphere around the food product during storage (Jouki et al., 2014). Consequently, it is crucial to examine whether the addition of EO nanoemulsions affects the gas barrier performance of these films. Given that edible coatings are applied directly to food surfaces, their structural integrity and sensory properties are critical determinants of consumer acceptance and commercial viability (Bahrami et al., 2019). Thus, the combined physicochemical and mechanical characteristics of edible films containing EO nanoemulsions must be carefully considered.

2.1.5.2 Physical Properties

2.1.5.2.1 Colour Attributes

Colour plays a decisive role in the overall acceptability of edible films, as it directly affects the visual quality of packaged foods. The optical properties of films are generally quantified using the CIE L*, a*, b* colour model, in which L* denotes brightness, a* represents the green-to-red coordinate, and b* reflects the blue-to-yellow coordinate. Previous studies have shown that incorporating essential oil (EO) nanoemulsions into biopolymer films can significantly alter these colour parameters. For example, alginate films containing thyme EO nanoemulsions exhibited increased positive b* values, resulting in a subtle yellow–green appearance, likely due to the light-absorbing phenolic compounds present in the oil (Acevedo-Fani et al., 2015, Jouki et al., 2014). Similarly, the addition of cinnamon EO nanoemulsions enhanced the yellowness of alginate-based films, with greater colour intensity observed at higher EO concentrations (Frank et al., 2018). In soluble soybean polysaccharide films, increasing levels of cinnamon EO nanoemulsions were associated with reductions in lightness and redness, alongside elevated b* values, producing a darker and more yellowish film matrix (Ghani et al., 2018). Conversely, the incorporation of rosemary and lemongrass EO nanoemulsions into banana starch films did not significantly modify the L*, a*, or b* parameters, indicating that the extent of colour alteration depends strongly on the intrinsic chemical composition and chromophoric properties of the essential oil used (Restrepo et al., 2018).

2.1.5.2.2 Film Thickness

Film thickness is a critical structural attribute that significantly affects the mechanical integrity and water vapor barrier efficiency of edible films (Almasi et al., 2020). Variations in thickness are often associated with the incorporation level and droplet characteristics of essential oil (EO) nanoemulsions within the film matrix (Acevedo-Fani et al., 2015).

Studies have demonstrated that increasing nanoemulsion concentration generally leads to thicker films. For instance, corn starch-based films formulated with 3% (v/v) nutmeg EO nanoemulsion exhibited greater thickness compared to those containing 1% (v/v), suggesting that higher EO loading contributes to increased film mass and structural buildup (Aisyah et al., 2018). Likewise, hydroxypropyl methyl cellulose (HPMC) films enriched with *Thymus daenensis* EO nanoemulsion were reported to be thicker than control films without nanoemulsion (Moghimi et al., 2017). The increase in thickness is primarily attributed to the added components of the nanoemulsion system—namely essential oil, surfactant, and aqueous phase—which elevate the total solid content and viscosity of the film-forming solution. When equal volumes of more viscous dispersions are cast, the resulting dried films tend to exhibit greater thickness (Erfanifar et al., 2023). Furthermore, higher concentrations of plasticizers

such as glycerol have been shown to enhance solution viscosity, thereby contributing to increased film thickness (Lin et al., 2025).

The influence of nanoemulsion incorporation on film thickness is not consistent across all polymer systems. In certain cases, the addition of EO nanoemulsions does not significantly alter film thickness. For example, basil seed gum films enriched with *Zataria multiflora* EO nanoemulsion exhibited thickness values between 114 and 130 μm, which were statistically comparable to those of the control films (Gahruie et al., 2017). Conversely, some studies have reported a reduction in thickness following nanoemulsion incorporation. Alginate-based films containing thyme and sage EO nanoemulsions were observed to be thinner than the corresponding control films (Acevedo-Fani et al., 2015). Similarly, incorporation of 2.5% and 5% (v/v) marjoram EO nanoemulsions into pectin films resulted in decreased thickness (Almasi et al., 2020). This reduction has been associated with the use of nanoemulsions possessing very small droplet sizes, which may promote partial volatilization or migration of essential oil components during drying, thereby decreasing the effective solid content contributing to film formation. Therefore, the ultimate impact of EO nanoemulsions on film thickness depends on both their compositional attributes and physicochemical properties, including droplet size distribution, concentration, and interaction with the polymer matrix (Shiryanpour et al., 2025).

2.1.5.2.3 Film Solubility

Film solubility in water is considered a key functional property when selecting edible films for specific food packaging applications, as it determines the film's stability and integrity upon contact with moisture. Studies have shown that incorporating EO nanoemulsions can significantly influence this parameter. For example, Ghani et al. (2018) observed that elevating the concentration of cinnamon essential oil (EO) nanoemulsions in soluble soybean polysaccharide films led to a gradual decrease in water solubility. Comparable findings were reported for banana starch films incorporated with lemongrass and rosemary EO nanoemulsions, where solubility at both 25 °C and 95 °C was lower than that of the control films (Wigati et al., 2025). This decline in solubility is primarily associated with the increased hydrophobic character imparted by dispersed EO droplets, which limit water diffusion into the polymer matrix and reduce its dissolution (Cui et al., 2023).

Similarly, basil seed gum films containing *Zataria multiflora* EO nanoemulsions exhibited diminished water solubility (Hashemi et al.). This effect may be attributed to the synergistic influence of enhanced hydrophobicity and the development of a denser polymeric network. Strengthening of the network structure is likely due to intermolecular hydrogen bonding

(dipole–dipole interactions) between hydroxyl groups of the polymer chains and the polar head groups of surfactants stabilizing the nanoemulsion droplets (Train et al., 2021).

2.1.5.3 Physico-Chemical Properties

2.1.5.3.1 Water Vapour Permeability

Water vapour permeability (WVP) is an important parameter for evaluating the barrier performance of edible films and coatings, as it reflects the material's ability to limit moisture transfer between the food product and the external environment (Gökkaya Erdem et al., 2021). The incorporation of essential oil (EO) nanoemulsions can markedly affect WVP, primarily due to the hydrophobic nature of EOs, which can hinder water diffusion within otherwise hydrophilic polysaccharide-based matrices (Kong et al., 2022). For instance, the inclusion of cinnamon EO nanoemulsion at a low level (0.2% v/v) in soluble soybean polysaccharide films did not produce a significant change in WVP compared to the untreated control. In contrast, increasing the nanoemulsion concentration to 0.4–0.8% (v/v) led to a notable decrease in WVP, indicating enhanced resistance to moisture transmission and improved barrier functionality (Ghani et al., 2018). This enhancement is attributed to the formation of a more hydrophobic and compact film structure, where well-dispersed nanoemulsion droplets create a tortuous pathway that limits water vapor transmission. Conversely, at higher concentrations, excessive interactions between polymer chains and nanoemulsion droplets may disturb matrix continuity, compromise structural integrity, and potentially diminish barrier performance (Zhang et al., 2024).Comparable observations have been documented in previous investigations. Acevedo-Fani et al. (2015) reported a pronounced reduction in the water vapour permeability of alginate films after incorporation of sage essential oil nanoemulsions. The improved barrier performance was primarily attributed to the fine droplet size of the nanoemulsion system, which enabled uniform distribution of the oil phase within the polymer matrix, thereby obstructing moisture diffusion pathways. Effective barrier enhancement is generally achieved at optimal nanoemulsion concentrations that facilitate homogeneous nanodroplet dispersion without inducing structural discontinuities in the film network (Dhar et al., 2015). Similarly, Hossain et al. (2018) demonstrated that methyl cellulose/cellulose nanocrystal (MC/CNC) composite films incorporated with a thyme–oregano essential oil nanoemulsion exhibited approximately a 9% decrease in WVP relative to neat MC films. This improvement was attributed to the combined tortuosity effect generated by the rigid CNC reinforcement and the well-dispersed oil nanodroplets, which compelled water vapour molecules to follow a more extended and complex diffusion pathway, thereby enhancing moisture barrier efficiency.

2.1.5.3.2 Moisture Absorption

Moisture absorption characteristics are also important for food stability. Pectin films containing marjoram EO nanoemulsions exhibited increased moisture absorption at higher EO levels (Kong et al., 2022). Alginate films with higher cinnamon EO nanoemulsion content also exhibited slightly increased moisture retention, although the moisture content remained within 10–12%. These variations may be associated with the presence of glycerol, which increases flexibility but may also enhance water affinity, or with the hydrophobic characteristics of EO droplets that alter water–matrix interactions (Neumann et al., 2018).

2.1.5.3.3 Mechanical Properties

Mechanical performance is a key determinant of the practical applicability of edible films in food packaging systems. Among the various mechanical parameters, tensile strength (TS) and elongation at break (EAB) are the most commonly employed indices to assess film behavior under stress (Moeini et al., 2022). Tensile strength represents the maximum stress a film can withstand before rupture, serving as an indicator of its structural robustness and resistance to mechanical damage during processing, handling, storage, and distribution (Gopal, 2025). Elongation at break, in contrast, measures the film's ability to stretch or deform before rupture, indicating its flexibility and capacity to conform to the shape of food products without tearing (Tafa et al., 2023). Generally, a higher EAB value is considered advantageous for packaging materials, as it improves film adaptability and wrapping performance. When formulating polysaccharide-based edible films, it is essential to consider the influence of environmental conditions, particularly relative humidity, since the water content absorbed by hydrophilic polymer matrices can significantly modify mechanical behavior. Water functions as a natural plasticizer, reducing intermolecular forces within the polymer chains and thereby increasing flexibility while decreasing tensile strength. Therefore, before mechanical testing, films must be conditioned under controlled humidity and temperature to ensure consistent and comparable results.

2.1.5.3.4 Tensile Strength

Tensile strength (TS) is a fundamental mechanical indicator that describes the maximum stress an edible film can tolerate prior to rupture. Incorporation of essential oil (EO) nanoemulsions frequently modifies this parameter due to structural alterations within the polymer matrix. For example, hydroxypropyl methyl cellulose films containing *Thymus daenensis* EO nanoemulsions exhibited a marked reduction in TS, decreasing from 36.2 ± 0.7 MPa (control) to 22.6 ± 0.7 MPa after nanoemulsion incorporation (Moghimi et al., 2017).

A comparable decline in TS was reported for corn starch films enriched with nutmeg EO nanoemulsions, where tensile values varied between 15.1 and 18.9 kgf/mm² depending on

nanoemulsion concentration, indicating that increasing EO levels progressively weakened the film structure (Aisyah et al., 2017). Similarly, pectin-based films formulated with 5% and 7.5% (v/v) marjoram EO nanoemulsions showed reduced tensile strengths of 1.9 MPa and 1.3 MPa, respectively (Kong et al., 2022). This reduction is generally attributed to decreased polymer–polymer interactions due to the presence of EO droplets, which act as structural discontinuities and increase film flexibility at the expense of mechanical resistance (Eslami et al., 2023). Conversely, some studies have reported an improvement in TS when specific EO nanoemulsions are incorporated. For instance, basil seed gum films containing 3% (v/v) Zataria multiflora EO nanoemulsion showed an increase in TS from 19.7 MPa to 34.6 MPa (Hashemi et al., 2017). Similarly, methylcellulose films incorporated with a blend of oregano and thyme EO nanoemulsions (7.5% w/w) exhibited an increase in TS from 54.2 to 71.7 MPa, which represents approximately a 30% enhancement (Lee et al., 2019). This improvement is linked to the formation of stronger intermolecular hydrogen bonds between hydroxyl-containing polymer chains and surfactant head groups surrounding the EO droplets, leading to a reinforced network structure (Li et al., 2025). However, in alginate-based films, the addition of thyme, sage, or lemongrass EO nanoemulsions did not cause significant variation in TS, with values remaining similar to the control films. Additionally, increasing the concentration of rosemary and lemongrass EO nanoemulsions up to 0.5% (v/v) did not significantly influence TS, which remained in the narrow range of 3.09 to 3.43 MPa (McClements et al., 2011). Such limited differences are typically attributed to the low level of nanoemulsion incorporated into these film matrices.

2.1.5.3.5 Elongation at break

Elongation at break (EAB) is a measure of film flexibility and extensibility, indicating the extent to which a material can deform before rupture. Incorporation of essential oil (EO) nanoemulsions has been shown to significantly influence this parameter in various biopolymer matrices. For instance, alginate films containing sage EO nanoemulsion exhibited markedly higher stretchability (78%) compared with control films (38%), whereas films formulated with lemongrass (32%) and thyme (41%) nanoemulsions displayed EAB values similar to or slightly above the control (Acevedo-Fani et al., 2015). These variations were associated with the electrostatic characteristics of the nanoemulsions, where repulsive interactions between similarly charged polymer chains increased intermolecular spacing and generated a plasticizing effect (Chiang et al., 2023).

A comparable enhancement in flexibility was observed in basil seed gum films enriched with *Zataria multiflora* EO nanoemulsion, where EAB increased from 21.6% in the control to 39.5%

(Erfanifar et al., 2023). Likewise, incorporation of rosemary and lemongrass EO nanoemulsions (0.5% w/w) improved the elongation of banana starch films to 20.45 ± 1.5% and 23.54 ± 0.8%, respectively, compared with 10.98 ± 1.2% for untreated films (Perdones et al., 2012). This improvement is generally attributed to the weakening of intermolecular forces within the polymer matrix, as dispersed oil droplets reduce hydrogen bonding density and enhance chain mobility (Liao et al., 2021).

However, the effect is not universal. In methyl cellulose films, incorporation of an oregano–thyme EO blend nanoemulsion resulted in only a marginal increase in elongation, from 19.3% to 20.0% (Hossain et al., 2019). Additionally, the presence of plasticizers such as glycerol can further amplify flexibility, corn starch films containing nutmeg EO nanoemulsion and 30% (v/v) glycerol exhibited an EAB of 52.8%, reflecting the combined plasticizing action of glycerol and EO droplets in reducing intermolecular cohesion within the film network (Aisyah et al., 2018).

2.1.5.3.5 Antimicrobial Activity

Numerous essential oils (EOs) have been reported to exhibit strong antimicrobial activity when tested under in vitro conditions against foodborne pathogens and spoilage-associated microorganisms. In one study, Kong et al. (2022) developed alginate-based edible films incorporated with nanoemulsions of thyme, lemongrass, and sage essential oils. The antimicrobial performance of these films was evaluated using TSA supplemented with NaCl as a model solid food medium to mimic real food system conditions. The control alginate films exhibited no antibacterial effect, showing microbial growth comparable to untreated plates. However, the incorporation of thyme EO nanoemulsion markedly enhanced the antibacterial activity of the films, while lemongrass and sage EO nanoemulsion films did not produce noticeable inhibition. This strong inhibitory response associated with thyme EO is attributed to its high thymol content, a phenolic compound capable of interacting with microbial cell membrane proteins via hydrophobic forces, thereby increasing membrane permeability and disturbing cellular function (Kowalczyk et al., 2020). Similarly, basil seed gum-based edible films loaded with Zataria multiflora EO nanoemulsion displayed improved antibacterial activity against Bacillus cereus and Escherichia coli when analyzed through broth dilution assays, whereas the control films lacked inhibitory effects (Gahruie et al., 2017). Moghimi et al. (2017) showed that incorporating *Thymus daenensis* essential oil nanoemulsions into hydroxypropyl methyl cellulose (HPMC) films markedly improved their antimicrobial performance. The modified films inhibited a diverse range of Gram-negative bacteria, including *E. coli*, *S. typhi*, *S. dysenteriae*, *S. flexneri*, *A. baumannii*, and *K. pneumoniae*, as well as Gram-positive

organisms such as *S. aureus*, *S. epidermidis*, *B. subtilis*, *E. faecalis*, *E. faecium*, and MRSA. In comparison to untreated HPMC films, the nanoemulsion-containing films demonstrated substantially stronger antibacterial effects. This bioactivity is largely attributed to phenolic constituents, particularly thymol and carvacrol, which compromise microbial membrane integrity, enhance permeability, and disrupt essential cellular functions. In a related study, Aisyah et al. (2018) observed that starch-based films supplemented with nutmeg essential oil nanoemulsions produced visible antibacterial inhibition zones against *S. aureus* and *E. coli*. The antimicrobial intensity increased progressively with higher nanoemulsion incorporation levels, suggesting a concentration-responsive mechanism. Likewise, Ghani et al. (2018) incorporated cinnamon essential oil nanoemulsions into soluble soybean polysaccharide films and reported enhanced antibacterial activity, further supporting the role of nanoemulsion delivery systems in improving the functional performance of biodegradable packaging materials. The antimicrobial efficacy of the films was influenced by nanoemulsion concentration, with formulations containing 0.8% cinnamon EO nanoemulsion effectively suppressing both Gram-positive and Gram-negative bacteria. In contrast, lower concentrations (0.4% and 0.6%) demonstrated partial or selective antibacterial activity. Collectively, these studies highlight that nanoemulsification significantly enhances the dispersion, stability, and bioavailability of essential oils within polymer matrices. Improved distribution of active compounds within the film structure facilitates stronger interactions with microbial cell membranes, thereby amplifying antimicrobial performance across diverse biopolymer-based edible film systems.

2.1.6 Importance of Packaging in Fresh-Cut Fruits and Vegetables

Fruits and vegetables constitute a vital part of a balanced and healthy diet due to their richness in essential micronutrients, dietary fiber, and a wide range of bioactive phytochemicals. The micronutrient profile of vegetables primarily includes vitamins and minerals that are required in small quantities but play indispensable roles in regulating numerous physiological and metabolic functions in the human body. Despite their low required intake levels, deficiencies of these micronutrients are associated with several health disorders. According to dietary recommendations issued by the USDA, an individual should consume approximately three to five servings of vegetables each day (Benjamin, 2011), while a total daily intake of about 400 g of fruits and vegetables is strongly encouraged (Woodside et al., 2013).

Driven by consumer demand for convenience and reduced preparation time, minimally processed fruits and vegetables have gained substantial popularity in modern food retail systems (De Corato, 2020). Fresh agricultural commodities are increasingly transformed into ready-to-eat (RTE) or ready-to-cook (RTC) products to enhance usability while largely retaining their

fresh-like sensory and nutritional attributes (Abdul Khalil et al., 2018). Over the past three decades, the market for minimally processed produce has expanded significantly across Europe. Similarly, in the United States, packaged salads and fresh-cut vegetables represent some of the fastest-growing product categories in supermarkets (Santeramo et al., 2018). In Asian markets, fresh-cut fruits and vegetables account for a considerable proportion of retail food sales (De Corato, 2020). The International Fresh-cut Produce Association (IFPA) defines fresh-cut produce as fruits or vegetables that are trimmed, peeled, washed, and cut into fully usable forms, followed by packaging to deliver convenience, nutritional value, and freshness to consumers. Minimal processing, often described as a "mild technology," involves operations such as peeling, slicing, washing, application of sanitizing agents, and drying. Although these processes improve convenience, they disrupt the natural structural integrity of fresh produce, rendering it more prone to deterioration compared to intact raw materials (Banerjee et al., 2016). Mechanical damage incurred during processing increases susceptibility to microbial contamination by facilitating the survival and proliferation of spoilage and pathogenic microorganisms. The majority of microorganisms responsible for food spoilage and foodborne infections are Gram-negative bacteria, which constitute approximately 80–90% of reported cases. These include species belonging to genera such as *Pseudomonas*, *Enterobacter*, and *Erwinia*. In addition to bacterial contamination, various yeasts and molds also play a major role in food deterioration (Abdul Khalil et al., 2018). Industrial processing further accelerates the deterioration of minimally processed fruits and vegetables by inducing biochemical and physiological changes. These include elevated respiration rates, enhanced oxidative reactions, membrane degradation, enzymatic browning, and progressive loss of tissue firmness and texture. Consequently, maintaining the sensory attributes, nutritional quality, and microbial safety of fresh-cut produce remains a significant challenge for the food industry. Various preservation strategies, such as refrigeration, use of chemical preservatives, mild thermal treatments, microwave processing, reduction of water activity, ionizing radiation, high-pressure processing, pulsed electric fields, pulsed light, ozone treatment, and hurdle technology which integrates multiple preservation approaches to ensure product safety and quality have been explored (Siddiqui et al., 2011). Nevertheless, appropriate packaging plays a central and indispensable role in preserving the overall quality of fresh-cut products. Although petroleum-based packaging materials have traditionally been used, growing environmental concerns and sustainability issues have led to a shift away from such materials. Additionally, conventional packaging can pose risks of chemical migration into food due to direct contact with the product. As a result, increasing attention is being directed toward the development and application of

biopolymer-based packaging systems. Extensive research efforts have focused on producing biomass-derived packaging materials, several of which have already been successfully commercialized within the food industry.

2.1.7 Starch-based biopolymer

Starch-based biopolymers are increasingly recognized as strong candidates for replacing petroleum-derived plastics, particularly in packaging applications where environmental sustainability is a key concern (Tagliapietra et al., 2021). Growing awareness of the ecological impact of synthetic plastics has encouraged the exploration of renewable biopolymer sources, among which starch stands out due to its abundance, biodegradability, and low cost. Starch is a glucose-based polysaccharide found widely in nature and is commonly extracted from crops such as maize, potato, cassava, and wheat, which are produced in large quantities worldwide (Arruda et al., 2025). In addition to these conventional sources, interest is rising in starch recovery from agricultural byproducts including rice bran, corn husk, potato peels, and banana peels as a means of reducing waste and promoting circular resource utilization (Maqsood et al., 2025). The use of starch obtained from such waste streams lowers raw material costs while supporting sustainable waste management practices. As a result, starch-derived films and coatings are receiving increasing attention for use in food packaging, medical products, and other environmentally focused applications (Singh et al., 2024). One of the advantageous properties of starch is its natural ability to form continuous films. When processed appropriately, starch can produce transparent, flexible, and biodegradable films suitable for coating or packaging applications. These materials can degrade naturally without generating harmful residues, offering a clear environmental benefit compared with plastics derived from petroleum (Gonçalves et al., 2024). Moreover, incorporating starch into material development aligns with circular economy strategies, wherein material production and disposal are designed to minimize environmental burden and encourage resource recovery. Despite these advantages, native starch faces challenges that limit its direct substitution for conventional plastics. Issues such as poor mechanical strength, high water sensitivity, and structural instability restrict its performance in packaging environments where barrier properties and durability are essential. For these reasons, ongoing research is focused on modifying starch chemically, physically, or through blending to improve its functional performance and extend its application range (Onyeaka et al., 2024). Starch is a polysaccharide composed mainly of two glucose polymers, amylose and amylopectin, whose ratios depend on the botanical origin. Amylose is largely a linear chain of glucose residues linked through α-(1-4) bonds, whereas amylopectin is a highly branched macromolecule containing both α-(1-4) linkages and α-(1-6) branch points (Zhu and

Gilbert, 2024). In most starches, amylopectin predominates over amylose. At the molecular level, amylose typically forms helical conformations, while amylopectin develops a branched, network-like structure. The organization of these two components results in a semi-crystalline granule structure that exhibits birefringence when observed under polarized light (Varghese et al., 2024). Upon heating in the presence of water, starch granules absorb water, expand, and progressively lose their ordered crystalline arrangement in a process referred to as gelatinization. During this transition, amylose diffuses out of the granules and contributes to the formation of a viscous matrix. Subsequent cooling promotes partial realignment of amylose and amylopectin chains, known as retrogradation, which affects the texture, rigidity, and storage stability of starch-based systems (Lin et al., 2023).

2.1.8 Protein-Based Biopolymers

Biopolymeric materials derived from proteins are increasingly explored as sustainable alternatives to conventional petroleum-based plastics because of their film-forming capacity, biodegradability, and effective gas barrier performance. These materials are typically produced from naturally occurring proteins such as soy protein, whey protein, casein, gelatin, and wheat gluten, each contributing distinct mechanical, structural, and functional attributes to the resulting films (Selvam et al., 2025). Beyond conventional protein sources, agro-industrial residues are now recognized as valuable raw materials for protein-based biopolymer production. Byproducts such as soybean and sunflower oilseed meals remaining after oil extraction, wheat and rice bran, corn gluten meal, and residues from fish and poultry processing industries are rich in protein content. These underutilized resources provide cost-effective and environmentally sustainable feedstocks for the development of biodegradable protein-based films and packaging systems (Abedini et al., 2022). The unique performance of protein-based films is closely linked to the structural nature of proteins themselves. Proteins are composed of amino acids with diverse chemical functionalities, including hydrophilic and hydrophobic side chains. This diversity allows proteins to form various intermolecular interactions such as hydrogen bonding, ionic interactions, and hydrophobic associations which play an important role in determining the film's cohesiveness, flexibility, and barrier properties (Hadidi et al., 2022). By changes in processing conditions, pH, plasticizer content, and protein source, the physical behavior and functional performance of protein-based biopolymer films can be tailored to meet specific application requirements.

2.1.9 PHA and PLA

Polyhydroxyalkanoates (PHA) and polylactic acid (PLA) represent two of the most promising bioplastics for advancing sustainable food packaging systems. These polymers are

predominantly produced via microbial fermentation processes that utilize renewable carbon-rich substrates originating from agricultural by-products such as corn stover, sugarcane bagasse, rice husk, fruit peel waste, and other lignocellulosic materials (Dalton et al., 2022). Harnessing such residues not only aids in waste valorization but also reduces dependence on edible crops, thereby improving the environmental sustainability and lowering the carbon footprint of bioplastic manufacturing. PHA comprises a diverse group of microbial polyesters synthesized by bacteria under nutrient-limiting conditions, while PLA is an aliphatic thermoplastic polyester formed through the polymerization of lactic acid generated from carbohydrate fermentation (Stublić et al., 2024). Both polymers exhibit desirable biodegradability and compostability, making them suitable alternatives to conventional plastics in eco-friendly packaging applications.

2.2 *Cyamopsis Tetragonoloba*

Cyamopsis tetragonoloba, commonly known as guar, is a leguminous plant extensively utilized as a staple crop in India's drought-prone and arid regions (Asati et al., 2021). Underutilized edible legumes in the Indian desert, spanning states like Rajasthan, Haryana, Punjab, and Gujarat, include *Prosopis cineraria*, *Cyamopsis tetragonoloba*, and *Acacia senegal* (Vishnyakova and Frolov, 2023). Unexplored edible legumes, such as *Prosopis cineraria*, *Cyamopsis tetragonoloba*, and *Acacia senegal*, are prominent in the Indian desert regions, including Rajasthan, Haryana, Punjab, and Gujarat (Vishnyakova and Frolov, 2023). These legumes exhibit remarkable drought resistance, adaptability to degraded soils, and minimal dependency on surface water, thriving under conditions of abundant sunlight and low relative humidity during their growth season. Consequently, *Cyamopsis tetragonoloba* (guar) has emerged as a sustainable and economically viable crop for arid and semi-arid regions (Soltani et al., 2024). *Cyamopsis tetragonoloba* are rich in flavonoids and isoflavonoids, which constitute a significant class of natural phenolic compounds, with flavonoids representing approximately half of all phenolics found in plants (Sharma, 2021). Guar contains a favorable amino acid profile, with crude protein content ranging from approximately 33% to 45%. However, the inclusion of guar meal in broiler diets is limited by the presence of anti-nutritional factors such as guar gum (β-mannan), saponins, and trypsin inhibitors. These compounds have been shown to impede growth in poultry, nonetheless, at lower concentrations, certain anti-nutritional factors like β-mannan and saponins can have beneficial effects on avian health and performance. β-mannan, in particular, is considered a key anti-nutritional factor when higher quantities of guar meal are incorporated into poultry diets (Hussain et al., 2012).In addition to being a source of essential nutrients for both people and animals, *cyamopsis tetragonoloba* is

used as a primary ingredient in many other products, including biogas, guar korma, guar churi, alcoholic drinks, guar gum, and oil shown in Fig. 2.2 (Sharma et al., 2011). The distribution of guar bean harvest usage is approximately 35%-40% for human and animal consumption, 50%-55% for industrial purposes, 5% for medicinal applications, and other uses (Kumar et al., 2017). Guar gum, extracted from the seed endosperm, is the primary reason for the crop's economic value, particularly in agriculture. Guar gum is a high molecular weight polysaccharide with hydrophilic properties and gel-forming capacity, ranging in color from white to yellowish-white and lacking a distinct odor (Sharma et al., 2018). It is widely used across industries such as food, cosmetics, paper, mining, and petroleum. In addition, guar straw is commonly used as animal feed, particularly for camels and sheep (Ghodki et al., 2021). Recent research efforts have focused on developing biobased and biodegradable materials as alternatives to fossil fuel-derived plastics, particularly for food packaging applications (Bangar et al., 2023). The safety and freshness of food products are highly dependent on packaging, and the limitations of conventional plastic packaging, particularly in accurately displaying expiration dates, contribute significantly to food waste and foodborne illnesses (Jafarzadeh et al., 2024). Lignocellulosic biomass, composed of cellulose, lignin, and hemicellulose, offers great potential due to its biodegradability, biocompatibility, and sustainability (Blasi et al., 2023). The circular economy model advocates for the reuse and recycling of nutrients and bioactive compounds from agri-food processing waste, promoting a waste-free value chain (Yoha and Moses, 2023).

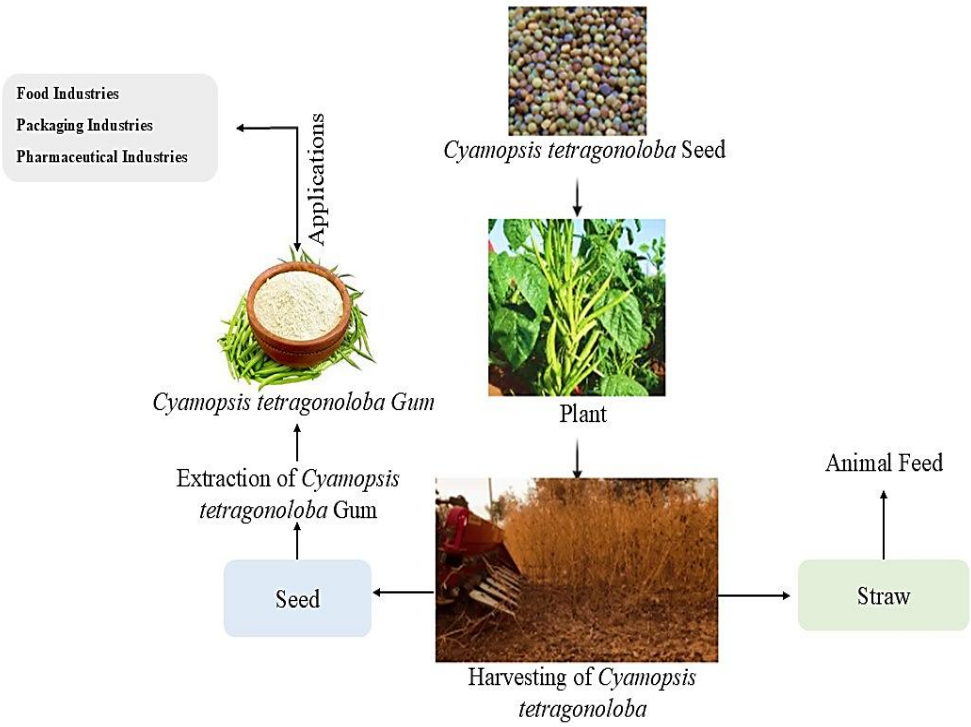

Fig. 2.2 Production process of *Cyamopsis tetragonoloba* Straw

Improving the application and utilization of genetically modified or seed proteins in human diets is limited. While some studies have explored the extraction, characterization, and functional properties of guar meal, more comprehensive research is needed to address these gaps. To further advance the industrial applications of guar gum-based composites, additional studies should focus on cost comparisons between traditional commercial adsorbents and non-traditional alternatives. Furthermore, evaluating the potential for recycling spent adsorbents could promote zero waste discharge, contributing to more sustainable practices in the industry.

2.2.1 Nutritional Profile of *Cyamopsis tetragonoloba*

Cyamopsis tetragonoloba provides a significant amount of dietary fiber, which aids in decreasing calorie density and minimizing the glycemic response. Additionally, they serve as an excellent source of protein (Rebello et al., 2014). In contrast, the ash, fat, moisture, protein, and crude fiber content in *Cyamopsis tetragonoloba* gum and seeds are 4.53 g, 3.32 g, 10.0 g, 33.25 g, and 11.6 g, and 3.33 to 4.96 g, 1.70 to 2.47 g, 8.37 to 8.80 g, and 25.80 to 30.52 g per 100 g of carbohydrate content, respectively (Badr et al., 2014, Yousif et al., 2013). The chemical composition of guar straw includes in vitro dry matter digestibility (56.9%), organic matter (88.5%), cellulose (33.3%), protein (12.4%), and crude fiber (30.5%) (Bhatt et al., 2012, Lamba et al., 2002). *Cyamopsis tetragonoloba* is rich in various nutrients and is recommended as a

protein source to meet dietary requirements.The most abundant fatty acid in *Cyamopsis tetragonoloba* beans is cis-linolenic acid, followed by cis-oleic acid and palmitic acid. Guar is a valuable source of iron and also contains significant amounts of other minerals such as zinc and copper (Sharma et al., 2017). Guar beans possess various pharmacological properties, including anticancer, antidiabetic, antiulcer, anticoagulant, antimicrobial, anti-asthmatic, and anti-inflammatory activities (Sharma et al., 2014). Legumes, in comparison to cereals, may serve as a more effective alternative in addressing these health issues. Notably, despite being an atypical legume, guar beans fulfill these requirements due to their high content of carbohydrates (35–59.1%), protein (24.5–35%), and bioactive substances. Research has demonstrated that guar beans have multiple beneficial pharmacological effects, including anti-cancer, anti-ulcer, anti-diabetic, anticoagulant, antimicrobial, anti-asthmatic, cholinergic effects, anti-inflammatory properties, and cellular protection (Manikpuri et al., 2023). A substantial quantity of *cyamopsis tetragonoloba* is obtained as guar meal, also referred to as Korma and Churi, during the process of extracting guar gum from the seeds. This guar meal is commonly utilized as cattle feed. The proximate composition of guar gum includes protein (3.73-5 g), ash (0.83-0.7 g), crude fiber (1.24 g), fat (1.50-0.7 g), and carbohydrates (81.02-80 g) per 100 g (Prabaharan et al., 2011, Hamdani et al., 2017). The proximate composition of guar gum includes protein (3.73-5 g), ash (0.83-0.7 g), crude fiber (1.24 g), fat (1.50-0.7 g), and carbohydrates (81.02-80 g) per 100 g (Prabaharan et al., 2011, Hamdani et al., 2017).

2.2.2 Bioactive Compounds of *Cyamopsis tetragonoloba*

Cyamopsis tetragonoloba is a rich source of various bioactive compounds such as flavonoid content includes quercetin, daidzein, kaempferol, and kaempferol-3-arabinosides. Additionally, the polyphenolic constituents include gallotannins, gallic acid derivatives, myricetin-7-glucoside-3-glycoside, chlorogenic acid, ellagic acid, 2,4,3-trihydroxybenzoic acid, texasin-7-O-glucoside, and *p*-coumaryl quinic acid (Tran et al., 2020). Plant bioactive compounds are categorized as secondary metabolites, which can have pharmacological or toxic effects on humans and animals. These organic molecules produced by plants are not essential for their growth, development, or reproduction (Višnjevec et al., 2024). The qualitative and quantitative analysis of bioactive compounds in plant materials primarily depends on the selection of an appropriate extraction method. The efficiencies of both conventional and non-conventional extraction methods largely rely on critical input parameters, including understanding the plant matrix, the chemistry of bioactive compounds, and scientific expertise (Azmir et al., 2013). Also, including significant levels of ascorbic acid and condensed tannins, along with phenolic acids such as caffeic acid, gallic acid, gentisic acid, and p-coumaric. Additionally, it features

astragalin, p-hydroxycinnamyl, and coniferyl alcohol (Sharma et al., 2011). Furthermore, phytochemical analysis of the crude methanolic and flavonoid-enriched fractions obtained from the pods/seeds of *Cyamopsis tetragonoloba* was performed to identify putative flavonoids and isoflavonoids using column chromatography and thin-layer chromatography techniques. This purification process was followed by a comparative analysis of the antioxidant and anticancer activities between the crude methanolic and flavonoid-enriched fractions, shedding light on the impact of extraction procedures on the combined effects of the extracts (Asati et al., 2021). Sharma et al. (2017) and Joshi et al. (2023) reported various bioactive compounds in guar, as shown in Fig. 2.3 and Table 2.3. Overall, guar contains a substantial number of bioactive compounds and exhibits a wide range of biological functions that are beneficial to human health.

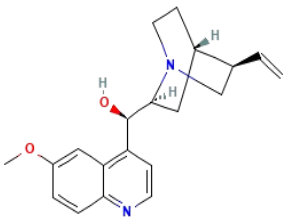

Quinone

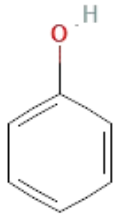

Phenol

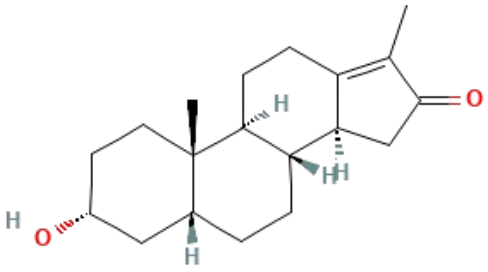

Steroids

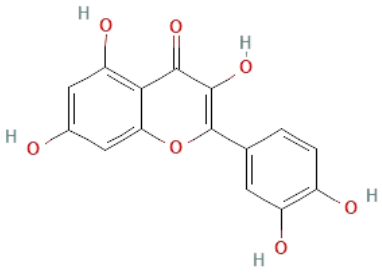

Quercetin

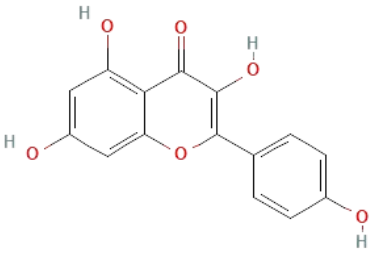

Kaempferol

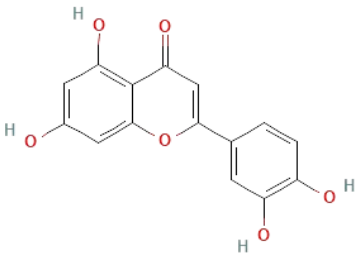

Luteolin

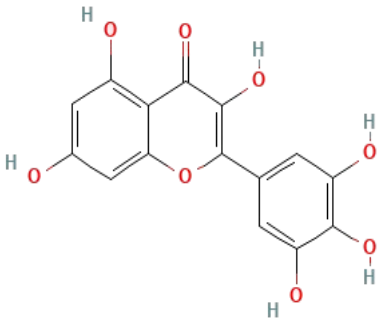

Myricetin

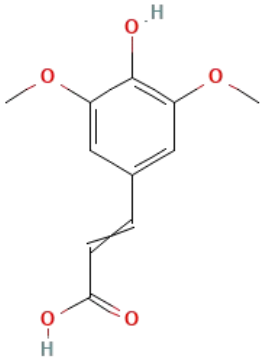

Sinapic acid

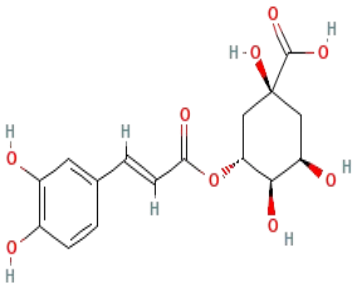

Cholorogenic acid

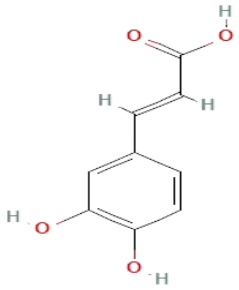

Caffeic acid

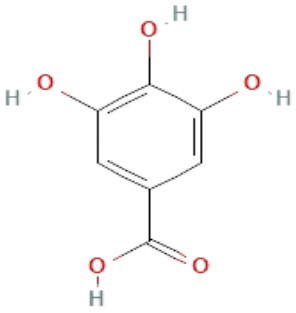

Gallic acid

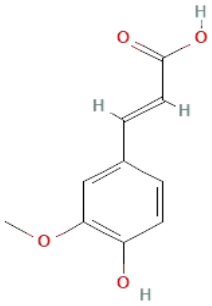

Ferulic acid

Fig. 2.3 The chemical structure of Bioactive compounds presents in *Cyamopsis tetragonoloba*

Table 2.3 Extraction methods and application of *Cyamopsis tetragonoloba*

Source	**Method of Extraction**	**Compounds**	**Yield (%)**	**Applications**	**References**
Cyamopsis tetragonoloba barks, leaves	Methanolic Extraction	Flavonoid and iso Flavonoid	80-90	Antioxidant activity Anti-cancerous activity	Asati et al., 2021
Cyamopsis tetragonoloba Seed	n-Hexane, Ethyl Acetate, Acetone, Ethanol and	Quinone, phenol, steroids, flavonoids (quercetin, kaempferol, luteolin,	27-73.1 56.4-85.7 42.5-97.6 83.3-97.1 94.5-98	-	Ganatra et al., 2013, Joshi et al., 2023

	Methanol Extraction	myricetin, and catechin), glycosides, terpenoid, tannin,			
Cyamopsis tetragonoloba Pod	Methanol and Hexane extraction	Flavonoids	80-90	Antioxidant Activity, Anticancer activity	Asati et al., 2021
Cyamopsis tetragonoloba Seed and Leaves	Ethanol and Methanol Extraction	Total Flavonoids and Total Phenolic Content	0.006003-0.020467 0.00522	Antioxidant activity	Sharma et al., 2017
Cyamopsis tetragonoloba Bean	Ethanolic extract	Tannins	-	Anti-hyperglycemic effect	Mukhtar et al., 2006
Cyamopsis tetragonoloba Seed	Methanolic Extraction	Total Flavonoids and Total Phenolic Content (Sinapic acid, cholorogenic acid, caffeic acid, gallic acids and ferulic acid)	292.39 20.58	Antioxidant activity,	Kheto et al., 2023, Sharma et al., 2017

2.2.2.1 Anticancer

Numerous scientific studies have emphasized the pharmacological potential of bioactive compounds derived from plants, known as phytochemicals, particularly in the pursuit of novel and highly effective anticancer agents (Shukla et al., 2015). In a study by Badr et al. (2014), the sulphorhodamine-B (SRB) assay was employed to evaluate the anticancer efficacy of guar seed extract against several human cancer cell lines, including prostate cancer (PC3), colon cancer

(HCT116), and intestinal carcinoma (CACO-2). The results indicated that guar seed extract exhibited anticancer activity, with the highest inhibitory concentration (IC50) values observed against CACO-2 (101.0 µg/ml), HCT116 (41.0 µg/ml), and PC-3 (40.5 µg/ml) cell lines, respectively shown in fig. 2.4. Additionally, guar gum has been recognized as a potential ingredient in anticancer therapies, particularly for colorectal cancer treatment (Mondal et al., 2023). The cytotoxic properties of guar seed extract are linked to the presence of various flavonoids, such as daidzein, genistein, quercetin, and kaempferol (Soehnlen et al., 2011). The Guar gum-capped copper oxide nanoparticles (CuO NPs/GG) exhibit significant physicochemical properties. Guar gum (GG) hydrogel was used as a natural and eco-friendly medium for the synthesis of CuO NPs. This study examines the catalytic activity of the CuO NPs/GG nanocomposite and its role in inhibiting cancer cell growth. The anti-kidney cancer effects of the nanocomposite were evaluated through an MTT assay to assess cytotoxicity. This assay was conducted on normal human endothelial cells (HUVECs) and human kidney cancer cell lines, including ACHN, CaKi-2, and HEK293, to determine the nanocomposite's selective toxicity towards cancer cells (Li et al., 2024). Administering small doses of anticancer agents directly to the colon's inner lining may help eliminate small tumors that naturally form in this area, potentially reducing the need for surgical procedures.

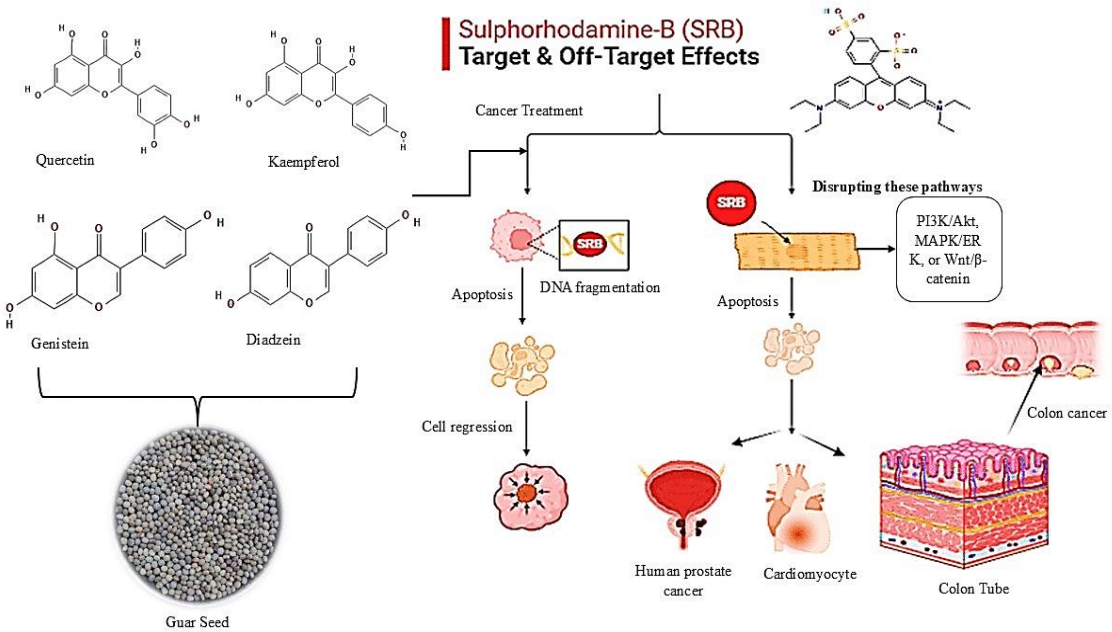

Fig. 2.4 Anticancer mechanism of *Cyamopsis tetragonoloba* seed

2.2.2.2 Antioxidant activity

Polysaccharides have shown the ability to effectively neutralize a diverse array of free radicals formed during biological and chemical reactions. The antioxidant mechanism of polysaccharides, which contributes to the regulation of oxidative stress in the circulatory system, is facilitated by the presence of electron-donating or hydrogen-donating functional groups attached to the polysaccharide chains shown in fig. 2.5. Plant-based food products are typically characterized by the presence of both antioxidants and anti-nutritional factors. Antioxidants play a crucial role in mitigating oxidative damage induced by reactive oxygen species (ROS), thereby reducing the risk of cardiovascular, neurodegenerative, and aging-related diseases, including various cancers (Hamdani and Wani, 2017). In vitro antioxidant experiments conducted by Wang et al. (2013) demonstrated that regioselective sulfation at the C-2 and C-3 positions and lower molecular weight significantly enhanced antioxidant activities. These modifications resulted in a much stronger scavenging ability of 1,1-diphenyl-2-picrylhydrazyl (DPPH) and hydroxyl radicals compared to the known C-6-sulfated derivative. Aydogdu et al. (2023) reported that guar gum films containing *Aronia melanocarpa* extract exhibited an antioxidant activity of approximately 62.07%. Hamdani and Wani (2017) investigated, the nutritional and non-nutritional properties of guar gum and demonstrated that it exhibited notable antioxidant activity. Their findings indicated that guar gum effectively chelated metal ions and scavenged DPPH radicals, highlighting its significant antioxidant potential.

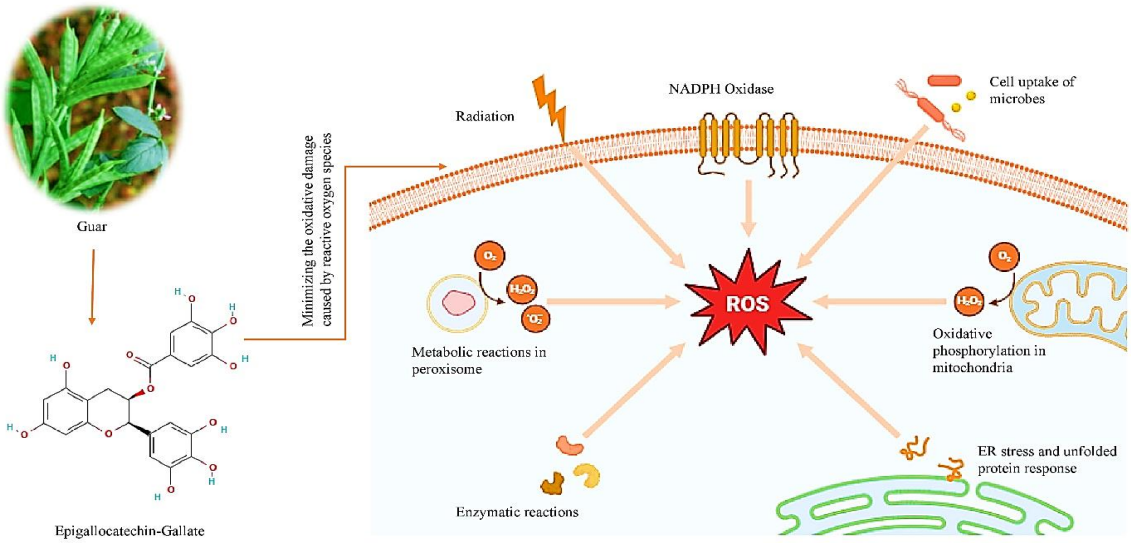

Fig. 2.5 Mechanism action of *Cyamopsis tetragonoloba* due to the existence of Epigallocatechin gallate

2.2.2.3 Anti-inflammatory

Diabetes mellitus (DM) is recognized as a major metabolic and inflammatory disorder with severe global health consequences. The signaling pathways activated directly by hyperglycemia play a crucial role in the pathogenesis of diabetic complications, primarily through the generation of reactive oxygen species (ROS), oxidative stress, and subsequent cellular apoptosis. As a result, the primary strategy in diabetes management often emphasizes the reduction of postprandial blood glucose levels (Volpe et al., 2018, Adewole et al., 2024). *Cyamopsis tetragonoloba* (guar gum) has been shown to exert anti-inflammatory effects on the intestinal epithelium by activating TLR2 and dectin-1 receptors, and by upregulating SOCS-1 expression via the JAK and cSrc signaling pathways, as illustrated in fig. 2.6. While guar gum's microbial metabolites contribute to these effects, the intact guar gum itself may also provide therapeutic benefits in the prevention or management of intestinal inflammatory diseases (Hung and Suzuki, 2017). Additionally, the combination of guar gum with other excipients in a single dosage form could optimize the physicochemical properties to achieve desired therapeutic outcomes (Jhundoo et al., 2021). *Cyamopsis tetragonoloba* (guar gum) exhibits significant potential as an anti-inflammatory agent, particularly in managing intestinal inflammatory diseases through its interaction with key signaling pathways. Its high viscosity and ability to modulate drug release make it a promising excipient for specialized therapeutic formulations.

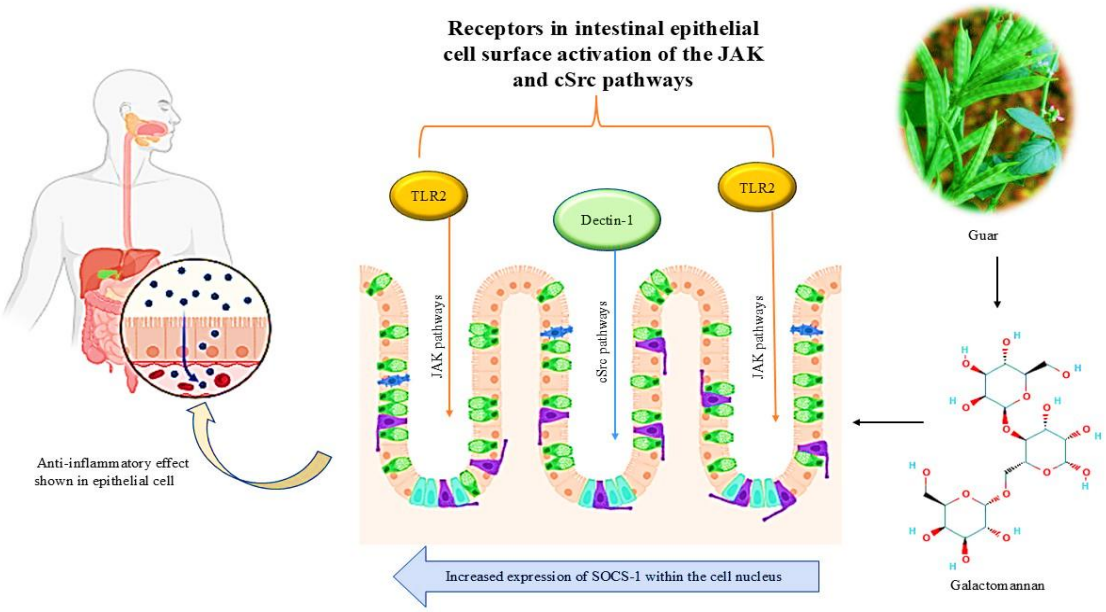

Fig. 2.6 Mechanism of action of galactomannan shows anti-inflammatory effects of *Cyamopsis tetragonoloba* gum on intestinal epithelial cells

2.2.2.4 Antidiabetic

Diabetes mellitus is a chronic and complex condition characterized by a partial, complete, or relative deficiency in insulin secretion by pancreatic β-cells, or by impaired insulin function. This disorder is associated with significant changes in plasma lipid and lipoprotein profiles, increasing the risk of premature atherosclerosis, coronary artery disease, and myocardial infarction (Yedjou et al., 2023). A 14-day administration of guar gum notably improved hyperglycemia in STZ-induced diabetic rats, demonstrated by a significant reduction in serum glucose levels and a corresponding increase in serum insulin levels is shown in fig. 2.7. Moreover, guar gum was effective in lowering insulin resistance, improving insulin sensitivity, and enhancing β-cell function (Nasry et al., 2013). The guar gum diet also led to significant decreases in serum cholesterol, triacylglycerols, LDL-C, and the atherogenic index. Compared to glibenclamide, guar gum showed superior effectiveness in treating hyperlipidemia and hyperglycemia in diabetic rats. As a result, guar gum is recommended as a reliable dietary fiber for diabetic patients (Saeed et al., 2013). The antihyperglycemic effects of certain plants are mainly due to their ability to restore pancreatic tissue function, increase insulin production, inhibit glucose absorption in the intestines, or enhance metabolite processing in insulin-dependent pathways.

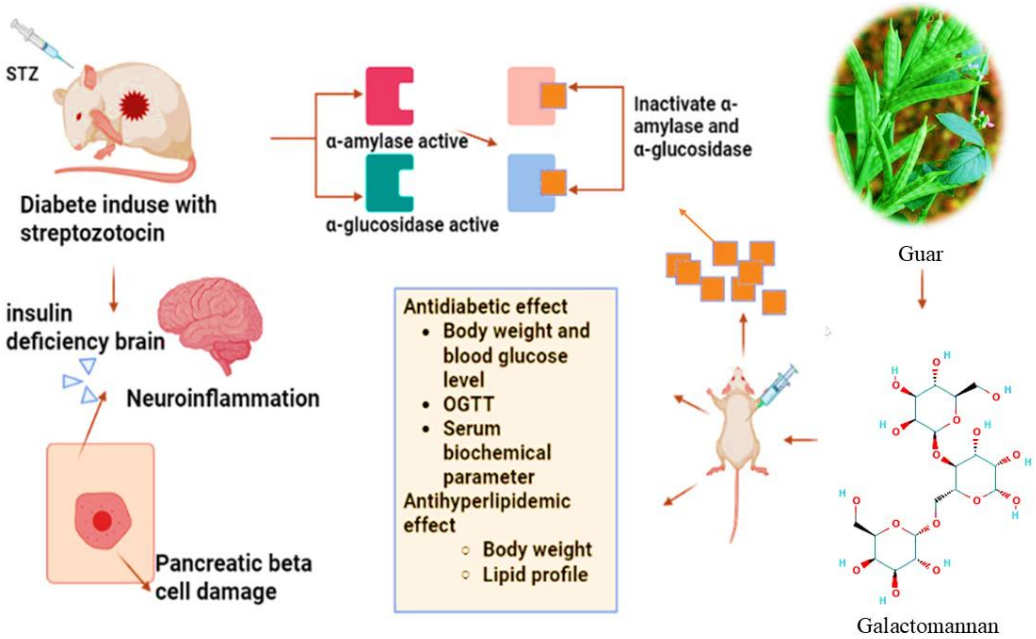

Fig. 2.7 Antidiabetic mechanism of galactomannan *Cyamopsis tetragonoloba*

2.2.3 Utilizations of *Cyamopsis tetragonoloba*

The increasing global demand for *Cyamopsis tetragonoloba* in recent decades has driven intensified research and breeding efforts in its primary cultivation regions, including India, the United States, Pakistan, Australia, and parts of southern Europe. Within Europe, the Russian Federation, alongside Germany, the Netherlands, Italy, France, Spain, and the United Kingdom, stands as one of the largest importers of guar gum, reflecting its extensive industrial and commercial applications (Vishnyakova et al., 2023).

2.2.3.1 Food applications of *Cyamopsis tetragonoloba*

Cyamopsis tetragonoloba, has gained attention as a novel food additive due to its multifaceted applications in the food industry and its endospermic seeds for the commercial extraction of guar gum. Valued by both manufacturers and consumers for its economical and natural characteristics, guar gum is extensively employed for its thickening, stabilizing, binding, and suspending properties in various liquid-solid systems shown in Table 2.4. Its solubility in cold water and ability to generate viscosity even at low concentrations make it a versatile additive (Morris et al., 2010). In food applications, guar gum influences the behavior of water, a common component, altering the texture and stability of products (Tahmouzi et al., 2023). Chemically, guar gum is composed of a mannose backbone with galactose side chains, which interact with starch, potentially inhibiting amylopectin retrogradation and affecting the amylose network. This interaction contributes to its ability to soften and retard the firming of baked goods, making it an effective additive in reducing staling (Kohajdová and Karovičová, 2008). Bread containing guar gum exhibits lower crust temperatures and a lighter crust color post-baking, attributed to an enhanced Maillard reaction facilitated by guar gum's influence on water diffusion and interaction with reducing sugars (Mohammadi Golchin et al., 2021). In pasta and noodle systems, guar gum enhances the cohesion and mechanical strength of the product, while in dairy products like yogurt, it improves viscosity and sensory properties (Sandhu et al., 2015, Lee et al., 2016). Additionally, guar gum's application as a dietary fiber in low glycemic-index food products is well recognized, with emerging uses in the development of biodegradable films for food packaging and as a wall material for flavor encapsulation (Gupta and Variyar, 2018). Its inclusion in meat products, such as chicken nuggets, has been shown to improve sensory and chemical characteristics (Yadav et al., 2013). Guar gum is also used in beverages for viscosity control and calorie reduction, and it serves as a non-caloric dietary fiber in capsule form. Its safety and efficacy extend to pet foods, salad dressings, sauces, relishes, ketchup, and canned soups, where it enhances stability, appearance, and texture. In frozen foods and meat products, guar gum binding properties improve texture and moisture retention, while in ice cream, it enhances chewiness and resistance to heat shock (Thombare et al., 2016). Furthermore, guar

gum has potential applications in low-fat chocolate production, where it can replace cocoa butter, offering benefits for individuals with diabetes by increasing the hardness and melting point of the chocolate as cocoa butter content decreases (Amir et al., 2013). Moreover, guar gum acts as an excellent stabilizer and surface capping agent, particularly in the context of coating silver nanoparticles with CMC or guar gum, which has been shown to affect the quality of mango fruits, including weight loss, firmness, and respiration rate (Hmmam et al., 2021). It has also been reported to reduce oil uptake in fried products (Sakhale et al., 2011). The growing demand for food, driven by a rising global population, has led to the generation of substantial amounts of waste and by-products in the agro-food industry. This has prompted the development of strategies to reduce waste through valorization, with a focus on conserving resources and minimizing environmental impact (Tomar et al., 2023). Common types of food-processing waste include offcuts, trimming waste, defective products, and by-products, highlighting the need for efficient resource utilization in food manufacturing. Concerns over the high production costs, toxicity, and potential health hazards associated with nanomaterials have led researchers to explore more cost-effective and environmentally friendly alternatives, such as cellulose nanoparticles. These nanoparticles, produced with tunable properties, have shown good compatibility with industrial products and offer promising potential when reinforced with biopolymers like guar gum (Palanichamy et al., 2023). Notably, the processing of *Cyamopsis tetragonoloba* gum powder generates significant quantities of lignocellulosic material, underscoring the importance of exploring sustainable applications for guar waste (Suthar, 2006). In conclusion, guar gum stands out as a versatile and valuable additive in the food industry, offering significant benefits in terms of texture, stability, and health-related applications. Its compatibility with other biopolymers and potential in biodegradable packaging materials further enhances its importance. As the demand for sustainable and efficient food production grows, guar gum role in reducing waste and enhancing product quality will likely continue to expand. The ongoing research into its applications underscores its potential to contribute to both food innovation and environmental sustainability. Guar gum is utilized for several industrial applications owing to its capacity to create hydrogen bonds with water molecules. Furthermore, it possesses a remarkable water-thickening capacity, surpassing other agents (such as Arabic and Tragacanth gums or cornflour) by a factor of eight, requiring just a minimal quantity to attain adequate viscosity. Consequently, diminished needs lower expenses, rendering the process cost-effective **(**Tahmouzi et al., 2023). In the past decade, notable advancements in guar farming have been realised in several areas of the Southern Federal District and the Lower Volga region of Russia. Furthermore, the State Register of Breeding

Achievements was augmented with 10 guar cultivars, nine of which are domestically developed. This fact is anticipated to influence the advancement of domestic gum manufacturing. Guar can further serve as animal feed and as green manure. Like other legumes, it establishes symbiotic relationships with nitrogen-fixing rhizobia and arbuscular mycorrhizal fungi (Vishnyakova et al., 2023). Consequently, the incorporation of this legume crop into agricultural production in Russia would enhance the advancement of sustainable agriculture and the technological autonomy of the national oil production sector.

Table 2.4 Applications of *Cyamopsis tetragonoloba* in the food industries

Use of *Cyamopsis tetragonoloba*	**Function**	**Mechanism**	**References**
Thickening agent	Increase viscosity and texture of food	Gums are hydrophilic biopolymers with a high molecular weight used in the food industry to regulate the rheological and functional characteristics of food items	Himashree et al., (2022)
Stabilizer	Prevent separation of component	Guar gum plays a crucial function in stabilising ice cream due to its water-binding characteristics.	Mudgil et al. (2014)
Emulsifier	Enhance water and oil binding	Emulsion stabilizer by increasing the viscosity of the aqueous phase, hence reducing the rate of separation between the water and oil phases	Kamer, (2024)

Dietary fiber source	Promote gut health and regulate digestion	Guar gum has an impact on inflammatory bowel disorder cause and intestinal microbiota activity	Paudel et al. (2024)
Gluten substitute	Provide elasticity and viscosity in gluten-free products	Utilised in gluten-free bakery product compositions to replicate gluten-like properties.	Pach et al. (2018)
Fat replacement	Enhanced the stability of meat emulsions by optimizing technological functionality and mitigating oxidative degradation.	The substitution of fat with guar or xanthan gum significantly enhanced emulsion stability and improved cooking yield	Rather et al. (2016)
Edible film	Produces edible films and coatings for preservation	Guar gum-based films act as a barrier to moisture and gas exchange, improving the shelf life of fresh produce and minimally processed foods	Gull et al. (2024)
Prebiotic	Promotes the growth of beneficial microorganisms	Guar gum hydrolysates are fermented by gut microbiota, producing short-chain fatty acids that enhance intestinal health	Zhang et al. (2024)

2.2.3.2 Packaging Industries

The rapid growth of the world population is a major factor behind the rise of the food business, resulting in a higher need for food packaging films. Currently, plastics derived from petrochemicals are the most commonly used materials for food packaging. However, the

widespread use of these plastics, sourced from unsustainable and finite petrochemical resources, poses serious environmental challenges, as they take years to degrade naturally, and their incineration releases harmful chemicals (Jiang et al., 2023). Guar gum, known for its safe, non-toxic, and cost-effective properties, is extensively utilized in various industries. In the food industry, guar gum is particularly employed in bakery and dairy products, beverages, and processed foods as an efficient gelling, thickening, softening, and preservative agent (Sharahi et al., 2023). *Cyamopsis tetragonoloba* finds applications in both the packaging industries, as illustrated in Table 1b. Bandyopadhyay et al. (2019) reported the production of hydrogel food packaging films made from a combination of bacterial cellulose, guar gum, polyvinyl pyrrolidone, and carboxymethyl cellulose. The introduction of guar gum to this composite significantly enhanced the mechanical and barrier properties of the films. Furthermore, the qualities of chitosan-guar gum composite films have been improved by incorporating active agents or blending with other polymers such as polyvinyl alcohol and gum ghatti, which have been shown to enhance the films' properties (Sharma et al., 2024). According to Parida and Biswal (2024), the resulting material exhibits greater flexibility and tensile strength compared to virgin guar gum, making it a viable alternative to synthetic polymeric materials in modern food packaging. Saurabh et al. (2018) developed a biodegradable active packaging film based on guar gum, incorporating grape pomace extract into optimized guar gum films. The effectiveness of these pomace extract-based active films was compared with cling film for extending the shelf-life of minimally processed irradiated pomegranate arils. The developed film, treated with a radiation dose of 5 KGy, extended the shelf-life of irradiated arils (2 KGy) to 12 days, compared to 8 days for samples packaged in cling film. Additionally, Bhat et al. (2022) produced a chitosan-guar gum active packaging film incorporating different concentrations of moringa extract using a solvent casting technique. This active packaging film exhibited superior antibacterial activity against *E. coli* and *S. aureus* due to the presence of moringa extract in the chitosan-guar gum-polyvinyl alcohol matrix, as compared to the control film. Overall, the integration of guar gum into various polymeric matrices has demonstrated significant potential in enhancing the mechanical, barrier, and antibacterial properties of food packaging films. These advancements suggest that guar gum-based materials could serve as effective, biodegradable alternatives to traditional synthetic polymers. The ability of guar gum to improve shelf-life and provide antimicrobial protection further underscores its value in modern food packaging applications present in Table 2.5. As research continues, guar gum's role in sustainable packaging solutions is likely to expand, contributing to reduced environmental impact.

Table 2.5 Applications of *Cyamopsis tetragonoloba* in the packaging industries

Source	**Film matrix**	**Packaging Material**	**Applications**	**References**
Watermelon rind Extract	Guar Gum	Active packaging film	Weight loss, color, Firmness and TSS changes of fresh-cut bananas	Wang et al. (2023)
Gum Gatti and cetrimide	Guar Gum	Active biobased films	Higher tensile strength, elongation at break, Thermal stability, good miscibility and good antimicrobial activity	Narasagoudr et al. (2023)
Hyacinth bean	Guar Gum	Intelligent packaging films	The water vapor barrier ability, TS, EAB, thermal stability, and free radical scavenging activity and monitor freshness of chilled shrimp and pork	Huang et al. (2023)
Wood wool	Guar Straw	Balls	Maintain the relative humidity and temperature inside the onion storage structure	Ghodki et al. (2021)
Grape pomace extract	Guar Gum	Biodegradable active film	Improve the shelf-life of minimally processed fresh-produce	Saurabh et al (2018)

Moringa extract	Guar Gum	Active packaging film	Endowed with better structural, physicochemical and mechanical properties	Bhat et al. (2022)
Walnut green husk extract	Guar Gum	Active packaging film	Good physical properties, and great potential in ensuring food quality and extending shelf-life fresh cut apple	Jiang et al. (2022)
Bael fruits	Guar Gum	Biodegradable packaging material	Prepare a biobased, bio renewable, and biodegradable cloth-to-cloth, cloth-to-paper, and paper-to-paper adhesive using natural ingredients	Sharma et al. (2021)
Macadamia skin	Guar Gum	Bio composite edible fim	Increase in tensile strength, reduction in percentage of elongation at break of films and high antimicrobial property	Saberi et al. (2017)

2.2.4 Pharmaceutical Industries

The galactomannan derived from *Cyamopsis tetragonoloba* exhibits mucoadhesive properties, antioxidant activity, gelling capability, and susceptibility to enzymatic degradation. Coupled with its wide regulatory acceptance, these attributes render it an ideal material for pharmaceutical applications and as a carrier in drug delivery systems (Alooparampil et al., 2023). *Cyamopsis tetragonoloba* is utilized for drug delivery in the colon because of its drug release-retarding characteristics and vulnerability to microbial breakdown in the large intestine. The gelling feature inhibits medication release from the dosage form and is prone to breakdown

in the intestinal environment (Patel et al., 2014). The drug release kinetics indicated that the release mechanism involves the expansion of the highly porous guar gum tablet, succeeded by erosion and diffusion processes. This delivery technique showed considerable promise for chronic therapeutic uses, especially in managing hypertension. The viability of employing GG for TB therapy was investigated by analyzing the relationship between the mannose moiety of GG and mannose receptors in human beings, to augment both mucosal and systemic immune responses via efficient vaccination methods (Karakus et al., 2019 and Amjed et al., 2024). Despite the limitations of guar gum biopolymer, including pH-dependent solubility, unregulated hydration rate, diminished viscosity during storage, and susceptibility to microbial degradation, the modification of GG functional groups and the synthesis of its derivatives enhance the physicochemical features of this gum (Sharahi et al., 2024). Inflammatory bowel disease (IBD) induces inflammation in the colonic region, which can lead to severe complications if left untreated. Chemically modified guar gum (GG)-based drug delivery systems, such as matrix tablets and interpenetrating polymer network (IPN) hydrogels, have been extensively studied for their therapeutic potential in IBD management. These formulations have demonstrated efficacy in delivering 5-aminosalicylic acid specifically to the colonic region, providing a targeted approach for IBD treatment (Mahto et al., 2019). The treatment of colorectal cancer requires targeted medicine delivery to the afflicted area. Recent improvements have concentrated on in situ forming gels and hydrogels engineered for colon-targeted administration of anticancer medicines. In situ cross-linked hydrogels utilizing guar gum dialdehyde and chitosan, specifically designed for colorectal cancer treatment. Their research emphasized the combined therapeutic benefits of curcumin and aspirin on colon cancer. These hydrogels significantly reduced medication absorption in the small intestine and upper gastrointestinal tract, facilitating regulated and localised drug release precisely at the colorectal location (Dalei et al., 2023 and Manna et al., 2024). The low toxicity, biocompatibility, biodegradability, and natural abundance of guar gum have facilitated its use as a medicinal excipient, as shown in Table 2.6. The adaptable and pH-responsive characteristics of guar gum render it a viable medication delivery system.

Table 2.6 Applications of *Cyamopsis tetragonoloba* in the pharmaceutical industries

Pharmaceutical Applications of *Cyamopsis tetragonoloba*			
Guar Derivatives	**Drug**	**Applications**	**References**

Carboxymethyl guar gum	Ceftazidime	Wound healing	Manna et al. (2015)
Guar gum oleate-*graft*-poly (methacrylic acid)	Ibuprofen	Colon-targeted drug delivery	Seeli et al. (2017)
Guar gum succinate sodium alginate beads	Ibuprofen	Colon-specific drug delivery system	Seeli et al. (2016)
Poly (diethylene glycol dimethacrylate) grafted carboxymethyl guar gum	Diclofenac sodium	Controlled overdose drug delivery	Giri et al. (2016)
Alginate guar gum hydrogel	5-aminosalicylic acid (5-ASA)	Colon targeted drug delivery	Mahto and Mishra (2019)
Guar Gum Nano silica	Diclofenac sodium	Transdermal diclofenac delivery	Giri et al. (2013)
Chemically cross-linked chitosan, guar gum and PVA	Methotrexate	Drugs used in colorectal cancer	Zarbab et al. (2023)
Capped guar gum	5 Fluorouracil	Drugs used in colorectal cancer	Kumar et al. (2019)
Carboxymethyl guar gum and gelatin	Ciprofloxacin	Drug use for antibiotic	Ghosh et al. (2018)
Chemically cross-linked guar gum with glycidyl methacrylate	Hydrocortisone	Drug used in ulcerative colitis	Reis et al. (2022)
Oxidized guar gum and chitosan	Curcumin and Aspirin	Drugs used in colorectal cancer	Dalei et al. (2023)
Capped guar gum	5-Fluorouracil	Drugs used in colorectal cancer	Kumar et al. (2017)

Graft copolymerized guar gum	5-amino salicylic acid	Drugs used in inflammatory bowel disease	Mahto and Mishra (2019)

2.2.5 Environmental Impact and Sustainability Considerations

Guar (*Cyamopsis tetragonoloba*) is a legume crop from arid and semi-arid areas that has gained popularity in sustainable agriculture due to its byproduct, guar straw. As the world focuses on renewable energy and sustainability, guar straw has garnered attention as a sustainable resource. However, like any agricultural product used for industrial purposes, scaling up its production comes with environmental concerns. The most critical problem is water usage, especially in areas that require irrigation. Although guar has some drought tolerance, its high-water demand raises sustainability issues in water-scarce regions. Life cycle assessments (LCAs) of guar production emphasize water use as a major environmental challenge. On the positive side, converting guar straw into bioenergy or biochar has been identified as a strategic method for reducing waste and producing renewable energy. Research indicates that this practice reduces the carbon footprint of guar cultivation and promotes more sustainable agricultural practices (Gahane et al., 2022, Mealing, 2021). Guar straw plays a vital role in sustainable agriculture, particularly in arid regions like the southwestern United States, where it can be used as a feedstock for bioenergy production. This not only helps manage waste but also supports carbon neutrality efforts. Additionally, cultivating guar on degraded lands improves soil health and helps combat desertification (Patel, 2024). Economically, guar straw adds value by generating revenue through bioenergy and industrial applications. Techno-economic analyses have emphasized the need to optimize agricultural practices and technologies to maximize profitability while minimizing environmental harm, ensuring that guar farming remains both viable and sustainable (Summers et al., 2021). Social sustainability is another important factor in assessing guar straw utilization. Practices such as straw management in guar cultivation can create employment opportunities and increase the income of rural communities in arid regions. However, these benefits come with social challenges, such as the disruption of traditional farming practices and competition from global markets (Mealing, 2021). Overall, the environmental and sustainability issues surrounding guar straw are complex, involving water and land use, bioenergy production, and socio-economic factors. The benefits of using guar straw, particularly for bioenergy, are significant but must be carefully balanced to avoid

potential negative impacts on both the environment and society. With ongoing research, guar straw has the potential to contribute to a more sustainable bio-economy.

2.3 *Cucumis callosus*

The Cucurbitaceae family has been extensively explored by researchers and industries for its nutritional richness and potential therapeutic properties (Mukherjee et al., 2022). However, numerous fruits within this family remain underutilized and scientifically underexplored, particularly in the context of key food and pharmaceutical applications (Macha et al., 2025). Interestingly, these underutilised fruits are often rich in essential nutrients, bioactive phytoconstituents, and potent antioxidants, making them a promising candidate for developing functional foods and therapeutic agents (Kumar et al., 2022). Despite their adaptability to marginal soils, resilience to climatic stresses, and integration into traditional food systems, many of these fruits have not received appropriate attention in mainstream research and commercial development (Bhrijvasi et al., 2024). Notably, underutilized fruits play an important role in supporting traditional diets, local food security, and ethnomedicinal practices across diverse geographical regions (Tak et al., 2024). Among these underutilized members of the Cucurbitaceae family, *Cucumis callosus* (Rottl.) Cogn is considered a promising yet neglected species, which is native to the arid and semi-arid regions of India, particularly the northwestern states. This plant is traditionally cultivated during the rainy season and is well adapted to harsh agro-climatic conditions (Deepika et al., 2024). Historically, various parts of *C. callosus* have been used in traditional medicinal systems for managing a range of ailments. For example, its seeds are recognized for their astringent and cooling properties, which are beneficial in treating bilious disorders and mucosal inflammations (Goyal et al., 2009). Although such traditional knowledge, scientific validation, and functional characterization, the nutraceutical and therapeutic potential of this plant remain limited, demanding further investigation. In addition, this fruit exhibits a wide range of pharmacological properties, including anthelmintic, anticancer, antioxidant, antidiabetic, and diuretic activities, which contribute to its traditional use in the treatment of skin diseases and snake bites (Chand et al., 2012). Additionally, its effectiveness in managing *tumpley* disease in cattle has been reported by Panda et al. (2018). *Cucumis callosus* (Rottl.) is highly relied upon in traditional medicine among the ethnic communities of Rajasthan and Gujarat, where indigenous societies use it as cogn. fruit for the treatment of urinary disorders such as urethral irritation, urinary retention, and dribbling of urine. These clinical characteristics of urolithiasis, a pathological condition marked by the formation of calculi, particularly calcium oxalate stones, within the urinary tract. Based on ethnopharmacological relevance and preliminary findings, it has been found that the

hydroethanolic extract of *C. callosus* fruit shows therapeutic effects by mitigating the severity of calcium oxalate-induced urolithiasis (Choudhary et al., 2023). There is limited data available on the traditional medicinal use of *Cucumis callosus. Cucumis callosus*, locally known as Kachri, is widely recognized in Rajasthan and neighbouring states under various language names, *kachri* or *kaohariya* in Rajasthan, *kothimbola* in Gujarat, *chibdin* in Goa, *shinde* in Maharashtra, *pehtool* in eastern Uttar Pradesh, *gurmi* in Nepal, and *chibhadin* in Punjab and Haryana, South Asia, reflecting its widespread use across regions (Gojia and Vyas, 2015). Additionally, products made from kachri—such as jam, jelly, preserves, drinks, pickles, dried fruits, and vegetables have demonstrated economic potential and may help address nutritional deficiencies in tribal communities (Pessarakli, 2016 and Deepika et al., 2023)). Taxonomically, *C. callosus* is classified as a non-dessert form of *Cucumis melo var. callosus*, a drought-resistant and underutilized cucurbit species with promising potential for cultivation in arid and semi-arid regions (Ramyashree et al., 2024). This fruit exhibits small stalks and monoecious flowers with thick, spreading hairs. Its yellow blossoms give rise to large, egg-ovoid fruits measuring approximately 4.5–6 cm in length and weighing between 50–200 g. *Callosus* fruit shows a variable rind coloration, ranging from yellow to light and dark green patterns, and contains a prominent seed cavity (Samadia et al., 2024). While immature fruits possess a bitter flavor, ripening transforms them into a palatable and nutritionally rich food source (Patel and Rauf, 2017). Nutritionally, *C. callosus* is a rich source of carbohydrates, proteins, and essential micronutrients, including fat-soluble vitamins (A, D, E, and K), and minerals such as iron, zinc, calcium, and potassium (Pessarakli, 2016). The fruit of *Cucumis callosus* contains a diverse range of approximately 32 phytochemical constituents, including alkaloids, flavonoids, tannins, glycosides, carbohydrates, proteins, and several other components (Choudhary et al., 2023). Detailed phytochemical analysis further highlights the presence of amino acids, saponins, and phytosterols, which are attributed to a wide spectrum of therapeutic effects (Patel and Rauf, 2017). It also plays vital role in the diet of rural communities, although its consumption has declined due to urbanization and the growing dependence on synthetic dietary supplements. Nevertheless, local populations continue to collect kachri fruits in limited quantities for household use (Chand et al., 2012). Traditionally, its use has been associated with the treatment of various diseases such as menstrual irregularities, jaundice, gastrointestinal disturbances, dropsy, fever, infections, and sciatica. Pharmacological studies further demonstrate its anti-inflammatory, analgesic, and antioxidant activities (Chand et al., 2012a, Chand et al., 2012b and Vaghasiya et al., 2024). Value-added products derived from kachri, such as jams, jellies, beverages, pickles, dried fruit snacks, and chutneys, not only enhance its marketability but also

contribute to the nutritional security and economic upliftment of tribal and rural populations (Gpyal et al., 2009). These functional food products have also shown potential in reducing postharvest losses by extending shelf life (Mann et al., 2013). The growing interest in traditional and nutritionally superior food sources, particularly those with therapeutic properties, underscores the need to reassess the potential of *C. callosus*. Effective commercial exploitation and value addition through innovative processing technologies can not only address nutritional deficiencies in tribal and rural communities but also enhance their economic value. This review aims to explore the traditional knowledge, comprehensive bioactivity, and vital applications of the underutilized *Cucumis callosus* fruit. In India, neglected and unexplored species hold great promise for strengthening global nutrition, particularly as the world's population grows and the demand for food increases each year.

2.3.1 Nutritional Profile of *Cucumis Callosus*

The compositional profile of kachri shows a well-balanced proximate composition with high protein content. The kachri fruit has a high nutritional profile because of significant amounts of ascorbic acid (vitamin C) and alkaloids per 100 g of the edible section, as well as low crude fiber content (Nandal and Bhardwaj, 2014). Carbohydrates, lipids and fatty acids, protein and amino acids, and organic acids are all examples of macronutrients abundant in kachri fruit. Kachri contains potential phytochemicals like phenolic chemicals, chlorophyll, carotenoids, and volatile compounds, as well as flavonoids and other polyphenols (Meena et al., 2016). Kachri has several significant minerals, including calcium, phosphorus, iron, copper, and zinc. These minerals have varying levels of bioavailability depending on each mineral's rate of absorption and are essential for the body's many metabolic processes (Kumar et al., 2021). Total ash, as well as the minerals, earthy elements, and metallic salts that are adhered to the fruit, are crucial in determining the quality of the fruit. Several authors have analyzed the proximate components of kachri, which are summarised in Table 2.7, including ash (1.46-11.8 g/100 g), crude fibre (0.23-1.46 g/100 g), Fat (1.28-6.82 g/100 g), and Moisture (88.3-88.8 g/100 g), respectively (Chande t al., 2012 and Meena et al., 2016). Kachri offers a sufficient quantity of protein while being low in fat, which is typically favoured in a calorie-controlled diet (Pessarakli, 2016). Protein content in Kachri has been reported to range from 22.06 to 23.84 g/100g (Mitharwal et al., 2022). Carbohydrates, including sugars, sugar alcohols, and fiber, are the primary source of starch and energy. Carbohydrate content affects a food product's texture, structure, and overall acceptability, along with other sensory attributes (Anonymous, 2010). Kachri is high in carbohydrates (61.21g/100g), compared to Ker (18.2g), Khejri (14.5g), and Phog (15.73g), respectively (Meena et al., 2016, Embuscado, 2014 and John et al., 2013). Still,

considering the widespread prevalence of micronutrient deficiency, it is essential to make every effort to conserve these supplies. Applying heat to anything to remove moisture does more than just reduce moisture content, it may also alter the nutritional value of what has been dried. Accordingly, the fruit serves as a rich source of nutrients, with protein functioning as a key structural element, and is recommended as part of the diet to meet the body's protein needs.

Table 2.7 Nutritional and bioactive composition of *Cucumis callosus*

Component	***Cucumis Callosus* g/100g**	**References**
Ash	1.46-11.8	Goyal et al. (2009), Panda et al. (2018), Pessarakli, (2016), Nadal and Bhardwaj, (2014), Meena et al. (2016) and Kumar et al. (2022)
Moisture	88.3-88.8	
Fat	1.28-6.82	
Protein	22.06-23.84	
Crude fibre	0.23-1.46	
Carbohydrate	7.45-61.21	
Total Phenolic Content g GAE/100g	0.0117-0.056	
Total Flavenoid content g RE and QE/ 100g	0.000471-0.240	
Crude Alkaloids	0.01296	
Tannins	0.000177	
Saponins	0.00728	
Calcium	0.00009	
Phosphorus	0.000003-0.0000029	
Iron	0.000182	
Copper	0.0000046	
Zinc	0.00052	
Vitamin C	0.02981	

2.3.2 Areas of Distribution and Harvesting of *Cucumis Callosus*

Cucumis callosus is a horticultural crop that grows in dry places with low relative humidity levels and various soil types such as gravely soil, regur Soil, sandy loam, and argillaceous mud with a slightly alkaline pH (Pessarakli, 2016). Climatic conditions and semi-desert environments are abundant in important natural resources, especially drought-resistant fruits and vegetables (John et al., 2013)). It is historically distributed between the equator's (40°) N and (40°) S, covering sections of North Africa, Pakistan, Iran, and Afghanistan, as well as India, followed by Malaysia, China, and Australia. As stated by Akashi et al., (2022), an analysis of the herbaria and also identification data suggests that germplasm-gathering excursions for this

taxon must be focused on open brightness areas in Tamil Nadu, Rajapalayam, Telangana's Rangareddy, Karnataka's Bellary, Maharashtra's Dhule, Thana, Pune, Odisha, as well as Rajasthan's well as Sujchi Saharan. It is referred to by a variety of regional names, including (kachri) in Rajasthan and Haryana, (chipper) in Punjab, as well as (pehtool) in eastern Uttar Pradesh. It goes by a variety of regional names, including chipper in Punjab, kachri in Rajasthan, Haryana, pehtool in eastern Uttar Pradesh, as well as numerous other names throughout the rest of the (Tanaka et al., 2007, Dwivedi et al., 2010, Parthasarathy and Sambandam, 2005). The Indian species *Cucumis callosus* was considered the ancestor of *C. melo* due to its free compatibility with *Cucumis melo* and the regular behaviour of chromosomes during diakinesis. *Cucumis callosus* is a wild variety found in India, as well as a species comparable to *Cucumis trigonus* (Meghwal et al., 2022). *Cucumis callosus* is cultivated in arid and semi-arid regions of India, particularly across the Aravalli range of Rajasthan, the border regions of Haryana, Rajasthan, and parts of Gujarat, where the agroclimatic conditions for its growth (Liu, 2003). The crop is generally sown during the kharif and summer seasons, uses minimal water resources, and grows in low-humidity environments. In states like Haryana and Rajasthan, an intercropping system is practiced wherein *C. callosus* is grown alongside cotton (*Gossypium spp.*) and pearl millet (*Pennisetum glaucum*), optimizing land use and promoting sustainable agriculture (Chand et al., 2012b). The growing season typically begins in mid-April and continues through mid-June, followed by profuse blooming of yellow flowers, with fruit development occurring shortly after. The fruits are soft, oblong to ellipsoid, marked with distinct green variegated patterns, and attain full maturity from September to November, which is the ideal period for large-scale harvesting and collection (Deepika et al., 2023). Tiny fruit size, prolonged maturation times, hard flesh, bitterness, and tolerance to biological as well as chemical stress are all wild qualities that might have been lost through domestication.

2.3.3 Bioactivity of *Cucumis callosus*

Fruit and vegetables, as well as plant-based foods, are usually recommended for consumption with high bioactivity of phytochemicals shown in Table 2.8, it improves the nutritional content as well as overall food quality by modifying color, taste, texture, and flavor, as well as provide therapeutic benefits in addition to basic nourishment to lower the likelihood of chronic disease development (Sood et al., 2012). Phytochemicals are also non-nutritive chemical plant compounds that occur naturally in plants. A phytochemical study of the *Cucurbitaceae* family reveals the existence of a variety of phytochemicals, such as tannins, glycosides, terpenoids, polysaccharides, saponins, resins, carotenoids, as well as phytosterols (Mukherjee et al., 2022 and Katiyar et al., 2012). Plant-based bioactive compounds, in addition to the food business,

are gaining acceptance as also being active components because of their use in pharmaceuticals lower characteristics of toxicity, particularly derived from edible plant species commonly employed along with ethnomedicine (Quideau et al., 2011 and Kumar et al., 2022). The total phenolic content in kachri typically ranges from 0.0117 to 0.056 g GAE/mg extract, while saponin levels are found at 0.000471–0.240 g RE and QE/100 g. Additionally, phenolic compounds offer plants defence mechanisms to neutralize ROS to live as well as protect against molecular damage, which is harm from bacteria, herbivores, and insects. The alcoholic extract of *Cucumis callosus* was assessed for its antioxidant activity in vitro through the utilization of the DPPH radical scavenging activity and hydrogen peroxide radical scavenging activity assay (Pessarakli, 2016, Chand et al., 2012b and Kumar et al., 2022). Saponins possess hemolytic properties, exhibit expectorant action, and have cytotoxic, anticancer, and anti-mutagenic activities. They can help reduce the risk of human tumors by preventing the proliferation of cancerous cells. Additionally, saponins are used to control bleeding and treat wounds due to their ability to precipitate and coagulate red blood cells (Katiyar et al., 2012). Tannins, also known as tannoids, are a kind of biomolecule found in plants that are produced by the phytochemical process. Tannins have astringent characteristics that help wounds and inflamed mucous membranes heal faster. Tannins have the potential to act as metal ion chelators, donate protons, and form strong hydrogen bonds, thereby enhancing their role as effective biological antioxidants. Hydrolyzable tannins are responsible for scavenging free radicals (Kapoor et al., 2020). In comparison to Kair, *Cucumis melo* var. *agrestis* (Kachri) also contains phytoconstituents such as saponins, which are primarily known to improve the immune system, lower blood cholesterol levels, and reduce the risk of intestinal tumors (Varadharajan et al., 2016). Likewise, Soam et al., 2013 reported various bioactive compounds including Imidazo(4,5-E) 1,2,4-triazin-6-one, Perhydro(4,5,7)trimethyl-3-thioxo /4,5,7-trimethyl-3-thioxooctahydro6H-imidazo (4,5)(1,2,4) triazin-6-one, 1-Diphenylsilyloxy-butane or butoxy-diphenyl-silane, 2-α-Naphthylimino-2,3-dihydro-4H1, 3-benzothiazin-4-one/2-β-naphthylimino-2,3-dihydro-4-H-1,3-benzothian-4-one, 3-Methyl-1-phenethyl-4- phenyl propionyloxy piperdine, palladium, bis2-butyl-8-quinolinolato, 2,5-Dichloro(4,6)bis-1-methyl-1H benzoimidazol-(2yl-isophthalic acid), dimethyl-ester, 5(H-Indeno1),2-b(pyrazin5-one), (6,7,8)-tribromo9-ethoxycarbonyl-N, N-diethyl1,2,3,4-tetrahydro, wilforine, wilfortrine, which are existing in the fruit as shown in (Fig. 2.8). Notably, compounds like 1-diphenylsilyloxy-butane, butoxy-diphenyl-silane, and certain quinolinolato complexes are not alkaloids but represent organosilicon derivatives, metal complexes, and heterocyclic compounds, highlighting the phytochemical complexity of the plant. Overall, it has a substantial number of

bioactive compounds and exhibits a wide range of biological functions that are beneficial to our health.

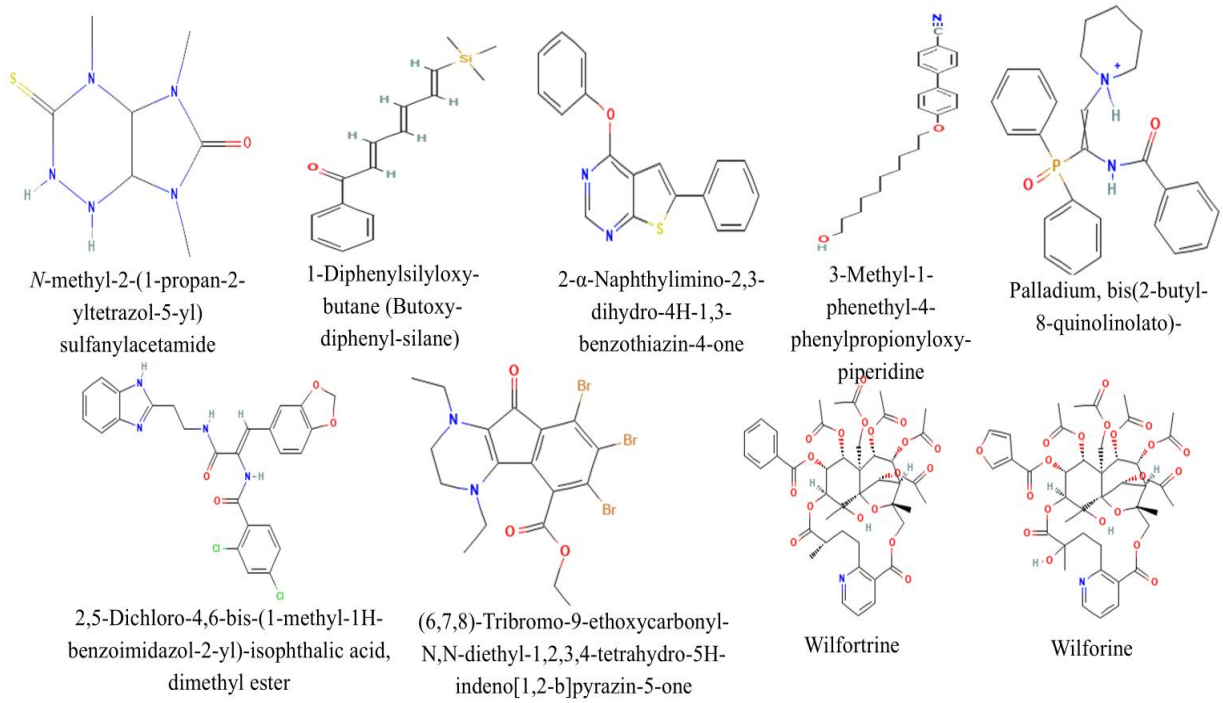

Fig. 2.8 Alkaloids and other bioactive compounds identified in *Cucumis callosus*

Table 2.8 Highlights of *Cucumis callosus* biological activity and phytochemical

Product	**Extraction technique**	**Bioactivity**	**References**
Pericarp	Conventional extraction (Methanolic extract)	Anti-diabetic α-amylase enzyme assay α-glycosidase enzyme assay	Chand et al. (2012) a
	Conventional extraction (Methanolic and Ethenolic extract)	Antimicrobial Minimum inhibitory concentration (MIC Zone of inhibition-Disk diffusion method.	Chand et al. (2012) b
Seeds	Alcoholic extract	Antioxidant activity DPPH radical scavenging activity-Hydrogen peroxide	Chand et al. (2012) b
Fruit	Conventional extraction	Anti-diabetic Antioxidant activity	Panda et al. (2018)

	(Methanolic extract)	Anti-Hyperlipidaemic activity	
Seeds	Conventional extraction (Aqueous extract)	Antioxidant activity DPPH radical scavenging activity- Hydrogen peroxide	Chand et al. (2012) a
Leaves	Conventional extraction (Ethenolic extract)	Cardioprotective and antioxidant activity	Kohajdova et al. (2013)
Fruit	Conventional extraction (Methanolic extract)	In vitro anticancer assay -Trypan blue exclusion assay - MTT assay In vivo anticancer assay	Panda et al. (2018)
Fruit	Ethyl acetate, Methanol, n-hexane, and water extraction	Antioxidant Activity DPPH radical scavenging activity ABTS assay FRAP assay	Nandal and Bhardwaj, (2014)
Phytochemicals of *Cucumis callosus* and their bioactivity			
Fruit (α and β – amyrins, Taraxerol, Lupeol, Cycloartenol,dehydro cycloartnol, Euphol, Tirucallol, Ellagitanins, Quercetin-3-rutinoside, Cucurbitacin –B)	Conventional extraction (Ethenolic extract)	Antioxidant, Anticancer, Anti-inflammatory, Antimicrobial, Detoxification, Antihyperglycemic, *Antidiabetic*	Guo et al. (2016)
Seed (Ferulic acid, Syringic acid, Methyl Gallate, Sinapic acid hexoside, Caffeoyl glucose (1,6-Di-O-galloyl glucoside) and (b) flavonol and their derivatives (Quercitrin, Chrysin, Malvidin-3-*O*-glucoside). Glycosyringic acid, Malvidin-3-*O*-glucoside and Quercitrin)	Methanolic Extraction	Anti-oxidant, Anti-inflammatory, Anticancer, Antidiabetic, Antiendotoxic, neuroprotective, Cardioprotective and Hepatoprotective effects	Deepika et al. (2023)
Pericarp	Methanolic Extraction	Cucurbitacin B, a triterpenoid, and	Panda et al. (2018)

		Ebenone leucopentaacetate	
Seed Ferulic acid, Syringic acid, Methyl gallate, Sinapic acid hexoside, Caffeoyl glucose, 1,6-di-O-galloyl glucoside, Glycosyringic acid, Quercitrin, Chrysin, Malvidin-3-O-glucoside	Methanolic Extraction	Anti-oxidant, Anti-inflammatory, Anticancer, Antidiabetic, Antiendotoxic, neuroprotective, Cardioprotective and Hepatoprotective effects	Deepika et al. (2023)

2.3.4 Biological Activities of *Cucumis callosus*

2.3.4.1 Anticancer and gastroprotective effects

Cucurbitacin B (CuB) is shown to be an anticancer agent in plants of the *Cucumis* genus. *Cucumis callosus* (MFCC) contains Cucurbitacin B (CuB) and ebenone leucopentaacetate (ELP), both of which have anticancer effects against EAC-carrying mice (Panda et al., 2018). The tetracyclic triterpenoid cucurbitacin B (CuB) targets many signalling pathways linked to tumour growth and has strong anticancer action. In vitro studies with pancreatic cancer cell lines (Panc-1 and MiaPaCa-2) and in vivo studies with Panc-1 xenograft models showed that CuB inhibited the tyrosine phosphorylation of STAT3, STAT5, and JAK2. Inducing cell cycle arrest and apoptosis, this suppression of the JAK/STAT signalling cascade leads to the downregulation of key oncogenic and anti-apoptotic proteins like c-Myc, cyclins, survivin, Bcl-xL, and Bcl-2, while simultaneously enhancing tumour suppressors like p53 (Zhang et al., 2022). We hypothesize that a comparable mechanism underlies the cytotoxic effects of MFCC in EAC-bearing mice, specifically the downregulation of JAK and STAT proteins. These proteins are essential for tumour cell proliferation and apoptosis, respectively. It shows that CuB's anticancer efficacy in different cancer models is mostly due to its capacity to disrupt important survival pathways (Wang et al., 2024). Additionally, its gastroprotective properties mediated by free radical scavenging, lipid peroxidation reduction, and mucosal defence enhancement may complement its anticancer potential by mitigating gastrointestinal side effects commonly associated with chemotherapy and NSAID use (Pathak et al., 2025 and Mohammed et al., 2025)). The gastro-protective activity of *Cucumis callosus* is characterized by scavenging of free radicals (ROS), decreased lipid peroxidation, and decreased vascular permeability (ROS), as well as increased mucosal barrier strength and presence of triterpenoids and sterols cause these effects (Gill et al., 2011). Peptic ulcers, also known as stomach ulcers,

are mucosal lesions of the gastrointestinal tract that develop due to an imbalance between aggressive factors and the mucosal defense mechanism (Vishwakarma et al., 2017). They are primarily associated with *Helicobacter pylori* infection and prolonged use of non-steroidal anti-inflammatory drugs (NSAIDs), which significantly compromise the integrity of the mucosal lining (Fig. 1h). *Cucumis callosus* contains the phytochemical substance Lupeol, which provides significant protection against stomach ulcers in all species (Tripathi et al., 2016). In *Cucumis callosus*, the presence of alkaloids and flavonoids has been reported to contribute to its ulcer-protective properties. Additionally, polyphenols play an important role in reducing free acidity, total acidity, and gastric acid volume, thereby supporting gastrointestinal health. Beyond these effects, the polyphenolic compounds exhibit strong antioxidant activity, immunomodulatory potential, and anti-inflammatory action, which collectively enhance their therapeutic relevance. Notably, due to their natural origin, these bioactive constituents are associated with fewer adverse effects compared to synthetic agents, making them particularly promising for anticancer applications

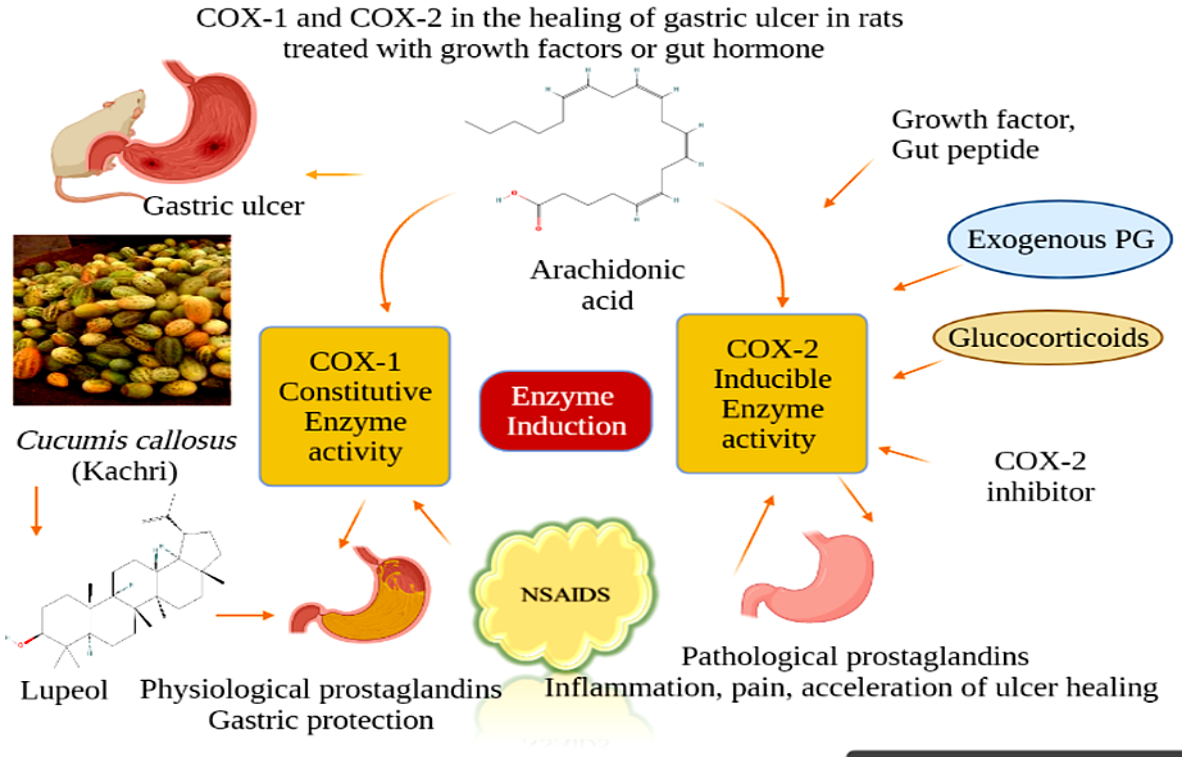

Fig. 2.9 Mechanism of antiulcer with COX-1, COX-2, and prostaglandins

2.3.4.2 Antioxidant and anti-hyperglycemic Activity

Numerous related metabolism and oxidative stress ailments, cancer, neurological disorders, and cardiovascular diseases have been linked to an excess of ROS (reactive oxygen species). *Cucumis callosus* contains a phenolic component known as Quercetin-3-rutinoside, which has

been found to have an anti-hyperglycemic effect via various modes of action, including inhibiting important enzymes such as a-amylase, a-glucosidase, and aldose-reductase (Chand et al., 2012 a). Some of these degenerative and chronic illnesses are caused by free radicals and oxidative stress and exceed the body's natural antioxidant system, which results from an imbalance in the system's oxidative processes. *Cucumis callosus* Cogn seed extract shows notable antioxidant activity, suppresses pain, scavenges radicals, and decreases ROS-induced oxidative stress (Kawamura et al., 2018). Quercetin enhances the antioxidant defence system and preserves oxidative homeostasis by influencing both the non-enzymatic and enzymatic antioxidant defence systems, as well as regulating signalling pathways like as MAPK, NRFB, AMPK, and others activated by ROS (Qi et al., 2022). By influencing redox-sensitive pathways such as NF-κB and p38MAPK/iNOS, quercetin enhances the cellular antioxidant response and mitigates oxidative damage, thereby contributing to the prevention and attenuation of disease progression. Quercetin has been reported to promote disease recovery by upregulating the expression of TNF receptor-associated factor 3 (TRAF3) while downregulating NF-κB-inducing kinase, leading to a reduction in pro-inflammatory signalling. Furthermore, in models of acute spinal cord injury, quercetin confers neuroprotective effects by elevating superoxide dismutase (SOD) activity, reducing malondialdehyde (MDA) levels, and suppressing the p38MAPK/iNOS signaling pathway (Liu et al., 2018). In the human body, the antioxidant properties of phenolic compounds as well as the decrease in levels of oxidative stress are both demonstrated (Tramutola et al., 2017). Free radical inhibitors can slow down age-related degenerative processes as well as the ageing process of individual cells (Yao et al., 2013). Quercetin-3-rutinoside exhibits anti-hyperglycemic effects by inhibiting key carbohydrate-metabolizing enzymes such as α-amylase, α-glucosidase, and aldose reductase, thereby modulating postprandial glucose levels (Fig. 2.10). The inhibition of these enzymes slows down the breakdown of complex carbohydrates and, consequently, the absorption of glucose into the bloodstream. This helps to maintain post-meal glucose homeostasis and has a positive effect on type 2 diabetes (Yao et al., 2013). Overall, the evidence highlights that *Cucumis callosus*, particularly through its phenolic component quercetin-3-rutinoside, exhibits potential antioxidant and anti-hyperglycemic activities. By inhibiting free radicals and modulating both enzymatic and non-enzymatic antioxidant defense systems, it effectively reduces oxidative stress and restores redox balance. Collectively, these mechanisms suggest that *Cucumis callosus* could be a valuable therapeutic component to overcome oxidative stress-related disorders, metabolic syndromes, and degenerative diseases, while offering a natural alternative with minimal side effects.

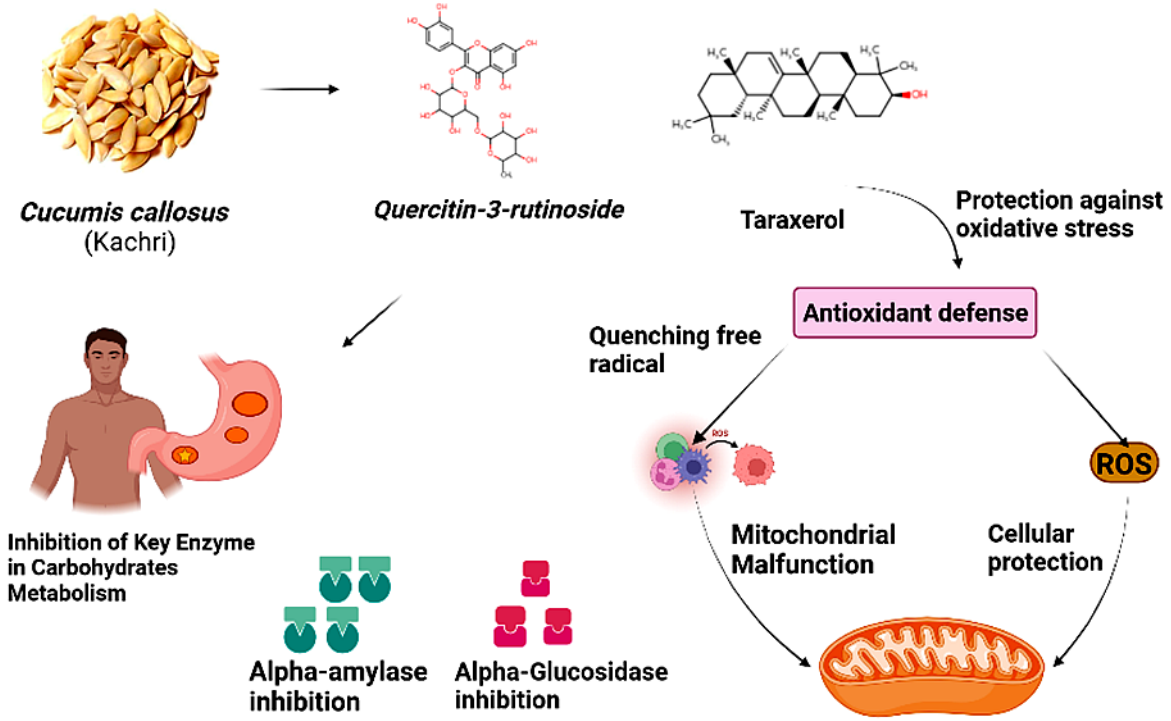

Fig. 2.10 Mechanism of action of *Cucumis callosus* due to the existence of Quercetin-3-rutinoside and Taraxerol

2.3.4.3 Anti-Inflammatory Activity

The root of *Cucumis callosus* was utilized for its anti-inflammatory and analgesic activity, and during initial phytochemical analysis of *Cucumis callosus* fruit extract of methanol (MECC), the existence of primary flavonoids, alkaloids, tannins, saponins, and triterpenoids was revealed. While *Cucumis callosus* root has been investigated for anti-inflammatory and analgesic effects, and fruit extract for nephroprotection, no detailed study has yet been conducted on the phytochemistry and pharmacology of fruit parts (pulp, peel, or seeds) with respect to inflammation. Taraxerol is a pentacyclic triterpenoid compound known for its potent anti-inflammatory activity, which is primarily attributed to its ability to modulate key molecular targets involved in inflammation. Taraxerol interferes with the activation of TAK1 and Akt, which inhibits LPS-induced iNOS, COX-2, TNF-α, IL-6, and IL-1β expressions and suppresses NF-κB activations by blocking IKK and MAPK signalling pathway in RAW264.7 macrophages (Khanra et al., 2017). Taraxerol shows anti-inflammatory effects by targeting key signalling pathways implicated in inflammatory reactions. It specifically disrupts the activation of TGF-β-activated kinase 1 (TAK1) and protein kinase B (Akt), which are essential upstream mediators in the inflammatory signalling process. Taraxerol inhibits TAK1 and Akt, thereby suppressing

the lipopolysaccharide (LPS)-induced expression of pro-inflammatory mediators such as inducible nitric oxide synthase (iNOS), cyclooxygenase-2 (COX-2), tumour necrosis factor-alpha (TNF-α), interleukin-6 (IL-6), and interleukin-1β (IL-1β) in RAW264 macrophage cells. Moreover, taraxerol blocks the activation of nuclear factor kappa B (NF-κB) by preventing the development of the IκB kinase (IKK) complex and altering the mitogen-activated protein kinase (MAPK) signalling pathway (Panda et al., 2016). Male rats weighing 170-220g were grouped into four categories, with six animals in each category. . Group I acted as the control category. MECC was used to treat groups II and III (200 and 400 mg kgG1 b.w). As a control, Indomethacin was given to Group IV (10 mg kgG1) (Dhara et al., 2000). The right-hand paws of rats were given a (0.1) mL injection of a freshly made 1% carrageenan solution to cause acute oedema. For comparison, the control paw was the left non-inflamed paw (0.9%, 0.1 mL saline injected). MECC demonstrated significant P (0.01), comparable anti-inflammatory effects to those of the conventional anti-inflammatory medication indomethacin. MECC (400 mg/kg G1) showed good action when compared to other models and significantly decreased (61%) carrageenan-induced rat paw oedema. The effects of the *Cucumis callosus* root methanol extract on various analgesic models (acetic acid-induced writhing, tail flicking, and hot plate method), as well as acute and chronic anti-inflammatory models, were observed (Choudhary et al., 2024). Treatment with *Cucumis callosus* fruit extract resulted in a significant reduction of osteopontin (OPN) expression in the affected animals. Ethylene glycol-induced nephrotoxicity led to upregulation of OPN in renal tissues, whereas administration of the extract reduced both OPN expression and the number of OPN-positive cells, indicating its potential renoprotective effect (Kumar et al., 2012). The phytochemical Taraxerol in Fig. 1i demonstrated the highest anti-inflammatory activity by inhibition (LPS-induced iNOS, COX-2, TNF-α, IL-6, and IL-1β) and suppression (NF-κB) of factors associated with the process of inflammation.

2.3.4.4 Anti-diabetic activity

Diabetes mellitus is a chronic metabolic condition caused by a lack of insulin, it disrupts glucose uptake and metabolic processes and causes a variety of short-term and long-term clinical problems. MECC's hypoglycemic activity was tested on diabetic rats induced with STZ (Streptozotocin). MECC effectively lowered blood glucose levels in diabetic rats at doses of 200 and 400 mg/kg toward normal control (Verma et al., 2015). MECC's hypoglycemic action could be attributed to increased insulin release from existing islets of Langerhans cells. To stimulate pancreatic cells, the oral hypoglycemic drug glibenclamide, which has been utilized to treat diabetes mellitus for many years, is compared to the plasma glucose-lowering activity. MECC contains secondary metabolites that have been associated with anti-diabetic effects,

which may be influenced by its antioxidant characteristics (Kumar et al., 2012 and Verma et al., 2015). Diabetic rats treated with MECC showed significant improvements in body weight compared to STZ controls, indicating MECC effectively prevented weight loss in diabetic rats (Dhara et al., 2000). The antidiabetic mechanism of quercetin-3-rutinoside shows multiple therapeutic actions targeting hyperglycaemia and associated metabolic disturbances. In diabetic rats induced with streptozotocin (STZ), which leads to insulin deficiency and pancreatic beta-cell damage, quercetin-3-rutinoside demonstrated inhibition of the carbohydrate-metabolising enzymes α-amylase and α-glucosidase. This enzymatic inhibition reduces glucose absorption, which helps to control blood glucose levels, and it also regulates neuroinflammatory responses associated with insulin deficiency in the brain. *Cucumis callosus* fruit contains significant bioactive compounds, Quercetin-3-rutinoside and lupeol, which have been reported (Fig. 2.11) to be responsible for regulating blood glucose levels and also improving glucose tolerance, reducing blood levels of glucose, GHb, TC, TG, LDL-c, and NEFA, increasing the content of HDL-c, adiponectin, as well as glycogen (Guo et al., 2016 and Prajapati et al., 2017). In diabetic rats, quercetin-3-rutinoside and lupeol reduced hyperglycemia and hyperlipidemia, and their antidiabetic effect is on body weight, blood glucose level, OGTT, Serum biochemical parameters, as well as the antihyperlipidemic effect, body weight, as a result of its lipid profile (Arora et al., 2011). The chloroform fraction of the methanolic extract of *Cucumis callosus* fruits has demonstrated significant antidiabetic potential, as evidenced by its ability to lower elevated blood glucose levels, lipid profile parameters, serum glutamate pyruvate transaminase (SGPT), serum glutamate oxaloacetate transaminase (SGOT), and serum urea in alloxan-induced diabetic rats. Additionally, it was found to enhance high-density lipoprotein (HDL) cholesterol and total protein levels. The underlying mechanism of its antidiabetic effect is likely attributed to the stimulation of insulin secretion from the remaining functional pancreatic β-cells, the release of insulin from its bound form, and/or the attenuation of oxidative stress through its antioxidant properties.

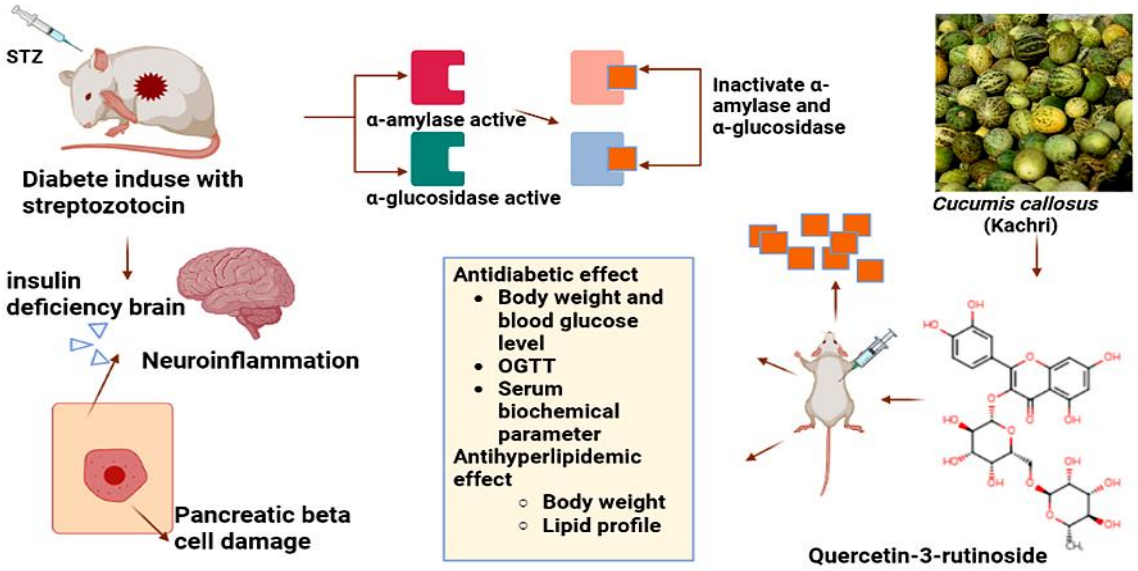

Fig. 2.11 Antidiabetic mechanism of quercetin-3-rutinoside *Cucumis callosus*

2.3.4.5 Cardiotoxicity

The cardioprotective activity of *Cucumis callosus* is well demonstrated by boosting antioxidant enzyme activity and lowering lipid oxidation. Doxorubicin-induced oxidative stress is suggested by experimental results to be caused by free radical production in cardiac cells (Ahmed et al., 2011). The ROS produced, radicals like superoxide and hydroxyl, have the possibility of damaging various intracellular components (Fig. 2.12). Heart tissue is particularly prone to free-radical injury because it has low levels of detoxifying enzymes like superoxide dismutase, catalase, and glutathione." Please also add a reference to this sentence (Hassan et al., 2025). Furthermore, doxorubicin accumulates in the heart tissue because of its strong affinity for the phospholipid components of cell membranes in the cardiac muscle cell (Phaniendra et al., 2015). Animals treated with DOX exhibited reduced SOD (superoxide dismutase) activity, while those pre-treated with *Cucumis callosus* demonstrated a dose-dependent increase in SOD activity (Rahbardar et al., 2022). Roemerine, a bioactive alkaloid derived from *Cucumis callosus*, exhibits significant cardioprotective effects, particularly against doxorubicin-induced cardiotoxicity. It enhances the activity of essential endogenous antioxidants such as glutathione, superoxide dismutase (SOD), and catalase, and it decreases free radical buildup and increases superoxide elimination. Treatment with Cucumis callosus, along with increased activity of superoxide dismutase, catalase, and glutathione, was associated with the prevention of doxorubicin-induced tissue damage and oxidative stress. Thus, *Cucumis callosus*, through its roemerine content, holds potential in attenuating cardiotoxicity by modulating oxidative stress pathways (Rahbardar et al., 2022). *Cucumis callosus*, therefore, demonstrates significant cardio-protective activity by down-regulating the DOX-induced

oxidative stress and up-regulating factors such as superoxide dismutase, catalase, and glutathione activity.

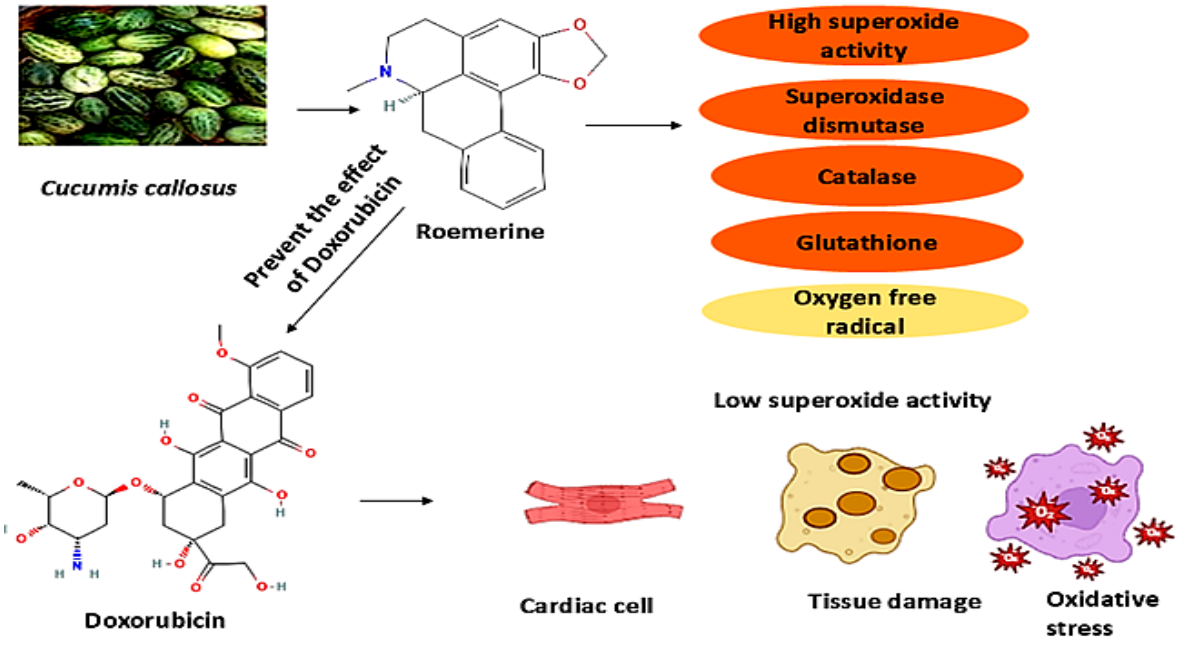

Fig. 2.12 Cardiotoxicity mechanism of roemerine of *Cucumis callosus*

2.3.4.6 Anti-urolithiatic

The efficiency of the anti-urolithiatic agent and its potential to protect the kidneys were assessed using a previously established rat model of hyperoxaluric calcium oxalate urolithiasis. The model covered a variety of targets, including the glyco-oxalate pathways, oxidant/antioxidant balance, metabolic pathways, mineral interaction, and regulation of extracellular matrix protein. Essentially, the extract from *Cucumis* fruit rectified the condition of excessive oxalate in the urine, prevented the formation of crystals, lowered the accumulation of crystals in the kidneys, reduced the oxidation of lipids, raised the activity of antioxidant enzymes such as glutathione (GSH) and catalase (CAT), and suppressed the production of osteopontin (OPN) (Choudhary et al., 2023). In conclusion, the findings revealed that *Cucumis callosus* fruit extract could exhibit significant anti-urolithiatic potential by targeting multiple pathological mechanisms associated with calcium oxalate stone formation. Through correction of hyperoxaluria, inhibition of crystal nucleation and aggregation, and reduction of renal crystal deposition, the extract effectively mitigates urolithiasis progression. Its antioxidant activity, marked by enhanced GSH and CAT levels, further protects renal tissue from oxidative injury, while suppression of osteopontin expression reduces crystal retention within the kidneys. Collectively, these outcomes highlight the therapeutic promise of *Cucumis callosus* as a natural, multi-targeted approach for the prevention and management of kidney stone disease.

2.3.5 Industrial application of *Cucumis callosus* in food

Cucumis callosus is a fruit that is not widely used or popular worldwide. However, it is more popular in semi-arid regions where it naturally grows as a secondary crop. It is frequently encountered on the shelves of vegetable shops in urban areas of India. This species is not currently part of India's conservation initiatives, as there is no identified direct threat of genetic degradation.The native population mostly consumes it in various forms, such as pickles, chutney, vegetables, jam, papdi, salad, squash, mouth freshener, juice, and acidulant, all of which are made by sun-drying (.Deepika et al., 2024) *The Cucumis callosus* cream obtained after drying the fruits is used as a souring agent in combination with other spices to make spice premixes and mouth fresheners (Gadekar et al., 2023). The declining rate drying phenomenon was noted in all of the drying runs for *Cucumis callosus* slices, thin-layer dried at various drying temperatures and thicknesses, including solar drying. The temperature and slice thickness had a substantial impact on the ascorbic acid concentration throughout the drying process of *Cucumis callosus* slices. Preserving the physical integrity and nutritional quality of *Cucumis callosus* during harvesting and post-harvest processing necessitates the use of specialised procedures. Controlled environment storage and minimum processing techniques are crucial for prolonging the usefulness and shelf life of food (Gojiya et al., 2015). The strong and resilient texture of *Cucumis callosus* makes it well-suited for use in pickles and preserves, where its crispness may be greatly appreciated. Moreover, its ability to assimilate flavors makes it suitable for producing items imbued with distinct tastes, hence increasing customer attraction and product distinctiveness (Smit et al., 2019). *Citrus paradisi* (grapefruit) was utilized in biscuit formulation. Incorporation of 5% dietary fiber from this citrus source during baking yielded biscuits with high consumer acceptability, demonstrating the potential of citrus by-products in functional bakery products (Kohajdova et al., 2013). Kuna et al. (2018), reported that *Citrus jambhiri* is an underutilized fruit used in pickle preparation and various value-added products. Irradiation at 0.25–0.5 kGy has been reported to preserve nutritional quality while reducing anti-nutritional compounds, thereby improving overall product stability and shelf life. Similarly, juice prepared from dried *Citrus aurantifolia* has been successfully processed using a continuous non-thermal juice pasteurizer employing an electric field. This method resulted in a juice product with superior nutritional value and a significantly lower microbial load compared to conventionally processed juice, highlighting its potential for producing safer and more nutrient-retentive citrus-based beverages (Altemimi et al., 2018). Overall, *Cucumis callosus* offers a promising prospect for the food processing sector to introduce new ideas and expand the variety of the worldwide food resources. The unique nutritional composition and

functional characteristics of this substance encourage further investigation and use in the creation of novel food items that appeal to health-conscious individuals seeking a varied diet. Through the resolution of current obstacles and the utilization of its complete capabilities, *C. callosus* can make a substantial impact on the improvement of food product quality and nutritional content, hence encouraging improved health outcomes.

2.3.6 Non-food applications of *Cucumis callosus*

In addition to increasing texture, the fibrous composition of *Cucumis callosus* can be utilized in the creation of nutritional supplements and functional meals that target the promotion of gastrointestinal health. The significant antioxidant activity of *Cucumis callosus* plays a crucial role in counteracting oxidative stress, therefore decreasing the likelihood of developing chronic ailments, including cancer and cardiovascular disorders. In addition, the high fiber content facilitates digestion and supports regular bowel motions, enhancing gastrointestinal health (Deva et al., 2019). Nevertheless, there are problems associated with harnessing the potential of *Cucumis callosus* in food processing. These factors encompass customer reception, where a lack of familiarity with the product may impede its market assimilation, and the requirement for standardized processing methods to guarantee product safety and uniformity (Kshash et al., 2023). Furthermore, the complete examination of the economic feasibility of cultivating *Cucumis callosus* on a large scale for commercial purposes has yet to be undertaken. Further investigation should prioritize the enhancement of farming methods, the creation of inventive food items, and the execution of thorough evaluations of both nutrition and toxicity to guarantee the secure use of goods derived from *Cucumis callosus* (Knez et al., 2023). The *Hemotocarpus validus* fruit can be employed as a natural food and dye colourant due to its high concentration of cyanidin-rich anthocyanins and pelargonidin. These natural-based colorants are anticipated to gain broader acceptance and adoption among consumers, as demonstrated by the increasing preference for natural alternatives over synthetic colorants in current consumer trends (Bohra et al., 2020). In another study, pectin extracted from the underutilized fruit *Averrhoa bilimbi* demonstrated significant potential as a biopolymer, showing suitability for the development of edible films. This highlights its promise as a distinctive biodegradable alternative for application in smart packaging of both food and non-food products (Shafie et al., 2020).

Chapter 2.4 Hypothesis

Based on the critical synthesis of literature, it is hypothesised that the valorisation of guar (*Cyamopsis tetragonoloba*) straw as a renewable source of nanocellulose and the incorporation of bioactive phytochemicals from Kachri (*Cucumis callosus*) extract can together yield a functionally superior, biodegradable packaging film with enhanced mechanical, barrier, and preservative performance suitable for fresh-cut fruits such as apples and pears. The extraction of nanocellulose from guar straw, when optimised through controlled alkaline, bleaching, and mechanical treatments, is expected to produce nanoscale fibrils with high crystallinity, aspect ratio, and surface reactivity that can act as both reinforcing agents and Pickering stabilisers within a nanoemulsion system. The integration of Kachri extract, rich in phenolic and flavonoid compounds, within this nanocellulose-stabilised matrix is anticipated to generate synergistic interactions through hydrogen bonding and interfacial adsorption, thereby enhancing film cohesion and conferring antioxidant and antimicrobial activity. The nanoemulsion-based formulation will enable uniform dispersion and controlled release of bioactive compounds, minimising phase separation and promoting long-term stability of functional activity. Consequently, the resulting film is expected to demonstrate higher tensile strength, improved elongation at break, reduced water-vapour and oxygen permeability, and sustained radical-scavenging and microbial inhibition capacity compared with conventional polysaccharide-based biodegradable films. When applied to cut fruits, this bioactive film is anticipated to delay enzymatic browning, minimise weight loss, and suppress microbial proliferation, thereby extending storage stability without compromising sensory attributes. Overall, the study hypothesises that the synergistic integration of guar-straw nanocellulose and Kachri extract via nanoemulsion technology can produce an environmentally sustainable, bioactive, and high-performance packaging film that exemplifies circular bioeconomy principles and offers a viable alternative to petroleum-based plastics in postharvest fruit preservation system.

Chapter 3 Materials and Methods

3.1 Materials

Guar (*Cyamopsis tetragonoloba*) straw and Kachri (*Cucumis callosus*) fruits were procured from Bodiwali village (29.4750° N, 75.2989° E), Fatehabad district, Haryana, India. All reagents and chemicals employed in the study were of analytical or chromatographic grade. Phenolic reference standards and routine laboratory reagents, including Folin–Ciocalteu reagent, sodium carbonate, hydrochloric acid, gallic acid, caffeic acid, *p*-coumaric acid, copper sulfate, sodium hydroxide, and petroleum ether, were obtained from reputable chemical suppliers in India. Additional chemicals such as sodium nitrite, sodium potassium tartrate, hydrogen peroxide, sulfuric acid, cetyltrimethylammonium bromide (CTAB), sodium dodecyl sulfate (SDS), ethylenediaminetetraacetic acid (EDTA), sodium tetraborate, urea, glycine, phosphate buffer salts, DTNB (5,5′-dithiobis-(2-nitrobenzoic acid)), 1-anilino-8-naphthalenesulfonate (ANS), ethanol, and DPPH were purchased from certified national and international vendors. Throughout the study, all solutions were prepared using ultrapure Milli-Q water, and analytical procedures were performed with Class A calibrated glassware to maintain accuracy and reproducibility.

3.2 Methods

3.2.1 Preparation of *Cyamopsis tetragonoloba* Straw Sample

The collected plant materials were thoroughly rinsed with distilled water to eliminate surface dust and extraneous particles. *Cyamopsis tetragonoloba* straw was dried at 60°C for 8 h in a controlled laboratory oven (Kaizen Imperial, New Delhi, India). After drying, the samples were using a mechanical mixer grinder (Sujata Supermix 900 W, Mumbai, India). The resulting powders were transferred into airtight glass containers and stored at ambient temperature (approximately 27°C) until further experimental use.

3.2.2 Proximate analysis of *Cyamopsis tetragonoloba* straw

The proximate composition of guar straw powder was determined in accordance with the standard analytical protocols prescribed by the Association of Official Analytical Chemists (AOAC, 2010).

3.3 Functional properties of *Cyamopsis tetragonoloba* straw

3.3.1 Bulk Density

The bulk density of *C. tetragonoloba* straw powder was determined following the procedure described by Shashikant et al. (2022). The powder sample was carefully introduced into a

graduated cylinder up to the 5 mL mark without applying pressure. The cylinder was gently tapped ten times to allow particle settling and to reduce inter-particle void spaces. Bulk density was calculated as the ratio of sample mass to the corresponding occupied volume and expressed in g/cm³. Tapped density was assessed by placing 5 g of the powder into a graduated cylinder and subjecting it to continuous tapping until no further reduction in volume was observed. The tapped density was computed as the ratio of the sample mass to the final compacted volume and reported in g/cm³.

3.3.2 Oil and Water Holding Properties

The water-holding capacity (WHC) and oil-holding capacity (OHC) of guar straw powder were evaluated according to the method of Chawla et al. (2020), with slight modifications. Briefly, 1 g of the sample was transferred into a pre-weighed centrifuge tube, followed by the addition of 10 mL distilled water (for WHC) or soybean oil (for OHC). The mixture was allowed to equilibrate at room temperature for 30 min to ensure adequate hydration or oil absorption. Subsequently, the tubes were centrifuged at 5000 rpm for 5 min (Beckman Coulter Avanti J-26XP, Hamburg, Germany). The supernatant was carefully decanted, and the tube containing the retained residue was reweighed. WHC and OHC were expressed as grams of water or oil retained per gram of dry sample (g/g).

3.3.3 Emulsifying properties

The emulsifying behavior of guar straw powder was investigated following the protocol reported by Rani et al. (2025). A 2% (w/v) aqueous dispersion of the powder was prepared and centrifuged at 10,000 × g to eliminate insoluble particles. Emulsion formation was carried out using a low-energy homogenization approach by gradually incorporating 2 mL soybean oil into 10 mL of the aqueous phase under continuous stirring at 1500 rpm for 2 h using a SPINOT magnetic stirrer (MC 02, Kolkata, India). The formation of a stable, milky-white emulsion indicated successful emulsification. The height of the emulsified layer was recorded using a graduated cylinder, and emulsifying activity was calculated based on the proportion of the emulsified layer relative to the total emulsion volume in eq 1 and 2.

$$\text{Emulsifying activity (\%)} = \frac{(\text{Emulsified layer height})}{(\text{Height of the total content})} \times 100 \quad (1)$$

Emulsion stability was evaluated by subjecting the emulsion to thermal treatment at 80 °C followed by centrifugation at 1500 rpm for 5 min. Emulsion stability was calculated as follows:

$$\text{Emulsifying Stability (\%)} = \frac{(\text{Emulsified layer after heating})}{(\text{Emulsified layer before heating})} \times 100 \quad (2)$$

3.3.4 Foaming capacity and stability

The foaming characteristics of *Cyamopsis tetragonoloba* straw powder were evaluated following the procedure described by Rani et al. (2025). A 2g powder was mixed in 20 ml of water powder was prepared and stirred magnetically at 500 rpm for 30 min to ensure uniform hydration. The dispersion was then centrifuged at 8,000 × g for 20 min to obtain the soluble fraction, which was used for foaming analysis. The recovered fraction was subjected to high-speed blending for approximately 10 min to induce foam formation. Immediately after whipping, the sample was transferred into a 250 mL graduated cylinder. The initial liquid volume and the total volume after foaming were recorded to determine foaming capacity and related parameters. Foam stability was evaluated after allowing the foam to stand undisturbed for 20 min at room temperature.

$$\text{Foaming capacity (\%)} = \frac{(\text{Whipped volume} - \text{the volume before whipping})}{(\text{The volume before whipping})} \times 100 \qquad (3)$$

After 20 min change in foam volume was measured as foam stability.

$$\text{Foaming stability (\%)} = \frac{(\text{Volume after resting} - \text{Volume before whipping})}{(\text{Volume before whipping})} \times 100 \qquad (4)$$

3.4 Characterization of *Cyamopsis tetragonoloba* straw

3.4.1 Fourier-transform infrared analysis (FTIR)

Fourier-transform infrared spectra of the powdered samples were recorded using an ATR-diamond crystal accessory attached to a PerkinElmer Spectrum IR 2 instrument, operated through IR-Solution 2 software. Air was used as the background reference prior to sample measurement. Spectral acquisition was performed in the mid-infrared region over a wavenumber range of 4000–400 cm^{-1} at a resolution of 4 cm^{-1}. For analysis, 10 mg of *C. tetragonoloba* straw powder was uniformly blended with 100 mg of KBr and placed on the ATR crystal surface. The resulting spectra were interpreted to identify characteristic functional groups.

3.4.2 Scanning electron microscope (SEM)

Surface morphology and structural features of the guar straw samples were examined using a Field Emission Scanning Electron Microscope (FESEM), specifically the JEOL JSM-7610F Plus model. The instrument was coupled with an Energy Dispersive Spectroscopy (EDS) unit to enable elemental characterization. For analysis, dried samples were mounted on a 2 mm elevated sample stub using carbon adhesive tape to ensure proper adhesion. Prior to imaging, specimens were sputter-coated with a thin layer of gold using a JEOL smart coater for 2 min to enhance conductivity. Micrographs were captured at 500× magnification under an accelerating voltage of 20.0 kV with a working distance of approximately 8.0 mm.

3.4.3. Thermo-gravimetric analysis (TGA)

The thermal degradation behavior of *Cyamopsis tetragonoloba* straw powder was investigated following the protocol reported by Rani et al. (2025). Thermogravimetric measurements were conducted using a PerkinElmer TGA 5000 instrument. Approximately 15 mg of accurately weighed sample was placed in an aluminum pan (PerkinElmer, 0219-0071) for analysis.

Thermal stability was assessed over a temperature range of 10–900°C at a constant heating rate of 10°C/min. To prevent oxidative reactions during analysis, the experiment was carried out under a continuous nitrogen atmosphere with a purity of 99.999%.

3.4.4 X-ray diffraction (XRD)

The crystalline characteristics of guar straw powder were determined using X-ray diffraction analysis according to the method described by Chawla et al. (2020). Diffraction measurements were performed using a PANalytical X'Pert Pro diffractometer (Netherlands) equipped with Cu Kα radiation operated at 30 kV and 30 mA. The powdered sample was uniformly distributed in an aluminum sample holder to ensure a flat and even surface. Diffraction data were collected over a 2θ range of 5° to 80° with a step size of 0.01° and a scanning duration of 10 s per step.

3.5 Ethanolic extraction from *Cyamopsis tetragonoloba* straw

An ethanolic extract of guar straw was prepared following the method outlined by Kumar et al. (2020). Briefly, 1 g of powdered sample was combined with 10 mL ethanol (solid-to-solvent ratio 1:10, w/v) and subjected to continuous agitation at 150 rpm for 24 h at 35°C using an orbital shaker. Following extraction, the solvent was evaporated under refrigerated conditions (4–7°C) to yield a concentrated extract containing bioactive constituents. The concentrated extract was then stored in airtight glass vials at −18°C until further analysis.

3.5.1 Determination of total phenols content

The total phenolic content (TPC) was determined by applying the Folin–Ciocalteu colorimetric assay with slight modifications to the standard procedure. Approximately 0.1 g of each sample was extracted with 10 mL of ethanol under appropriate conditions. From the prepared extract, 250 µL was transferred into a test tube and reacted with 10 µL of Folin–Ciocalteu reagent. Subsequently, 100 µL of 7.5% (w/v) sodium carbonate solution was incorporated into the reaction mixture. The contents were thoroughly mixed and allowed to stand at room temperature for 30 min to permit color development. Following incubation, absorbance was measured at 765 nm using a UV–Visible spectrophotometer (Evolution™ One/One Plus UV-1800, Shimadzu, Kyoto, Japan). A calibration curve was prepared using standard gallic acid solutions dissolved in methanol. The TPC values were calculated from the standard curve and expressed as milligrams of gallic acid equivalents per gram of sample (mg GAE/g).

3.5.2 Determination of total flavonoid content

Total flavonoid content (TFC) of *Cyamopsis tetragonoloba* straw extract was determined using the aluminum chloride colorimetric assay with slight modifications. Briefly, 1 g of finely powdered sample was extracted with 10 mL ethanol. Following centrifugation for 5 min at 2500 rpm, the supernatant was collected for further analysis. An aliquot of 1 mL extract was combined with 1 mL of 10% (w/v) aluminum chloride solution and 1 mL of 5% (w/v) sodium nitrite solution. The reaction mixture was allowed to stand for 6 min, after which 10 µL of 1 M sodium hydroxide was added to initiate color development. Absorbance of the resulting chromophore was measured at 510 nm using a UV–Visible spectrophotometer (UV-2600, Shimadzu Corporation, Kyoto, Japan).

3.5.3 DPPH (2,2-diphenyl picrylhydrazyl) radical-scavenging activity

The antioxidant potential of the extracts was evaluated using the DPPH radical scavenging assay with minor procedural adjustments. Ascorbic acid served as the reference standard for generating the calibration curve. For the analysis, 10 mg of guar straw sample was dissolved in 10 mL ethanol to obtain the working extract. An aliquot of 250 µL of this extract was mixed with 2.0 mL of 0.1 mM DPPH solution prepared in methanol. The reaction mixture was incubated at room temperature for 30 min in the absence of light to allow interaction between antioxidants and DPPH radicals. After incubation, absorbance was recorded at 517 nm using a UV–Visible spectrophotometer. Radical scavenging activity was determined based on the percentage decrease in absorbance, corresponding to the discoloration of DPPH from deep violet to pale yellow.

3.5.4 Quantification of polyphenolic compounds

Polyphenolic constituents present in the ethanolic extract of *C. tetragonoloba* straw were analyzed using Ultra-Performance Liquid Chromatography (UPLC). Separation was carried out on a Waters ACQUITY UPLC system (Waters Corporation, Milford, USAChromatographic separation was carried out using a reversed-phase C18 column (250 × 4.6 mm, 5 µm particle size). The mobile phase consisted of 1% (v/v) acetic acid in distilled water and acetonitrile in a volumetric ratio of 70:30. The solvent system was delivered under isocratic conditions at a constant flow rate of 1.0 mL/min. A 20 µL aliquot of the prepared extract was injected into the chromatographic system. Column temperature was maintained at 30°C to ensure consistent retention behavior and reproducible peak resolution. Detection of separated analytes was performed using a photodiode array (PDA) detector set at 280 nm.

3.5.6 Antimicrobial efficacy

The antimicrobial activity of *Cyamopsis tetragonoloba* straw extract was evaluated against selected microorganisms, including *Bacillus subtilis*, *Escherichia coli*, and *Aspergillus niger*,

using a modified agar well diffusion technique. Fresh microbial cultures (approximately 1×10^6 CFU/mL) were uniformly spread onto Mueller–Hinton agar plates to obtain a confluent microbial lawn. Wells of 6 mm diameter were aseptically created in the inoculated agar medium using a sterile cork borer. The extract was initially dissolved in dimethyl sulfoxide (DMSO), and 20 µL of this solution was carefully introduced into each well. The inoculated plates were incubated at 37°C for 24 h to allow sufficient microbial growth and diffusion of the extract into the surrounding agar matrix. Antimicrobial effectiveness was determined by measuring the diameter of the inhibition zones formed around each well, expressed in millimeters.

3.5.7 Cytotoxicity

The cytotoxic response of the prepared samples was assessed using the A549 human lung carcinoma cell line obtained from the National Centre for Cell Science (Pune, India). Cell viability was determined employing the MTT colorimetric assay. Briefly, cells were seeded in 96-well microplates at a density of 1×10^4 cells per well and allowed to attach for 24 h in Dulbecco's Modified Eagle Medium (DMEM) supplemented with 10% fetal bovine serum and 1% penicillin–streptomycin. Cultures were maintained at 37°C in a humidified incubator with 5% CO_2. Following the initial incubation period, cells were exposed to varying concentrations of the test extracts. Stock solutions were prepared in DMSO and diluted with culture medium to achieve the required treatment concentrations. After 24 h of treatment, 5 mg/mL MTT solution was added to each well, and the plates were further incubated for 2 h to permit formation of formazan crystals. Untreated cells served as the control group, while wells containing medium without MTT functioned as blanks. Subsequently, the medium was carefully removed, and the resulting formazan crystals were dissolved in 100 µL DMSO. Absorbance was measured at 540 nm using a microplate reader (Multiskan FC, Thermo Scientific).

3.5.8 Amylase Inhibition Assay

The inhibitory effect of *Cyamopsis tetragonoloba* straw extract on α-amylase activity was evaluated using a modified starch–iodine colorimetric method. Inhibition of α-amylase delays starch hydrolysis and subsequent glucose release, which is relevant for controlling postprandial hyperglycemia. To prepare the substrate solution, 500 mg of soluble starch was dissolved in 25 mL of 0.4 M sodium hydroxide and heated at 100°C for 5 min to achieve complete solubilization. After cooling to room temperature, the pH was carefully adjusted to 7.0 using hydrochloric acid, and the final volume was brought to 100 mL with distilled water. Extract solutions were prepared at varying concentrations in acetate buffer (pH 6.5). For the assay, 200 µL of the extract was combined with 400 µL starch solution and 200 µL of α-amylase enzyme

solution (20 µg/mL). The reaction mixture was incubated at 25°C for 5 min to allow enzymatic activity. The reaction was subsequently terminated by adding 800 µL of 0.1 M hydrochloric acid. Thereafter, 2 mL of iodine reagent was introduced to develop the starch–iodine complex. Absorbance was measured at 650 nm using a UV–Visible spectrophotometer to quantify residual starch and determine enzyme inhibition. The percentage inhibition of α-amylase was calculated relative to the control using the following equation (5):

$$\text{Amylase inhibitory activity (\%)} = 1 - \frac{(ODb - ODa)}{(ODd - ODc)} \times 100 \quad (5)$$

where ODb represents the absorbance of the reaction mixture containing starch and enzyme, ODs corresponds to the absorbance of the mixture containing extract, starch, and enzyme, and ODc refers to the absorbance of the control (starch without enzyme).

3.5.9 Lipase Inhibition Assay

Pancreatic lipase inhibitory activity was assessed according to a modified procedure described by Kumar et al. (2020). Lipase inhibition plays a significant role in reducing dietary fat digestion, thereby contributing to cholesterol regulation and weight management. The substrate solution consisted of a mixture containing sodium taurocholate and glycerol trioleate prepared in TES buffer (pH 7.0). Test extracts at different concentrations were prepared in the same buffer system for analysis. Test extracts at different concentrations were also prepared using the same TES buffer. For the enzymatic reaction, 200–1000 µL of lipase enzyme solution was combined with 200–1000 µL of the extract solution and 200 µL of the prepared substrate mixture in a test tube. The reaction system was incubated at 37°C for 30 min to permit lipid hydrolysis.

Following incubation, absorbance was recorded at 550 nm using a spectrophotometer. Lipase inhibitory activity was calculated according to Equation (7):

$$\text{Lipase Inhibition (\%)} = 1 - \frac{(OD2 - OD1)}{(OD4 - OD3)} \times 100 \quad (6)$$

where OD_2 represents the absorbance of the reaction mixture containing extract, substrate, and lipase enzyme, OD_1 corresponds to the mixture containing extract and substrate without enzyme, OD_3 denotes the control containing substrate and enzyme without extract, and OD_4 refers to the absorbance of the substrate solution alone.

3.6 Determination of lignocellulosic material

The lignocellulosic constituents of *Cyamopsis tetragonoloba* straw, including cellulose, hemicellulose, and lignin, were quantified using a gravimetric approach as described by Marlett et al. (1980) and Nago et al. (2022). The following procedures were employed to estimate individual fiber fractions.

3.6.1 Acid detergent fiber (ADF)

Acid detergent fiber was determined by treating the straw powder with 100 mL of cetyltrimethylammonium bromide (CTAB) solution prepared in 0.5 M sulfuric acid. The mixture was subjected to reflux heating for 60 min to facilitate removal of soluble components. After digestion, the residue was thoroughly rinsed with warm distilled water followed by acetone to eliminate residual detergent. The washed material was then dried at 104°C in a hot-air oven (Kaizen Imperial, New Delhi) until constant weight was obtained.

$$\text{Acid detergent fiber (\%)} = \frac{(W1-W2)}{W} \times 100 \quad (7)$$

W_1 represents the mass of the crucible containing the acid detergent fiber (ADF)-treated sample after drying

W_2 denotes the mass of the empty crucible

W corresponds to the initial weight of the straw powder used for analysis

3.6.2 Acid detergent lignin (ADL)

Acid detergent fiber was slowly added to 72% H2SO4 for the digestion of ADF. After being digested, the ADF was rinsed with hot distilled water and filtered through a filter paper and resultant residue dried in hot air oven at 104 °C until it reached a consistent weight.

$$\text{Acid detergent lignin (\%)} = \frac{(W1-W2)}{W} \times 100 \quad (8)$$

W_1 denotes the mass of the crucible containing the sulfuric acid (H_2SO_4)-treated sample after drying

W_2 represents the mass of the empty crucible

W corresponds to the initial weight of the straw powder subjected to analysis

The residue left over after five hours of heating at 540 °C in a muffle furnace was used to calculate the ash content.

$$\text{Ash (\%)} = \frac{(W1-W2)}{W} \times 100 \quad (9)$$

W_1 represents the mass of the crucible containing the ash residue after incineration

W_2 denotes the mass of the empty crucible

W corresponds to the initial weight of the straw powder taken for analysis

3.6.3 Neutral detergent fiber (NDF)

The neutral detergent fiber (NDF) solution was formulated using sodium dodecyl sulfate (SDS) in combination with ethylenediaminetetraacetic acid (EDTA). The prepared mixture was heated to boiling and subsequently maintained under reflux conditions for 60 min to ensure complete extraction. After completion of the reflux process, the resulting residue was thoroughly rinsed with hot distilled water, followed by washing with acetone to remove residual impurities. The cleaned residue was then dried in a hot air oven at 104 °C until a constant weight was achieved.

Neutral detergent fiber (%) = $\frac{(W1-W2)}{W} \times 100$ (10)

W_1 denotes the mass of the crucible containing the sample residue after treatment with the acid detergent fiber (ADF) solution and subsequent drying.

W_2 represents the mass of the empty crucible.

W corresponds to the initial weight of the straw powder used for the analysis.

Hemicellulose content was obtained by subtracting Acid Detergent Fiber (ADF) from Neutral Detergent Fiber (NDF):

$$\text{Hemicellulose} = \text{NDF} - \text{ADF}$$

Cellulose content was determined as the difference between Acid Detergent Fiber (ADF) and Acid Detergent Lignin (ADL):

$$\text{Cellulose} = \text{ADF} - \text{ADL}$$

Lignin content was calculated by subtracting ash content from Acid Detergent Lignin (ADL):

$$\text{Lignin} = \text{ADL} - \text{Ash}$$

3.7 Extraction of cellulose from guar straw

Cellulose was isolated from guar straw powder through an alkali delignification process, followed by conversion into nanocellulose via acid hydrolysis. Initially, 20 g of straw powder was dispersed in 400 mL of distilled water and maintained at 70 °C for 4 h to remove water-soluble impurities. The suspension was centrifuged at 10,000 rpm for 20 min (REMI Ltd., Mumbai, India), and the recovered solid fraction was dried at 55 °C in a tray dryer (Labfit India Pvt. Ltd., Gujarat, India). The dried material was subsequently subjected to alkaline treatment for delignification and purification of cellulose. Sodium hydroxide solution (5–10%, w/v) was applied at a fiber-to-solution ratio of 1:20, and the mixture was treated at 27–75 °C for 60–120 min in a Kaizen hot air oven (Imperial, New Delhi). The alkali-treated fibers were then bleached twice using a mixture of 24% hydrogen peroxide and 4% NaOH, maintaining a 1:1 fiber-to-bleaching solution ratio at 45 °C for 2 h to obtain purified cellulose.

For nanocellulose production, 20 g of the bleached cellulose was hydrolyzed using 30–40% (v/v) sulfuric acid at a fiber-to-acid ratio of 1:30 under continuous magnetic stirring for 2–4 h. The hydrolysis reaction was terminated by dilution with cold deionized water, followed by centrifugation at 10,000 rpm for 20 min to remove residual acid. Washing was repeated multiple times until the supernatant attained neutral pH (≈7.0). The resulting nanocellulose was dried at

50 °C for 12 h in a tray dryer and stored in airtight glass containers for subsequent characterization.

3.7.1 Optimization of the extraction process

Response surface methodology (RSM) is commonly used for optimize the best condition by analysing the relationship between one or more independent variables (Factors) and multiple dependent variables (response). In this study, Response Surface Methodology (RSM) was employed to optimize two different extraction processes. For cellulose extraction, three independent variables were selected: sodium hydroxide concentration (%), extraction time (min), and temperature (°C). Likewise, during the conversion of cellulose into nanocellulose, sulfuric acid concentration (%), reaction time (min), and temperature (°C) were considered as the key independent parameters. In both cases, the extraction yield (%) of cellulose and nanocellulose was taken as the response (dependent variable) for optimization. The experimental design matrix and the total number of experimental runs for each process are presented in Tables 3.1 and 3.2, respectively.

Table 3.1 Experimental design for optimization cellulose extraction process

Runs	**Factor 1 A: NaOH (%)**	**Factor 2 A: Time (min)**	**Factor 3 A: Temperature (°C)**	**Yield (%) Experimental**
1	7.5	120	51	
2	5	60	75	
3	7.5	120	51	
4	10	60	75	
5	3.29	120	51	
6	7.5	120	51	
7	5	60	27	
8	10	180	27	
9	10	60	27	
10	10	180	75	

11	7.5	120	51	
12	7.5	120	51	
13	5	180	75	
14	7.5	120	51	
15	7.5	120	91.41	
16	11.71	120	51	
17	7.5	221.04	51	
18	7.5	18.96	51	
19	5	180	27	
20	7.5	120	10.584	

Table 3.2 Experimental design for optimization nanocellulose extraction process

Runs	**Factor 1 A:H_2So_4 (%)**	**Factor 2 A: Time (min)**	**Factor 3 A: Temperature (℃)**	**Yield (%) Experimental**
1	30	4	75	
2	30	4	27	
3	40	2	27	
4	40	4	75	
5	30	2	27	
6	35	1.318	51	
7	30	2	75	
8	35	3	91.36	
9	35	3	51	
10	35	3	51	
11	35	3	51	

12	35	3	51	
13	43.40	3	51	
14	40	4	27	
15	35	3	51	
16	40	2	75	
17	35	4.68	51	
18	35	3	10.63	
19	26.59	3	51	
20	35	3	51	

3.7.2 Purity of cellulose

Cellulose purity was evaluated through acetic–nitric digestion followed by anthrone-based colorimetric quantification, with minor modifications to the method reported by Kamboj et al. (2025). Approximately 0.45–2.5 g of the cellulose-containing sample was dispersed in 100 mL distilled water to obtain a homogeneous suspension. From this suspension, 10 mL was transferred into a 1200 rpm homogenizer and processed for 5 min to ensure proper dispersion. The resulting suspension was carefully decanted, and the residual pellet was subjected to further chemical digestion. The residue was treated with 1 mL acetic–nitric reagent and heated thoroughly to achieve complete hydrolysis and additional removal of non-cellulosic components. To minimize sample loss during heating, a glass marble was placed over the reaction tube. The tubes were maintained in a boiling water bath for 30 min and subsequently centrifuged at 5000 rpm for 5 min. After discarding the supernatant, the pellet was washed repeatedly with 10 mL distilled water to eliminate remaining reagents and impurities. The purified residue was dried at 104°C until constant weight was attained and allowed to cool to room temperature prior to solubilization. An aliquot of 1.5 mL was further diluted with 150 mL distilled water and transferred into test tubes. Anthrone reagent was then added, and the reaction mixture was heated in a boiling water bath for 16 min to facilitate color development. After cooling in an ice bath for 3 min to terminate the reaction, absorbance was recorded at 620 nm using a UV–Visible spectrophotometer to determine cellulose content.

3.7.3 Characterization of Cellulose and confirming the conversion of guar straw to nanocellulose

3.7.3.1 Particle Size and zeta potential

The particle size of cellulose and nanocellulose suspensions was analysed with the help of Nano (Malvern, UK) in accordance with the methodology followed by Adeniyi et al. (2022).

3.7.3.2 Fourier-transform infrared spectroscopy (FTIR)

The identification of functional groups in the samples was performed by following the previously reported methodology described in Section 3.4.1.

3.7.3.3 Scanning electron microscope (SEM)

The surface morphology and microstructural characteristics of the samples were examined using FESEM, following the methodology described in Section 3.4.2.

3.7.3.4 Thermogravimetric analysis (TGA)

The thermal stability and degradation behavior of the samples were evaluated using thermogravimetric analysis (TGA) following the methodology described in Section 3.4.3.

3.7.3.5 Crystallinity analysis (XRD)

The crystallographic properties of the samples were examined using X-ray diffraction (XRD), following the procedure outlined earlier in Section 3.4.4.

3.7.3.6 Differential scanning calorimetry (DSC)

Differential scanning calorimetry (DSC) was employed to investigate the thermal transition characteristics of the samples following the procedure described by Zhang et al. (2023), with slight adjustments. Approximately 0.9 mg of each sample was accurately weighed and sealed in an aluminum pan prior to analysis. The temperature program was conducted over a range of 27°C to 450°C at a constant heating rate of 10°C/min. An inert nitrogen atmosphere was maintained at a flow rate of 20 mL/min to prevent oxidative degradation during heating. The resulting thermograms were analyzed using TA Instruments TRIOS software.

3.8 Preparation of *Cucumis callosus* peel, pulp and seed powder sample

Cucumis callosus fruits were cleaned using distilled water to remove impurities, then samples were subsequently subjected to oven drying at 45°C for 24 h, (Kaizen Imperial, New Delhi, India). After drying, the materials were using a mechanical mixer grinder (Sujata Supermix 900 W, Mumbai, India). The resulting powders were stored in airtight glass containers and stored at ambient temperature (approximately 27°C) until further experimental use.

3.8.1 Proximate analysis

The proximate composition of the samples was determined following the methodology described in Section 3.2.2. Standard analytical procedures were employed to quantify moisture, ash, crude protein, crude fat, and total carbohydrate contents.

3.8.2 Characterization of different parts of *Cucumis callosus* fruit

3.8.2.1 Determination of functional groups

Fourier transform infrared (FTIR) spectroscopy was employed to characterize the functional groups and investigate possible intermolecular interactions within the samples, following the methodology described in Section 3.4.1. The spectra were recorded over the specified wavenumber range to identify characteristic absorption bands corresponding to specific molecular vibrations.

3.8.2.2 Phase transition analysis

Differential scanning calorimetry (DSC) was carried out to evaluate the thermal transition behavior of the samples in accordance with the methodology described in Section 3.7.3.6. Thermograms were recorded to determine characteristic transitions, including glass transition temperature (Tg), melting temperature (Tm), and associated enthalpy changes, thereby assessing thermal stability and structural modifications.

3.8.2.3 Thermal decomposition

The weight loss profiles were performed to evaluate the thermal stability and degradation behavior of the samples in accordance with the methodology described in Section 3.4.3.

3.8.2.4 Crystallinity analysis

The diffraction patterns were recorded over the specified 2θ range to evaluate the degree of crystallinity, structural organization, and any phase transformations of the sample were investigated in accordance with the methodology described in Section 3.4.4.

3.8.2.5 Morphological analysis

Field emission scanning electron microscopy (FESEM) was employed to examine the surface morphology and microstructural features of the samples in accordance with the methodology described in Section 3.4.2. High-resolution micrographs were obtained to assess surface topology, particle distribution, and structural integrity.

3.9 Preparation of extract from *Cucumis callosus* peel, pulp and seed powder

An ethanolic and methanolic extract of *Cucumis callosus* peel powder was prepared according to the method reported by Rani et al. (2025) with minor modifications. Briefly, 15 g of samples powder was combined with 150 mL of 70% (v/v) ethanol and subjected to continuous agitation at 35°C for 48 h to facilitate extraction of bioactive constituents. Following extraction, the solvent was removed under refrigerated conditions to obtain a concentrated extract, which was subsequently utilized for further experimental procedures.

3.9.1 Biochemical analysis

3.9.1.1 Colouring pigment analysis

Pigment content was determined using an acetone-based extraction method adapted from previously reported procedures. Approximately 2 g of sample was homogenized with 25 mL of 80% (v/v) acetone to ensure complete pigment extraction. The homogenate was centrifuged at 2200 rpm for 8 min to separate the soluble fraction. The absorbance of the supernatant was measured at 663.6 nm, 646.6 nm, and 470 nm using a UV–Visible spectrophotometer. Recorded absorbance values were used to calculate the concentrations of respective pigments.

3.9.1.2 Ascorbic acid

Vitamin C content was quantified using a dye titration method. Approximately 2 g of samples was homogenized in 3% metaphosphoric acid to stabilize ascorbic acid during extraction. The homogenate was filtered, and 2 mL of the filtrate was titrated against a standardized dye solution in a conical flask until a persistent pink endpoint was achieved. The ascorbic acid concentration was calculated based on the volume of dye consumed during titration.

3.9.1.3 Determination of total phenol content

Total phenolic content of the samples was estimated according to the method described in Section 3.5.1.

3.9.1.4 Determination of total flavonoid content

Total flavonoid content was determined following the procedure outlined in Section 3.5.2.

3.9.1.5 HPLC Analysis

High-performance liquid chromatography (HPLC) was employed for detailed profiling of bioactive constituents as described previously.

3.9.1.6 Antioxidant activity

The antioxidant activity of the samples was evaluated in accordance with the procedure described in Section 3.5.3 to assess their free radical scavenging potential.

3.9.2 Antinutritional factor

3.9.2.1 Phytic acid

The phytic acid composition of the sample was determined using the method of Ojinnaka et al. (2013). 2 g of powdered sample was extracted with 50 ml of 0.2 N HCL and shaken for 35 min using an orbital shaker (Thermo Scientific, Mumbai, India), then filtered the extract for analysis. For the preparation of the standard, sodium phytate was used and diluted to the desired concentration for calibration. The reading was recorded at absorbance 519 nm using a spectrophotometer.

3.9.2.2 Oxalic acid

The titration method used for the analysis of oxalate content according to Ojinnaka et al. (2016). A 2 g sample was dispersed in 100 mL of distilled water with 5 mL of 6 M HCl and heated at

100 °C for 1 h. The pH of the sample was set to 4.0–4.5 using methyl red indicator and ammonium hydroxide after cooling. The solution was reheated to 90 °C, filtered to remove precipitates, and treated with 10 mL of 5% $CaCl_2$ under continuous stirring. Precipitates were dissolved with 20% H_2SO_4.mL after the mixture was centrifuged (3500 × g, 5 min) after being cooled overnight at 4 °C. The endpoint was pale pink after titrating against 0.05 M $KMnO_4$.

3.9.2.3 Tannin content

Tannin content was quantified based on a modified vanillin–HCl colorimetric method adapted from Zhang et al. (2024). The sample was extracted with methanol and centrifuged (REMI PR-24, REMI Ltd., Mumbai, India) for 15 minutes. This was reacted with 5.1 mL of freshly prepared vanillin–HCl reagent, composed of 4% vanillin in methanol combined with 8% hydrochloric acid in equal proportions. The reaction mixture was kept standing at ambient temperature (27 ℃) for 20 min. Readings were recorded at 500 nm using a UV–visible spectrophotometer.

3.9.2.4 Antimicrobial activity

The antimicrobial activity of the samples was evaluated in accordance with the procedure described in Section 3.5.6 to determine their inhibitory effect against selected microbial strains.

3.10.1 Formulation of nanocellulose-polyphenolic complex

Nanocellulose–polyphenolic complexes were prepared to facilitate controlled covalent interaction as described by Bains et al. (2025), with slight modifications. In brief, 1.5 g of nanocellulose powder was dispersed in 150 mL distilled water and heated at 40°C to obtain a uniform suspension. The pH of the dispersion was adjusted to 7.0 using 0.1 M NaOH under continuous stirring to ensure system stability. Subsequently, predetermined concentrations of *Cucumis callosus* peel extract (25, 50, 75, 100, 150, 200, 250, and 1000 mg) were gradually incorporated into the nanocellulose suspension. A constant stirring speed of 700 rpm was maintained for 40 min using a magnetic stirrer (Electronics and Instrumentation Engineering Pvt. Ltd., Gujarat, India) to promote homogeneous interaction and effective complex formation.

3.10.2 Determination of nanocellulose-polyphenolic complex binding efficiency

Binding efficiency of guar straw-derived nanocellulose–polyphenolic conjugates was evaluated following the procedure outlined by Chawla et al. (2023), with minor modifications. The prepared complexes were subjected to centrifugation at 30 kDa molecular weight cut-off membrane filters and rotated at 4500 rpm for 25 min to separate unbound phenolic compounds. The retained fraction was repeatedly washed with distilled water to ensure removal of any residual free phenolics. Binding efficiency (BE) of the complexes was subsequently calculated using the corresponding equation (Eq.) (11):

$$\text{Phenolic binding ration \%} = \frac{(\text{Total phenolic acid content} - \text{Dialyzed phenolic content})}{(\text{Total phenolic acis content})} \times 100 \quad (11)$$

3.10.3 Determination of functional properties of native nanocellulose and nanocellulose-polyphenolic complex

3.10.3.1 Bulk density

Bulk density of the prepared samples was assessed using the procedure outlined in Section 3.3.1.

3.10.3.2 Water absorption and oil absorption capacity

Water absorption capacity (WAC) and oil absorption capacity (OAC) of nanocellulose (NC) and nanocellulose–polyphenolic complexes (NPC) were determined following the protocol described in Section 3.3.2. These measurements were conducted to evaluate the hydration and lipid-binding behavior of the developed materials.

3.10.3.3 Foaming properties and stability

Foam formation and stability characteristics of the samples were examined according to the method specified in Section 3.3.4. These parameters were analyzed to assess the ability of the complexes to entrap air and maintain foam integrity over time.

3.10.4 Physicochemical properties

3.10.4.1 Total phenols content

Total phenolic content of the samples was quantified using the procedure detailed in Section 3.5.1. The analysis aimed to determine the concentration of phenolic constituents present in the formulations.

3.10.4.2 Total flavonoid content

Total flavonoid levels were estimated as per the methodology described in Section 3.5.2.

3.10.4.3 Antioxidant activity

The radical scavenging potential of the samples was assessed following the protocol provided in Section 3.5.3.

3.10.5 Quantification of polyphenolic compounds

Quantitative profiling of bioactive compounds was performed using high-performance liquid chromatography (HPLC), in accordance with the method described in Section 3.5.4.

3.10.6 Surface hydrophobicity (SH)

Surface hydrophobicity of nanocellulose (NC) and nanocellulose–polyphenolic complexes (NPC) was assessed using a fluorescence probe technique as described by Liu et al. (2021). Sample dispersions were prepared in 10 mM phosphate buffer (pH 7.0) at concentrations ranging from 0.2 to 2 mg/mL and allowed to equilibrate for 3 min. Subsequently, 20 µL of 8-

anilino-1-naphthalenesulfonic acid (ANS) solution was introduced into 4 mL of each dispersion. ANS selectively interacts with hydrophobic domains exposed on the sample surface. Fluorescence intensity was recorded using a spectrofluorometer at an excitation wavelength of 390 nm and an emission wavelength of 470 nm.

3.11 Characterization of nanocellulose-polyphenolic complex

3.11.1 Particle size

Particle size distribution of the prepared samples was analyzed following the protocol outlined in Section 3.7.3.1.

3.11.2 Fourier transform infrared spectroscopy

Functional groups and intermolecular interactions within the samples were investigated using FTIR spectroscopy. Spectral analysis was carried out according to the procedure described in Section 3.4.1, and the resulting spectra were interpreted to identify characteristic absorption bands corresponding to specific molecular vibrations.

3.11.3 Thermogravimetric analyzer

Thermal degradation behavior and compositional stability of the samples were examined using thermogravimetric analysis as described in Section 3.4.3. Weight loss profiles were recorded as a function of increasing temperature to evaluate thermal resistance and decomposition characteristics.

3.11.4 Differential Scanning Calorimetry

Thermal transition properties of the samples were determined by differential scanning calorimetry following the methodology detailed in Section 3.7.3.6. The obtained thermograms were analyzed to identify characteristic transition temperatures, including glass transition temperature (Tg) and melting temperature (Tm), along with associated enthalpic changes.

3.11.5 Scanning electron microscopy

The surface morphology and microstructural characteristics of the samples were examined using field emission scanning electron microscopy (FESEM) following the methodology described in Section 3.4.2. The micrographs were recorded to evaluate surface topology, structural uniformity, and morphological alterations.

3.11.6 X-ray diffraction

Diffraction patterns were recorded to evaluate the degree of crystallinity, structural organization, and potential phase modifications of the samples were investigated using X-ray diffraction (XRD) following the methodology described in Section 3.4.4.

3.12 Preparation of nanoemulsion

3.12.1 Preparation of Nanocellulose-Based Nanoemulsion

Nanocellulose-based nanoemulsions were prepared following the method described by Begum et al. (2024), with suitable modifications to optimize formulation composition and processing conditions. Ginger oil was used as the oil phase, while Tween 80 and lecithin served as surfactant and co-surfactant, respectively. Nanocellulose acted as a stabilizing biopolymeric component in the aqueous phase. Initially, predetermined concentrations of ginger oil (1–4ml/100ml v/v), Tween 80 (0.5–1ml/100ml v/v), and lecithin (0–2g/100g w/v) were added to distilled water containing a fixed nanocellulose concentration of 1.5g/100g (w/v). The mixtures were homogenized using a magnetic stirrer at 1100 rpm for 30 min to obtain a uniform nanoemulsion. The nanoemulsions were then subjected to high-pressure homogenization for droplet size reduction. Homogenization was carried out at a pressure range of 200–300 MPa for 16 passes. The number of passes was optimized based on preliminary trials to achieve nanoscale droplet size with acceptable stability and minimal aggregation. A total of sixteen nanoemulsion formulations were prepared according to the experimental design, varying the concentrations of Tween 80, ginger oil, and lecithin while maintaining constant nanocellulose content. The detailed formulation matrix is presented in Table 3.3. The resulting nanoemulsions were collected in clean glass vials and stored at room temperature for further physicochemical and stability analyses.

Table 3.3 Experimental design for the preparation of nanocellulose-based nanoemulsions with varying surfactant and oil concentrations

Sample code	**Nanocellulose (g/100ml)**	**Tween 80 (ml/100ml)**	**Ginger Oil (ml/100ml)**	**Lecithin (g/100ml)**
NC1	1.5	0.5	1	0
NC2	1.5	0.5	2	0
NC3	1.5	0.5	3	0
NC4	1.5	0.5	4	0
NC5	1.5	1	1	0
NC6	1.5	1	2	0
NC7	1.5	1	3	0
NC8	1.5	1	4	0
NC9	1.5	0.5	1	0.5
NC10	1.5	0.5	2	1

NC11	1.5	0.5	3	1.5
NC12	1.5	0.5	4	2
NC13	1.5	1	1	0.5
NC14	1.5	1	2	1
NC15	1.5	1	3	1.5
NC16	1.5	1	4	2

3.12.2 Preparation of Nanoemulsion Incorporated with *Cucumis callosus* Peel Extract

Nanoemulsions were developed using the protocol described by Ngwabebhoh et al. (2018), with modifications to incorporate *Cucumis callosus* peel extract and to optimize formulation stability. Nanocellulose concentration was maintained at 1.5 g/100 mL in all formulations, serving as the primary stabilizing agent. Tween 80 (1 mL/100 mL) and lecithin (1 g/100 mL) were used as surfactant and co-surfactant, respectively, while ginger oil (2 mL/100 mL) constituted the oil phase. The peel extract concentration was varied from 0.1 to 1.0 mg/100 mL. Based on the peel extract concentration, the nanoemulsions were coded sequentially from NE1 to NE10, as shown in Table 3.4, under continuous magnetic stirring at 1000 rpm for 35 min to ensure uniform dispersion. The prepared nanoemulsions were stored in glass vials and allowed to stand at room temperature for visual stability assessment.

Table 3.4 Optimization of *Cucumis callosus* peel extract concentration for nanoemulsion development

Sample code	**Nanocellulose (g/100ml)**	**Tween 80 (ml/100ml)**	**Ginger Oil (ml/100ml)**	**Lecithin (g/100ml)**	**Peel extract (mg/100ml)**
NE1	1.5	1	2	1	0.1
NE2	1.5	1	2	1	0.2
NE3	1.5	1	2	1	0.3
NE4	1.5	1	2	1	0.4
NE5	1.5	1	2	1	0.5
NE6	1.5	1	2	1	0.6
NE7	1.5	1	2	1	0.7

NE8	1.5	1	2	1	0.8
NE9	1.5	1	2	1	0.9
NE10	1.5	1	2	1	1

3.12.3 Formulation of Sodium Alginate–Based Nanoemulsion

Based on creaming index results, optimized Pickering nanoemulsions were further formulated with sodium alginate to enhance structural integrity and film-forming potential. In these formulations, nanocellulose (1.5 g/100 mL), Tween 80 (1 mL/100 mL), ginger oil (2 mL/100 mL), lecithin (1 g/100 mL), sodium alginate (0.4 g/100 mL), and varying concentrations of peel extract (0.1–0.8 mg/100 mL) were combined. The formulations were designated as NSE1 to NSE8 according to peel extract concentration present in Table 3.5.

Table 3.5 Optimization of sodium alginate concentration in nanocellulose-based nanoemulsions incorporated with peel extract

Sample code	**Nanocellulose (g/100ml)**	**Tween 80 (ml/100ml)**	**Ginger Oil (ml/100ml)**	**Lecithin (g/100ml)**	**Sodium alginate ((g/100ml))**	**Peel Extract (mg/100ml)**
NSE1	1.5	1	2	1	0.1	0.4
NSE2	1.5	1	2	1	0.2	0.4
NSE3	1.5	1	2	1	0.3	0.4
NSE4	1.5	1	2	1	0.4	0.4
NSE5	1.5	1	2	1	0.5	0.4
NSE6	1.5	1	2	1	0.6	0.4
NSE7	1.5	1	2	1	0.7	0.4
NSE8	1.5	1	2	1	0.8	0.4

3.12.4 Preparation of Guar Gum–Based Nanoemulsions

To further investigate the effect of polysaccharide reinforcement on nanoemulsion stability and rheological behavior, guar gum was incorporated into selected sodium alginate–based Pickering nanoemulsions. The guar gum concentration was varied from 0.1 to 0.5 g/100 mL, while maintaining constant levels of nanocellulose (1.5 g/100 mL), Tween 80 (1 mL/100 mL), ginger

oil (2 mL/100 mL), lecithin (1 g/100 mL), sodium alginate (0.4 g/100 mL), and peel extract (0.3 mg/100 mL). These formulations were coded as NG1 to NG5 as shown in Table 3.6.

Table 3.6 Optimization of guar gum concentration in sodium alginate–nanocellulose nanoemulsions

Sample Code	Nanocellulose (g/100ml)	Tween 80 (ml/100 ml)	Ginger Oil (ml/100 ml)	Lecithin (g/100ml)	Sodium alginate (g/100ml)	Peel Extract (mg/100 ml)	Guar gum (g/100ml)
NG1	1.5	1	2	1	0.3	0.4	0.1
NG2	1.5	1	2	1	0.3	0.4	0.2
NG3	1.5	1	2	1	0.3	0.4	0.3
NG4	1.5	1	2	1	0.3	0.4	0.4
NG5	1.5	1	2	1	0.3	0.4	0.5

3.12.5 Evaluation of the Physicochemical Stability of the Nanoemulsion

3.12.5.1 Creaming index

This property of nanoemulsions was monitored over a 30-day storage stability using a standardized evaluation protocol (Tosif et al., 2022), with minor modifications. For this analysis, 15 mL of each freshly prepared nanoemulsion was transferred into glass vials and stored under ambient conditions at 27 °C. The samples were visually examined at regular intervals of 5 days to monitor phase separation and physical stability. The creaming index was determined using Equation (12).

$$\text{Creaming index (\%)} = \frac{(Height\ of\ seprated\ layer\ of\ nanoemulsion)}{(Total\ height\ of\ nanoemulsion)} \times 100 \qquad (12)$$

3.12.5.2 Droplet size and zeta potential

Physicochemical characterization of the nanoemulsions was carried out to determine their droplet size profile and electrokinetic stability. Measurements were obtained using a zeta potential analyzer based on dynamic light scattering principles, in line with the approach reported by Onaizi (2022).

3.12.5.3 Antimicrobial activity

The antimicrobial efficacy of the samples was evaluated as described in Section 3.5.6 to assess their inhibitory activity. Amphotericin (25, 50 and 100 µg/well) and DMSO served as positive and negative controls, respectively.

3.12.6 Characterization of nanoemulsion

3.12.6.1 Rheology of nanoemulsion

The flow and viscoelastic characteristics of the nanocellulose-based nanoemulsions were determined using a controlled-stress rheometer (MARS III, USA) equipped with a 35 mm parallel plate assembly. The measurements were carried out under optimized experimental conditions adapted from previously reported methodologies, with appropriate modifications (Tosif et al., 2024, Miao et al., 2022). Before rheological measurements, the nanoemulsion samples were gently mixed and centrifuged at 4000 rpm for 10 min to remove any entrapped air bubbles and ensure uniformity. The linear viscoelastic region over a stress range from 0.1–1000 Pa at a fixed frequency of 1 Hz. Measurements were conducted over a temperature range of 5–50 °C to assess the temperature-dependent viscoelastic behaviour. Additionally, shear viscosity measurements were performed in rotational ramp mode using a constant gap of 1.0 mm, with shear rates varied over a defined range to assess the flow behaviour and shear-thinning characteristics of the nanoemulsion formulations.

3.12.6.2 Scanning electron microscope (SEM) of nanoemulsion

The surface morphology of the nanocellulose-based nanoemulsions was characterized using scanning electron microscopy (SEM). A small amount of sample was spread onto clean glass slides and allowed to dry at ambient conditions. The dried specimens were then affixed onto aluminum stubs using conductive carbon adhesive tape and coated with a thin layer of gold to enhance electrical conductivity. Imaging was carried out at various magnifications under an accelerating voltage of 15 kV to observe structural features.

3.12.6.3 Fourier Transform Infrared (FTIR) Analysis

Functional groups of the nanoemulsions were characterized using ATR-FTIR spectroscopy (PerkinElmer, China). For spectral acquisition, the samples were positioned directly onto the ATR crystal surface to ensure proper contact. The spectra were collected within the range of 4000–400 cm^{-1} at a resolution of 4 cm^{-1}, and several scans were accumulated and averaged to improve signal quality. A background spectrum was recorded and subtracted before sample analysis to eliminate instrumental and atmospheric interference.

3.13 Preparation of Ternary Blend and Bioactive Composite Films

Nanocellulose-based ternary blend and bioactive composite films were prepared following the method of Tosif et al. (2025) and Kasle et al., (2025) with modifications.

3.13.1 Optimization of Glycerol Concentration

The effect of the concentration of glycerol on film properties was optimized. Film-forming solutions containing nanocellulose (1.5 g/100 mL), sodium alginate (0.3 g/100 mL), and guar gum (0.3 g/100 mL) were prepared in 100 mL of double-distilled water formulations shown in

Table 2g. The solutions were mixed using a magnetic stirrer at 800 rpm for 30 min to obtain a homogeneous dispersion. Glycerol was added as a plasticizer at varying concentrations (0.1–0.6 mL/100 mL), followed by further stirring at 1000 rpm for 1h min. Based on mechanical strength, flexibility, puncture resistance, and water vapour barrier properties, the optimized glycerol concentration (0.1 mL/100 mL) was selected for further film preparation.

3.13.2 Preparation of functional with *Cucumis callosus* Peel Extract

Three control films were prepared to evaluate the individual contribution of each biopolymer. The nanocellulose (NC) control film was prepared using nanocellulose (1.5 g/100 mL), the sodium alginate (SA) control film using SA (0.3 g/100 mL), and the guar gum (GG) control film using GG (0.3 g/100 mL). All control films were plasticized with the optimized glycerol concentration and processed under identical conditions. Composite films were subsequently prepared using the optimized glycerol concentration. Two formulations were developed: a composite film without peel extract (NEW) and a bioactive composite film containing peel extract (NE). For both formulations, an aqueous suspension of nanocellulose (1.5 g/100 mL) was prepared and mixed with Tween 80 (1 mL/100 mL), ginger oil (2 mL/100 mL), and lecithin (1 g/100 mL) to form a nanoemulsion system. To this mixture, sodium alginate (0.3 g/100 mL) and guar gum (0.3 g/100 mL) were added under continuous stirring. The peel extract (0.4 mg/100 mL) was incorporated only in the NE formulation, while it was excluded from the NEW formulation presented in Table 3.7 and 3.8. The resulting film-forming solutions were stirred at 700 rpm for 35 min, followed by glycerol addition and further mixing at 1000 rpm for 1h min. The prepared film-forming solutions were poured onto leveled glass Petri dishes and allowed to dry in a hot-air tray dryer (stainless steel chamber, Rami, Ahmedabad, India) at 50 °C for 24 h to facilitate solvent evaporation. Once completely dried, the formed films were gently detached from the plates and stored in a desiccator at room temperature (approximately 28 °C) for equilibration prior to further analysis.

Table 3.7 Glycerol concentrations optimization for ternary blend films

Sample Code	**Nanocellulose (g/100 mL)**	**Sodium Alginate (g/100 mL)**	**Guar Gum (g/100 mL)**	**Glycerol (mL/100 mL)**
G0.1	1.5	0.3	0.3	0.1
G0.2	1.5	0.3	0.3	0.2
G0.3	1.5	0.3	0.3	0.3
G0.4	1.5	0.3	0.3	0.4
G0.5	1.5	0.3	0.3	0.5

G0.6	1.5	0.3	0.3	0.6

Table 3.8 Composition of control and composite films prepared using optimized glycerol concentration

Sample Code	**Nanocellulose (g/100 mL)**	**Tween 80 (mL/100 mL)**	**Ginger Oil (mL/100 mL)**	**Lecithin (g/100 mL)**	**Sodium Alginate (g/100 mL)**	**Peel Extract (mg/100 mL)**	**Guar Gum (g/100 mL)**	**Glycerol (mL/100 mL)**
NC	1.5	–	–	–	–	–	–	0.4
SA	–	–	–	–	0.3	–	–	0.4
GG	–	–	–	–	–	–	0.3	0.4
NEW	1.5	1	2	1	0.3	–	0.3	0.4
NE	1.5	1	2	1	0.3	0.4	0.3	0.4

3.13.3 Mechanical and Physicochemical Characterization of Films

3.13.3.1 Tensile strength (TS) and elongation at breakage (EB)

Tensile strength (TS) and elongation at break (%EB) were measured using a universal texture testing instrument (Model 3345, Instron Corporation, Norwood, USA) in accordance with American Society of Mechanical Engineers standard testing protocols and previously established procedures to assess the mechanical behaviour of the produced films. We used Eqs. (13) and (14) to calculate the parameters TS and %EB, respectively. Films with enhanced mechanical integrity were chosen for in-depth description and additional application-based assessment.

$$\text{TS (MPa)} = \left[\frac{(Maximum\ force\ at\ break\ during\ specimen\ break\ (F))}{(The\ initial\ cross\ (cm) - section\ area\ of\ film\ (cm)}\right] \quad (13)$$

$$\text{EB (\%)} = \left[\frac{(Film\ length\ after\ deformation - original\ length\ of\ film\ (cm))}{(Initial\ length\ of\ film\ (cm)}\right] \times 100 \quad (14)$$

3.13.3.2 Thickness

The thickness of the prepared films was determined using a precision digital micrometer (Digimatic Micrometer, Mitutoyo Corporation, Kawasaki, Japan) in accordance with the procedure reported by Chawla et al. (2023).

3.13.3.3 Water Vapor Permeability (WVP)

Water vapor permeability (WVP) of the films was determined following the procedure outlined by Chawla et al. (2023). A weighing bottle containing approximately 5 g of anhydrous calcium chloride was sealed with the test film and tightly secured to prevent vapor leakage. The initial mass of the assembly was recorded and then placed in a humidity-controlled chamber maintained at 27 °C and 75% RH using a saturated sodium chloride solution. After 24 h of exposure, the bottles were reweighed, and the moisture gain was used to calculate WVP.

3.13.3.4. Moisture Content and Transparency

The residual moisture present in the film samples was determined by oven-drying to constant mass. Pre-weighed film specimens were placed in a controlled drying environment with phosphorus pentoxide (P_2O_5) as a desiccant and maintained at 60 °C for 24 h. After the drying period, the samples were cooled in a desiccator and weighed again. The moisture percentage was calculated from the reduction in mass relative to the initial weight of the films.

Optical transparency was assessed by measuring the light transmittance of rectangular film strips (1 × 5 cm) at 660 nm using a UV–visible spectrophotometer. Transparency values were derived from the recorded absorbance data using Eq. (15).

$$\text{Transmittance (\%)} = \left(\frac{Absorbance\ (A660)}{Thickness\ (mm)}\right) \quad (15)$$

3.13.3.5 Puncture strength

Puncture properties of the film samples were evaluated following the procedure described by Alexandre et al. (2016). Circular film specimens were fixed in a test holder (52.6 mm diameter) and penetrated using a cylindrical probe (3 mm diameter) at a constant crosshead speed of 1 mm/s.

3.13.3.6 Antimicrobial activity

The antimicrobial performance of the developed packaging films was evaluated as described in Section 3.12.5.3 to determine their inhibitory effect against selected foodborne and spoilage microorganisms.

3.13.4 Characterization of films

3.13.4.1 Morphological Analysis

The surface morphology of the developed film samples was examined using a field emission scanning electron microscope (FESEM) (Hitachi SU3500, Hitachi High-Technologies Corporation, Tokyo, Japan). Film specimens were carefully sectioned and mounted on metallic stubs using double-sided conductive carbon tape to ensure proper adhesion. Microstructural observations were performed at magnifications of 500× and 1000× to evaluate surface homogeneity and detect possible structural irregularities.

3.13.4.2 Functional Group Analysis (FTIR)

Fourier-transform infrared spectroscopy was employed to investigate the chemical structure and intermolecular interactions of the film samples. Spectral measurements were conducted using an FTIR spectrometer (ALPHA, Bruker, Germany) at ambient temperature.

Spectra were recorded following the operational conditions described previously (Section 3.10.6.3), and the resulting absorption bands were analyzed to identify characteristic functional groups present in the films.

3.13.4.3 Thermogravimetric Analysis (TGA)

Thermal stability and degradation behavior of the film samples were assessed using thermogravimetric analysis with a DTG-60 instrument (Shimadzu). Approximately 7 mg of accurately weighed sample was placed in a sample pan and subjected to heating from 25°C to 600°C at a constant rate of 10°C/min under controlled atmospheric conditions.

3.13.4.4 X-ray Diffraction (XRD) Analysis

X-ray diffraction analysis was performed to examine the crystalline characteristics and structural organization of the films. Diffraction patterns were obtained using an X'Pert PRO MPD diffractometer (PANalytical, Netherlands). Data acquisition was carried out over the specified scanning range under standard operational settings to evaluate crystalline and amorphous regions.

3.13.4.5 Differential Scanning Calorimetry (DSC)

The thermal transition properties of the control and functional film samples were examined using differential scanning calorimetry (DSC). The measurements were conducted on a DSC instrument (TA Instruments Q2000, TA Instruments, New Castle, USA) equipped with a single-furnace system and precise temperature control sensors. The samples were sealed in standard aluminum pans prior to analysis to ensure accurate thermal evaluation.

3.13.5 Biodegradability of packaging film

3.13.5.1 Dry method

The biodegradability of the prepared films was evaluated using a pot burial method under dry soil conditions, followed method of Kamboj et al. (2025) with suitable modifications. Plastic pots with a total height of 12.5 cm were filled with 1 kg of air-dried garden soil, and circular film samples (90 mm diameter) were accurately weighed and buried in the soil at a depth of 9 cm. The pots were maintained under ambient laboratory conditions at a temperature of 27 ± 5 °C and a relative humidity of 70 ± 5% throughout the experimental period. The soil was kept under dry conditions, and no water was added or sprayed during the study. Biodegradation of the films was monitored at predetermined intervals of 0, 3, 6, 9,12,15, 18 and 21 days. At each

interval, the film samples were carefully removed, gently cleaned to eliminate soil residues, air-dried at room temperature, and visually documented through photography to observe changes such as surface deterioration, cracking, and fragmentation, thereby assessing the extent of biodegradation over time.

3.13.5.2 Moist soil method

Biodegradation of the film samples under moist soil conditions was evaluated using a soil burial method with suitable modifications. Film specimens with dimensions of 2 × 2 cm were buried in 100 g of fresh garden soil placed in sterile Petri plates. To maintain moisture of soil conditions, 50 mL of distilled water was added uniformly to the soil. The Petri plates were maintained under controlled incubation conditions at 30 °C throughout the experimental period. Film degradation was monitored at regular time intervals, and the samples were periodically retrieved by carefully removing the soil covering the films. Film degradation was monitored by periodic visual observation, and samples were photographed at intervals of 1–2 days. Before each observation, the soil covering the film surface was carefully removed, and after documentation, the film was reburied to allow degradation to continue under identical conditions.

3.13.5.3 Oven-Assisted Soil Method

The biodegradation of film samples was evaluated using an oven-assisted soil burial method. Film specimens (1 × 1 cm) were prepared and placed in containers containing 100 g of fresh soil. Each film sample was buried at the center of the soil matrix to ensure uniform exposure to microbial activity. Soil moisture was adjusted by adding 50 mL of distilled water to maintain adequate hydration. The containers were then incubated in an oven at 30 °C to accelerate microbial degradation under controlled conditions. Throughout the incubation period, visual observations were recorded, and photographs were taken at regular intervals (every 1–2 days) to monitor structural changes and degradation behavior of the films.

3.13.5.4 Enzymatic Degradation

An enzymatic degradation study was performed to evaluate the stability of the film samples. Approximately 10 mg of the film was used for the analysis. A cellulase enzyme solution was prepared at a concentration of 0.02 wt% relative to the film weight in 60 mL of sodium phosphate buffer (pH 7.2). Subsequently, 24 mL of distilled water was added to 6 mL of the prepared cellulase solution to obtain the final reaction medium. The film sample was then completely immersed in the enzyme solution and incubated at 25 °C for a period of 1–3 days. During the incubation period, visual observations were recorded, particularly noting the

formation of oil droplets floating on the surface, attributed to the amphiphilic characteristics of the film matrix.

3.14 Shelf-life study of cut fruit

The shelf-life evaluation was performed using fresh-cut apple and pear slices as representative climacteric fruits with high post-cut physiological activity and susceptibility to moisture loss, enzymatic browning, and texture deterioration during refrigerated storage. These fruits were selected because their climacteric nature makes them suitable models for assessing the ability of biodegradable films to reduce weight loss and control postharvest quality changes. Apple slices were included as a moderately firm fresh-cut fruit model, whereas pear slices were selected due to their comparatively softer texture and faster deterioration tendency after cutting. Thus, the use of both fruits allowed comparative evaluation of the packaging performance under different climacteric fruit matrices. This analysis was carried out by packaging fresh-cut apple and pear slices using the prepared film formulations and comparing them with unwrapped samples as per method Dong et al., (2025) and McHugh and Senesi, (2000). Fresh apples and pears were washed thoroughly, peeled, and cut into uniform slices using a sterile stainless-steel knife. Approximately 2-3 g of freshly cut fruit, each slices was wrapped with the respective films. The nanocellulose (NC), sodium alginate (SA), and guar gum (GG) films were used as control packaging materials and compared with the NEW (composite film without peel extract) and NE (bioactive composite film containing peel extract). Unwrapped fruit slices were used as the negative control. All wrapped and unwrapped samples were stored at a controlled refrigerated temperature (4–5 °C) for a period of 12 days. At 3-day intervals, the fruit samples were weighed to determine changes in weight during storage, and the wrapped films were visually inspected to assess moisture loss and permeability behaviour. The percentage reduction in fruit weight was calculated using Eq. (21), following the procedure described by Vonnie et al. (2022).

3.15 Physicochemical Analysis of Fresh-Cut Fruits

The quality attributes of fresh-cut apple and pear slices covered with different film formulations were assessed during refrigerated storage. The treatments included nanocellulose (NC), sodium alginate (SA), guar gum (GG), a composite film without peel extract (NEW), and a bioactive composite film containing peel extract (NE). Their performance was compared with uncoated fruit slices, which acted as the control group. The samples were stored at 4 °C and analyzed at 0, 3, 6, 9, and 12 days of storage. Changes in color parameters, percentage weight reduction, textural firmness, microbial count, total phenolic content, and antioxidant capacity were recorded throughout the storage period. In addition, the headspace gas composition inside the

packaged samples was measured at each sampling interval to monitor internal atmospheric changes. To evaluate physical parameters such as colour, firmness, weight loss, and internal gas composition, unwrapped fruit slices were used as the control. For biochemical (total phenolics and antioxidant activity) and microbiological analyses, untreated and unwrapped slices were used as the reference. All experiments were conducted in triplicate, and mean values were utilized for further data analysis.

3.15.1 Proximate of cut fruits

The proximate analysis of the samples was carried out according to the methodology outlined in Section 3.2.2.

3.15.2 Weight Loss and pH Value

Mass reduction of wrapped and unwrapped apple and pear slices was monitored during refrigerated storage (4–5 °C). Samples were placed in pre-weighed plastic trays, and changes in mass were recorded at predetermined intervals. The pH of wrapped and unwrapped apple slices was measured according to Pourdarbani et al. (2022), with minor modifications. Approximately 4 g of sample was homogenized with 10 mL of distilled water using a motorized pestle, and the pH of the resulting slurry was recorded using a digital pH meter (LAQUAtwin-pH-22, HORIBA Scientific).

3.15.3 Total Soluble Solids (TSS) and Titratable Acidity

Physicochemical attributes of fresh-cut apple and pear samples, including soluble solids concentration and acidity, were evaluated in accordance with Wang et al. (2023). Fruit material was macerated with distilled water to form a homogeneous mixture. The extract was clarified through filtration and centrifugation at 5000 × g for 10 min to obtain a clear liquid phase for analysis. TSS was determined using a refractometer (ZRS-6060, Prayaag Technologies) and expressed in degrees Brix (°Brix). Acidity was quantified by neutralizing the filtrate with 0.1 M sodium hydroxide using phenolphthalein as the indicator, and results were reported as percentage titratable acidity.

3.15.4 Color Value

The surface color of the fresh-cut fruit samples was determined using a portable colorimeter (ColorFlex EZ, HunterLab, Reston, USA) according to standardized procedures. Color parameters were recorded in the CIE L*, a*, and b* system, where L* indicates lightness, a* represents the red–green coordinate, and b* corresponds to the yellow–blue coordinate. Measurements were taken at three different positions on each sample to account for surface heterogeneity. All analyses were conducted in triplicate, and the average values were used for statistical interpretation.

3.15.5 Firmness

The firmness of the fruit samples was measured using a texture analysis system (Instron 5943, Instron Corporation, Norwood, USA) equipped with a 2 mm cylindrical stainless-steel probe. The analysis was performed following the method described by Luo et al. (2024) to evaluate changes in textural resistance during storage.

3.15.5 Total phenolic content

The total phenolic content (TPC) of the samples was determined following the procedure described in Section 3.5.1.

3.15.6 Antioxidant Capacity

The antimicrobial performance of the developed packaging films was evaluated as described in Section 3.10.5.2 to determine their inhibitory effect against selected foodborne and spoilage microorganisms.

3.15.7 Ascorbic Acid Content

The ascorbic acid concentration of the samples was determined according to the method described earlier in Section 3.9.3.1.2.

3.15.8 Respiration Rate

Respiratory activity of wrapped and unwrapped apple and pear slices was evaluated according to Tosif et al. (2023) by monitoring carbon dioxide production within sealed systems. To assess the effect of film packaging on metabolic behavior, approximately 5 g of fruit slices from each treatment were placed in airtight glass containers (200 mL) and held at 28 °C for 24 h. At selected intervals, headspace gas was sampled using an airtight syringe and injected into a gas chromatograph (Hitachi Model 163) equipped with a thermal conductivity detector and a CTR-1 column (Alltech Associates, Inc.). Helium was employed as the carrier gas at a flow rate of 40 mL/min. Operational temperatures were set at 55 °C for the injector, 100 °C for the detector, and 55 °C for the column. The respiration rate was calculated from the quantified CO_2 concentration and expressed relative to sample mass. All analyses were performed in triplicate to ensure precision and to assess the influence of film packaging on fruit metabolic activity.

3.16 Statistical Data Analysis

All experimental determinations were carried out in triplicate (n = 3), and the results were expressed as mean ± standard deviation. Statistical computations were performed using GraphPad Prism software (version 9.0, GraphPad Software Inc., San Diego, CA, USA). Data were subjected to one-way analysis of variance (ANOVA) to assess significant differences among treatments, followed by Tukey's multiple comparison test. A significance level of $P < 0.05$ was adopted for all statistical evaluat

Chapter 4 Results and Discussion

This chapter presents a comprehensive interpretation of the experimental findings obtained during this research. The results arising from various stages of experimentation, including extraction, characterization, formulation, and performance evaluation, are systematically discussed to establish clear relationships between material composition, processing conditions, and functional behaviour. Each result is interpreted in the context of the research objectives and supported through comparison with relevant published literature to explain the observed trends and underlying mechanisms. Emphasis is placed on understanding variations in formulation and structural attributes that influence physicochemical, mechanical, barrier, and functional properties of the developed bio-based packaging systems. Overall, this section demonstrates the findings collectively validate the proposed hypothesis and contribute to the development of sustainable and functional packaging materials. The colourimetric analysis revealed clear differences in the visual characteristics of *Cyamopsis tetragonoloba* guar straw and *Cucumis callosus* fruit peel, reflecting their distinct botanical composition and pigment profiles. Guar straw exhibited mean L*, a*, and b* values of 53.95 ± 0.89, 1.75 ± 0.16, and 13.05 ± 0.52, respectively, indicating comparatively higher lightness with a near-neutral a* value and moderate yellow tonality. This color profile is typical of dried lignocellulosic residues, where cellulose, hemicellulose, and lignin contribute to a pale yellow to brown appearance with minimal green pigmentation. In contrast, *Cucumis callosus* fruit peel showed L*, a*, and b* values of 50.26 ± 0.20, −5.09 ± 0.11, and 23.62 ± 0.35, respectively, demonstrating slightly lower lightness, a pronounced green chromatic component, and a significantly higher yellow contribution. The negative a* value confirms the presence of residual chlorophyll, while the elevated b* value suggests a strong influence of polyphenolic compounds and carotenoid pigments inherent to fruit peels. Overall, the comparative L*a*b* profiles highlight the straw's relatively uniform, lightly colored lignocellulosic nature versus the peel's pigment-rich, green–yellow appearance, underscoring their differential suitability for bio-based applications where color, phenolic content, and aesthetic properties are critical considerations.

(A) Cyamopsis tetragonoloba

(B) *Cucumis callosus* Peel

Fig. 4.1 Raw biomass materials used in the study: (A) *Cyamopsis tetragonoloba* (guar) straw and (B) *Cucumis callosus* peel

4.1 Proximate analysis

Guar straw powder is a light brown, fibrous material with a gritty consistency, making it suitable for biobased products. The results of the proximate analysis of Cyamopsis tetragonoloba straw are presented in Table 4.1, indicating that the moisture content was determined to be 4.43%, a critical parameter for evaluating the shelf life of food products. Additionally, the fat content was observed to be 0.30%, and the protein content was found to be 4.89%, with limited nutritional energy but potential for functional ingredient applications. The ash content in the straw was determined to be 2.16%, and the fiber content was recorded at 39.65%. These results show that *Cyamopsis tetragonoloba* straw could serve as a sustainable raw material for bioproducts. High fiber value underscores the lignocellulosic nature of the material, which is characterized by a substantial presence of cellulose, hemicellulose, and lignin (Abdel Kader et al., 2025). *C. tetragonoloba* straw as a source for nanocellulose extraction, bio-based polymer production, and structural reinforcement in biodegradable composites due to higher fiber content (Sholokhova et al., 2025). Furthermore, the high fiber fraction suggests potential applicability in food systems as a source of dietary fiber with associated techno-functional benefits, including bulk enhancement and water retention capacity.

Table 4.1 Proximate analysis of Guar (*Cyamopsis tetragonoloba*) straw

Proximate Composition	**Observation**
Moisture (%)	4.43±0.20
Fat (%)	0.30±0.10
Ash (%)	2.16±0.11
Fiber (%)	39.65±0.10

Protein (%)	4.89±0.08

Data are presented as mean ± SD (n = 3)

4.2 Techno-functional properties

Essential criteria in food processing include techno-functional qualities, including water solubility and oil absorption, foam and emulsion properties and stabilisation. These qualities directly and indirectly influence food quality, therefore supporting the acceptability and integration of components into food formulations (Kumar et al., 2022). Table 4.2 shows the techno-functional characteristics of *Cyamopsis tetragonoloba* straw: bulk density, tapped density, emulsifying property, and stability, reported as 0.34 g/cm^3, 0.58 g/cm^3, 41.92 %, and 49.99 %, respectively. The notable oil-binding capacity of guar straw suggests a positive contribution to the textural properties of food products by retaining substantial amounts of oil. This retention is critical for minimizing the loss of oil and volatile aromatic compounds during food processing (Wang et al., 2023). Water-binding capacity refers to the capability of a material to hold water molecules when subjected to centrifugal force, which encompasses different forms of water, such as total bound water, physically trapped water, and hydrodynamic water (Liu et al., 2024). The water-holding and oil absorption capacities of guar straw are 5.08 g/g and 4.85 g/g, respectively, suggesting its capacity to retain moisture and lipids, which is critical for preserving nutrients and volatile compounds during processing. The techno-functional properties of *C. tetragonoloba* straw highlight its multifunctionality as a food ingredient. Water- and oil-binding capacities, emulsifying ability, and bulk density make it suitable for incorporation into diverse food systems. Beyond improving product texture and stability, the valorization of guar straw into food applications provides an environmentally sustainable pathway by converting an underutilized agricultural residue into a high-value functional ingredient.

Table 4.2 Techno-functional properties of Guar (*Cyamopsis tetragonoloba*) straw

Functional properties	**Composition**
Bulk density g/cm³	0.34±0.15
Tapped density g/cm³	0.58±0.80
Water-holding capacity g/g	5.08±0.38
Oil absorption capacity g/g	4.85±0.60
Emulsifying property %	41.92±0.56
Emulsifying stability %	49.99±0.21

Data are presented as mean ± SD (n = 3)

4.3 Characterization of Guar Straw

4.3.1 Fourier transmission infrared spectroscopy

Fourier transmission infrared spectroscopy mainly identifies the chemical bonds that absorb infrared energy at various frequencies or wavelengths. The FTIR analysis of straw powder mainly reveals the stretching vibrations of hydroxyl groups, C-H bonds, and carbonyl groups. The observed phenomena include the stretching vibration of the O atom, the stretching of the glycosidic bond (C-O-C) in the polysaccharide, and the existence of the furanoid ring in the sugar units (Srikanth et al., 2015). Fig. 4.2 shows that O—H at 3675.38 cm^{-1} shows the alcohol stretching vibrations at variable intensity in guar straw. The vibrational band within the range of 3267–3333 cm^{-1} corresponds to the (C—H) carbonyl group at 3279 cm^{-1}, exhibiting medium to acute intensity indicative of H-bonded and stretched vibrations (Ghatak, 2023). Moreover, the existence of (C—H and N—H) corroborated the alkyne and amine salt, specifically at stretching vibrations of 2907.26 cm^{-1} and 2987.81 cm^{-1} with varying intensity, while the stretching range at 1599.16 cm^{-1} indicated (N—H) bonding (Rašeta et al., 2025). Moreover, peaks at 1406.45 cm^{-1} and 1393.93 cm^{-1} correspond to the sulfonyl chloride stretching vibration (S=O), while the vibrational band in the range of 1200-1275 cm^{-1} is attributed to the (C–O) alkyl aryl ether at 1249.98 cm^{-1}, exhibiting considerable intensity. At 1065.91 cm^{-1} and 1056.59 cm^{-1}, the peaks correspond to the stretching of primary alcohol (C–O) and sulfoxide (S=O), respectively. A noticeable peak at 892.08 cm^{-1} and 618.05 cm^{-1} signifies C=C and C–O–C linkages in cellulose and hemicellulose bonding, respectively (Nazar et al., 2025). The peaks at 430.50 cm^{-1} and 406.62 cm^{-1} correspond to the stretching of the (C—I) group. The strong absorption bands observed around 1055 cm^{-1} and 892 cm^{-1} are shown (C—O) stretching and β-glycosidic linkage, confirming the presence of cellulose and hemicellulose, which support the high fiber content. In this context, Sun et al. (2000) and Xiao et al. (2001) demonstrated that the spectra of wheat straw fibres, produced by both methods, are characterised by peaks at 3422 cm−1 and 1056 cm−1, which correspond to the stretching vibrations of O—H and C—O, respectively. This analysis revealed functional groups confirming its polysaccharide-rich composition and cellulose, hemicellulose, and lignin functional groups, confirming its lignocellulosic composition (Ramírez-Estrada et al., 2022). O–H and C–H stretching vibrations indicated alcohol and hydrogen-bonded groups, while C–O–C and β-glycosidic linkages confirmed the presence of cellulose and hemicellulose, supporting the high fiber content (Ramírez-Estrada et al., 2025). Additional N–H and sulfonyl groups suggest minor amine and sulfoxide functionalities. These functional groups form the fibrous morphology observed in SEM, where the sample displayed a heterogeneous surface with cylindrical wax rods, tubular

structures, and irregular, rod-like fibers, reflecting the presence of both crystalline cellulose and amorphous matrix components (Mutlu et al., 2025). These structural features highlight the straw's potential as a fibrous and functional ingredient in food or bioproduct applications.

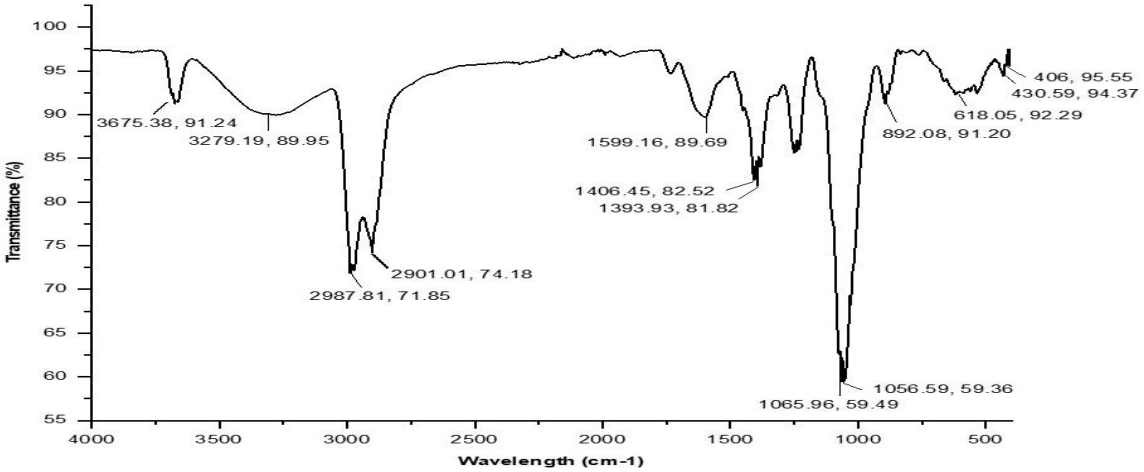

Fig. 4.2 FTIR Spectroscopy spectrum of *Cyamopsis tetragonoloba* straw

4.3.2 Surface morphology

The microstructure and surface morphology micrographs of guar straw were obtained by Scanning Electron Microscopy (SEM) (Xu et al., 2022). Fig. 4.3 demonstrates that low molecular weight and high molecular weight guar straw exhibit distinct characteristics in solid-state preparations. The outer surface image displays several cylindrical wax rods, each measuring up to 100µm, positioned at various angles. The clusters of rods are unevenly distributed throughout the epidermal surface, showing a propensity to aggregate in the interstices between the straw veins. This structural analysis shows that the straw possesses mechanical strength and potential for applications in bio-composites and packaging materials, where surface morphology and fiber networks can influence strength, barrier properties, and interfacial interactions (Kossalbayev et al., 2025). These structural features correlate with FTIR results, which confirmed the presence of cellulose, hemicellulose, and lignin through characteristic functional groups, and with XRD data showing a semi-crystalline structure (Xu et al., 2025). The fibrous microstructure observed in SEM also explains the thermal behavior seen in TGA, where moisture and volatiles are lost at 262.30 °C and amorphous components decompose below 453.40 °C, while crystalline cellulose remain thermally stable (Hindi et al., 2025 and Ma et al., 2025). SEM observations shown visual representation of the straw powder and its influence on thermal stability. The carbon and oxygen molecules synthesised from guar straw powder largely exhibit various morphologies, characterised by irregular surfaces and narrow, road-like structures with uneven edges. The average diameter of the fibre was around

2.5 µm. Amer et al. (2007) reported that morphological variability of barley straw and visualised its hollow tubular structure. The tubular structure of the wax crystalloids is associated with the presence of diketones in the wax.

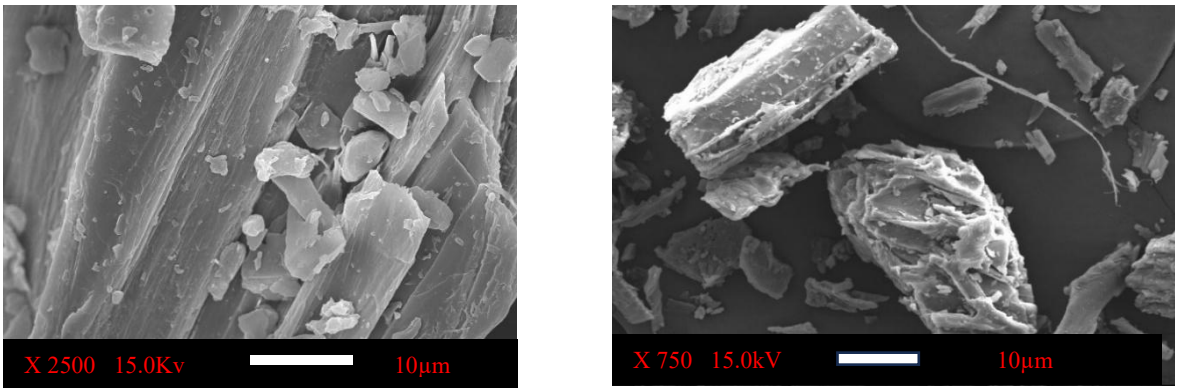

A **B**

Fig. 4.3 Microstructure of Guar straw using Scanning Electron Microscopy (SEM)

4.3.3 X-ray diffraction pattern

Internal strain and crystalline structure of different sizes of straw powder were revealed through X-ray diffraction patterns, as shown in Fig. 4.4, which shows that guar straw powder showed 2θ peaks at values 19.89˚ to 23.96˚, which clearly showed the sharp peaks of the guar straw, revealing its amorphous behaviour. Similar behaviour has been observed by (Hernandez et al., 2018) for the XRD behaviour of the corn straw, in which the diffraction peaks of 2θ were observed at 16˚ and 22˚, which was related to the crystalline behaviour of corn straw powder. To determine the samples' "degree of crystallinity - *DoC*" (also known as "crystalline area"), which is dependent on the total area or intensity that each component of the study contributes to the overall diffraction pattern (Hernandez et al., 2018). The degree of crystallinity of the guar straw sample is 73%, calculated by using eq. 1. Whereas, the crystallinity of corn stalk powder and superfine grinding treated corn stalk fibers was 58.14% and 64.27%, this indicates that the crystal structure of the superfine-ground corn stalk fibres was superior to that of the coarse corn stalk powder. The crystallinity aligns with the fibrous structures observed in SEM, whereas crystallinity of cellulose, providing structural integration (Alzarieni et al., 2025). The TGA profile shows initial weight loss at 262.30 °C corresponds to moisture and volatiles, while final decomposition of organic compounds (carbohydrates and proteins) below 453.40 °C reflects the thermal degradation of amorphous regions (Addagada and Nair, 2025). The residual mass after 453.40 °C indicates that the crystalline cellulose fiber contributes to higher thermal stability. These results also confirm that the mechanical forces during superfine grinding did not entirely disrupt the crystalline structures of the cellulose (Zhao et al., 2013). In contrast to

this study, guar straw has a high degree of crystallinity and has great potential for use in packaging materials, bio-composites, and other fields where it is used for increased thermal stability and mechanical strength.

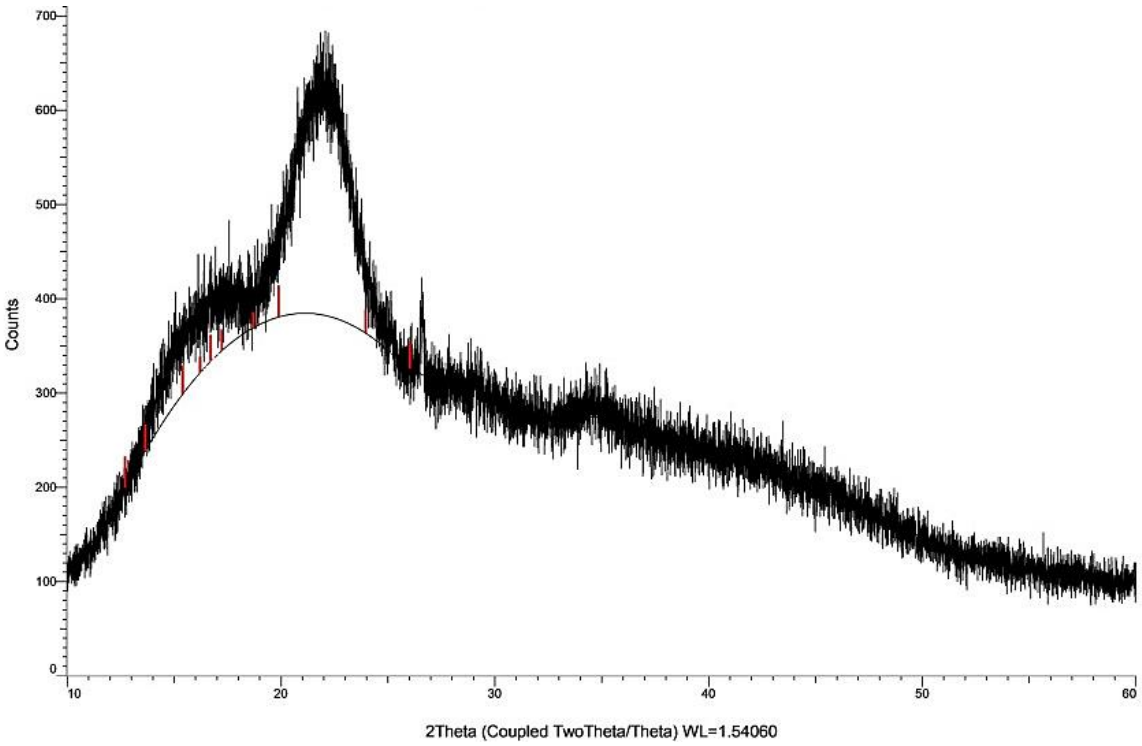

Fig. 4.4 X-ray diffraction pattern of *Cyamopsis tetragonoloba* straw

4.3.4 Thermogravimetric analysis

A thermogravimetric analyser is used to check the change in mass upon increasing the system temperature. It is used to obtain the substances' decomposition temperatures and oil volatility (Jaglan et al., 2023). Perkin Elmer TGA 4000 (710 Bridgeport Avenue, Shelton, USA) was used for thermogravimetric analysis, and the graph of the guar straw powder obtained is shown in Fig. 4.5. In the curve, it is revealed that the Tg value for the straw powder was 76.596˚ with a lower temperature, and with an increase in temperature Tg value is decreased 25.918˚. Therefore, as the temperature increases, the sample weight decreases, leading to a change in mass during thermal treatment. The TGA curve showed distinct stages of weight reduction. In guar straw, a weight loss of 0.508 mg was recorded at 262.30 °C, which can be attributed to the removal of moisture along with the release of volatile compounds present in the biomass. There was about 1.941 mg of weight loss observed at temperatures below 262.30 ℃ due to the decomposition of organic compounds, such as carbohydrates and proteins, present in the straw. The thermal stability observed in TGA correlates with the XRD results, as the crystalline cellulose resists thermal decomposition longer than the amorphous lignin and hemicellulose

components identified by FTIR and visualized in SEM (Hasan et al., 2025). These components break down into smaller molecular fragments that volatilize at elevated temperatures, reducing sample mass. At around 453.40 °C, the decomposition of inorganic constituents of the straw begins, leaving a residual sample weight of approximately 0.915 mg (Sharma et al., 2023).

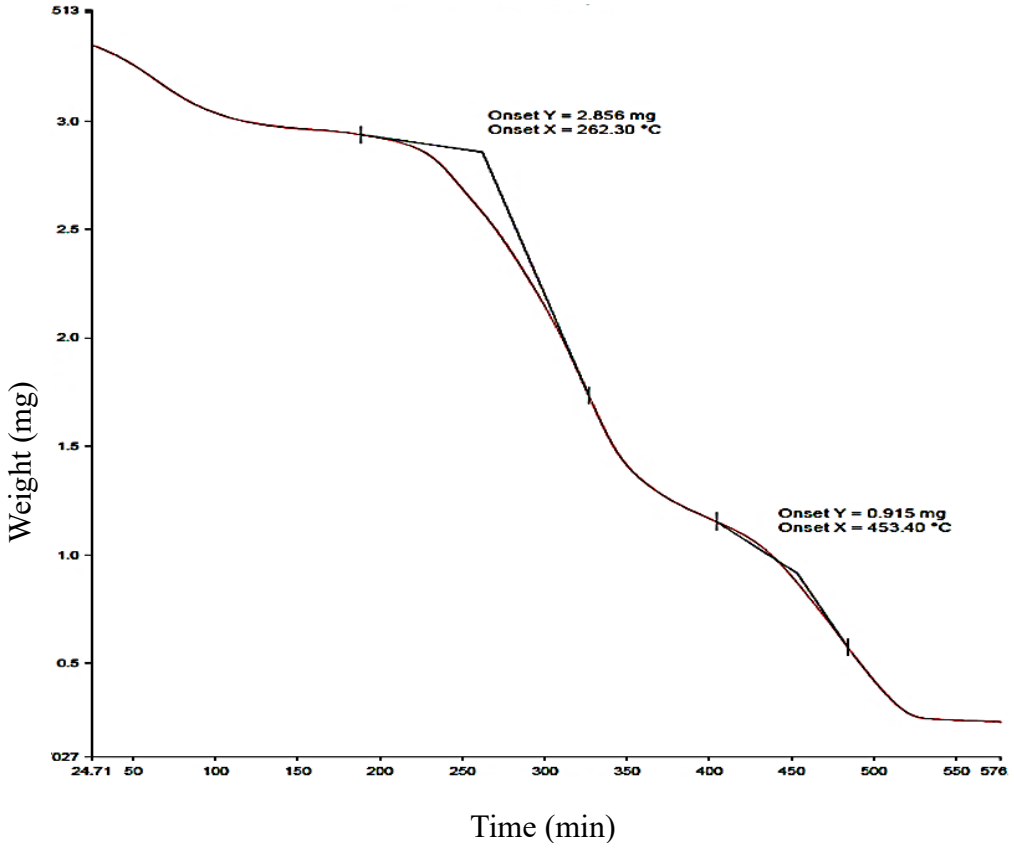

Fig. 4.5 Thermogravimetric analysis of *Cyamopsis tetragonoloba* straw

Overall, the integration of FTIR, SEM, XRD, and TGA results demonstrates that guar straw powder consists of crystalline cellulose fibrils embedded within an amorphous lignin–hemicellulose matrix. This structural arrangement determines its morphological characteristics, thermal stability, and overall suitability for applications that demand improved mechanical strength and heat resistance, including bio-composites and sustainable packaging materials.

4.4 Ethanolic extraction

The ethanolic extraction of *Cyamopsis tetragonoloba* straw yielded a 4.50% extract. This extraction percentage indicates a higher concentration of bioactive compounds in the guar straw powder. These bioactive compounds possess nutraceutical and functional properties that contribute to BMI reduction through various biochemical mechanisms (Kumar et al., 2020).

4.4.1 Phytochemical analysis

The total flavonoid content was quantified using a quercetin standard curve at 510 nm, while the total phenolic content was determined following the method described by Kumar et al.

(2023), employing gallic acid as the standard at 765 nm. The values obtained were 3.83 mg QE/g and 4.15 mg GAE/g, respectively. Whereas, the extract exhibited strong antioxidant activity measured by the 1,1-diphenyl-2-picrylhydrazyl (DPPH) radical scavenging method, and it was 42.06 %. According to Arora et al., (2011), the highest antioxidant activity of wheat straw (70.8%) and TPC (9.8 mg/mL), respectively. The presence of phenolic and flavonoid compounds supports its role in enhancing antioxidant capacity, which may help in protecting food systems from oxidative deterioration. Furthermore, valorizing guar straw for its bioactive compounds contributes to sustainable resource utilization, adding economic and functional value to an agricultural residue that is often discarded.

4.4.2 Quantification of polyphenols through HPLC

Polyphenolic substances include flavonoids, phenolic acids, tannins, lignans, and coumarins. Consequently, two conjugated polyphenolic compounds, specifically chlorogenic acid, caffeic acid, vanillic acid, and cinnamic acid, were quantified by High-Performance Liquid Chromatography, with the findings illustrated in Fig. 4.6. The results demonstrated an optimal chromatographic profile and effective separation of the phenolic components by High-Performance Liquid Chromatography. The chromatogram indicates that guar straw extract had significantly larger levels of Cinnamic acid (8.44 mg/kg), with relative areas of 24.38% and a retention time of 49.45 min, compared to Vanillic acid (0.49 mg/kg), which had relative areas of 19.71% and a retention time of 1.71 min. Vanillic acid, a hydroxybenzoic acid derivative, is frequently reported in lignocellulosic residues as a product of lignin degradation (Martínková et al., 2023). It exhibits radical-scavenging and antimicrobial activity, which may complement the functionality of cinnamic acid, thereby enhancing the overall bioactive potential of guar straw.

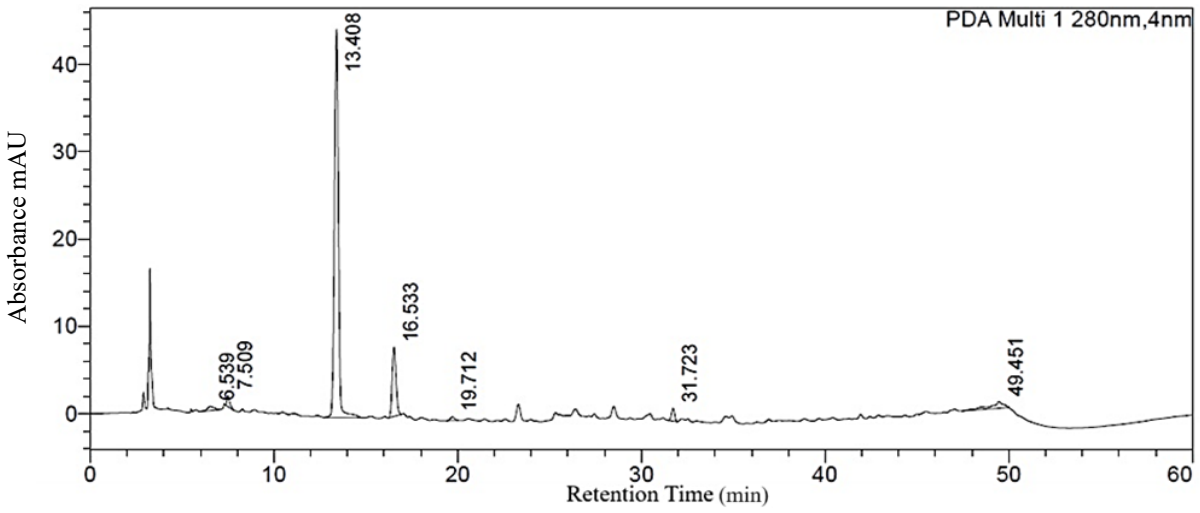

Fig. 4.6 HPLC Chromatograph of Ethanolic *Cyamopsis tetragonoloba* straw

4.4.3 Antimicrobial efficiency of *Cyamopsis tetragonoloba* straw extract

Antimicrobial activity is measured by zone of inhibition in (mm) for the guar straw extract shown and Table 4.3. The guar straw powder extract showed antimicrobial efficacy against *Bacillus subtilis, Escherichia coli*, and *Aspergillus niger* microorganisms. The control (Chloramphenicol), exhibits the highest zone of inhibition, with *E. coli* showing significant (p<0.05) largest zone (28.17 mm), followed by *B. subtilis* (21.83 mm) and *A. niger* (18.88 mm), indicating strong antimicrobial activity. At lower concentrations (6.5 µL/mL), *B. subtilis* shows significantly (p<0.05) higher (6.16 mm) zone of inhibition than *E. coli* (2 mm) and *A. niger* (1.09 mm). However, at 12.5 and 25 (µL/mL), zone of inhibition of *B. subtilis* (6.66 to 7 mm) and *E. coli* (3.26 to 3.90 mm) are significantly higher than *A. niger* (1.92 to 2.48 mm). At 50 (µL/mL), *B. subtilis* (7.33 mm) showed significantly higher zone of inhibition than *E. coli* (6.33 mm) and *A. niger* (4.26 mm), whereas E. coli and A. niger showed statistically significant differences ($p < 0.05$) among the treatments. At the highest concentration (100 µL/mL), *B. subtilis* (10.83 mm), *E. coli.* (8.16 mm) and *A. niger* (6.19), with the difference being statistically significant (p<0.05). These results indicate that microbial activity varies with extract concentration, with B. subtilis generally more susceptible, and significant differences between *E. coli* and *A. niger* occur at intermediate and high concentrations. Higher concentrations of guar straw extract (50 and 100 µL/mL) exhibited greater antimicrobial activity. The observed antimicrobial activity can be attributed to the polyphenolic constituents of guar straw, notably cinnamic acid and vanillic acid, which have been widely reported to exhibit radical-scavenging, membrane-disrupting, and antimicrobial properties. Cinnamic acid is known to alter microbial cell wall integrity, inhibit enzyme activity, and interfere with microbial metabolic pathways, particularly in Gram-positive bacteria, thereby explaining the heightened susceptibility of *B. subtilis* (Jaramillo Jimenez et al., 2024 and Guzman, 2014). The reduced sensitivity of *E. coli* may be linked to the structural complexity of the Gram-negative outer membrane, which provides additional resistance to bioactive compounds (Saxena et al., 2023). The moderate antifungal activity observed against *A. niger* suggests that phenolic acids in guar straw may partially inhibit fungal cell wall synthesis and hyphal growth. Overall, the antimicrobial analysis shows that *C. tetragonoloba* straw extract exerts a concentration-dependent inhibitory effect, with greater efficacy against Gram-positive bacteria, thereby underscoring its potential as a sustainable source of natural antimicrobials for applications in food preservation, biobased packaging, and related industrial sectors

Table 4.3 Antimicrobial efficiency *of Cyamopsis tetragonoloba* straw extract

Sample (µL/mL)	***Bacillus subtilis* (mm)**	***Escherichia coli* (mm)**	***Aspergillus niger* (mm)**
Control	21.83 ± 0.28^{aB}	28.17 ± 0.29^{aA}	18.88 ± 0.24^{aC}
6.5	6.16 ± 0.30^{cdA}	2.17 ± 0.29^{fB}	1.09 ± 0.07^{fC}
12.5	6.66 ± 0.58^{cdA}	3.26 ± 0.30^{eB}	1.92 ± 0.06^{eC}
25	7.00 ± 0.72^{cdA}	3.90 ± 0.09^{dB}	2.48 ± 0.11^{dC}
50	$7.33\pm0.^{37cA}$	6.33 ± 0.35^{cB}	4.26 ± 0.28^{cC}
100	10.83 ± 0.31^{bA}	8.16 ± 0.39^{bB}	6.19 ± 0.40^{bC}

Values are expressed as mean ± SD. Different lowercase superscripts (a–c) within a column indicate significant differences ($p < 0.05$), while different uppercase superscripts (A–C) within a row denote significant differences ($p < 0.05$).

4.4.4 Cytotoxicity of guar straw extract

In-vitro anticancer efficacy of guar straw extracts was assessed using the A549 lung cancer cell line, a non-metastatic human lung cancer model. Cells were treated with varying extract concentrations (0-50 µL/mL) for 24 h. Cell viability was determined by the MTT assay and is shown in Fig. 4.7. The control (0 µL/mL) shows high cell viability, and it is statistically significant ($p<0.05$) compared with lower concentrations. Cell viability showed a gradual reduction as the concentration increased (0.78 to 6.25 µL/mL), indicating that although the reduction is significant ($p < 0.05$), these values are relatively high. Furthermore, at 12.5 µL/mL, cell viability decreases and shows a significant ($p<0.05$) difference relative to lower concentrations. Whereas the lowest viability was observed at 2.5 µL/mL and 50 µL/mL, with significant ($p < 0.05$) differences between them, indicating the highest cytotoxic effect. The results showed that guar straw has greater cytotoxicity, with an IC_{50} value of 43.23 %, indicating its good ability to inhibit the proliferation of lung cancer cells. This increased cytotoxic potential may be attributed to its chemo-preventive and cell-killing properties, highlighting its potential as a therapeutic agent. According to Geies et al. (2020), at a 50% concentration, the IC_{50} value for the cytotoxic activity of rice straw lignin on the A549 cell line is 17.9 µL/mL. Guar Straw is non-toxic, has good physicochemical compatibility and biodegradability, making it an attractive substrate for cancer medication delivery. The statistical analysis showed that the effect of concentration on cell viability ($p<0.05$), with higher concentration having greater cytotoxicity.

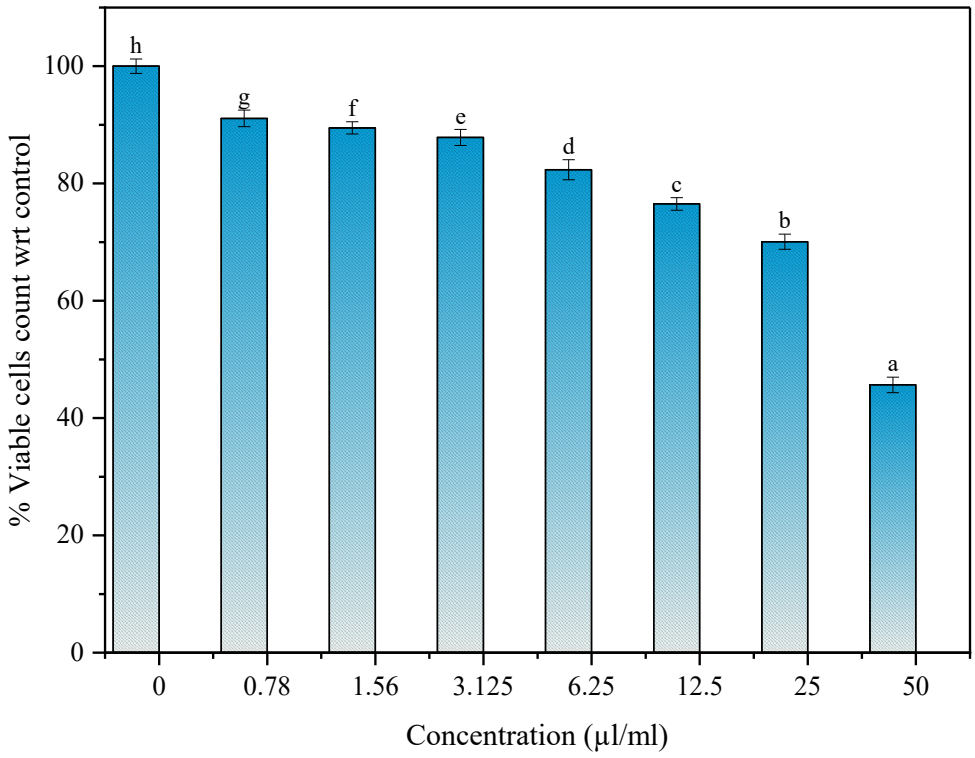

Fig. 4.7 Cytotoxicity of *Cyamopsis tetragonoloba* straw extract. Data are presented as mean ± SD (n = 4). $^{a–h}$ Means with the same superscript in a column are significantly (p<0.05) from each other.

4.4.5 Amylase inhibition assay

The digestive enzyme α-amylase plays a significant role in the breakdown of glucose from starch in the gut. When the activity of amylase is reduced, the quantity of small-molecule sugars derived from starch decreases to regulate blood glucose levels (Cheng et al., 2017). The percentage of amylase inhibition and the IC_{50} values are presented in Table 4.4. Guar straw powder extract was analysed at concentrations ranging from 200 to 1000 µg/mL. The highest inhibition of amylase activity was observed at 1000 µg/mL, with a significantly (p < 0.05) greater inhibition rate of 90.99%. In contrast, the extract at 200 µg/mL exhibited a significantly (p < 0.05) lower inhibition rate of 79.52% compared to those at 400, 600, and 800 µg/mL, which showed inhibition rates of 80.14%, 82.70%, and 87.30%, respectively. The findings indicate that amylase inhibition increased with higher doses, suggesting that guar straw extract may possess potential antidiabetic properties. Guar straw extract contains several phenolic and flavonoid compounds that are known to inhibit carbohydrate-digesting enzymes such as amylase. It contains flavonoid or tannin derivatives and phenolic compounds (gallic and ferulic

acid) that interfere with the enzymatic activity by binding to the protein's active site, which shows amylase inhibitory effects. According to Meng et al. (2019), buckwheat straw showed a 70.94% decrease in amylase activity at a dosage of 100 mg. As compared, guar straw exhibited a higher percentage of amylase inhibition, attributable to its elevated fiber content. This study underscores the essential function of dietary fiber in glycemic control. Fiber significantly reduces postprandial blood glucose levels by inhibiting glucose transport, decreasing glucose concentration in the small intestine, delaying starch degradation, and directly blocking carbohydrate-digesting enzymes like amylase.

4.4.6 Lipase inhibition assay

The percentage of lipase inhibition and IC_{50} values of guar straw powder extract are presented in Table 4.4. 1000 µg/mL concentrations of the extract exhibited significantly ($p < 0.05$) higher lipase inhibition, with inhibition rates of 71.86%. In contrast, the extract at 200 µg/mL showed a significantly ($p < 0.05$) lower inhibition of 14.32%. Additionally, concentrations of 400, 600, 800 µg/mL demonstrated significantly different ($p < 0.05$) levels of inhibition, with values of 28.34%, 37.60%, and 58.46%, respectively. These results show a dose-dependent increase in lipase inhibition, as guar straw contains flavonoids and phenolic compounds that are lipase inhibitors. These compounds interact with lipase through hydrogen bonding and hydrophobic interactions, reducing the enzyme's ability to hydrolyse dietary fats.

Table 4.4 Amylase and lipase inhibition assay of different *Cyamopsis tetragonoloba* straw

Concentration of Sample (µg/mL)	**% Inhibition of Amylase**	**% Inhibition of Lipase**
200	79.52 ± 0.65^{a}	14.32 ± 0.77^{a}
400	80.14 ± 0.93^{b}	28.34 ± 0.86^{b}
600	82.70 ± 0.75^{c}	37.60 ± 0.80^{c}
800	87.30 ± 0.84^{d}	58.46 ± 0.32^{d}
1000	90.99 ± 0.32^{e}	71.86 ± 0.28^{e}

Data are presented as mean ± SD (n = 3)

Different uppercase superscripts $^{a\text{-}e}$within the same evaluation are significantly different ($p<0.05$) from each other

4.5 Determination of cellulose, hemicellulose, and lignin

The lignocellulosic composition of guar straw powder, including cellulose, hemicellulose, and lignin, was determined using the Van Soest method shown in the figure. 4.8. The results showed that the pure cellulose in guar straw constitutes approximately 49.61±0.58% it is major

structural polysaccharide component in plant cell walls. Whereas lignin provides the structural rigidity and resistance to microbial degradation, it was found 18.45±0.62%. A higher lignin content requires more delignification, and it decreases digestibility. Hemicellulose, a heteropolysaccharide associated with cellulose microfibrils in plant cell walls, was found to be present at 20.15 ± 0.74%. It contributes significantly to maintaining the structural integrity of the cell wall and enhances its capacity to retain water. The structural characteristics of guar straw affect the texture and cellulose yield, depending on its genetic, morphological, and compositional characteristics.

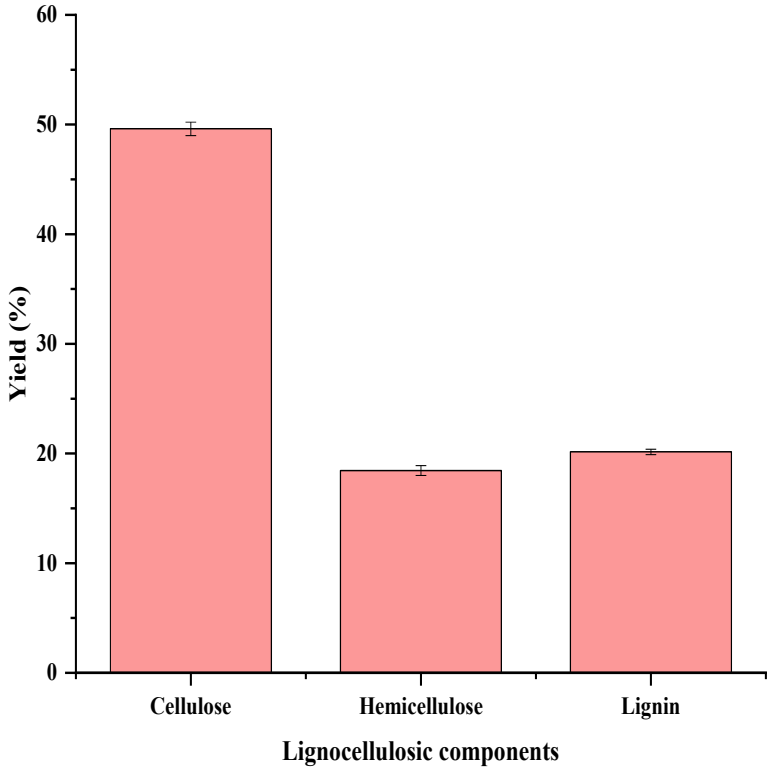

Fig. 4.8 The yield of lignocellulosic components in *Cyamopsis tetragonoloba* straw is expressed as mean ± standard deviation (SD) from independent replicates. Error bars represent the standard deviation of the mean.

4.5.1 Optimization of parameters

Response Surface Methodology (RSM) based on a Central Composite Design (CCD) was applied to optimize the process variables influencing cellulose yield. Three independent factors were selected for the study: sodium hydroxide concentration, reaction temperature, and extraction time. Each variable was evaluated at three coded levels—low (−1), center (0), and

high (+1)—as presented in Table 4.5. A second-order (quadratic) regression model was developed to describe the relationship between the independent variables and the response. The adequacy and statistical significance of the model were assessed using analysis of variance (ANOVA). The mathematical expression of the fitted response surface model is given below (Eq. 10):

$$\text{Yield (\%)} = 41.70 - 2.59A - 1.36B - 0.84C - 1.66AB - 2.12AC - 2.86BC - 0.81A^2 - 0.75B^2 + 0.03C^2 \quad (10)$$

where A represents the sodium hydroxide concentration (% w/w), B denotes the reaction time (min), and C corresponds to the extraction temperature (°C). The coded and actual values of these independent variables are provided in Table 4.6. Among the 20 experimental trials, the highest cellulose yield (48.82%) was obtained in run 19, which was in close agreement with the predicted value of 48.58%, indicating good model accuracy. The optimum extraction conditions identified by the RSM model were 5% (w/w) NaOH concentration, 27 °C reaction temperature, and 180 min extraction time. Under these conditions, the experimental cellulose yield reached 48.82%, with an overall desirability value of 0.99, confirming the effectiveness of the optimization process. The ANOVA results for the quadratic response surface model (Eq. 10) are presented in Table 4.7. The model exhibited an F-value of 182.37 (Table 4.6), demonstrating high statistical significance. The probability of obtaining such a large F-value due to random variation was only 0.01%, indicating strong model adequacy and reliability. Reaction temperature, sodium hydroxide concentration, and extraction time significantly influenced cellulose yield, as their *p*-values were less than 0.05 (Table 4.6). The coefficient of determination (R^2) for the fitted model was 0.9939, suggesting excellent agreement between experimental and predicted values. A *p*-value below 0.05 indicates that the corresponding factors significantly affect the response and validates the statistical robustness of the regression model (Thakur et al., 2020). Alkaline pretreatment using NaOH is recognized as an efficient and cost-effective approach for lignocellulosic biomass processing, as it disrupts ester linkages and facilitates the removal of lignin and hemicellulose, thereby enriching cellulose content (Tharunkumar et al., 2024). Similarly, Ding et al. (2025) reported that alkali treatment of cotton straw under optimized conditions (10.46% NaOH, 90 °C, 7.19 h) resulted in a cellulose yield of 43.87%, closely matching the predicted value of 43.92%, further supporting the effectiveness of alkali-based extraction strategies.

Table 4.5 Ranges of the factors used in central composite design for alkali hydrolysis of cellulose

Factors	Actual level of coded factors		
	-1 (Low)	0 (centre)	+1 (High)
NaOH (%)	5	7.50	10
Time (min)	60	120	180
Temperature (°C)	27	33.50	75

Table 4.6 Model fitness as evaluated through Analysis of Variance (ANOVA), confirming the statistical reliability of the selected models.

Source	Sum of Squares	df	Mean Square	F-value	p-value	
Model	265.73	9	29.53	182.37	< 0.0001	Significant
A-NaOH	91.85	1	91.85	567.31	< 0.0001	
B-Time	25.17	1	25.17	155.47	< 0.0001	
C-Temperature	9.70	1	9.70	59.89	< 0.0001	
AB	20.67	1	20.67	127.69	< 0.0001	
AC	36.13	1	36.13	223.13	< 0.0001	
BC	65.44	1	65.44	404.18	< 0.0001	
A^2	9.63	1	9.63	59.49	< 0.0001	
B^2	8.31	1	8.31	51.30	< 0.0001	
C^2	0.0184	1	0.0184	0.1139	0.7427	
Residual	1.62	10	0.1619			
Lack of Fit	0.8883	5	0.1777	1.22	0.4178	not significant
Pure Error	0.7307	5	0.1461			
Cor Total	267.35	19				

Table 4.7 Experimental setup and results for the central design matrix for alkali treatment of Cellulose

Sr. No.	NaOH (%)	Time (min)	Temperature (°C)	Experimental yield (g/100g)	Purity of cellulose (%)

1	7.5	120	51	41.49±0.58^{de}	99.53±0.47^{b}
2	5	60	75	42.39±0.70^{ef}	99.24±0.63^{b}
3	7.5	120	51	41.38±0.63^{cde}	99.41±0.45^{b}
4	10	60	75	44.62±0.61^{g}	99.67±0.33^{b}
5	3.29	120	51	43.16±0.63^{fg}	84.76±0.83^{a}
6	7.5	120	51	40.90±0.79^{cde}	99.57±0.13^{b}
7	5	60	27	42.56±0.77^{ef}	99.34±0.56^{b}
8	10	180	27	36.12±0.49^{ab}	99.78±0.28^{b}
9	10	60	27	36.30±0.14^{ab}	99.71±0.26^{b}
10	10	180	75	33.01±0.21^{a}	99.79±0.21^{b}
11	7.5	120	51	41.89±0.98^{de}	99.58±0.66^{b}
12	7.5	120	51	41.28±0.18^{cde}	99.56±0.52^{b}
13	5	180	75	37.20±0.90^{abc}	99.44±0.44^{b}
14	7.5	120	51	41.90±0.85^{de}	99.42±0.46^{b}
15	7.5	120	91.41	39.80±0.53^{bcd}	99.51±0.52^{b}
16	11.71	120	51	34.54±0.50^{a}	99.83±0.24^{b}
17	7.5	221.04	51	36.69±0.42^{abc}	99.54±0.57^{b}
18	7.5	18.96	51	41.34±0.73^{cde}	99.42±0.69^{b}
19	5	180	27	48.82±0.46^{h}	99.39±0.60^{b}
20	7.5	120	10.58	42.73±0.89^{fg}	99.59±0.58^{b}

Results are expressed as mean ± standard deviation. Mean values within a row bearing different lowercase superscripts (a–h for cellulose yield and a–b for cellulose purity) differ significantly ($p < 0.05$) according to Duncan's Multiple Range Test across 20 experimental runs. The comparison between predicted and observed values indicated that the model was significant and showed a strong correlation coefficient (Fig. 1). The response surface graphs (Fig. 2A–C) depict the combined effects of sodium hydroxide concentration, extraction time, and temperature on cellulose yield. Fig. 4.9 (A) A reveals a decrease in cellulose yield with higher NaOH concentration and longer extraction time, suggesting a non-linear interaction, where high-alkali hydrolysis increases delignification of cellulose, leaving more cellulose available for extraction. Fig. 4.9 (B) shows a significant interaction between NaOH concentration and temperature, where both variables showed delignification and cellulose yield recovery. In contrast, Fig. 4.9(C) shows the effect of time and temperature on cellulose yield. The contour lines show the effects of increasing time and temperature on both variables, and cellulose yield

decreases. Fig. 4.10 illustrates the experimental and model-predicted cellulose yield values. The data points closely align along the 45-degree reference line (Y = X), indicating a model reliability and minimal deviation between predicted and observed results.

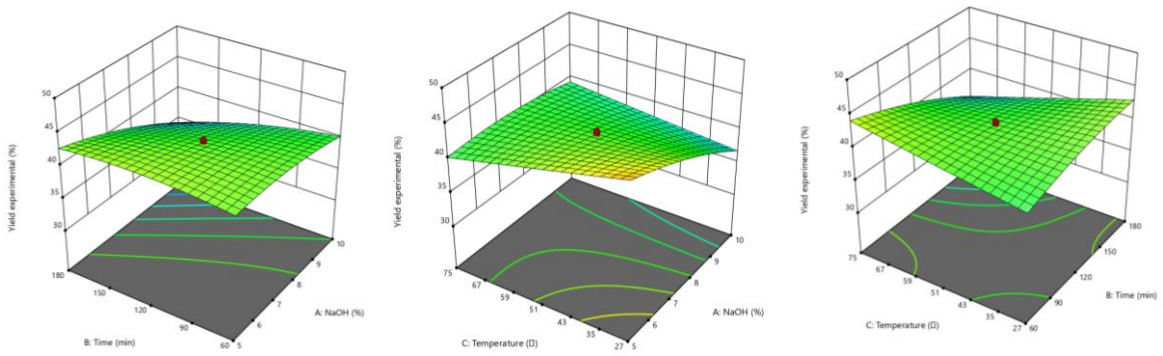

Fig. 4.9 (A, B, C) (A) Interaction plot showing the relationship between NaOH concentration (%) and extraction time (h). (B) Contour plot illustrating the interaction between NaOH concentration (%) and temperature (°C). (C) Contour plot depicting the combined effect of temperature (°C) and extraction time (h).

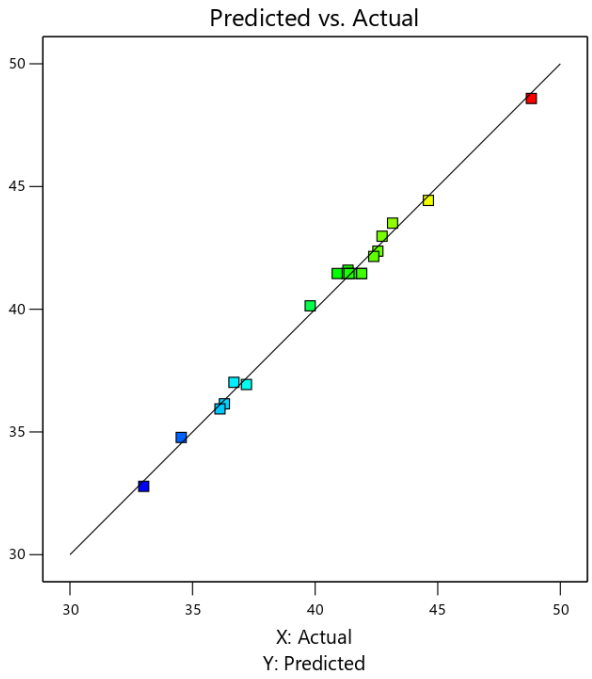

Fig. 4.10 Predicted vs. Actual graph

4.5.2 Purity of cellulose

The purity of cellulose with different NaOH concentrations during the extraction process from guar straw was present in Table 4.7. At lower concentrations (3.29%), the cellulose purity was lowest 84.76% due to improper delignification of lignocellulosic material and it is shown significant difference (p<0.05) with other treatments. Whenever, NaOH concentration was

increased to 5% the purity percentage of cellulose was good, found values between 99.24% to 99.44%, which shown effective removal of hemicellulose and lignin while cellulose yield was higher. Further increase to 7.5 % NaOH enhanced the purity, reaching maximum purity was 99.41-99.59% as higher alkali levels promote more efficient lignin solubilization. Whereas, purity percentage of cellulose was increase with NaOH concentration higher, the purity 99.67% to 99.83%, respectively, was obtained at 10–11.71% NaOH, these concentrations can negatively affect cellulose yield. Therefore, 5% NaOH was selected as the optimal concentration for further experiments because it provides a good balance between cellulose purity and maximum yield while decrease the excessive alkali usage. This data clearly shows the effectiveness of NaOH for the extraction of cellulose from guar straw. It highlights the importance of choosing the right concentration for best result and further use for conversion of nanocellulose.

4.5.3 Conversion of cellulose to nanocellulose

Optimization of nanocellulose yield from cellulose was carried out using Response Surface Methodology (RSM) based on a three-factor Central Composite Design (CCD). A total of 20 experimental runs were generated, and the corresponding design matrix along with the observed responses are presented in Tables 4.8 and 4.10. The independent variables selected for optimization were sulfuric acid concentration (%), reaction temperature, and hydrolysis time (min). Each variable was evaluated at three coded levels: low (−1), center (0), and high (+1), as summarized in Table 4.8. The adequacy and statistical significance of the developed quadratic model were assessed using analysis of variance (ANOVA). The second-order polynomial equation representing the response surface model is given below (Eq. 11):

$$\text{Yield (\%)} = 61.48-4.03A-1.51B-6.18C+0.17AB+2.88AC-0.43BC-1.40A^2-3.65B^2-0.32C^2 \quad (11)$$

where A represents the sulfuric acid concentration (% w/w), B denotes the hydrolysis time (h), and C corresponds to the reaction temperature (°C). The coded and actual values of these independent variables are presented in Table 4.8.

The optimum conditions for nanocellulose production were obtained at a sulfuric acid concentration of 30%, reaction temperature of 27 °C, and hydrolysis time of 2 h. Under these optimized parameters, the experimental yield of nanocellulose was 70.21%, which closely matched the predicted value of 70.43%, with an overall desirability value of 1.0 as estimated by the RSM model. The analysis of variance (ANOVA) results for the quadratic response surface model (Eq. 11) are presented in Table 4.9. The model showed an F-value of 251.82,

indicating high statistical significance. The probability of obtaining such a large F-value due to random error was only 0.01%, confirming the adequacy and reliability of the fitted model. The main factors—acid concentration, reaction temperature, and hydrolysis time—exhibited significant effects on nanocellulose yield, as their *p*-values were less than 0.05 (Table 4.9). However, the interaction between acid concentration and time was found to be statistically non-significant ($p > 0.05$). The coefficient of determination (R^2) was 0.9976, demonstrating excellent agreement between the predicted and experimental values. A *p*-value below 0.05 indicates statistical significance of the model terms and confirms the validity of the regression analysis (Thakur et al., 2020).

Table 4.8 Factor ranges employed in the central composite design for nanocellulose production through acid hydrolysis.

Factors	**Actual level of coded factors**		
	-1 (Low)	**0 (centre)**	**+1 (High)**
H2So4 (%)	30	35	40
Time (h)	2	3	4
Temperature (°C)	27	51	75

Table 4.9 Model adequacy was assessed using Analysis of Variance (ANOVA), which confirmed the statistical validity of the selected models.

Source	**Sum of Squares**	**df**	**Mean Square**	**F-value**	**p-value**	
Model	1049.41	9	116.60	251.82	< 0.0001	Significant
A-H2So4	221.89	1	221.89	479.21	< 0.0001	
B-Time	31.04	1	31.04	67.04	< 0.0001	
C-Temperature	520.95	1	520.95	1125.09	< 0.0001	
AB	0.2485	1	0.2485	0.5367	0.4806	
AC	66.18	1	66.18	142.93	< 0.0001	
BC	1.49	1	1.49	3.21	0.1033	
A^2	28.31	1	28.31	61.14	< 0.0001	
B^2	191.64	1	191.64	413.89	< 0.0001	
C^2	1.56	1	1.56	3.36	0.0967	

Residual	4.63	10	0.4630			
Lack of Fit	1.38	5	0.2765	0.4257	0.8149	not significant
Pure Error	3.25	5	0.6495			
Cor Total	1054.04	19				

Table 4.10 Experimental setup and results for the central design matrix for acid treatment for nanocellulose extraction

Sr. No.	H_2SO_4 (%)	Time (h)	Temperature (°C)	Experimental yield (g/100g)
1	30	4	75	49.21 ± 0.40^{b}
2	30	4	27	68.11 ± 0.49^{jk}
3	40	2	27	55.79 ± 0.33^{fg}
4	40	4	75	47.00 ± 0.24^{a}
5	30	2	27	70.21 ± 0.89^{kl}
6	35	1.31	51	54.31 ± 0.40^{ef}
7	30	2	75	53.09 ± 0.66^{de}
8	35	3	91.36	50.21 ± 0.37^{bc}
9	35	3	51	62.01 ± 0.73^{hi}
10	35	3	51	60.18 ± 0.36^{gh}
11	35	3	51	61.11 ± 0.91^{hi}
12	35	3	51	61.12 ± 0.95^{hi}
13	43.40	3	51	51.23 ± 0.23^{cd}
14	40	4	27	54.34 ± 0.44^{ef}
15	35	3	51	62.23 ± 0.56^{hi}
16	40	2	75	50.12 ± 0.29^{bc}
17	35	4.68	51	48.34 ± 0.59^{ab}
18	35	3	10.63	71.21 ± 0.39^{l}
19	26.59	3	51	64.12 ± 0.66^{ij}
20	35	3	51	62.15 ± 0.35^{hi}

Data were presented as mean ± standard deviation. Mean values within a row with different lowercase superscripts (a-k), for yield of nanocellulose and significantly different (p<0.05) from each other based on Duncan's multiple range test for 20 runs.

The 3D contour graph response surface plots and the predicted vs. actual graph value relation shown the efficiency of the developed model in optimizing nanocellulose extraction conditions. The 3D surface plots (Fig. 4.11 A–C) represent the interaction between H_2SO_4, extraction time, and temperature on nanocellulose yield. In Fig. 4.11 (A), higher acid concentrations and prolonged extraction times resulted in reduced yield, likely due to over-hydrolysis and degradation of cellulose chains. Fig. 4.11 B demonstrates a notable interaction between acid concentration and temperature, where low level of nanocellulose yield, with excessive acid and temperature led to decreasing nanocellulose recovery due to acid-induced breakdown. Fig. 4.11 C shown more extraction times at elevated temperatures also negatively impacted yield, supporting the need to avoid bad conditions during hydrolysis. The predicted vs. actual plot (Fig. 4.12) shows a strong correlation between experimental and predicted values, with data points closely aligned along the 45° line, indicating high model accuracy and reliability. Overall, the model underscores the importance of control conditions of variables to maximize nanocellulose yield while preserving structural integrity.

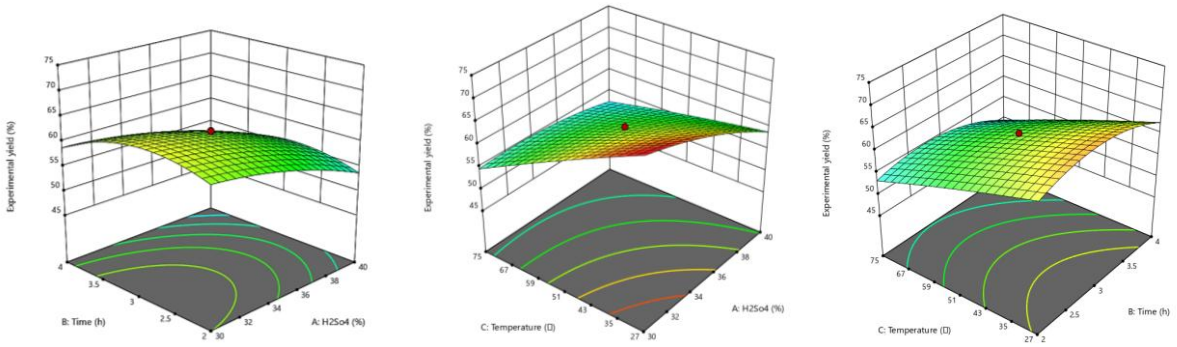

Fig. 4.11 (A–C) Response surface and contour plots showing the interactions among process variables: (A) H_2SO_4 concentration (%) versus reaction time (h); (B) H_2SO_4 concentration (%) versus temperature (°C); and (C) temperature (°C) versus reaction time (h).

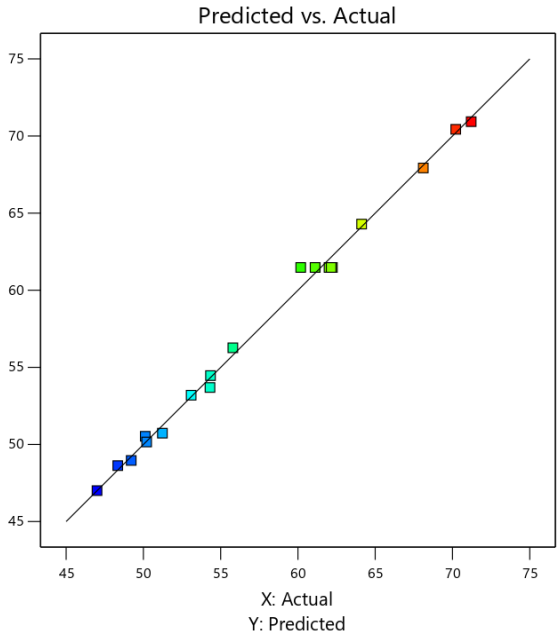

Fig. 4.12 Predicted vs. Actual graph

4.5.4 Characterization of cellulose and nanocellulose

4.5.4.1 Particle size

The nanoscale dimensions of cellulose and nanocellulose were confirmed through particle size analysis, as shown in Fig. 4.13, detailing both particle size distribution and zeta potential values. The cellulose sample exhibited an average particle size of 520.9 ± 0.78 nm with a surface charge of -20.2 ± 10.6 mV. In contrast, the nanocellulose sample displayed a reduced particle size of 296.0 ± 0.41 nm and a surface charge of -13.3± 10.1 mV. Alkali hydrolysis using sodium hydroxide effectively reduces cellulose particle size by selectively degrading the amorphous regions within the cellulose matrix. This process induces the fragmentation of cellulose fibres, yielding finer and more uniform particles. During hydrolysis, increased crystallinity and disruption of intermolecular hydrogen bonds facilitate particle size reduction, thereby enhancing the material's surface properties. Whereas, acid hydrolysis was performed using sulfuric acid, imparting half-ester sulfate groups to the nanocellulose surface, which led to a significant negative charge distribution (Chawla et al., 2023).

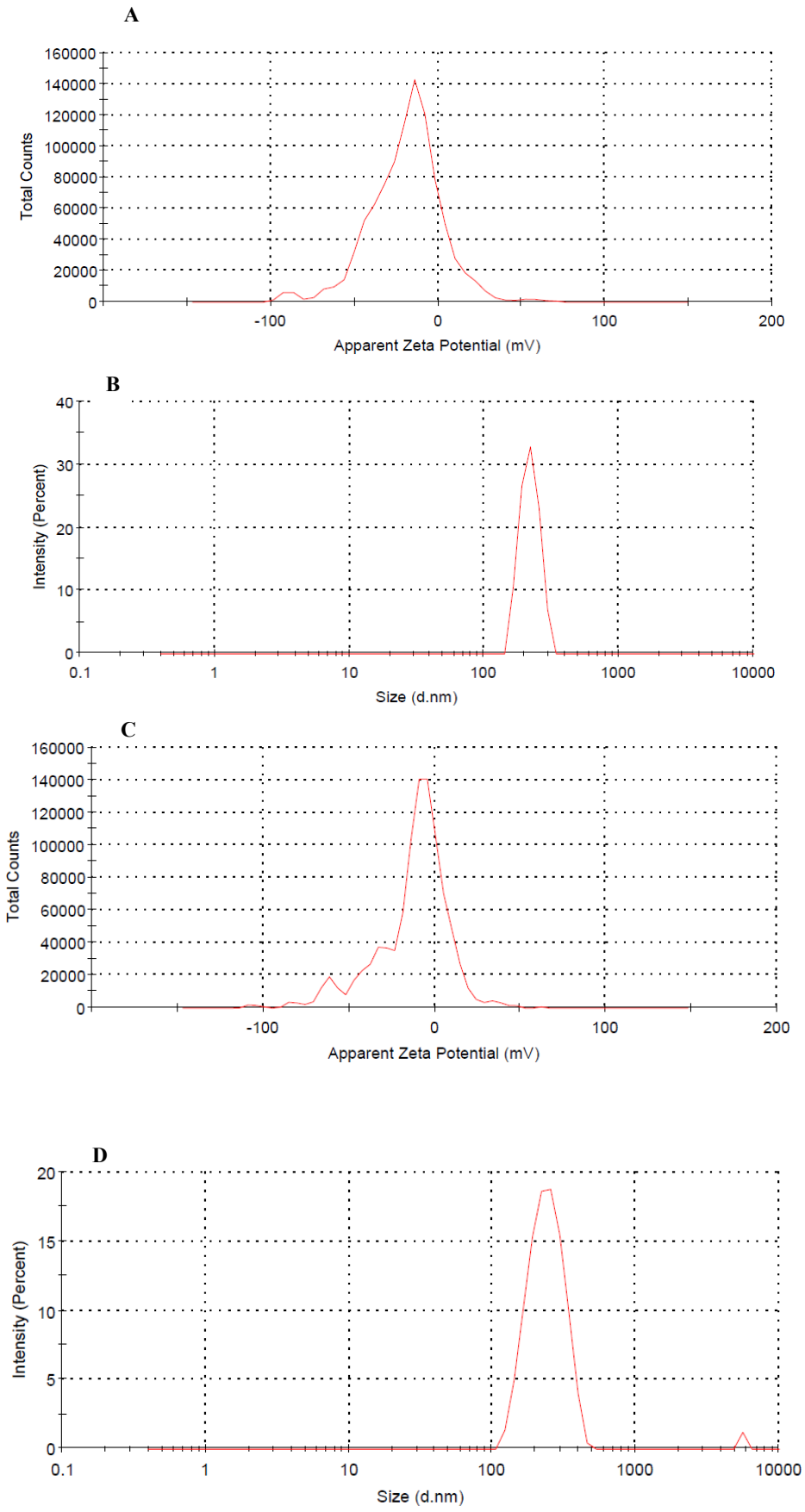

Fig. 4.13 Characterization of guar straw cellulose (A zeta potential and B particle size) and nanocellulose (C zeta potential and D particle size)

4.5.4.2 Determination of functional group

FTIR analysis was conducted to characterize the functional groups present in cellulose and nanocellulose over the wavenumber range of 4000–400 cm^{-1} (Table 4.11, Fig. 4.14). A prominent broad band centered around 3327 cm^{-1} was attributed to O–H stretching vibrations, reflecting strong intermolecular and intramolecular hydrogen bonding within the cellulose matrix. In cellulose samples, absorption bands spanning 3327 to 559 cm^{-1} indicated the presence of typical polysaccharide functional groups, including hydroxyl (O–H), aliphatic C–H, methylene (CH_2), and ether (C–O–C) linkages. The band near 1510 cm^{-1}, associated with aromatic vibrations of lignin, was substantially reduced or nearly absent after chemical treatment, confirming lignin removal. Similarly, the decreased intensity at 1426 cm^{-1} further supported the elimination of non-cellulosic components. The absorption peak at 1373 cm^{-1} corresponded to C–H bending vibrations, while the reduced band around 1258 cm^{-1} suggested effective removal of hemicellulose during treatment (Kaushik and Singh, 2011). An intensified signal near 897 cm^{-1}, characteristic of β-1,4-glycosidic linkages, verified the cellulose structure in treated fibers (Guo et al., 2024). For nanocellulose, the spectral profile showed absorption bands between 3328 and 609 cm^{-1}, corresponding to O–H, C–H, CH_2, C–O–C, and C–O groups, indicating that the fundamental cellulose framework remained preserved after nanoscale processing. The consistent broad O–H stretching band observed between 3326 and 3340 cm^{-1} across all samples also highlights the hydrophilic nature and moisture affinity of cellulose and nanocellulose materials (Trivedi et al., 2023).

The transformation of rice straw into nanocellulose is characterized by chemical modifications, such as the removal of non-cellulosic components and the functionalization of the cellulose structure, which improve its versatility and functionality for various applications (Sharma et al., 2023).

Table 4.11 Comparison of Functional groups in cellulose and nanocellulose

Wavelength (cm^{-1})	**Stretching Bond**	**Functional Group**	**Cellulose Transmittance (%)**	**Nanocellulose Transmittance (%)**	**Interpretation**

3327.50	O–H stretching (hydrogen bonded)	Hydroxyl group	92.57	–	Broad O–H stretch, strong hydrogen bonding in cellulose
3328.39	O–H stretching (hydrogen bonded)	Hydroxyl group	–	85.66	Slight shift and reduced intensity in NC, indicates increased hydrogen bonding
2891.87	C–H stretching (alkyl group)	Alkyl group (methylene/methyle)	–	89.94	Present only in NC, shows stability of aliphatic chains
1419.88	CH_2 symmetric bending/deformation	Methylene group	86.63	–	Indicates intact CH_2 groups in cellulose
1365.62	CH_2 symmetric bending/deformation	Methylene group	–	91.15	Present in NC, shift may reflect structural rearrangement

1156.90	C–O–C asymmetric stretching (glycosidic linkages)	Ether linkage (β-1,4-glycosidic)	–	88.35	Appears clearly in NC, indicates enhanced exposure of glycosidic bonds
1023.27	C–O stretching in primary alcohol	Primary/Secondary alcohol group	86.87	–	Higher in cellulose, less alteration of C–O groups
1024.07	C–O stretching in primary alcohol	Primary/Secondary alcohol group	–	66.47	Lower intensity in NC, suggests partial cleavage or rearrangement
873.03	β-glycosidic linkage (C1–H deformation)	Anomeric proton (C1–H in pyranose ring)	91.90	–	Strong peak in cellulose, intact β-linkage
894.21	β-glycosidic linkage (C1–H deformation)	Anomeric proton (C1–H in pyranose ring)	–	89.57	Slightly reduced in NC, still preserved
670.50	C–H bending and skeletal vibration	Alkyl group (methylene/methyl)	–	89.20	Only in NC, more skeletal vibration due to smaller fibril size

608.98	C–O skeletal vibration and ring deformation	Primary/Secondary alcohol group	-	87.24	Strong in cellulose, linked to intact polysaccharide structure
559.00	C–O skeletal vibration and ring deformation	Primary/Secondary alcohol group	93.50		Decreased in NC, implies partial disruption of cellulose ring

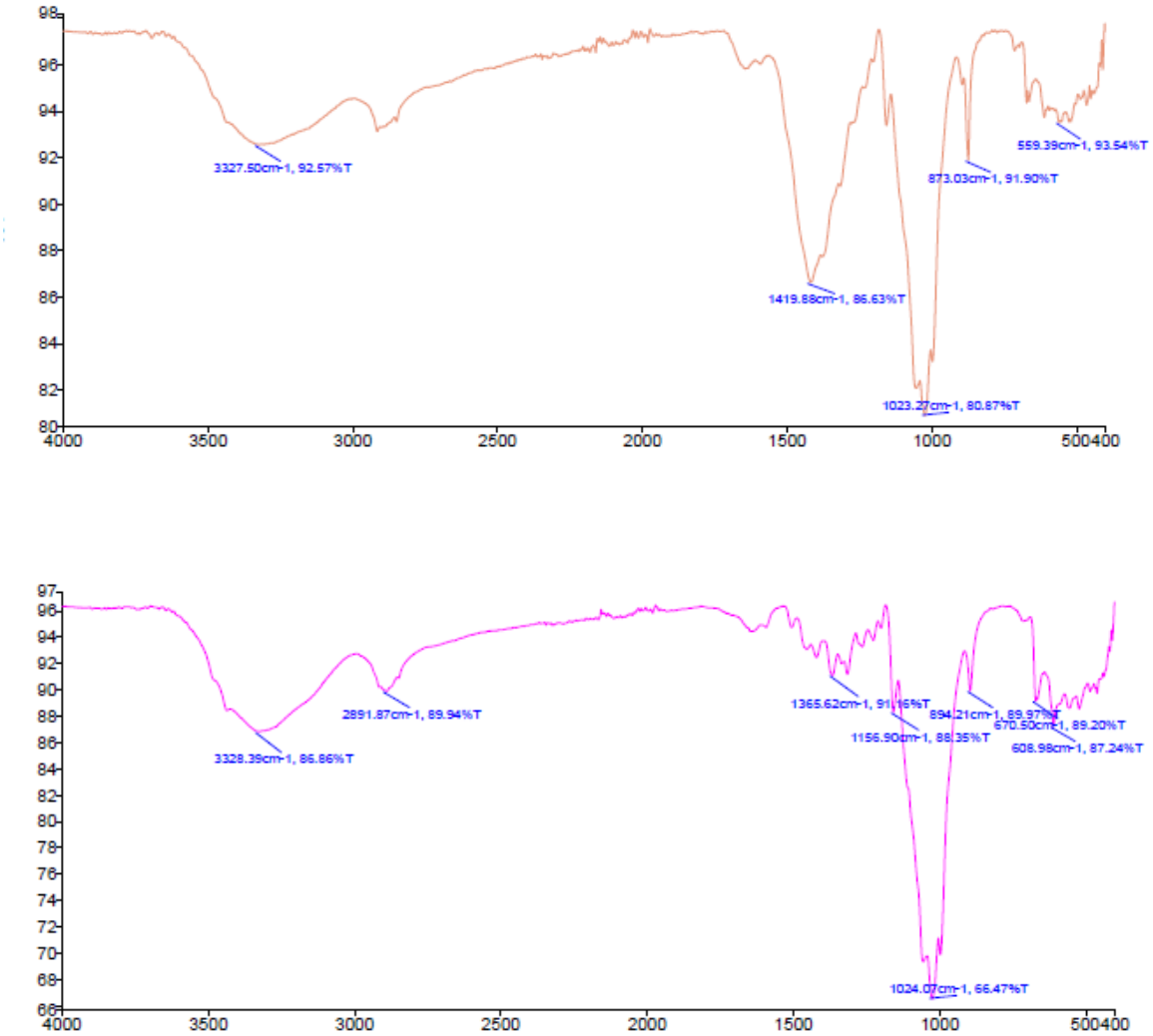

Fig. 4.14 FTIR Spectroscopy spectrum of guar straw cellulose (A) and nanocellulose (B)

4.5.4.3 Crystallinity determination using (XRD)

To compare the crystallinity of cellulose to the nanocellulose, X-ray diffraction was used and result is shown in Fig. 3c. Herein, the crystallinity of cellulose (Fig. 4.15) represents the sharp crystalline peak at 2θ = 22.27˚, along with crystalline structure, a different amorphous region was found at 2θ = 15.00˚. This pattern shown that semi-crystalline nature of cellulose within polymer matrix. Whereas, in the nanocellulose (Fig. B) shows a broader and sharper crystalline peak was decrease at 2θ = 21.40˚, it's nearby the amorphous pattern minimum at 2θ = 17.23˚. Moreover, amorphous region was increased from 30˚ to 50˚, the crystallinity of nanocellulose decreased as a result of chemical hydrolysis. The X-ray diffractogram of cowpea husk showed prominent diffraction peaks at approximately 15.4°, 22°, and 34° (2θ), which are characteristic of cellulose crystalline structures. After alkaline treatment followed by bleaching, the crystallinity index increased to 77%, indicating efficient elimination of amorphous constituents such as hemicellulose and lignin. This improvement reflects the formation of cellulose-enriched fibers with a more ordered crystalline arrangement compared to the raw material (Masanabo et al., 2025). In contrast, nanocellulose samples exhibited a noticeable reduction in peak intensity, suggesting an increase in the amorphous fraction. This phenomenon may be attributed to the partial disruption of crystalline domains during acid hydrolysis and the fragmentation of cellulose fibrils into nanoscale structures. Likewise, nanocellulose isolated from soybean straw displayed distinct reflections near 16° and 22.5° (2θ), corresponding to the (101) and (200) planes, respectively. These diffraction signals are typical of cellulose type I, indicating that the native crystalline framework was largely retained after the nanocellulose preparation process (Souza et al., 2020).

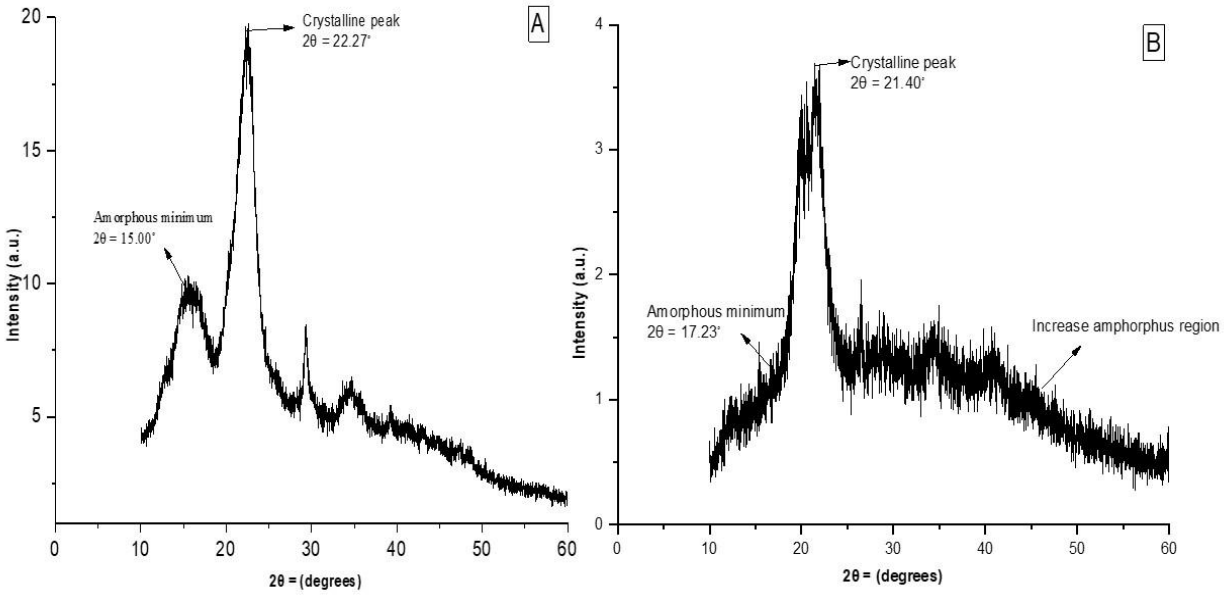

Fig. 4.15 X-ray diffraction pattern of guar straw cellulose (A) and nanocellulose (B)

4.5.4.4 Thermal stability analysis

Cellulose and nanocellulose weight loss was observed at heating temperatures ranging from 30 to 600°C. The thermogravimetric analysis (TGA) curve for samples shown the weight loss in different phase, as depicted in Fig. 4.16. The initial weight loss in cellulose 6.911 mg, was observed at 46.59 ℃, which is due to loss of surface moisture content. The major mass reduction due to decomposition of cellulose chains, particularly the breakdown of glycosidic linkages and other thermally unstable components at 233.60 °C by reducing the weight of cellulose to 6.356 mg. In contrast with nanocellulose (Fig B) represent the thermal stability, firstly degradation of nanocellulose was started at higher temperature 311.42 °C, with a weight loss 5.543 mg, shows the enhanced thermal stability. This is due to the removal of amorphous part during acid hydrolysis and the increased order of the nanocellulose structure. A second, more gradual degradation was occurred at 454.01 °C, with a remaining mass of 0.991 mg, corresponding to the carbonization or char formation phase.

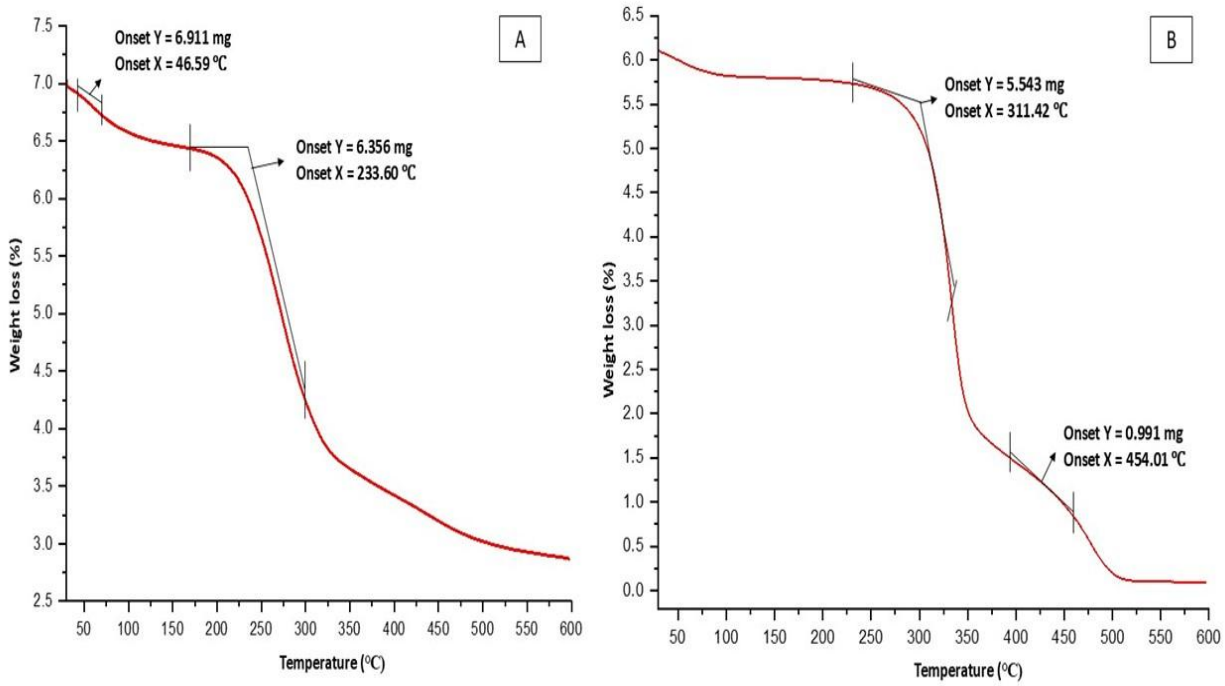

Fig. 4.16 Thermogravimetric analysis of guar straw cellulose (A) and nanocellulose (B)

4.5.4.5 Surface morphology

The morphology and microstructure of cellulose and nanocellulose were analysed using scanning electron microscopy, and the results are shown in Fig. 4.17 (A and B). The micrograph revealed an irregular network of fibrils with a rough surface. The rough surface and no fiber bundles or micro-structure are observed it confirming that the lignin and hemicellulose are removed by using alkali treatment. Whereas, in Fig. 4.17 B, the porous and web-like structure with nanoscale fibrils is shown. This structural conversion shows that the acid hydrolysis treatment effectively removed amorphous fractions, exposing crystalline particles and converting cellulose into nanoparticles.

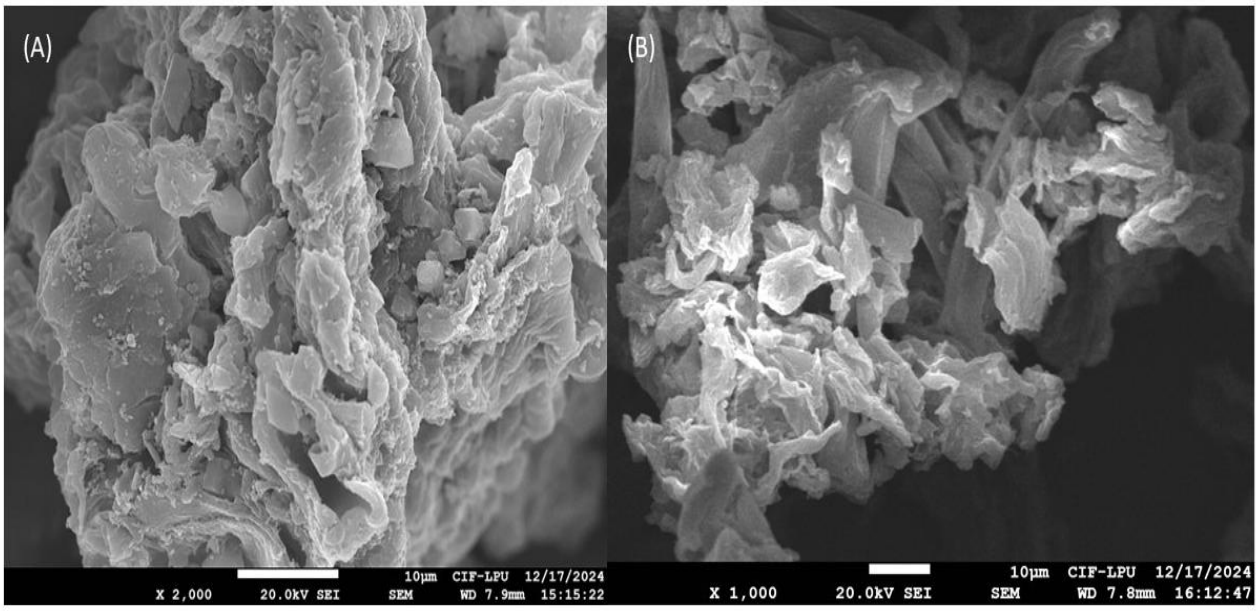

Fig. 4.17 Morphological analysis of guar straw cellulose (A) and nanocellulose (B)

4.6 Proximate analysis of *Cucumis callosus* (Seed, peel and pulp)

The moisture content in fruit pulp was significantly ($p < 0.05$) higher (76.73%) compared to the seed (27.45%) and peel (21.50%), indicating the pulp has higher water content. Ash content of *Cucumis callosus* seed (2.96 %) shows a non-significant ($p < 0.05$) difference with peel (2.83%), and both were significantly higher than pulp (1.06 %). It shows that higher inorganic components are found in non-edible parts of fruit. The fat content showed a highly significant difference ($p < 0.05$) in each part of the fruit. The seed has fat content (6.43 %), in the peel, moderate fat content was found (0.53 %), and the pulp contains a negligible amount (0.06 %). Crude fibre content showed significant ($p < 0.05$) variation, the peel had the highest fibre content (8.13 ± 0.92%), as compared to the seed (1.90 ± 0.06%) and pulp (1.78 ± 0.04%). However, protein content showed a significant difference ($p < 0.05$) in all parts, with the highest amount of protein found in the seed (23.51 %), moderate in the peel (3.79 %), and lowest in the pulp (0.36 %), which indicates that the seed is a concentrated source of plant-based protein. Whereas, carbohydrate content in pulp, peel and seed was shown to be significantly different ($p < 0.05$) from each other, (79.99%), (71.35 %) and (39.65 %), respectively. The proximate composition and statistical comparisons of seed, peel and pulp are shown in Table 4.12.The pulp, being moisture- and carbohydrate-rich, contributes primarily to energy and palatability; the seed, rich in protein and fat, offers concentrated nutrients for functional and fortified foods; and the fibre- and mineral-rich peel holds promise as a functional ingredient in dietary formulations. Chaudhary et al. (2025) reported that *Cucumis callosus* peel on a dry basis contains moisture, ash, fat, crude fibre, protein, and carbohydrates, 9.59%, 8.18%, 6.89%,

29.34%, 9.34% and 36.66%, respectively. Okiti et al. (2024) observed in *Cucumis callosus* seeds proximate profiling, including moisture (12.3%), carbohydrate (10.23%), crude fat (50.85%), crude fibre (2.72%), crude protein (20.2%), and ash (1.59%) in unfermented samples on a dry basis. No previous study has examined the *Cucumis callosus* fruit pulp proximate composition, so findings of this research are compared with those of fruits belonging to the same botanical family (*Cucurbitaceae*), such as melon (*Cucumis melo*), which has reported nutritional composition of fruit pulp, such as moisture (25.50 %), crude fat (1.08 %), crude protein (9.33 %), ash (4.16 %), crude fibre (7.10 %), and carbohydrate (52.83 %) of dried powdered sample (David and Ngbada, 2025).

Table 4.12 Proximate composition of *Cucumis callosus* peel, pulp and seed

Fruit parts	Seed (%)	Peel (%)	Pulp (%)
Moisture	27.45 ± 0.96^{b}	21.50 ± 1.45^{a}	76.73 ± 0.70^{c}
Ash	2.96 ± 0.75^{b}	2.83 ± 0.15^{b}	1.06 ± 0.15^{a}
Fat	6.43 ± 0.50^{c}	0.53 ± 0.05^{b}	0.06 ± 0.11^{a}
Crude Fibre	1.90 ± 0.06^{b}	8.13 ± 0.92^{c}	1.78 ± 0.04^{a}
Protein	23.51 ± 0.03^{c}	3.79 ± 0.35^{b}	0.36 ± 0.041^{a}
Carbohydrate	39.65 ± 0.71^{a}	71.35 ± 1.05^{b}	79.99 ± 1.13^{c}

Data are presented as mean ±SD (n=3), $^{a\text{-}c}$Means with the same lowercase superscript in a row do not vary significantly

4.6.1 Characterization of *Cucumis callosus* (Seed, peel and pulp)

4.6.1.1 Determination of functional group

The FTIR spectra determine the functional groups present in different parts of *Cucumis callosus,* such as peel, pulp, and seed, which are shown in Fig. 4.18 (a, b, and c). Peel exhibits absorption bands at 3322.10 cm^{-1} (O–H) stretching of hydroxyl groups in polysaccharides and phenolics, 2923.10 cm^{-1} and 2853.51 cm^{-1} (C–H stretching of aliphatic chains) (Williams, 2019). Whereas, at 1742.81 cm^{-1} 1622.81 cm^{-1} and 1524.02 cm^{-1}, and 1156.27–1046.25 cm^{-1} C=O stretching of esters and carboxylic acids indicating pectin and uronic acids, amide I and II bands of proteins and C–O–C and C=O stretching of glycosidic linkages, respectively, these peaks are confirming the presence of polysaccharides, proteins, and phenolic compounds (Gaweł-Bęben et al., 2022). According to Gowtham et al. (2022), seed and peel of *Cucurbita pepo* ftir analysis reveals the chrateristic peaks at 3004.24 to 3421.05 cm^{-1} which indicates O-H functional group cm^{-1}, 2924 cm^{-1}, (C–H stretching), 1743 cm^{-1} (carbonyl ester), 1651 cm^{-1}

(amide I) and 1535 cm^{-1} (amide II), respectively. Seed, peel and pulp are rich sources of polysaccharides, lipids, and proteins. The pulp of *Cucumis callosus* showed multiple absorption peaks including, peaks at 3279.29 cm^{-1}, 3012.33 cm^{-1}, 2923.90 cm^{-1}, and 2854.43 cm^{-1}, suggest the existence of O–H stretching vibrations, hydroxyl groups from carbohydrates, phenolic constituents, and bound water molecules, shown the hydrophilic nature of the pulp, C–H stretching vibrations of aliphatic CH_2 and CH_3 groups, characteristic of cellulose, hemicellulose, and pectic substances (Kpodo et al., 2023 and Chaudhary, and Gupta, 2025). A distinct, sharp band at 1742.61 cm^{-1} (C=O stretching vibrations), shows the presence of esterified carbonyl groups such as methyl esters of galacturonic acid found in pectin (Pais et al., 2023). The peak at 1628.19 cm^{-1} represents C=C stretching or amide I (C=O) vibrations, indicating the contribution of aromatic phenolics and proteins. Absorptions at 1542.56 cm^{-1} and 1511.66 cm^{-1} are associated with amide II (N–H bending) and aromatic C=C stretching, confirming the presence of protein and lignin-like aromatic compounds. The peaks at 1425.91 cm^{-1} and 1377.71 cm^{-1} correspond to CH_2 bending and C–H deformation, associated with cellulosic structures. The 1331.86 cm^{-1} band represents C–N stretching vibrations, confirming amine or amide linkages in proteins. Some peaks observed at 1247.56 cm^{-1}, 1148.20 cm^{-1}, 1084.60 cm^{-1}, and 1034.62 cm^{-1} C–O–C asymmetric stretching, C=O stretching, and C–C skeletal vibrations, characteristic of glycosidic linkages in polysaccharides such as pectin and cellulose. The band at 920.34 cm^{-1} is assigned to C–O–H bending in pyranose rings, while peaks at 845.27 cm^{-1} and 776.33 cm^{-1} correspond to C–H deformation and β-glycosidic linkages, confirming the carbohydrate backbone. In the lower wavenumber region, absorptions at 663.52 cm^{-1}, 610.52 cm^{-1}, and 589.47 cm^{-1} are attributed to C–H out-of-plane bending and aromatic skeletal vibrations, indicating phenolic and lignin-related compounds. Peak at 420.53 cm^{-1}, the metal–oxygen (M–O) bending vibrations, represent the presence of mineral complexes such as calcium or magnesium pectates embedded in the polysaccharide network (Rahmati et al., 2025). Kpoda et al. (2023) reported that absorption peaks were determined for pectins from the different Cucurbitaceae species. The broad peak within the range of 3500 to 3000 cm−1 corresponds to the O–H stretching vibration band. The occurrence of this peak agreed with previous reports of extracted polysaccharides. The seed spectrum displayed a broad O–H peak at 3324.93 cm^{-1}, C–H stretching at 2918.13 and 2850.67 cm^{-1}, amide I and II bands at 1621.28 and 1542.04 cm^{-1}, and strong polysaccharide-associated peaks at 1096.21–1018.62 cm^{-1}, along with lipid-associated C–H bending near 861.23 cm^{-1}. In the melon seed peaks, some peaks at 1,744 cm−1 (C=O ester bond), 1,644 and 2,062 cm−1, reveal the presence of C=C and C=C, respectively (Rahimdokht et al., 2016). Overall, the FTIR analysis shows that the peel is

rich in structural polysaccharides, proteins, and phenolics; the pulp is a rich source of pectins and carbohydrates. The seed is composed of proteins, lipids, and polysaccharides.

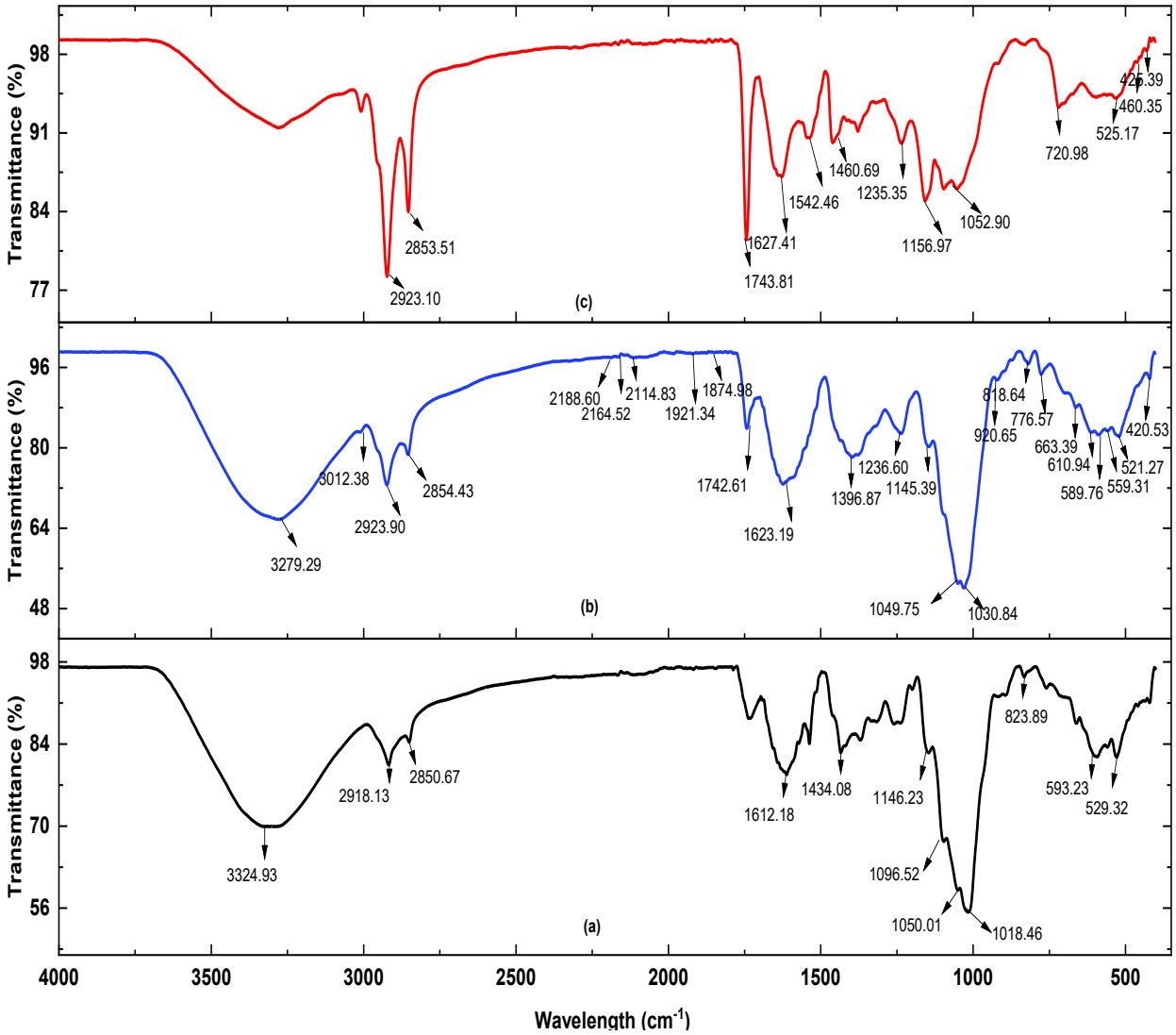

Fig. 4.18 Fourier Transform Infrared Spectroscopy analysis of *Ccucmis callosus* peel (a), pulp (b) and seed (c)

4.6.1.2 X-ray differaction

The crystallinity of different parts of *Cucumis callosus* (peel, pulp and seed) was compared, and the results are shown in Fig. 4.19 (a, b and c). Herein, the crystalline peaks were observed at 2θ=21.36˚, 2θ=20.31˚, and 2θ=21.31˚ for peel, pulp and seed, respectively. These peaks show the presence of cellulosic microfibrils and other structurally organised polysaccharides (Gaweł-Bęben et al., 2022 and Caballero-Gutiérrez et al., 2025). Crystalline regions are due to intermolecular hydrogen bonding and van der Waals interactions between linear polysaccharide backbones (Liu et al., 2020). The minimum amorphous area was found at 2θ = 24.97˚ peel, 2θ=25.89˚ pulp, and 2θ=25.97˚ seed. This region is due to the presence of non-crystalline

polysaccharides such as hemicellulose and pectin, which contain irregular branching (Adharsh and Sontakke, 2023). Whereas monosaccharide residues (e.g., arabinose, galactose, rhamnose), and functional substitutions (–COOH, –OCH_3) are also found, amorphous polysaccharides and phenolics provide elasticity, water affinity, and functional activity (Chen et al., 20205). Gade et al., (2022), reported that the crystallinity peaks of the ash gourd, watermelon, pumpkin and musk melon seeds were at 20.81, 20.25, 19.90 and 19.75, respectively.

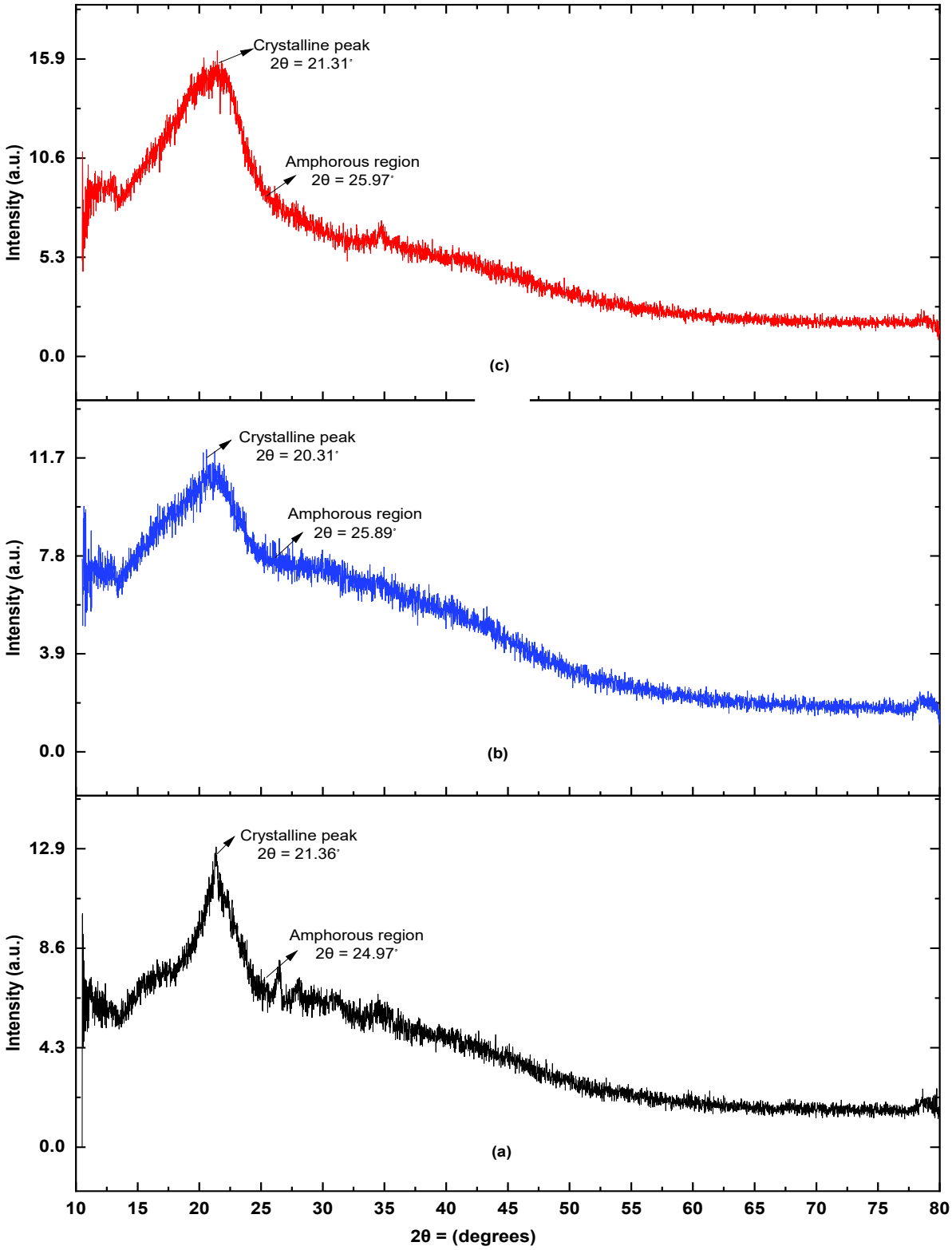

Fig. 4.19 X-diffraction analysis of *Cucumis callosus* peel (a), pulp (b) and seed (c)

4.6.1.3 Thermogravimetric analysis

The thermogravimetric analysis curve determined the sample weight loss at different stages as shown in Fig. 4.20. In the initial stage, a minor weight loss was due to evaporation of moisture and volatile compounds, where in the peel decreased from 10.623 mg (100%) to 9.933 mg

(93.50%), pulp from10.168 mg (100%) to 9.401 mg (92.46%), and seed from 19.377 mg (100%) to 19.260 mg (99.40%). In the second stage, weight loss in peel, pulp, and seed is 8.785 mg (82.70%), 9.039 mg (88.91%), and 18.093 mg (93.36%), respectively, indicating partial degradation of organic constituents, including the decomposition of hemicellulose, pectin, and amorphous polysaccharides. In the third stage, major degradation in the samples due to decomposition of hemicellulose, pectin, and amorphous polysaccharides occurs in the peel. Gade et al. (2022) reported that the lowest onset temperature of watermelon seeds (29.8 °C), pumpkin (30.8 °C), ash gourd (40.5 °C) and musk melon seed (42.4 °C). Thermal decomposition of in Cucurbit peel, moisture loss (30–151 °C = 4.47%), firstly devolatilization (151 to 317 °C = 52.52%), and secondary reactions (317 and 800 °C = 18.16%) (Bashir et al., 2024).

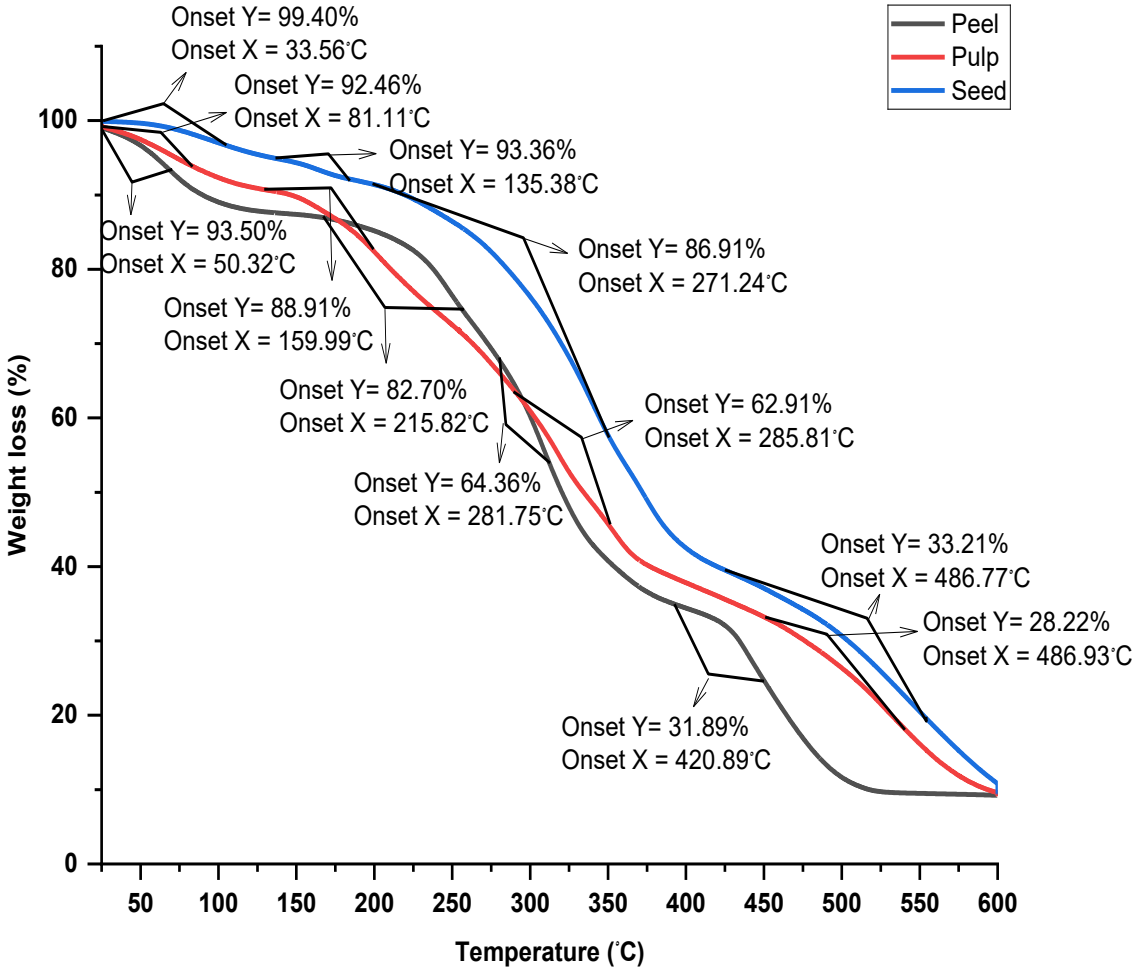

Fig. 4.20 Thermogravimetric analysis (TGA) of *Cucumis callosus* peel, pulp and seed

4.6.1.4 Differential Scanning Calorimetry

The evaluation of melting behaviour analyze using a Differential Scanning Calorimetry (DSC) of peel, pulp and seed of *Cucumis callosus* fruit samples exhibits different thermal characteristics, indicating the stability of samples shown in Fig. 4.21. According to this analysis peel sample showed exothermic peaks at 431.94 ℃ and endothermic peaks at 357.60 ℃, with corresponding enthalpy changes (ΔH) of 1809.27 J/g in Fig 1D (a). In contrast with pulp and seed samples displayed comparable peaks with enthalpy changes of 138.46 J/g at 29.68 ℃ and 110.47 ℃ and 60.65 J/g, at 32.34 ℃ and 109.03 ℃, respectively, as shown in Fig. 1D (b, c). The peel of *Cucumis callosus* fruit shows maximum enthalpy and the highest decomposition temperature, which shows that this peel has high thermal stability. The peel of watermelon shows the endothermic transition peaks at 30–145 °C (Chaudhari et al., 2015).

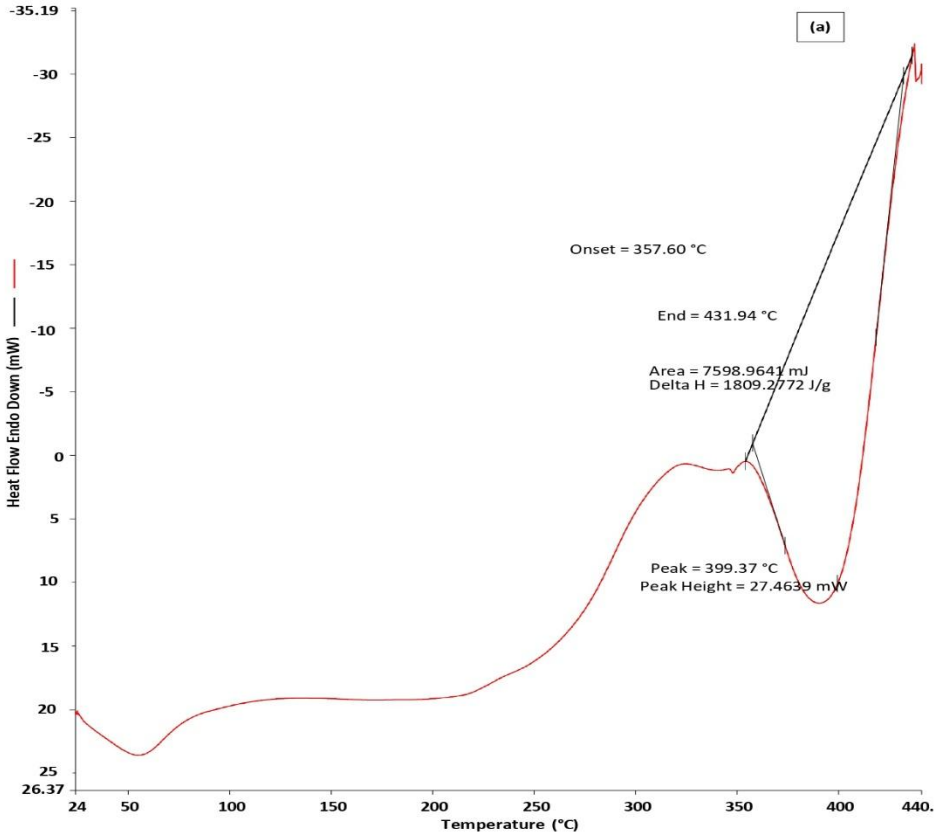

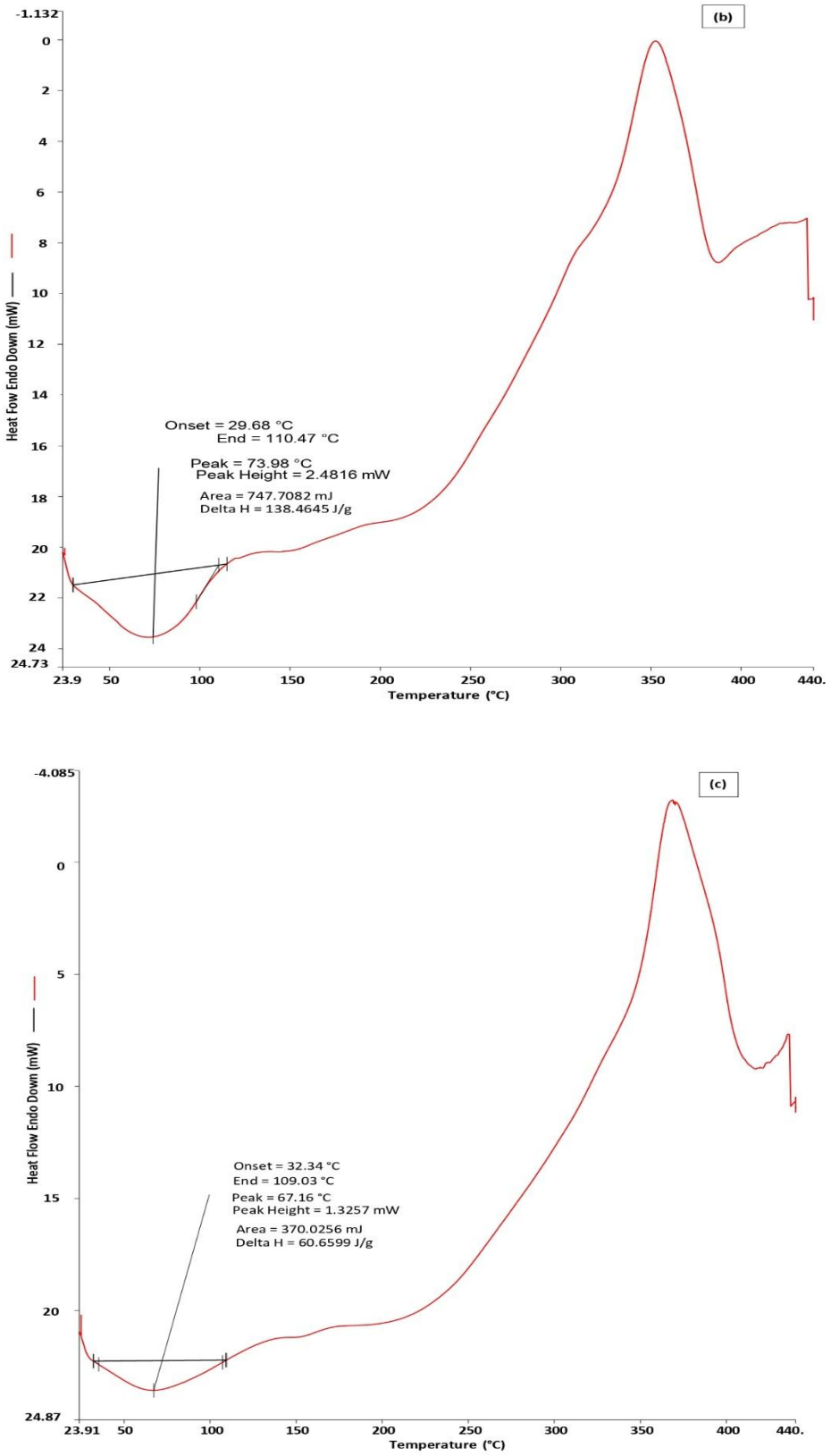

Fig. 4.21 Differential Scanning calorimetry (DSC) of *Cucumis callosus* Peel (a), pulp (b) and seed (c)

4.6.1.5 Surface morphology

The surface morphology of *Cucumis callosus* peel, pulp, and seed was analysed using a scanning electron microscope (SEM) presented in Fig. 4.22 (a-f). Under a magnification of 500^x and 1000^x presented the peel in fig 5 (a-b) revealed irregular, sharp edges and rough surfaces. The lamellar arrangement and layered appearance suggest the presence of fibrous cell-wall residues rich in lignocellulosic material. The pulp particles in Fig. 5 (c,d) exhibited a distinctly compact and granular morphology, showing a smooth area, and the surface appeared uneven with small pore, and micro-cracks. The seed micrographs, Fig. (e,f) displayed discrete, small, and roughly spherical particles with variable sizes. The fine granular structure with minor surface roughness suggests a protein- and lipid-rich matrix. Zhao et al., (2025), study on Cucumis melo seeds provides detailed SEM analysis showing reticulated seed coat morphology and surface ultrastructure resembling those of thin-skinned melon varieties. Mallek-Ayadi et al., (2022), study on Cucumis melo pulp reports microstructural features consistent with compact granular morphology with uneven surfaces and micro-cracks. The rough and fragmented surface further reflects the disruption of plant tissue during processing, exposing internal fibrous networks. Such morphological characteristics are typical of plant-derived peel materials and support their potential application as reinforcing agents in biopolymer-based composites and as functional ingredients in food systems.

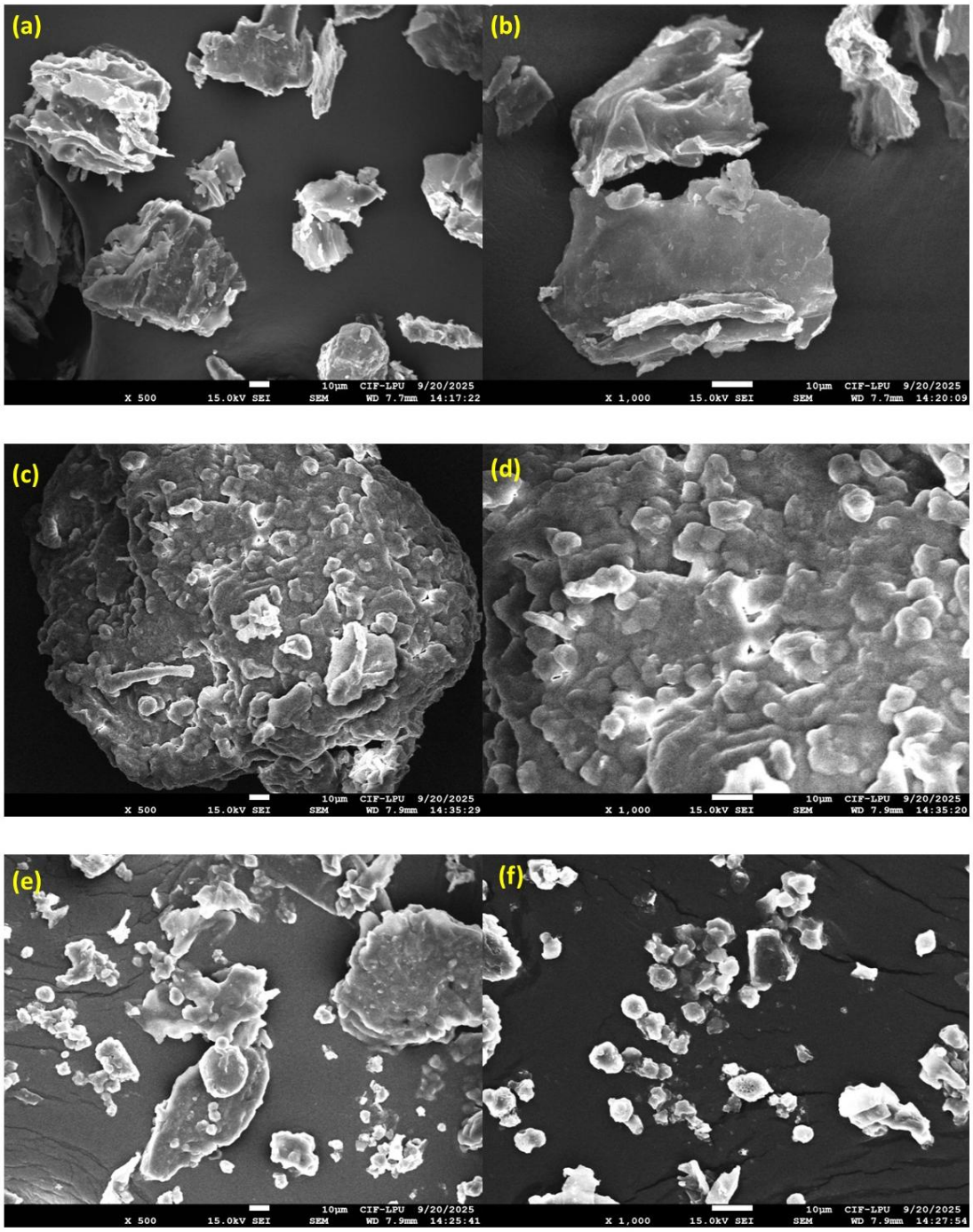

Fig. 4.22 SEM micrograph of *Cucumis callosus* (Peel (a-b), pulp (c-d) and seed (e-f)

4.6.2 Extraction of *Cucumis callosus* fruit

The ethanol extract yield of the peel, pulp, and seed of *Cucumis callosus* was recorded as the highest (21.4%), followed by the seed (10.8%) and peel (7.3%).

4..6.2.1 Physicochemical analysis

The peel showed the highest total phenolic content (390.84 mg GAE/100 g) and total flavonoid content (324.60 mg QE/100 g), followed by the seed (337.86 and 167.02 mg/100 g, respectively), while the pulp exhibited the lowest concentrations (236.83 and 124.68 mg/100

g) shows significant difference ($p < 0.05$) with each other. These results suggest that the peel is particularly rich in secondary metabolites with strong reducing capacity and radical-scavenging potential (Hussain et al., 2022). Vitamin C content in the pulp (34.86%) shows a significantly higher difference ($p < 0.05$) than the peel (18.87 %) and seed (17.92 %). The higher ascorbic acid content in the pulp may be due to its metabolically active parenchymatous tissue and natural role in protecting fruit tissue from oxidative stress. The phenolic and flavonoid content, antioxidant activity were found to be highest in the peel (67.76 %), intermediate in the seed (52.34 %), and lowest in the pulp (34.89 %). Fundo et al. (2018), reported melon seed total phenolic concentration (229.13 µg/g), antioxidant activity (653.67 µg/g). Melon peels contain the highest total phenolic content (0.087 mgGAE/g), as compared to the seed (0.042 mgGAE/g) and the rind (0.026 mgGAE/g. Chemical composition of polyphenolic, flavonoid compounds, Vitamin C and antioxidant activity are shown in Table 4.13.

Table 4.13. Physicochemical composition of different of *Cucumis callosus*

Chemical composition	Peel	Pulp	Seed
Total phenolic content (mgGAE/100g)	390.84 ± 1.76^{c}	236.83 ± 0.46^{a}	337.86 ± 1.51^{b}
Total flavonoid content (mgQE/100g)	324.60 ± 1.05^{c}	124.68 ± 1.95^{a}	167.02 ± 1.99^{b}
Vitamin C (%)	18.87 ± 0.70^{b}	34.86 ± 0.55^{c}	17.92 ± 0.69^{a}
Antioxidant activity (%)	67.76 ± 0.61^{c}	34.89 ± 0.95^{a}	52.34 ± 0.86^{b}

Data are shown as mean ± SD

Different uppercase superscripts $^{a\text{-}c}$within the column are significantly different ($p<0.05$) from each other

4.6.2.2 Biochemical profiling

4.6.2.2.1 Chlorophyll and carotenoid content

The photosynthetic pigment contents of different parts of *Cucumis callosus* peel, pulp and seed showed a significant difference ($p < 0.05$) from each other presented in Table 4.14. The peel exhibited the highest pigment content, with chlorophyll a (17.21mg/g), chlorophyll b (15.38mg/g), and carotenoids (2.42mg/g), followed by the seed 1.61, 1.80, and 1.32mg/g, respectively. The pulp showed the lowest amount of pigments, 0.56 mg/g for chlorophyll a, 0.67 mg/g for chlorophyll b, and 0.50 mg/g for carotenoids. The peel, being the outermost light-

exposed region, contained abundant chloroplasts and photosynthetic structures, which explains its elevated concentrations of chlorophyll and carotenoids.

Table 4.14 Photosynthetic pigment content of different parts of *Cucumis callosus*

Pigments	Peel	Pulp	Seed
Chlorophyll a (mg/g)	17.21±0.60^{c}	0.56±0.062^{a}	1.61±0.075^{b}
Chlorophyll b (mg/g)	15.38±0.03^{c}	0.67±0.034^{a}	1.80±0.95^{b}
Carotenoids (mg/g)	2.42±0.11^{c}	1.32±0.083^{b}	0.50±0.073^{a}

Data are shown as mean ± SD

4.6.2.2.2 Quantification of polyphenols through HPLC

Polyphenolic compounds such as flavonoids, phenolic acids, tannins, lignans, and coumarins are essential bioactives that contribute significantly to the antioxidant and enzyme inhibitory potential of plant-based extracts. The HPLC chromatograms of the peel Fig.4.23 (a), pulp, (b), and seed, (c) extracts recorded at 280 nm revealed distinct phenolic profiles, showing efficient resolution and quantification of individual compounds. In the peel extract, major peaks appeared at retention times of 31.97 and 41.02min, showing phenolic compounds are caffeic acid (83.65 mg/kg) and ferulic acid (3231.01 mg/kg). The pulp extract exhibited major peaks at 16.52, 33.08, and 41.88 min, indicating that the compounds were found, such as chlorogenic acid, caffeic acid, and ferulic acid, 4.97 mg/kg, 3.88 mg/kg and 204.73 mg/kg. The seed extract displayed peaks at 31.95 and 40.98 min, representing caffeic acid (81.66 mg/kg) and ferulic acid (2710.13 mg/kg). The higher cinnamic and caffeic acid levels in the seed fraction explain its superior antioxidant and enzyme inhibitory performance compared to peel and pulp. Overall, the total phenolic composition was highest in peel at different retention times, and relative peak intensities confirmed the successful chromatographic separation and the predominance of hydroxycinnamic acid derivatives in the seed extract, indicating its potential as a rich natural source of bioactive phenolics with strong functional and nutraceutical relevance.

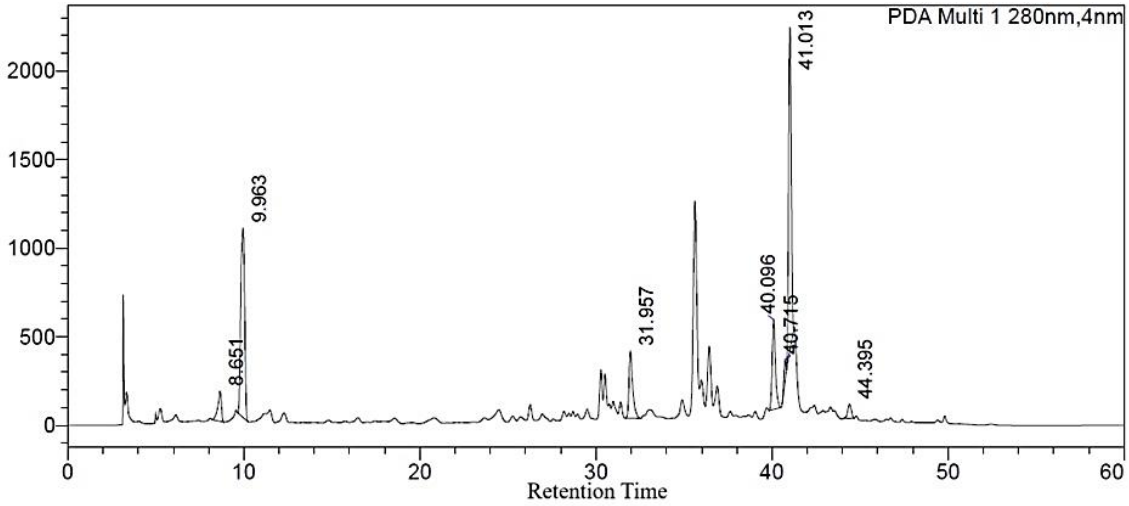
PDA Multi 1 280nm,4nm
41.013
9.963
40.096
31.957
40.715
8.651
44.395
Retention Time

(a)

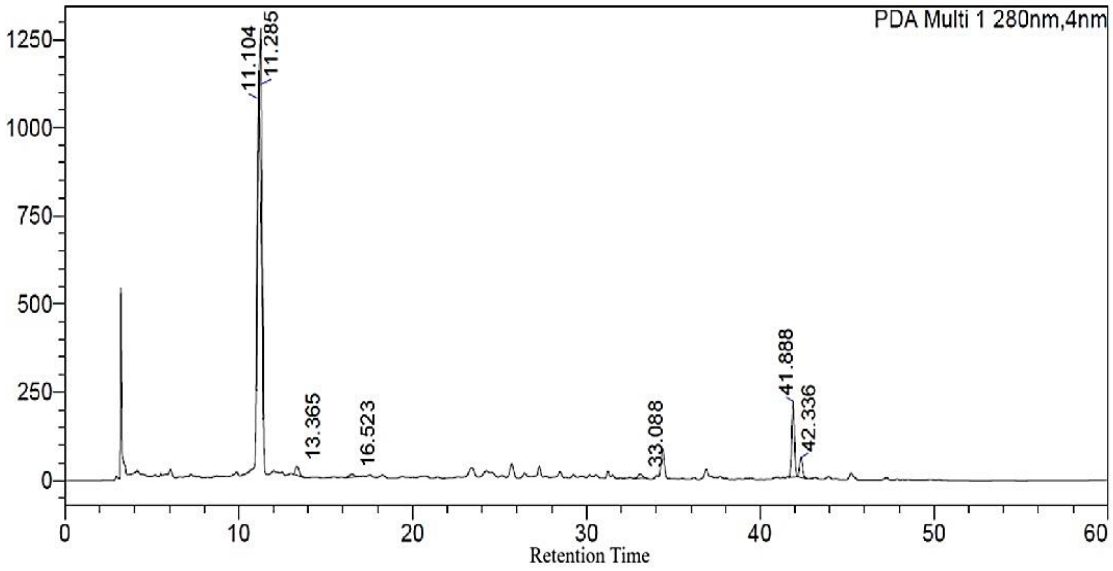
PDA Multi 1 280nm,4nm
11.104
11.285
41.888
13.365
16.523
33.088
42.336
Retention Time

(b)

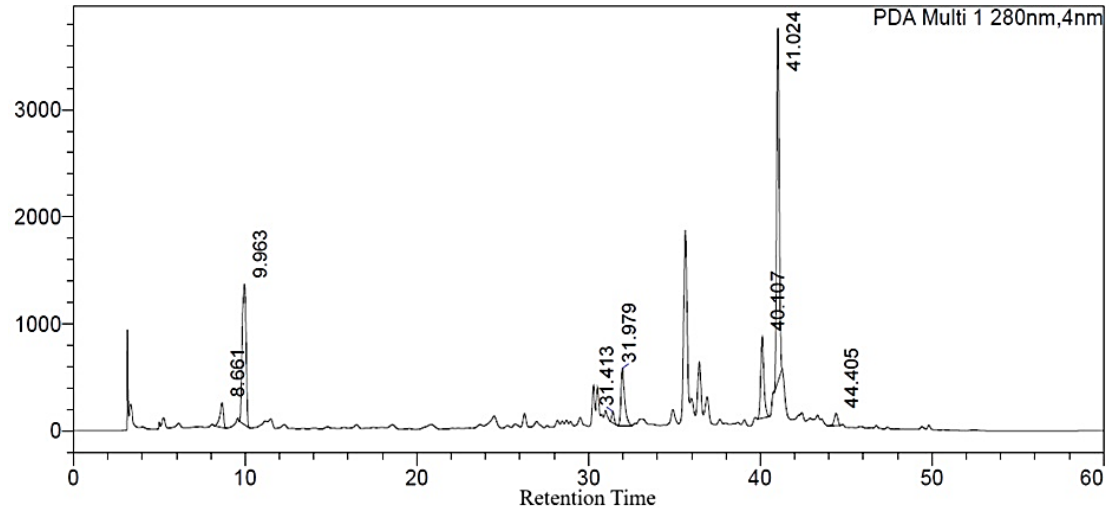
PDA Multi 1 280nm,4nm
41.024
9.963
40.407
31.979
31.413
8.661
44.405
Retention Time

(c)

Fig. 4.23 HPLC Chromatograph of Ethanolic *Cucumis callosus* peel (a), pulp (b) and seed (c)

4.6.2.2.3 Antinutritional factors

The analysis of anti-nutritional factors, phytic acid, tannins, and oxalic acid in the peel, pulp, and seed of *Cucumis callosus* in presented in Table 4.15. The phytic acid content shows a significant difference ($p < 0.05$) among the samples, being highest in the seed (32.91 mg/g), as compared to the pulp (23.54 mg/g) and peel (19.42 mg/g). This shows that the seed possesses greater mineral-chelating capacity, while the lower phytic acid in peel and pulp enhances mineral bioavailability (Ramesh et al., 2022). The tannin content showed a significant difference ($p < 0.05$), with the seed (13.65 mg/g) showing the highest concentration, the peel (12.52 mg/g) moderate, and the pulp (10.76 mg/g) the lowest. The high tannin levels in the seed and peel indicate reduced protein digestibility but higher antioxidant potential, whereas the lower tannin content in the pulp suggests better digestibility and improved sensory characteristics (Ojo, 2022). Similarly, oxalic acid content showed significant variation ($p < 0.05$), being highest in the pulp (0.028 mg/g), followed by the peel (0.026 mg/g) and lowest in the seed (0.020 mg/g). Although these differences are small numerically, they are statistically significant, implying tissue-specific variations in oxalate accumulation. Overall, all three factors, phytic acid, tannins, and oxalic acid, differed significantly among the peel, pulp, and seed, with the seed showing the highest anti-nutritional load, the peel moderate, and the pulp being nutritionally superior due to its significantly lower levels of anti-nutritional compounds**.**

Table 4.15 Antinutritional compounds in *Cucumis callosus* peel, pulp and seed

Factors	Peel	Pulp	Seed
Phytic acid (mg/g)	19.42 ± 1.27^{a}	23.54 ± 1.30^{b}	32.91 ± 1.90^{c}
Tannin content (mg/g)	12.52 ± 0.15^{b}	10.76 ± 0.06^{a}	13.65 ± 0.91^{c}
Oxalic acid (mg/g)	0.026 ± 0.04^{b}	0.028 ± 0.03^{c}	0.020 ± 0.02^{a}

Data are shown as mean ± SD

Different uppercase superscripts $^{a\text{-}c}$within the column are significantly different ($p<0.05$) from each other

4.6.3 Antimicrobial efficiency

Antimicrobial activity of *Cucumis callosus* extracts of peel, pulp, and seed was evaluated against *Escherichia coli* and *Staphylococcus aureus*, as shown in Fig. 4.24. At a concentration of 1 mg/mL, all extracts exhibited measurable antibacterial activity. Against *E. coli*, the peel extract (P_1) showed the largest zone of inhibition (11.50 mm), followed by the pulp (Pu_1) and seed (S_1) extracts (11.00 mm). In the case of *S. aureus*, the seed extract (S_1) showed the highest

inhibition (13.00 mm), followed by the peel (11.00 mm) and pulp (11.00 mm) extracts. No inhibition zones were observed at 0.5 mg/mL or 0.25 mg/mL concentrations, except for the seed extract, which showed mild inhibition (10.00 mm) against *S. aureus* at 0.5 mg/mL. The standard antibiotic ampicillin exhibited markedly higher inhibition zones in all assays, confirming assay reliability. For *E. coli*, ampicillin showed inhibition zones of 17.00 mm (pulp), 17.00 mm (peel), and 19.00 mm (seed). Against *S. aureus*, inhibition zones of 19.25 mm (peel), 18.25 mm (pulp), and 20.50 mm (seed) were observed. These values significantly exceeded those of the natural extracts, demonstrating the expected potency of the synthetic antibiotic. Overall, the results confirm that the seed extract (S_1) of *C. callosus* possesses the strongest antibacterial potential, especially against *S. aureus*, followed by the peel and pulp extracts. Neglo et al. (2021) reported that the peel, pulp, and seed extracts of watermelon (*Citrullus lanatus*) exhibited antibacterial activity with inhibition zones of 12 mm, 7.6 mm, and 11 mm, respectively, against *Escherichia coli*, and 20 mm, 13 mm, and 14 mm, against *Staphylococcus aureus*.

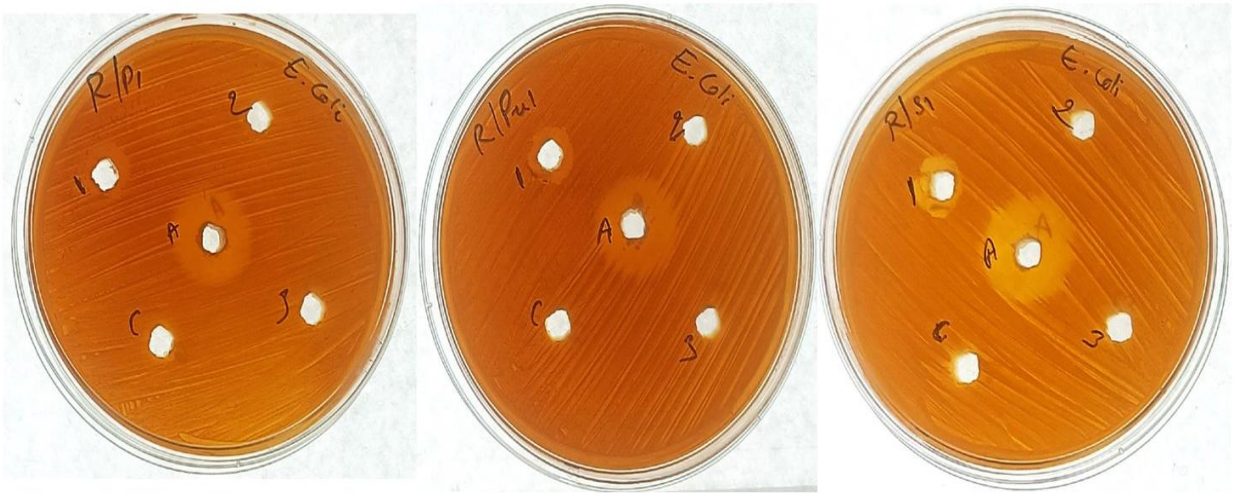

(a)

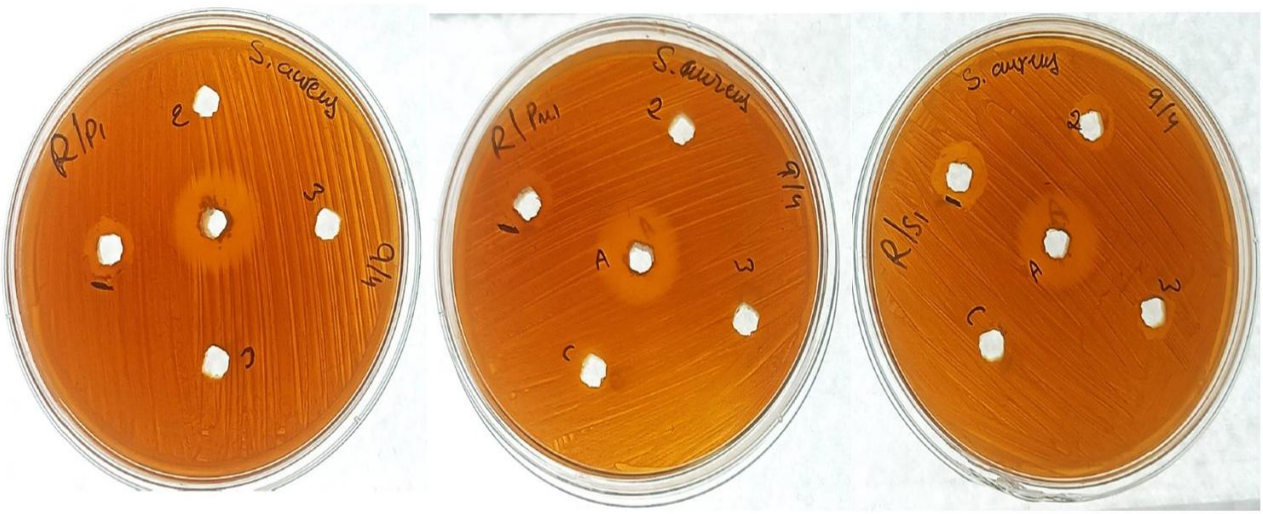

(b)

Fig. 4.24 Zone of inhibition in *Cucumis callosus* peel, pulp and seed against *Escherichia coli* (a) and *Staphylococcus aureus* (b)

4.6.4 Binding efficiency

The interaction between guar straw–derived nanocellulose and the ethanolic *Cucumis callosus* peel extract was found to be concentration dependent, and the corresponding binding efficiencies are presented in Table 4.16. Among the tested formulations, NC0.2 and NC0.5 exhibited significantly higher (p<0.05) binding efficiencies compared to the other concentrations. This enhanced interaction can be attributed to the greater availability of surface hydroxyl groups on nanocellulose, which promote hydrogen bonding and hydrophobic interactions with polyphenolic constituents. In contrast, NC0.025 showed the lowest binding efficiency, indicating limited interaction at this concentration. No significant differences ($p > 0.05$) were observed between NC0.050 and NC0.1, as well as between NC0.075 and NC1, suggesting comparable polyphenol binding capacities within these concentration ranges. The highest interaction observed at NC0.2 and NC0.5 may also be associated with the formation of stronger intermolecular associations, potentially involving quinone-mediated covalent linkages. Conversely, the reduced binding at NC0.025% could be related to preferential nanocellulose–nanocellulose interactions, which limit the availability of active binding sites for phenolic compounds. Additionally, optimal binding was observed at neutral pH (pH 7), indicating that reduced proton interference under these conditions favors stable complex formation between nanocellulose and polyphenols, consistent with previously reported findings (Peng et al., 2023).

Table 4.16 The nanocellulose-phenol interaction efficiency at different polyphenol concentrations

NPC	*Cucumis callosus* extract (%)	Binding ratio (%)
NPC0.025	0.025	97.12 ± 0.05^{a}
NPC0.050	0.05	97.88 ± 0.03^{b}
NPC0.075	0.075	98.83 ± 0.06^{c}
NPC0.1	0.1	98.47 ± 0.02^{b}
NPC0.2	0.2	99.36 ± 0.08^{c}
NPC0.5	0.5	99.37 ± 0.04^{c}
NPC 1	1	98.86 ± 0.07^{c}

Data are presented as mean ± SD (n = 3). Mean values within a column with different lowercase superscripts (a-c) within the column are significantly different ($p < 0.05$) from each other

4.6.5 Techno-functional properties of the nanocellulose-polyphenolic complex

The functional properties of the nanocellulose-polyphenolic complex, as shown in Table 4.17, indicate promising applications in food and biopolymer formulations. The WHC was measured at 2.82 g/g, demonstrating a good ability to retain water, which benefits extending the shelf life of foods. The OHC of the complex was found to be 1.34 g/g, showing a low affinity for lipophilic substances, which can aid in flavour retention (Abdullah et al., 2023). Emulsion properties and stability were observed at 29.92 % and 24.36%, respectively. Additionally, the foaming capacity was 10.45%, foaming stability was 6.72%, and swelling capacity was 9.21 ml/g, making it a suitable dietary fibre source (Tian et al., 2024). Furthermore, the lower bulk density (0.38 ± 0.03 g/cm³) and true density (0.23 ± 0.02 g/cm³) indicate a porous structure, which is excellent for formulation in low-density materials such as light-textured or expanded food items.

Table 4.17 Techno-functional properties of nanocellulose-polyphenolic complex

Functional Properties	**Composition**
Water Holding Capacity (WHC) g/g	2.82 ± 0.75
Oil Holding Capacity (OHC) g/g	1.34 ± 0.63
Emulsion Ability (EA) %	29.92 ± 0.23
Emulsion Stability (ES) %	24.36 ± 0.89
Foaming Capacity (FC) %	10.45 ± 0.94
Foaming Stability (FS) %	6.72 ± 0.51

Swelling Capacity ml/g	9.21 ± 0.56
Bulk Density g/cm^3	0.38 ± 0.03
True Density g/cm^3	0.23 ± 0.02

Data are presented as mean ± SD (n = 3)

4.6.6 Quantification of total phenolic content, total flavonoid content and DPPH radical-scavenging activity

As shown in the Table. 4.18, the antioxidant activity, total phenolic and total flavonoid content of the nanocellulose–polyphenolic complex showed significant phenolic content. The total phenolic content (TPC) and total flavonoid content (TFC) were found as 290.93 mg GAE/g and 224.45 mg QE/g, respectively. The phenolic composition represents crucial antioxidants (phenolic acids, flavonoids, and tannins), known for their role in neutralizing free radicals and preventing oxidative cell damage (Kumar et al., 2020). The radical scavenging activity of the polyphenolic complex was found 72.67%, indicating a high scavenging capacity to help eliminate free radicals, which have been identified as causes of cellular damage and ageing (Patil et al., 2024).

Table 4.18 Phytochemical properties of nanocellulose-polyphenolic complex

Phytochemical composition	**Composition**
Total phenolic content (mgGAE/g)	290.93±1.13
Total flavonoid content (mgQE/g)	224.45±0.98
Radical scavenging (%)	72.67±0.19

Data are shown as mean ± SD (n = 3)

4.6.7 Determination of polyphenolic compounds

Polyphenolic compounds present in the nanocellulose polyphenolic complex were analysed using HPLC, as shown in Fig. 4.25. The chromatographic analysis revealed three different peaks, which showed variation in polyphenolic compounds. At 7.550 min, the most predominant phenolic acid was found, such as p-coumaric/ferulic acid, with 61.109% of the total area. The good quantity of the p-coumaric/ferulic could be the main contributor to the antioxidant activity of the extract. Chlorogenic acid contributing 23.466% of the total area with a retention time of 6.083 min, reflecting its relevance in modulating oxidative pathways and

enhance bioactivity of the complex. Caffeic acid was observed at 6.917 min with 15.425% of the total area. It is known to its strong antioxidant activity. Whereas, the lower concentration of compounds is important due to their anti-inflammatory and antimicrobial properties (Patil et al., 2024). These findings similar with previous study

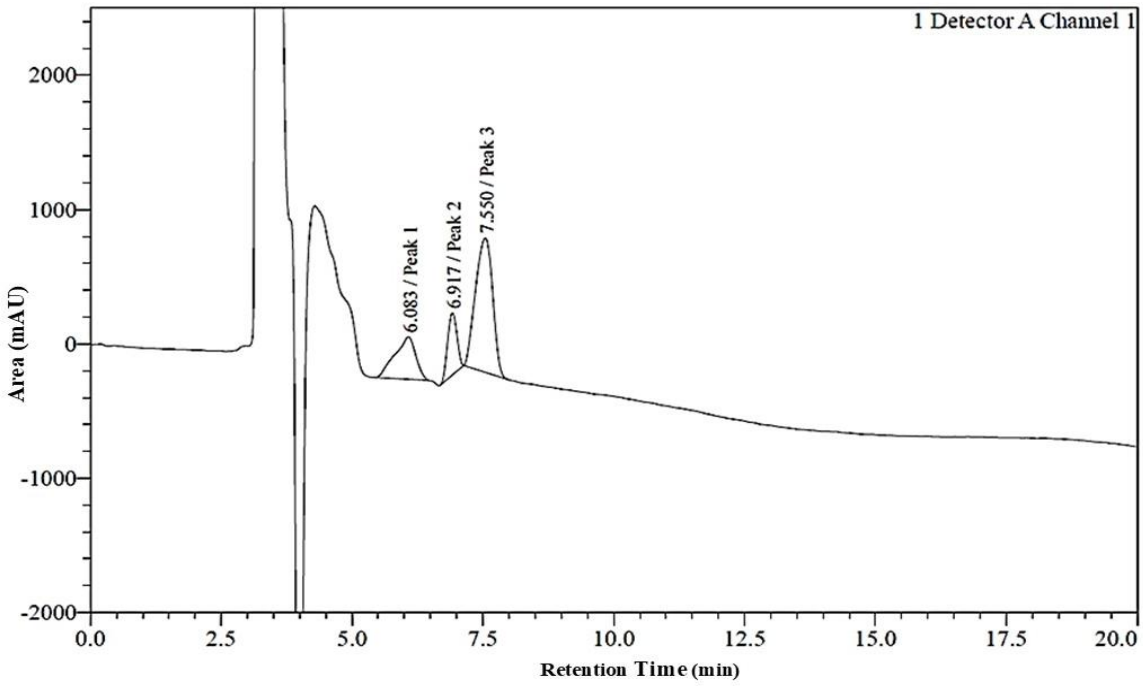

Fig. 4.25 HPLC Chromatograph of nanocellulose- polyphenolic complex

4.6.8 Hydrophobic characteristics of the surface

The surface hydrophobicity of the polyphenolic complex (0.48 a.u./mg·ml^{-1}) was higher compared to the native nanocellulose (0.15 a.u./mg·ml^{-1}). The hydrophobicity was increased with the hydrophobic groups or by introducing new hydrophobic aromatic moieties, thereby increasing fluorescence reactivity and surface hydrophobicity. According to Hu et al. 2017, the modification of cellulose with polyphenolic compounds increased the hydrophobicity from a water angle of 21˚ to 74˚. The study showed that surface modification through various spectroscopic and microscopic analyses increased dispersibility in organic solvents due to increased hydrophobicity. Surface functionalization with polyphenol compounds introduces aromatic hydrophobic groups that mask hydroxyl groups on nanocellulose. This enhances surface hydrophobicity and enables applications such as oil-water separation, advanced coatings, and green composite materials (Iqbal et al., 2022).

4.6.9 Characterization of native nanocellulose and nanocellulose- polyphenolic complex

4.6.9.1 Fourier Transform Infrared Spectroscopy (FTIR)

The Fourier Transform Infrared Spectroscopy (FTIR) analysis of native nanocellulose and nanocellulose–polyphenolic complex showed the differences in their functional group present in samples (Fig. 4.26). In the spectrum of native nanocellulose red line were absorbed broad peak at 3330.43 cm^{-1}, which signifies a O–H stretching vibration, representing of intramolecular hydrogen bonding in cellulose. Whereas, nanocellulose–polyphenolic complex (black line) shows a slightly shifted O–H band at 3362.3 cm^{-1}, suggesting enhanced hydrogen bonding interactions due to polyphenolic attachment. The presence of hydroxyl groups was evident from the prominent absorption bands in the 3400-3200 cm^{-1} region, attributed to O–H stretching vibrations (Wahyudi et al., 2025). Peaks at 2980.80 cm^{-1} and 2901.24 cm^{-1} in the phenolic complex and native nanocellulose respectively, correspond to asymmetric and symmetric C–H stretching of methyl and methylene groups, which are less prominent in native nanocellulose. The absorption peaks at 3451 cm-1 and around 2899 cm-1 were attributed to the O-H and C-H stretching vibrations, respectively (Wulandari, et al., 2016). The carbonyl group (C=O) stretching vibration appears more shown in the native nanocellulose at 1726.28 cm^{-1}, indicating ester or carboxylic acid contributions. Peaks at 1591.49 cm^{-1} and 1358.65 cm^{-1} in the complex are attributed to aromatic skeletal vibrations and C–O stretching, respectively, confirming the presence of polyphenolic structures. The band at 1051.77 cm^{-1} and 1055.16 cm^{-1} in both samples corresponds to the bending mode of absorbed water, but appears more intense in the complex, suggesting increased hydrophilicity. The peak absorption at 1644 cm-1 was reported as the O-H vibration of absorbed water. The peak for C-H and C-O vibrations contained in the polysaccharide rings of cellulose is around 1382 cm-1 (Mandel et al., 2011). The fingerprint region (1055.16–1033.00 cm^{-1}) shows strong C–O–C and C–O stretching vibrations in both samples, but the slight shifts and differences in intensity indicate structural modifications upon complexation (Djanas et al., 2024). stretching vibrations between 1225 and 1075 cm−1 and C-O single bond stretching vibrations between 1150 and 1040 cm−1. The 900–700 cm−1 spectral region is associated with out-of-plane deformation vibrations of the C-H group. This region is important because it helps in determining the type of aromatic substitution (Abbas et al., 2017). The vibration of C-O-C in pyranose ring indicated by the absorption peak at 1060 cm-1. The transmittance dip at 524.78 cm^{-1} in the complex compared to 560.71 cm^{-1} in the native cellulose further supports the modification of the nanocellulose backbone due to polyphenolic binding. The shift observed peaks of native nanocellulose compared to the polyphenolic complex support the chemical modification of nanocellulose backbone upon complex formation.

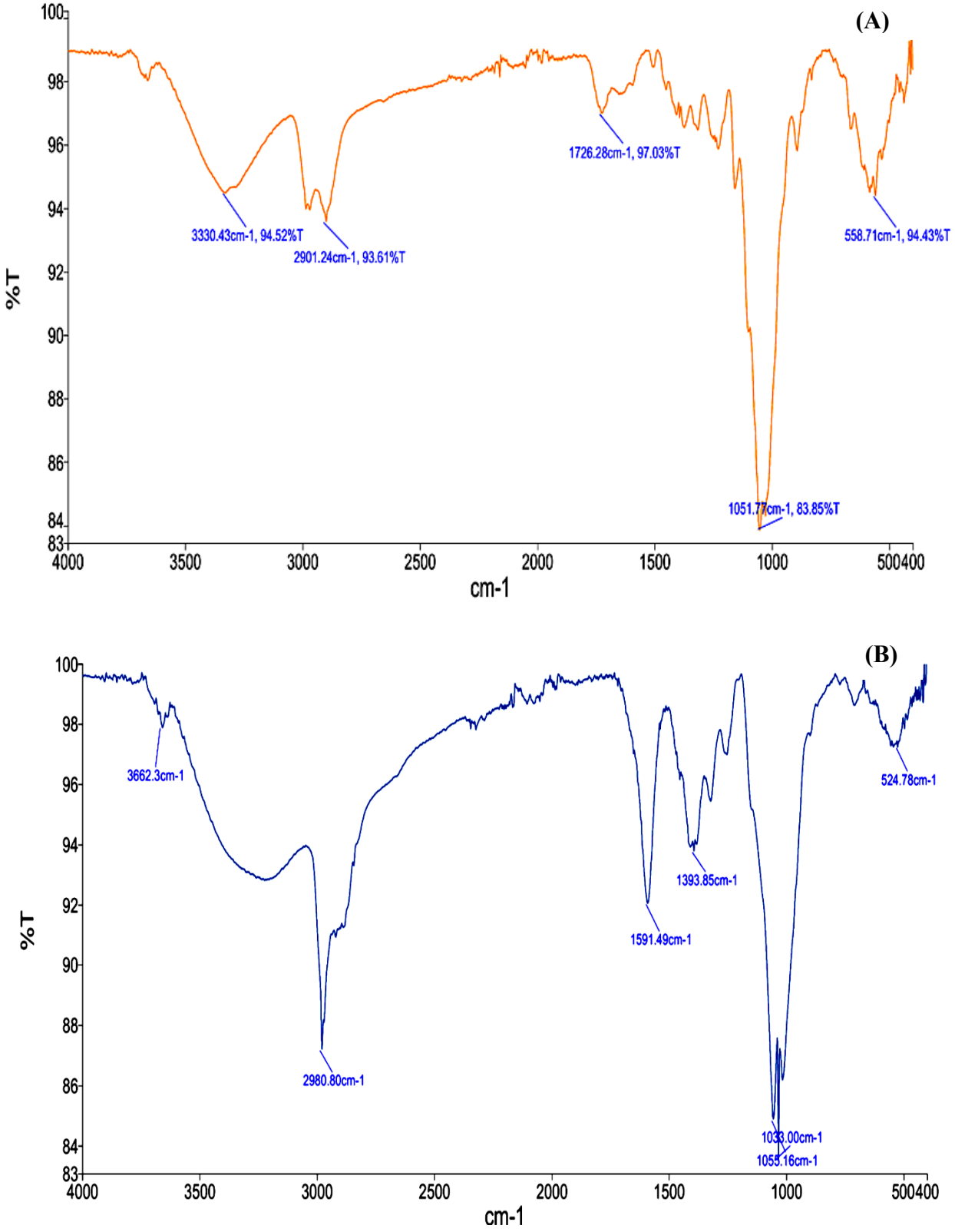

Fig. 4.26 Fourier Transform Infrared Spectroscopy analysis of guar straw nanocellulose (A)

and nanocellulose–polyphenolic complex (B)

4.6.9.2 X-diffraction analysis

The X-diffraction analysis of native nanocellulose (green curve) and nanocellulose–polyphenolic complex (blue curve) reveals clear structural differences due to complex formation, shown in fig. 4.27. Native nanocellulose shows a strong crystalline peak at about 2θ=22.18° and an amorphous minimum at 2θ=19.00°, indicating a high crystallinity index of 67.86%. In contrast, the nanocellulose–polyphenolic complex exhibits a broader and shifted crystalline peak near 2θ=21.63° and an amorphous minimum shifted to 2θ=17.88°. There is an evident increase in the amorphous background in the complex, corresponding to a significantly lower crystallinity index of 22.51%. This decreases in crystallinity and increase in amorphous content suggest that polyphenol binding disrupts the ordered cellulose crystalline regions by interfering with hydrogen bonding and molecular packing. As a result, the nanocellulose chains adopt a more disordered structure, confirming successful complex formation and indicating altered physical and mechanical properties compared to native nanocellulose. According to Hossen et al., found that crystallinity index increased due to chemical hydrolysis from about 5.5% in raw fiber to approximately 29% in nanocellulose. On conversion of nanocellulose into polyphenolic complex, show that surface modifications lead to decreased crystallinity due to disruption of hydrogen bonding and packing, aligning with the observed lowered crystallinity index in nanocellulose–polyphenolic complexes (Raju et al., 2023).

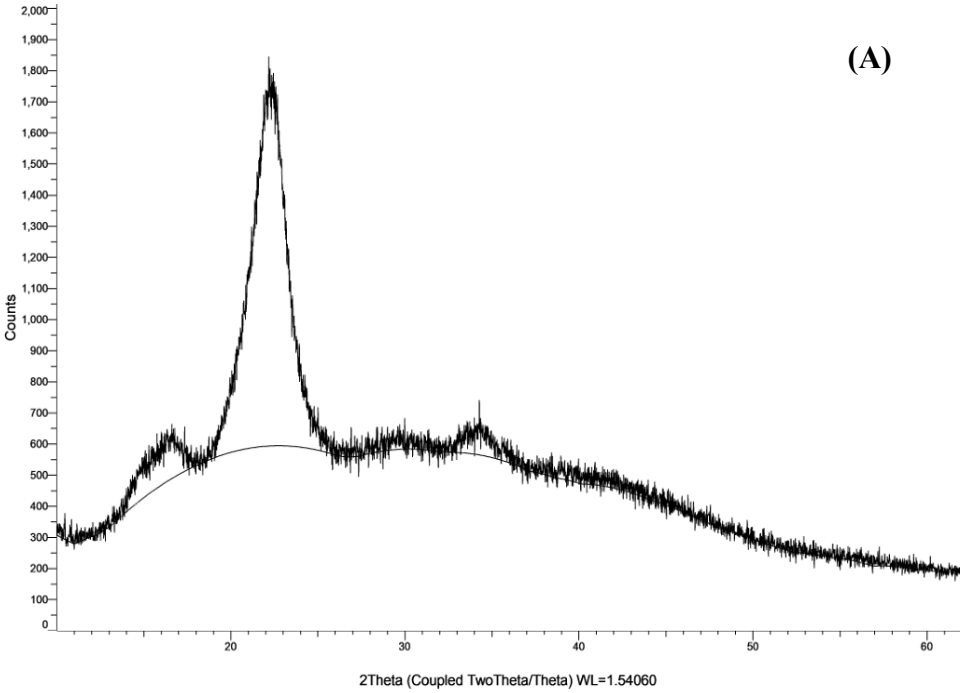

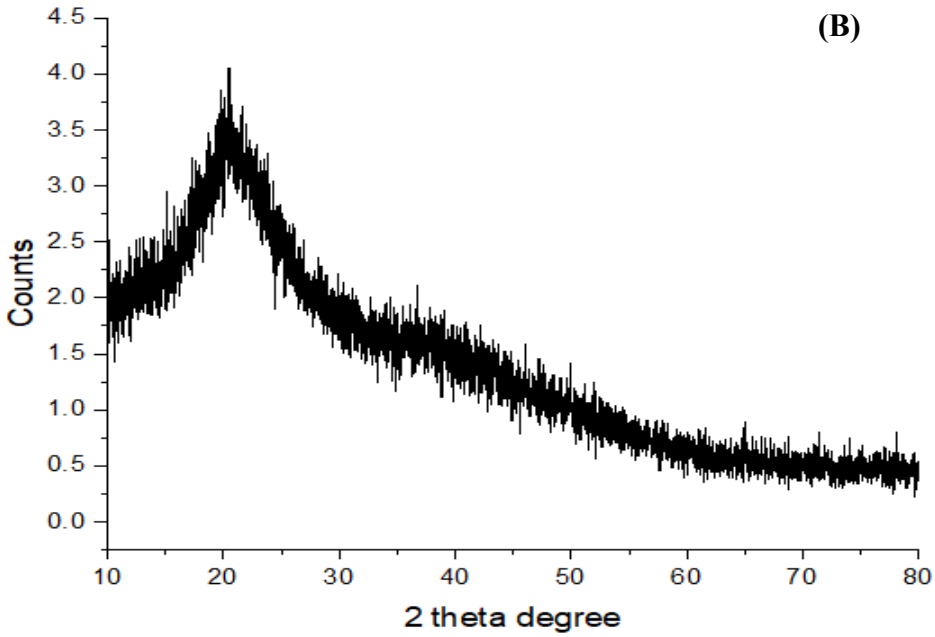

Fig. 4.27 X-diffraction analysis guar straw nanocellulose (A) and nanocellulose–polyphenolic complex (B)

4.6.10.3 Thermogravimetric analysis

The decomposition behaviour and thermal stability of nanocellulose and nanocellulose–polyphenolic complex were evaluated using thermogravimetric analysis (TGA), and the results are represented in Fig 4.28. In both samples, thermal degradation is indicated in three distinct phases. The weight loss of the polyphenolic complex was observed, 87.59 % 58.69 % and 25.51 % for the native nanocellulose, 92.67 % and 88.68 %, in the nanocellulose polyphenolic complex, respectively. The initial stage weight loss at 184.67 ℃ and 113. 69 ℃ for the nanocellulose and polyphenolic complex was observed due to evaporation of absorbed moisture and degradation of nanocellulose. Whereas, in the second stage, degradation was noted at 281.64 ℃ for nanocellulose and 172.77 ℃ complex, which can be due to the depolymerization and breakdown of C-C and C-O bonds in the ring structures, resulting in the formation of CO, CO2, and H_2O as well as decomposition of the phenyl group, respectively. In the final stage for sample nanocellulose was observed at 464.27 ℃ due to decomposition of the remaining cellulose residues and any other organic materials present in the nanocellulose. The gradual decrease in mass in this range indicates the continuous breakdown of nano-cellulose and other organic components into smaller quantities in the form of more stable compounds remaining as ash content (Xu et al., 2022). Whereas, final degradation in polyphenolic complex at 270.55 ℃ which is due to combustion of volatile and carbon content.

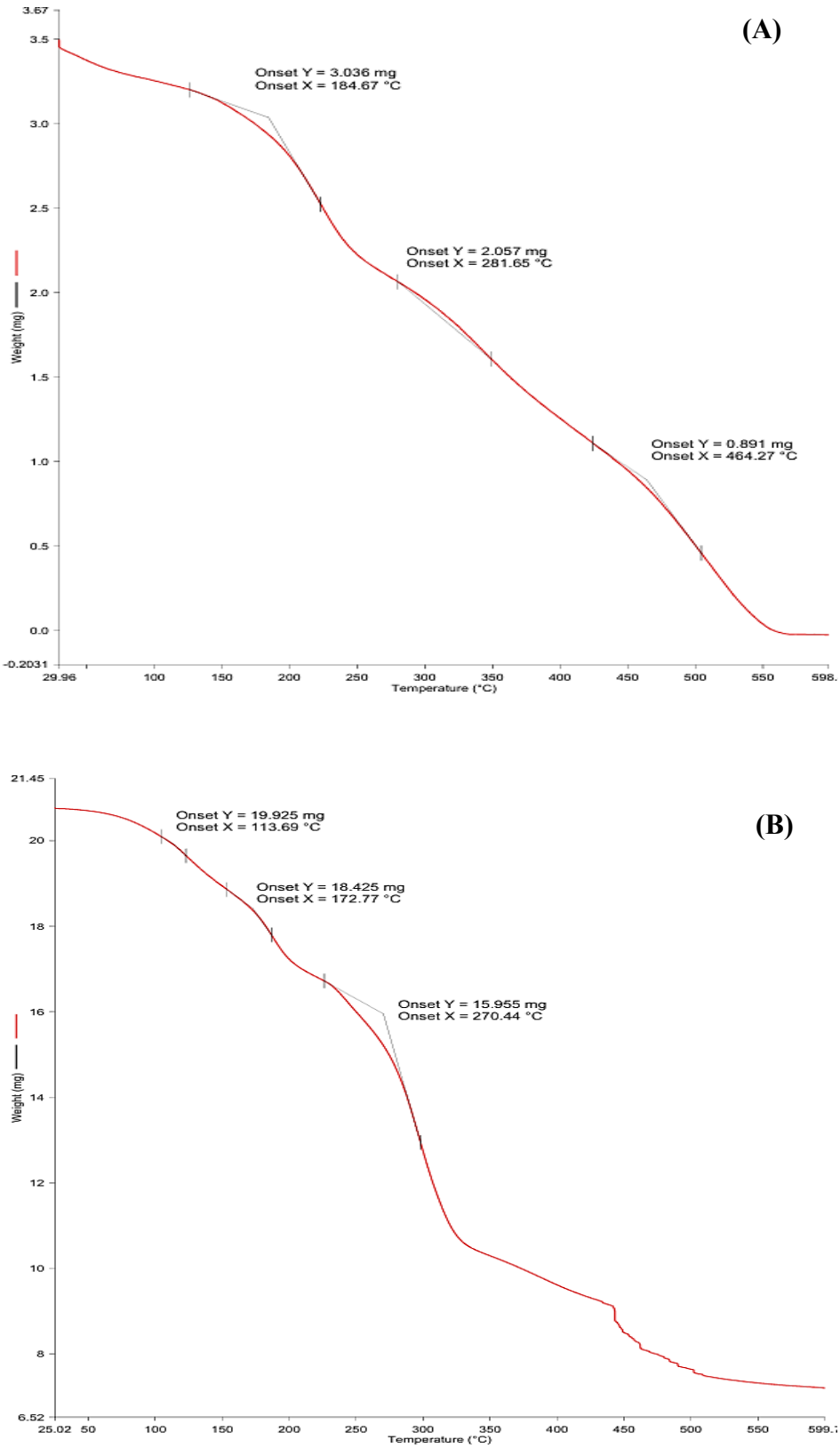

Fig. 4.21 Thermogravimetric analysis of guar straw nanocellulose (A) and nanocellulose–polyphenolic complex (B)

4.6.9.4 Differential Scanning Calorimetry

The Differential Scanning Calorimetry (DSC) thermograms of native nanocellulose and the nanocellulose–polyphenolic complex determine the heat transfer, showing changes in thermal

behavior upon complex formation in fig 4.29. Native nanocellulose exhibited a first endothermic peak at 56.38 °C (ΔH = 148.21 J/g), and the nanocellulose–polyphenolic complex at 95.69 °C (ΔH = 169.92 J/g), due to the moisture evaporation, in complex stronger hydrogen bonding polyphenols and nanocellulose hydroxyl groups, which delays moisture loss. followed by a major degradation-of nanocellulose at 119.01 °C (ΔH = 169.92 J/g) and a final decomposition stage at 324.63 °C (ΔH = 20.20 J/g). Whereas, in complex also exhibited multiple degradation peaks at 200.21 °C (ΔH = 57.04 J/g) and 332.58 °C (ΔH = 119.02 J/g), with higher onset and peak temperatures compared to native nanocellulose, indicating enhanced thermal stability. The observed shifts to higher decomposition temperatures and reduced ΔH values for intermediate transitions in the complex suggest that polyphenolic moieties restrict polymer chain mobility and form additional hydrogen bonds, thereby improving the structural rigidity and thermal resistance of nanocellulose. These results confirm successful complex formation and a stabilization effect imparted by polyphenol incorporation. Albitres et al. (2022) found through DSC and thermogravimetric analysis that nanocellulose composites with additives show higher degradation temperatures and changes enthalpy compared to native nanocellulose. Similarly, Kaur et al., found that nanocellulose shows an endothermic peak due to moisture evaporation at around 50–60 °C and a major degradation phase at 200–300 °C. Chemical modification, during formulation of polyphenol complexation, leads to shifts in these transitions to higher temperatures due to stronger intermolecular hydrogen bonding and restricted polymer chain mobility.

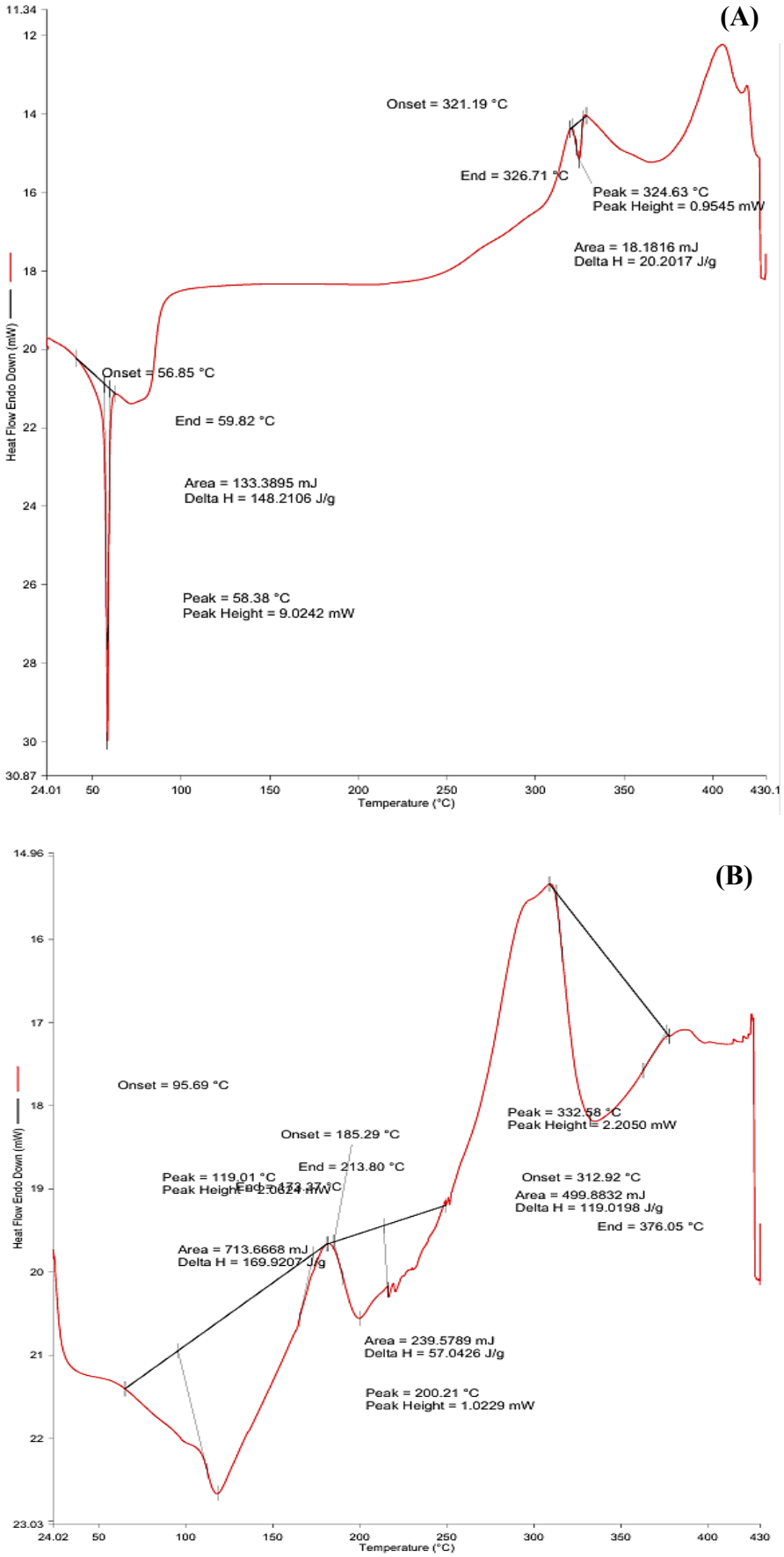

Fig. 4.29 Differential Scanning Calorimetry of guar straw nanocellulose (A) and nanocellulose–polyphenolic complex (B)

4.6.9.5 Surface morphology examined by FE-SEM

The surface morphology of guar straw nanocellulose and polyphenolic complex was analyzed and the results are characterized in Fig. The surface shown in Fig. 4.30 (A and B), elongated, fibrous structures with a smooth surface, and nanocellulose are shown in microfibril form. Due to acid hydrolysis, fibrous bundles break into finer fibrils and a more uniform distribution of fibrillar particles without significant agglomeration, indicating good colloidal stability. In contrast, polyphenolic complex morphology appears rough, irregular distribution, more compact fibrous and crystal formation due to hydrogen bonding and hydrophobic interactions between nanocellulose hydroxyl groups and phenolic compounds. Osterberg et al., 2023, reported that polyphenolic compounds interact with nanocellulose via hydrogen bonding and hydrophobic interactions between hydroxyl groups and aromatic rings. These interactions lead to a rougher, more compact fibrous surface morphology with some crystal-like formations due to self-assembly and cross-linking effects often observed in lignin-like nanoparticle systems.

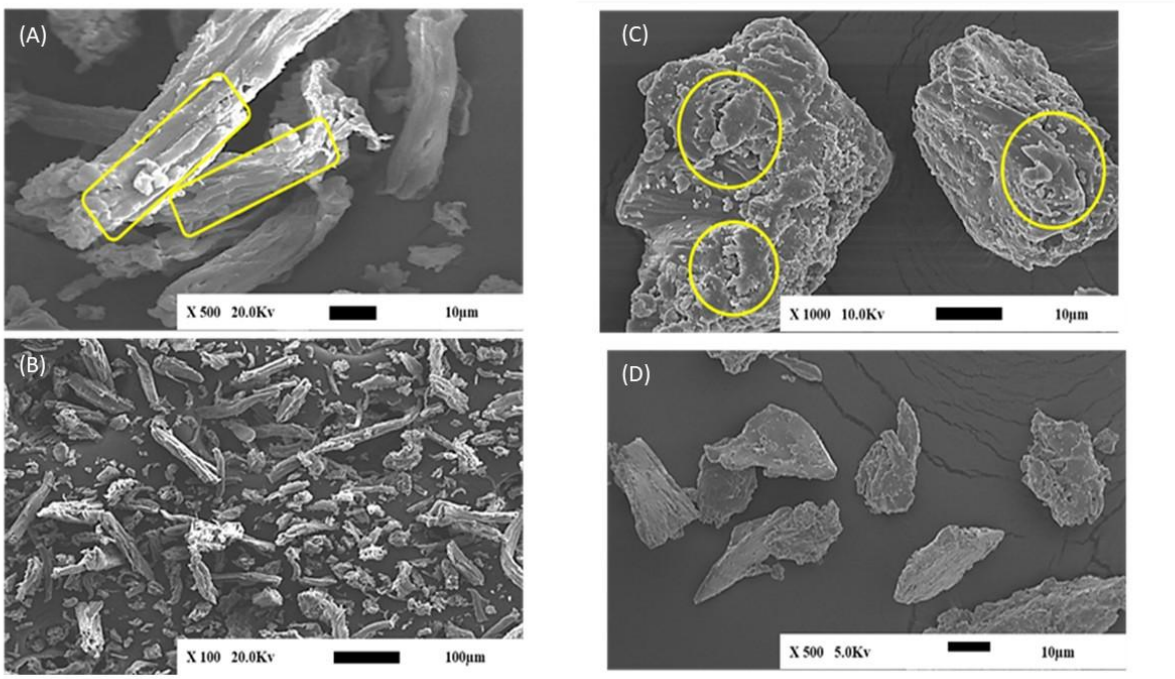

Fig. 4.23 Surface morphology of guar straw nanocellulose (A,B) and nanocellulose–polyphenolic complex (C,D)

The interaction between guar straw polysaccharides and Kachri polyphenols is mainly governed by hydrogen bonding and non-covalent molecular interactions. Guar straw polysaccharides contain abundant hydroxyl groups, while Kachri polyphenols possess phenolic –OH groups and aromatic structures, which can interact with the polysaccharide matrix through intermolecular

hydrogen bonding. These interactions may promote better molecular compatibility between the polysaccharide chains and polyphenolic compounds, resulting in a more compact and cohesive film network. The formation of such interactions can influence film properties by improving structural integrity, reducing free volume within the polymer matrix, and modifying water sensitivity and permeability behaviour. In addition, the incorporation of Kachri polyphenols contributes functional activity to the films, particularly antioxidant potential, due to the presence of phenolic hydroxyl groups capable of donating hydrogen atoms or electrons. Therefore, hydrogen bonding between guar straw polysaccharides and Kachri polyphenols plays an important role in regulating both the physicochemical properties and functional performance of the developed films.

4.7 Physical and chemical stability of nanoemulsion

4.7.1 Creaming index of nanocellulose-based nanoemulsion

The creaming index is an important parameter for assessing the physical and gravitational stability of dispersed systems, as it shows the droplet phase separation during storage. In the present investigation, no detectable creaming index was observed for samples NC1 to NC12, indicating that these formulations did not form stable dispersions or were unable to maintain a uniform dispersed phase for quantitative evaluation. The absence of measurable creaming in these samples suggests immediate destabilisation, phase separation, or insufficient emulsification, rendering them unsuitable for further stability analysis. Whereas formulations NC13 to NC16 exhibited measurable creaming indices, confirming the successful formation of dispersed systems. The representative vial image (Fig. 4.31 and 4.32) illustrates the formation of a thin cream layer at the top of the nanoemulsion after storage, which was used as a visual reference for determining emulsion stability. The ratio of the cream layer height to the total height of the nanoemulsion enabled the calculation of the creaming index, providing a quantitative measure of phase separation and physical stability.The creaming index values of NC13 (0.53 ± 0.81%), NC14 (0.49 ± 0.35%), and NC15 (0.57 ± 0.65%) were remarkably low, remaining well below 1%. Such low values indicate excellent resistance to gravitational separation, reflecting effective stabilization of droplets within the continuous phase shown in Table 4.19 and fig 4.25. This enhanced stability can be attributed to adequate emulsifier adsorption at the oil–water interface, resulting in the formation of a coherent interfacial film that restricts droplet movement and aggregation (Ravera et al., 2025). Adding ginger oil to a nanoemulsion can enhance both its stability and bioavailability, thereby improving the preservation of fruit quality (Showkat et al., 2025). The stability of the nanoemulsion was due to the combined action of Tween 80, lecithin, and nanocellulose. Tween 80 effectively reduced

interfacial tension and provided steric stabilization, while lecithin acted synergistically with Tween 80 to form a compact and elastic interfacial film, thereby minimizing droplet aggregation (Bąk and Podgórska, (2016). Nanocellulose further enhanced stability by increasing continuous-phase viscosity and acting as a Pickering stabilizer through irreversible adsorption at the oil–water interface, effectively suppressing creaming and coalescence (Teo et al., 2022).

Fig. 4.31 Representative vial image of the nanoemulsion showing a small cream layer formed at the top during storage, indicating minimal creaming behaviour and good physical stability of the formulation

Table 4.19 Optimisation and different formulation of nanocellulose-based nanoemulsions with varying surfactant and oil concentrations

Sample code	**Creaming Index (%)**	**Droplet Size (nm)**
NC1	-	-
NC2	-	-
NC3	-	-
NC4	-	-
NC5	-	-
NC6	-	-
NC7	-	-
NC8	-	-
NC9	-	-
NC10	-	-
NC11	-	-
NC12	-	-

NC13	0.53±0.81	191.7 ± 7.31
NC14	0.49±0.35	188.8 ± 5.37
NC15	0.57±0.65	192.3 ± 4.11
NC16	0.61±0.20	247.4 ± 8.38

Data are presented as mean ± SD (n = 3).

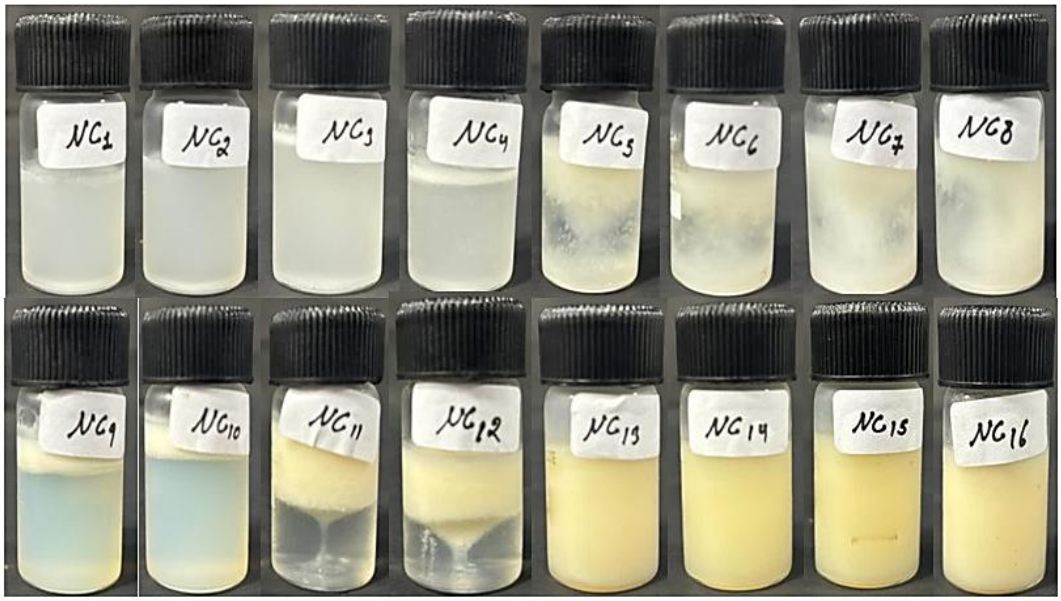

Fig. 4.32 Nanocellulose (NC), Tween 80 (T), Ginger Oil (G), Lecithin (L), NC1 (NC-1, T-0.5, G-1, L-0), NC2 (NC-1, T-0.5, G-2, L-0), NC3 (NC-1, T-0.5, G-3, L-0), NC4 (NC-1, T-0.5, G-4, L-0), NC5 (NC-1, T-1, G-1, L-0), NC6 (NC-1, T-2, G-1, L-0), NC7 (NC-1, T-3, G-1, L-0), NC8 (NC-1, T-4, G-1, L-0), NC9 (NC-1, T-0.5, G-1, L-0.5), NC10 (NC-1, T-0.5, G-1, L-1), NC11 (NC-1, T-0.5, G-1, L-1.5), NC12 (NC-1, T-0.5, G-1, L-2), NC13 (NC-1, T-0.5, G-1, L-0.5), NC14 (NC-1, T-0.5, G-2, L-1), NC15 (NC-1, T-0.5, G-3, L-1.5), NC16 (NC-1, T-0.5, G-4, L-2)

4.7.1.1 Droplet size and zeta potential of nanocellulose-based nanoemulsion

The droplet size of various nanoemulsion formulations demonstrated an increasing trend with elevated oil concentrations. Among the samples, NC16 exhibited the largest average droplet size (247.4 ± 8.38), while NC13, NC14, and NC15 displayed smaller sizes of 191.7 ± 7.31 nm, 188. 8± 5.75nm, and 192.3 ± 4.11 nm, respectively, representative in Fig. 4 .26. The zeta potential values of the optimized nanoemulsion formulations ranged from −5.17 to −19.3 mV, indicating differences in surface charge and electrokinetic stability among the samples. NC14 exhibited the highest negative zeta potential (−19.3±0.21 mV), suggesting strong electrostatic repulsion between droplets and enhanced colloidal stability. In contrast, NC13 showed a comparatively low zeta potential (−5.17±0.32 mV), indicating weak electrostatic stabilization,

which may increase the susceptibility of droplets to aggregation and reduce physical stability shown in fig. 4.33. For Pickering nanoemulsions, the droplet sizes of PN1, PN2, PN3, and PN4 were recorded at 193.2 nm, 259.6 nm, 262.2 nm, and 368.1 nm, with corresponding polydispersity index (PDI) values of 0.411, 0.284, 0.311, and 0.368, respectively (Begum et al., 2024). Similar observations were reported by Winuprasith et al. (2015), who noted that increasing the concentration of micro-fibrillated cellulose in emulsions resulted in larger droplet sizes, likely due to increased viscosity and inefficient mixing. This may promote droplet aggregation as the nanocellulose content rises. Onaizi (2022) further explained that at a constant emulsifier concentration, an increase in the volume fraction of the oil phase can limit the availability of emulsifier molecules to stabilize the newly formed oil droplets. Consequently, droplet coalescence may occur, leading to the formation of larger droplets. Continued coalescence may eventually destabilize the system, potentially resulting in phase separation, with the timeframe for such separation depending on multiple factors, including surfactant efficiency, oil type and concentration, and energy input during emulsification. Hence, the stability of the nanoemulsions formulated in this study may decline as the oil concentration increases.

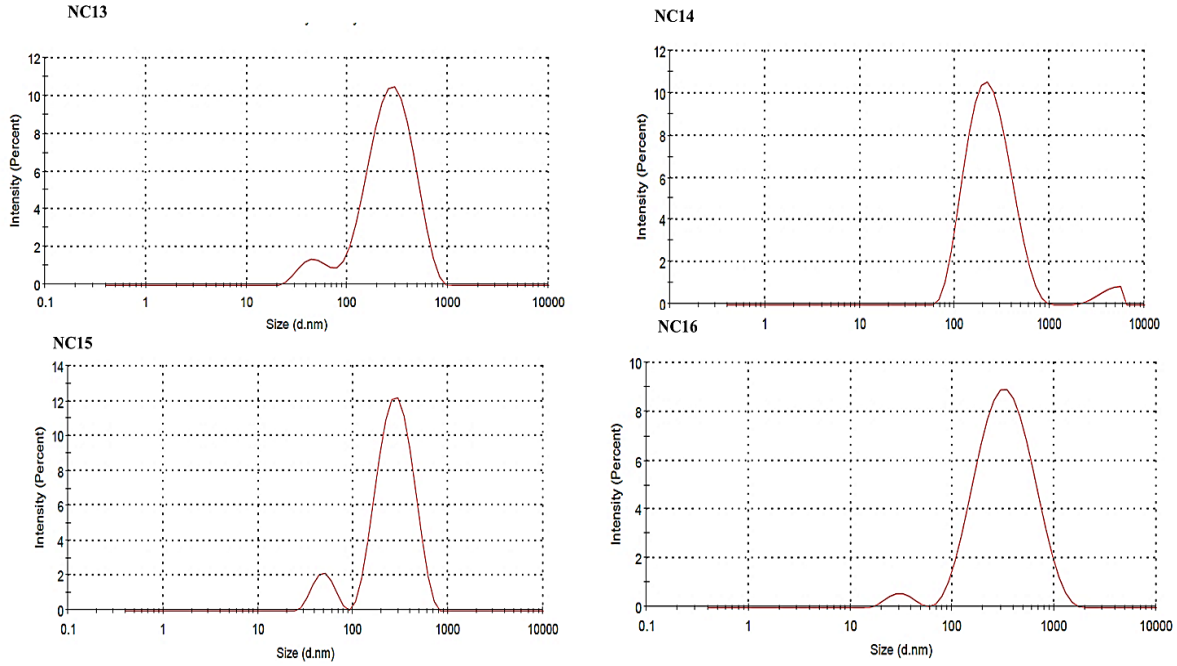

Fig. 4.33 Droplet size of Nanocellulose Nanoemulsion (NC13, NC14, NC15 and NC16)

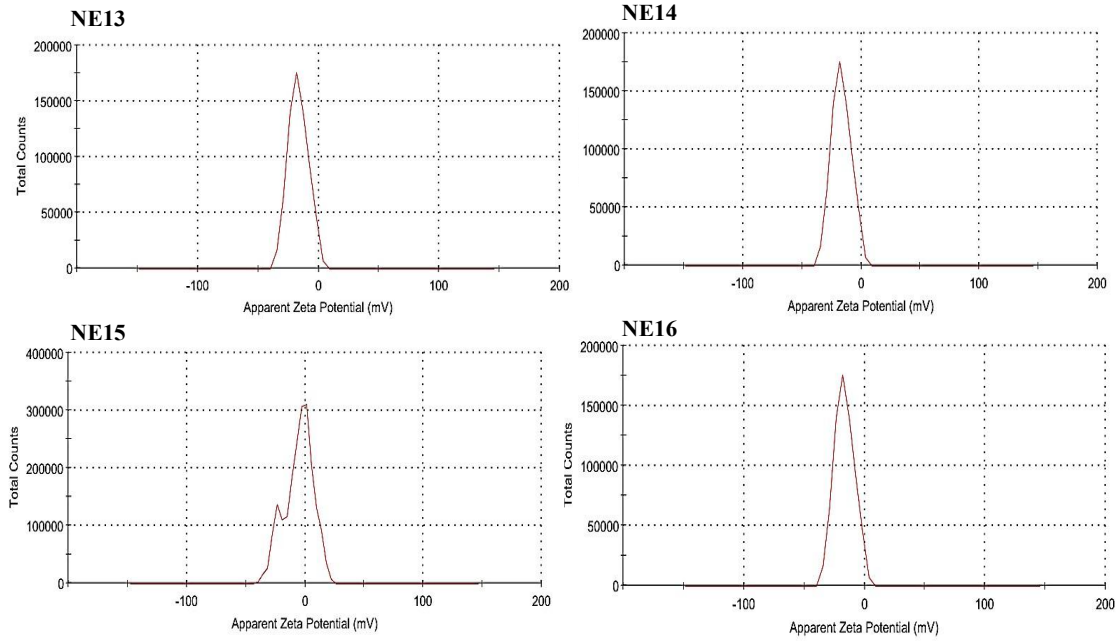

Fig. 4.34 Zeta potential of Nanocellulose Nanoemulsion (NC13, NC14, NC15 and NC16)

4.7.2 Creaming index of nanoemulsion incorporated with *Cucumis callosus* fruit peel extract

The creaming index of the formulated nanoemulsions was monitored over a storage period of 30 days in Table 4.20 and fig 4.35. The results demonstrated a gradual increase in the creaming index for all formulations, indicating progressive destabilization of the nanoemulsion system with storage time due to gravitational separation of droplets (Boostani et al., 2020). At the initial stage (0 day), all samples exhibited low creaming index values (<1%), confirming good physical stability immediately after preparation. However, with increasing storage duration, a significant rise in creaming index was observed, as reflected by the different uppercase superscripts within each formulation. At each storage interval, significant differences ($p < 0.05$) were observed among formulations, as shown by different lowercase superscripts, whereas values sharing identical superscripts were not significantly different, indicating comparable stability. At Day 0, NE4 (0.39 ± 0.09%) exhibited significantly lower creaming ($p < 0.05$) than NE1 (0.74 ± 0.15%) and NE10 (0.81 ± 0.38%), whereas NE3 and NE8 (both 0.62%) did not differ significantly ($p > 0.05$) from each other. This trend persisted throughout storage, with NE4 consistently showing significantly lower creaming index values ($p < 0.05$) at all time points (1.17 ± 0.29% at Day 5, 2.45 ± 0.35% at Day 10, 3.85 ± 0.32% at Day 15, 5.13 ± 0.42% at Day 20, 6.27 ± 0.37% at Day 25, and 7.31 ± 0.41% at Day 30), confirming superior physical stability. In contrast, formulations NE1, NE2, NE9, and NE10 exhibited significantly higher creaming index values ($p < 0.05$) by Day 20 (6.24–6.42%) and could not be evaluated thereafter

due to emulsion breakdown, indicating pronounced physical instability and could not be evaluated thereafter due to emulsion breakdown, indicating pronounced physical instability. Some nanoemulsion formulations exhibited emulsion breakage during prolonged storage, as evidenced by complete phase separation into a distinct cream layer and a clear serum layer, beyond which creaming index values could not be recorded. Some nanoemulsion formulations (NE1, NE2, NE9, and NE10) exhibited emulsion breakage during prolonged storage, as evidenced by complete phase separation into a cream layer and a serum layer, beyond which creaming index values could not be determined. This instability is due to the non-optimal concentration of *Cucumis peel* extract, which resulted in either insufficient or excessive interfacial stabilization. At lower extract concentrations, inadequate polyphenol-mediated interfacial reinforcement led to increased droplet mobility, whereas at higher concentrations, excess solids likely promoted droplet aggregation and destabilization (Sarkhel et al., 2025). Consequently, prolonged gravitational separation and droplet growth caused irreversible emulsion breakdown during storage.

Table 4.20 Optimization of *Cucumis callosus* peel extract concentration for nanoemulsion development

Peel extract (%)	**0 Day**	**5 Day**	**10 Day**	**15 Day**	**20 Day**	**25 Day**	**30 Day**
NE1	0.74 ± 0.15^{ec}	1.92 ± 0.35^{dB}	3.51 ± 0.48^{cB}	4.98 ± 0.43^{bA}	6.42 ± 0.46^{aA}	–	–
NE2	0.66 ± 0.22^{eD}	1.75 ± 0.31^{dD}	3.31 ± 0.39^{cD}	4.87 ± 0.37^{bB}	6.24 ± 0.44^{aC}	–	–
NE3	0.62 ± 0.11^{gE}	1.69 ± 0.28^{fE}	3.26 ± 0.41^{eE}	4.84 ± 0.65^{dc}	6.19 ± 0.39^{cD}	7.35 ± 0.41^{bA}	8.27 ± 0.55^{aA}
NE4	0.39 ± 0.09^{gG}	1.17 ± 0.29^{fJ}	2.45 ± 0.35^{eJ}	3.85 ± 0.32^{dI}	5.13 ± 0.42^{cI}	6.27 ± 0.37^{bf}	7.31 ± 0.41^{af}
NE5	0.54 ± 0.13^{gf}	1.53 ± 0.26^{fG}	3.01 ± 0.32^{eG}	4.65 ± 0.58^{dE}	6.05 ± 0.33^{cE}	7.14 ± 0.39^{bB}	8.01 ± 0.71^{aC}
NE6	0.47 ± 0.03^{gH}	1.27 ± 0.44^{fI}	2.64 ± 0.38^{eI}	4.03 ± 0.34^{dH}	5.34 ± 0.40^{cH}	6.51 ± 0.43^{bE}	7.58 ± 0.29^{aE}
NE7	0.53 ± 0.19^{gG}	1.41 ± 0.29^{fH}	2.82 ± 0.77^{eH}	4.18 ± 0.16^{dG}	5.54 ± 0.61^{cG}	6.67 ± 0.35^{bD}	7.72 ± 0.40^{aD}
NE8	0.62 ± 0.35^{gE}	1.63 ± 0.31^{fF}	3.13 ± 0.39^{ef}	4.47 ± 0.38^{dE}	5.85 ± 0.24^{cf}	7.01 ± 0.42^{bC}	8.14 ± 0.46^{aB}

NE9	0.73 ± 0.23^{dC}	1.85 ± 0.53^{cC}	3.41 ± 0.52^{cC}	4.76 ± 0.43^{bD}	6.24 ± 0.38^{aC}	–	–
NE10	0.81 ± 0.38^{eA}	1.96 ± 0.35^{dA}	3.62 ± 0.41^{cA}	4.98 ± 0.39^{bA}	6.41 ± 0.45^{aB}	–	–

Values are expressed as mean ± SD (n = 3). Different lowercase superscripts (a–e) within a row indicate significant differences ($p < 0.05$) among storage days for the same sodium alginate formulation, whereas different uppercase superscripts (A–H) within a column represent significant differences ($p < 0.05$) among *Cucumis callosus* peel extract samples (NG1–NG58) on the same storage day.

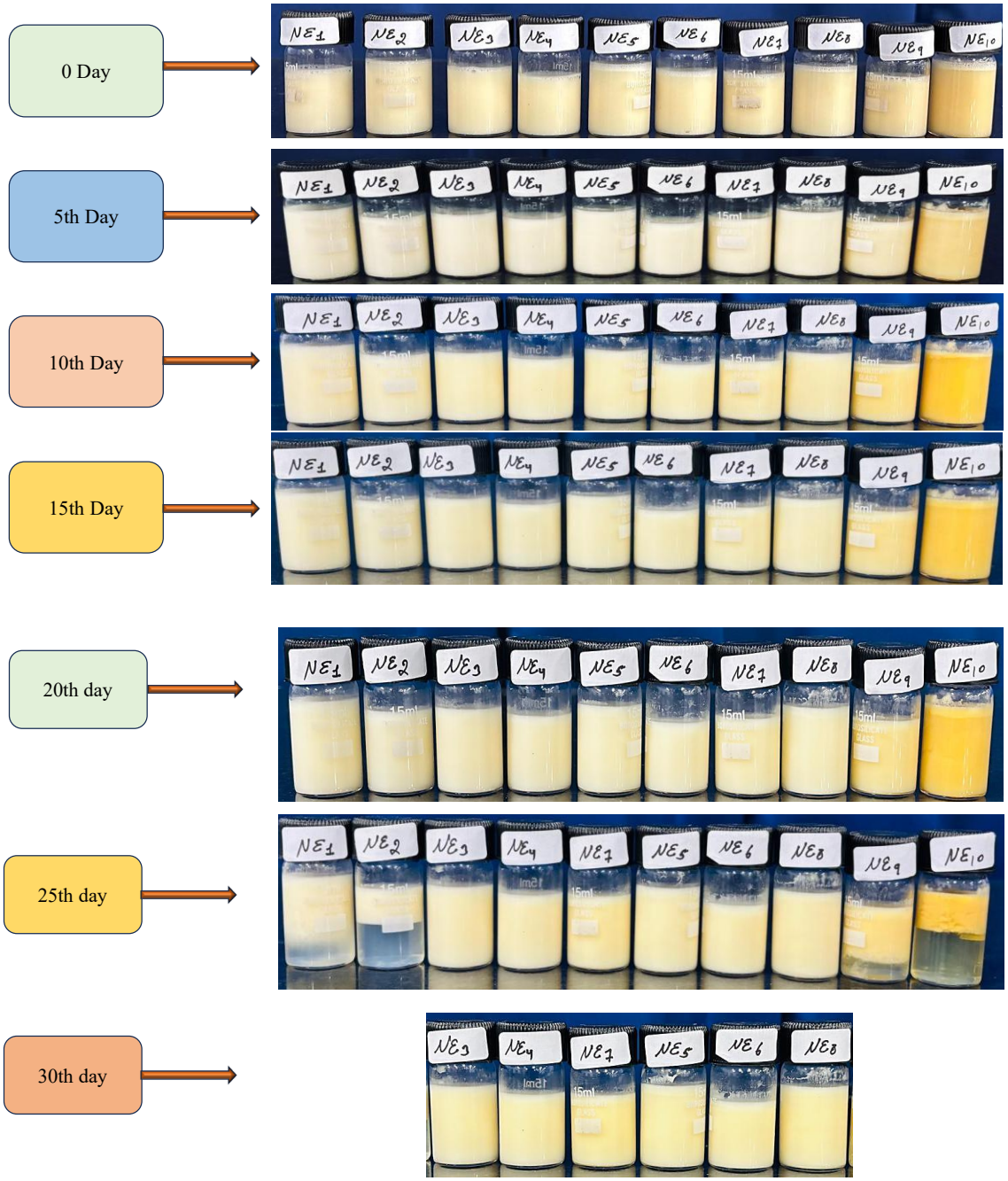

Fig. 4.35 Visual stability assessment of nanoemulsions (NE1–NE10) during storage at 0, 5, 10, 15, 20, 25, and 30 days, illustrating progressive creaming, phase separation, and emulsion breakage in certain formulations over time.

4.7.3 Creaming index of sodium alginate–based nanoemulsion

The creaming index of sodium alginate–based nanoemulsions (NS1–NS8) was evaluated over a storage period of up to 30 days to assess their physical stability, as shown in Table 4.21 and fig 4.36. Overall, the creaming index showed a significant increase ($p < 0.05$) with storage time, indicating progressive gravitational separation of oil droplets during storage. At Day 0, all

formulations exhibited low creaming index values ranging from 0.52 ± 0.15% (NS3) to 1.08 ± 0.29% (NS1), confirming good initial stability; however, significant differences ($p < 0.05$) were observed among formulations, while samples sharing identical lowercase superscripts were not significantly different ($p > 0.05$), indicating comparable initial stability. Throughout storage, NS3 (0.3% sodium alginate) consistently showed significantly lower creaming index values than NS1 and NS2 at all time points, increasing from 0.52 ± 0.15% (Day 0) to 1.39 ± 0.88% (Day 5), 2.65 ± 0.23% (Day 10), 3.94 ± 0.18% (Day 15), 5.11 ± 0.51% (Day 20), and finally 7.08 ± 0.50% (Day 30), demonstrating superior physical stability. In contrast, NS1 and NS2 exhibited significantly higher creaming indices, reaching 10.35 ± 0.41% and 9.87 ± 0.71% at Day 30, respectively, indicating reduced stability due to insufficient interfacial reinforcement at lower sodium alginate concentrations. Formulations NS4–NS8 (0.4–0.8% sodium alginate) showed measurable creaming only up to Day 10 (values exceeding 4–5%), after which no data could be recorded due to emulsion breakage, likely caused by excessive polymer concentration leading to increased viscosity, polymer-induced droplet aggregation, and restricted emulsifier mobility. At higher concentrations (NS4–NS8), excessive sodium alginate caused polymer-induced droplet aggregation, restricted emulsifier diffusion, and heterogeneous gel-like structuring, resulting in emulsion breakage during extended storage (Bai et al., 2018). Thus, the stability of the nanoemulsions was governed by a balance between viscosity enhancement and interfacial stabilization, explaining the significant and non-significant differences observed among formulations (Branco et al., 2020). Overall, the results confirm that both storage duration and sodium alginate concentration significantly influenced creaming behavior, with 0.3% sodium alginate (NS3) providing an optimal balance between viscosity enhancement and interfacial stabilization, while non-significant differences among certain formulations at specific time points indicate comparable stability performance.

Table 4.21 Optimization of sodium alginate concentration in nanocellulose-based nanoemulsions incorporated with peel extract

Sodium Alginate (%)	**0 Day**	**5 Day**	**10 Day**	**15 Day**	**20 Day**	**25 Day**	**30 Day**
NSE1	1.08 ± 0.29^{gA}	2.96 ± 0.44^{fA}	5.01 ± 0.22^{eA}	6.54 ± 0.67^{dA}	8.13 ± 0.33^{cA}	9.28 ± 0.64^{bA}	10.35 ± 0.41^{aA}
NSE2	0.89 ± 0.25^{gB}	2.54 ± 0.32^{fB}	4.42 ± 0.45^{eB}	5.97 ± 0.25^{dB}	7.62 ± 0.40^{cB}	8.79 ± 0.39^{bB}	9.87 ± 0.71^{aB}
NSE3	0.52 ± 0.15^{gH}	1.39 ± 0.88^{fH}	2.65 ± 0.23^{eH}	3.94 ± 0.18^{dD}	5.11 ± 0.51^{cD}	6.17 ± 0.87^{bc}	7.08 ± 0.50^{ac}
NSE4	0.63 ± 0.10^{gG}	1.74 ± 0.79^{fG}	3.31 ± 0.56^{eG}	4.81 ± 0.21^{dc}	–	–	–

NSE5	0.69 ± 0.13^{gf}	1.87 ± 0.41^{ff}	3.58 ± 0.37^{ef}	–	–	–	–
NSE6	0.73 ± 0.11^{gE}	1.95 ± 0.19^{fE}	3.72 ± 0.31^{eE}	–	–	–	–
NSE7	0.79 ± 0.08^{gD}	2.12 ± 0.29^{fD}	3.95 ± 0.19^{eD}	–	–	–	–
NSE8	0.84 ± 0.19^{gc}	2.31 ± 0.73^{fc}	4.18 ± 0.22^{ec}	–	–	–	–

Data are presented as mean ± SD (n = 3). Different lowercase superscript letters ($^{a–g}$) within the same row indicate significant differences ($p < 0.05$) among storage days for the same sodium alginate formulation, while different uppercase superscript letters ($^{A–H}$) within the same column denote significant differences ($p < 0.05$) among different sodium alginate samples (NSE1–NSE8) on the same storage day.

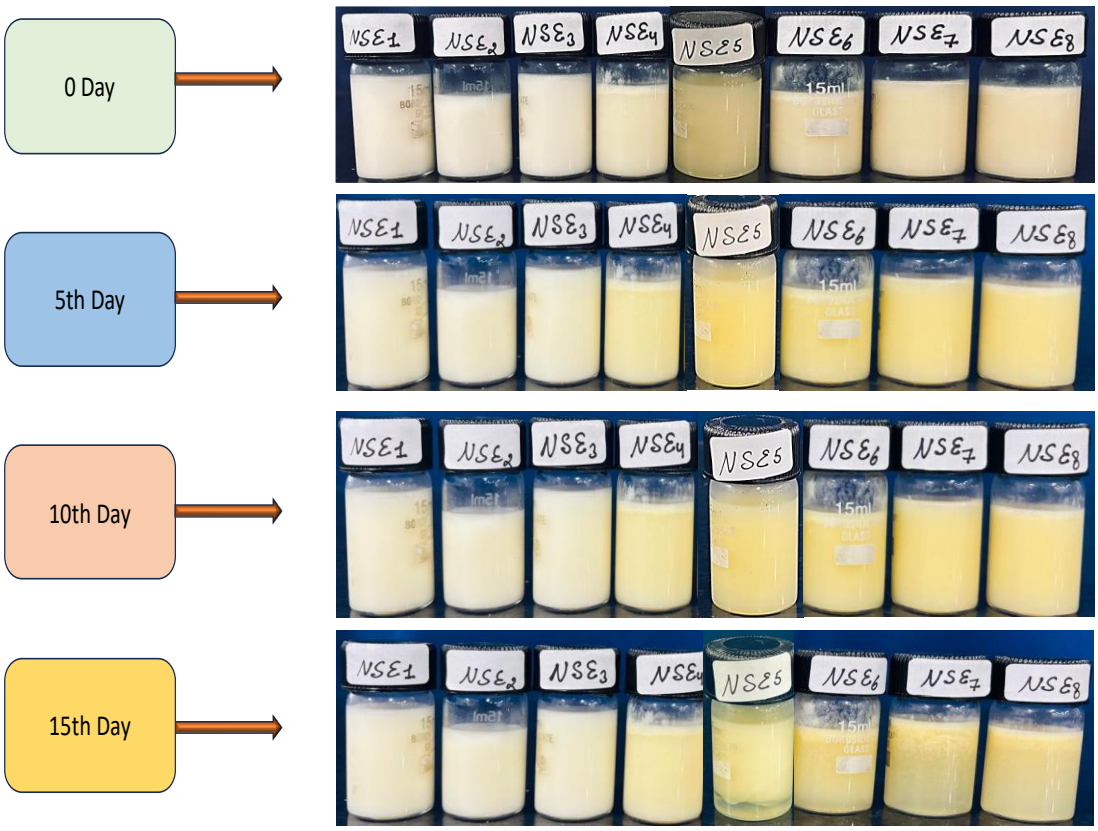

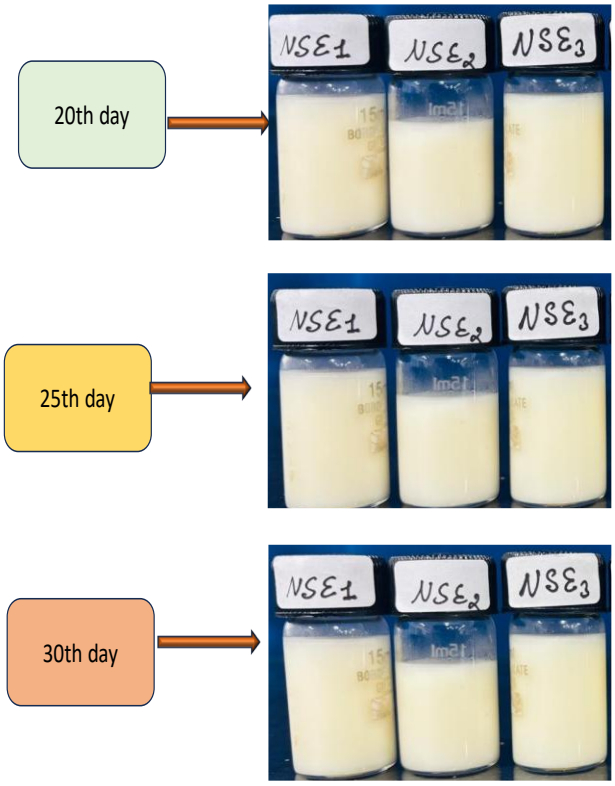

Fig. 4.36 Visual stability assessment of nanoemulsions (NSE1–NSE8) during storage at 0, 5, 10, 15, 20, 25, and 30 days, illustrating progressive creaming, phase separation, and emulsion breakage in certain formulations over time.

4.7.4 Creaming index of guar gum-based nanoemulsion

The creaming index of guar gum–based nanoemulsions (NG1–NG5) increased significantly ($p < 0.05$) with storage time for all formulations, indicating progressive gravitational separation during storage in Table 4.22 and Figure 4.37. At Day 0, all samples exhibited low creaming index values ranging from 0.45 ± 0.04% (0.3% guar gum) to 0.75 ± 0.11% (0.5% guar gum), confirming good initial physical stability. Significant variations ($p < 0.05$) in guar gum concentrations were detected across storage intervals, as indicated by different lowercase superscripts. Values with the same superscript did not differ significantly, suggesting similar stability. With increasing storage duration, the creaming index increased significantly ($p < 0.05$) for all formulations, as evidenced by different uppercase superscripts within each guar gum concentration. By Day 10, creaming index values ranged from 2.35 ± 0.31% (0.3%) to 3.79 ± 0.20% (0.5%), which further increased to 4.96–6.82% by Day 20. At the end of storage (Day 30), the highest creaming index was observed for 0.5% guar gum (9.28 ± 0.30%), while the lowest was recorded for 0.3% guar gum (7.29 ± 0.62%), indicating significantly better stability at this concentration. Overall, nanoemulsions containing 0.3% guar gum consistently exhibited

significantly lower creaming index values throughout storage, suggesting optimal stabilization due to a balanced increase in continuous-phase viscosity and effective restriction of droplet mobility (Ribeiro et al., 2024). In contrast, higher guar gum concentrations (0.4–0.5%) resulted in significantly higher creaming, likely due to excessive polymer content causing reduced interfacial flexibility and enhanced droplet aggregation (Farshi et al., 2019). These results confirm that both guar gum concentration and storage time significantly influenced creaming behavior, with 0.3% guar gum identified as the most suitable concentration for minimizing creaming and enhancing nanoemulsion stability.

Table 4.22 Optimization of guar gum concentration in nanoemulsions

Sample code	**0 Day**	**5 Day**	**10 Day**	**15 Day**	**20 Day**	**25 Day**	**30 Day**
NG1	0.60 ± 0.15^{gC}	1.55 ± 0.79^{fC}	3.15 ± 0.46^{eC}	4.65 ± 0.38^{dC}	5.96 ± 0.82^{cC}	7.35 ± 0.55^{bC}	8.42 ± 0.26^{aC}
NG2	0.52 ± 0.09^{gD}	1.38 ± 0.45^{fD}	2.84 ± 0.54^{eD}	4.22 ± 0.16^{dD}	5.48 ± 0.21^{cD}	6.79 ± 0.33^{bD}	7.95 ± 0.44^{aD}
NG3	0.45 ± 0.04^{gE}	1.20 ± 0.28^{fE}	2.35 ± 0.31^{eE}	3.78 ± 0.54^{dE}	4.96 ± 0.18^{cE}	6.22 ± 0.19^{bE}	7.29 ± 0.62^{aE}
NG4	0.68 ± 0.13^{gB}	1.72 ± 0.50^{fB}	3.48 ± 0.58^{eB}	5.02 ± 0.20^{dB}	6.44 ± 0.64^{cB}	7.89 ± 0.27^{bB}	8.93 ± 0.38^{aB}
NG5	0.75 ± 0.11^{gA}	1.88 ± 0.12^{fA}	3.79 ± 0.20^{eA}	5.36 ± 0.22^{dA}	6.82 ± 0.26^{cA}	8.24 ± 0.39^{bA}	9.28 ± 0.30^{aA}

Values are expressed as mean ± SD (n = 3). Different lowercase superscripts (a–g) within a row indicate significant differences ($p < 0.05$) among storage days for the same sodium alginate formulation, whereas different uppercase superscripts (A–H) within a column represent significant differences ($p < 0.05$) among guar gum samples (NG1–NG58) on the same storage day.

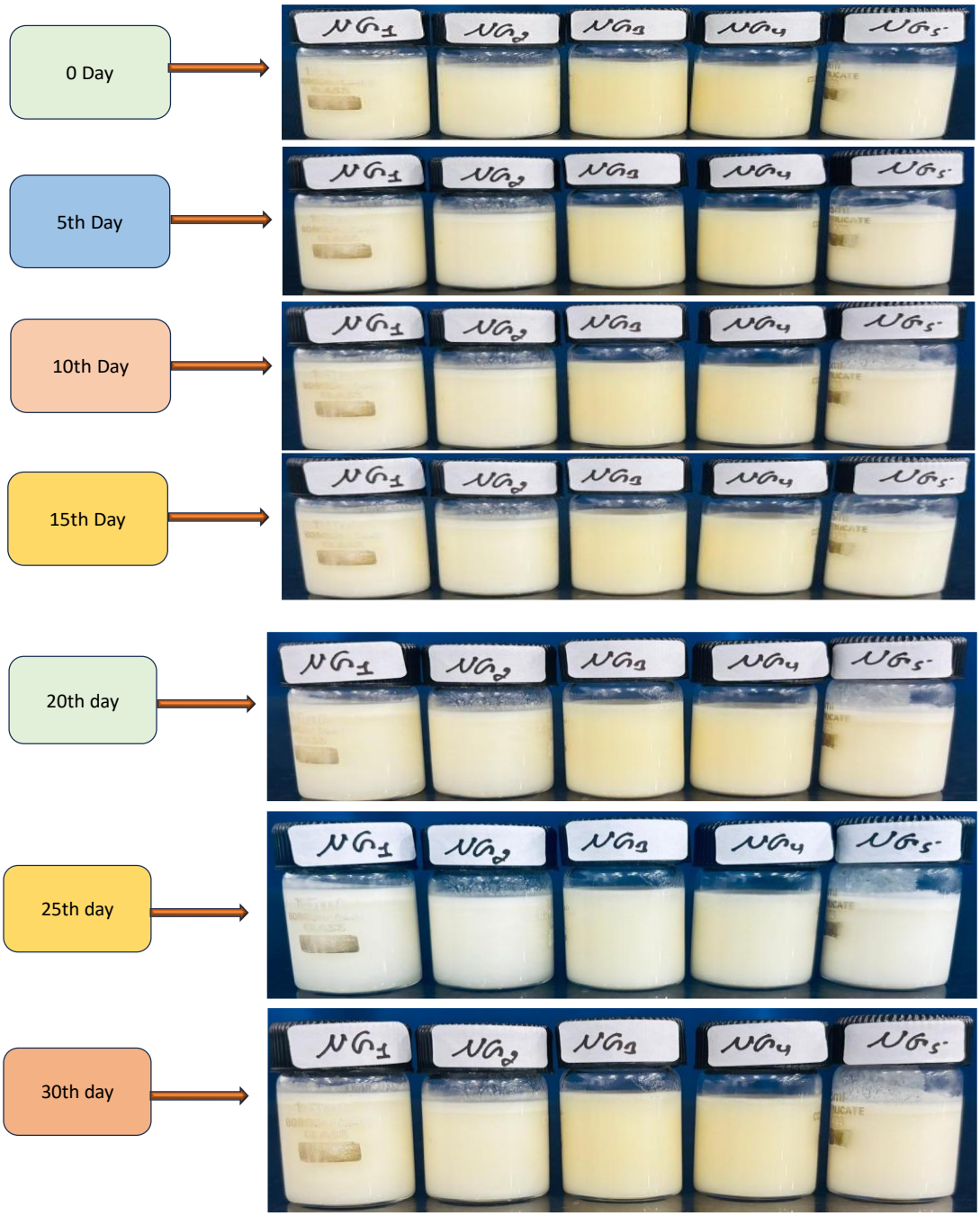

Fig. 4.37 Visual stability assessment of nanoemulsions (NG1–NG5) during storage at 0, 5, 10, 15, 20, 25, and 30 days, illustrating progressive creaming, phase separation, and emulsion breakage in certain formulations over time.

4.7.5 Droplet Size and Zeta potential of optimized nanoemulsions

The droplet size and zeta potential of nanoemulsions formulated with nanocellulose, ginger oil, and polysaccharide stabilizers such as, sodium alginate and guar gum at a fixed concentration of Tween 80 were quantified, and the results are depicted in Fig. 4.38. The droplet size analysis shown differences among the formulations, with NG3 exhibiting the smallest mean droplet size

(147.09 ± 4.16 nm), followed by NE4 (152.98 ± 6.09 nm), while NSE4 showed the largest droplet size (164.72 ± 5.25 nm). This trend indicates that the type and concentration of stabilizing polysaccharide significantly influenced emulsification efficiency and droplet breakup. The smaller droplet size observed for NG3 can be attributed to the effective viscosity enhancement and steric stabilization provided by guar gum, which restricted droplet mobility and suppressed droplet coalescence during homogenization. The zeta potential measurements further supported the droplet size results. The nanoemulsions exhibited negative surface charge values of −14.6±0.81 mV for NE4, −17.5±0.32 mV for NSE3, and −20.6±49 mV for NG3, indicating electrostatic stabilization of the dispersed droplets. The higher absolute zeta potential observed for NG3 suggests stronger electrostatic repulsion between droplets, which minimized droplet aggregation and contributed to the formation of finer and more stable droplets. In contrast, the comparatively lower zeta potential magnitude of NE4 reflects weaker electrostatic repulsion, making the system more dependent on steric and viscosity-based stabilization mechanisms. The observed correlation between droplet size and zeta potential demonstrates that formulations possessing higher absolute surface charge and enhanced continuous-phase viscosity produced smaller droplet sizes and improved physical stability. According to Stokes' law, smaller droplets exhibit reduced gravitational separation, thereby lowering creaming tendency (Hussain et al., 2017). Conversely, formulations with larger droplet sizes and lower zeta potential magnitude are more susceptible to droplet collision, coalescence, and phase separation during storage. Additionally, nanocellulose contributed to interfacial reinforcement and Pickering-type stabilisation, however, its stabilising efficiency was significantly influenced by its interaction with the selected polysaccharide (Teo et al., 2022). Natural polysaccharide stabilisers, such as sodium alginate and guar gum, can effectively form stable nanoemulsions (Teixé-Roig et al., 2022 and Basu et al., 2025). Overall, the results confirm that the synergistic interaction between guar gum, nanocellulose, and electrostatic surface charge plays a critical role in governing droplet size distribution and nanoemulsion stability. The superior performance of NG3, characterized by the smallest droplet size and highest absolute zeta potential, highlights its enhanced resistance to droplet aggregation and creaming compared to NE4 and NSE4.

(a)

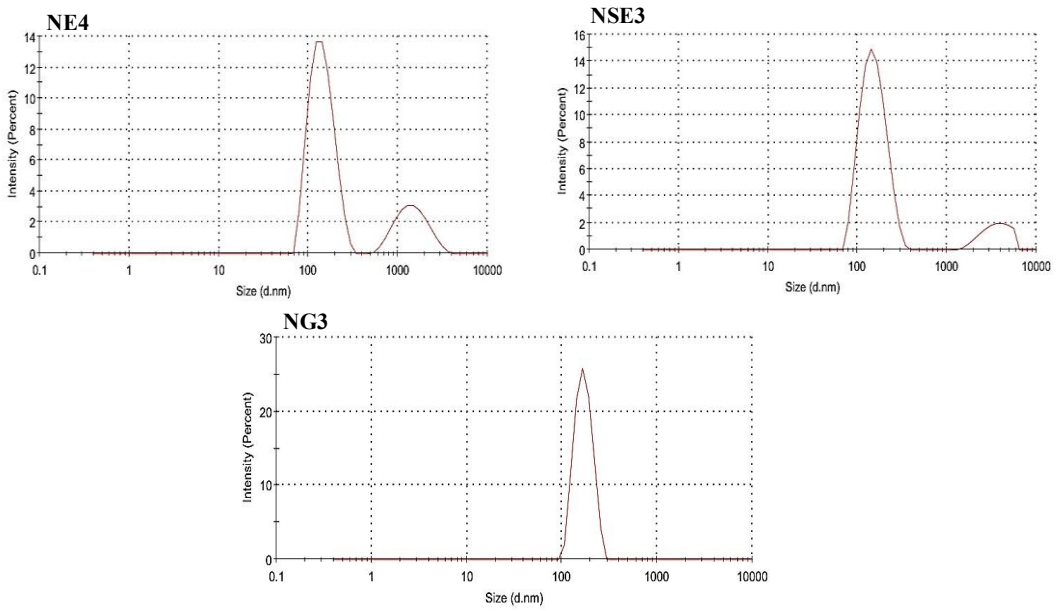

(b)

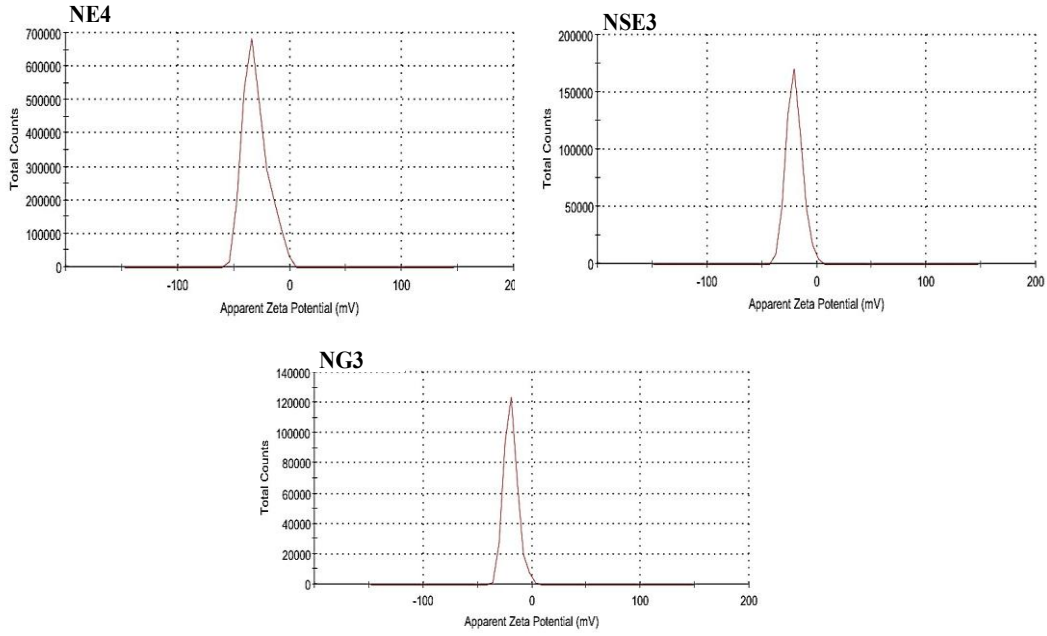

Fig. 4.38 (a) Droplet size distribution and (b) zeta potential distribution of nanoemulsion formulations NE4, NSE3, and NG3

4.7.6 Rheology of nanoemulsions

The rheological behavior of the formulated nanoemulsion was analysed through steady shear and dynamic oscillatory measurements in order to elucidate the underlying microstructural organization and interaction mechanisms governing its flow and viscoelastic properties. The

combined interpretation of viscosity, shear stress, storage modulus (G′), and loss modulus (G″) as shown in Fig. 4.39. When shear rate increases then polymer chains undergo progressive alignment along the flow direction, entanglements are partially released, and weak physical junctions are disrupted, leading to a reduction in viscosity to 15–25 Pa·s (NG3), 10–15 Pa·s (NSE3), 8–10 Pa·s (NE4), and 4–6 Pa·s (NC14). High viscosities arise from the formation of a polymer-dominated transient network, where nanocellulose fibrils act as rigid scaffolds, hydrocolloid chains (guar gum and/or alginate) contribute flexible, highly hydrated backbones, and lecithin-stabilized oil droplets behave as physical fillers. The viscosity hierarchy reflects differences in polymer chain flexibility, entanglement density, and network connectivity. Quintana-Martinez et al. (2018) report strong shear-thinning (non-Newtonian, Carreau model fit) in 30% sunflower oil emulsions with 0.5–1% guar gum and lecithin, viscosity drops ~3 orders of magnitude up to 1000 s^{-1}, attributed to guar chain interlocking deformation at high shear. Higher guar increases zero-shear η_0 (10–164 Pa·s) and resistance to flow, mirroring your polymer-dominated networks. Nanoemulsion/gum ratios (e.g., xanthan) increase zero-shear viscosity and shear-thinning, higher gum yields gel-like behavior with droplet fillers (Alfaro-Rodríguez et al., 2022). Shear stress increased continuously with shear rate for all samples, with values ranging from 60–80 Pa at 0.1 s^{-1} to 900–1000 Pa at 100 s^{-1} for NG3, and proportionally lower values for NSE3, NE4, and NC14. Mechanistically, shear stress represents the force required to deform and mobilize the polymer network. Guar gum contributes long, flexible galactomannan chains capable of forming dense entanglement domains, while alginate provides semi-rigid chains that resist deformation (Sharma et al., 2021). Nanocellulose fibrils further increase stress transmission by acting as load-bearing elements (Baron et al., 2025). Whereas NC14 has lower extensive polymer–polymer connectivity, resulting in lower resistance to flow. The storage modulus (G′) increased with angular frequency from 120–150 Pa to 800–900 Pa for NG3, 80–100 Pa to 600–700 Pa for NSE3, 60–70 Pa to 400–500 Pa for NE4, and 30–40 Pa to 200–250 Pa for NC14 over the frequency range of 0.1–100 rad·s^{-1}. G′ represents the elastic energy stored within the polymer network during oscillatory deformation. G′ represents the elastic energy stored within the polymer network during oscillatory deformation. At low frequencies, polymer chains have sufficient time to relax through segmental motion and disentanglement, resulting in lower elastic response (Mirigian, et al., 2021). In guar gum-CNC hydrogels, G′ increases from ~150 Pa (low ω) to higher values over 0.1–100 rad·s^{-1}, with G′ >> G″ indicating elasticity from H-bonded networks, low-frequency relaxation allows disentanglement. Polymer-nanoparticle gels show frequency-independent G′ dominance at high ω, as deformation outpaces relaxation times (Mangel et al., 2016). The higher G′ values of NG3

reflect a greater density of elastic junctions arising from synergistic guar gum–alginate interactions. Loss modulus (G″) increased with the addition of polysaccharide in all nanoemulsion formulations, indicating enhanced viscous energy dissipation under faster deformation conditions. At low frequencies (0.1 rad s^{-1}), G″ values were approximately 40–50 Pa for NG3, 30–35 Pa for NSE3, 20–25 Pa for NE4, and 15–20 Pa for NC14. With increasing frequency up to 100 rad s^{-1}, G″ rose to approximately 300–400 Pa for NG3, 200–250 Pa for NSE3, 150–180 Pa for NE4, and 100–120 Pa for NC14. At low frequencies, polymer chains have sufficient mobility to dissipate energy through viscous flow (Teymoory et al., 2025). As frequency increases, rapid deformation enhances internal friction, increasing viscous losses. However, G″ remains consistently lower than G′, indicating that elastic energy storage dominates over viscous dissipation (Shanmuka et al., 2025). Emulsions containing synergistic hydrocolloids in NG3 and NSE3, which were develop dense, elastic polymer networks capable of resisting deformation and storing mechanical energy, while formulations dominated by nanocellulose alone (NC14) form weaker, less interconnected structures.

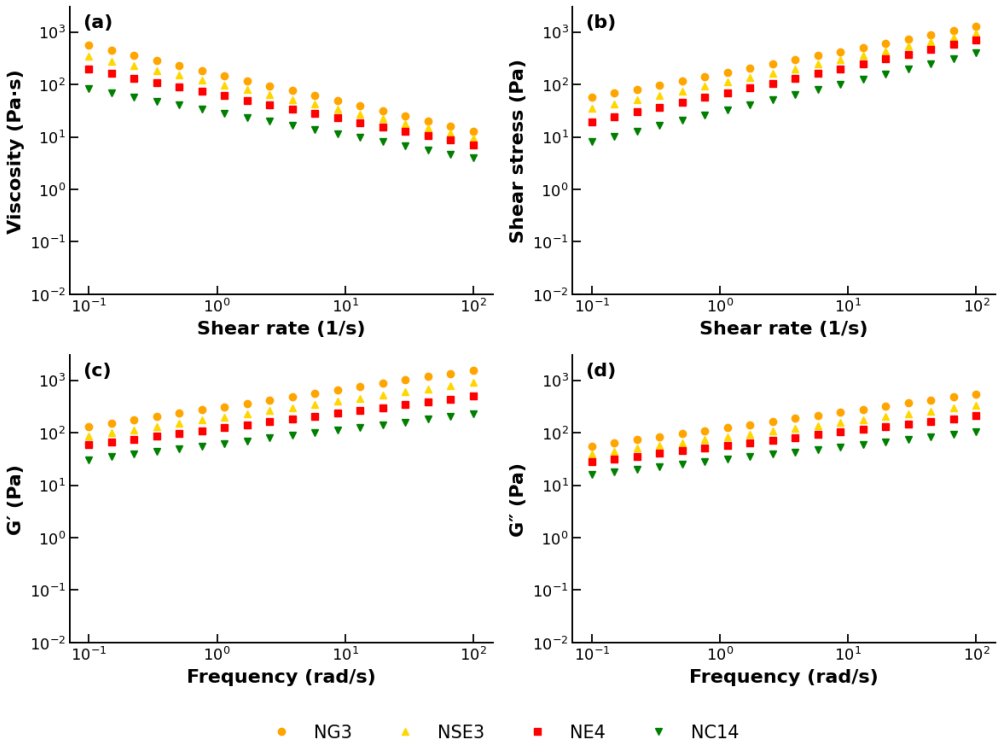

Fig. 4.39 Rheological behavior of nanoemulsion formulations NG3, NSE3, NE4, and NC14: (a) apparent viscosity as a function of shear rate, (b) shear stress versus shear rate, (c) storage modulus (G′), and (d) loss modulus (G″) as a function of angular frequency

4.7.7 Field emission scanning electron microscopy (FESEM)

The combined SEM and rheological observations demonstrate that the viscoelastic behavior of the nanoemulsion systems is directly governed by composition-dependent microstructural organization and polymer-level interactions shown in fig 4.40. In NC14, the SEM micrograph shows sparsely distributed oil droplets embedded in a loosely connected nanocellulose matrix, indicating limited polymer–polymer contact and weak network formation, this microstructure allows greater polymer chain mobility and explains the low resistance to flow and weak elastic response observed rheologically (Ghasemi et al., 2025). Incorporation of peel extract in NE4 produces a more uniform droplet distribution within a moderately interconnected polymeric matrix, where polyphenolic constituents promote hydrogen bonding and interfacial adsorption at the oil–polymer interface, leading to effective droplet immobilization and controlled polymer bridging without excessive network densification (Chen et al., 2024). This balanced microstructure accounts for the stable shear-thinning behaviour and moderated viscoelastic response of NE4. In contrast, NSE3 exhibits a denser and more heterogeneous morphology characterized by closely packed droplets embedded in a corrugated continuous phase, arising from sodium-alginate-driven chain overlap and ionic junction zone formation that significantly restricts polymer mobility and enhances elastic dominance. The enhanced stability of the single emulsions at room temperature can be attributed to the presence of sufficient CNCs, sodium alginate, and lecithin, which collectively formed a robust interfacial network surrounding the oil droplets, while lecithin predominantly localized at the oil–water interface and facilitated effective interfacial stabilization (Maeda et al., 2025). NG3 displays the most compact and cohesive microstructure due to synergistic interactions between guar gum and sodium alginate reinforced by nanocellulose fibrils, resulting in extensive chain entanglement and a highly interconnected network capable of resisting deformation (Ribeiro et al., 2024). Overall, the progressive transition from NC14 to NG3 confirms that peel-extract-mediated interfacial stabilization governs controlled network formation in NE4, whereas alginate-induced ionic networking dominates structural densification in NSE3, establishing a clear structure–property relationship between nanoemulsion microstructure and rheological behavior.

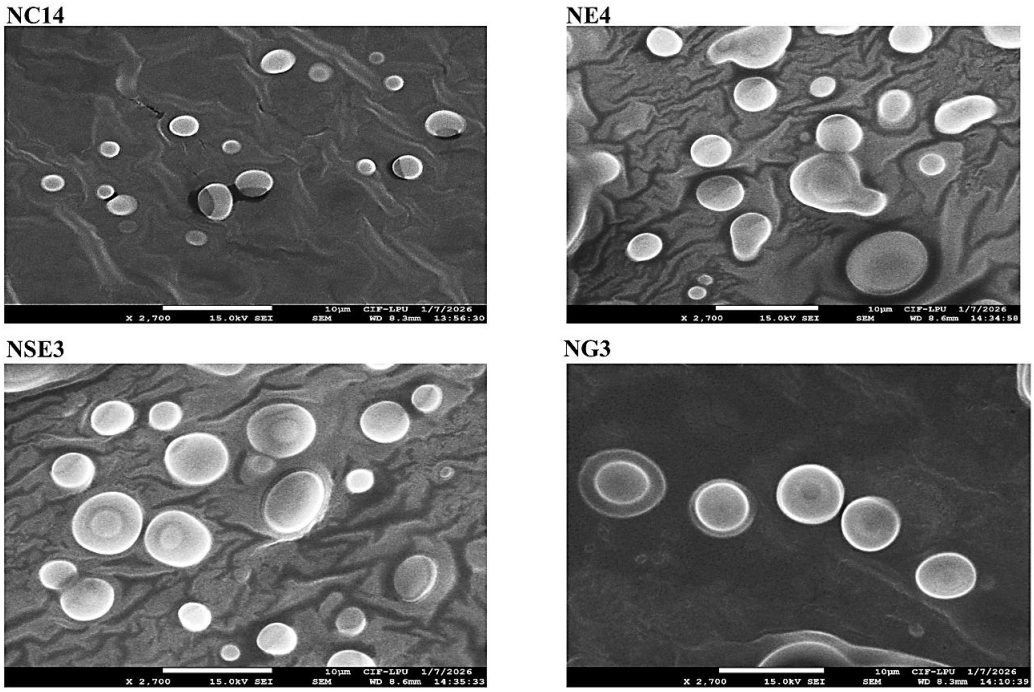

Fig. 4.40 Scanning electron microscopy (SEM) micrographs of nanoemulsion formulations NC14, NE4, NSE3, and NG3

4.7.8 Functional group determination

The FTIR spectra of four emulsion samples, such as NC14, NE4, NSE3 and NG3, reveal the characteristic functional group present in each formulation, which is shown in Fig. 4.41. For the Guar gum-based nanoemulsion (NG3) shown, the broad O–H stretching band was observed at 3307 cm^{-1} and peaks were found in NSE3, NE4 and NC14, including 3355 cm^{-1}, 3437 cm^{-1}, and 3347 cm^{-1}, respectively. This is due to the increased hydrogen bonding and reorientation of hydroxyl groups at the oil–water interface in the emulsified systems. The peak around 890 cm^{-1} is specifically associated with β-glycosidic linkages between glucose units, confirming the cellulose-type polysaccharide structure (Yang et al., 2017). Similarly, C–H stretching band at 2922 cm^{-1} in NG3 became more stable and symmetric stretching near 2927 cm^{-1} in NSE3 and NE4, reflecting enhanced contribution of lipid chains and stronger hydrophobic interactions essential for emulsion stabilization. The band associated with bound water and amide I vibrations, located at 1638 cm^{-1} in NG3, shifted slightly to the range of 1464 cm^{-1} in the emulsified samples, suggesting intensified polymer–water and emulsifier–water interactions surrounding the dispersed oil droplets. In addition, the CH_2 bending vibration at 1332 cm^{-1}, observed predominantly in NE4, further confirms the involvement of hydrophobic moieties from the oil phase. The absorption bands observed at 1408 and 1180 cm^{-1} are attributed to C–

O bending and angular deformation vibrations characteristic of phenolic groups. The prominent peak at 1065 cm^{-1} corresponds to O–C stretching vibrations of the anhydroglucose ring, which is commonly associated with flavonoid-related structures (Liang et al., 2019). The polysaccharide backbone vibrations, represented by C–O–C and C–O stretching bands at 1333 and 1082 cm^{-1} in NG, showed minor shifts to 1205–1079 cm^{-1} (NSE3) and 1094–1088 cm^{-1} (NE4 and NC14), indicating conformational rearrangement of the polysaccharide chains to accommodate interfacial adsorption without disrupting the fundamental glycosidic structure. A weak band at 2127 cm^{-1} detected in NE4 was attributed to overtone or combination vibrations arising from nano-scale structural reorganization rather than new chemical bond formation. The presence of ester groups from the Tween 80 or oil components in the nanoemulsion may be responsible for the C=O stretching vibrations indicated by the absorption peaks seen in the range of 1700–1600 cm−1 (Tosif et al., 2025).

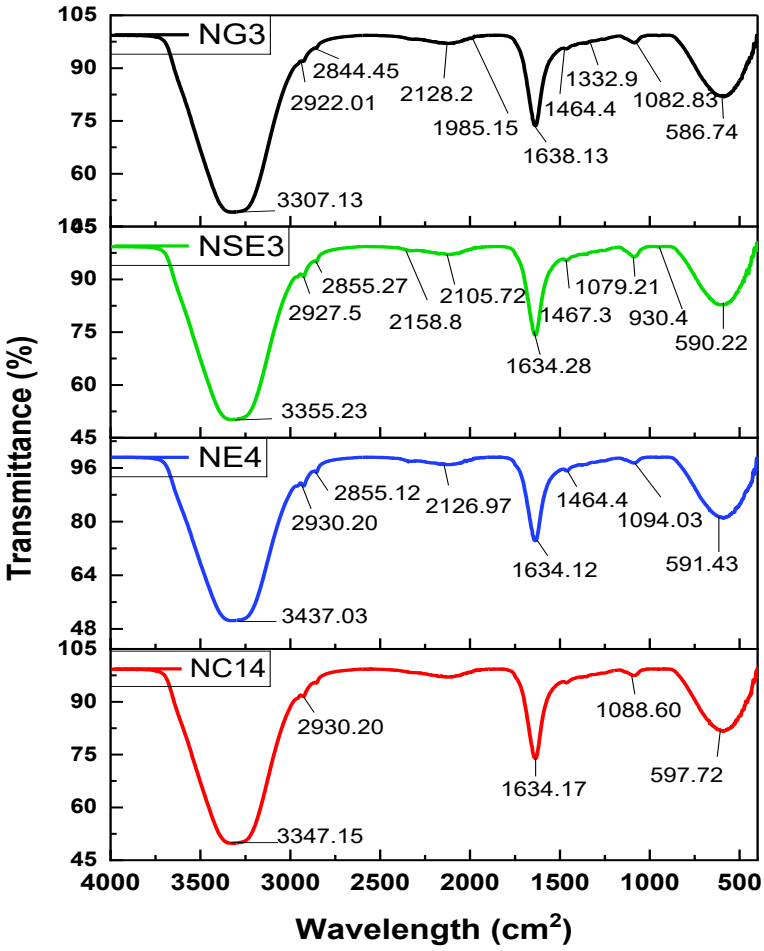

Fig. 4.41 Functional group determination presents in NC14, NE4, NSE3, and NG3 nanoemulsion

4.7.9 Antimicrobial analysis

The antimicrobial activity of the formulated samples (NGE, NSE, NCE, and NC) against *Staphylococcus aureus* and *Escherichia coli* showed a concentration-dependent zone of inhibition in Fig. 4.42 and 4.43. For both bacterial strains, the positive control (ampicillin) exhibited significantly higher ($p < 0.05$) antibacterial activity against both microorganisms across all concentrations. At 100% concentration of the sample, NGE showed a higher zone of inhibition against *S. aureus* (26.69±0.60 mm) compared to *E. coli* (19.89±0.73 mm), followed by a significantly lower ($p < 0.05$) zone at 50% and 25% concentrations, confirming a dose-dependent response. NSE showed lower antimicrobial activity then NG at 100%, 50% and 25 %, 22.76±0.56 mm, 14.81±0.47mm, and 8.28±0.17mm, respectively, against *S. aureus*, with significantly lower inhibition zones ($p < 0.05$) but significantly higher than NCE and NC for both bacterial strains. While NCE and NC exhibited the lowest inhibition zones, which were significantly reduced ($p < 0.05$) at decreasing concentrations, at 100 % to 25 %, shown 16.95±0.33mm, to 4.7±0.41mm and 10.86±0.37mm to 3.17±0.28mm against *S. aureus*, whereas 10.29 0.84mm to 3.92 0.49mm and 8.31 0.36mm to 2.28 0.15mm against *E. coli* antimicrobial activity. Higher antibacterial activity of NGE and NSE due to the higher availability and effective diffusion of bioactive constituents, which may disrupt cell wall integrity, alter membrane permeability, and interfere with essential metabolic pathways.

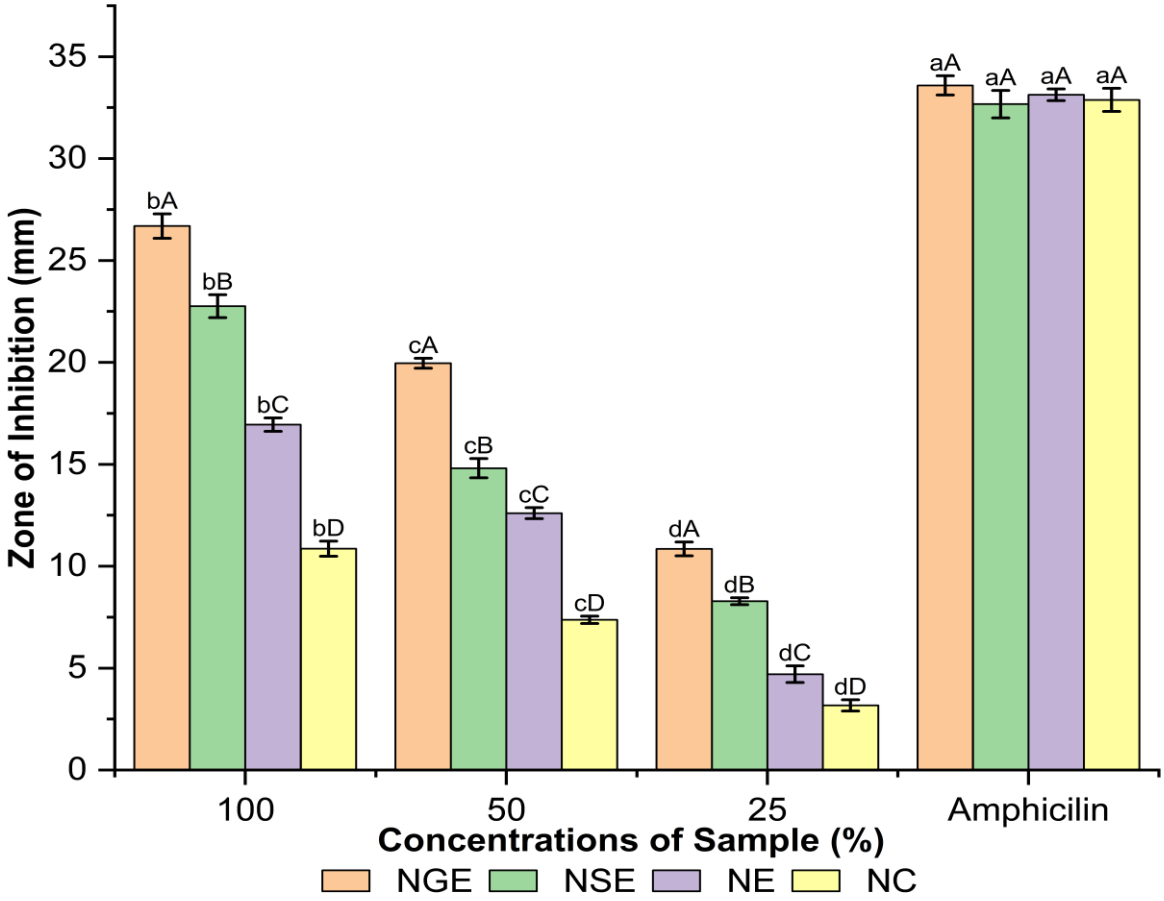

Fig. 4.35 Zone of inhibition against *S. aureus* of formulated nanoemulsions. Results are presented as mean ± standard deviation (n = 3). Different lowercase letters (a–d) above the bars indicate significant differences among treatments at the same concentration, whereas uppercase letters (A–D) represent significant differences among concentrations within the same treatment ($p < 0.05$, Duncan's multiple range test).

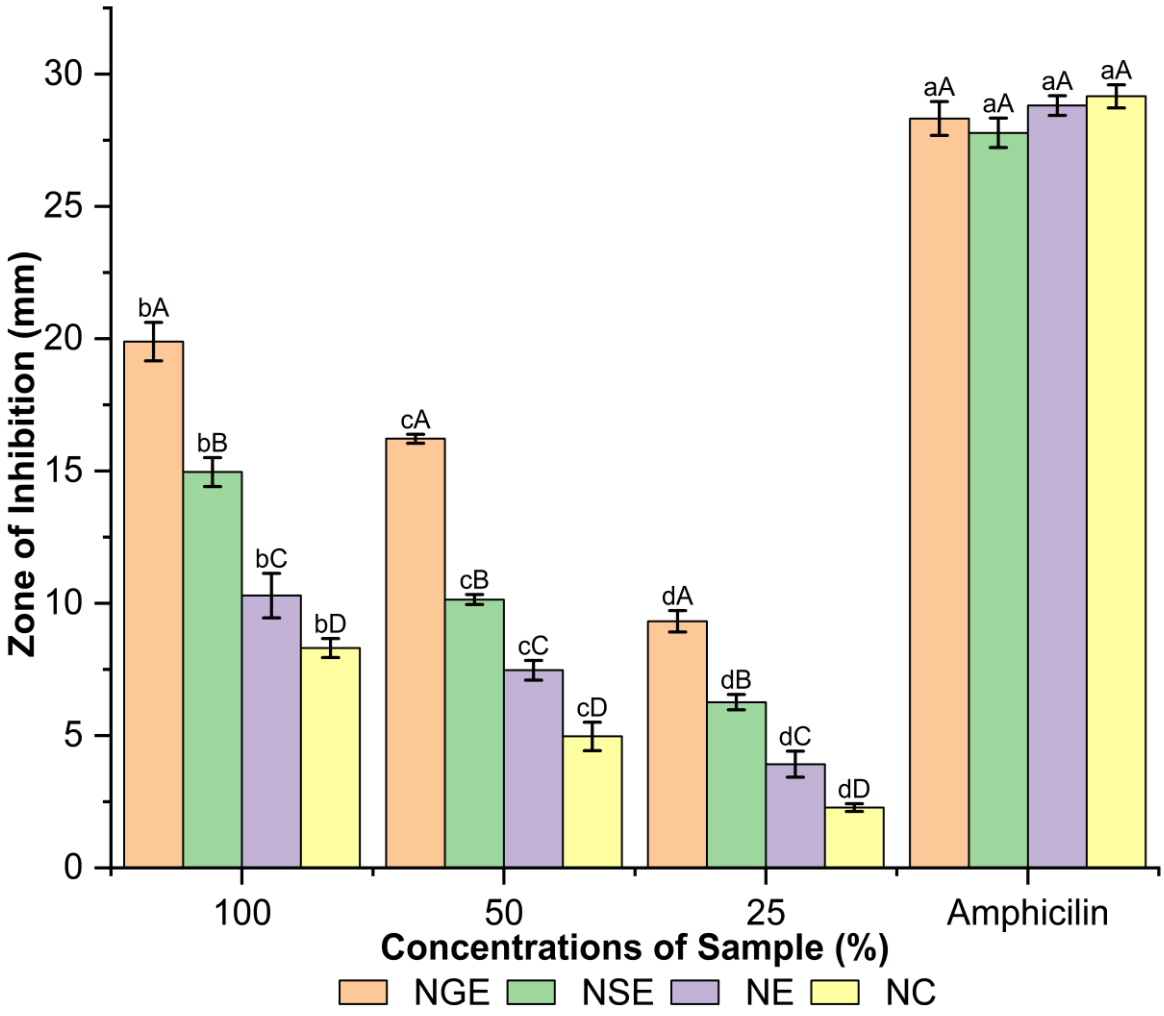

Fig. 4.43 Zone of inhibition against *E. coli* of formulated nanoemulsions. Data are presented as mean ± standard deviation (n = 3). Different lowercase letters (a–d) above the bars indicate significant differences among treatments at the same concentration, while uppercase letters (A–D) indicate significant differences among concentrations within the same treatment ($p < 0.05$, Duncan's multiple range test).

4.8 Mechanical and physicochemical properties of glycerol-based packaging films

The mechanical strength and physicochemical stability of glycerol-plasticized packaging films are critical determinants of their structural integrity, flexibility, barrier efficiency, and overall performance in food packaging applications. The incorporation of glycerol as a plasticizer significantly influences tensile behavior, elongation capacity, moisture affinity, solubility, and thermal characteristics of the developed films, as shown in fig. 4.44.

4.8.1 Evaluation of tensile strength (TS) and elongation at break (EB)

Mechanical properties, including tensile strength (TS) and elongation at break (EB), were evaluated to optimize the glycerol concentration in the formulated films, and the results are presented in Table 4.23. A total of six glycerol-based formulations (G0.1–G0.6) were assessed,

and the results showed that glycerol concentration significantly influenced the mechanical behaviour of the films. Lower glycerol concentrations produced films with higher tensile strength, whereas increasing glycerol content progressively reduced TS and improved film flexibility. The highest TS was observed in G0.1 (42.80 ± 0.61 MPa), followed by G0.2 (39.62 ± 0.82 MPa), indicating the formation of a compact and rigid polymer network with restricted chain mobility. This behaviour may be attributed to strong intermolecular hydrogen bonding among guar straw polysaccharide chains and between the polysaccharide matrix and *Cucumis callosus* polyphenols. The abundant hydroxyl groups present in both guar straw polysaccharides and *C. callosus* phenolic compounds can promote hydrogen-bond formation, leading to improved molecular compatibility, compactness, and load-bearing capacity of the film network. With increasing glycerol concentration, TS gradually decreased in G0.3 (36.93 ± 0.77 MPa), G0.4 (34.44 ± 0.63 MPa), G0.5 (30.56 ± 0.51 MPa), and G0.6 (28.19 ± 0.79 MPa). This reduction suggests that excessive plasticization weakened intermolecular interactions within the film matrix. Glycerol, being a low-molecular-weight plasticizer rich in hydroxyl groups, can compete with polysaccharide–polysaccharide and polysaccharide–polyphenol hydrogen-bonding sites. As a result, the original compact network becomes more flexible due to increased free volume and enhanced chain mobility, but its resistance to tensile stress decreases. Therefore, the decline in TS at higher glycerol concentrations can be associated with glycerol-induced disruption or loosening of hydrogen-bonded polymer–polyphenol interactions.

In contrast, elongation at break showed an opposite trend and increased significantly with glycerol concentration. EB increased from 28.47 ± 0.75% in G0.1 to 66.73 ± 0.88% in G0.6, demonstrating enhanced flexibility and ductility of the films. The higher EB values at elevated glycerol concentrations are related to increased polymer chain mobility, greater free volume, and reduced brittleness, which allow the film matrix to deform and elongate under applied stress. This indicates that mechanical behaviour is closely associated with the internal molecular arrangement of the films, where a dense hydrogen-bonded network favours tensile strength, while a more plasticized and less tightly packed structure promotes extensibility.

Although higher glycerol levels improved elongation, excessive plasticization caused a considerable reduction in tensile strength, making such formulations less suitable for packaging applications. Notably, G0.4 exhibited an optimal balance between tensile strength (34.44 ± 0.63 MPa) and elongation at break (61.30 ± 0.72%), indicating effective plasticization without excessive weakening of the polymer network. At this concentration, glycerol likely provided sufficient flexibility while retaining adequate hydrogen-bonding interactions among guar straw polysaccharides, *C. callosus* polyphenols, nanocellulose, and the film-forming matrix.

Therefore, G0.4 was selected as the optimized glycerol concentration for further characterization, as natural polymer-based films require a balance between mechanical strength and flexibility for practical packaging applications.

Nanocellulose–emulsion-templated packaging films are commonly developed in combination with other biopolymers to exploit synergistic interactions that cannot be achieved using nanocellulose alone. Although nanocellulose provides high stiffness, aspect ratio, and hydrogen-bonding capacity, films composed solely of nanocellulose are often brittle and difficult to process. Blending nanocellulose with flexible film-forming biopolymers and bioactive polyphenols enables the formation of a composite network in which each component contributes a complementary structural and functional role. In this system, guar straw polysaccharides provide the continuous film-forming matrix, nanocellulose reinforces the structure through hydrogen bonding, glycerol regulates chain mobility, and Kachri (*Cucumis callosus*) polyphenols contribute both molecular interactions and antioxidant functionality.

The observed results are consistent with previous reports on polysaccharide-based films, where low glycerol concentrations generally produced compact hydrogen-bonded networks with higher tensile strength, whereas moderate glycerol levels improved flexibility without severe structural weakening. Tijani et al. (2024) reported that starch/glycerol films containing 10–15% glycerol showed tensile strength above 35 MPa due to dense hydrogen-bonded networks that restricted polymer chain mobility. Similarly, Lau et al. (2022) observed that 20–30% glycerol produced an optimal balance between TS and EB in pectin-based films. The present G0.4 formulation showed comparable behaviour, suggesting that controlled glycerol incorporation can balance hydrogen bonding, plasticization, and mechanical performance in guar straw polysaccharide–*Cucumis callosus* polyphenol-based composite films.

Table 4.23 Effect of glycerol concentration on tensile strength and elongation at break of the films

Sample code	Tensile strength (MPa)	Elongation at break (%)
G0.1	42.80 ± 0.61^{a}	28.47 ± 0.75^{f}
G0.2	39.62 ± 0.82^{b}	34.92 ± 0.68^{e}
G0.3	36.93 ± 0.77^{c}	48.65 ± 0.81^{d}
G0.4	34.44 ± 0.63^{d}	61.30 ± 0.72^{c}
G0.5	30.56 ± 0.51^{e}	63.21 ± 0.91^{b}
G0.6	28.19 ± 0.79^{f}	66.73 ± 0.88^{a}

Data are presented as mean ± standard deviation (n = 3). Mean values within the same row followed by different lowercase letters (a–e) are significantly different ($p < 0.05$), as determined by analysis of variance (ANOVA) followed by post hoc tests.

4.8.2 Water vapor transmission rate (WVTR)

The water vapour transmission rate (WVTR) of the nanocellulose–sodium alginate–guar gum emulsion-templated films was strongly influenced by glycerol concentration, as shown in Table 4.24. WVTR values ranged from 2.30 ± 0.63 g/m²·day in G0.4 to 8.61 ± 0.77 g/m²·day in G0.6, indicating a clear composition-dependent moisture barrier behaviour. At lower glycerol concentration, G0.1 showed a WVTR of 4.48 ± 0.51 g/m²·day, which may be associated with the hydrophilic nature of the polysaccharide-based matrix containing abundant hydroxyl groups that promote water vapour sorption and diffusion.

With increasing glycerol concentration, WVTR increased to 5.42 ± 0.33 g/m²·day in G0.2 and 6.35 ± 0.22 g/m²·day in G0.3. This increase can be attributed to glycerol-induced plasticization, which enhances polymer chain mobility, increases free volume, and creates additional pathways for water molecule transport. Glycerol may also compete with intermolecular hydrogen bonding among nanocellulose, sodium alginate, guar gum, and *Cucumis callosus* polyphenolic compounds, thereby loosening the compactness of the film network.

Notably, G0.4 exhibited the lowest WVTR value of 2.30 ± 0.63 g/m²·day, demonstrating optimal moisture barrier performance. Mechanistically, this reduction may be explained by the formation of a more balanced and compact emulsion-templated microstructure. At this concentration, glycerol likely provided sufficient chain mobility for better film formation without excessive disruption of intermolecular interactions. Simultaneously, nanocellulose reinforcement, sodium alginate–guar gum compatibility, and possible hydrogen bonding with *Cucumis callosus* polyphenols contributed to improved matrix cohesion. The dispersed emulsion droplets may further increase the tortuosity of the diffusion pathway, thereby limiting continuous water vapour transport across the film matrix.

However, further increases in glycerol concentration in G0.5 and G0.6 sharply increased WVTR to 7.46 ± 0.55 and 8.61 ± 0.77 g/m²·day, respectively. At these higher levels, excessive glycerol increased the hydrophilicity and free volume of the film matrix, weakened polymer–polymer and polymer–polyphenol interactions, and facilitated moisture uptake and transport. Overall, these findings indicate that glycerol plays a dual role in regulating WVTR. Moderate glycerol concentration improves film-forming ability, matrix compactness, and barrier efficiency, whereas excessive glycerol acts as a moisture-attracting plasticizer that compromises water vapour resistance. Therefore, G0.4 was selected as the optimized

formulation due to its lowest WVTR and superior moisture barrier characteristics, making it suitable for biodegradable packaging applications.

4.8.3 Thickness

The thickness of the nanocellulose–sodium alginate–guar gum emulsion-templated films was significantly influenced by glycerol concentration, as presented in Table 4.21. Film thickness varied from 0.15 ± 0.003 mm in G0.5 to 0.20 ± 0.002 mm in G0.6, indicating that glycerol content strongly affected film-forming behaviour and matrix consolidation. At lower glycerol concentration, G0.1 showed a thickness of 0.19 ± 0.002 mm, which may be associated with limited plasticization and relatively rigid polymer chains that restricted flow, rearrangement, and uniform packing during casting. As glycerol concentration increased to intermediate levels, film thickness decreased to 0.18 ± 0.003 mm in G0.3 and 0.16 ± 0.002 mm in G0.4. This reduction suggests that moderate glycerol incorporation enhanced polymer chain mobility, allowing more efficient molecular rearrangement and denser packing of the emulsion-templated network during solvent evaporation. Mechanistically, glycerol at controlled levels may facilitate better dispersion of emulsion droplets and nanocellulose fibrils within the sodium alginate–guar gum matrix. In addition, possible hydrogen-bonding interactions among nanocellulose, sodium alginate, guar gum, and *Cucumis callosus* polyphenolic compounds may contribute to improved matrix cohesion and compactness, thereby reducing void spaces and producing thinner films with greater structural uniformity. However, at higher glycerol concentrations, excessive plasticization increased free volume and weakened intermolecular interactions within the film network. Consequently, film thickness increased again in G0.6 to 0.20 ± 0.002 mm, indicating less effective matrix consolidation. At this concentration, polymer chains may become overly flexible, reducing their ability to pack tightly around the emulsion droplets and nanocellulose framework. Excess glycerol may also compete for hydrogen-bonding sites within the polymer–polyphenol network, thereby loosening the matrix and increasing structural spacing. Overall, these results demonstrate that glycerol concentration critically governs film thickness by regulating polymer mobility, hydrogen-bonding interactions, and packing efficiency within the emulsion-templated matrix. The formulation G0.4 exhibited an optimal balance by producing a relatively thin and compact film structure, which is favourable for packaging applications requiring uniform thickness and consistent mechanical and barrier performance.

4.8.4 Puncher strength

Puncture strength reflects the resistance of packaging films to localized mechanical deformation and is a critical parameter for assessing their suitability for handling, stacking, and protection against sharp or concentrated loads. As shown in Table 4.20, the puncture strength of the nanocellulose–sodium alginate–guar gum emulsion-templated films increased from 19.6 ± 0.41 N in G0.1 to a maximum of 25.7 ± 0.47 N in G0.4, followed by a decline to 18.4 ± 0.43 N in G0.6. This trend indicates a strong dependence of puncture resistance on glycerol concentration, matrix compactness, and intermolecular cohesion.

At lower glycerol concentration, G0.1 showed comparatively lower puncture strength, which may be attributed to limited plasticization and a relatively rigid and brittle polymer network. Such a matrix has reduced ability to deform and redistribute localized stress around the puncture site, resulting in earlier crack initiation and lower resistance to concentrated loading. With increasing glycerol concentration from G0.2 to G0.4, puncture strength increased significantly from 21.8 ± 0.38 N to 25.7 ± 0.47 N. Mechanistically, moderate glycerol plasticization enhanced polymer chain mobility and allowed better stress distribution under point loading. At the same time, nanocellulose reinforcement and emulsion-templated domains may have acted as energy-dissipating structures, limiting crack propagation and improving resistance to puncture.

The highest puncture strength observed in G0.4 suggests the formation of a mechanically balanced and cohesive film network. At this optimized glycerol level, sufficient flexibility was achieved without excessive weakening of the polymer matrix. Possible hydrogen-bonding interactions among nanocellulose, sodium alginate, guar gum, and *Cucumis callosus* polyphenolic compounds may have further contributed to matrix integrity, compactness, and resistance against localized deformation. The hydroxyl-rich structure of the polysaccharide components and *C. callosus* polyphenols can promote intermolecular interactions, improving compatibility within the composite matrix and supporting effective load transfer during puncture testing.

Beyond the optimal glycerol concentration, further increases in glycerol content in G0.5 and G0.6 reduced puncture strength to 22.1 ± 0.39 N and 18.4 ± 0.43 N, respectively. This decline may be due to over-plasticization, where excessive glycerol increases free volume, weakens polymer–polymer and polymer–polyphenol interactions, and reduces the reinforcing efficiency of nanocellulose within the matrix. As a result, the film becomes softer and less resistant to concentrated mechanical force, allowing easier deformation and rupture under localized stress. Overall, the results demonstrate that G0.4 represents the optimized formulation, where the combined effects of controlled glycerol plasticization, nanocellulose reinforcement, emulsion

templating, and possible hydrogen-bonding interactions with *Cucumis callosus* polyphenols produced a mechanically robust matrix with superior puncture resistance. This property is particularly important for biodegradable packaging applications requiring resistance to tearing, piercing, and mechanical damage during handling, storage, and transportation.

4.8.5 Toughness

Toughness represents the total energy absorbed by a film before fracture and reflects the combined contribution of tensile strength and elongation capacity. As presented in Table 4.20, the toughness of the nanocellulose–sodium alginate–guar gum emulsion-templated films increased from 1.84 ± 0.14 MJ/m³ in G0.1 to a maximum of 3.98 ± 0.21 MJ/m³ in G0.4, followed by a slight decline to 3.41 ± 0.16 MJ/m³ in G0.6. This trend highlights the critical role of glycerol concentration in balancing matrix strength, flexibility, and energy absorption capacity.

At lower glycerol concentration, G0.1 showed comparatively low toughness, which may be attributed to limited plasticization and the formation of a rigid and relatively brittle polymer network. Restricted polymer chain mobility reduces the ability of the film matrix to deform under stress, leading to early fracture and lower energy absorption before failure. As glycerol concentration increased from G0.2 to G0.4, toughness improved significantly from 2.47 ± 0.09 MJ/m³ to 3.98 ± 0.21 MJ/m³. Mechanistically, moderate glycerol plasticization enhanced polymer chain mobility while maintaining sufficient intermolecular cohesion within the nanocellulose-reinforced, emulsion-templated matrix.

The maximum toughness observed in G0.4 suggests the formation of a mechanically balanced film network with improved resistance to fracture. At this concentration, glycerol likely provided adequate flexibility without excessive weakening of the polymer matrix. In addition, possible hydrogen-bonding interactions among nanocellulose, sodium alginate, guar gum, and *Cucumis callosus* polyphenolic compounds may have contributed to improved matrix compatibility, cohesion, and load transfer. The hydroxyl-rich structure of the polysaccharide components and *C. callosus* polyphenols can support intermolecular interactions, allowing the film to absorb and dissipate more energy during deformation. The dispersed emulsion droplets may also have functioned as stress-relief and energy-dissipating domains, delaying crack initiation and propagation under mechanical loading. This synergistic effect of controlled plasticization, nanocellulose reinforcement, emulsion templating, and polymer–polyphenol interactions contributed to the superior toughness of G0.4. Beyond the optimal glycerol concentration, further increases in glycerol content in G0.5 and G0.6 reduced toughness despite higher elongation at break. This reduction may be due to over-plasticization, where excessive

glycerol increases free volume, weakens polymer–polymer and polymer–polyphenol interactions, and reduces the reinforcing efficiency of nanocellulose. As a result, the matrix becomes softer and yields prematurely under applied stress, reducing its total energy absorption capacity.

Overall, the highest toughness observed in G0.4 confirms that this formulation achieved the most favourable balance between strength and extensibility. The results demonstrate that optimized glycerol concentration, nanocellulose reinforcement, emulsion templating, and possible hydrogen-bonding interactions with *Cucumis callosus* polyphenols collectively contributed to the development of mechanically resilient biodegradable packaging films.

4.8.6 Moisture Content and Transparency

The moisture content and transparency of the nanocellulose–sodium alginate–guar gum emulsion-templated films varied significantly with glycerol concentration, as shown in Table 4.25. Moisture content decreased from 6.92 ± 0.84% in G0.1 to a minimum of 5.65 ± 1.21% in G0.4, indicating improved matrix compactness and reduced availability of free hydrophilic sites for water binding at the optimized glycerol level. At lower glycerol concentration, limited plasticization may have restricted polymer chain rearrangement, resulting in a less compact structure with relatively higher moisture retention. The lowest moisture content observed in G0.4 may be attributed to the formation of a more cohesive and compact film network. At this concentration, glycerol likely provided sufficient chain mobility for effective packing of nanocellulose, sodium alginate, and guar gum within the emulsion-templated matrix. In addition, possible hydrogen-bonding interactions among the hydroxyl-rich polysaccharide components, nanocellulose, and *Cucumis callosus* polyphenolic compounds may have reduced the number of free hydroxyl groups available for water adsorption. The improved matrix cohesion and reduced free volume contributed to lower moisture uptake in G0.4. However, further increase in glycerol concentration led to higher moisture content, reaching 8.69 ± 1.34% in G0.6. This increase can be attributed to the hygroscopic nature of glycerol and its ability to attract and retain water molecules. Excessive glycerol may also increase free volume, weaken polymer–polymer and polymer–polyphenol interactions, and create a more open matrix structure, thereby facilitating moisture absorption within the film network. Transparency also varied with glycerol concentration and increased progressively from 0.85 ± 0.15 in G0.1 to a maximum of 1.51 ± 0.05 in G0.4. This improvement in optical clarity may be related to enhanced polymer chain mobility, better film-forming ability, and more homogeneous dispersion of nanocellulose fibrils, emulsion droplets, and *Cucumis callosus* polyphenolic compounds within the matrix. A uniform and compact microstructure reduces phase separation

and light scattering, thereby improving film transparency. At higher glycerol concentrations, transparency decreased from 1.18 ± 0.08 in G0.5 to 0.96 ± 0.12 in G0.6. This reduction may be associated with excessive plasticization, increased moisture uptake, and microstructural heterogeneity, which can enhance light scattering across the film surface. Overall, G0.4 exhibited the lowest moisture content and highest transparency, confirming it as the optimized glycerol concentration for producing moisture-resistant and visually clear biodegradable packaging films.

Table 4.25 Effect of glycerol concentration on the mechanical properties of emulsion-templated nanocellulose–sodium alginate–guar gum packaging films

Sample	Glycerol (mL/100 mL)	Tensile strength (MPa)	Elongation at break (%)	Toughness (MJ/m^3)	Puncture strength (N)
G0.1	0.1	42.80 ± 0.61^{f}	28.47 ± 0.75^{a}	1.84 ± 0.14^{a}	19.6 ± 0.41^{a}
G0.2	0.2	39.12 ± 0.54^{e}	36.92 ± 0.68^{b}	2.47 ± 0.09^{b}	21.8 ± 0.38^{b}
G0.3	0.3	36.93 ± 0.49^{d}	48.14 ± 0.72^{c}	3.15 ± 0.19^{c}	23.9 ± 0.50^{c}
G0.4	0.4	34.44 ± 0.63^{c}	61.30 ± 0.72^{d}	3.98 ± 0.21^{e}	25.7 ± 0.47^{d}
G0.5	0.5	31.62 ± 0.71^{b}	63.84 ± 0.81^{e}	3.56 ± 0.18^{d}	22.1 ± 0.39^{b}
G0.6	0.6	28.19 ± 0.79^{a}	66.73 ± 0.88^{f}	3.41 ± 0.16^{cd}	18.4 ± 0.43^{a}

Values are expressed as mean ± SD (n = 3). Within each row, means bearing different lowercase letters (a–e) differ significantly according to ANOVA followed by post-hoc testing.

Table 4.26 Effect of glycerol concentration on the physicochemical and barrier properties of emulsion-templated nanocellulose–sodium alginate–guar gum packaging films

Sample	Thickness (mm)	WVTR ($g/m^2 \cdot day$)	Moisture content (%)	Transparency (Abs_{660})
G0.1	0.19 ± 0.002^{c}	4.48 ± 0.51^{c}	6.92 ± 0.84^{c}	0.85 ± 0.15^{a}
G0.2	0.18 ± 0.003^{b}	5.42 ± 0.33^{d}	6.41 ± 0.76^{c}	1.02 ± 0.29^{b}
G0.3	0.18 ± 0.003^{b}	6.35 ± 0.22^{e}	5.98 ± 0.68^{b}	1.24 ± 0.47^{c}
G0.4	0.16 ± 0.002^{a}	2.30 ± 0.63^{a}	5.65 ± 0.21^{a}	1.51 ± 0.53^{d}
G0.5	0.15 ± 0.003^{a}	7.46 ± 0.55^{f}	7.12 ± 0.95^{d}	1.18 ± 0.88^{c}
G0.6	0.20 ± 0.002^{d}	8.61 ± 0.77^{g}	8.69 ± 0.34^{e}	0.96 ± 0.62^{b}

Results are reported as mean ± SD (n = 3). Means within the same row bearing different lowercase letters (a–e) are significantly different according to ANOVA followed by post-hoc analysis ($p < 0.05$).

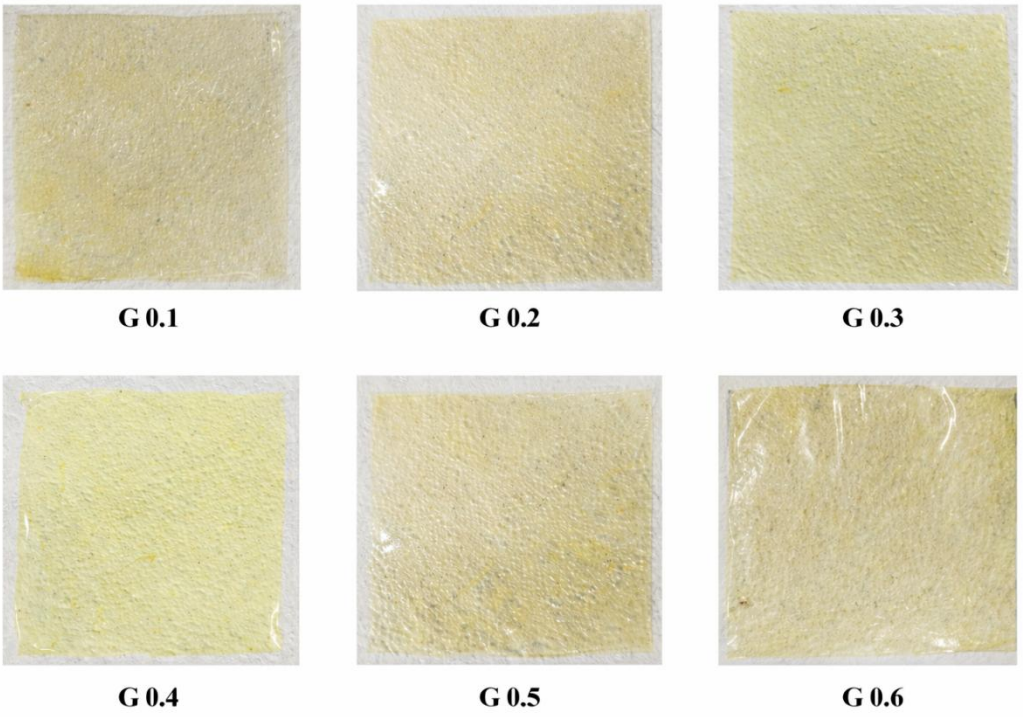

Fig. 4.44 Visual appearance of nanoemulsion-templated nanocellulose–sodium alginate–guar gum packaging films prepared with different glycerol concentrations: G0.1 (0.1 mL/100 mL), G0.2 (0.2 mL/100 mL), G0.3 (0.3 mL/100 mL), G0.4 (0.4 mL/100 mL), G0.5 (0.5 mL/100 mL), and G0.6 (0.6 mL/100 mL)

4.9 Comparison of mechanical and physicochemical attributes of functional and control films

The mechanical strength and physicochemical characteristics of the glycerol-plasticized control films such as, (NC) nanocellulose, (SA) sodium alginate, and (GG) guar gum—were systematically compared with the emulsion-templated composite film without *Cucumis callosus* extract (NEW) and the functional film incorporated with *Cucumis callosus* peel extract (NE) to elucidate the influence of matrix composition and bioactive integration on film performance. The incorporation of emulsifiers, essential oil, and peel extract was expected to modulate intermolecular interactions within the polymeric network, thereby affecting tensile properties, flexibility, moisture sensitivity, solubility, thickness, and barrier behavior. The comparative mechanical and physicochemical parameters of all developed films are presented in Fig. 4.45.

4.9.1 Tensile strength (TS) and elongation at break (EB)

The tensile strength (TS) and elongation at break (EB) of the films varied significantly with polymer composition and the incorporation of the emulsion template and *Cucumis callosus* extract, as shown in Table 4.22. The NC control film exhibited a TS of 28.50 ± 0.56 MPa and a

relatively low EB of 31.5 ± 0.61%, which can be attributed to the rigid nanocellulose-dominated network formed through extensive intermolecular hydrogen bonding among cellulose hydroxyl groups. This dense network effectively transfers applied stress but restricts polymer chain mobility, resulting in limited extensibility.

The SA control film exhibited a lower TS of 22.1 ± 0.24 MPa and a higher EB of 48.9 ± 0.43%, reflecting the flexible nature of sodium alginate chains. The presence of carboxylate groups in sodium alginate may promote chain mobility and slippage during tensile deformation, thereby improving extensibility. In contrast, the GG control film exhibited the lowest TS of 17.4 ± 0.77 MPa but the highest EB among the control films, 62.4 ± 0.38%. This behaviour may be associated with the highly branched structure of guar gum, which limits effective stress transfer but allows greater molecular rearrangement during stretching.

A pronounced improvement in mechanical performance was observed in the NEW composite film without *Cucumis callosus* extract, which showed a TS of 35.90 ± 0.67 MPa and an EB of 54.2 ± 0.44%. This enhancement is mainly attributed to synergistic interactions among nanocellulose, sodium alginate, and guar gum within the emulsion-templated matrix. Nanocellulose acts as a reinforcing scaffold and forms hydrogen-bonded junctions with alginate and guar gum, while the emulsion template promotes a more homogeneous microstructure. This organized matrix can redistribute applied stress more effectively and suppress crack initiation. Therefore, the balanced combination of rigid nanocellulose domains and flexible polysaccharide chains resulted in simultaneous improvement in strength and flexibility.

The NE functional film, containing *Cucumis callosus* extract within the emulsion-templated matrix, exhibited the highest TS of 38.71 ± 0.90 MPa and EB of 71.3 ± 0.29% among all samples. The increase in TS indicates improved interfacial adhesion between the emulsion droplets and the polymer matrix, which may be associated with hydrogen bonding and secondary interactions between *Cucumis callosus* polyphenolic compounds and the hydroxyl- and carboxyl-rich polysaccharide chains. The phenolic hydroxyl groups of *C. callosus* extract may interact with nanocellulose, sodium alginate, and guar gum, improving matrix compatibility, cohesion, and load transfer. At the same time, the substantial increase in EB suggests that the extract-loaded emulsion droplets acted as flexible and energy-dissipating domains within the film network. These domains may increase chain mobility, delay crack propagation, and allow greater deformation before rupture. Thus, the emulsion-templated architecture provided a hierarchical structure in which nanocellulose contributed load-bearing ability, sodium alginate and guar gum provided flexibility and film-forming capacity, and *Cucumis callosus* extract contributed to both molecular interactions and functional

reinforcement. Overall, these results demonstrate that emulsion templating significantly enhanced the mechanical performance of nanocellulose-based films, while incorporation of *Cucumis callosus* extract in the NE film produced the most favourable balance between tensile strength and extensibility. The improved performance of NE may be attributed to the combined effects of nanocellulose reinforcement, polysaccharide compatibility, emulsion-mediated stress dissipation, and possible hydrogen-bonding interactions between *Cucumis callosus* polyphenols and the polymer matrix, making it suitable for advanced functional and active packaging applications.

4.9.2 Water vapor transmission rate (WVTR)

The water vapour transmission rate (WVTR) of the films showed significant variation depending on polymer composition, emulsion templating, and incorporation of *Cucumis callosus* peel extract, as shown in Table 4.23. The NC control film exhibited a relatively higher WVTR of 4.48 ± 0.51 g/m²·day, which can be attributed to the hydrophilic nature of nanocellulose and the presence of abundant hydroxyl groups that facilitate water vapour sorption and diffusion through the film matrix. The SA control film showed a moderately increased WVTR of 5.42 ± 0.33 g/m²·day, reflecting the hydrophilic nature of sodium alginate and the availability of free carboxylate groups that may enhance moisture transport. In contrast, the GG control film exhibited a further increase in WVTR of 6.35 ± 0.22 g/m²·day, which may be associated with the loosely packed and highly flexible guar gum network, providing less resistance to water vapour permeation.

A substantial reduction in WVTR was observed in the NEW composite film without *Cucumis callosus* peel extract, which exhibited a WVTR of 2.30 ± 0.63 g/m²·day, indicating improved moisture barrier performance. This reduction may be attributed to the formation of a denser and more compact polymer network resulting from hydrogen bonding and physical entanglement among nanocellulose, sodium alginate, and guar gum. Nanocellulose can act as a reinforcing phase, while alginate and guar gum contribute to continuous film formation and matrix flexibility. In addition, the emulsion-templated structure may increase diffusion tortuosity by disrupting continuous pathways for water vapour migration across the film matrix.

The NE functional film, containing *Cucumis callosus* peel extract within the emulsion-templated matrix, showed a slightly higher but still low WVTR of 3.18 ± 0.47 g/m²·day compared with NEW. The marginal increase in WVTR may be attributed to the presence of polar phytochemical constituents in *C. callosus* extract, particularly phenolic hydroxyl groups, which can introduce additional moisture-binding sites within the matrix. However, the WVTR of NE remained significantly lower than that of the individual control films, indicating that the

extract-loaded emulsion system maintained an effective barrier structure. The improved barrier performance of NE may be associated with the combined effects of emulsion templating, nanocellulose reinforcement, and possible hydrogen-bonding interactions between *Cucumis callosus* polyphenols and the polysaccharide matrix. These interactions may improve matrix compatibility and cohesion, while dispersed emulsion droplets can function as discontinuous domains that increase the tortuous path for water vapour diffusion. Therefore, although *C. callosus* extract introduced some polar groups into the film matrix, the overall emulsion-templated architecture restricted moisture migration effectively. Overall, these results demonstrate that emulsion templating markedly enhanced the moisture barrier properties of nanocellulose-based films. Incorporation of *Cucumis callosus* peel extract in the NE film caused only a minor increase in WVTR compared with NEW, without compromising overall barrier performance. This balance between reduced moisture transmission and added bioactive functionality highlights the suitability of the NE film for active and biodegradable packaging applications.

4.9.3 Thickness

The thickness of the films varied significantly depending on polymer composition, emulsion templating, and incorporation of *Cucumis callosus* peel extract, as shown in Table 4.23. The NC control film exhibited a thickness of 0.19 ± 0.02 mm, reflecting the dense packing of nanocellulose fibrils driven by strong intermolecular hydrogen bonding among cellulose hydroxyl groups. The SA control film showed a slightly lower thickness of 0.18 ± 0.03 mm, which may be attributed to the flexible nature of sodium alginate chains that allows better flow and levelling during film casting. Similarly, the GG control film exhibited a comparable thickness of 0.18 ± 0.03 mm, which may be associated with the high molecular weight and branched structure of guar gum. Although guar gum increases solution viscosity, its film-forming ability still supports relatively uniform spreading during casting. A noticeable reduction in thickness was observed in the NEW composite film without *Cucumis callosus* peel extract, which exhibited a thickness of 0.16 ± 0.02 mm. This decrease indicates improved matrix consolidation arising from synergistic interactions among nanocellulose, sodium alginate, and guar gum. Nanocellulose can form hydrogen-bonded junctions with alginate and guar gum, while the emulsion-templated structure promotes efficient polymer chain rearrangement during solvent evaporation. These interactions allow tighter molecular packing, reduced void volume, and formation of a thinner and more compact film matrix. The NE functional film, incorporating *Cucumis callosus* peel extract within the emulsion-templated matrix, exhibited a slightly higher thickness of 0.17 ± 0.02 mm compared with NEW. This

marginal increase may be attributed to the presence of extract-loaded emulsion droplets, which introduce additional solid content and localized structural expansion within the polymer network. The phenolic constituents of *C. callosus* peel extract may also interact with nanocellulose, sodium alginate, and guar gum through hydrogen bonding and secondary interactions. These interactions can slightly increase matrix spacing while maintaining structural cohesion and uniformity. Overall, the results indicate that emulsion templating contributes to the development of thinner and more compact composite films by improving polymer compatibility and matrix consolidation. Incorporation of *Cucumis callosus* peel extract in the NE film caused only a minimal increase in thickness, without compromising structural uniformity. This suggests that the extract was effectively incorporated within the emulsion-templated polysaccharide matrix, supporting the suitability of the NE film for active biodegradable packaging applications.

4.9.4 Puncher strength

Puncture strength reflects the resistance of films to localized mechanical stress and is a critical parameter for packaging materials subjected to handling, stacking, and accidental impact. As shown in Table 4.26, the NC control film exhibited a puncture strength of 19.6 ± 0.41 N, which can be attributed to the rigid but relatively brittle nanocellulose network formed through extensive hydrogen bonding among cellulose hydroxyl groups. Although this network provides stiffness, it has limited ability to dissipate localized stress under point loading. The SA control film exhibited a moderately higher puncture strength of 21.8 ± 0.38 N, which may be attributed to the flexible nature of sodium alginate chains that enables partial stress redistribution during puncture deformation. In contrast, the GG control film displayed a puncture strength of 23.9 ± 0.50 N, which may be associated with the elastic and deformable nature of the guar gum matrix. Although guar gum has a relatively loosely packed structure, its flexibility may help absorb localized force before rupture. A further improvement in puncture strength was observed in the NEW composite film without *Cucumis callosus* peel extract, which exhibited the highest puncture strength of 25.7 ± 0.47 N. This enhancement may be linked to synergistic interactions among nanocellulose, sodium alginate, and guar gum within the emulsion-templated matrix. Nanocellulose acts as a reinforcing framework that restricts crack initiation, while sodium alginate and guar gum provide flexibility and film-forming continuity. The emulsion-templated structure may also promote uniform stress distribution and delay crack propagation under puncture loading. Thus, the balanced combination of stiffness and flexibility enabled the NEW film to absorb and redistribute localized force more effectively. The NE functional film,

incorporating *Cucumis callosus* peel extract within the emulsion-templated matrix, showed a slightly reduced but still high puncture strength of 22.1 ± 0.39 N compared with NEW. This marginal decrease may be attributed to the presence of extract-loaded emulsion droplets and polyphenolic constituents, which can introduce localized plasticization and increase matrix deformability. However, possible hydrogen-bonding interactions between *C. callosus* polyphenols and the polysaccharide matrix may help maintain matrix cohesion and prevent excessive mechanical weakening. Therefore, although the incorporation of *C. callosus* peel extract slightly reduced maximum puncture force, the NE film retained adequate resistance to localized mechanical stress.

Overall, these results demonstrate that emulsion templating significantly improved puncture strength by enhancing stress redistribution, matrix cohesion, and crack resistance. Incorporation of *Cucumis callosus* peel extract in the NE film slightly reduced puncture strength compared with NEW but maintained sufficient mechanical robustness for practical active and biodegradable packaging applications.

4.9.5 Moisture Content and Transparency

The moisture content and transparency of the films showed significant dependence on polymer composition, emulsion templating, and incorporation of *Cucumis callosus* peel extract, as shown in Table 4.27. The NC control film exhibited the highest moisture content of 11.35 ± 0.42%, which can be attributed to the highly hydrophilic nature of nanocellulose and the abundance of free hydroxyl groups that readily interact with water molecules through hydrogen bonding. The SA film showed a reduced moisture content of 9.28 ± 0.37%, indicating partial restriction of water uptake due to ionic interactions among alginate chains, although the presence of carboxylate groups still favours moisture absorption. A further decrease was observed in the GG film, with a moisture content of 7.27 ± 0.31%, which may be associated with the branched guar gum structure that allows polymer chain rearrangement and reduces water entrapment within the matrix. A pronounced reduction in moisture content was observed in the NEW composite film without *Cucumis callosus* peel extract, which exhibited a value of 6.70 ± 0.28%. This reduction indicates the formation of a compact and well-integrated polymer network. The improved moisture resistance of NEW may be attributed to strong intermolecular hydrogen bonding and physical entanglement among nanocellulose, sodium alginate, and guar gum, which reduce free volume and limit the availability of hydrophilic sites for water binding. Notably, the NE functional film, containing nanocellulose, sodium alginate, guar gum, and *Cucumis callosus* peel extract, exhibited the lowest moisture content of 4.91 ± 0.24% among all formulations. The superior moisture resistance of NE may be mechanistically attributed to

the emulsion-templated architecture, where extract-loaded emulsion domains are immobilized within the polymer matrix. These domains can increase diffusion tortuosity and reduce direct interaction between water molecules and hydrophilic groups. In addition, possible hydrogen-bonding interactions between *C. callosus* polyphenolic compounds and the polysaccharide matrix may reduce the number of free hydroxyl and carboxyl groups available for water binding, thereby improving moisture resistance. Transparency followed a complementary trend. The NC film showed the lowest transparency value of 0.85 ± 0.06 Abs_{660}, which may be due to light scattering from densely packed nanocellulose fibrils and structural heterogeneity. Transparency improved in the SA and GG films, with values of 1.02 ± 0.05 and 1.24 ± 0.04 Abs_{660}, respectively, reflecting improved matrix uniformity and chain mobility. The NEW film exhibited the highest transparency of 1.51 ± 0.05 Abs_{660}, indicating the formation of a highly homogeneous and well-dispersed composite structure. Although the transparency of the NE film was slightly lower at 1.18 ± 0.06 Abs_{660}, this decrease may be attributed to the intrinsic colour and light-absorbing phytochemicals present in *Cucumis callosus* peel extract. The presence of phenolic compounds can increase light absorption and scattering, leading to a moderate reduction in optical clarity. However, the transparency remained within an acceptable range for packaging applications, especially where active functionality and moisture resistance are prioritized.

Overall, the results demonstrate that the NE functional film achieved the best balance between low moisture content and acceptable transparency. The combined effects of emulsion templating, nanocellulose reinforcement, polysaccharide compatibility, and possible hydrogen-bonding interactions with *Cucumis callosus* polyphenols contributed to improved moisture resistance while maintaining suitable optical properties for active biodegradable packaging applications.

Table 4.26 Mechanical properties of control, composite, and functional emulsion-templated films

Sample code	**Tensile strength (MPa)**	**Elongation at break (%)**	**Puncture strength (N)**
NC Control	28.50 ± 0.56^{c}	31.5 ± 0.61^{a}	19.6 ± 0.41^{b}
SA Control	22.10 ± 0.24^{b}	48.9 ± 0.43^{c}	21.8 ± 0.38^{c}
GG Control	17.40 ± 0.77^{a}	62.4 ± 0.38^{d}	23.9 ± 0.50^{c}
NEW	35.90 ± 0.67^{d}	54.2 ± 0.44^{c}	25.7 ± 0.47^{d}

NE	38.71 ± 0.90^{e}	71.3 ± 0.29^{e}	22.1 ± 0.39^{c}

Values are expressed as mean ± SD (n = 3). Means within the same row marked with different lowercase letters (a–e) indicate significant differences based on ANOVA followed by post hoc tests ($p < 0.05$).

Table 4.27 Physicochemical and barrier properties of control, composite, and functional emulsion-templated films

Sample code	**Moisture content (%)**	**Transparency (Abs_{660})**	**Thickness (mm)**	**WVTR ($g/m^2 \cdot day$)**
NC Control	11.35 ± 0.42^{e}	0.85 ± 0.06^{a}	0.19 ± 0.02^{c}	4.48 ± 0.51^{c}
SA Control	9.28 ± 0.37^{d}	1.02 ± 0.05^{b}	0.18 ± 0.03^{b}	5.42 ± 0.33^{d}
GG Control	7.27 ± 0.31^{c}	1.24 ± 0.04^{c}	0.18 ± 0.03^{b}	6.35 ± 0.22^{e}
NEW	6.70 ± 0.28^{b}	1.51 ± 0.05^{d}	0.16 ± 0.02^{a}	2.30 ± 0.63^{a}
NE	4.91 ± 0.24^{a}	1.18 ± 0.06^{c}	0.17 ± 0.02^{b}	3.18 ± 0.47^{b}

Data are presented as mean ± SD (n = 3). Mean values with different lowercase (a-e) alphabets within a row, respectively, based on analysis of variance (ANOVA) and post hoc tests

Fig. 4.45 Visual representation of nanocellulose-based control and nanoemulsion-templated packaging films.

Note: (NC) nanocellulose control film, (SA) sodium alginate control film, and (GG) guar gum control film, all plasticized with glycerol. (NEW) The emulsion-templated composite film prepared using nanocellulose, sodium alginate, guar gum, Tween 80, ginger oil, and lecithin without peel extract (NE) represents the functional emulsion-templated film with nanocellulose, sodium alginate, guar gum, Tween 80, ginger oil, and lecithin incorporating *Cucumis callosus* peel extract.

4.10 Antimicrobial property of packaging films

The antimicrobial activity of the developed films exhibited a significant concentration-dependent response against *Staphylococcus aureus* and *Escherichia coli*, with inhibition zones increasing significantly ($p < 0.05$) with increasing concentration, as shown in figs. 4.346 and 4.47. For *S. aureus*, at 10 mg/mL, inhibition zones increased from 10.12 ± 0.28 mm for the nanocellulose control film (NC) to 16.71 ± 0.15 mm (GG) and 18.19 ± 0.74 mm (SA), followed by significantly higher values of 22.13 ± 0.26 mm (NEW) and 25.56 ± 0.16 mm (NE). The lower antimicrobial activity of NC can be attributed to nanocellulose acting primarily as a structural matrix with limited inherent antibacterial properties. The GG and SA control films, plasticized with glycerol, showed significantly higher inhibition than NC due to improved hydration and swelling behavior, which enhanced diffusion of antimicrobial compounds into the surrounding medium. The emulsion-templated composite film (NEW), composed of nanocellulose, sodium alginate, guar gum, Tween 80, ginger oil, and lecithin, exhibited significantly higher antibacterial activity because ginger oil contains bioactive terpenoids capable of disrupting bacterial membranes, while emulsifiers improved dispersion and release of hydrophobic compounds. The NE formulation demonstrated the significantly highest inhibition, which is attributed to the incorporation of *Cucumis callosus* peel extract providing additional phenolic and flavonoid compounds that act synergistically with ginger oil to enhance membrane disruption and microbial inhibition. As concentration decreased to 5 mg/mL and 2.5 mg/mL, inhibition zones became significantly lower ($p < 0.05$), ranging from 5.44 ± 0.51 to 12.37 ± 0.26 mm and 2.31 ± 0.42 to 6.89 ± 0.75 mm, respectively, confirming dose-dependent antimicrobial behavior. A similar trend was observed for *E. coli*, where inhibition zones increased significantly from 7.10 ± 0.13 mm (NC) to 28.55 ± 0.66 mm (NE) at 10 mg/mL, indicating improved penetration of nanoemulsion-delivered bioactive compounds even through the Gram-negative outer membrane barrier. Ampicillin exhibited significantly higher inhibition zones ($p < 0.05$) of approximately 28–31 mm, validating experimental sensitivity. Overall, the enhanced antimicrobial performance of NEW and NE films is attributed to the emulsion-templated structure enabling controlled release of bioactive agents, while synergistic

interactions between ginger oil and peel-derived phenolics resulted in superior antibacterial efficacy compared with control films.

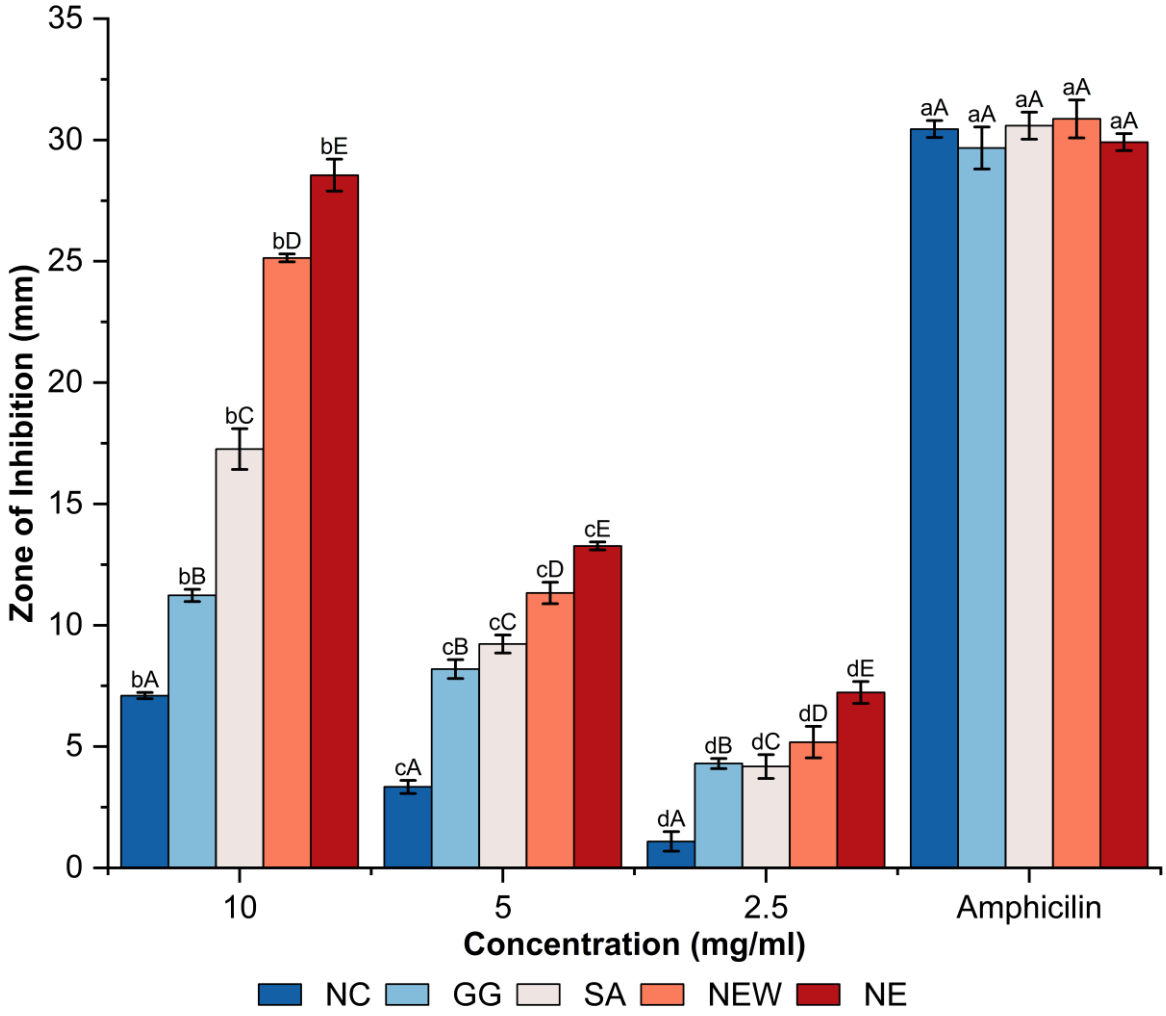

Fig. 4.46 Antimicrobial activity of formulated packaging film against *Escherichia coli*

Note: (NC) nanocellulose control film, (SA) sodium alginate control film, and (GG) guar gum control film. (NEW) The emulsion-templated composite film prepared using nanocellulose, sodium alginate, guar gum, Tween 80, ginger oil, and lecithin without peel extract (NE) represents the functional emulsion-templated film with nanocellulose, sodium alginate, guar gum, Tween 80, ginger oil, and lecithin incorporating *Cucumis callosus* peel extract. Data are presented as mean ± standard deviation (n = 3). Different lowercase letters indicate significant differences among concentrations within the same formulation, while different uppercase letters indicate significant differences among film formulations at the same concentration ($p < 0.05$).

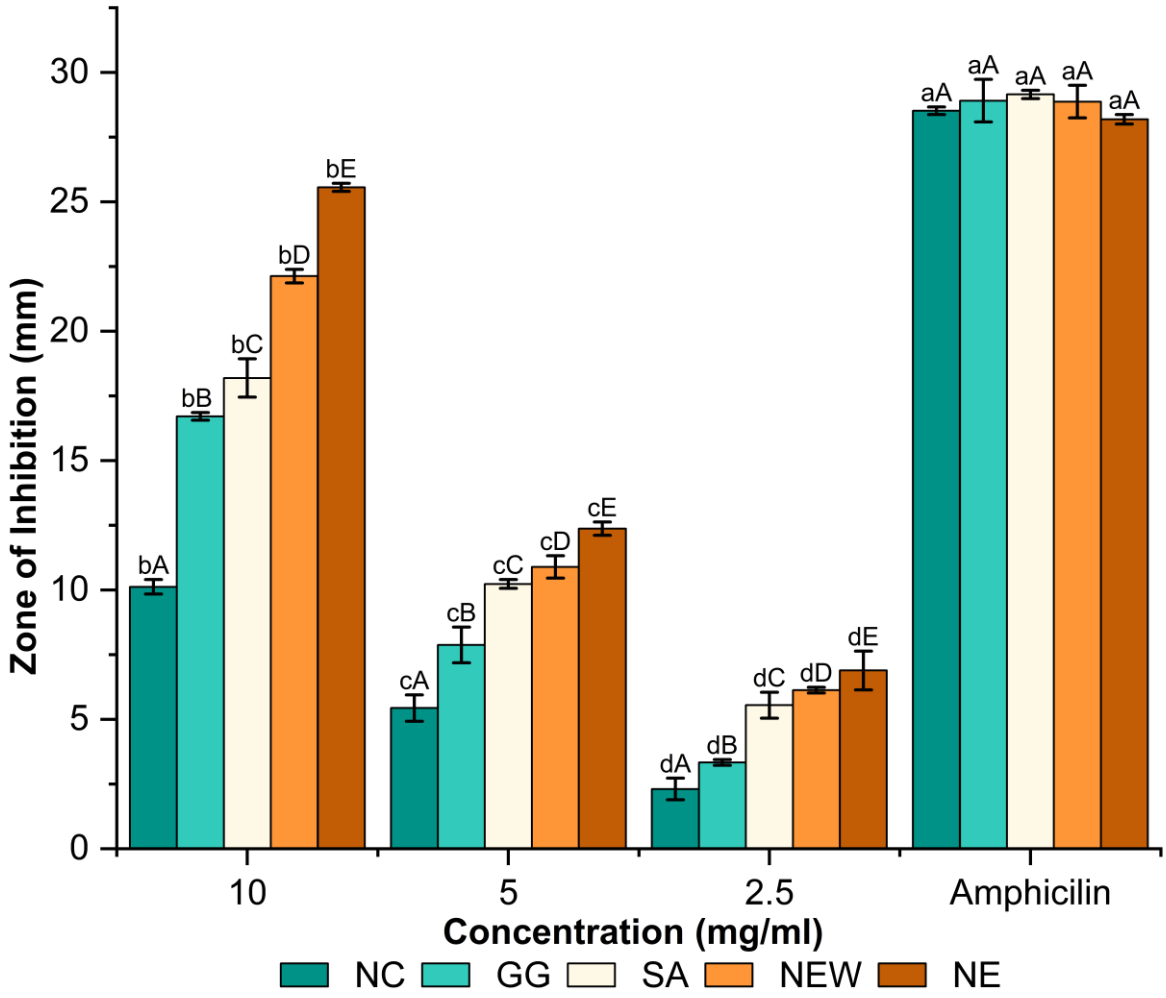

Fig. 4.47 Antimicrobial activity of formulated packaging film against *Staphylococcus aureus*

Note: (NC) nanocellulose control film, (SA) sodium alginate control film, and (GG) guar gum control film. (NEW) The emulsion-templated composite film prepared using nanocellulose, sodium alginate, guar gum, Tween 80, ginger oil, and lecithin without peel extract (NE) represents the functional emulsion-templated film with nanocellulose, sodium alginate, guar gum, Tween 80, ginger oil, and lecithin incorporating *Cucumis callosus* peel extract. Data are presented as mean ± standard deviation (n = 3). Different lowercase letters indicate significant differences among concentrations within the same formulation, while different uppercase letters indicate significant differences among film formulations at the same concentration ($p < 0.05$).

4.11 Characterization of packaging films

4.11.1 Fourier transform infrared spectroscopy (FTIR)

The FTIR spectra of the nanocellulose emulsion film (NC), sodium alginate emulsion film (SA), guar gum emulsion film (GG), composite nanoemulsion film (NEW), and functional emulsion-templated film (NE) provide detailed insight into the molecular interactions governing film formation and functional differentiation in fig 4.48. All films exhibited a broad

absorption band in the 3600–3200 cm^{-1} region, corresponding to O–H stretching vibrations of hydroxyl groups from polysaccharides, glycerol, and hydrogen-bonded water in the emulsion continuous phase, confirming extensive hydrogen bonding as the primary stabilization mechanism. In the NC, SA, and GG films, this band appeared at ~3270–3308 cm^{-1}, reflecting relatively uniform hydrogen-bond environments dominated by intra- and intermolecular interactions within individual polymer matrices. In the NEW film, the O–H band shifted to ~3289 cm^{-1} with noticeable broadening, indicating increased hydrogen-bond complexity due to the coexistence of multiple polysaccharides, glycerol plasticization, and emulsion interfaces. In contrast, the NE film exhibited a broader O–H band centered at ~3315 cm^{-1}, signifying a more heterogeneous hydrogen-bonding environment arising from structured polymer–surfactant–oil interfaces, characteristic of a functionally optimized emulsion-templated system. The C–H stretching vibrations at ~2939–2920 cm^{-1} (asymmetric) and ~2853–2843 cm^{-1} (symmetric) were present in all films due to polysaccharide backbones but showed markedly higher intensity in the NEW and NE films, confirming the incorporation and stabilization of aliphatic chains from the dispersed lipid phase and surfactants. Films containing sodium alginate (SA, NEW, and NE) displayed characteristic carboxylate stretching vibrations, with asymmetric $–COO^-$ bands at ~1595–1591 cm^{-1} and symmetric bands at ~1459–1413 cm^{-1}, confirming the ionic nature of alginate and its participation through electrostatic interactions without chemical modification. The absorption near ~1650–1645 cm^{-1}, attributed to H–O–H bending of bound water and overlapping carboxylate vibrations, further reflects the hydrophilic and emulsion-rich nature of these systems. All films showed strong absorptions in the fingerprint region (1200–1030 cm^{-1}) corresponding to C–O–C and C–O stretching vibrations of glycosidic linkages, along with minor bands near ~895–870 cm^{-1} indicative of β-glycosidic structures, demonstrating preservation of polysaccharide backbones across all formulations. Importantly, the absence of new ester or carbonyl peaks near ~1720 cm^{-1} across all films confirms that film formation occurred via non-covalent interactions rather than chemical cross-linking. Collectively, these results indicate that while NC, SA, and GG films represent simpler hydrogen-bonded emulsion networks, the NEW film exhibits enhanced interaction complexity due to polymer blending and lipid incorporation, and the NE film is distinguished by a highly organized interfacial architecture and heterogeneous hydrogen-bonding environment, which underpins its functional performance without altering the intrinsic chemistry of the biopolymers.

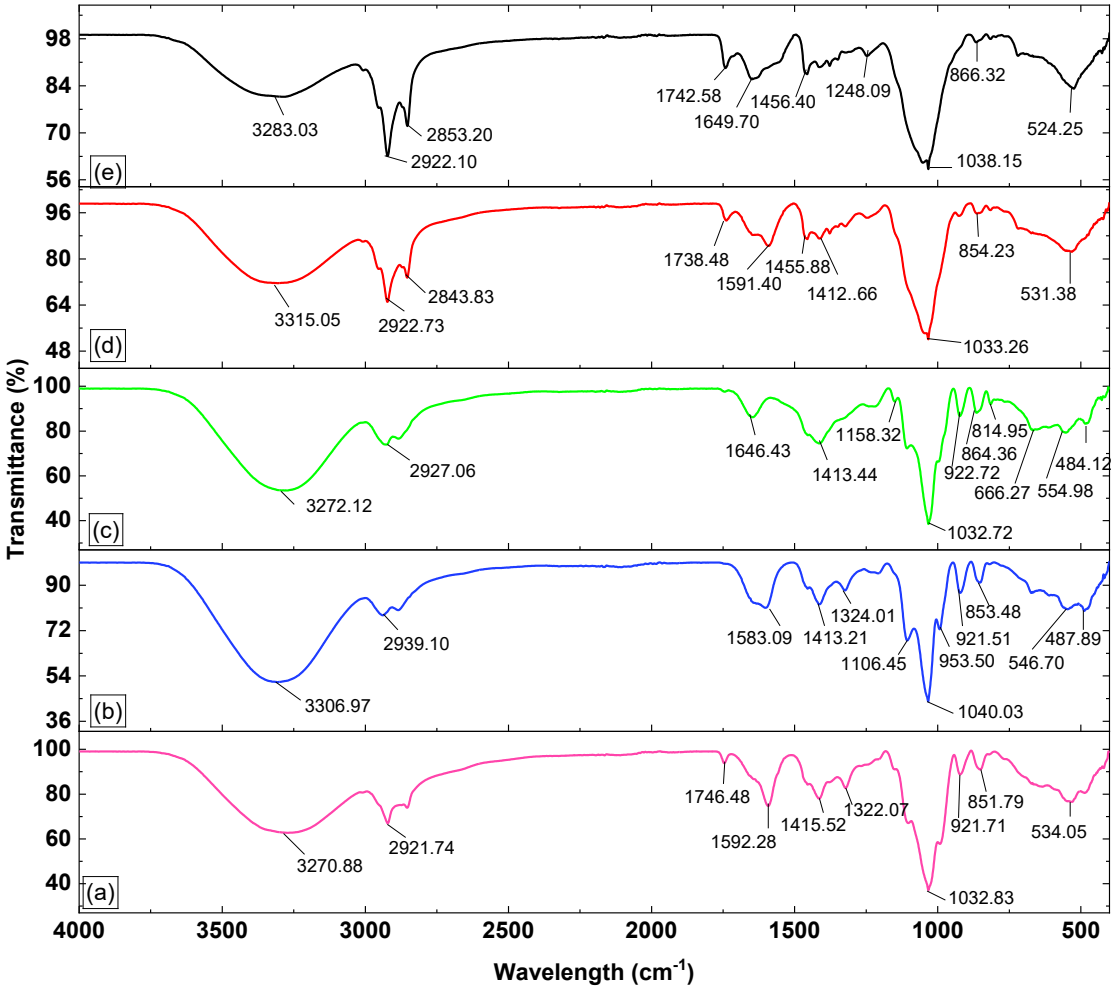

Fig. 4.48 FTIR spectra of emulsion-based packaging films: (a) nanocellulose nanoemulsion film (NC), (b) sodium alginate emulsion film (SA), (c) guar gum emulsion film (GG), (d) composite emulsion film (NEW), and (e) functional nanoemulsion-templated film (NE)

4.11.2 Degree of crystallinity (XRD)

The comparative XRD analysis of the emulsion-based films nanocellulose (NC), sodium alginate (SA), guar gum (GG), composite emulsion film (NEW), and functional emulsion-templated film (NE), reveals a systematic reduction in structural order with increasing formulation complexity as shown in fig. 4.49. The NC film exhibits a broad diffraction halo centered at $2\theta \approx 21.47°$, corresponding to short-range ordering of cellulose chains, indicating partial retention of local crystalline domains despite disruption of long-range crystallinity by emulsification and plasticization. In contrast, the SA film shows a diffuse maximum at $2\theta \approx 22.71°$, reflecting limited molecular ordering driven by hydrogen bonding and ionic interactions among alginate chains, while remaining predominantly amorphous due to the irregular distribution of mannuronic and guluronic units and the presence of bound water. The GG film

displays a broad halo at 2θ ≈ 20.37°, consistent with the inherently amorphous nature of galactomannan polymers, where extensive side-chain substitution restricts efficient chain packing. Upon polymer blending in the NEW film, the diffraction maximum shifts to 2θ ≈ 20.11° with increased peak broadening, indicating enhanced disruption of ordered regions due to interpenetration of multiple polysaccharide chains, glycerol plasticization, and the presence of a dispersed lipid phase, which collectively increase intermolecular spacing and suppress crystalline alignment. The NE film exhibits the broadest and least intense halo centered at 2θ ≈ 19.78°, signifying the highest amorphous character among all samples, this pronounced loss of order is mechanistically attributed to emulsion templating, where polymer chains reorganize around surfactant-stabilized oil droplets, leading to increased free volume, reduced chain regularity, and dominance of short-range interactions over crystalline packing. Importantly, the absence of sharp diffraction peaks in all films confirms that no new crystalline phases are formed and that the observed structural evolution arises solely from physical interactions and interfacial organization, with NE distinguished by the most disordered yet structurally integrated emulsion network, favorable for enhanced flexibility and functional performance.

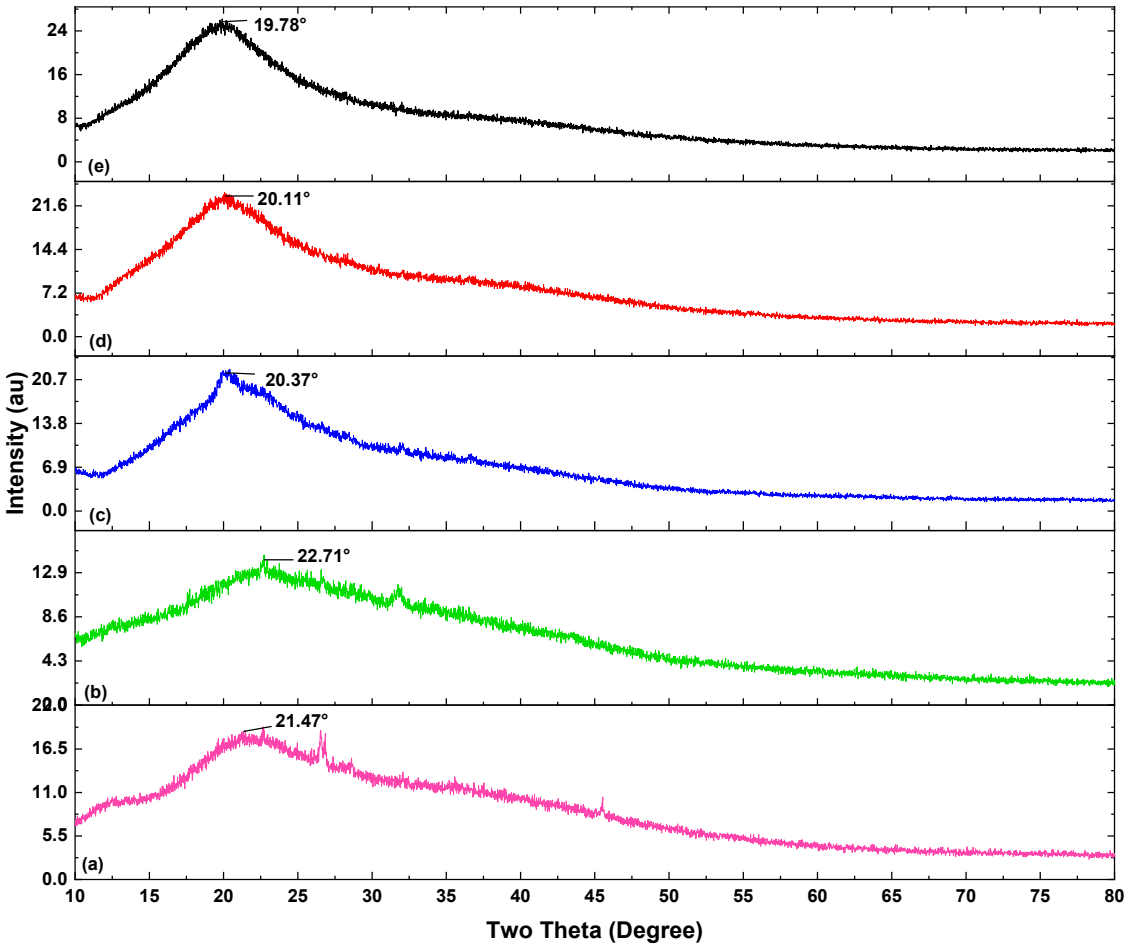

Fig. 4.49 X-ray diffraction (XRD) patterns of emulsion-based packaging films: (a) nanocellulose emulsion film, (b) sodium alginate emulsion film, (c) guar gum emulsion film, (d) composite emulsion film, and (e) functional emulsion-templated film

4.11.3 Field emission scanning electron microscopy (FESEM)

The scanning electron micrographs of the nanocellulose (NC), sodium alginate (SA), guar gum (GG), composite emulsion film (NEW), and functional emulsion-templated film (NE) reveal progressive changes in surface morphology that reflect differences in polymer compatibility, interfacial interactions, and emulsion structuring mechanisms in fig 4.50. The NC film exhibits a relatively rough and heterogeneous surface with visible fibrillar features and localized agglomeration, which can be attributed to partial aggregation of nanocellulose domains and non-uniform packing within the emulsion matrix, resulting from strong inter-fibrillar hydrogen bonding and limited chain mobility during drying. The SA film shows a comparatively smoother but still irregular surface, characterized by micro-cracks and uneven regions, indicative of shrinkage stresses generated during solvent evaporation and the intrinsically brittle nature of alginate-rich matrices governed by ionic and hydrogen-bond interactions. In contrast, the GG film presents a more continuous yet slightly granular morphology, reflecting the predominantly amorphous nature of guar gum, however, minor phase heterogeneities suggest insufficient interfacial stabilization within the emulsion system. A marked improvement in surface uniformity is observed in the NEW film, which displays a denser and more compact morphology with reduced surface defects, demonstrating enhanced polymer compatibility arising from the synergistic blending of nanocellulose, alginate, and guar gum in the presence of glycerol. This improvement is mechanistically attributed to increased intermolecular hydrogen bonding and plasticization, which promote chain rearrangement and better packing around dispersed emulsion droplets. Nevertheless, faint streaks and micro-domains are still discernible, indicating partial interfacial instability of the dispersed phase. The NE film, however, exhibits the smoothest, most homogeneous, and defect-free surface morphology among all samples, with an absence of cracks, voids, or phase-separated regions. This superior microstructural integrity is attributed to effective emulsion templating, wherein surfactant-stabilized oil droplets act as structural templates that facilitate uniform polymer redistribution and interfacial cohesion. The presence of functional components enhances polymer–surfactant–oil interactions, leading to a tightly integrated network dominated by hydrogen bonding, electrostatic interactions, and hydrophobic associations. Consequently, the NE film forms a compact and continuous matrix, which correlates well with its higher amorphous character observed in XRD analysis and the heterogeneous hydrogen-bonding environment identified in

FTIR spectra. Overall, the SEM results confirm that increasing formulation complexity and emulsion templating progressively improve structural homogeneity, with the NE film representing the most optimized architecture for functional applications.

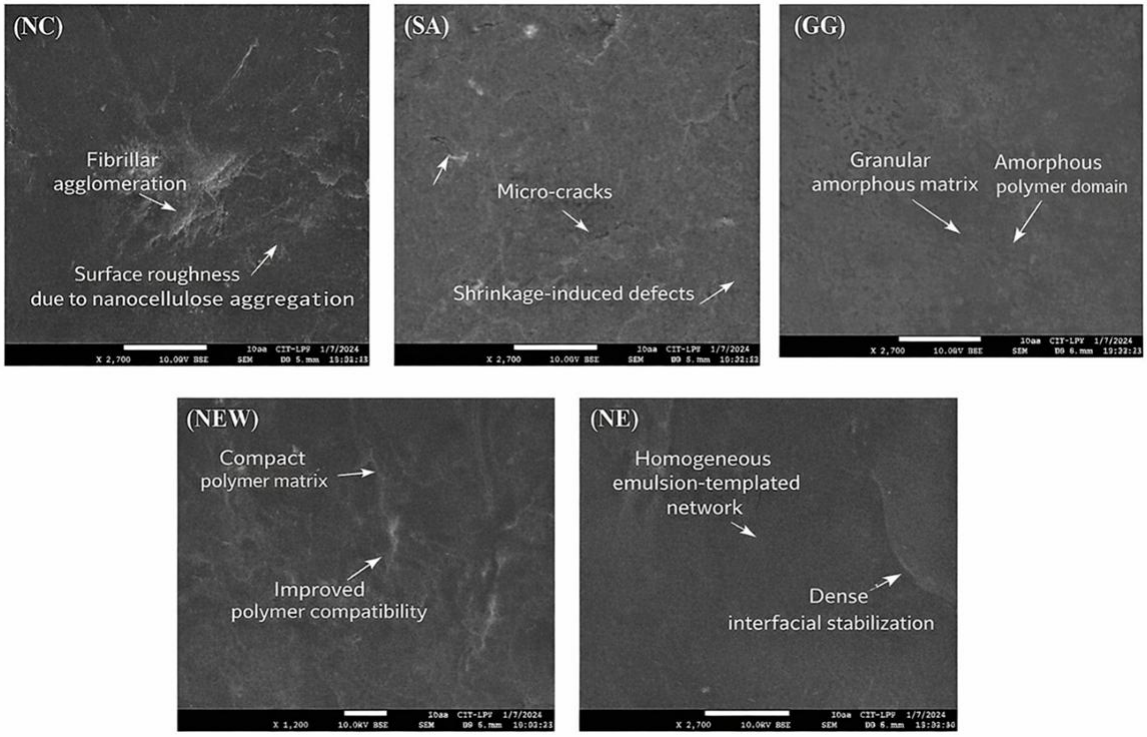

Fig. 4.50 FESEM micrographs of emulsion-based packaging films: (NC) nanocellulose emulsion film, (SA) sodium alginate emulsion film, (GG) guar gum emulsion film, (NEW) composite emulsion film, and (NE) functional emulsion-templated film

4.11.4 Thermogravimetric analysis (TGA)

Thermogravimetric analysis (TGA) was carried out to examine the thermal degradation behavior and weight-loss characteristics of the emulsion-based films. Fig. 4.51 presents the thermogravimetric curves of a (NC) nanocellulose emulsion film, b (SA) sodium alginate emulsion film, c (GG) guar gum emulsion film, d (NEW) composite emulsion film, and e (NE) functional emulsion-templated film. All samples exhibited a three-stage thermal degradation profile, which is typical of polysaccharide-based polymeric materials. The initial weight loss below approximately 120–150 °C observed for all films is attributed to the evaporation of physically adsorbed and bound moisture associated with hydroxyl-rich polymer matrices. Among the samples, films a–c (NC, SA, and GG) showed relatively higher initial mass loss, indicating greater hydrophilicity and free water binding, whereas films d and e (NEW and NE) exhibited reduced moisture loss, suggesting restricted water mobility due to stronger intermolecular interactions and a more compact network structure. The major degradation stage

occurred between approximately 220 and 420 °C, corresponding to the thermal decomposition of the polysaccharide backbone involving glycosidic bond cleavage and polymer chain scission. The NC (a) and GG (c) films showed an earlier onset of degradation, indicating comparatively lower thermal stability. The SA (b) film exhibited slightly improved thermal resistance, which can be attributed to ionic interactions within the alginate structure. In contrast, the NEW composite emulsion film (d) showed a noticeable shift of the main degradation region toward higher temperatures, reflecting enhanced thermal stability arising from synergistic interactions among nanocellulose, sodium alginate, and guar gum. Notably, the NE functional emulsion-templated film (e) demonstrated the highest thermal stability, as evidenced by the delayed onset of degradation, reduced mass-loss rate, and higher residual mass at elevated temperatures. The improved thermal behavior of NE is attributed to the emulsion-templated architecture and the incorporation of functional constituents, which promote matrix compactness, restrict polymer chain mobility, and enhance char formation. The increased residual mass observed for films d and e at higher temperatures further confirms improved resistance to thermal decomposition.

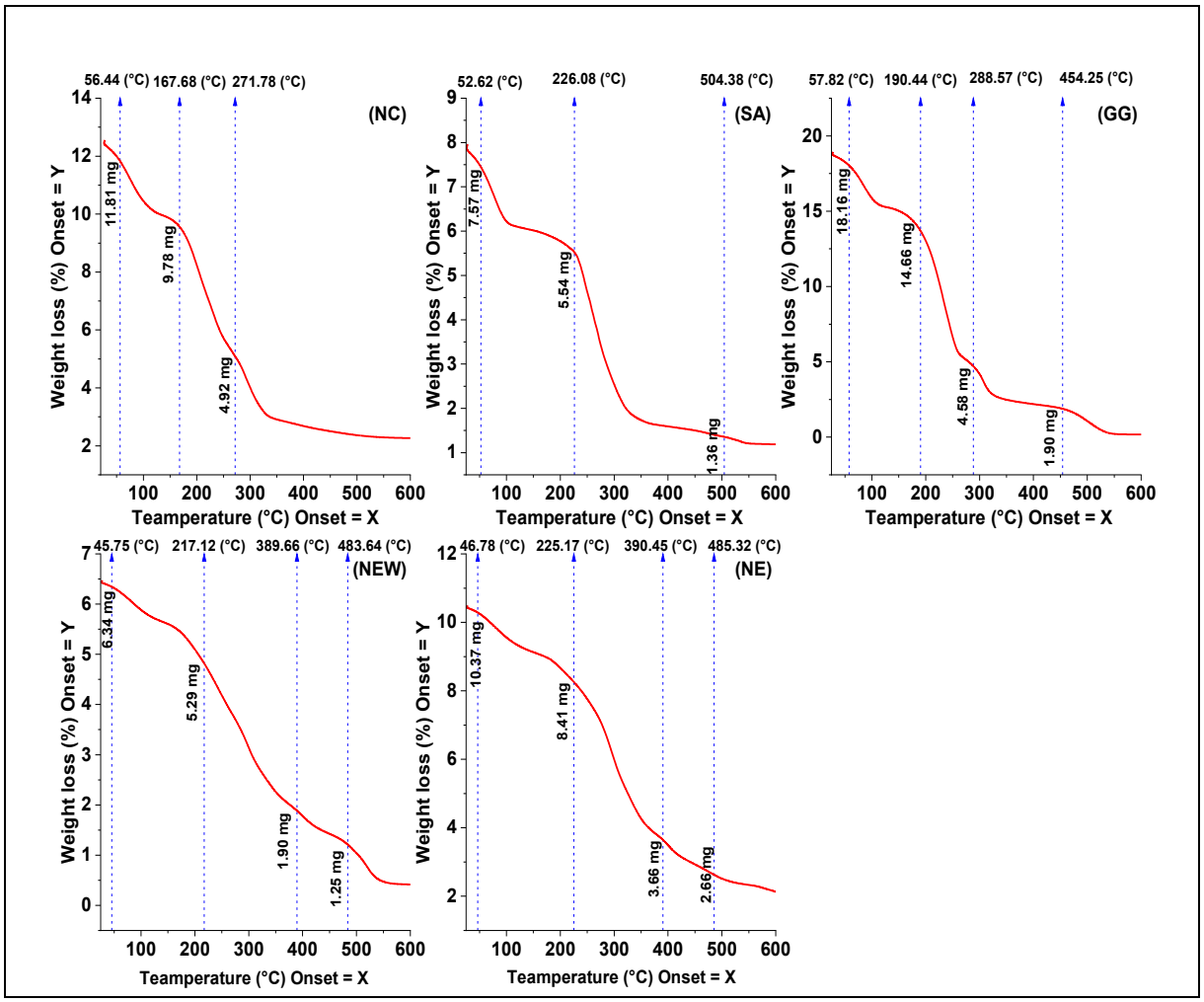

Fig. 4.51 Thermogravimetric analysis (TGA) curves of emulsion-based packaging films: Note: (NC) nanocellulose emulsion film, (SA) sodium alginate nanoemulsion film, (GG) guar gum nanoemulsion film, (NEW) composite emulsion film, and (NE) functional nanoemulsion-templated film. The profiles illustrate the multi-stage thermal degradation behavior and the comparative thermal stability of individual polymer, composite, and functional films.

4.11.5 Differential scanning calorimetry (DSC)

Differential scanning calorimetry (DSC) was used to investigate the occurrence of physical and structural transitions in the emulsion-based films during heating, and the results are presented in Fig. 4.52. The DSC thermograms of NC (nanocellulose emulsion film), SA (sodium alginate emulsion film), GG (guar gum emulsion film), NEW (composite emulsion film), and NE (functional emulsion-templated film) exhibit distinct endothermic transitions, reflecting the influence of polymer composition and emulsion templating on thermal behavior. The DSC curve of the NC film shows a prominent endothermic transition with an onset temperature of 119.79 °C, a peak temperature of 133.31 °C, and an enthalpy change (ΔH) of 346.48 J/g, which is attributed to the disruption of extensive hydrogen bonding and the removal of bound water associated with the highly ordered nanocellulose network. In comparison, the SA film displays an endothermic peak at 138.72 °C with a lower ΔH of 279.72 J/g, followed by a secondary transition at 291.09 °C (ΔH = 195.87 J/g), indicating thermal relaxation and decomposition of alginate chains stabilized by ionic interactions. The GG film exhibits broader thermal transitions, with a first peak at 129.71 °C (ΔH = 229.82 J/g) and a second peak at 264.76 °C (ΔH = 253.00 J/g), suggesting gradual rearrangement and degradation of the branched guar gum structure. In contrast, the NEW composite emulsion film shows a single, shifted endothermic transition with an onset at 136.03 °C, a peak at 137.09 °C, and a significantly reduced ΔH of 188.05 J/g. The reduction in enthalpy compared to the individual polymer films indicates the formation of a more homogeneous and compact polymer network due to synergistic interactions among nanocellulose, sodium alginate, and guar gum, which reduces the energy required for thermal transitions. Notably, the NE functional emulsion-templated film exhibits a stabilized endothermic peak at 146.01 °C with the lowest enthalpy change (ΔH = 47.36 J/g) among all samples. The substantial decrease in ΔH suggests restricted polymer chain mobility and reduced ordered domains, resulting from the emulsion-templated architecture and the incorporation of functional peel extract within the polymer matrix.

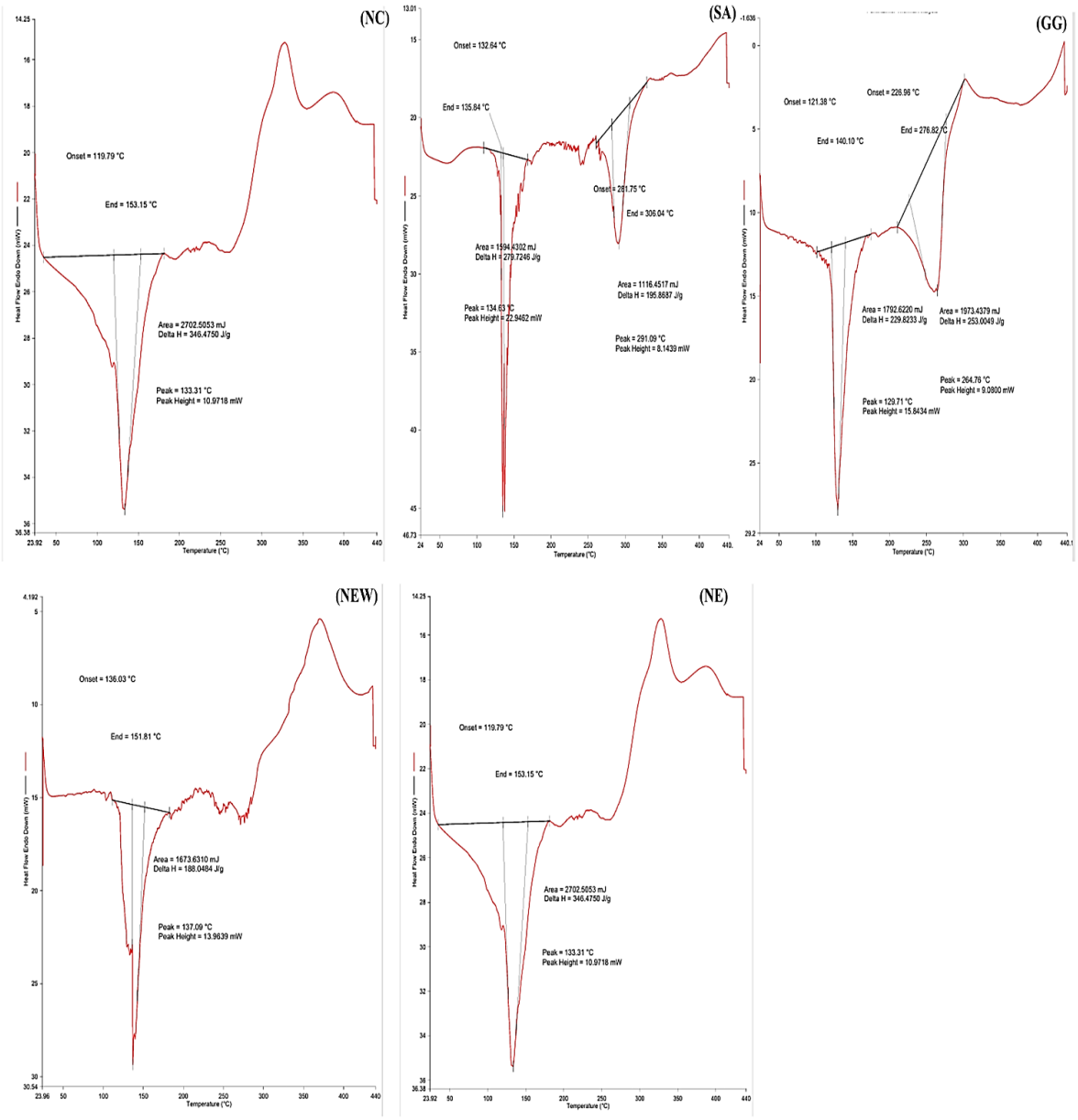

Fig. 4.52 Differential scanning calorimetry (DSC) thermograms of nanoemulsion-based packaging films showing thermal transitions, including onset temperature, peak temperature, end temperature, and enthalpy change (ΔH):

Note: NC—nanocellulose emulsion film, SA—sodium alginate emulsion film, GG—guar gum emulsion film, NEW—composite emulsion film (nanocellulose–sodium alginate–guar gum), and NE—functional emulsion-templated film incorporating peel extract. The curves illustrate the effect of polymer composition and emulsion templating on thermal stability and phase-transition behaviour of the packaging films.

4.12 Biodegradability of packaging films

4.12.1 Soil burial method

The biodegradation of the developed packaging films was further substantiated by morphological changes observed during the soil burial test, as illustrated in Fig. 4.53-4.60, in conjunction with the quantitative weight loss data presented in Tables 4.28 and 4.29. Initially, all films exhibited smooth, intact surfaces, indicating structural integrity before burial. With increasing burial time, progressive surface deterioration became evident, marked by discoloration, roughening, cracks, pits, and fragmentation, which intensified at later stages. These morphological alterations correspond well with the increasing weight loss values, confirming that biodegradation proceeded through a surface-erosion–dominated mechanism followed by bulk degradation. Sodium alginate films showed early and pronounced surface disintegration, consistent with their high weight loss (56.36% at day 18), due to rapid moisture absorption and microbial enzymatic attack. Nanocellulose and guar gum films exhibited comparatively slower morphological degradation, retaining partial structural continuity, which aligns with their lower weight loss values (24.73% and 20.79%, respectively). In contrast, the composite film without extract (NEW) displayed extensive surface cracking and fragmentation, corresponding to its higher weight loss (67.68%), indicating that polymer blending produced a less compact matrix vulnerable to microbial penetration. Notably, the nanoemulsion-based functional film containing bioactive extract (NE) showed the most severe morphological damage, including pronounced erosion and fragmentation, in agreement with its maximum weight loss (73.19%). Mechanistically, moisture-induced swelling, disruption of intermolecular hydrogen bonding, and nanoemulsion-induced microvoid formation enhanced microbial colonization and enzymatic hydrolysis of polymer chains.

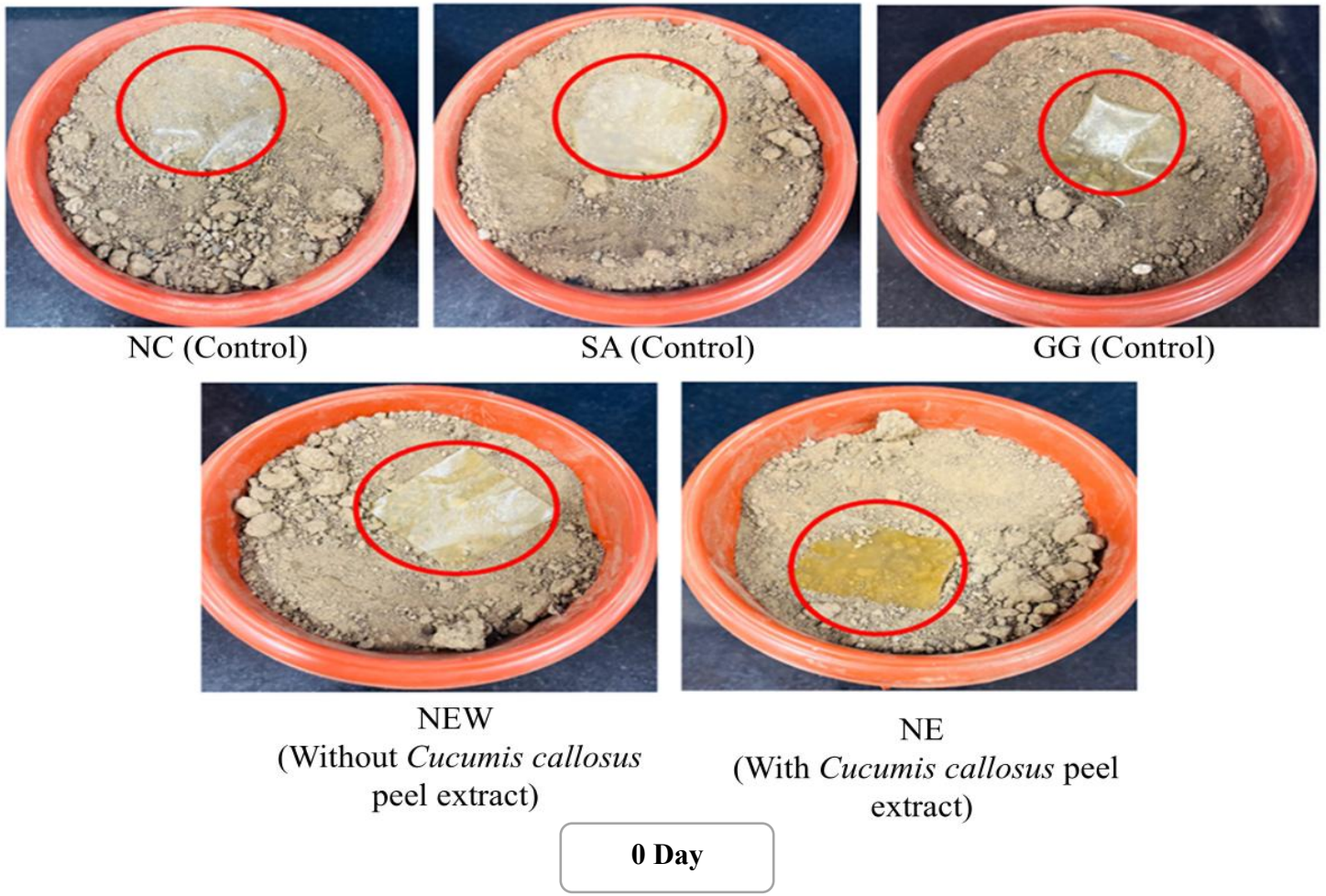

Fig. 4.53 Degradation study of biodegradable film samples during soil burial method on 0 day

Note: NC: Nanocellulose, SA: Sodium alginate, GG: Guar gum, NEW: Nanocellulose, sodium alginate, and guar gum without *Cucumis callosus* peel extract, and NE: Nanocellulose, sodium alginate, and guar gum with *Cucumis callosus* peel extract functional film.

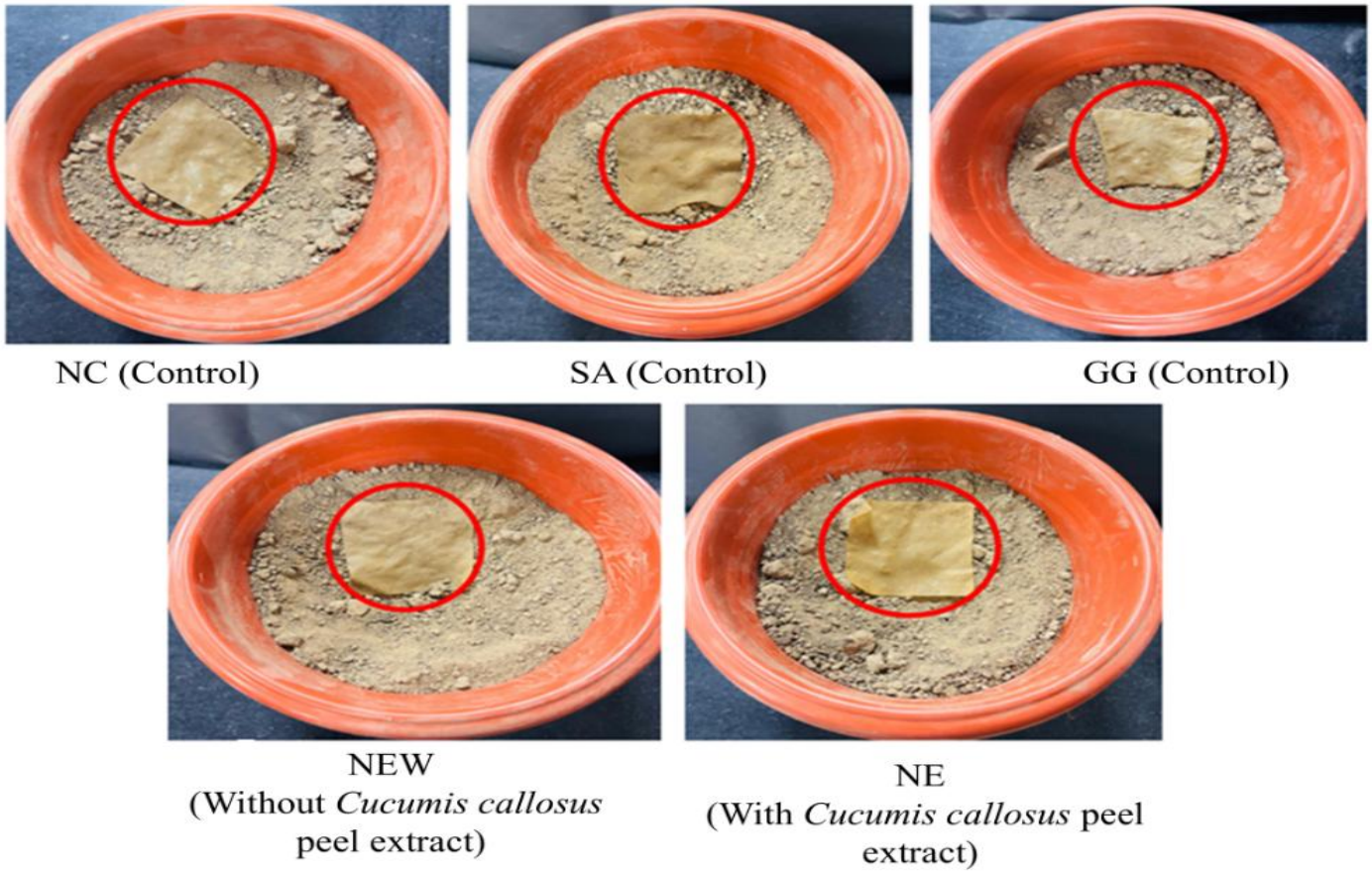

Fig.4.54 Degradation study of biodegradable film samples during soil burial method on the 3rd day

Note: NC: Nanocellulose, SA: Sodium alginate, GG: Guar gum, NEW: Nanocellulose, sodium alginate, and guar gum without *Cucumis callosus* peel extract, and NE: Nanocellulose, sodium alginate, and guar gum with *Cucumis callosus* peel extract functional film.

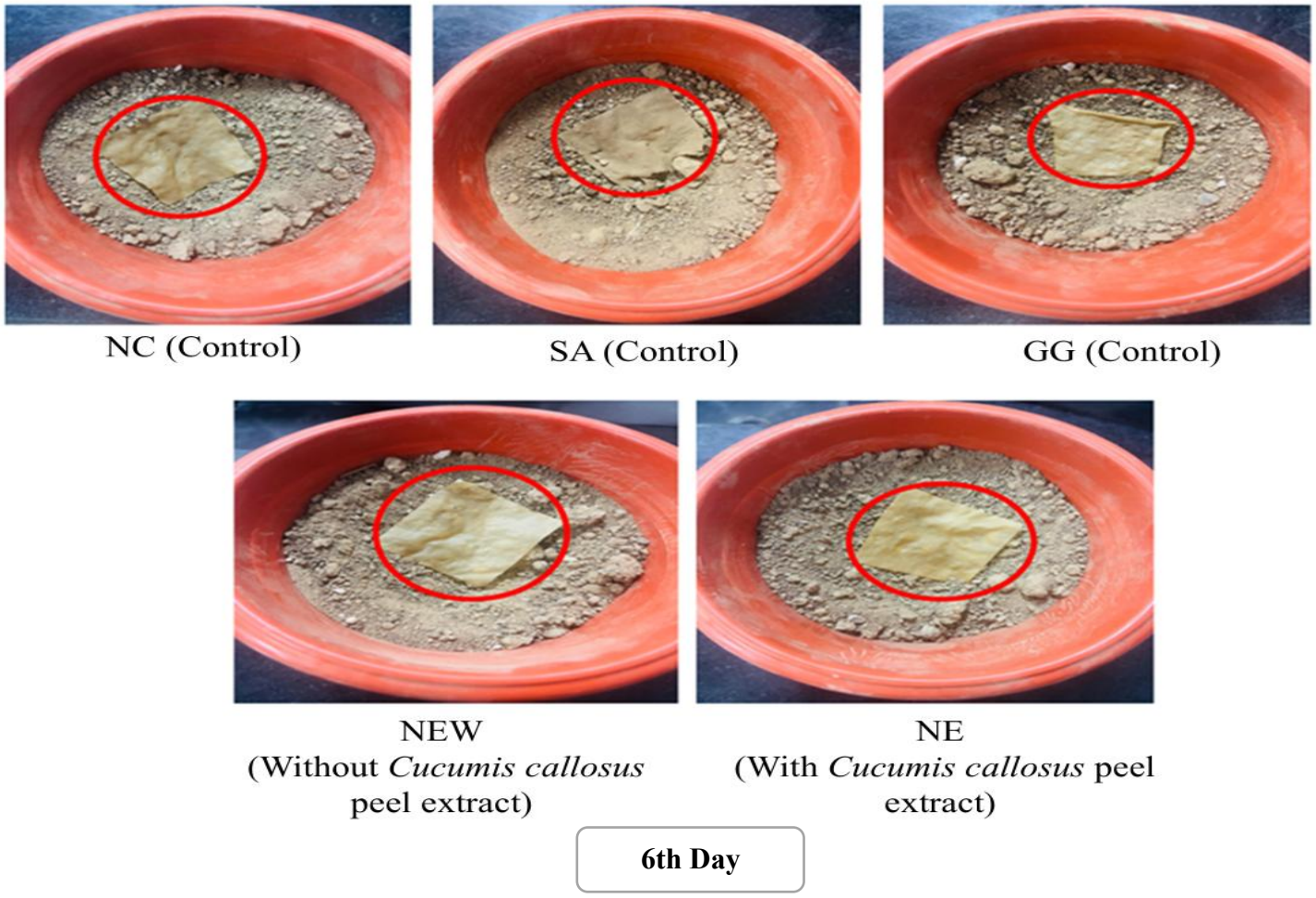

Fig. 4.55 Degradation study of biodegradable film samples during soil burial method on the 6th day

Note: NC: Nanocellulose, SA: Sodium alginate, GG: Guar gum, NEW: Nanocellulose, sodium alginate, and guar gum without *Cucumis callosus* peel extract, and NE: Nanocellulose, sodium alginate, and guar gum with *Cucumis callosus* peel extract functional film.

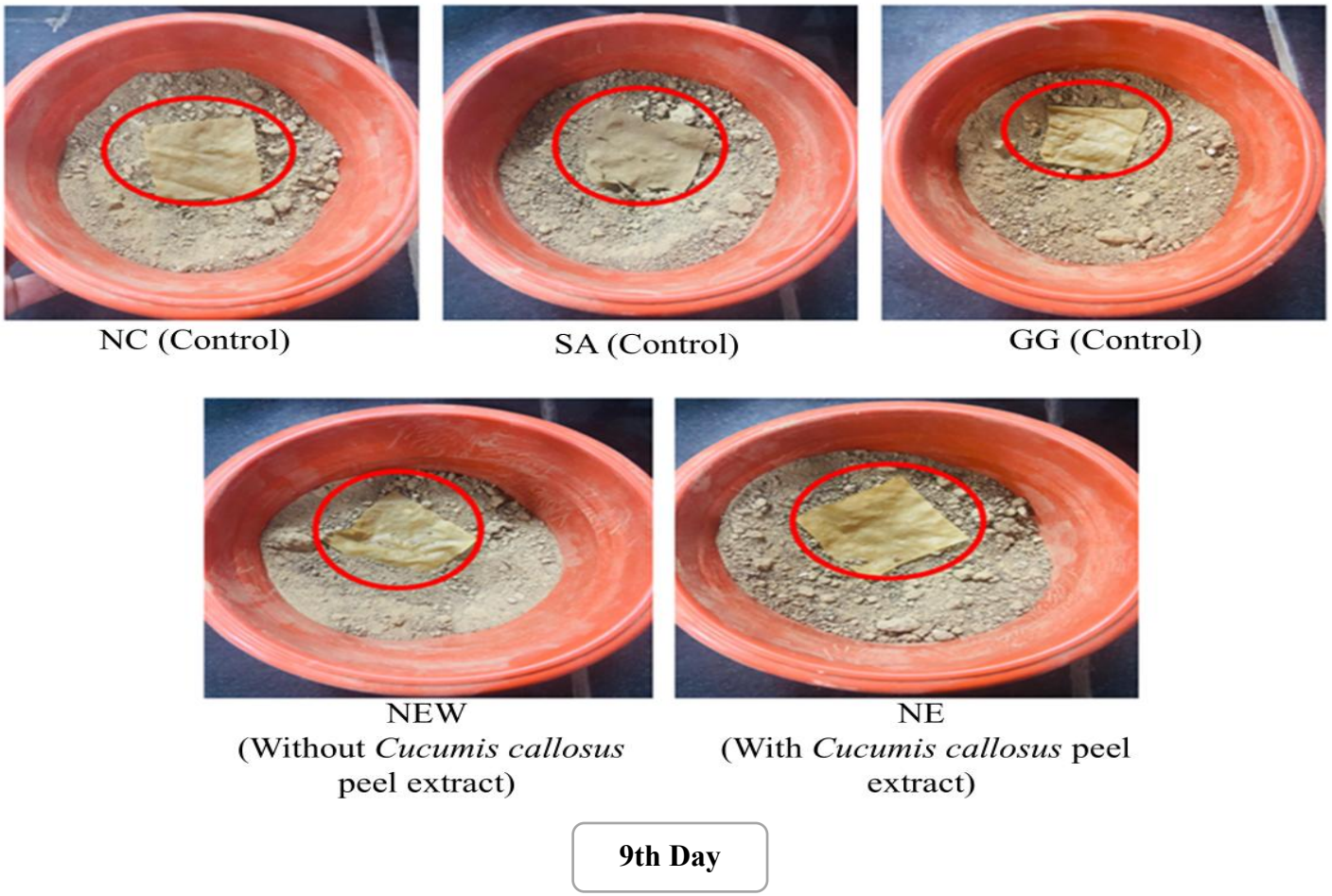

Fig. 4.56 Degradation study of biodegradable film samples during soil burial method on the 9th day

Note: NC: Nanocellulose, SA: Sodium alginate, GG: Guar gum, NEW: Nanocellulose, sodium alginate, and guar gum without *Cucumis callosus* peel extract, and NE: Nanocellulose, sodium alginate, and guar gum with *Cucumis callosus* peel extract functional film.

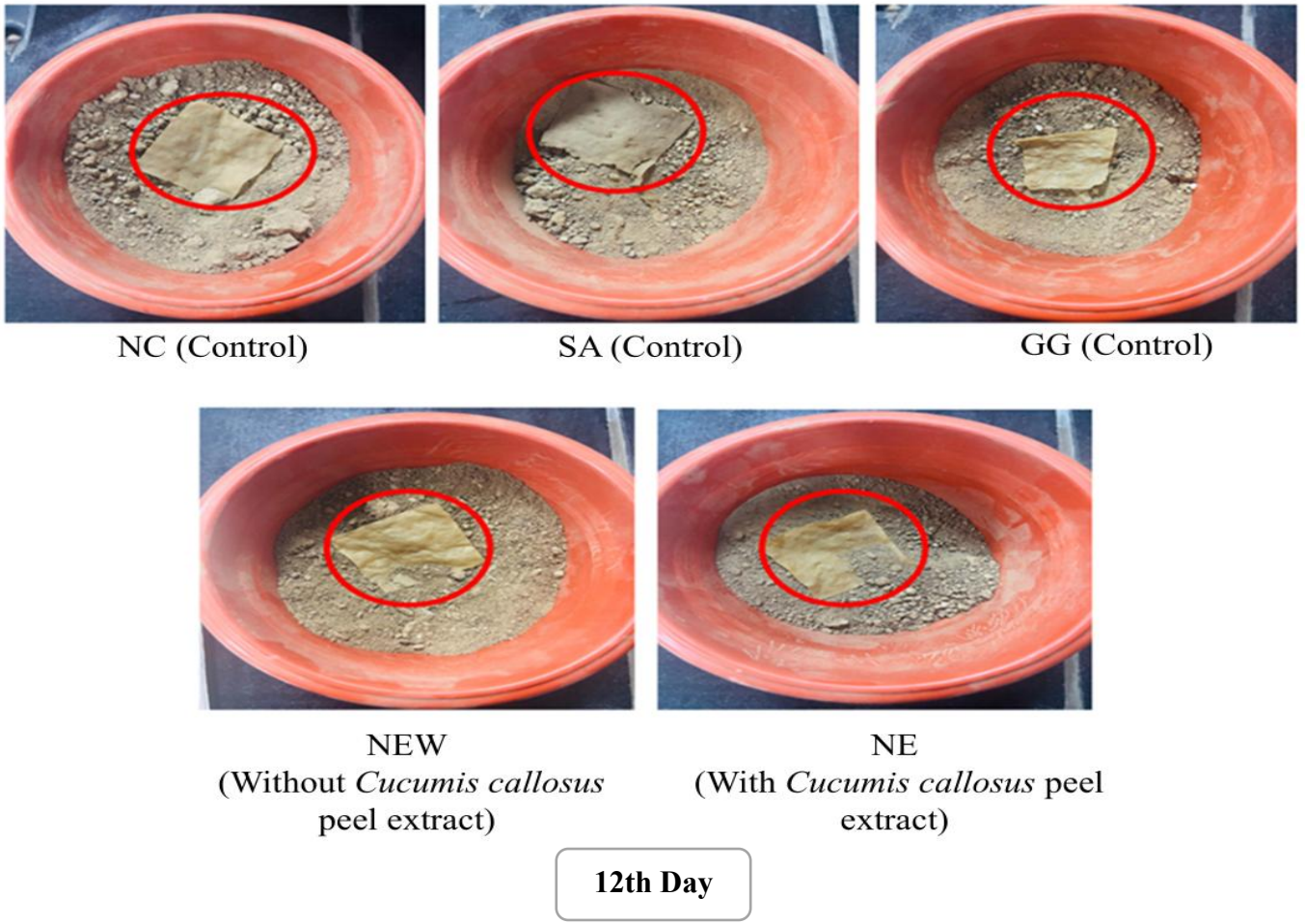

Fig. 4.57 Degradation study of biodegradable film samples during soil burial method on the 12th day

Note: NC: Nanocellulose, SA: Sodium alginate, GG: Guar gum, NEW: Nanocellulose, sodium alginate, and guar gum without *Cucumis callosus* peel extract, and NE: Nanocellulose, sodium alginate, and guar gum with *Cucumis callosus* peel extract functional film.

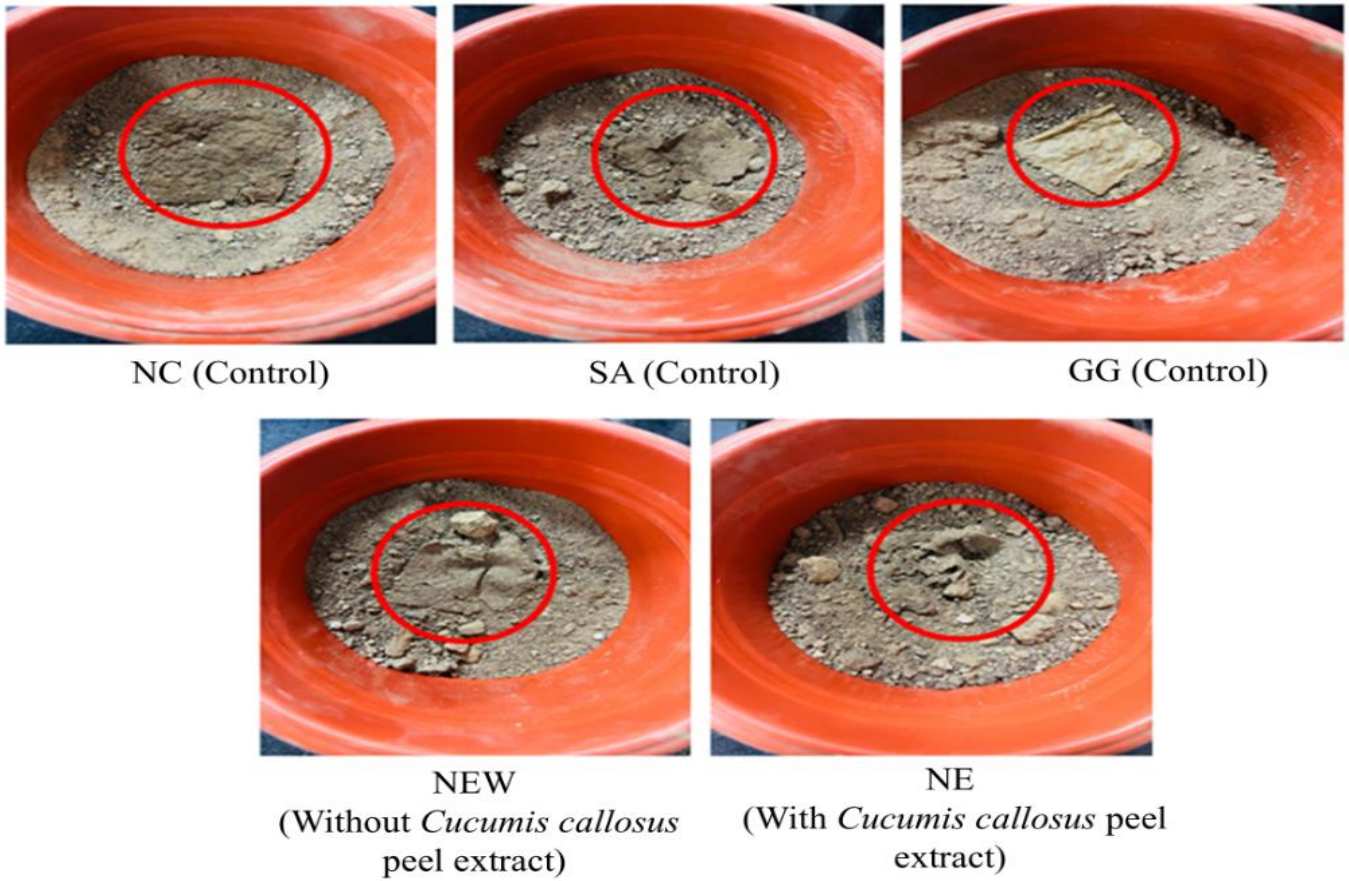

Fig. 4.58 Degradation study of biodegradable film samples during soil burial method on the 15th day

Note: NC: Nanocellulose, SA: Sodium alginate, GG: Guar gum, NEW: Nanocellulose, sodium alginate, and guar gum without *Cucumis callosus* peel extract, and NE: Nanocellulose, sodium alginate, and guar gum with *Cucumis callosus* peel extract functional film.

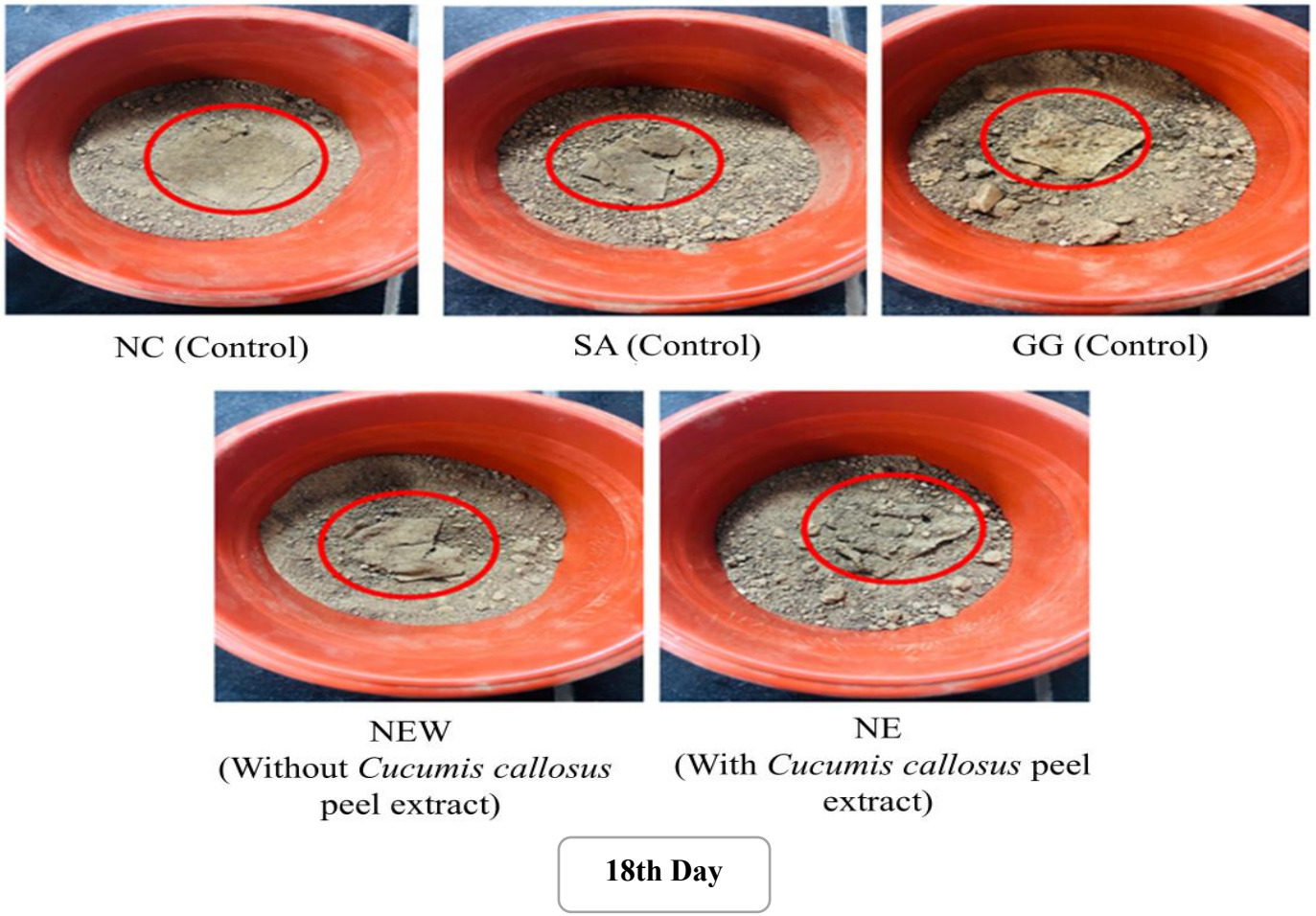

Fig. 4.59 Degradation study of biodegradable film samples during soil burial method on the 18th day

Note: NC: Nanocellulose, SA: Sodium alginate, GG: Guar gum, NEW: Nanocellulose, sodium alginate, and guar gum without *Cucumis callosus* peel extract, and NE: Nanocellulose, sodium alginate, and guar gum with *Cucumis callosus* peel extract functional film.

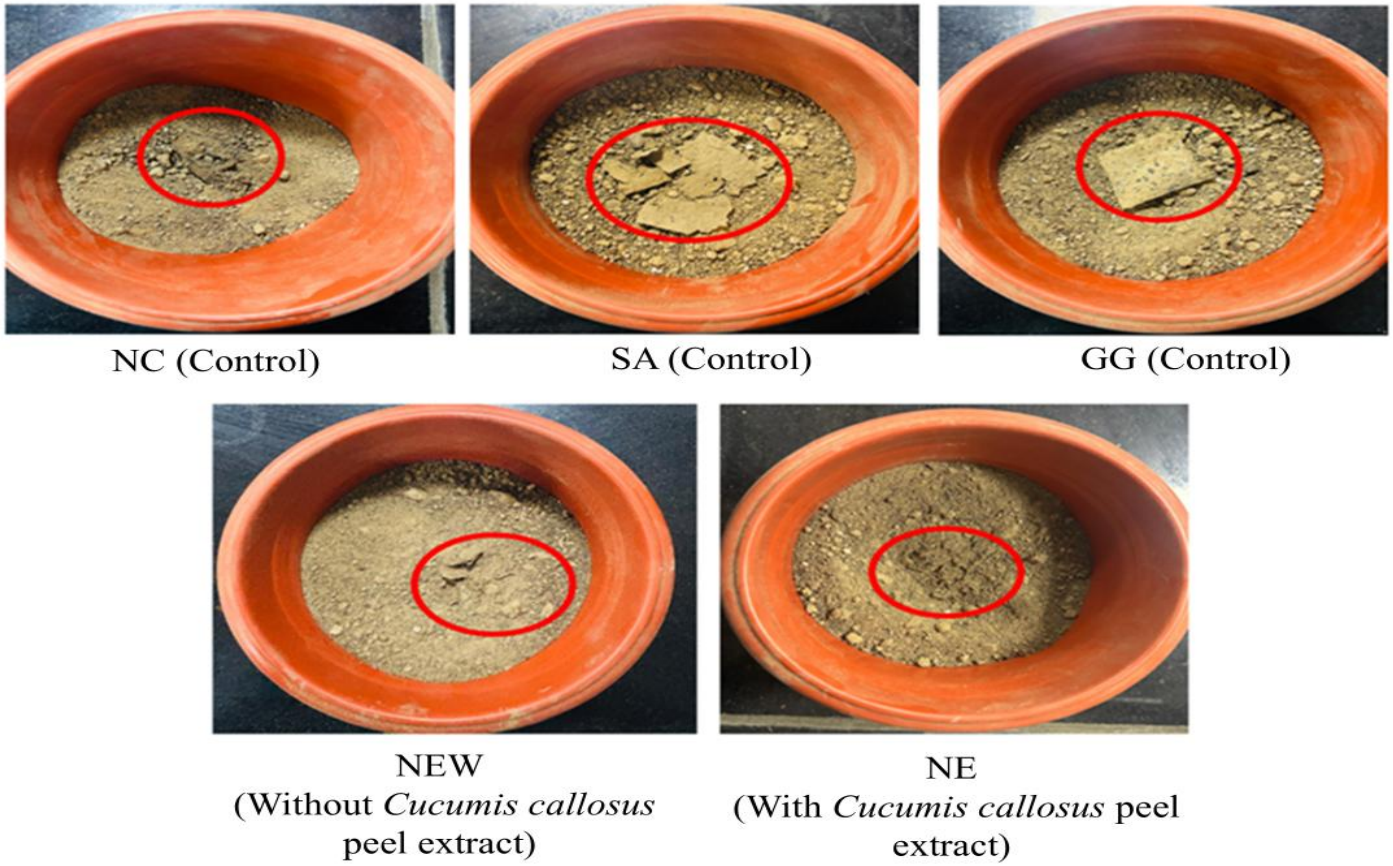

Fig. 4.60 Degradation study of biodegradable film samples during soil burial method on the 21st day

Note: NC: Nanocellulose, SA: Sodium alginate, GG: Guar gum, NEW: Nanocellulose, sodium alginate, and guar gum without *Cucumis callosus* peel extract, and NE: Nanocellulose, sodium alginate, and guar gum with *Cucumis callosus* peel extract functional film.

Table 4.28 Actual Weight of Packaging Films

Packaging Film	Actual Weight (g)
Nanocellulose	0.93 ± 0.05
Sodium alginate	0.55 ± 0.07
Guar gum	0.98 ± 0.04
Nanocellulose nanoemulsion-based guar gum–sodium alginate film (without extract)	0.57 ± 0.06
Nanocellulose nanoemulsion-based guar gum–sodium alginate film (with extract)	0.62 ± 0.03

Values are expressed as mean ± standard deviation.

Table 4.29 Weight loss (%) of samples stored under different packaging films in soil degradation process

Days	NC Control (%)	SA Control (%)	GG Control (%)	NEW Composite (%)	NE Functional Film (%)
0	0.00 ± 0.00^{aA}	0.00 ± 0.00^{aA}	0.00 ± 0.00^{aA}	0.00 ± 0.00^{aA}	0.00 ± 0.00^{aA}
3	3.23 ± 0.05^{cB}	5.45 ± 0.08^{aB}	2.97 ± 0.02^{dB}	3.51 ± 0.06^{bB}	3.13 ± 0.03^{cB}
6	5.38 ± 0.02^{cC}	9.09 ± 0.07^{aC}	5.94 ± 0.03^{cC}	7.02 ± 0.09^{bC}	6.25 ± 0.05^{bC}
9	8.60 ± 0.07^{cD}	12.73 ± 0.05^{aD}	7.92 ± 0.06^{dD}	10.53 ± 0.02^{bD}	9.38 ± 0.03^{cD}
12	11.83 ± 0.04^{dE}	16.36 ± 0.02^{cE}	10.89 ± 0.07^{eE}	19.04 ± 0.03^{bE}	21.50 ± 0.08^{aE}
15	15.98 ± 0.05^{df}	30.18 ± 0.03^{bf}	12.87 ± 0.02^{ef}	33.54 ± 0.07^{af}	39.63 ± 0.02^{af}
18	24.73 ± 0.03^{dG}	56.36 ± 0.07^{bG}	20.79 ± 0.05^{eG}	67.68 ± 0.04^{aG}	73.19 ± 0.06^{aG}

Results are reported as mean ± standard deviation. Within each row, values bearing distinct lowercase superscripts$^{(a–e)}$ differ significantly among film treatments, whereas within each column, different uppercase superscripts$^{(A–G)}$ denote significant variation over storage time.

4.12.2 Oven-Assisted Soil Method

The biodegradation behaviour of the developed packaging films was evaluated using an oven-assisted soil burial method, and the results, with time-dependent morphological changes, are shown in (Fig. 4.61-4.63). On Day 0, all films retained their original morphology with smooth and continuous surfaces, along with comparable initial weights (NC: 0.15 ± 0.02 g, SA: 0.19 ± 0.04 g, GG: 0.12 ± 0.05 g, NEW: 0.11 ± 0.02 g, NE: 0.13 ± 0.03 g), confirming the absence of pre-degradation and uniform baseline conditions. By Day 1–2, observable changes such as surface roughening, partial opacity loss, and marginal edge deformation were detected. These early alterations are attributed to soil moisture diffusion into the hydrophilic polymer matrices, resulting in polymer swelling and partial disruption of intermolecular hydrogen bonding, which increased chain mobility and surface permeability. This hydration-induced structural relaxation

facilitated microbial adhesion and initial colonization at the film–soil interface. By Day 3, extensive surface erosion, crack development, fragmentation, and partial incorporation of film residues into the soil matrix were evident. This stage of degradation is associated with enhanced microbial activity and enzymatic hydrolysis of glycosidic linkages, promoted by sustained moisture availability and elevated temperature conditions in the oven-assisted system. Sodium alginate and nanocellulose films exhibited faster deterioration due to their higher hydrophilicity and abundance of accessible functional groups, whereas guar gum films showed comparatively slower degradation because of their compact galactomannan structure, which limited enzymatic accessibility. The composite film without extract (NEW) demonstrated increased fragmentation, indicating that polymer blending generated a heterogeneous matrix with increased free volume, favoring moisture ingress and microbial penetration. The nanoemulsion-based functional film containing extract (NE) exhibited the highest extent of degradation by Day 3, which can be attributed to nanoemulsion-induced plasticization, microvoid formation, and interconnected diffusion pathways, collectively enhancing moisture transport, microbial colonization, and polymer chain scission. Overall, the day-wise degradation pattern reflects a transition from moisture-induced structural relaxation to microbially mediated bulk degradation, underscoring the critical role of film composition and microstructure in determining biodegradation behavior.

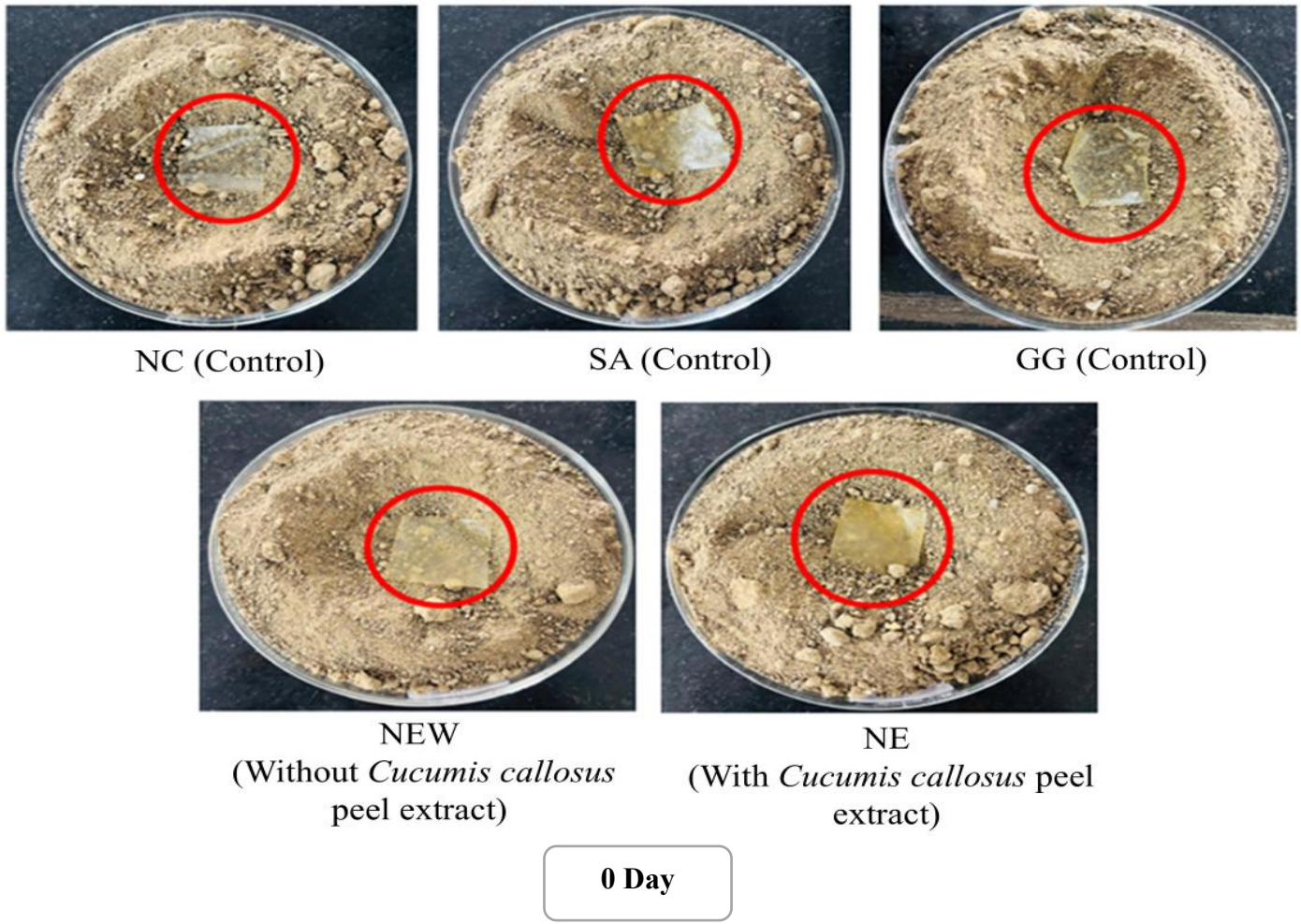

Fig. 4.61 Degradation study of biodegradable film samples during oven-assisted soil burial method on the 0 day

Note: NC: Nanocellulose, SA: Sodium alginate, GG: Guar gum, NEW: Nanocellulose, sodium alginate, and guar gum without *Cucumis callosus* peel extract, and NE: Nanocellulose, sodium alginate, and guar gum with *Cucumis callosus* peel extract functional film.

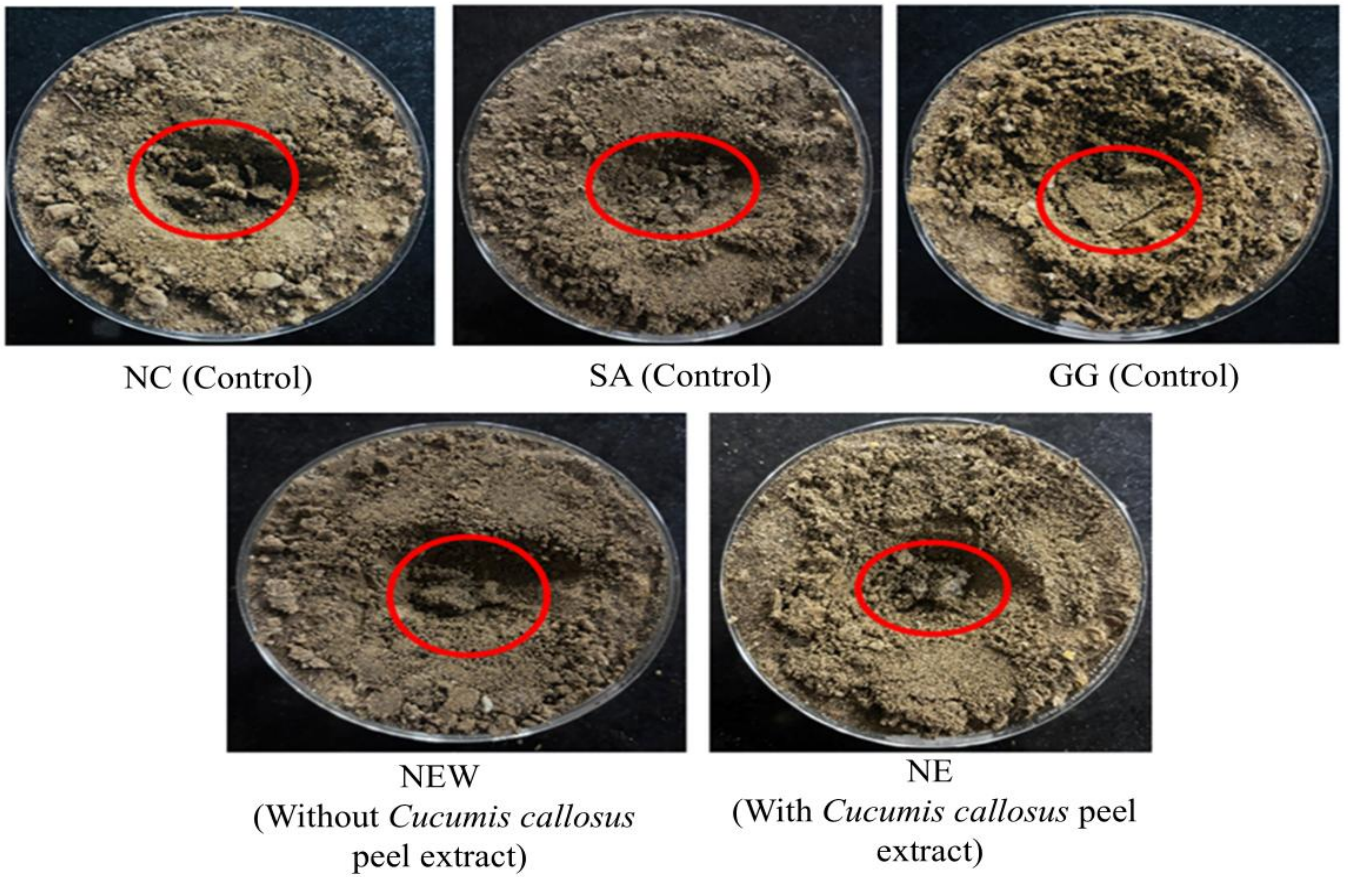

Fig. 4.62 Degradation study of biodegradable film samples during oven-assisted soil burial method on the 2nd day

Note: NC: Nanocellulose, SA: Sodium alginate, GG: Guar gum, NEW: Nanocellulose, sodium alginate, and guar gum without *Cucumis callosus* peel extract, and NE: Nanocellulose, sodium alginate, and guar gum with *Cucumis callosus* peel extract functional film.

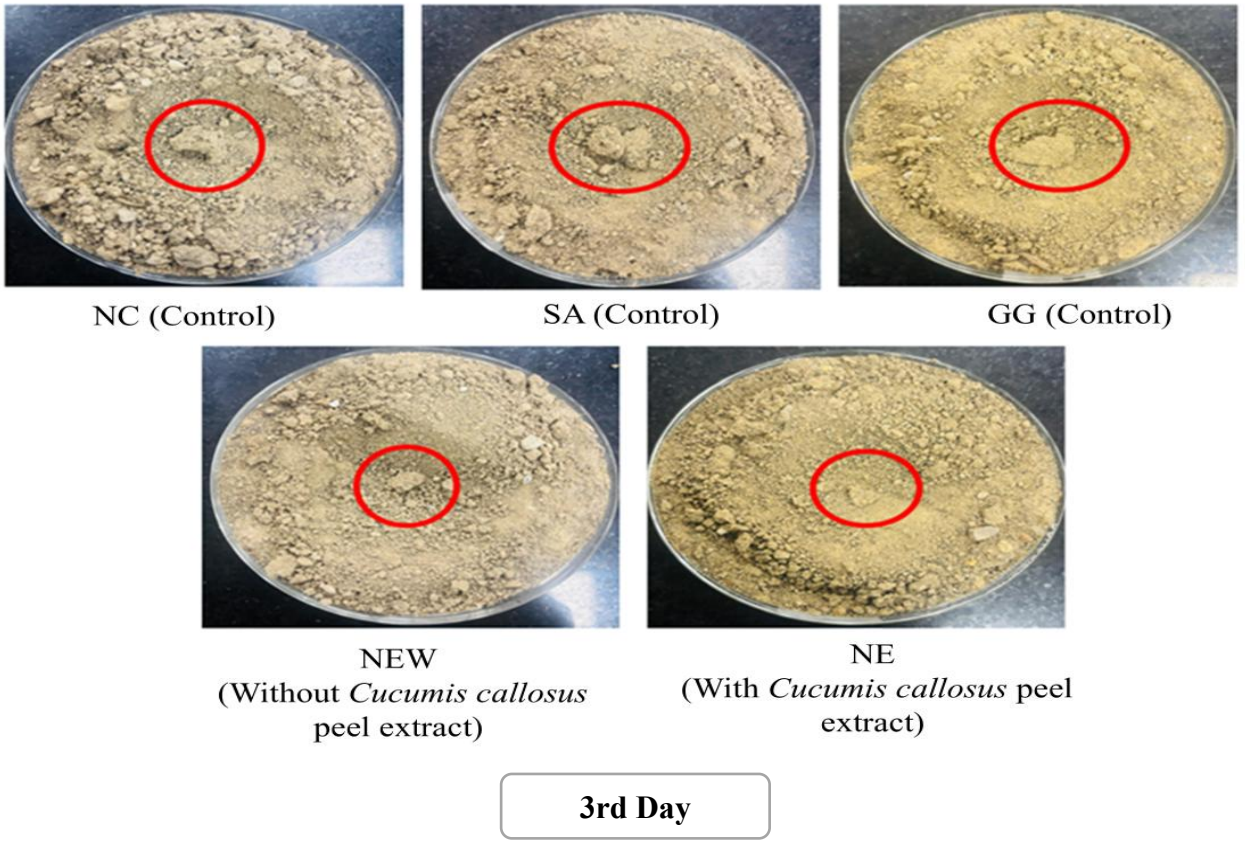

Fig. 4.63 Degradation study of biodegradable film samples during oven-assisted soil burial method on the 3rd day

Note: NC: Nanocellulose, SA: Sodium alginate, GG: Guar gum, NEW: Nanocellulose, sodium alginate, and guar gum without *Cucumis callosus* peel extract, and NE: Nanocellulose, sodium alginate, and guar gum with *Cucumis callosus* peel extract functional film.

4.12.3 Enzymatic degradation

The enzymatic degradation behavior of the developed packaging films was evaluated using a cellulase-mediated degradation assay, and the morphological changes observed at different 6time intervals are illustrated in Fig. 4.64 and 4.65. At Day 0, all films (NC, SA, GG, NEW, and NE) remained intact when immersed in the enzyme solution, retaining their original shape and transparency, indicating negligible immediate enzymatic action. After 2 days of enzymatic exposure, clear differences in degradation behavior became evident. The nanocellulose (NC) and sodium alginate (SA) films showed substantial disintegration, as indicated by the absence of intact film fragments and the appearance of dispersed residues within the solution, confirming effective cellulase-driven hydrolysis of β-1,4-glycosidic linkages. Guar gum (GG) films exhibited comparatively slower degradation, retaining partial structural fragments, which can be attributed to their galactomannan backbone that offers lower susceptibility to cellulase due to steric hindrance and limited enzyme accessibility. The composite film without extract (NEW) demonstrated enhanced degradation relative to single-polymer films, suggesting that polymer blending resulted in a less ordered matrix with increased enzyme-accessible domains. Notably, the nanoemulsion-based functional film containing extract (NE) showed the highest extent of enzymatic degradation, characterized by extensive fragmentation and the appearance of oily residues floating on the solution surface. This phenomenon is scientifically attributed to the amphiphilic nature of the NE film, where enzymatic breakdown of the polysaccharide matrix released entrapped hydrophobic components from the nanoemulsion, causing phase separation and oil flotation. Overall, the enzymatic degradation results confirm that film composition strongly governs susceptibility to enzymatic hydrolysis, with nanoemulsion incorporation significantly enhancing matrix accessibility and degradation kinetics, thereby supporting the biodegradable and enzyme-responsive nature of the developed functional packaging films**.**

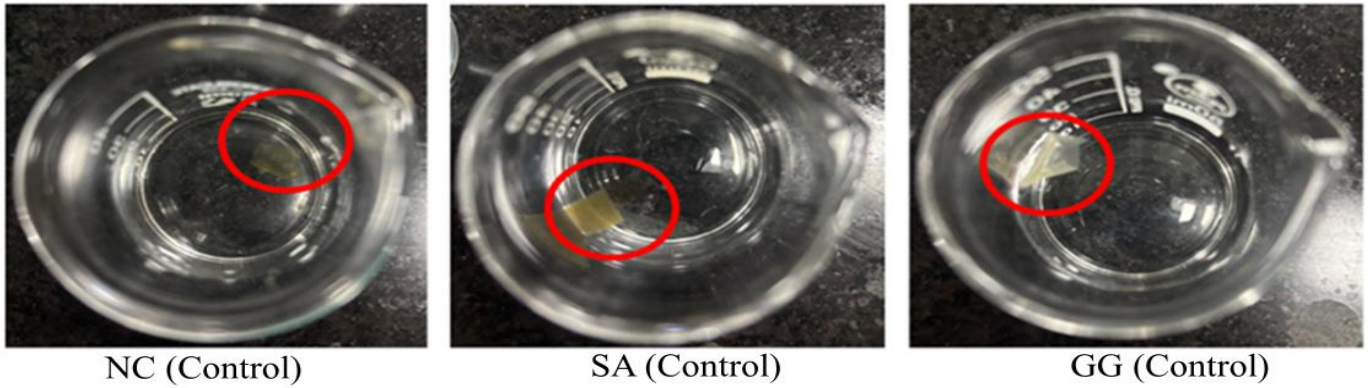

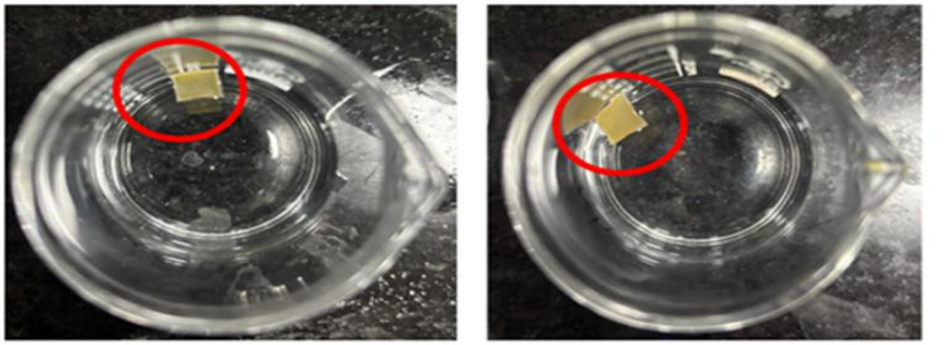

0 Day (12:00 PM)

Fig. 4.64 Degradation study of biodegradable film samples during enzymatic degradation method on the 0 day

Note: NC: Nanocellulose, SA: Sodium alginate, GG: Guar gum, NEW: Nanocellulose, sodium alginate, and guar gum without *Cucumis callosus* peel extract, and NE: Nanocellulose, sodium alginate, and guar gum with *Cucumis callosus* peel extract functional film.

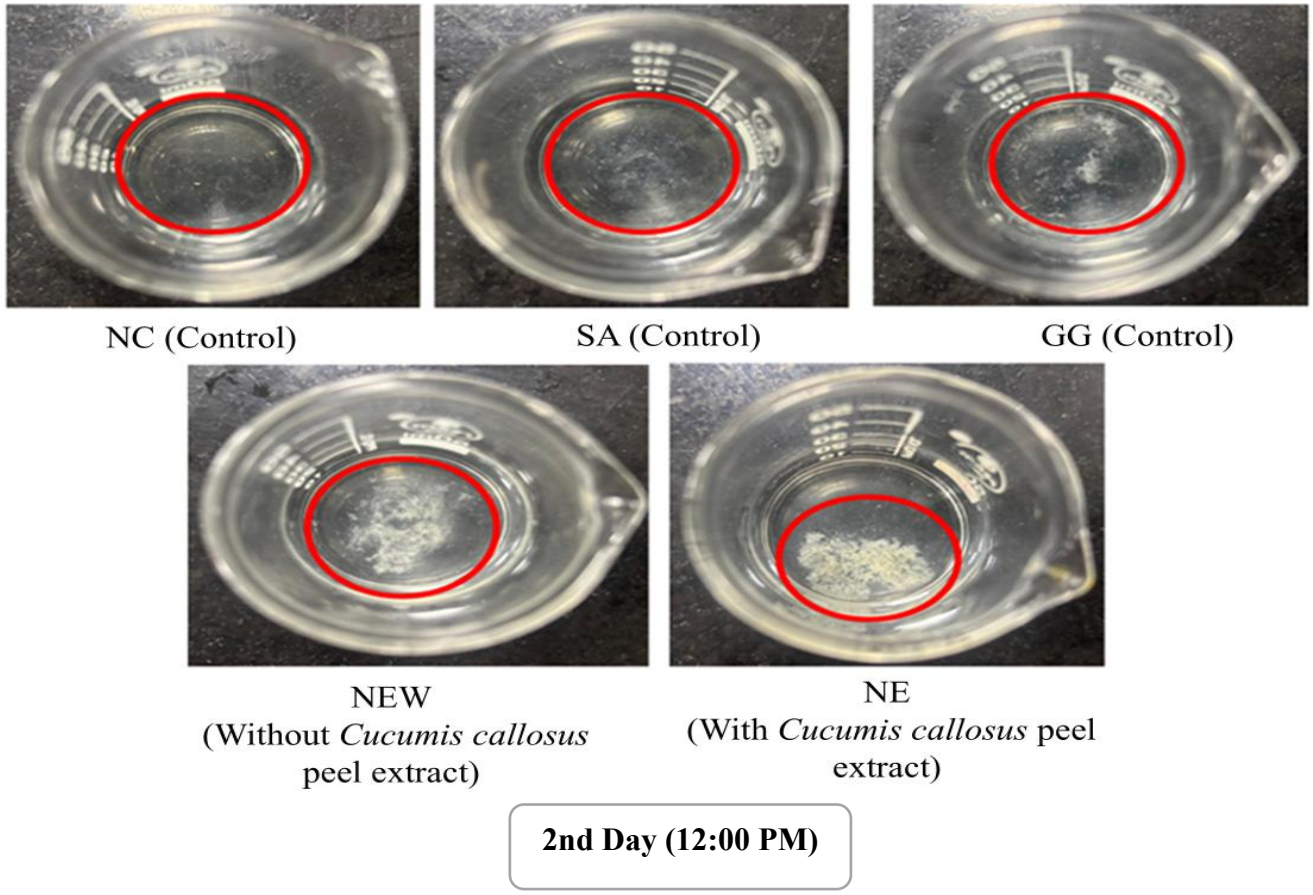

Fig. 4.65 Degradation study of biodegradable film samples during enzymatic degradation method on the 2nd day

Note: NC: Nanocellulose, SA: Sodium alginate, GG: Guar gum, NEW: Nanocellulose, sodium alginate, and guar gum without *Cucumis callosus* peel extract, and NE: Nanocellulose, sodium alginate, and guar gum with *Cucumis callosus* peel extract functional film.

4.13 Shelf-life study of Control and fresh-cut apple and pear slices in different packaging (Visual Representation)

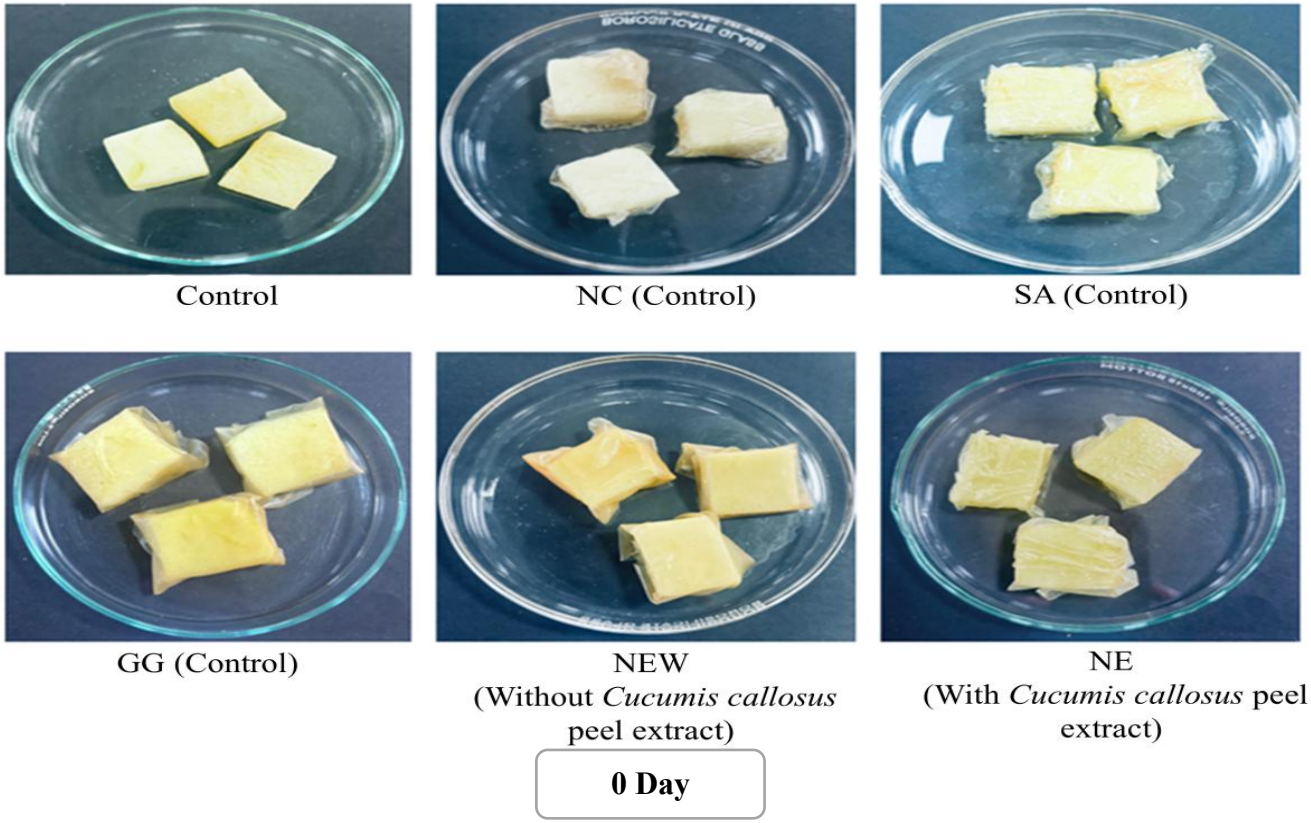

Fig. 4.66 Shelf-life study of fresh-cut apple slices in different packaging films at refrigerated temperature (4-7 ℃) at 0 day

Note: NC: Nanocellulose, SA: Sodium alginate, GG: Guar gum, NEW: Nanocellulose, sodium alginate, and guar gum without *Cucumis callosus* peel extract, and NE: Nanocellulose, sodium alginate, and guar gum with *Cucumis callosus* peel extract functional film.

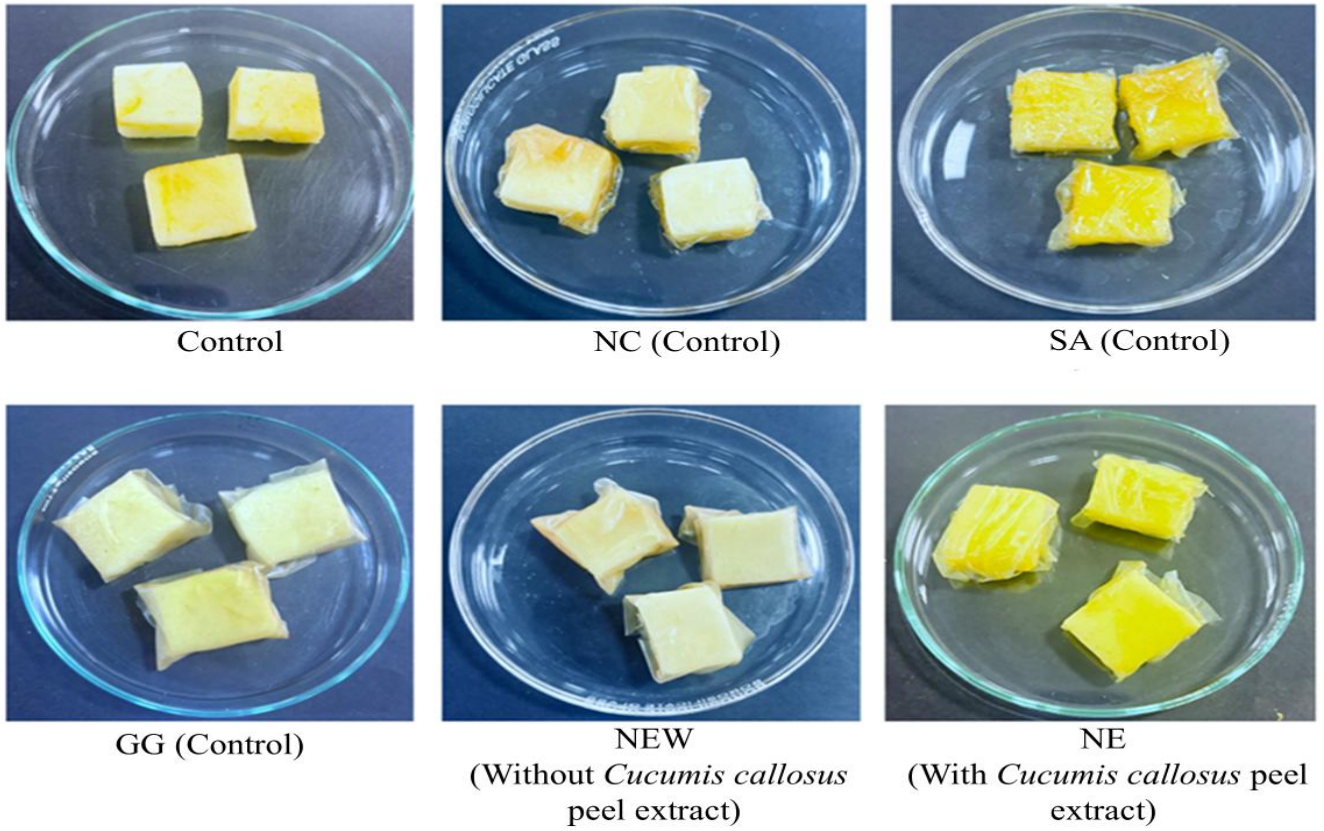

Fig. 4.67 Shelf-life study of fresh-cut apple slices in different packaging films at refrigerated temperature (4-7 ℃) on the 3rd day

Note: NC: Nanocellulose, SA: Sodium alginate, GG: Guar gum, NEW: Nanocellulose, sodium alginate, and guar gum without *Cucumis callosus* peel extract, and NE: Nanocellulose, sodium alginate, and guar gum with *Cucumis callosus* peel extract functional film.

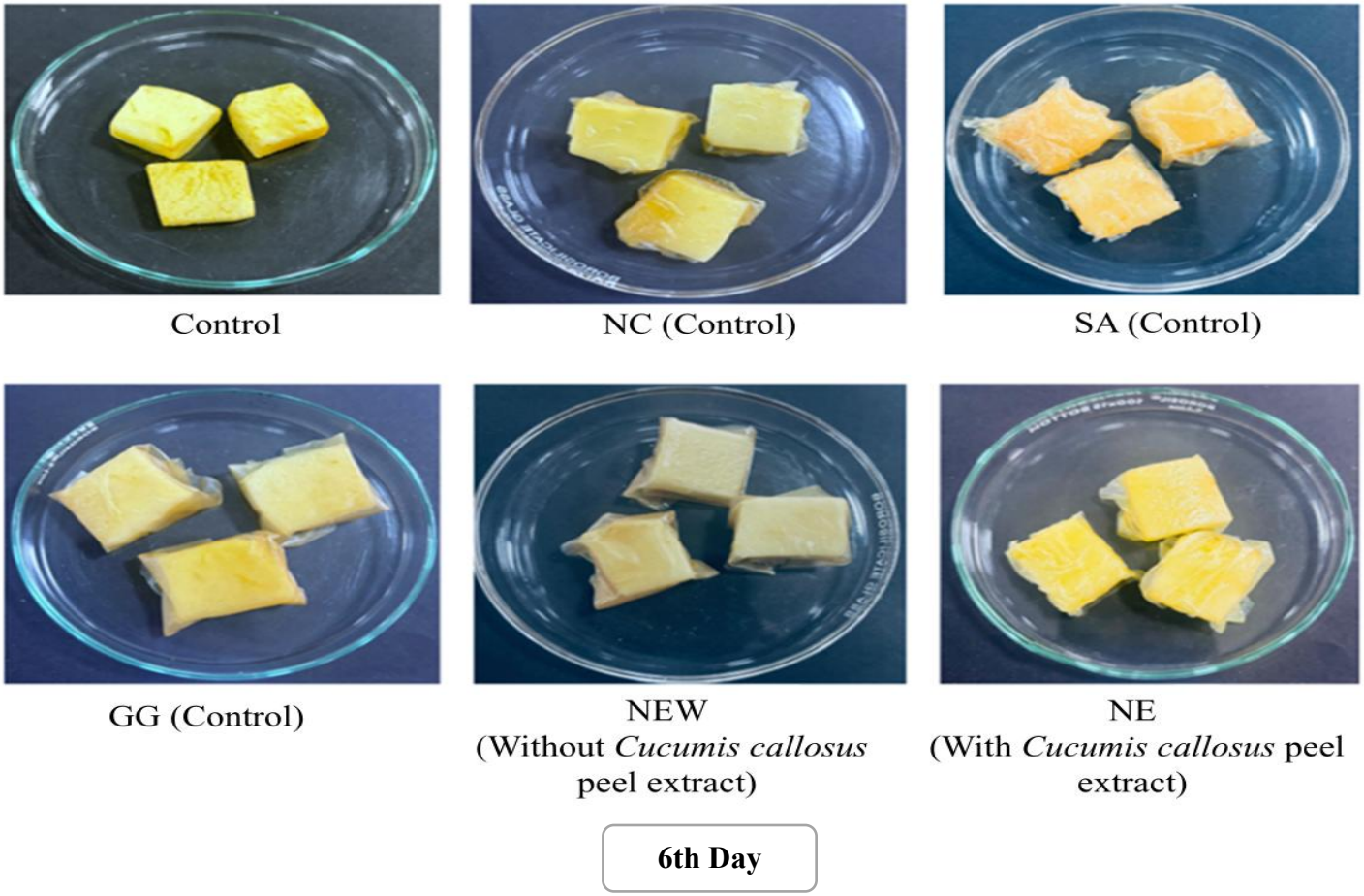

Fig. 4.68 Shelf-life study of fresh-cut apple slices in different packaging films at refrigerated temperature (4-7 ℃) on the 6th day

Note: NC: Nanocellulose, SA: Sodium alginate, GG: Guar gum, NEW: Nanocelluloses, sodium alginate, and guar gum without *Cucumis callosus* peel extract, and NE: Nanocellulose, sodium alginate, and guar gum with *Cucumis callosus* peel extract functional film.

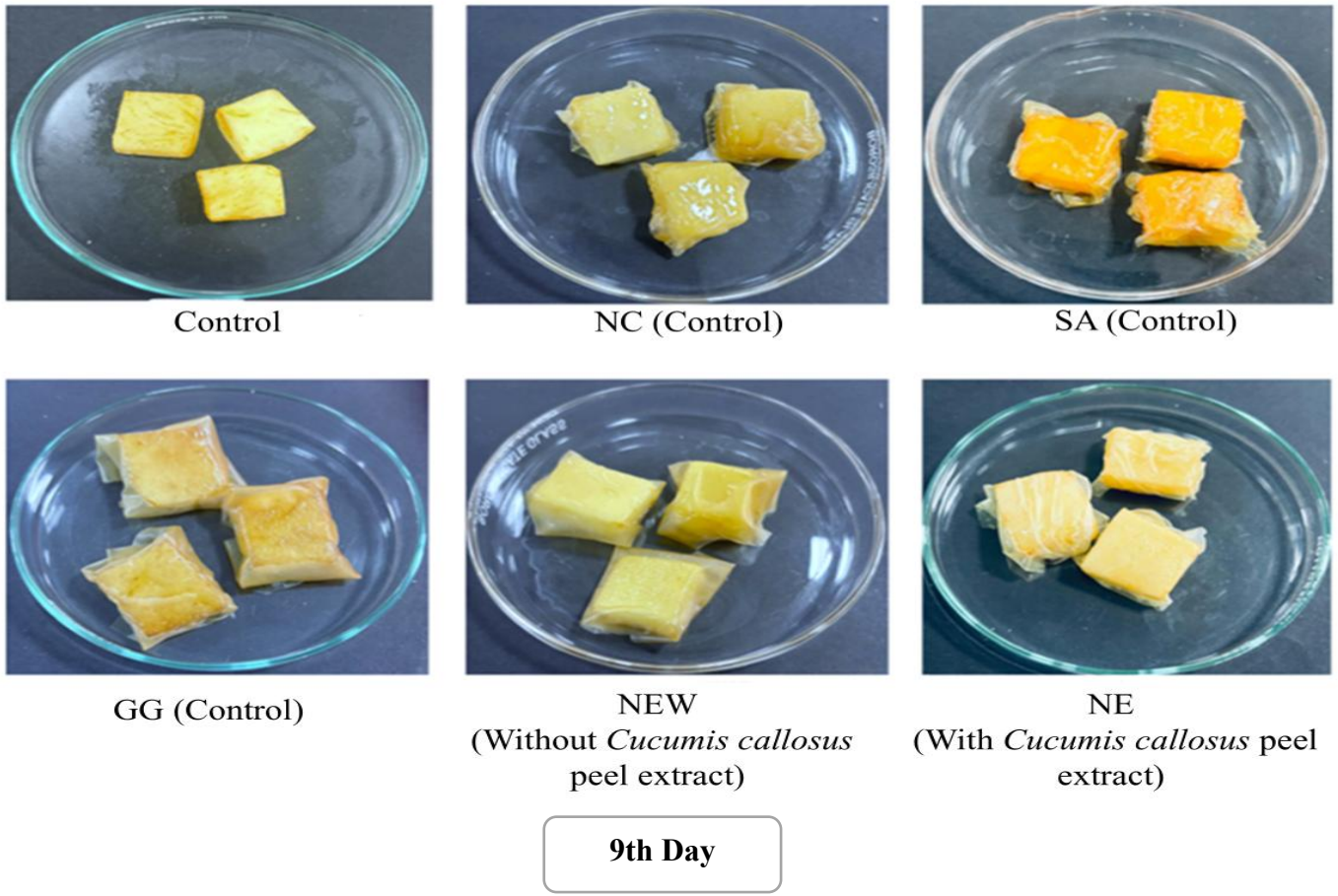

Fig. 4.69 Shelf-life study of fresh-cut apple slices in different packaging films at refrigerated temperature (4-7 ℃) on the 9th day

Note: NC: Nanocellulose, SA: Sodium alginate, GG: Guar gum, NEW: Nanocellulose, sodium alginate, and guar gum without *Cucumis callosus* peel extract, and NE: Nanocellulose, sodium alginate, and guar gum with *Cucumis callosus* peel extract functional film.

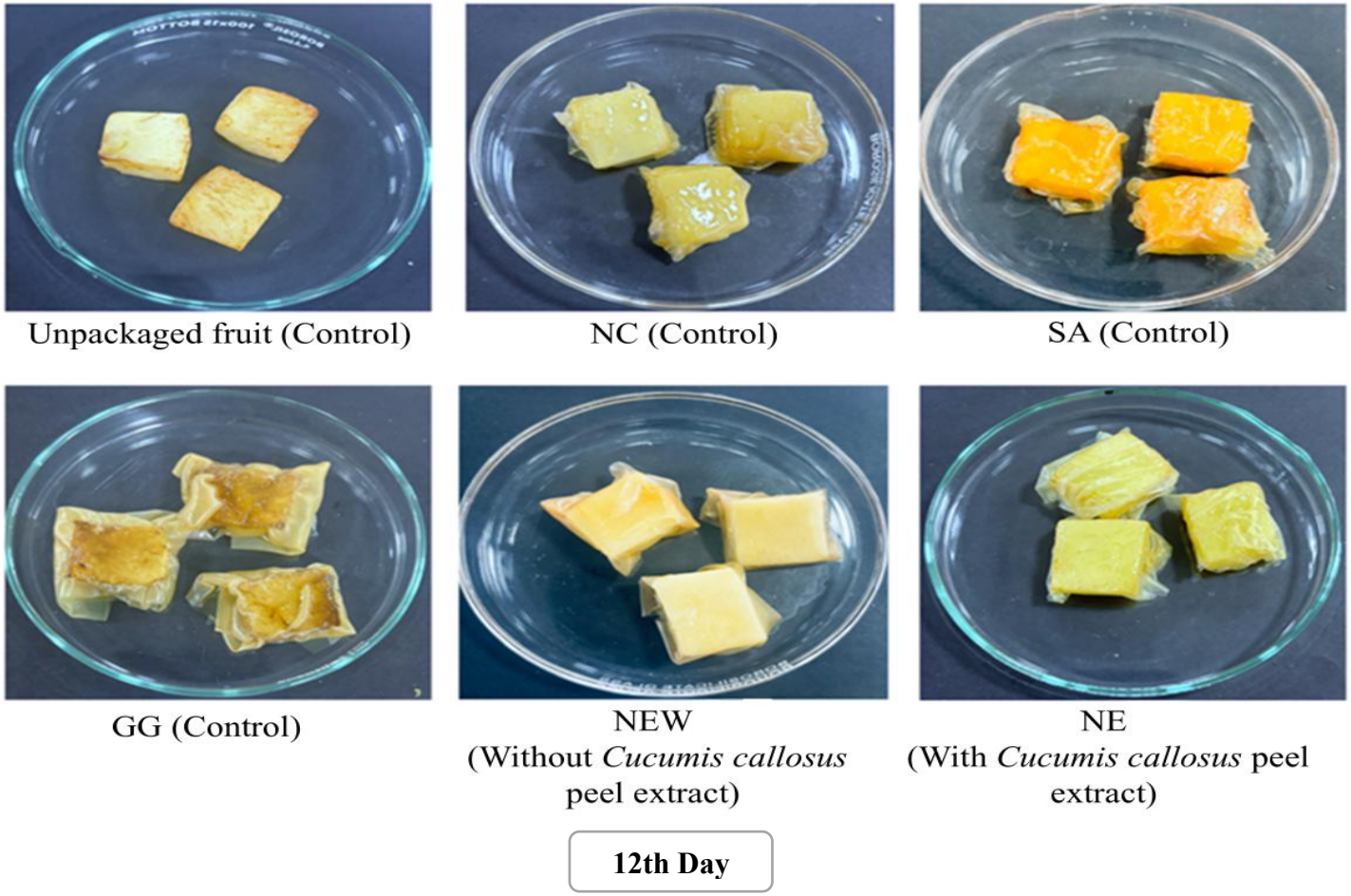

Fig. 4.70 Shelf-life study of fresh-cut apple slices in different packaging films at refrigerated temperature (4-7°C) on the 12th day

Note: NC: Nanocellulose, SA: Sodium alginate, GG: Guar gum, NEW: Nanocellulose, sodium alginate, and guar gum without *Cucumis callosus* peel extract, and NE: Nanocellulose, sodium alginate, and guar gum with *Cucumis callosus* peel extract functional film.

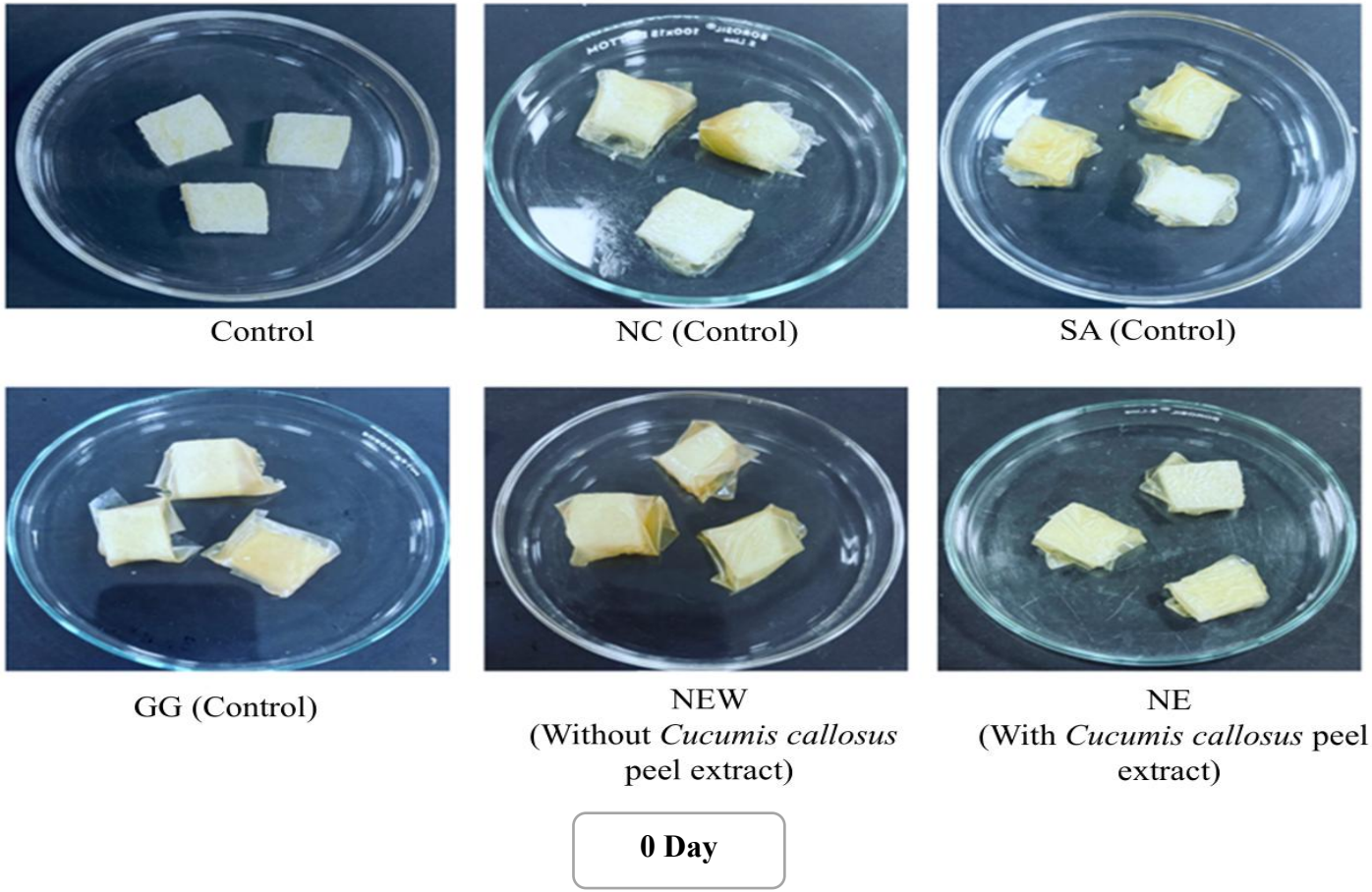

Fig. 4.71 Shelf-life study of fresh-cut pear slices in different packaging films at refrigerated temperature (4-7 ℃) on day 0.

Note: NC: Nanocellulose, SA: Sodium alginate, GG: Guar gum, NEW: Nanocellulose, sodium alginate, and guar gum without *Cucumis callosus* peel extract, and NE: Nanocellulose, sodium alginate, and guar gum with *Cucumis callosus* peel extract functional film.

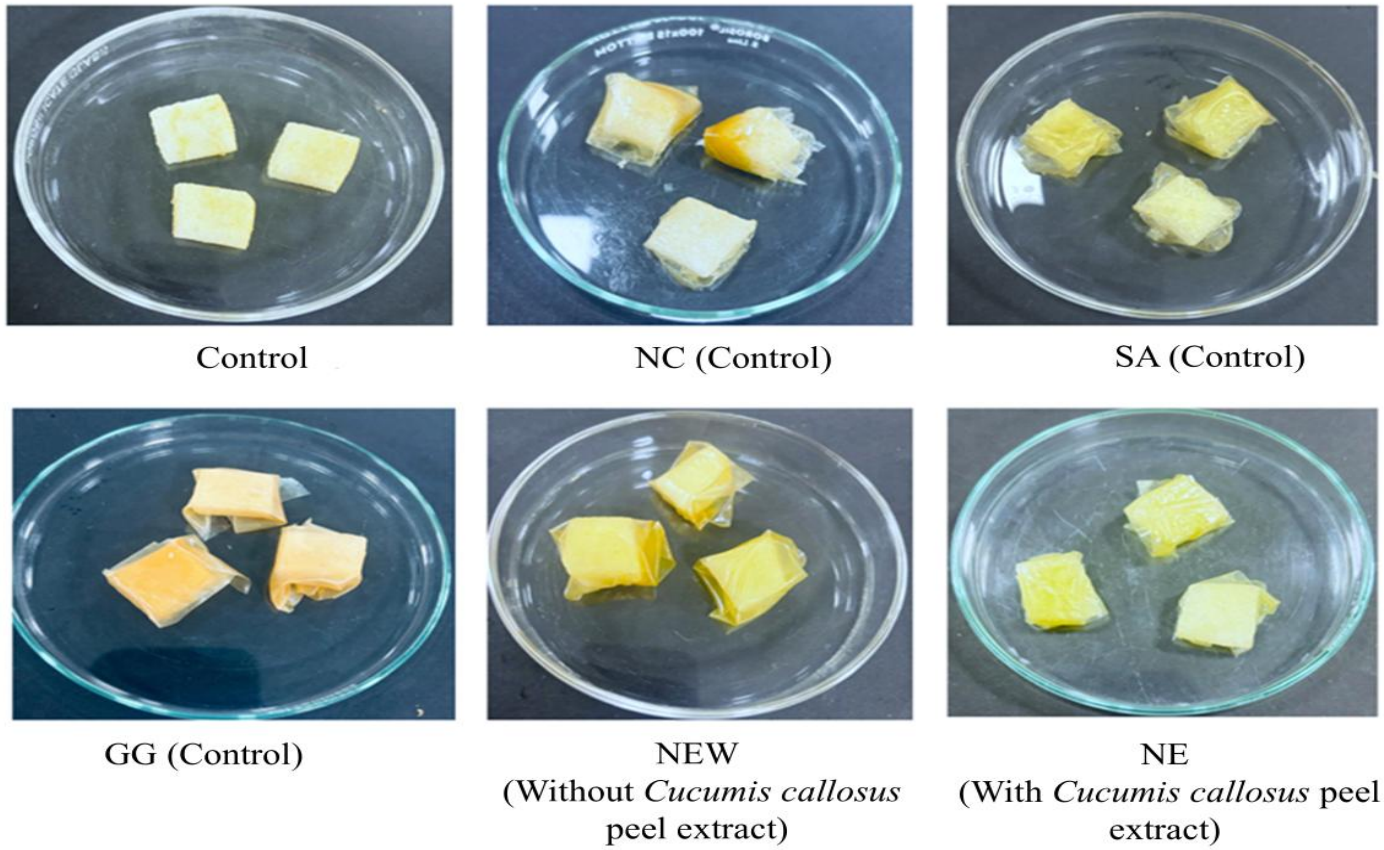

Fig. 4.72 Shelf-life study of fresh-cut pear slices in different packaging films at refrigerated temperature (4-7 °C) on the 3rd day.

Note: NC: Nanocellulose, SA: Sodium alginate, GG: Guar gum, NEW: Nanocellulose, sodium alginate, and guar gum without *Cucumis callosus* peel extract, and NE: Nanocellulose, sodium alginate, and guar gum with *Cucumis callosus* peel extract functional film.

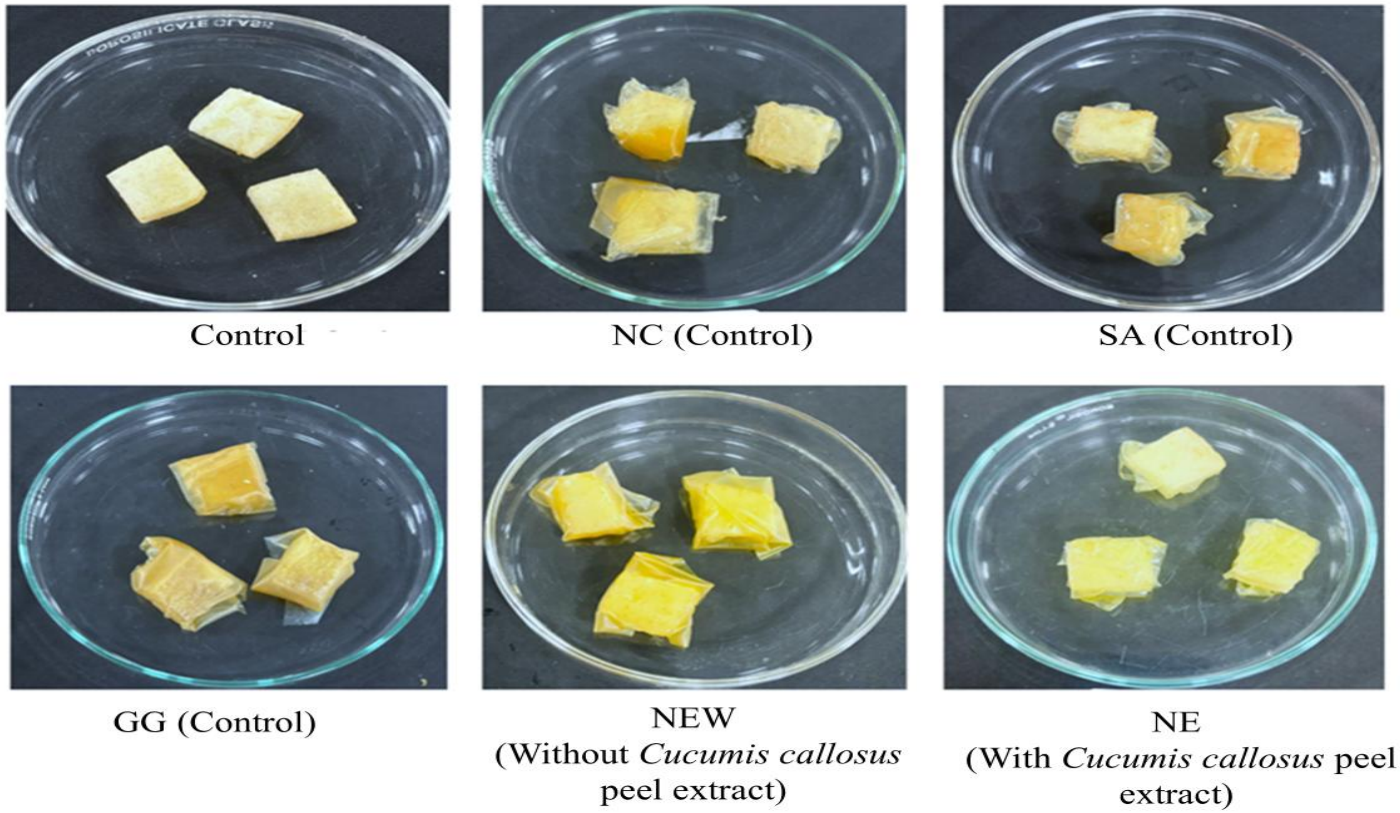

Fig. 4.73 Shelf-life study of fresh-cut pear slices in different packaging films at refrigerated temperature (4-7 °C) on the 6th day.

Note: NC: Nanocellulose, SA: Sodium alginate, GG: Guar gum, NEW: Nanocellulose, sodium alginate, and guar gum without *Cucumis callosus* peel extract, and NE: Nanocellulose, sodium alginate, and guar gum with *Cucumis callosus* peel extract functional film.

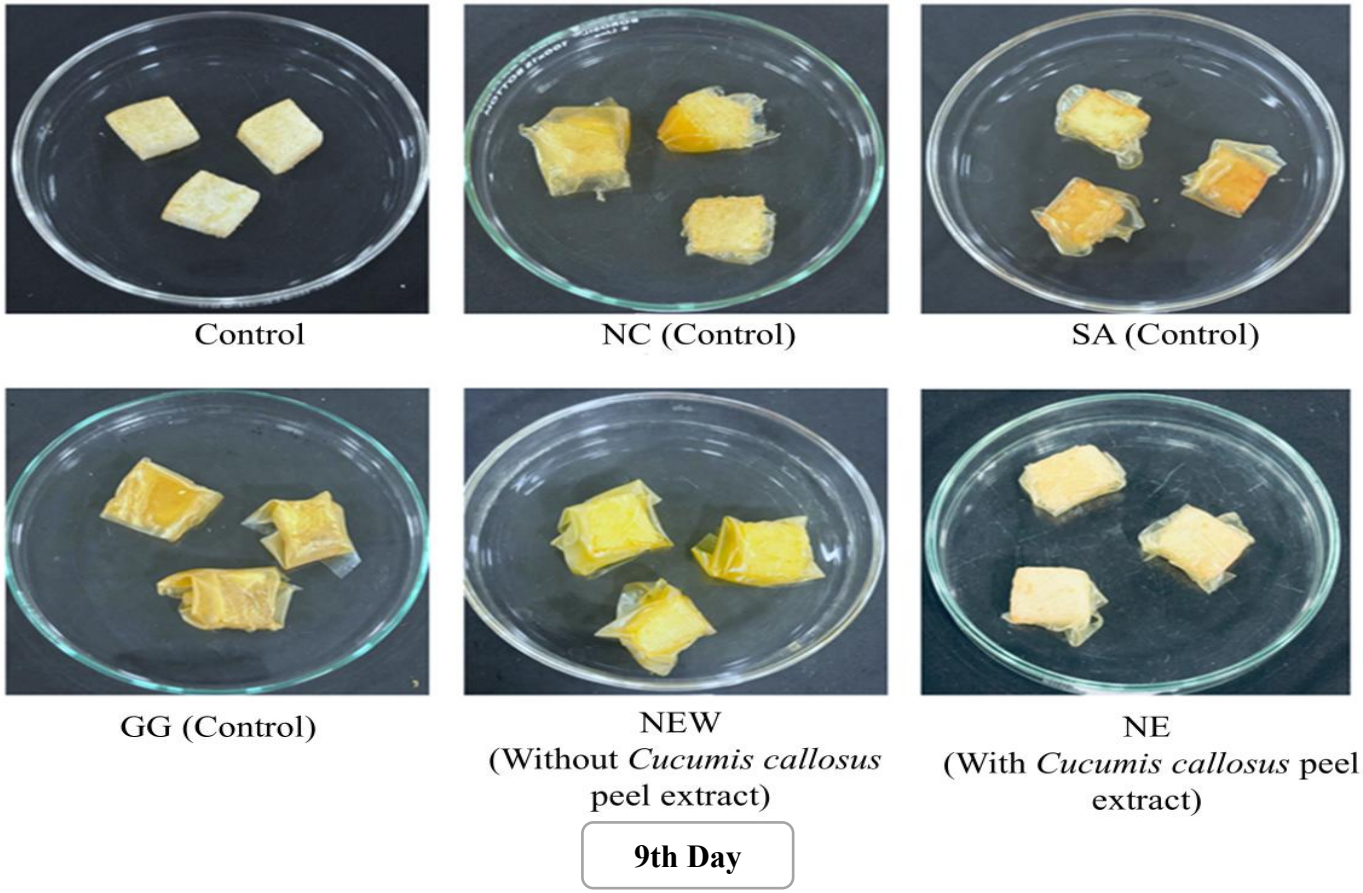

Fig. 4.74 Shelf-life study of fresh-cut pear slices in different packaging films at refrigerated temperature (4-7 °C) on the 9th day

Note: NC: Nanocellulose, SA: Sodium alginate, GG: Guar gum, NEW: Nanocellulose, sodium alginate, and guar gum without *Cucumis callosus* peel extract, and NE: Nanocellulose, sodium alginate, and guar gum with *Cucumis callosus* peel extract functional film.

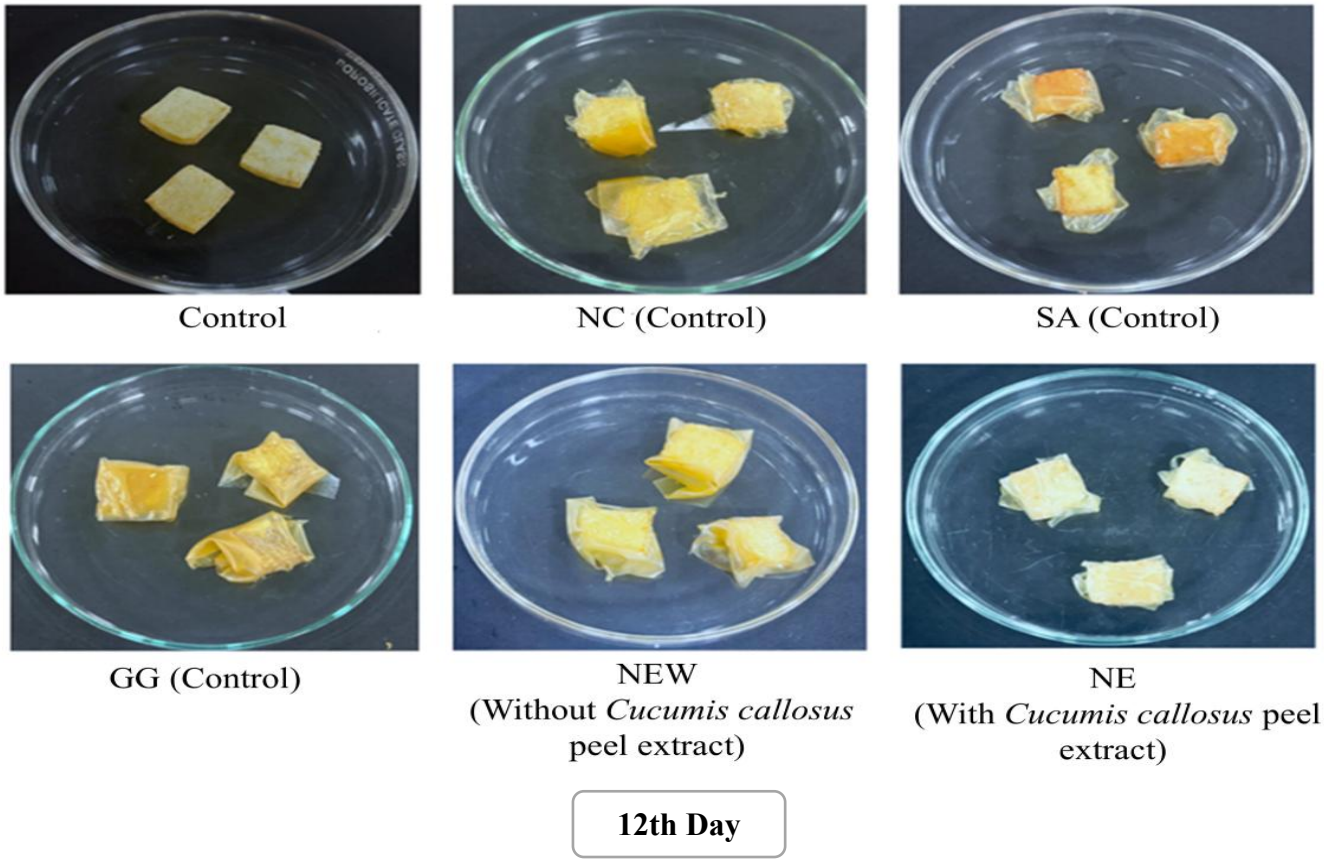

Fig. 4.75 Shelf-life study of fresh-cut pear slices in different packaging films at refrigerated temperature (4-7 ℃) on the 12th day

Note: NC: Nanocellulose, SA: Sodium alginate, GG: Guar gum, NEW: Nanocellulose, sodium alginate, and guar gum without *Cucumis callosus* peel extract, and NE: Nanocellulose, sodium alginate, and guar gum with *Cucumis callosus* peel extract functional film.

4.14 Shelf-Life Study of Control and Fresh-Cut Apple and Pear Slices in Different Packaging

Fresh-cut apple and pear slices were aseptically prepared and placed in sterile Petri plates to simulate controlled storage conditions. Cutting-induced tissue damage accelerates respiration, enzymatic browning, and moisture loss, and leading to rapid quality deterioration. Therefore, appropriate packaging interventions are essential to retard oxidative and microbial spoilage while maintaining physicochemical stability. In the present study, control (unpackaged) samples and packaged fresh-cut apple and pear slices were stored under refrigerated conditions in Petri plates, and their shelf-life behavior was systematically monitored. The comparative visual and quality changes observed during storage are presented in Fig. 4.66-4.70 for fresh-cut apple slices and in Fig. 4.71-4.75 for fresh-cut pear slices.

4.14.1 Moisture content

Moisture retention in fresh-cut fruits is influenced by water vapor diffusion, transpiration rate, tissue disruption caused by cutting, and the barrier efficiency of applied coatings or packaging systems. Cutting increases exposed surface area and accelerates moisture migration from fruit tissues to the surrounding environment, whereas edible coatings and packaging films act as semi-permeable barriers that moderate water vapor transmission and slow dehydration during storage. In fresh-cut apple slices, moisture content decreased significantly ($p < 0.05$) during the 12-day storage period in all treatments in fig. 4.76 and 4.77, as indicated by different uppercase superscripts (A–E) within each column shown in Tables 4.30 and 4.31, confirming a significant effect of storage time. The unpackaged control showed the greatest moisture loss, decreasing from 84.22 ± 0.11% on day 0 to 56.38 ± 0.26% on day 12, with each storage interval differing significantly from the previous one. At each storage day, the Control exhibited significantly lower moisture content than all packaged treatments, as reflected by different lowercase superscripts within the same row. Among packaged apple samples, nanocellulose (NC), sodium alginate (SA), and guar gum (GG) treatments, at the same storage intervals, values sharing the same lowercase letters did not differ significantly ($p > 0.05$). For example, on day 12, moisture contents of 65.58 ± 0.77% (NC), 69.70 ± 0.17% (SA), and 67.40 ± 0.66% (GG) carried the same lowercase superscript, indicating statistically comparable moisture retention. In contrast, the NEW treatment retained significantly higher moisture than NC, SA, and GG at all storage intervals beyond day 3, while the NE treatment consistently exhibited the highest moisture content, remaining significantly different ($p < 0.05$) from all other treatments on the same storage day. On day 12, moisture contents of 77.65 ± 0.37% (NEW) and 81.13 ± 0.18% (NE)

were significantly higher than those of all other treatments. A similar trend was observed in fresh-cut pear slices. Moisture content decreased significantly ($p < 0.05$) across storage days for all treatments, as shown by distinct uppercase superscripts (A–E) within each column. The unpackaged pear samples exhibited the highest moisture loss, declining from 87.68 ± 0.22% on day 0 to 61.90 ± 0.34% on day 12, and differed significantly from all packaged samples at each storage interval. Among the coated pear samples, NC and GG treatments did not differ significantly ($p > 0.05$) from each other at corresponding storage days, whereas SA showed intermediate moisture retention. On day 12, the moisture contents of 68.10 ± 0.35% (NC) and 69.92 ± 0.34% (GG) shared the same lowercase superscript, indicating no significant difference between these treatments. In contrast, the NEW treatment retained significantly higher moisture than NC, SA, and GG, while the NE treatment showed the highest moisture retention throughout storage. On day 12, the moisture contents of 80.20 ± 0.35% (NEW) and 84.68 ± 0.37% (NE) were significantly higher ($p < 0.05$) than those of all other treatments. These results demonstrate that NE was the most effective treatment in minimizing moisture loss and maintaining tissue hydration in both apple and pear slices during refrigerated storage.

Table 4.30 Changes in moisture content of fresh-cut apple slices as influenced by biodegradable packaging systems during refrigerated storage (0–12 days)

Day	**Control (%)**	**NC Control (%)**	**SA Control (%)**	**GG Control (%)**	**NEW Control (%)**	**NE Control (%)**
0	84.22 ± 0.11^{aA}	83.58 ± 0.52^{aA}	84.26 ± 0.22^{aA}	85.12 ± 0.17^{aA}	84.25 ± 0.79^{aA}	84.27 ± 0.12^{aA}
3	70.61 ± 0.23^{cB}	78.74 ± 0.34^{bB}	80.82 ± 0.41^{bB}	81.65 ± 0.63^{bB}	82.78 ± 0.84^{aB}	83.92 ± 0.15^{aA}
6	65.85 ± 0.44^{cC}	74.02 ± 0.25^{bB}	77.12 ± 0.45^{bB}	76.88 ± 0.44^{bB}	80.08 ± 0.85^{aB}	82.25 ± 0.26^{aB}
9	60.10 ± 0.15^{cD}	69.28 ± 0.16^{bC}	73.38 ± 0.26^{bC}	72.12 ± 0.55^{bC}	78.35 ± 0.76^{aC}	81.55 ± 0.27^{aC}
12	56.38 ± 0.26^{cE}	65.58 ± 0.77^{bC}	69.70 ± 0.17^{bD}	67.40 ± 0.66^{bD}	77.65 ± 0.37^{aC}	81.13 ± 0.18^{aC}

Results are expressed as mean ± standard deviation (n = 3). Different uppercase letters (A–E) within the same column indicate significant differences ($p < 0.05$), while different lowercase letters (a–c) within a row denote significant differences ($p < 0.05$) on the same storage day.

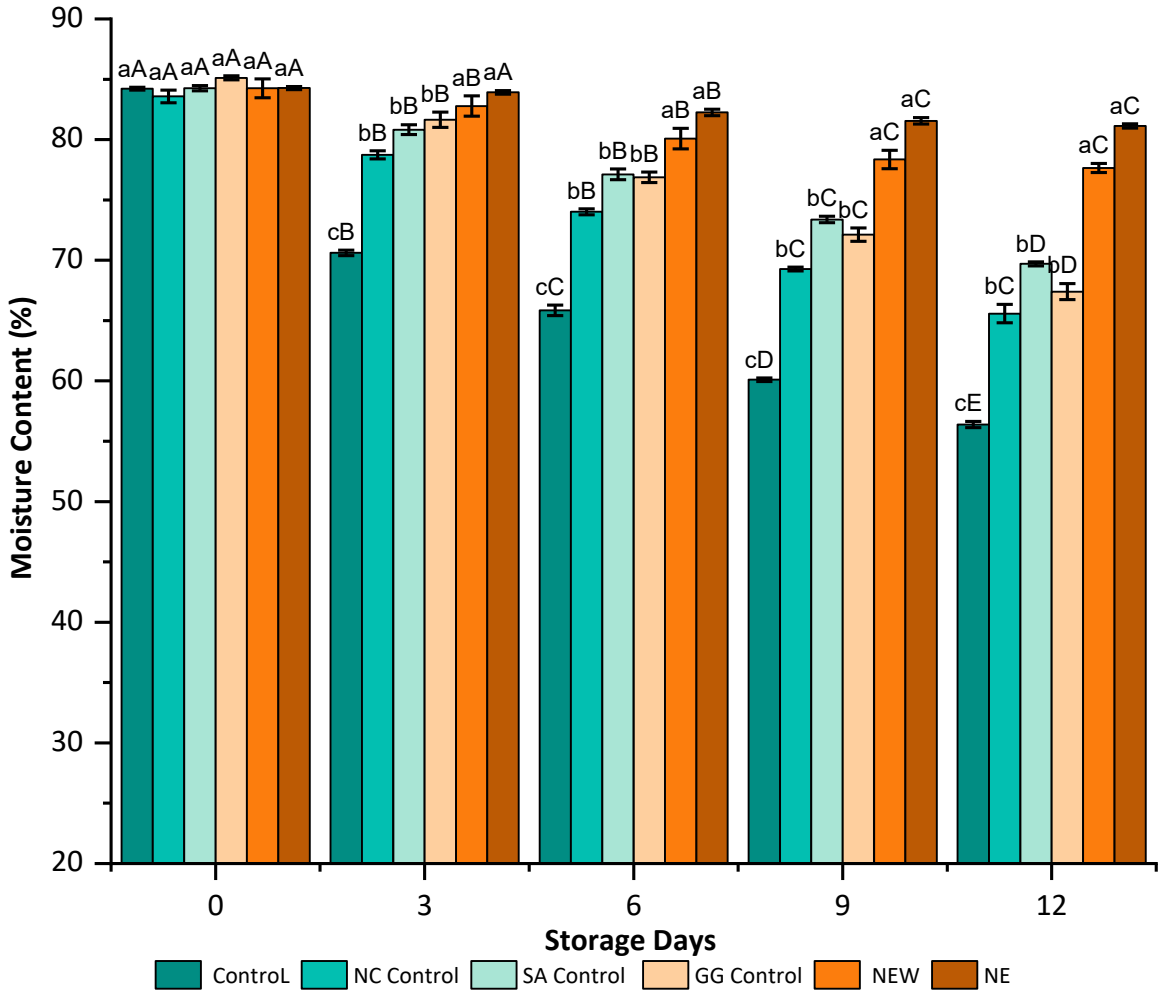

Fig. 4.76 Changes in moisture content (%) of fresh-cut apple slices during storage under different packaging materials

Note: NC: Nanocellulose, SA: Sodium alginate, GG: Guar gum, NEW: Nanocellulose, sodium alginate, and guar gum without *Cucumis callosus* peel extract, and NE: Nanocellulose, sodium alginate, and guar gum with *Cucumis callosus* peel extract functional film. Different lowercase letters denote significant differences among treatments within the same storage day, while different uppercase letters denote significant differences within the same treatment across storage days ($p < 0.05$).

Table 4.31 Changes in moisture content of fresh-cut pear slices as influenced by biodegradable packaging systems during refrigerated storage (0–12 days)

Day	Control (%)	NC Control (%)	SA Control (%)	GG Control (%)	NEW Control (%)	NE Control (%)
0	87.68 ± 0.22^{aA}	87.70 ± 0.73^{aA}	87.72 ± 0.24^{aA}	87.69 ± 0.23^{aA}	87.71 ± 0.22^{aA}	87.73 ± 0.23^{aA}

3	77.10 ± 0.25^{cB}	79.28 ± 0.26^{cB}	81.35 ± 0.27^{bB}	78.14 ± 0.25^{cB}	85.32 ± 0.26^{aB}	86.45 ± 0.28^{aB}
6	71.35 ± 0.28^{cC}	74.52 ± 0.29^{cC}	78.62 ± 0.30^{bC}	75.38 ± 0.28^{cC}	83.58 ± 0.29^{aC}	85.78 ± 0.31^{aB}
9	66.60 ± 0.31^{cD}	70.78 ± 0.32^{cD}	75.90 ± 0.33^{bD}	72.62 ± 0.31^{cD}	82.88 ± 0.32^{aC}	85.10 ± 0.34^{aB}
12	61.90 ± 0.34^{cE}	68.10 ± 0.35^{cE}	71.22 ± 0.36^{bE}	69.92 ± 0.34^{cE}	80.20 ± 0.35^{aD}	84.68 ± 0.37^{aB}

Values are reported as mean ± standard deviation (n = 3). $^{(A-E)}$ Mean values show significant (p<0.05) differences within the same column, and $^{(a-c)}$ mean values within the row indicate significant (p<0.05) differences on the same storage day.

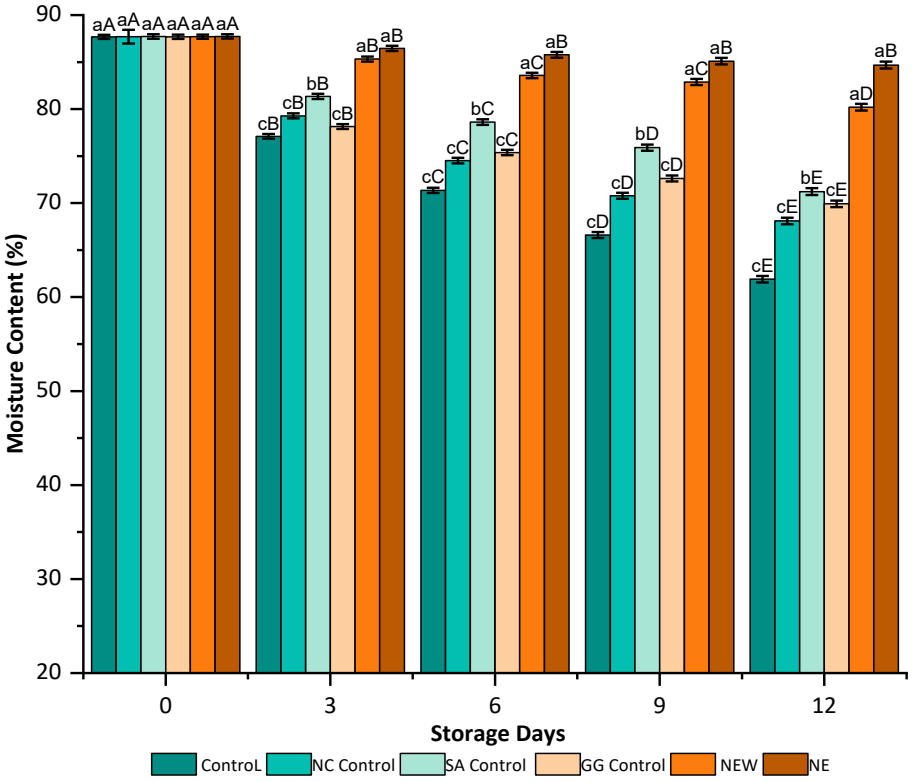

Fig. 4.77 Changes in moisture content (%) of fresh-cut pear slices during storage under different packaging materials

Note: NC: Nanocellulose, SA: Sodium alginate, GG: Guar gum, NEW: Nanocellulose, sodium alginate, and guar gum without *Cucumis callosus* peel extract, and NE: Nanocellulose, sodium alginate, and guar gum with *Cucumis callosus* peel extract functional film. Different lowercase letters denote significant differences among treatments within the same storage day, while different uppercase letters denote significant differences within the same treatment across storage days (p < 0.05).

4.14.2 Ash content

Ash content reflects the total mineral fraction of fruit tissues and is largely influenced by moisture loss and concentration effects during storage. In fresh-cut fruits, increases in ash content during storage are generally attributed to progressive dehydration rather than an actual gain in minerals. Packaging systems can regulate this apparent increase by limiting moisture migration and preserving tissue structure. In fresh-cut apples, ash content showed a consistent increase with storage duration across all treatments fig. 4.78 and 4.79, as indicated by the progressive change in uppercase superscripts within each column in Table 4.32 and 4.33. The unpackaged control exhibited the lowest ash values throughout storage, increasing from 0.25 ± 0.002% on day 0 to 0.32 ± 0.003% by day 12, indicating a gradual concentration effect due to unrestricted moisture loss under open storage conditions. Significant differences between storage intervals were observed from day 6 onwards, confirming a clear time-dependent effect on ash content. Among the packaged apple samples, ash content was significantly higher ($p < 0.05$) than that of the unpackaged control at corresponding storage days, as denoted by different lowercase superscripts within the same row. However, NC, SA, and GG treatments did not differ significantly ($p > 0.05$) from one another on the same storage day, particularly evident at day 12, where values of 0.38 ± 0.003% (NC), 0.40 ± 0.003% (SA), and 0.37 ± 0.003% (GG) shared common lowercase superscripts. This suggests comparable performance of these coatings in moderating moisture loss. In contrast, the NEW composite film (0.39 ± 0.003%) and NE film (0.42 ± 0.004%) exhibited significantly higher ash contents ($p < 0.05$) than the other packaged treatments, indicating superior control over moisture migration and enhanced retention of solids during storage. A similar pattern was observed in fresh-cut pears, although absolute ash values were higher than those recorded for apples. The unpackaged pear samples showed a steady and significant increase in ash content from 0.28 ± 0.002% on day 0 to 0.33 ± 0.003% by day 12, reflecting a pronounced concentration effect driven by moisture loss. Significant differences among storage days were observed from day 6 onwards, as reflected by the change in uppercase superscripts. For packaged pear samples, ash content remained consistently higher than that of the unpackaged control throughout storage. As observed in apples, NC, SA, and GG treatments did not differ significantly ($p > 0.05$) from one another within the same storage day, sharing common lowercase superscripts. At day 12, ash contents of 0.37 ± 0.001% (NC), 0.38 ± 0.002% (SA), and 0.36 ± 0.003% (GG) indicated comparable behavior among these coatings. Conversely, the NEW film (0.38 ± 0.001%) and NE film (0.40 ± 0.002%) retained significantly higher ash contents ($p < 0.05$) than all other treatments at the

corresponding storage interval, highlighting their improved effectiveness in limiting moisture loss and maintaining mineral concentration.

Table 4.32 Effect of biodegradable packaging films on ash content of fresh-cut apple slices during storage (0–12 days)

Day	Control (%)	NC Control (%)	SA Control (%)	GG Control (%)	NEW Control (%)	NE Control (%)	Control (%)
0	0.28 ± 0.002^{aA}	0.28 ± 0.003^{aA}		0.29 ± 0.003^{aA}	0.28 ± 0.002^{aA}	0.29 ± 0.003^{aA}	0.29 ± 0.001^{aA}
3	0.29 ± 0.004^{bA}	0.31 ± 0.001^{aA}		0.32 ± 0.004^{aA}	0.30 ± 0.006^{bA}	0.32 ± 0.001^{aA}	0.33 ± 0.003^{aA}
6	0.32 ± 0.001^{cB}	0.33 ± 0.002^{bB}		0.34 ± 0.001^{bB}	0.32 ± 0.001^{cB}	0.34 ± 0.003^{bB}	0.35 ± 0.001^{aB}
9	0.34 ± 0.001^{cC}	0.35 ± 0.001^{cC}		0.36 ± 0.001^{bC}	0.34 ± 0.001^{cC}	0.36 ± 0.001^{bC}	0.38 ± 0.001^{aC}
12	0.33 ± 0.003^{cC}	0.37 ± 0.001^{cD}		0.38 ± 0.002^{bD}	0.36 ± 0.003^{cD}	0.38 ± 0.001^{bD}	0.40 ± 0.002^{aD}

Values are expressed as mean ± SD (n = 3). Different uppercase letters (A–E) within a column and lowercase letters (a–c) within a row indicate significant differences ($p < 0.05$) on the same storage day.

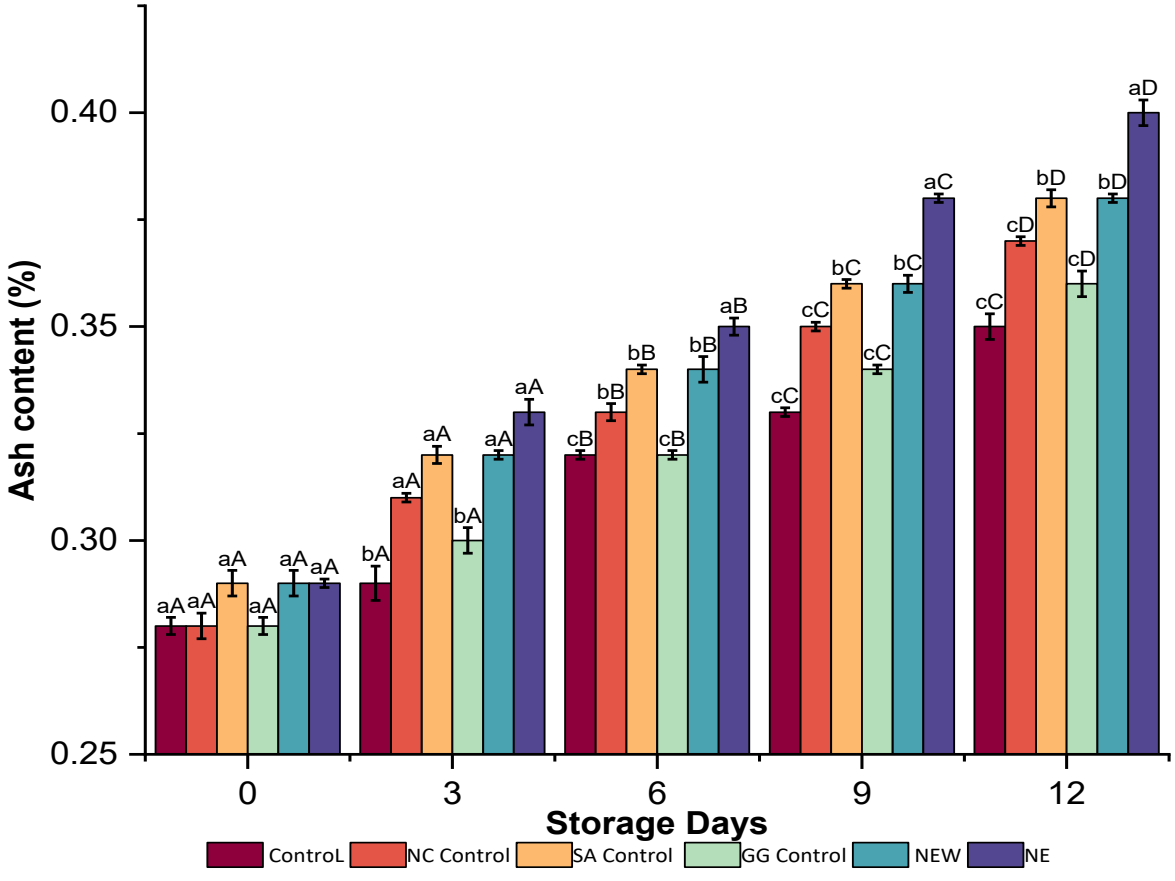

Fig. 4.78 Changes in ash content (%) of fresh-cut apple slices during storage under different packaging materials

Note: NC: Nanocellulose, SA: Sodium alginate, GG: Guar gum, NEW: Nanocellulose, sodium alginate, and guar gum without *Cucumis callosus* peel extract, and NE: Nanocellulose, sodium alginate, and guar gum with *Cucumis callosus* peel extract functional film. Different lowercase letters denote significant differences among treatments within the same storage day, while different uppercase letters denote significant differences within the same treatment across storage days ($p < 0.05$).

Table 4.33 Effect of biodegradable packaging films on ash content of fresh-cut pear slices during storage (0–12 days)

Day	**Control (%)**	**NC Control (%)**	**SA Control (%)**	**GG Control (%)**	**NEW Control (%)**	**NE Control (%)**
0	0.25 ± 0.002^{aA}	0.26 ± 0.001^{aA}	0.25 ± 0.002^{aA}	0.25 ± 0.003^{aA}	0.26 ± 0.002^{aA}	0.24 ± 0.003^{aA}
3	0.27 ± 0.002^{bA}	0.29 ± 0.002^{bA}	0.31 ± 0.004^{aA}	0.28 ± 0.002^{bA}	0.30 ± 0.001^{aA}	0.31 ± 0.001^{aA}
6	0.29 ± 0.003^{cB}	0.32 ± 0.003^{cB}	0.34 ± 0.003^{bB}	0.31 ± 0.003^{cB}	0.33 ± 0.003^{bB}	0.305 ± 0.002^{aB}
9	0.30 ± 0.001^{cB}	0.35 ± 0.002^{cC}	0.37 ± 0.002^{bC}	0.34 ± 0.001^{cC}	0.36 ± 0.003^{bC}	0.38 ± 0.003^{aC}
12	0.32 ± 0.003^{cC}	0.38 ± 0.003^{cD}	0.40 ± 0.002^{bD}	0.37 ± 0.004^{cD}	0.39 ± 0.002^{bD}	0.42 ± 0.003^{aD}

Values are expressed as mean ± SD (n = 3). Different uppercase letters (A–E) within a column and lowercase letters (a–c) within a row indicate significant differences ($p < 0.05$) on the same storage day.

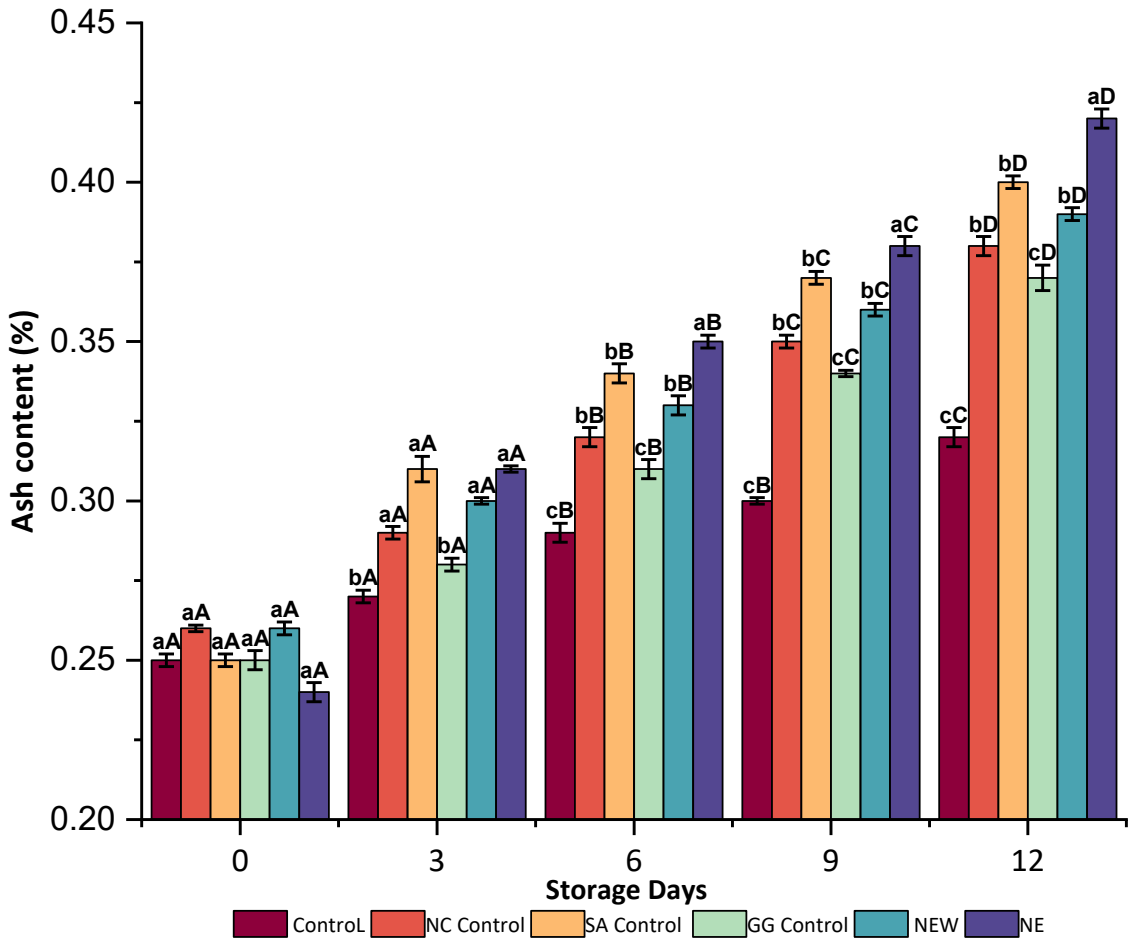

Fig. 4.79 Changes in ash content (%) of fresh-cut pear slices during storage under different packaging materials

Note: NC: Nanocellulose, SA: Sodium alginate, GG: Guar gum, NEW: Nanocellulose, sodium alginate, and guar gum without *Cucumis callosus* peel extract, and NE: Nanocellulose, sodium alginate, and guar gum with *Cucumis callosus* peel extract functional film. Different lowercase letters denote significant differences among treatments within the same storage day, while different uppercase letters denote significant differences within the same treatment across storage days ($p < 0.05$).

4.14.3 Fat content

Fat content, though a minor proximate component in fresh-cut fruits, exhibited measurable changes during storage that were influenced by storage duration and the type of biodegradable packaging film applied. In fresh-cut apple slices, fat content showed a significant decreasing trend ($p < 0.05$) over the 12-day storage period across all treatments in Tables 4.34 and 4.35. At day 0, fat content ranged between 0.17 and 0.19% among all treatments, with no significant differences ($p > 0.05$) observed, indicating uniform initial composition before storage, as shown in fig. 4.80 and 4.81. As storage progressed, the unpackaged apple samples exhibited the

greatest reduction in fat content, declining from 0.18% at day 0 to 0.07% by day 12. From day 3 onward, packaged apple samples retained significantly higher fat content ($p < 0.05$) than the unpackaged control at corresponding storage intervals. Among the coated samples, nanocellulose (NC), sodium alginate (SA), and guar gum (GG) treatments did not differ significantly ($p > 0.05$) from one another on the same storage day, indicating comparable performance of these polysaccharide-based films. In contrast, the NEW and NE treatments consistently maintained higher fat content than NC, SA, and GG during storage. The NE-treated apple samples showed the highest fat retention throughout the storage period, maintaining 0.14% fat at day 12, which was significantly higher ($p < 0.05$) than all other treatments. A similar storage-dependent decline in fat content was observed in fresh-cut pear slices. Initial fat content at day 0 ranged from 0.13 to 0.15%, with no significant differences ($p > 0.05$) among treatments. Fat content decreased significantly ($p < 0.05$) with increasing storage time in all treatments. The unpackaged pear samples showed the most pronounced reduction, decreasing from 0.14% at day 0 to 0.05% by day 12, and exhibited significantly lower fat content than all packaged samples at later storage stages. Among the coated pear samples, NC, SA, and GG treatments generally showed no significant differences ($p > 0.05$) from one another at corresponding storage intervals. In contrast, NEW and NE treatments retained significantly higher fat content ($p < 0.05$) throughout storage, with NE consistently maintaining the highest values. At day 12, NE-treated pear samples retained 0.11% fat, which was significantly higher than all other treatments. Overall, the higher fat retention observed in NEW- and NE-treated apple and pear slices can be attributed to their superior barrier efficiency, which moderated dehydration-related compositional changes and helped stabilize proximate composition during refrigerated storage.

Table 4.34 Effect of biodegradable packaging films on fat content of fresh-cut apple slices during storage (0–12 days)

Day	Control (%)	NC Control (%)	SA Control (%)	GG Control (%)	NEW Control (%)	NE Control (%)
0	0.18 ± 0.004^{aA}	0.19 ± 0.005^{aA}	0.18 ± 0.002^{aA}	0.17 ± 0.006^{aA}	0.18 ± 0.004^{aA}	0.19 ± 0.005^{aA}
3	0.16 ± 0.005^{bA}	0.17 ± 0.004^{aA}	0.17 ± 0.003^{aA}	0.15 ± 0.005^{bB}	0.16 ± 0.005^{aB}	0.18 ± 0.006^{aA}
6	0.13 ± 0.003^{cA}	0.15 ± 0.002^{bB}	0.14 ± 0.005^{bB}	0.14 ± 50.004^{cB}	0.15 ± 0.004^{bB}	0.16 ± 0.003^{aB}
9	0.11 ± 0.006^{cB}	0.13 ± 0.005^{cB}	0.12 ± 0.003^{bB}	0.13 ± 0.004^{cB}	0.14 ± 0.006^{bB}	0.15 ± 0.006^{aB}

12	0.07 ± 0.003^{eC}	0.10 ± 0.005^{cC}	0.11 ± 0.006^{bC}	0.09 ± 0.005^{cC}	0.12 ± 0.005^{bC}	0.14 ± 0.003^{aC}

Values are expressed as mean ± SD (n = 3). Different uppercase letters (A–E) within a column and lowercase letters (a–c) within a row indicate significant differences ($p < 0.05$) on the same storage day.

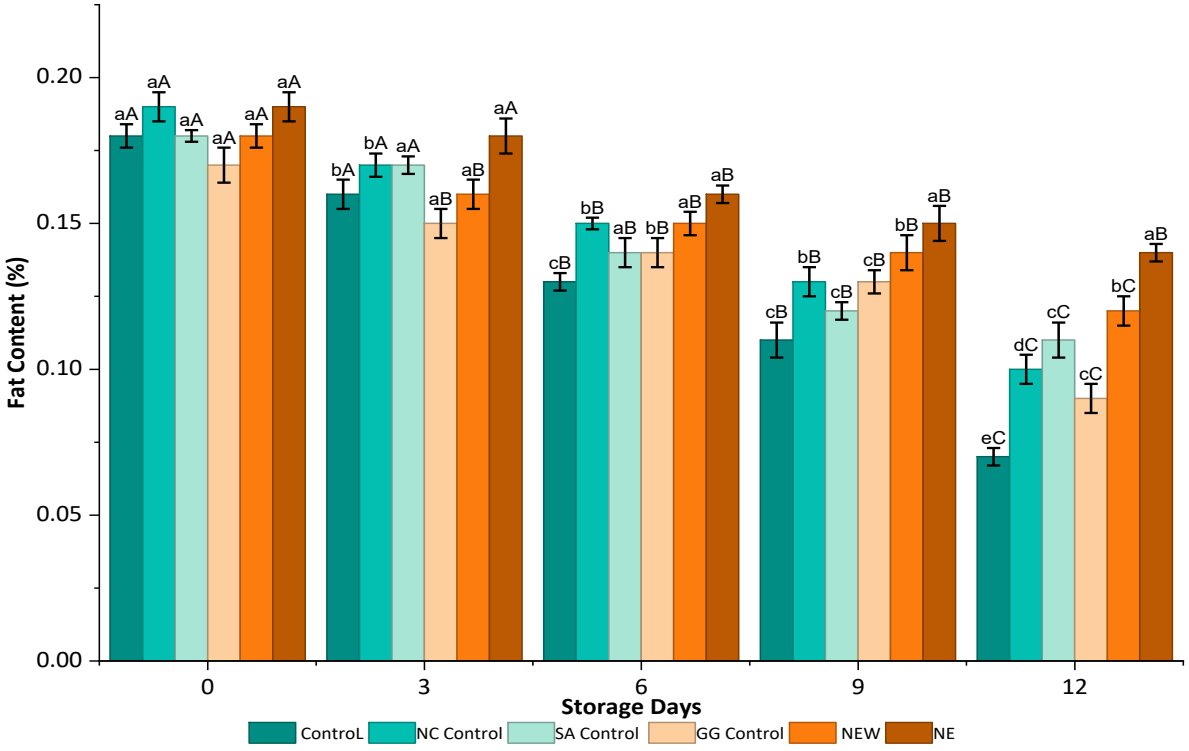

Fig. 4.80 Changes in fat content (%) of fresh-cut apple slices during storage under different packaging materials

Note: NC: Nanocellulose, SA: Sodium alginate, GG: Guar gum, NEW: Nanocellulose, sodium alginate, and guar gum without *Cucumis callosus* peel extract, and NE: Nanocellulose, sodium alginate, and guar gum with *Cucumis callosus* peel extract functional film. Different lowercase letters denote significant differences among treatments within the same storage day, while different uppercase letters denote significant differences within the same treatment across storage days ($p < 0.05$).

Table 4.35 Effect of biodegradable packaging films on fat content of fresh-cut pear slices during storage (0–12 days)

Day	Control (%)	NC Control (%)	SA Control (%)	GG Control (%)	NEW Control (%)	NE Control (%)
0	0.14 ± 0.006^{aA}	0.14 ± 0.004^{aA}	0.13 ± 0.003^{aA}	0.14 ± 0.005^{aA}	0.14 ± 0.004^{aA}	0.15 ± 0.006^{aA}

3	0.12 ± 0.004^{aA}	0.13 ± 0.005^{aA}	0.12 ± 0.003^{aA}	0.13 ± 0.006^{aA}	0.11 ± 0.005^{aA}	0.14 ± 0.007^{aA}
6	0.11 ± 0.003^{aB}	0.12 ± 0.004^{bB}	0.11 ± 0.004^{aB}	0.12 ± 0.005^{aB}	0.10 ± 0.004^{aB}	0.13 ± 0.006^{aB}
9	0.09 ± 0.005^{bB}	0.11 ± 0.006^{bB}	0.10 ± 0.004^{bB}	0.11 ± 0.004^{bB}	0.08 ± 0.006^{aB}	0.12 ± 0.005^{aB}
12	0.05 ± 0.006^{dC}	0.10 ± 0.004^{cC}	0.09 ± 0.005^{bC}	0.10 ± 0.004^{bC}	0.07 ± 0.005^{cC}	0.11 ± 0.004^{aC}

Values are expressed as mean ± SD (n = 3). Different uppercase letters (A–E) within a column and lowercase letters (a–c) within a row indicate significant differences ($p < 0.05$) on the same storage day.

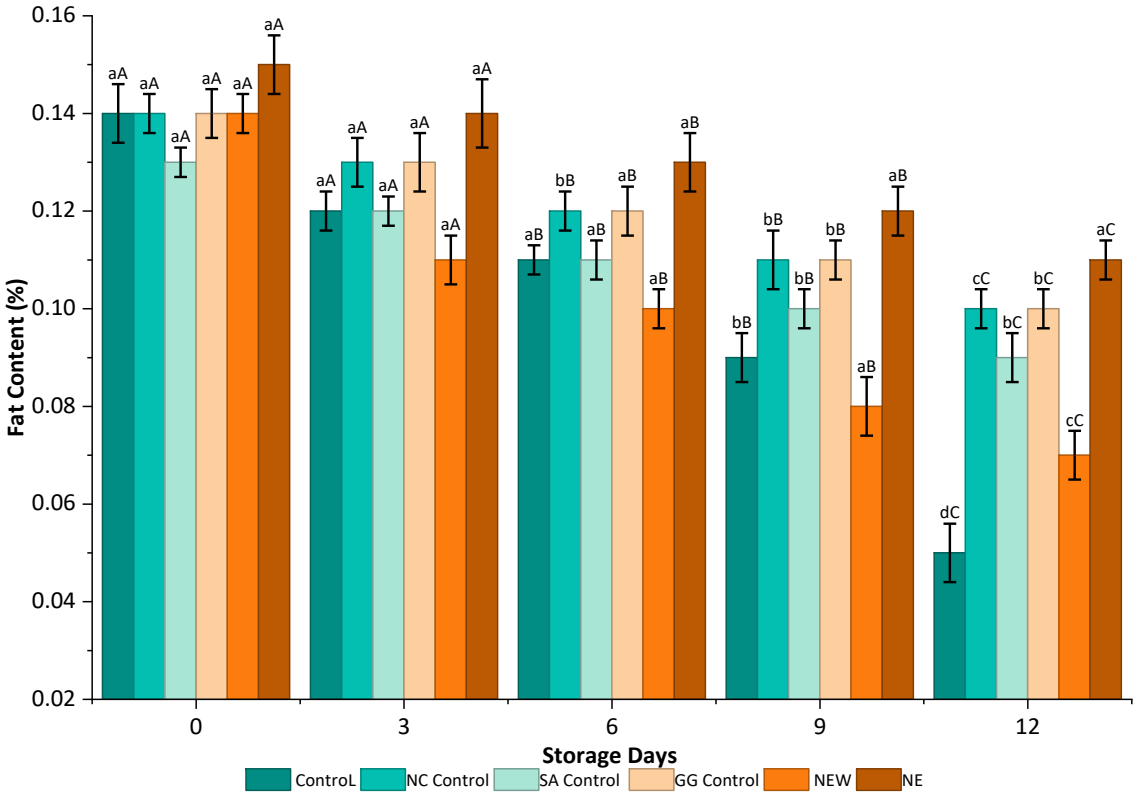

Fig. 4.81 Changes in fat content (%) of fresh-cut pear slices during storage under different packaging materials

Note: NC: Nanocellulose, SA: Sodium alginate, GG: Guar gum, NEW: Nanocellulose, sodium alginate, and guar gum without *Cucumis callosus* peel extract, and NE: Nanocellulose, sodium alginate, and guar gum with *Cucumis callosus* peel extract functional film. Different lowercase letters denote significant differences among treatments within the same storage day, while

different uppercase letters denote significant differences within the same treatment across storage days ($p < 0.05$).

4.14.4 Protein content

Protein content of fresh-cut apple and pear slices exhibited a consistent and statistically significant decline ($p < 0.05$) during refrigerated storage from day 0 to day 12 in fig. 4.82 and 4.83, irrespective of the packaging treatment applied, as shown in Tables 4.36 and 4.37. This reduction can be attributed to post-harvest metabolic activity, enzymatic degradation following tissue disruption, and partial loss of soluble nitrogenous compounds during storage. The extent of protein loss, however, was strongly influenced by the type of biodegradable packaging film, which modulated oxygen permeability and helped preserve cellular integrity. In fresh-cut apple slices, the initial protein content on day 0 ranged from 0.41 ± 0.002% to 0.44 ± 0.005%, with no significant differences ($p > 0.05$) observed among treatments, indicating uniformity of the raw material prior to storage. As storage progressed, protein content declined significantly within each treatment. The unpackaged control exhibited the most pronounced decrease, declining from 0.42 ± 0.003% on day 0 to 0.30 ± 0.004% by day 12, reflecting accelerated protein degradation under open storage conditions. In contrast, packaged apple samples consistently retained higher protein contents throughout storage. At day 12, apple slices treated with nanocellulose (NC), sodium alginate (SA), and guar gum (GG) retained 0.32 ± 0.003%, 0.33 ± 0.002%, and 0.34 ± 0.003% protein, respectively, with no significant differences ($p > 0.05$) among these treatments. The NEW and NE packaging systems demonstrated superior performance, retaining 0.34 ± 0.003% and 0.37 ± 0.002% protein, respectively, at day 12. Among all treatments, the NE film consistently maintained the highest protein content across all storage intervals, indicating enhanced preservation of protein integrity. In fresh-cut pear slices, although absolute protein values were consistently higher than those observed in apples, reflecting inherent compositional differences between the fruits. On day 0, protein content in pear slices ranged from 0.56 ± 0.003% to 0.60 ± 0.004%, with NE-treated samples exhibiting the highest initial protein level. Protein content decreased significantly ($p< 0.05$) during storage in all treatments. The unpackaged pear samples showed the greatest decline, decreasing from 0.57 ± 0.005% on day 0 to 0.44 ± 0.006% by day 12. Packaged pear samples retained significantly higher protein levels compared to the unpackaged control throughout storage. At day 12, NC-, SA-, and GG-treated pear slices retained 0.49 ± 0.005%, 0.50 ± 0.002%, and 0.48 ± 0.004% protein, respectively, with no significant differences ($p > 0.05$) among them. In contrast, the NEW and NE treatments showed enhanced protein retention, maintaining 0.51 ± 0.007% and 0.54 ± 0.004% protein, respectively. Overall, the results demonstrate that

biodegradable packaging films, particularly the NEW and NE formulations, effectively slowed protein degradation in fresh-cut apple and pear slices during refrigerated storage. The improved protein retention is likely associated with reduced oxygen exposure, lower oxidative stress, and better maintenance of tissue structure, thereby contributing to improved nutritional quality and extended shelf life of fresh-cut fruits.

Table 4.36 Changes in protein content of fresh-cut apple slices as affected by biodegradable packaging and storage duration (0–12 days)

Day	Control (%)	NC Control (%)	SA Control (%)	GG Control (%)	NEW Control (%)	NE Control (%)
0	0.42 ± 0.003^{aA}	0.43 ± 0.003^{aA}	0.41 ± 0.002^{aA}	0.42 ± 0.003^{aA}	0.43 ± 0.003^{aA}	0.44 ± 0.005^{aA}
3	0.40 ± 0.003^{bB}	0.41 ± 0.002^{aB}	0.39 ± 0.002^{cB}	0.40 ± 0.005^{bB}	0.42 ± 0.002^{aB}	0.43 ± 0.003^{aA}
6	0.38 ± 0.002^{cC}	0.37 ± 0.005^{bC}	0.36 ± 0.004^{bC}	0.38 ± 0.002^{cC}	0.39 ± 0.03^{bC}	0.41 ± 0.003^{aB}
9	0.33 ± 0.002^{dD}	0.35 ± 0.003^{bD}	0.34 ± 0.003^{c}	0.36 ± 0.003^{cD}	0.37 ± 0.004^{bD}	0.39 ± 0.001^{aC}
12	0.30 ± 0.004^{cE}	0.32 ± 0.003^{bE}	0.33 ± 0.002^{bE}	0.34 ± 0.003^{cE}	0.34 ± 0.003^{bE}	0.37 ± 0.002^{aD}

Values are expressed as mean ± SD (n = 3). Different uppercase letters (A–E) within a column and lowercase letters (a–c) within a row indicate significant differences ($p < 0.05$) on the same storage day.

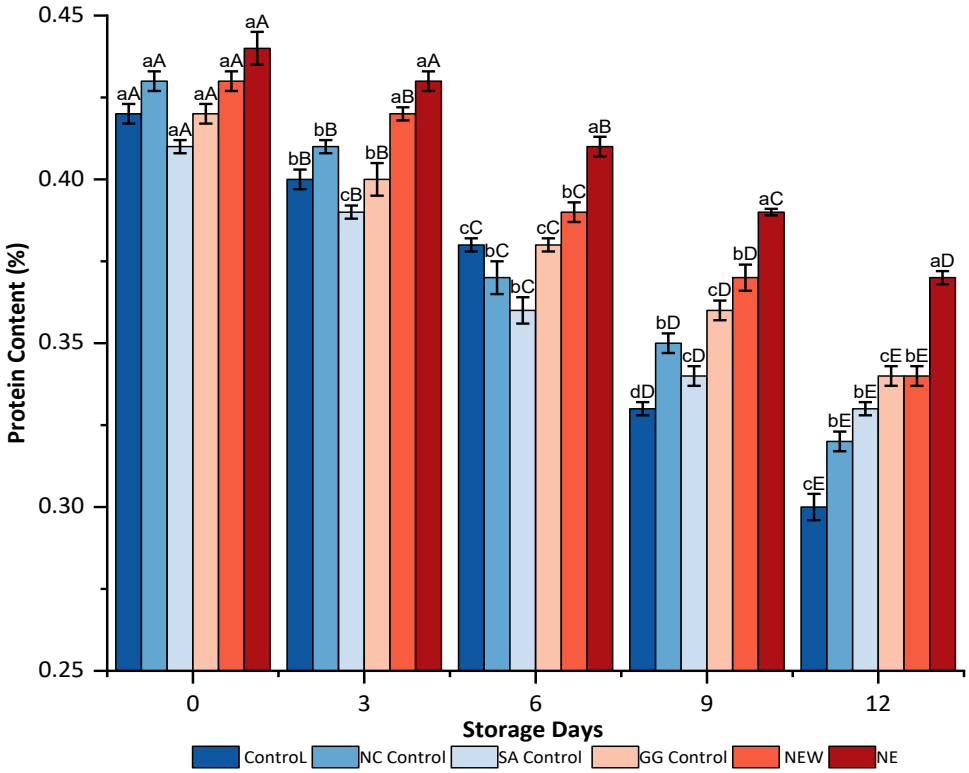

Fig. 4.82 Changes in protein content (%) of fresh-cut apple slices during storage under different packaging materials

Note: NC: Nanocellulose, SA: Sodium alginate, GG: Guar gum, NEW: Nanocellulose, sodium alginate, and guar gum without *Cucumis callosus* peel extract, and NE: Nanocellulose, sodium alginate, and guar gum with *Cucumis callosus* peel extract functional film. Different lowercase letters denote significant differences among treatments within the same storage day, while different uppercase letters denote significant differences within the same treatment across storage days ($p < 0.05$).

Table 4.37 Changes in protein content of fresh-cut pear slices as affected by biodegradable packaging and storage duration (0–12 days)

Day	**Control (%)**	**NC Control (%)**	**SA Control (%)**	**GG Control (%)**	**NEW Control (%)**	**NE Control (%)**
0	0.57 ± 0.005^{cA}	0.58 ± 0.006^{bA}	0.59 ± 0.005^{bA}	0.56 ± 0.003^{cA}	0.58 ± 0.005^{bA}	0.60 ± 0.004^{aA}
3	0.52 ± 0.005^{cB}	0.55 ± 0.006^{bB}	0.56 ± 0.005^{bB}	0.54 ± 0.001^{cB}	0.57 ± 0.004^{bB}	0.59 ± 0.003^{aA}
6	0.49 ± 0.006^{cC}	0.52 ± 0.005^{cC}	0.53 ± 0.004^{bC}	0.51 ± 0.006^{cC}	0.54 ± 0.005^{bB}	0.57 ± 0.007^{aB}
9	0.47 ± 0.005^{dD}	0.50 ± 0.006^{bD}	0.51 ± 0.005^{bD}	0.49 ± 0.001^{cD}	0.53 ± 0.006^{bC}	0.55 ± 0.003^{aC}
12	0.44 ± 0.006^{dE}	0.49 ± 0.005^{cE}	0.50 ± 0.002^{bE}	0.48 ± 0.004^{cE}	0.51 ± 0.007^{bD}	0.54 ± 0.004^{aC}

Values are expressed as mean ± SD (n = 3). Different uppercase letters (A–E) within a column and lowercase letters (a–c) within a row indicate significant differences ($p < 0.05$) on the same storage day.

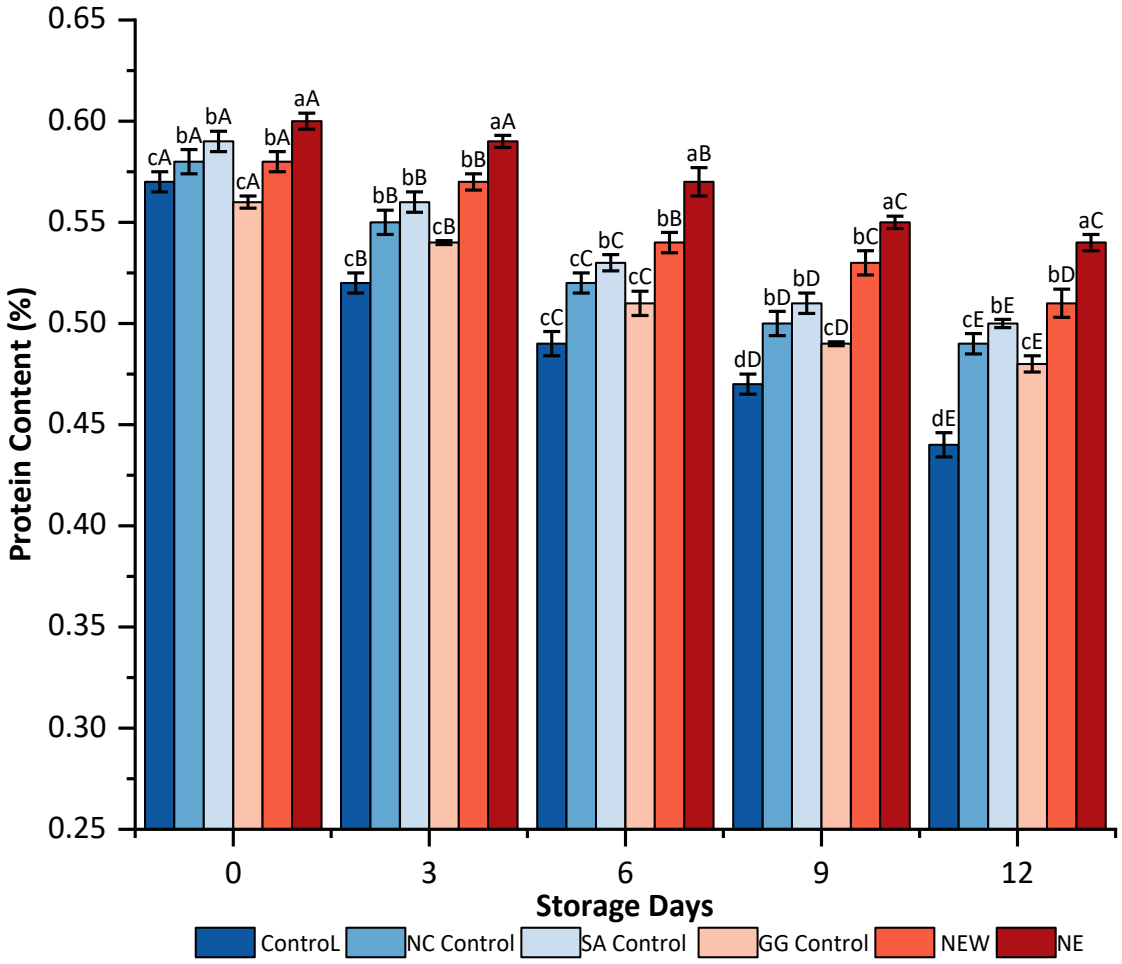

Fig. 4.83 Changes in protein content (%) of fresh-cut pear slices during storage under different packaging materials

Note: NC: Nanocellulose, SA: Sodium alginate, GG: Guar gum, NEW: Nanocellulose, sodium alginate, and guar gum without *Cucumis callosus* peel extract, and NE: Nanocellulose, sodium alginate, and guar gum with *Cucumis callosus* peel extract functional film. Different lowercase letters denote significant differences among treatments within the same storage day, while different uppercase letters denote significant differences within the same treatment across storage days ($p < 0.05$).

4.14.5 Fiber

Crude fiber content of fresh-cut apple and pear slices decreased significantly ($p< 0.05$) with increasing storage duration under refrigerated conditions, as represented in fig. 4.84 and 4.85, indicating progressive degradation of insoluble structural components following minimal processing presented in Tables 4.38 and 4.39. The magnitude of fiber loss was strongly dependent on the type of biodegradable packaging film applied, demonstrating the role of packaging in preserving cell wall integrity and limiting structural deterioration during storage.

In apple slices, crude fiber content at the onset of storage was comparable among all treatments, with values between 2.85 ± 0.04% and 2.87 ± 0.04%, indicating no significant initial variation. As storage advanced, fiber content declined in all samples, however, the decrease was most pronounced in the Control. From day 3 onward, unpackaged apple slices consistently exhibited significantly lower crude fiber content than all packaged samples. By day 12, fiber content in unpackaged apples dropped to 2.55 ± 0.05%, which was significantly lower ($p < 0.05$) than that observed in film-packaged treatments. Apple slices packaged with NC, SA, and GG films retained moderate fiber levels at day 12 (2.67 ± 0.05%, 2.69 ± 0.05%, and 2.61 ± 0.05%, respectively), with no significant differences among these treatments. In contrast, the NEW and NE packaging systems resulted in significantly higher crude fiber retention throughout storage. The NE film was the most effective, preserving 2.80 ± 0.05% crude fiber at day 12, a value significantly higher than all other treatments. Pear slices followed the same overall trend but maintained higher absolute fiber contents than apples due to intrinsic compositional differences. At day 0, crude fiber content ranged narrowly from 3.85 ± 0.11% to 3.87 ± 0.12%, with no significant differences among treatments. With increasing storage time, fiber content decreased significantly ($p < 0.05$) in all pear samples. The unpackaged pear slices experienced the greatest decline, reaching 2.89 ± 0.15% by day 12, which was significantly lower than all packaged treatments. Pear slices treated with NC, SA, and GG films retained intermediate fiber contents (3.42 ± 0.17%, 3.48 ± 0.18%, and 3.38 ± 0.16%, respectively), while slices packaged using NEW and NE films consistently maintained significantly higher crude fiber levels. At the end of storage, NE-treated pear slices retained the highest fiber content (3.78 ± 0.19%), followed by NEW (3.68 ± 0.18%). Overall, these findings demonstrate that biodegradable packaging films substantially influenced crude fiber preservation in fresh-cut fruits. Samples packaged with NEW and NE films maintained significantly higher fiber contents, whereas Controls showed significantly lower values due to enhanced structural degradation. The results underscore the importance of packaging design in preserving dietary fiber and structural quality during refrigerated storage of fresh-cut fruits.

Table 4.38 Evolution of crude fiber content in fresh-cut apple slices packaged using biodegradable films during storage (0–12 days)

Day	Control (%)	NC Control (%)	SA Control (%)	GG Control (%)	NEW Control (%)	NE Control (%)
0	2.85 ± 0.04^{aA}	2.87 ± 0.04^{aA}	2.86 ± 0.04^{aA}	2.85 ± 0.04^{aA}	2.86 ± 0.04^{aA}	2.87 ± 0.04^{aA}

3	2.75 ± 0.04^{bB}	2.78 ± 0.05^{bB}	2.82 ± 0.06^{aB}	2.79 ± 0.05^{bB}	2.83 ± 0.05^{aB}	2.86 ± 0.05^{aA}
6	2.68 ± 0.05^{cC}	2.73 ± 0.04^{bcC}	2.77 ± 0.05^{bC}	2.75 ± 0.05^{cC}	2.79 ± 0.06^{bC}	2.84 ± 0.05^{aB}
9	2.62 ± 0.06^{cD}	2.71 ± 0.05^{bcD}	2.72 ± 0.04^{bD}	2.68 ± 0.05^{cD}	2.76 ± 0.05^{bD}	2.81 ± 0.04^{aC}
12	2.55 ± 0.05^{cE}	2.67 ± 0.05^{bcE}	2.69 ± 0.05^{bE}	2.61 ± 0.05^{cE}	2.71 ± 0.05^{bE}	2.80 ± 0.05^{aC}

Data are expressed as mean ± SD (n = 3). Means within the same column bearing different uppercase letters (A–E) and within the same row bearing different lowercase letters (a–c) differ significantly ($p < 0.05$) on the same storage day.

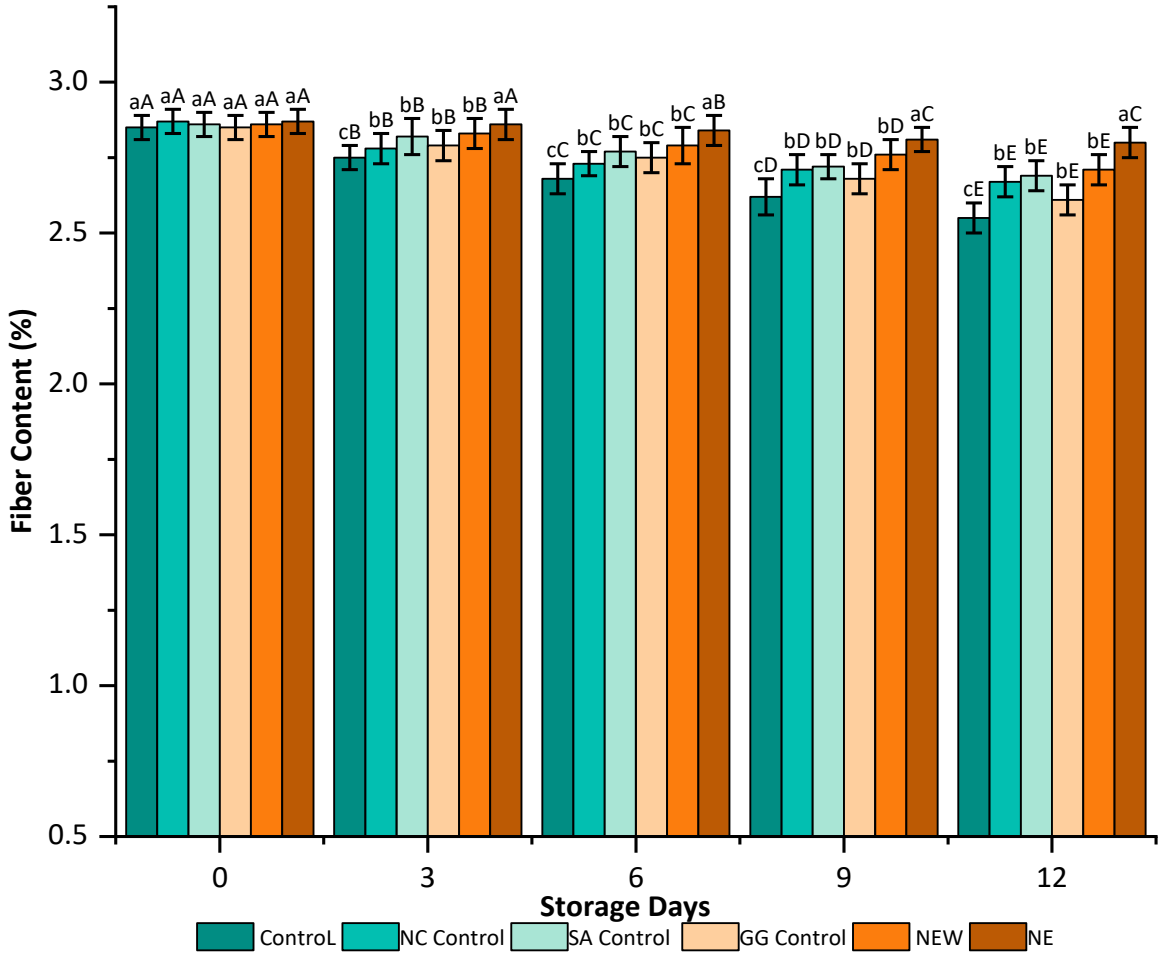

Fig. 4.84 Changes in fiber content (%) of fresh-cut apple slices during storage under different packaging materials

Note: NC: Nanocellulose, SA: Sodium alginate, GG: Guar gum, NEW: Nanocellulose, sodium alginate, and guar gum without *Cucumis callosus* peel extract, and NE: Nanocellulose, sodium alginate, and guar gum with *Cucumis callosus* peel extract functional film. Different lowercase letters denote significant differences among treatments within the same storage day, while

different uppercase letters denote significant differences within the same treatment across storage days ($p < 0.05$).

Table 4.39 Evolution of crude fiber content in fresh-cut pear slices packaged using biodegradable films during storage (0–12 days)

Day	Control (%)	NC Control (%)	SA Control (%)	GG Control (%)	NEW Control (%)	NE Control (%)
0	3.87 ± 0.10^{aA}	3.86 ± 0.11^{aA}	3.87 ± 0.12^{aA}	3.85 ± 0.11^{aA}	3.87 ± 0.12^{aA}	3.86 ± 0.12^{aA}
3	$3.61 \pm 0.1d^{B}$	3.70 ± 0.14^{bB}	$3.72 \pm 0.15b^{B}$	$3.69 \pm 0.13c^{B}$	3.83 ± 0.15^{aB}	3.84 ± 0.16^{aB}
6	$3.52 \pm 0.13d^{C}$	3.63 ± 0.15^{bC}	3.65 ± 0.16^{bC}	3.58 ± 0.14^{cC}	3.79 ± 0.16^{aC}	3.81 ± 0.17^{aC}
9	$3.23 \pm 0.14e^{D}$	$3.51 \pm 0.16d^{D}$	$3.59 \pm 0.17c^{D}$	$3.49 \pm 0.15d^{D}$	3.72 ± 0.17^{bD}	3.79 ± 0.18^{aD}
12	$2.89 \pm 0.15e^{E}$	$3.42 \pm 0.17d^{E}$	$3.48 \pm 0.18d^{E}$	3.38 ± 0.16^{cE}	3.68 ± 0.18^{bE}	3.78 ± 0.19^{aD}

Data are expressed as mean ± SD (n = 3). Means within the same column bearing different uppercase letters (A–E) and within the same row bearing different lowercase letters (a–c) differ significantly ($p < 0.05$) on the same storage day.

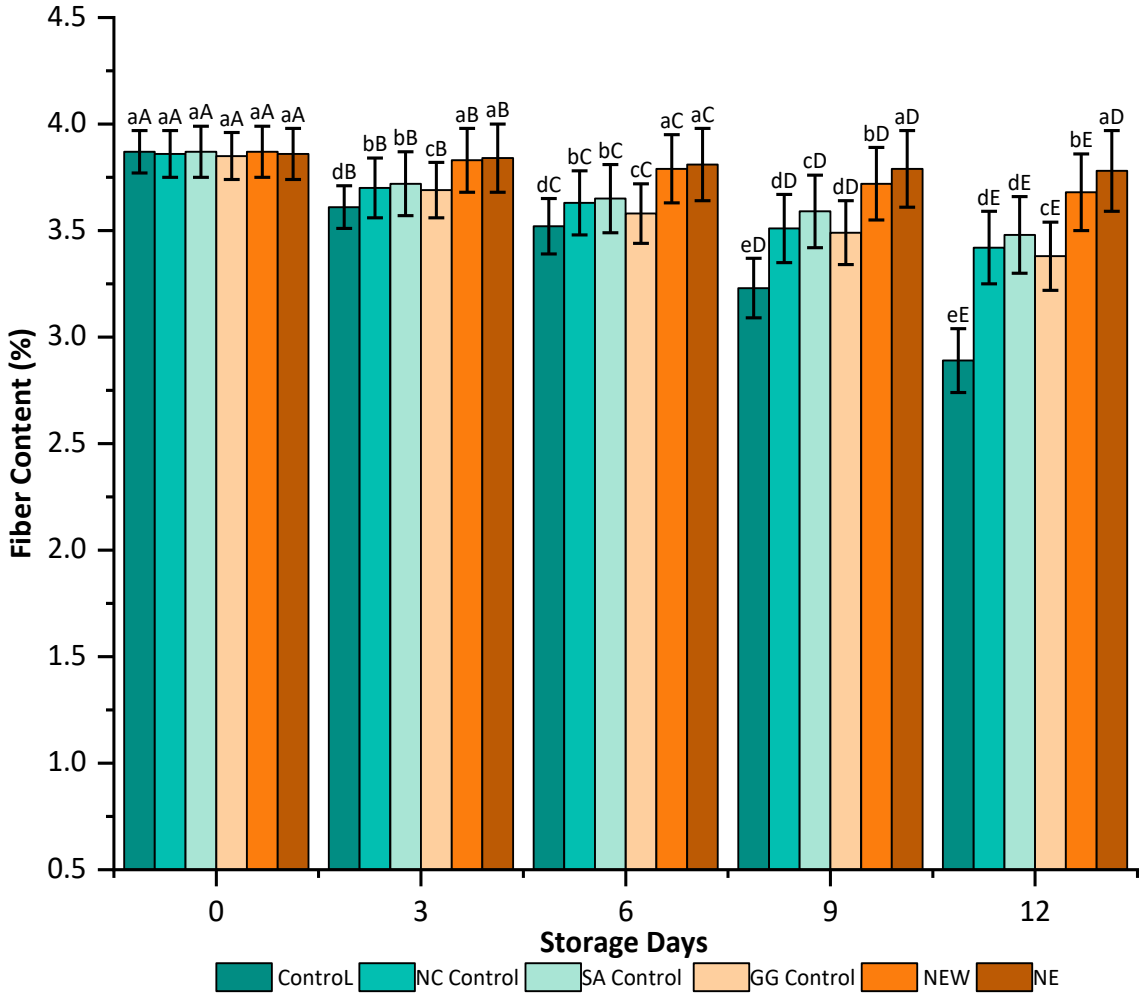

Fig. 4.85 Changes in fiber content (%) of fresh-cut pear slices during storage under different packaging materials

Note: NC: Nanocellulose, SA: Sodium alginate, GG: Guar gum, NEW: Nanocellulose, sodium alginate, and guar gum without *Cucumis callosus* peel extract, and NE: Nanocellulose, sodium alginate, and guar gum with *Cucumis callosus* peel extract functional film. Different lowercase letters denote significant differences among treatments within the same storage day, while different uppercase letters denote significant differences within the same treatment across storage days ($p < 0.05$).

4.15 Physicochemical evaluation of packaged and unpackaged cut apples and pears

4.15.1 Color (L value Lightness)

For fresh-cut apples, unpackaged samples exhibited a pronounced and continuous decline in L* value from 65.21 ± 0.35 on day 0 to 34.69 ± 0.15 by day 12, indicating severe surface darkening due to unrestricted oxygen exposure and enhanced polyphenol oxidase (PPO)–mediated oxidation of phenolic substrates showed in Tables 4.40 and 4.41. The progressive reduction in

lightness across storage days confirms a significant time-dependent browning reaction in control samples in fig 4.86 and 4.87. Among the packaged treatments, nanocellulose (NC), sodium alginate (SA), and guar gum (GG) films significantly ($p < 0.05$) retained higher L* values than the unpackaged control at all storage intervals, with day-12 values of 41.86 ± 0.26, 40.28 ± 0.54, and 41.12 ± 0.65, respectively. However, these films showed comparable lightness values within the same storage day (shared lowercase letters), suggesting similar but limited efficacy in suppressing enzymatic browning. The NEW composite film further improved color retention, maintaining a significantly higher L* value (50.84 ± 0.70) at day 12, indicating synergistic effects of polymer blending that reduced oxygen diffusion and moisture loss. Notably, the NE functional film exhibited the highest L* values throughout storage, decreasing only from 65.81 ± 0.25 to 52.23 ± 0.14, which was significantly ($p < 0.05$) higher than all other treatments on corresponding days, as reflected by distinct lowercase superscripts. This superior lightness retention is attributed to the formation of a dense, uniform surface barrier that restricted oxygen ingress, reduced PPO activity, and stabilized cellular integrity. A similar but more pronounced browning trend was observed in fresh-cut pears, reflecting their higher susceptibility to enzymatic discoloration (Yang et al., 2021). Unpackaged pear slices showed a sharp decline in L* value from 63.40 ± 0.40 on day 0 to 32.86 ± 0.28 by day 12, confirming extensive surface darkening under open storage conditions. Packaged pear samples demonstrated significantly higher L* values ($p < 0.05$) than the control across all storage days, with NC, SA, and GG films retaining moderate lightness (38.24–37.64 at day 12). However, these films did not differ significantly from each other within the same day, indicating comparable barrier performance. In contrast, the NEW composite film markedly delayed lightness loss, maintaining an L* value of 47.24 ± 0.54 at day 12, while the NE functional film preserved the highest lightness (48.62 ± 0.26), which was significantly ($p < 0.05$) higher than all other treatments, as indicated by distinct lowercase lettering in Table X. Overall, apples retained higher L* values than pears under identical treatments, indicating lower browning susceptibility, which may be attributed to differences in phenolic composition, PPO activity, and tissue microstructure. The statistically significant retention of L* values in NE- and NEW-treated samples demonstrates their effectiveness in suppressing enzymatic browning through controlled gas exchange, reduced oxidative stress, and stabilization of surface moisture. The superior performance of the NE film is mechanistically linked to the combined barrier and bioactive effects of the peel extract, which is rich in phenolic compounds and natural antioxidants. These bioactive constituents act as oxygen scavengers and PPO inhibitors, reducing quinone formation and interrupting pigment polymerisation pathways. Additionally,

the peel extract may stabilize cellular membranes and suppress reactive oxygen species (ROS) production, thereby further limiting oxidative discolouration.

Table 4.40 Effect of packaging treatments on L* value (lightness) of fresh-cut apples during storage (0–12 days)

Day	Control (%)	NC Control (%)	SA Control (%)	GG Control (%)	NEW Control (%)	NE Control (%)
0	65.21 ± 0.35^{bA}	65.34 ± 0.42^{bA}	65.18 ± 0.70^{bA}	65.26 ± 0.37^{bA}	65.48 ± 0.74^{bA}	65.81 ± 0.25^{aA}
3	58.34 ± 0.62^{cB}	60.24 ± 0.26^{bB}	59.18 ± 0.64^{bB}	59.86 ± 0.45^{bB}	60.84 ± 0.18^{aB}	61.12 ± 0.70^{aB}
6	49.86 ± 0.48^{cC}	53.48 ± 0.52^{bC}	52.26 ± 0.60^{bC}	53.12 ± 0.51^{bC}	55.92 ± 0.89^{aC}	56.84 ± 0.66^{aC}
9	41.12 ± 0.32^{cD}	46.68 ± 0.40^{bD}	45.24 ± 0.88^{bD}	46.02 ± 0.39^{bD}	52.36 ± 0.60^{aD}	53.68 ± 0.61^{aD}
12	34.69 ± 0.15^{cE}	41.86 ± 0.26^{bE}	40.28 ± 0.54^{bE}	41.12 ± 0.65^{bE}	50.84 ± 0.70^{aE}	52.23 ± 0.14^{aE}

Data are expressed as mean ± SD (n = 3). Means within the same column bearing different uppercase letters (A–E) and within the same row bearing different lowercase letters (a–c) differ significantly ($p < 0.05$) on the same storage day.

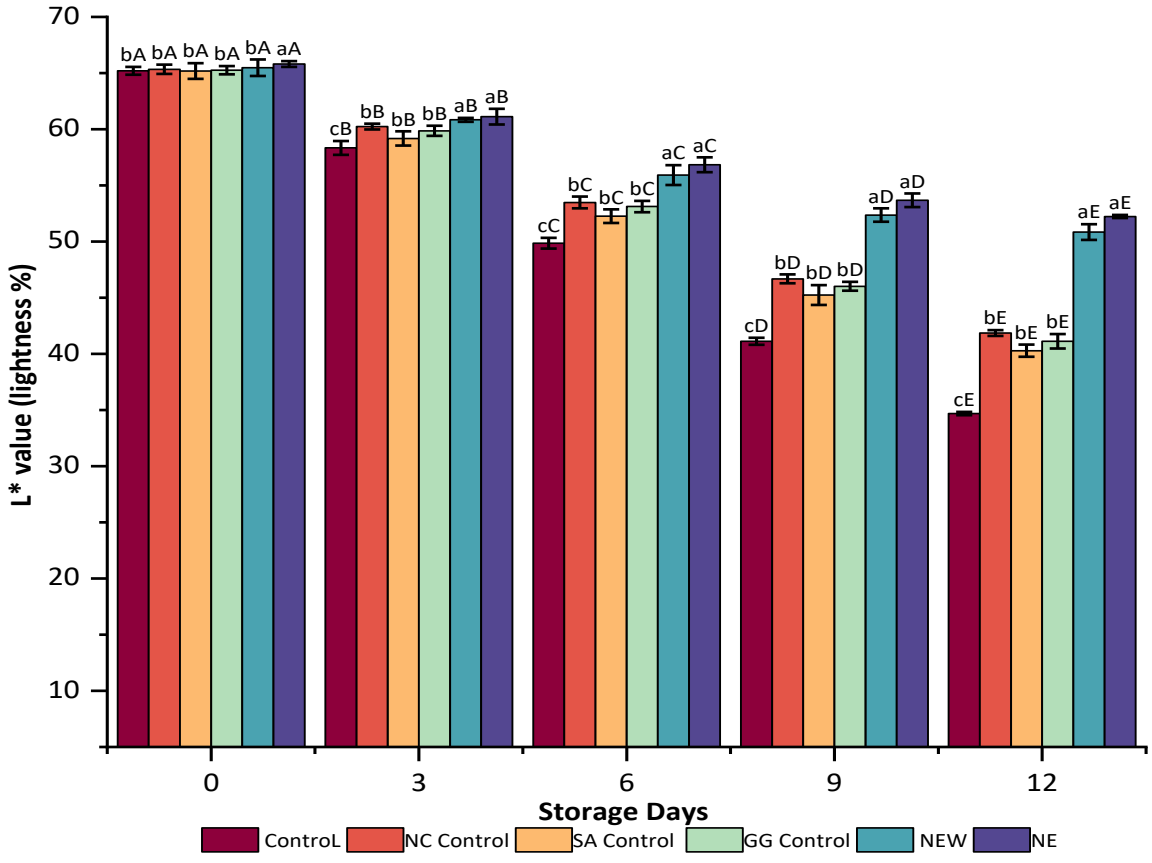

Fig. 4.86 Changes in L value (%) of fresh-cut apple slices during storage under different packaging materials

Note: NC: Nanocellulose, SA: Sodium alginate, GG: Guar gum, NEW: Nanocellulose, sodium alginate, and guar gum without *Cucumis callosus* peel extract, and NE: Nanocellulose, sodium alginate, and guar gum with *Cucumis callosus* peel extract functional film. Different lowercase letters denote significant differences among treatments within the same storage day, while different uppercase letters denote significant differences within the same treatment across storage days ($p < 0.05$).

Table 4.41 Effect of packaging treatments on L* value (lightness) of fresh-cut pears during storage (0–12 days)

Day	**Control (%)**	**NC Control (%)**	**SA Control (%)**	**GG Control (%)**	**NEW Control (%)**	**NE Control (%)**
0	63.40 ± 0.40^{cA}	63.55 ± 0.52^{bA}	63.48 ± 0.46^{bA}	63.60 ± 0.49^{bA}	63.92 ± 0.31^{aA}	64.10 ± 0.28^{aA}
3	55.86 ± 0.61^{cB}	57.92 ± 0.48^{bB}	57.40 ± 0.53^{bB}	57.86 ± 0.45^{bB}	59.84 ± 0.36^{aB}	60.42 ± 0.41^{aB}
6	46.90 ± 0.54^{cC}	49.85 ± 0.60^{bC}	49.26 ± 0.58^{bC}	49.72 ± 0.55^{bC}	52.48 ± 0.62^{aC}	53.36 ± 0.47^{aC}
9	38.74 ± 0.33^{cD}	41.60 ± 0.44^{bD}	41.05 ± 0.50^{bD}	41.52 ± 0.46^{bD}	45.36 ± 0.59^{aD}	46.28 ± 0.38^{aD}
12	32.86 ± 0.28^{cE}	38.24 ± 0.56^{bE}	37.64 ± 0.49^{bE}	38.10 ± 0.52^{bE}	47.24 ± 0.54^{aE}	48.62 ± 0.26^{aE}

Data are expressed as mean ± SD (n = 3). Means within the same column bearing different uppercase letters (A–E) and within the same row bearing different lowercase letters (a–c) differ significantly ($p < 0.05$) on the same storage day.

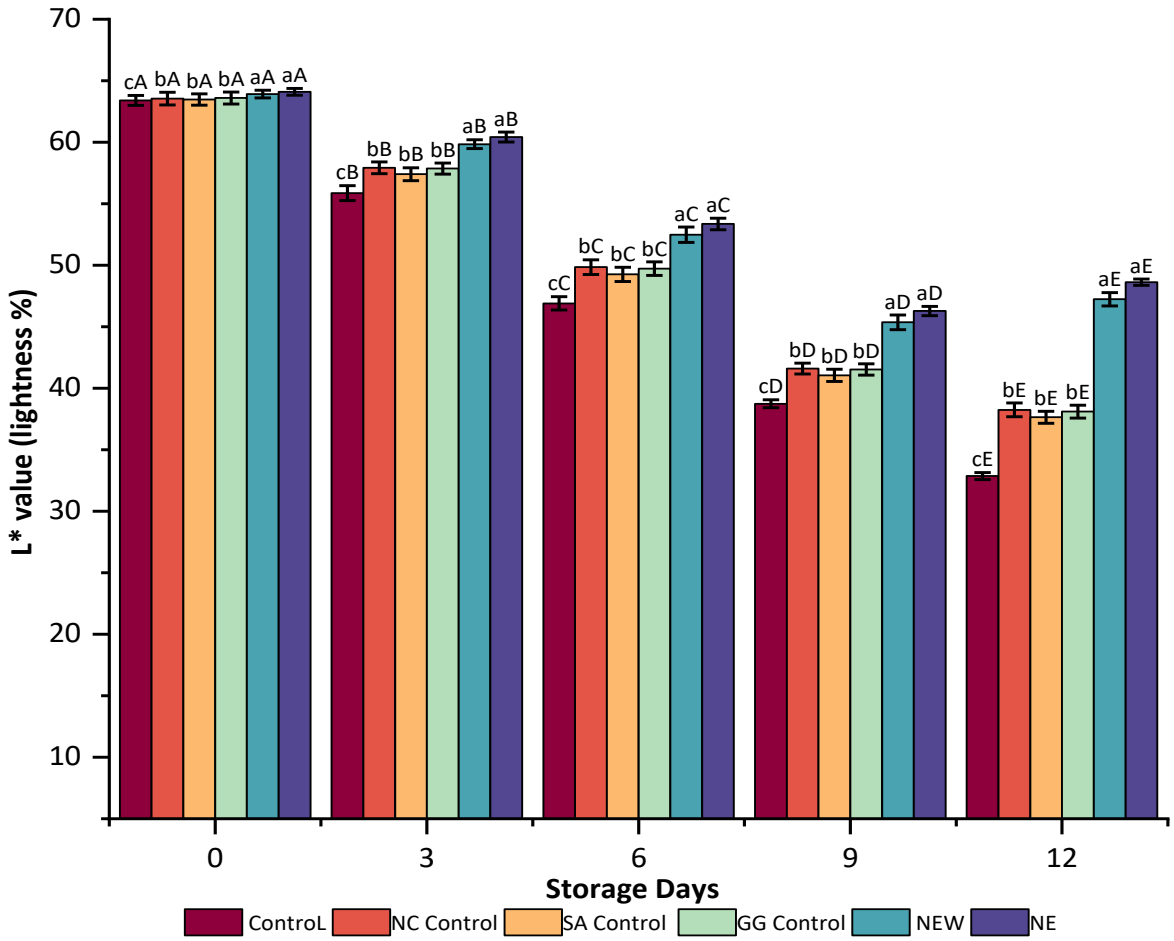

Fig. 4.87 Changes in L value (%) of fresh-cut pear slices during storage under different packaging materials

Note: NC: Nanocellulose, SA: Sodium alginate, GG: Guar gum, NEW: Nanocellulose, sodium alginate, and guar gum without *Cucumis callosus* peel extract, and NE: Nanocellulose, sodium alginate, and guar gum with *Cucumis callosus* peel extract functional film. Different lowercase letters denote significant differences among treatments within the same storage day, while different uppercase letters denote significant differences within the same treatment across storage days ($p < 0.05$).

4.15.2 Color (a value Redness)

For fresh-cut apples, the a* value, representing the development of redness and the progression of enzymatic browning, increased significantly ($p < 0.05$) in all treatments during the 0–12-day storage period (Table 4.42 and 4.43). Unpackaged apple slices exhibited the most pronounced increase in a* values, rising from 61.58 ± 0.77 on day 0 to 57.24 ± 0.35 (day 3), 53.16 ± 0.54 (day 6), 49.82 ± 0.70 (day 9), and finally 48.25 ± 0.88 by day 12, indicating severe surface discoloration as shown in fig. 4.88 and 4.89. The consistent shift in uppercase superscripts (A–E) confirms a statistically significant time-dependent increase in redness. Mechanistically, this

behaviour is attributed to cutting-induced tissue disruption, which collapses intracellular separation of enzymes and substrates and brings phenolic substrates into direct contact with polyphenol oxidase (PPO) in the presence of abundant molecular oxygen. PPO catalyzes the oxidation of o-diphenols to reactive o-quinones, which subsequently undergo non-enzymatic polymerisation into brown pigments, thereby intensifying surface redness and visual browning. Unrestricted oxygen diffusion in unpackaged samples further accelerates these reactions, while concurrent moisture loss and elevated respiration enhance oxidative stress at the cut surface. Among the packaged treatments, nanocellulose (NC), sodium alginate (SA), and guar gum (GG) films significantly ($p < 0.05$) suppressed redness development compared to the unpackaged control across all storage days. At day 12, NC-, SA-, and GG-coated apple slices recorded a* values of 50.86 ± 0.20, 50.12 ± 0.28, and 50.48 ± 0.51, respectively. However, the presence of common lowercase superscripts within the same storage day indicates no significant differences ($p > 0.05$) among these films, suggesting comparable but moderate efficacy. From a mechanistic perspective, these polysaccharide-based films function as semi-permeable barriers that partially restrict oxygen diffusion and reduce surface dehydration, thereby slowing PPO kinetics. Nevertheless, their hydrophilic nature and moderate gas permeability allow residual oxygen ingress, sustaining low-rate enzymatic oxidation and gradual pigment formation over extended storage. The NEW composite film exhibited improved color stability, with a* values decreasing from 61.64 ± 0.19 on day 0 to 59.26 ± 0.45 (day 3), 56.84 ± 0.66 (day 6), 55.12 ± 0.31 (day 9), and 54.12 ± 0.72 by day 12, which were significantly ($p < 0.05$) lower than those of NC, SA, and GG films. This enhanced performance is mechanistically linked to synergistic polymer–polymer interactions within the composite matrix, which increase chain entanglement, reduce free volume, and lower oxygen diffusivity. Improved moisture retention further limits the concentration of phenolic substrates at the surface, collectively suppressing enzymatic browning reactions. Notably, the NE functional film demonstrated the strongest inhibition of redness development throughout storage. Apple slices coated with NE showed only a marginal increase in a* values from 61.63 ± 0.80 on day 0 to 59.48 ± 0.73 (day 3), 57.36 ± 0.52 (day 6), 55.92 ± 0.30 (day 9), and 54.74 ± 0.68 by day 12, which were significantly ($p < 0.05$) lower than all other treatments at corresponding storage intervals. The superior efficacy of the NE film arises from the formation of a dense, uniform physical barrier that restricts oxygen ingress and moderates' moisture migration, and the presence of peel extract–derived bioactive compounds. These phenolic antioxidants act as oxygen scavengers and PPO inhibitors, chelate copper ions at the PPO active site, and reduce quinone intermediates back to their phenolic forms, thereby interrupting pigment polymerisation pathways and

suppressing redness development. A similar but more intense browning pattern was observed in fresh-cut pears, confirming their higher susceptibility to enzymatic discoloration. Unpackaged pear slices showed a sharp increase in a* values from 58.12 ± 0.36 on day 0 to 54.48 ± 0.50 (day 3), 50.36 ± 0.71 (day 6), 47.12 ± 0.17 (day 9), and 45.28 ± 0.82 by day 12, indicating extensive pigment formation under open storage conditions. The greater magnitude of redness development in pears is associated with higher intrinsic PPO activity, softer tissue structure, and weaker cellular integration, which accelerate phenolic oxidation following cutting. Packaged pear samples exhibited significantly ($p < 0.05$) lower a* values across all storage days. NC, SA, and GG films retained moderate redness control, with day-12 values ranging between 47.36 ± 0.85 and 47.86 ± 0.76, although differences among these treatments were not statistically significant within the same day. In contrast, the NEW composite film markedly delayed redness development, maintaining an a* value of 50.24 ± 0.22 at day 12, while the NE functional film preserved the highest color stability, recording 51.36 ± 0.30, which was significantly ($p < 0.05$) higher than all other treatments. Mechanistically, the peel extract incorporated into the NE film suppresses PPO-mediated oxidation, scavenges reactive oxygen species, stabilizes cellular membranes, and moderates metabolic activity, collectively delaying senescence-associated discoloration.

Table 4.42 Effect of packaging treatments on a* value (redness) of fresh-cut apples during storage (0–12 days)

Day	Control (%)	NC Control (%)	SA Control (%)	GG Control (%)	NEW Control (%)	NE Control (%)
0	61.58 ± 0.77^{bA}	61.42 ± 0.64^{cA}	61.36 ± 0.58^{cA}	61.44 ± 0.58^{cA}	61.64 ± 0.19^{aA}	61.63 ± 0.80^{aA}
3	57.24 ± 0.35^{bB}	56.12 ± 0.42^{cB}	56.36 ± 0.38^{cB}	56.24 ± 0.40^{cB}	59.26 ± 0.45^{aB}	59.48 ± 0.73^{aB}
6	53.16 ± 0.54^{bC}	52.14 ± 0.47^{cC}	52.36 ± 0.41^{cC}	52.28 ± 0.44^{cC}	56.84 ± 0.66^{aC}	57.36 ± 0.52^{aC}
9	49.82 ± 0.70^{cD}	50.26 ± 0.36^{bD}	50.04 ± 0.33^{bD}	50.18 ± 0.39^{bD}	55.12 ± 0.31^{aD}	55.92 ± 0.30^{aD}
12	48.25 ± 0.88^{cE}	50.86 ± 0.20^{bE}	50.12 ± 0.28^{bE}	50.48 ± 0.51^{bE}	54.12 ± 0.72^{aE}	54.74 ± 0.68^{aE}

Data are expressed as mean ± SD (n = 3). Means within the same column bearing different uppercase letters (A–E) and within the same row bearing different lowercase letters (a–c) differ significantly ($p < 0.05$) on the same storage day.

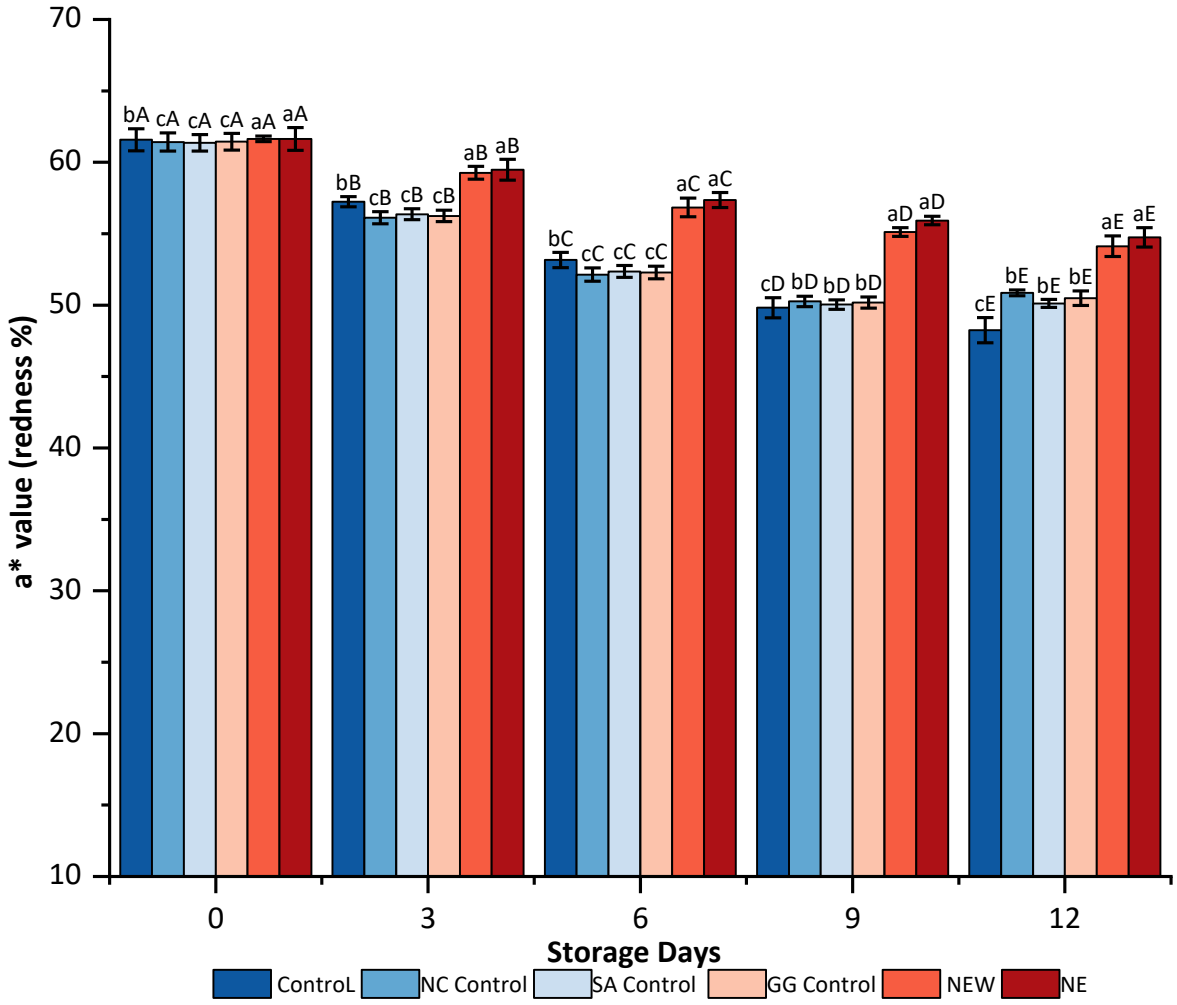

Fig. 4.88 Changes in a* value (%) of fresh-cut apple slices during storage under different packaging materials

Note: NC: Nanocellulose, SA: Sodium alginate, GG: Guar gum, NEW: Nanocellulose, sodium alginate, and guar gum without *Cucumis callosus* peel extract, and NE: Nanocellulose, sodium alginate, and guar gum with *Cucumis callosus* peel extract functional film. Different lowercase letters denote significant differences among treatments within the same storage day, while different uppercase letters denote significant differences within the same treatment across storage days ($p < 0.05$).

Table 4.43 Effect of packaging treatments on a* value (redness) of fresh-cut pears during storage (0–12 days)

Day	Control (%)	NC Control (%)	SA Control (%)	GG Control (%)	NEW Control (%)	NE Control (%)
0	58.12± 0.36^{bA}	57.94 ± 0.41^{cA}	57.88 ± 0.38^{cA}	57.96 ± 0.40^{cA}	58.24 ± 0.29^{aA}	58.30 ± 0.34^{aA}

3	54.48± 0.50^{bB}	53.42 ± 0.47^{cB}	53.56 ± 0.44^{cB}	53.48 ± 0.46^{cB}	55.36 ± 0.33^{aB}	55.72 ± 0.41^{aB}
6	50.36± 0.71^{bC}	49.38 ± 0.58^{cC}	49.52 ± 0.55^{cC}	49.46 ± 0.57^{cC}	52.84 ± 0.37^{aC}	53.18 ± 0.44^{aC}
9	47.12± 0.17^{cD}	47.86 ± 0.76^{bD}	47.36 ± 0.85^{cD}	47.54 ± 0.80^{cD}	51.12 ± 0.26^{aD}	51.68 ± 0.35^{aD}
12	45.28± 0.82^{cE}	47.86 ± 0.76^{bE}	47.36 ± 0.85^{bE}	47.54 ± 0.80^{bE}	50.24 ± 0.22^{aE}	51.36 ± 0.30^{aE}

Data are expressed as mean ± SD (n = 3). Means within the same column bearing different uppercase letters (A–E) and within the same row bearing different lowercase letters (a–c) differ significantly ($p < 0.05$) on the same storage day.

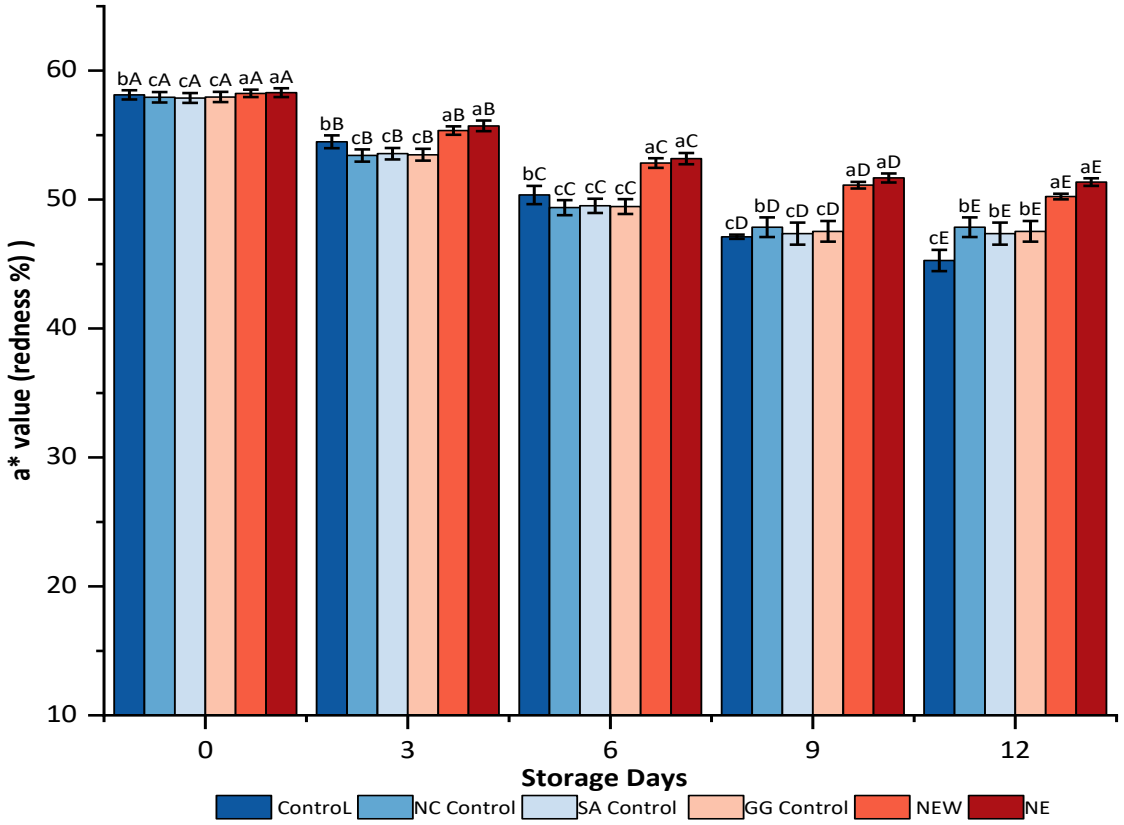

Fig. 4.89 Changes in a* value (%) of fresh-cut pear slices during storage under different packaging materials

Note: NC: Nanocellulose, SA: Sodium alginate, GG: Guar gum, NEW: Nanocellulose, sodium alginate, and guar gum without *Cucumis callosus* peel extract, and NE: Nanocellulose, sodium alginate, and guar gum with *Cucumis callosus* peel extract functional film. Different lowercase letters denote significant differences among treatments within the same storage day, while different uppercase letters denote significant differences within the same treatment across storage days ($p < 0.05$).

4.15.3 Color (b value yellowness)

The b* value, which reflects the degree of yellowness and is closely linked to carotenoid integrity and the progression of enzymatic browning, exhibited a significant ($p < 0.05$) decline in both fresh-cut apples and pears during storage (Table 4.44 and 4.45) and fig. 4.90 and 4.91. A reduction in b* values is indicative of carotenoid degradation, oxidative discoloration, and structural destabilization of chromoplast-associated pigments following tissue injury. In fresh-cut apples, unpackaged samples demonstrated the most pronounced loss of yellowness, with b* values decreasing progressively from 9.05 ± 0.55 on day 0 to 8.24 ± 0.65 (day 3), 7.15 ± 0.41 (day 6), 6.08 ± 0.29 (day 9), and ultimately 4.49 ± 0.41 by day 12. The systematic shift in uppercase superscripts (A–E) confirms a statistically significant time-dependent deterioration in yellowness. This rapid decline is primarily attributed to unrestricted oxygen availability, elevated polyphenol oxidase (PPO) and peroxidase activities, and oxidative degradation of carotenoid pigments, which are highly susceptible to reactive oxygen species generated as a consequence of cutting-induced cellular disruption. Packaged apple samples exhibited significantly ($p < 0.05$) higher b* values than the unpackaged control throughout storage. Among the control films, nanocellulose (NC), sodium alginate (SA), and guar gum (GG) coatings moderately delayed yellowness loss, retaining b* values of 5.86 ± 0.76, 5.74 ± 0.35, and 5.78 ± 0.57, respectively, by day 12. However, the presence of common lowercase superscripts within the same storage day indicates no significant differences ($p > 0.05$) among these treatments, suggesting comparable efficiency in restricting oxygen diffusion and slowing pigment oxidation. The NEW composite film showed enhanced preservation of yellowness, maintaining a significantly ($p < 0.05$) higher b* value of 6.92 ± 0.38 at day 12 compared to NC, SA, and GG treatments. This improvement is attributed to synergistic polymer–polymer interactions that reduced gas permeability, stabilized surface moisture, and slowed oxidative degradation of carotenoids. Notably, the NE functional film demonstrated the greatest retention of b* values across storage, with only a marginal decrease from 9.15 ± 0.31 on day 0 to 7.12 ± 0.40 by day 12. The consistently higher b* values observed for NE-treated samples (distinct lowercase superscripts) indicate superior protection against pigment oxidation. A similar but more severe trend was observed in fresh-cut pears, reflecting their higher susceptibility to pigment degradation. Unpackaged pear slices showed a sharp decline in b* values from 8.62 ± 0.32 on day 0 to 4.12 ± 0.28 by day 12, confirming extensive carotenoid breakdown under open storage conditions. All packaged pear samples retained significantly ($p < 0.05$) higher b* values than the control throughout storage. At day 12, NC-, SA-, and GG-treated pears exhibited b* values ranging from 5.24 ± 0.59 to 5.36 ± 0.52, with no statistically significant differences among these treatments. In contrast, the NEW composite film markedly delayed yellowness

loss in pears, maintaining a b* value of 6.48 ± 0.32 at day 12, while the NE functional film preserved the highest yellowness (6.72 ± 0.34), which was significantly ($p < 0.05$) higher than all other treatments. The superior performance of the NE film is mechanistically associated with peel extract–derived bioactive compounds that function as natural antioxidants and oxygen scavengers. These compounds suppress PPO-mediated oxidation, stabilize carotenoid structures, and reduce reactive oxygen species by delaying pigment degradation.

Table 4.44 Color attribute (b* value – yellowness) of packaged and unpackaged fresh-cut apples during storage

Day	Control (%)	NC Control (%)	SA Control (%)	GG Control (%)	NEW Control (%)	NE Control (%)
0	9.05 ± 0.55^{bA}	9.02 ± 0.19^{bA}	9.00 ± 0.80^{bA}	9.08 ± 0.73^{b}A	9.12 ± 0.86^{aA}	9.15 ± 0.31^{aA}
3	8.24 ± 0.65^{cB}	8.52 ± 0.38^{bB}	8.44 ± 0.27^{bB}	8.48 ± 0.46^{b}B	8.72 ± 0.29^{aB}	8.86 ± 0.80^{aB}
6	7.15 ± 0.41^{cC}	7.62 ± 0.62^{bC}	7.54 ± 0.41^{bC}	7.58 ± 0.33^{b}C	8.12 ± 0.45^{aC}	8.26 ± 0.76^{aC}
9	6.08 ± 0.29^{cD}	6.82 ± 0.50^{bD}	6.74 ± 0.28^{bD}	6.78 ± 0.15^{b}D	7.46 ± 0.34^{aD}	7.64 ± 0.65^{aD}
12	4.49 ± 0.41^{cE}	5.86 ± 0.76^{bE}	5.74 ± 0.35^{bE}	5.78 ± 0.57^{bE}	6.92 ± 0.38^{aE}	7.12 ± 0.40^{aE}

Data are expressed as mean ± SD (n = 3). Means within the same column bearing different uppercase letters (A–E) and within the same row bearing different lowercase letters (a–c) differ significantly ($p < 0.05$) on the same storage day.

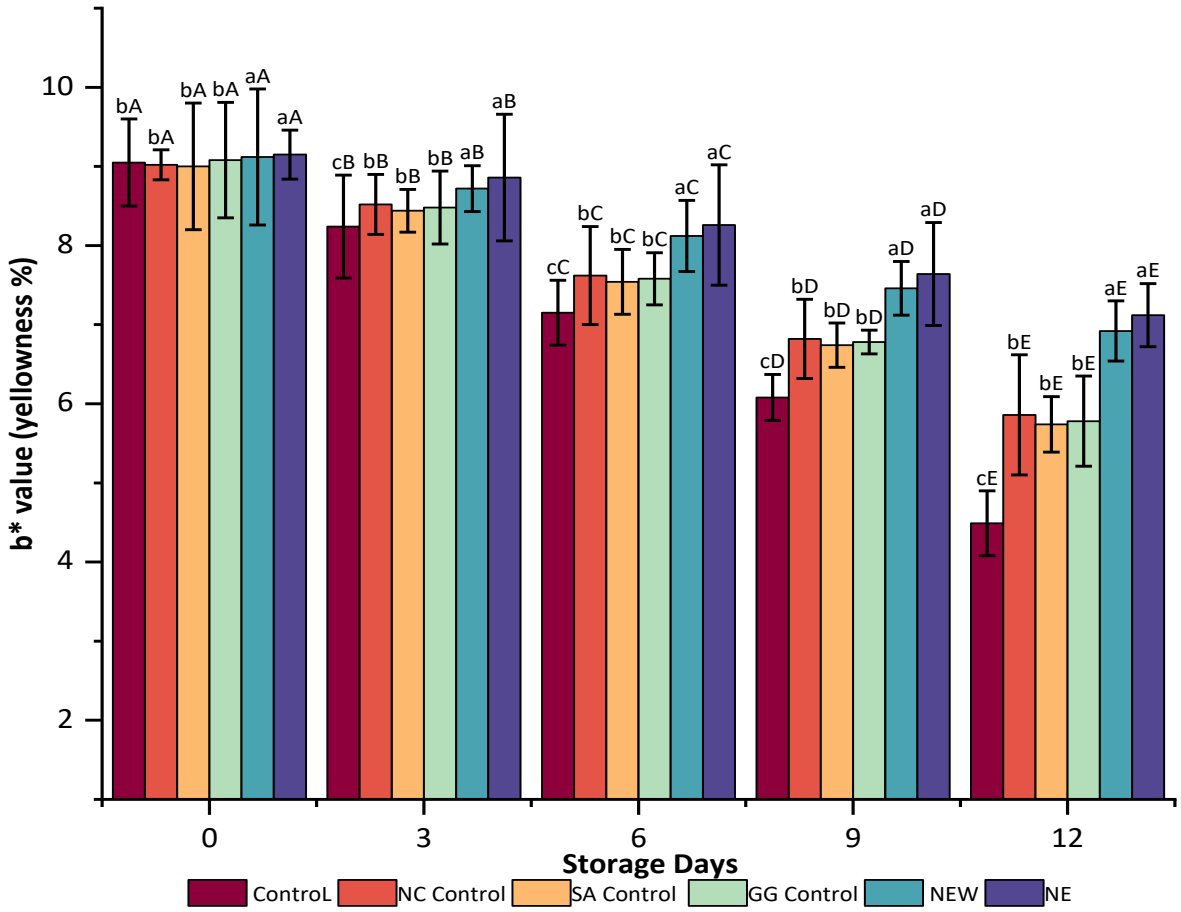

Fig. 4.90 Changes in b value (%) of fresh-cut apple slices during storage under different packaging materials

Note: NC: Nanocellulose, SA: Sodium alginate, GG: Guar gum, NEW: Nanocellulose, sodium alginate, and guar gum without *Cucumis callosus* peel extract, and NE: Nanocellulose, sodium alginate, and guar gum with *Cucumis callosus* peel extract functional film. Different lowercase letters denote significant differences among treatments within the same storage day, while different uppercase letters denote significant differences within the same treatment across storage days ($p < 0.05$).

Table 4.45 Color attribute (b* value – yellowness) of packaged and unpackaged fresh-cut pears during storage

Day	Control (%)	NC Control (%)	SA Control (%)	GG Control (%)	NEW Control (%)	NE Control (%)
0	8.62 ± 0.32^{bA}	8.60 ± 0.76^{bA}	8.58 ± 0.85^{bA}	8.64 ± 0.77^{bA}	8.70 ± 0.19^{aA}	8.74 ± 0.80^{aA}
3	7.86 ± 0.89^{cB}	8.10 ± 0.53^{bB}	8.02 ± 0.33^{bB}	8.06 ± 0.43^{bB}	8.34 ± 0.80^{aB}	8.48 ± 0.58^{aB}
6	6.74 ± 0.56^{cC}	7.22 ± 0.38^{bC}	7.14 ± 0.77^{bC}	7.18 ± 0.38^{bC}	7.76 ± 0.44^{aC}	7.94 ± 0.37^{aC}

9	5.62 ± 0.70^{cD}	6.28 ± 0.22^{bD}	6.20 ± 0.41^{bD}	6.24 ± 0.89^{bD}	6.92 ± 0.47^{aD}	7.14 ± 0.65^{aD}
12	4.12 ± 0.28^{cE}	5.36 ± 0.52^{bE}	5.24 ± 0.59^{bE}	5.28 ± 0.30^{bE}	6.48 ± 0.32^{aE}	6.72 ± 0.34^{aE}

Data are expressed as mean ± SD (n = 3). Means within the same column bearing different uppercase letters (A–E) and within the same row bearing different lowercase letters (a–c) differ significantly ($p < 0.05$) on the same storage day.

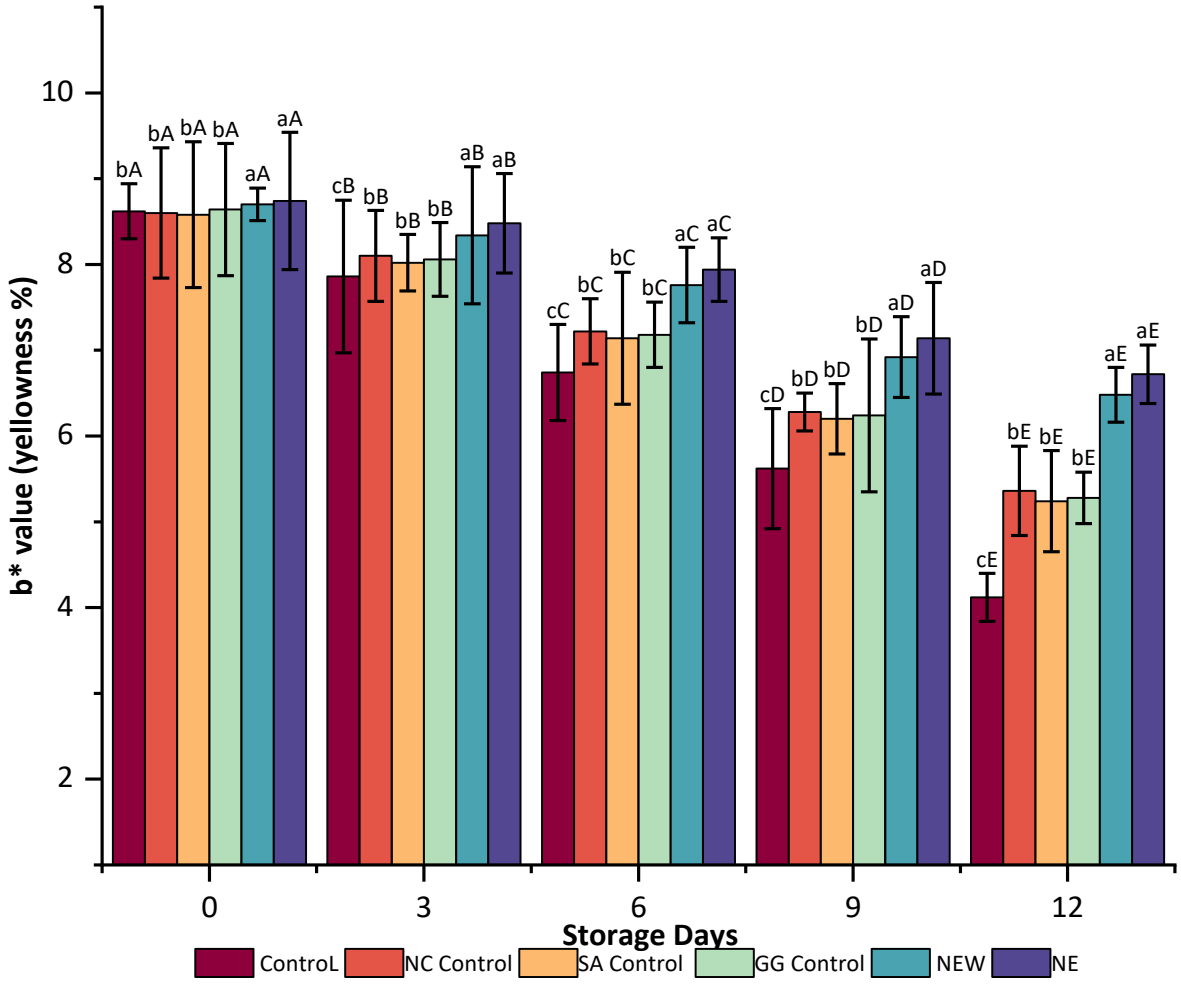

Fig. 4.91 Changes in b value (%) of fresh-cut pear slices during storage under different packaging materials

Note: NC: Nanocellulose, SA: Sodium alginate, GG: Guar gum, NEW: Nanocellulose, sodium alginate, and guar gum without *Cucumis callosus* peel extract, and NE: Nanocellulose, sodium alginate, and guar gum with *Cucumis callosus* peel extract functional film. Different lowercase letters denote significant differences among treatments within the same storage day, while different uppercase letters denote significant differences within the same treatment across storage days ($p < 0.05$).

4.15.4 Browning index (%)

The browning index is a critical quality parameter for minimally processed fruits, as it directly reflects enzymatic oxidation and surface discoloration during storage. In the present study, the unpackaged samples exhibited a significantly ($p < 0.05$) higher browning index throughout storage in fig. 4.92 and 4.93, with cut apples reaching 81.45 ± 0.33% and cut pears 58.32 ± 0.36% by day 12, primarily due to unrestricted oxygen exposure, moisture loss, and rapid activation of polyphenol oxidase (PPO), as shown in Tables 4.46 and 4.47. Among the control films, NC control apples (79.64 ± 0.22%) and NC film pears (52.15 ± 0.43%) showed comparatively high browning, which may be attributed to the hydrophilic nature and higher oxygen permeability of nanocellulose-rich matrices, offering limited resistance to oxidative reactions. In contrast, GG control apples (50.61 ± 0.43%) and GG film pears (41.10 ± 0.60%) exhibited significantly ($p < 0.05$) lower browning, likely due to improved moisture retention and reduced oxygen diffusion associated with the dense film-forming and viscous characteristics of gum-based polymers. Notably, the NEW composite film further suppressed browning in both apples (29.42 ± 0.24%) and pears (29.85 ± 0.27%), suggesting synergistic polymer interactions that enhanced film compactness and stabilized the fruit surface microenvironment. The NE functional film demonstrated the lowest browning index, with values of 11.84 ± 0.28% in apples and 17.60 ± 0.20% in pears, which were significantly ($p < 0.05$) lower than all other treatments. This superior antibrowning efficacy is attributed to the combined effects of strong oxygen-barrier properties, moisture regulation, and the presence of functional bioactive components that can scavenger reactive oxygen species and inhibit PPO-mediated phenolic oxidation.

Table 4.46 Changes in Browning Index (%) of Packaged and Unpackaged Fresh-Cut Apples

Day	**Control (%)**	**NC Control (%)**	**SA Control (%)**	**GG Control (%)**	**NEW Control (%)**	**NE Control (%)**
0	0.00 ± 0.00^{aE}	0.00 ± 0.00^{aE}	0.00 ± 0.00^{aE}	0.00 ± 0.00^{aE}	0.00 ± 0.00^{aE}	0.00 ± 0.00^{aE}
3	22.45 ± 0.28^{aD}	18.79 ± 0.47^{bD}	12.38 ± 0.29^{cD}	10.70 ± 0.64^{dD}	7.51 ± 0.18^{eD}	3.29 ± 0.12^{fD}
6	45.82 ± 0.35^{aC}	41.73 ± 0.11^{bC}	28.18 ± 0.32^{cC}	23.64 ± 0.22^{dC}	15.36 ± 0.44^{eC}	7.16 ± 0.20^{fC}
9	68.20 ± 0.34^{aB}	63.80 ± 0.34^{bB}	39.61 ± 0.31^{cB}	34.22 ± 0.17^{dB}	22.75 ± 0.23^{eB}	9.55 ± 0.10^{fB}
12	81.45 ± 0.33^{aA}	79.64 ± 0.22^{bA}	50.61 ± 0.43^{cA}	44.21 ± 0.31^{dA}	29.42 ± 0.24^{eA}	11.84 ± 0.28^{fA}

Data are expressed as mean ± SD (n = 3). Means within the same column bearing different uppercase letters (A–E) and within the same row bearing different lowercase letters (a–c) differ significantly ($p < 0.05$) on the same storage day.

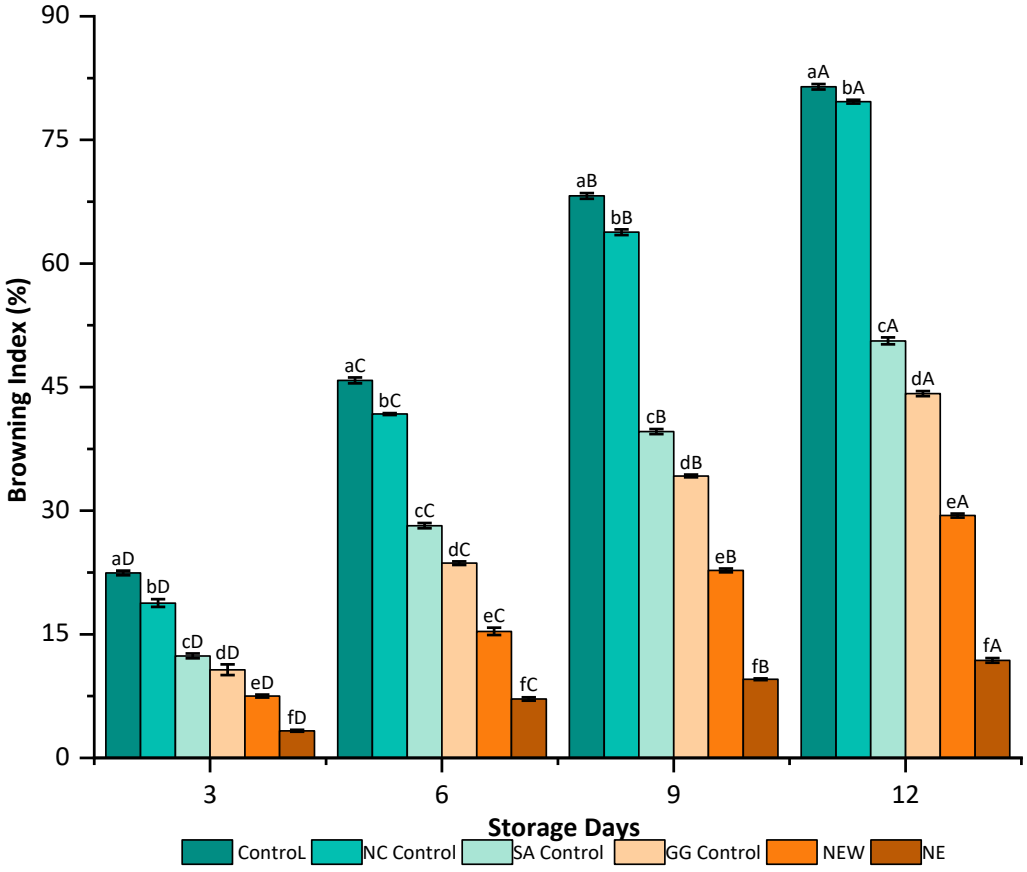

Fig. 4.92 Changes in Browning Index (%) of fresh-cut apple slices during storage under different packaging materials

Note: NC: Nanocellulose, SA: Sodium alginate, GG: Guar gum, NEW: Nanocellulose, sodium alginate, and guar gum without *Cucumis callosus* peel extract, and NE: Nanocellulose, sodium alginate, and guar gum with *Cucumis callosus* peel extract functional film. Different lowercase letters denote significant differences among treatments within the same storage day, while different uppercase letters denote significant differences within the same treatment across storage days ($p < 0.05$).

Table 4.47 Changes in Browning Index (%) of Packaged and Unpackaged Fresh-Cut Pears

Day	Control (%)	NC Control (%)	SA Control (%)	GG Control (%)	NEW Control (%)	NE Control (%)
0	0.00 ± 0.00^{aE}	0.00 ± 0.00^{aE}	0.00 ± 0.00^{aE}	0.00 ± 0.00^{aE}	0.00 ± 0.00^{aE}	0.00 ± 0.00^{aE}

3	12.80 ± 0.22^{aD}	10.90 ± 0.11^{bD}	9.40 ± 0.20^{cD}	8.25 ± 0.19^{dD}	6.10 ± 0.55^{eD}	3.95 ± 0.32^{fD}
6	28.40 ± 0.28^{aC}	24.10 ± 0.15^{bC}	21.60 ± 0.63^{cC}	19.50 ± 0.32^{dC}	14.85 ± 0.20^{eC}	9.60 ± 0.16^{fC}
9	43.55 ± 0.34^{aB}	38.20 ± 0.31^{bB}	33.75 ± 0.29^{cB}	30.55 ± 0.27^{dB}	22.40 ± 0.25^{eB}	13.95 ± 0.18^{fB}
12	58.32 ± 0.36^{aA}	52.15 ± 0.43^{bA}	46.40 ± 0.31^{cA}	41.10 ± 0.60^{dA}	29.85 ± 0.27^{eA}	17.60 ± 0.20^{fA}

Data are expressed as mean ± SD (n = 3). Means within the same column bearing different uppercase letters (A–E) and within the same row bearing different lowercase letters (a–c) differ significantly ($p < 0.05$) on the same storage day.

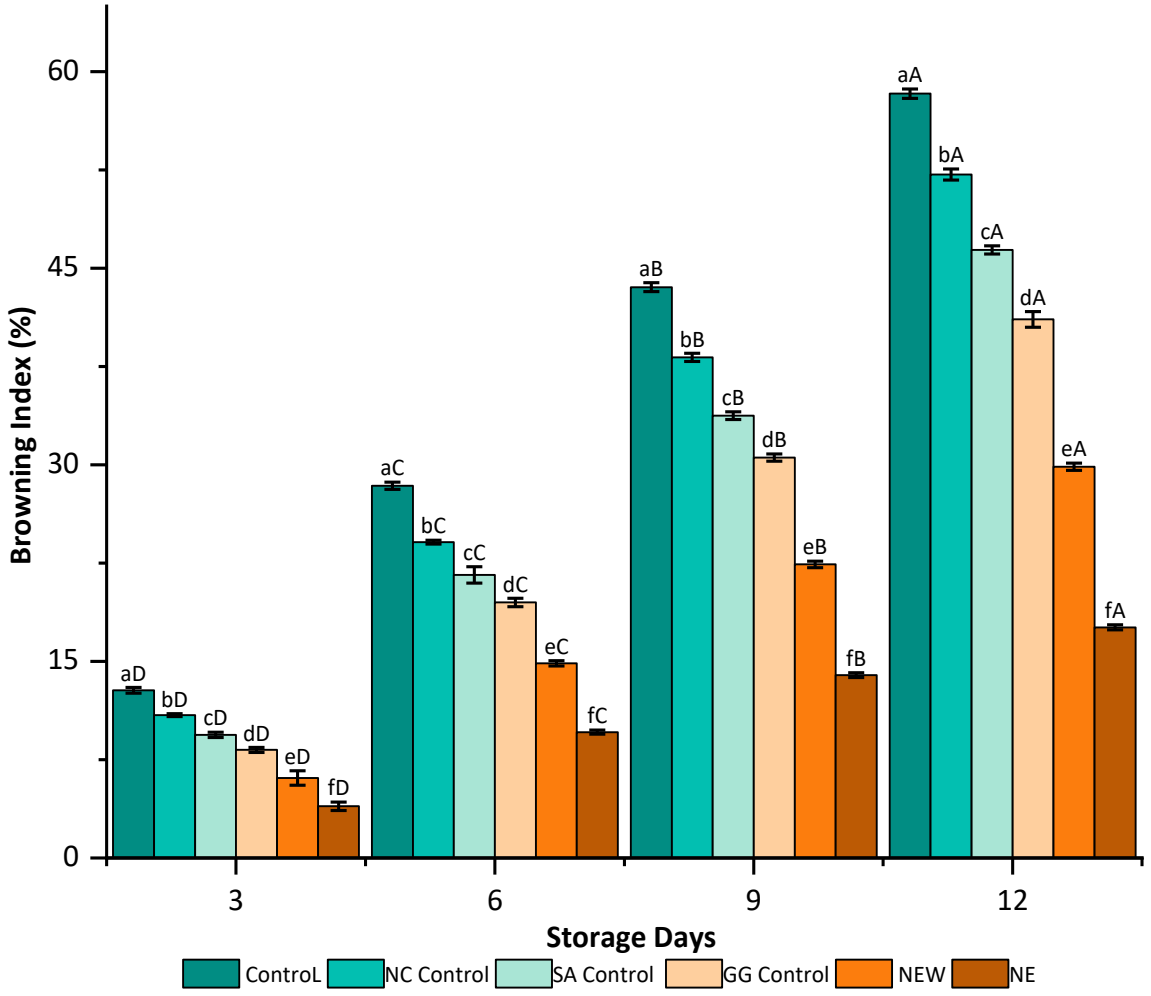

Fig. 4.93 Changes in Browning Index (%) of fresh-cut pear slices during storage under different packaging materials

Note: NC: Nanocellulose, SA: Sodium alginate, GG: Guar gum, NEW: Nanocellulose, sodium alginate, and guar gum without *Cucumis callosus* peel extract, and NE: Nanocellulose, sodium alginate, and guar gum with *Cucumis callosus* peel extract functional film. Different lowercase

letters denote significant differences among treatments within the same storage day, while different uppercase letters denote significant differences within the same treatment across storage days ($p < 0.05$).

4.15.5 Weight loss (%)

Weight loss is a key postharvest quality parameter reflecting water vapor transfer, transpiration rate, and tissue dehydration in fresh-cut fruits. Apple samples showed a progressive, treatment-dependent change in weight during storage, with weight-loss values ranging from 0.00 to 15.32% over 12 days, as shown in fig. 4.94 and 4.95. At day 0, all treatments exhibited 0.00% weight loss (3.00 g remaining) with no significant differences shown in Tables 4.48 and 4.49. By day 3, weight loss increased to 8.12% (2.76 g) in unpackaged apples, which was significantly ($p < 0.05$) higher than NC 7.00% (2.79 g), SA 6.80% (2.80 g), GG 6.70% (2.80 g), NEW 6.55% (2.80 g), and NE 6.42% (2.81 g) coated samples. On day 6, unpackaged apples showed a further increase to 11.20% (2.66 g), remaining significantly ($p < 0.05$) higher than NC 8.60% (2.74 g), SA 8.20% (2.75 g), GG 8.00% (2.76 g), NEW 7.60% (2.77 g), and NE 7.10% (2.79 g) treatments. By day 9, the highest weight loss was again observed in unpackaged apples 13.50% (2.60 g), whereas coated samples exhibited 9.60% (2.71 g) for NC, 9.20% (2.72 g) for SA, 8.80% (2.74 g) for GG, 8.30% (2.75 g) for NEW, and 7.80% (2.77 g) for NE, all being significantly ($p < 0.05$) lower than the unpackaged control. At the end of storage (day 12), unpackaged apples recorded the significantly ($p < 0.05$) higher weight loss of 15.32% (2.54 g remaining), whereas coated samples showed reduced losses of 10.26% (2.69 g) for NC, 9.90% (2.70 g) for SA, 9.50% (2.72 g) for GG, 9.10% (2.73 g) for NEW, and 8.70% (2.74 g) for NE. Overall, among all treatments, NE-coated apples exhibited significantly ($p < 0.05$) lower weight loss and higher weight retention, while unpackaged apples consistently showed significantly ($p < 0.05$) higher deterioration as compared to other treatments. Pear samples exhibited a pronounced, treatment-dependent increase in weight loss during storage, with values ranging from 0.00 to 29.92% over the 12 days. At day 0, all treatments showed 0.00% weight loss (3.00 g remaining) with no significant differences. By day 3, unpackaged pears recorded a weight loss of 8.25% (2.75 g), which was significantly ($p < 0.05$) higher than NC control 7.10% (2.79 g), SA control 6.42% (2.81 g), GG control 5.98% (2.82 g), NEW composite 4.80% (2.86 g), and NE functional film 3.55% (2.89 g). On day 6, weight loss increased sharply in unpackaged pears to 16.40% (2.51 g), remaining significantly ($p < 0.05$) higher than NC control 14.30% (2.57 g), SA control 12.90% (2.61 g), GG control 12.10% (2.64 g), NEW composite 9.65% (2.71 g), and NE functional film 6.95% (2.79 g). By day 9, unpackaged pears exhibited the highest weight loss of 22.85% (2.32 g), whereas coated samples showed significantly lower

losses of 20.42% (2.39 g) for NC, 18.20% (2.45 g) for SA, 16.95% (2.49 g) for GG, 13.42% (2.60 g) for NEW composite, and 9.88% (2.70 g) for NE functional film. At the end of storage (day 12), unpackaged pears recorded the significantly ($p < 0.05$) higher weight loss of 29.92% (2.10 g remaining), while coated pears showed reduced losses of 27.15% (2.19 g) for NC control, 23.74% (2.29 g) for SA control, 22.21% (2.33 g) for GG control, 17.45% (2.48 g) for NEW composite, and 12.55% (2.62 g) for NE functional film. Overall, among all treatments, NE functional film exhibited significantly ($p < 0.05$) lower weight loss and the highest weight retention, whereas unpackaged pears consistently showed significantly ($p < 0.05$) higher deterioration compared to coated samples throughout storage. Unpackaged samples exhibited a significantly ($p < 0.05$) higher weight loss during storage, reaching 15.32 ± 0.30% in cut apples and 29.92 ± 0.41% in cut pears by day 12, primarily due to unrestricted moisture diffusion and enhanced respiration associated with cellular disruption after cutting. Among the control films, nanocellulose-based packaging resulted in comparatively higher weight loss (10.26 ± 0.23% in apples and 27.15 ± 0.30% in pears), which may be attributed to the hydrophilic nature and moderate water vapor permeability of cellulose-rich matrices. In contrast, sodium alginate and guar gum control films significantly ($p < 0.05$) reduced moisture loss in both fruits, with weight loss values of 9.90 ± 0.25% and 9.50 ± 0.44% in apples, and 23.74 ± 0.18% and 22.21 ± 0.26% in pears, respectively, indicating improved moisture retention associated with enhanced polymer chain entanglement and film continuity. The NEW composite film further limited weight loss to 9.10 ± 0.34% in apples and 17.45 ± 0.43% in pears, suggesting synergistic interactions among polymeric constituents that reduced water vapor transmission. The NE functional film exhibited the lowest weight loss, with values of 8.70 ± 0.22% for apples and 12.55 ± 0.20% for pears, which were significantly ($p < 0.05$) lower than those of all other treatments. This effect is attributed to the formation of a dense interfacial barrier, enhanced water-binding capacity, and reduced transpiration rates, collectively contributing to improved moisture retention and delayed dehydration-induced quality deterioration in fresh-cut fruits. The reduction in weight of fresh-cut fruits is primarily attributed to moisture loss and the depletion of certain nutrients, which are utilized during the elevated respiration process triggered by mechanical damage incurred during cutting (Tao et al., 2019).

Table 4.48 Changes in weight loss (%) of Fresh-Cut Apples Stored under Different Packaging Conditions

Day	**Control (%)**	**NC Control (%)**	**SA Control (%)**	**GG Control (%)**	**NEW Control (%)**	**NE Control (%)**

0	0.00 ± 0.00^{aE}	0.00 ± 0.00^{aE}	0.00 ± 0.00^{aE}	0.00 ± 0.00^{aE}	0.00 ± 0.00^{aE}	0.00 ± 0.00^{aE}
3	8.12 ± 0.20^{aD}	7.00 ± 0.58^{bD}	6.80 ± 0.77^{cD}	6.70 ± 0.17^{dD}	6.55 ± 0.47^{eD}	6.42 ± 0.26^{fD}
6	11.20 ± 0.66^{aC}	8.60 ± 0.34^{bC}	8.20 ± 0.21^{cC}	8.00 ± 0.21^{dC}	7.60 ± 0.20^{eC}	7.10 ± 0.59^{fC}
9	13.50 ± 0.17^{aB}	9.60 ± 0.14^{bB}	9.20 ± 0.33^{cB}	8.80 ± 0.23^{dB}	8.30 ± 0.22^{eB}	7.80 ± 0.40^{fB}
12	15.32 ± 0.30^{aA}	10.26 ± 0.23^{bA}	9.90 ± 0.25^{cA}	9.50 ± 0.44^{dA}	9.10 ± 0.34^{eA}	8.70 ± 0.22^{fA}

Values are expressed as mean ± SD (n = 3). Means within the same column bearing different uppercase letters (A–E) and within the same row bearing different lowercase letters (a–f) differ significantly ($p < 0.05$) on the same storage day.

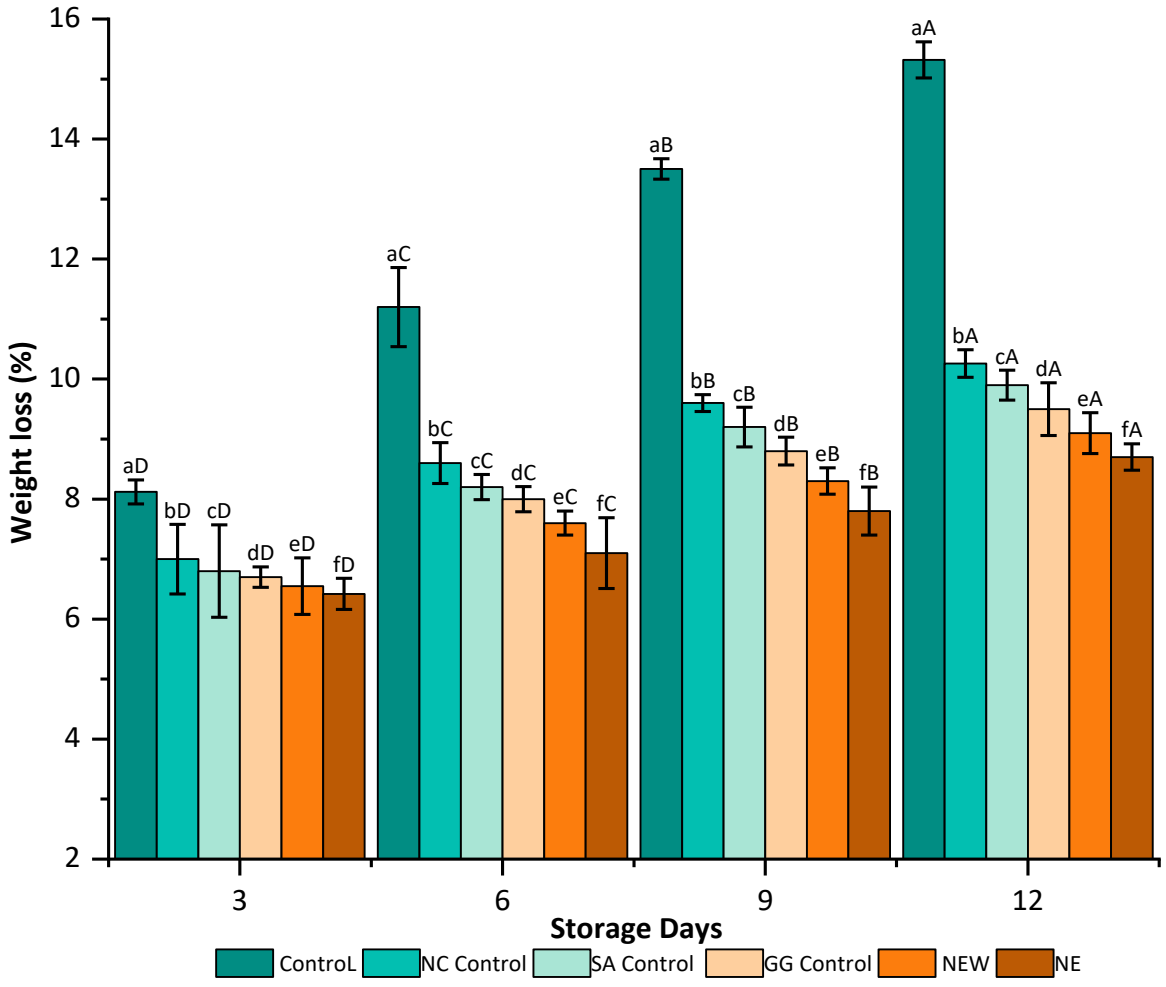

Fig. 4.94 Changes in Weight loss (%) of fresh-cut apple slices during storage under different packaging materials

Note: NC: Nanocellulose, SA: Sodium alginate, GG: Guar gum, NEW: Nanocellulose, sodium alginate, and guar gum without *Cucumis callosus* peel extract, and NE: Nanocellulose, sodium alginate, and guar gum with *Cucumis callosus* peel extract functional film. Different lowercase letters denote significant differences among treatments within the same storage day, while different uppercase letters denote significant differences within the same treatment across storage days ($p < 0.05$).

Table 4.49 Changes in weight loss (%) of Fresh-Cut pears Stored under Different Packaging Conditions

Day	**Control (%)**	**NC Control (%)**	**SA Control (%)**	**GG Control (%)**	**NEW Control (%)**	**NE Control (%)**
0	0.00 ± 0.00^{aE}	0.00 ± 0.00^{aE}	0.00 ± 0.00^{aE}	0.00 ± 0.00^{aE}	0.00 ± 0.00^{aE}	0.00 ± 0.00^{aE}
3	8.25 ± 0.47^{aD}	7.10 ± 0.65^{bD}	6.42 ± 0.76^{cD}	5.98 ± 0.13^{dD}	4.80 ± 0.22^{eD}	3.55 ± 0.11^{fD}
6	16.40 ± 0.39^{aC}	14.30 ± 0.22^{bC}	12.90 ± 0.20^{cC}	12.10 ± 0.41^{dC}	9.65 ± 0.17^{eC}	6.95 ± 0.35^{fC}
9	22.85 ± 0.80^{aB}	20.42 ± 0.57^{bB}	18.20 ± 0.94^{cB}	16.95 ± 0.32^{dB}	13.42 ± 0.27^{eB}	9.88 ± 0.18^{fB}
12	29.92 ± 0.41^{aA}	27.15 ± 0.30^{bA}	23.74 ± 0.18^{cA}	22.21 ± 0.26^{dA}	17.45 ± 0.43^{eA}	12.55 ± 0.20^{fA}

Values are expressed as mean ± SD (n = 3). Means within the same column bearing different uppercase letters (A–E) and within the same row bearing different lowercase letters (a–f) differ significantly ($p < 0.05$) on the same storage day.

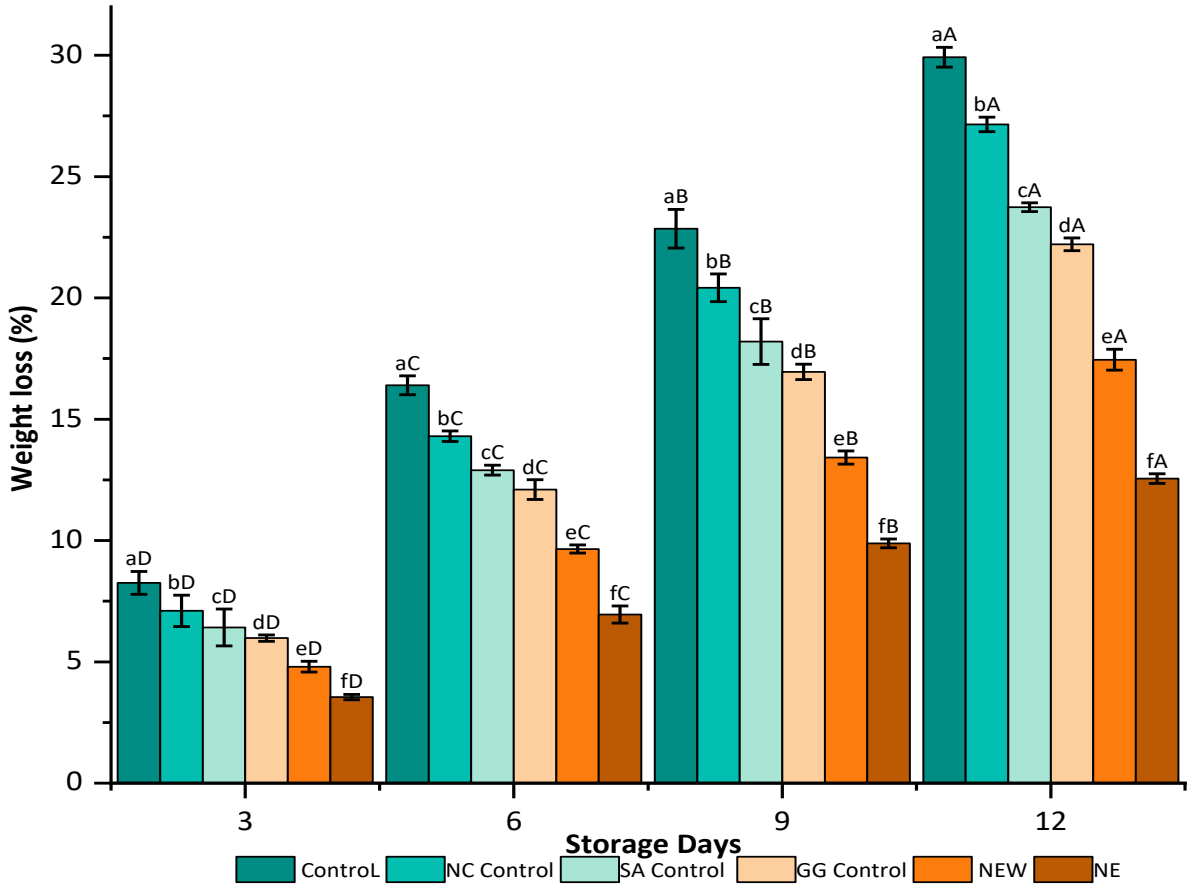

Fig.4.95 Changes in Weight loss (%) of fresh-cut pear slices during storage under different packaging materials

Note: NC: Nanocellulose, SA: Sodium alginate, GG: Guar gum, NEW: Nanocellulose, sodium alginate, and guar gum without *Cucumis callosus* peel extract, and NE: Nanocellulose, sodium alginate, and guar gum with *Cucumis callosus* peel extract functional film. Different lowercase letters denote significant differences among treatments within the same storage day, while different uppercase letters denote significant differences within the same treatment across storage days ($p < 0.05$).

4.15.6 pH

pH is a crucial biochemical indicator that reflects organic acid metabolism, respiration rate, and microbial activity in fresh-cut fruits during storage. In the present study, uncoated samples showed a progressive and significant ($p < 0.05$) increase in pH throughout storage representing in fig. 4.96 and 4.97, reaching 4.41 ± 0.04 in cut apples and 4.48 ± 0.03 in cut pears by day 12 presents in Tables 4.50 and 4.51. This increase can be attributed to accelerated respiration and metabolic consumption of organic acids, coupled with enhanced microbial activity under unrestricted exposure conditions. In contrast, all packaged samples exhibited a slower and controlled increase in pH, indicating delayed biochemical deterioration. Among the control

films, NC control showed comparatively higher pH values by day 12 (3.69 ± 0.05 in apples and 3.90 ± 0.05 in pears), which may be associated with the higher hydrophilicity and oxygen permeability of nanocellulose-based matrices, allowing continued metabolic activity. SA and GG control films resulted in significantly ($p < 0.05$) lower pH values in both fruits, with apples recording 3.74–3.77 and pears 3.86–3.81, suggesting improved regulation of gas exchange and reduced organic acid degradation due to enhanced film integrity. Notably, the NEW composite film further stabilized pH changes (3.82 ± 0.06 in apples and 3.76 ± 0.06 in pears), indicating synergistic interactions among polymeric components that restricted oxygen diffusion and respiration rate. The NE functional film demonstrated the most effective pH control, maintaining values of 3.90 ± 0.05 in apples and 3.69 ± 0.04 in pears, which were significantly ($p < 0.05$) lower than the uncoated samples. This enhanced pH stability is attributed to the formation of a dense interfacial barrier, reduced oxygen availability, and potential antimicrobial effects of functional constituents, collectively slowing organic acid depletion and microbial-mediated biochemical changes in fresh-cut apples and pears during storage.

Table 4.50 Changes in pH of Fresh-Cut Apples under Different Biodegradable Packaging Films

Day	Control	NC Control	SA Control	GG Control	NEW	NE
0	4.15 ± 0.06^{aE}	4.15 ± 0.07^{aA}	4.15 ± 0.06^{aA}	4.16 ± 0.02^{aA}	4.16 ± 0.04^{aA}	4.15 ± 0.09^{aA}
3	4.20 ± 0.04^{aD}	4.02 ± 0.06^{eB}	4.04 ± 0.08^{dB}	4.04 ± 0.05^{dB}	4.07 ± 0.06^{cB}	4.10 ± 0.05^{bB}
6	4.28 ± 0.05^{ac}	3.89 ± 0.06^{fc}	3.92 ± 0.03^{ec}	3.95 ± 0.06^{dc}	3.98 ± 0.06^{cc}	4.05 ± 0.04^{bc}
9	4.34 ± 0.04^{aB}	3.78 ± 0.05^{fD}	3.82 ± 0.08^{eD}	3.85 ± 0.03^{dD}	3.89 ± 0.05^{cD}	3.98 ± 0.07^{bD}
12	4.41 ± 0.04^{aA}	3.69 ± 0.05^{fE}	3.74 ± 0.07^{eE}	3.77 ± 0.05^{dE}	3.82 ± 0.06^{cE}	3.90 ± 0.05^{bE}

Values are expressed as mean ± SD (n = 3). Means within the same column bearing different uppercase letters (A–E) and within the same row bearing different lowercase letters (a–f) differ significantly ($p < 0.05$) on the same storage day.

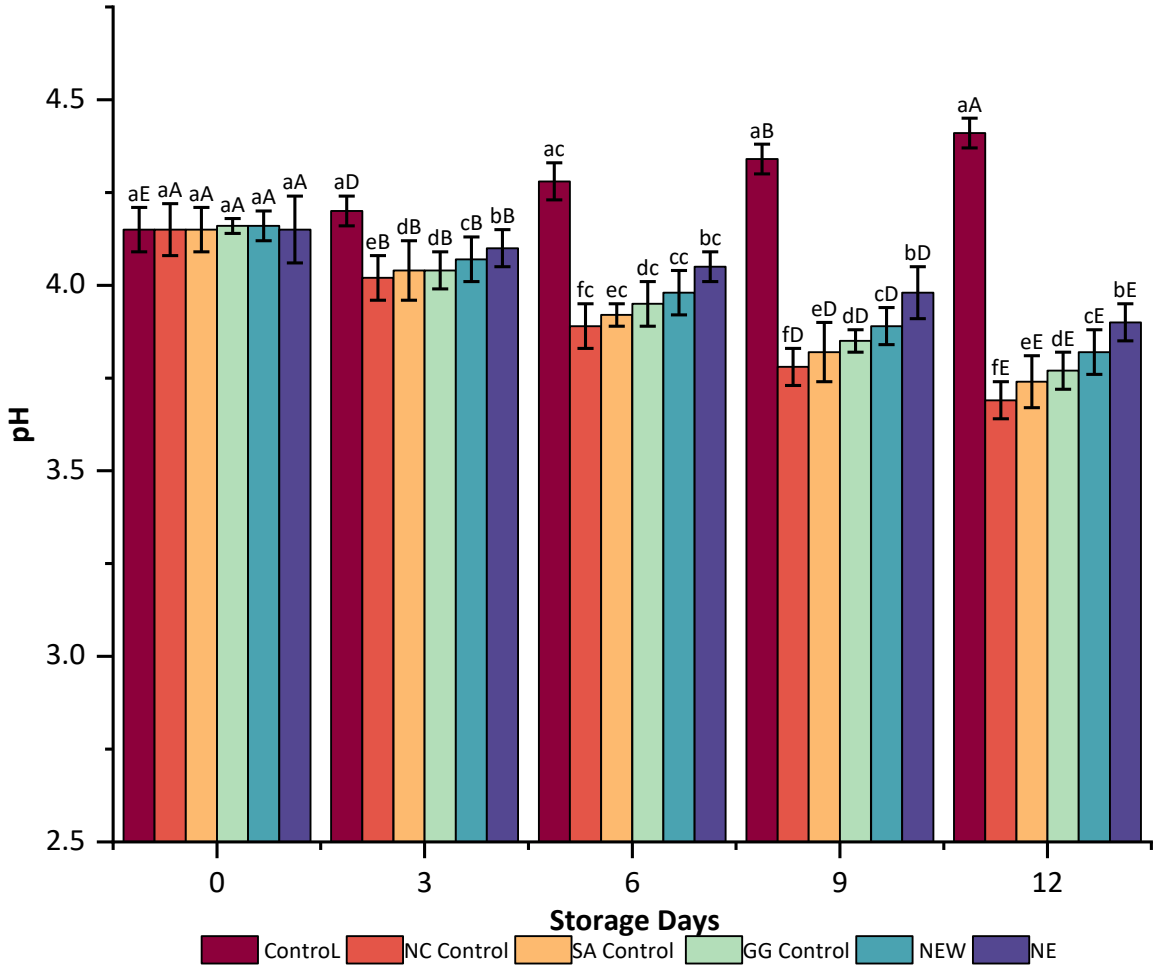

Fig.4.96 Changes in pH of fresh-cut apple slices during storage under different packaging materials

Note: NC: Nanocellulose, SA: Sodium alginate, GG: Guar gum, NEW: Nanocellulose, sodium alginate, and guar gum without *Cucumis callosus* peel extract, and NE: Nanocellulose, sodium alginate, and guar gum with *Cucumis callosus* peel extract functional film. Different lowercase letters denote significant differences among treatments within the same storage day, while different uppercase letters denote significant differences within the same treatment across storage days ($p < 0.05$).

Table 4.51 Changes in pH of Fresh-Cut Pears under Different Biodegradable Packaging Films

Days	Control	NC Control	SA Control	GG Control	NEW	NE
0	4.20 ± 0.04^{aE}	4.18 ± 0.03^{aA}	4.18 ± 0.04^{aA}	4.19 ± 0.05^{aA}	4.20 ± 0.04^{aA}	4.20 ± 0.08^{aA}
3	4.28 ± 0.08^{aD}	3.89 ± 0.05^{dB}	4.12 ± 0.06^{cB}	3.91 ± 0.04^{dB}	4.06 ± 0.02^{bB}	4.08 ± 0.04^{bB}
6	4.31 ± 0.04^{aC}	3.78 ± 0.05^{aC}	4.05 ± 0.04^{bC}	3.88 ± 0.04^{cC}	3.96 ± 0.03^{dC}	3.98 ± 0.06^{eC}

9	4.43 ± 0.04^{aB}	3.66 ± 0.08^{eD}	3.81 ± 0.02^{cD}	3.72 ± 0.04^{dD}	3.86 ± 0.05^{cD}	3.92 ± 0.04^{bC}
12	4.51 ± 0.04^{aA}	3.50 ± 0.03^{eE}	3.72 ± 0.05^{cE}	3.62 ± 0.03^{dE}	3.81 ± 0.06^{cD}	3.89 ± 0.04^{bC}

Values are expressed as mean ± SD (n = 3). Means within the same column bearing different uppercase letters (A–E) and within the same row bearing different lowercase letters (a–f) differ significantly ($p < 0.05$) on the same storage day.

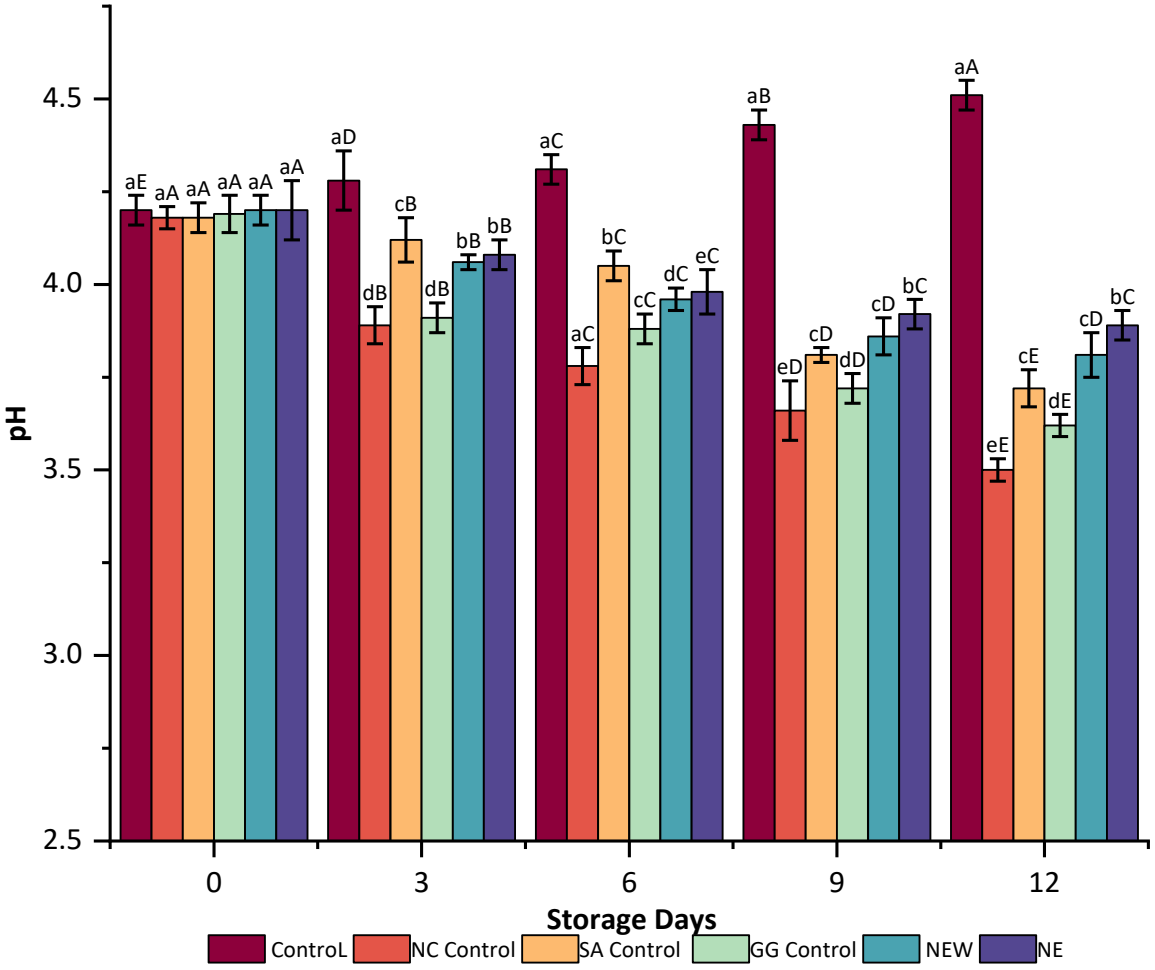

Fig. 4.97 Changes in pH of fresh-cut pear slices during storage under different packaging materials

Note: NC: Nanocellulose, SA: Sodium alginate, GG: Guar gum, NEW: Nanocellulose, sodium alginate, and guar gum without *Cucumis callosus* peel extract, and NE: Nanocellulose, sodium alginate, and guar gum with *Cucumis callosus* peel extract functional film. Different lowercase letters denote significant differences among treatments within the same storage day, while different uppercase letters denote significant differences within the same treatment across storage days ($p < 0.05$).

4.15.7 Total soluble solids (%)

Total soluble solids (TSS) serve as an integrative indicator of soluble sugar accumulation, carbohydrate metabolism, and moisture loss in fresh-cut fruits during storage, as shown in fig. 4.98 and 4.99. In the present study, TSS increased significantly ($p < 0.05$) with storage duration in both apple and pear slices, however, the rate and magnitude of increase were strongly dependent on the packaging system, reflecting differences in moisture barrier efficiency and metabolic regulation. Unpackaged samples consistently exhibited significantly higher TSS values than all packaged treatments at every storage interval presented in Tables 4.52 and 4.53. In fresh-cut apples, TSS increased from 12.10 ± 0.11% at day 0 to 13.80 ± 0.80% by day 12, while in pears, TSS rose from 14.10 ± 0.12% to 17.80 ± 0.61% over the same period. This significantly higher accumulation of soluble solids in unpackaged samples can be analytically attributed to rapid moisture loss, which concentrates soluble sugars, coupled with accelerated enzymatic hydrolysis of starch and structural carbohydrates under elevated respiration rates. Among the biodegradable packaging systems, nanocellulose (NC) films resulted in significantly higher TSS values than other packaged treatments, but significantly lower values than the unpackaged control. At day 12, NC-treated apple and pear slices recorded TSS values of 13.40 ± 0.17% and 15.22 ± 0.37%, respectively. This intermediate behavior suggests that NC films partially restricted moisture migration but still permitted sufficient water vapor transmission to allow moderate solute concentration and metabolic sugar formation. Sodium alginate (SA) and guar gum (GG) films further reduced TSS accumulation, exhibiting significantly lower TSS values than NC-treated samples. Final TSS values in apples were 13.01 ± 0.20% (SA) and 12.65 ± 0.46% (GG), while corresponding values in pears were 15.07 ± 0.21% (SA) and 15.27 ± 0.66% (GG). These results indicate improved moisture retention and partial suppression of carbohydrate-to-sugar conversion due to reduced oxygen ingress and lower respiration intensity. The composite (NEW) film demonstrated enhanced control over TSS evolution, maintaining significantly lower TSS values than NC, SA, and GG treatments at the end of storage (12.24 ± 0.38% in apples and 14.97 ± 0.28% in pears). This behavior reflects synergistic interactions among polymeric constituents, which likely reduced free volume within the film matrix, thereby restricting both moisture diffusion and metabolic activity. The functional (NE) film showed the most pronounced regulatory effect, consistently maintaining the significantly lowest TSS values throughout storage. By day 12, NE-treated apples and pears exhibited TSS values of 11.89 ± 0.67% and 14.89 ± 0.60%, respectively, which were significantly lower ($p < 0.05$) than all other treatments. Analytically, this indicates that the NE film most effectively limited moisture loss, suppressed respiration-driven sugar accumulation, and delayed enzymatic conversion of complex carbohydrates into soluble solids.

Table 4.52 Changes in Total Soluble Solids (%) of Fresh-Cut Apples under Different Biodegradable Packaging Films

Day	Control (%)	NC Control (%)	SA Control (%)	GG Control (%)	NEW Control (%)	NE Control (%)
0	12.10 ± 0.11^{aE}	11.80 ± 0.32^{bE}	11.58 ± 0.18^{eE}	11.41 ± 0.22^{dE}	11.13 ± 0.29^{eE}	10.95 ± 0.53^{fE}
3	12.60 ± 0.44^{aD}	12.30 ± 0.26^{bD}	12.01 ± 0.13^{cD}	11.78 ± 0.67^{dD}	11.44 ± 0.78^{eD}	11.15 ± 0.25^{fD}
6	13.10 ± 0.34^{ac}	12.80 ± 0.49^{bc}	12.42 ± 0.74^{cc}	12.09 ± 0.66^{dc}	11.79 ± 0.78^{ec}	11.46 ± 0.89^{fc}
9	13.45 ± 0.27^{aB}	13.10 ± 0.70^{bB}	12.71 ± 0.55^{cB}	12.37 ± 0.21^{dB}	12.01 ± 0.16^{eB}	11.66 ± 0.33^{fB}
12	13.80 ± 0.80^{aA}	13.40 ± 0.17^{bA}	13.01 ± 0.20^{cA}	12.65 ± 0.46^{dA}	12.24 ± 0.38^{eA}	11.89 ± 0.67^{fA}

Values are expressed as mean ± SD (n = 3). Means within the same column bearing different uppercase letters (A–E) and within the same row bearing different lowercase letters (a–f) differ significantly ($p < 0.05$) on the same storage day.

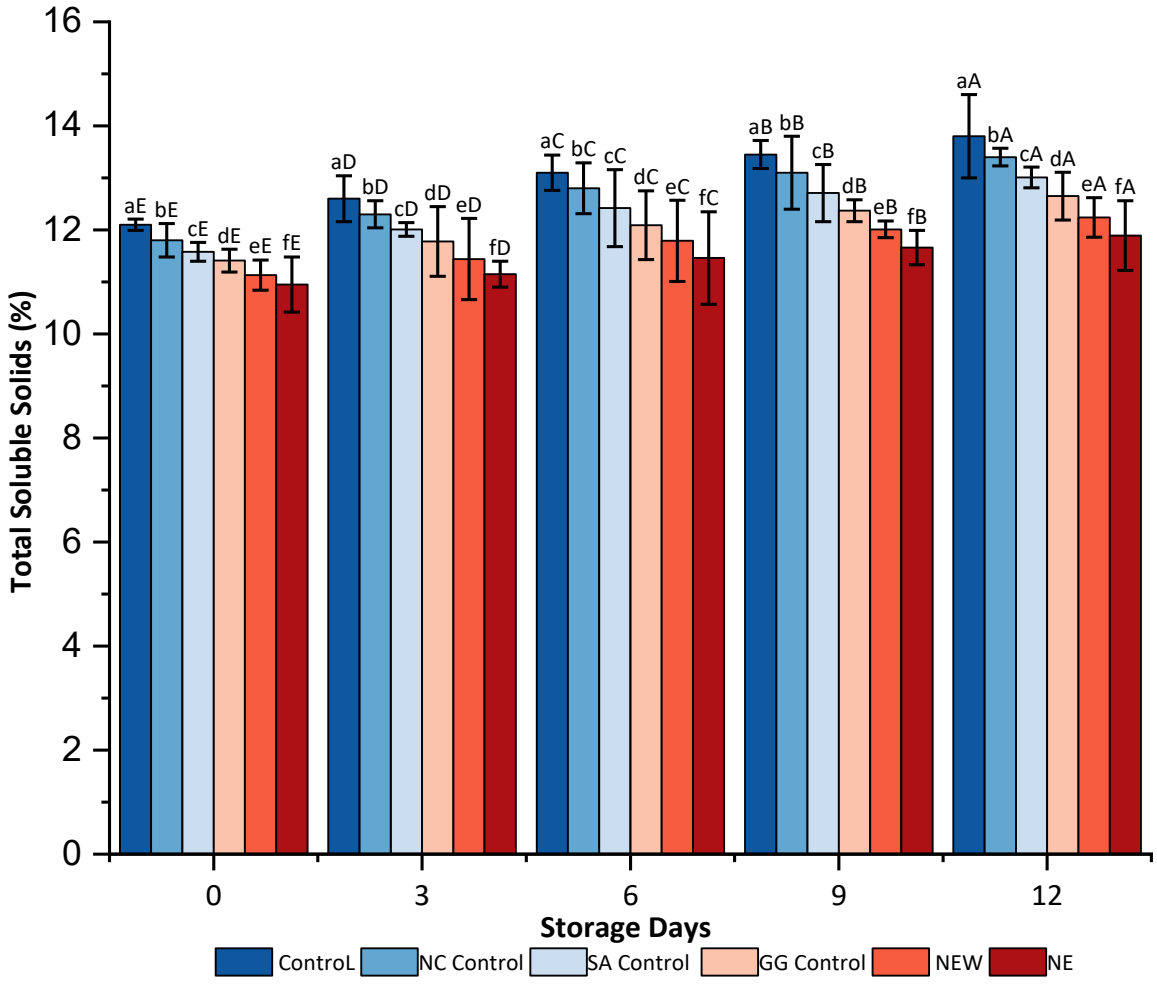

Fig. 4.98 Changes in Total Soluble Solids (%) of fresh-cut apple slices during storage under different packaging materials

Note: NC: Nanocellulose, SA: Sodium alginate, GG: Guar gum, NEW: Nanocellulose, sodium alginate, and guar gum without *Cucumis callosus* peel extract, and NE: Nanocellulose, sodium alginate, and guar gum with *Cucumis callosus* peel extract functional film. Different lowercase letters denote significant differences among treatments within the same storage day, while different uppercase letters denote significant differences within the same treatment across storage days ($p < 0.05$).

Table 4.53 Changes in Total Soluble Solids (%) of Fresh-Cut pears under Different Biodegradable Packaging Films

Day	**Control (%)**	**NC Control (%)**	**SA Control (%)**	**GG Control (%)**	**NEW Control (%)**	**NE Control (%)**
0	14.10 ± 0.12^{aE}	$14.12 \pm 0.32a^{E}$	$14.13 \pm 0.28a^{E}$	$14.12 \pm 0.62a^{E}$	$14.13 \pm 0.79a^{E}$	$14.09 \pm 0.43a^{E}$
3	15.60 ± 0.70^{aD}	$14.30 \pm 0.26e^{D}$	$14.52 \pm 0.33d^{D}$	$14.55 \pm 0.72b^{D}$	$14.44 \pm 0.68c^{D}$	14.23 ± 0.55^{fD}
6	16.10 ± 0.44^{ac}	14.89 ± 0.19^{bc}	14.68 ± 0.54^{cc}	$14.85 \pm 0.36b^{c}$	$14.79 \pm 0.18d^{c}$	$14.36 \pm 0.19e^{c}$
9	17.45 ± 0.37^{aB}	15.04 ± 0.40^{bB}	$14.92 \pm 0.65d^{B}$	$15.12 \pm 0.28c^{B}$	$14.87 \pm 0.26d^{B}$	$14.50 \pm 0.52e^{B}$
12	17.80 ± 0.61^{aA}	15.22 ± 0.37^{bA}	15.07 ± 0.21^{cA}	$15.27 \pm 0.66b^{A}$	$14.97 \pm 0.28d^{A}$	$14.89 \pm 0.60e^{A}$

Values are expressed as mean ± SD (n = 3). Means within the same column bearing different uppercase letters (A–E) and within the same row bearing different lowercase letters (a–f) differ significantly ($p < 0.05$) on the same storage day.

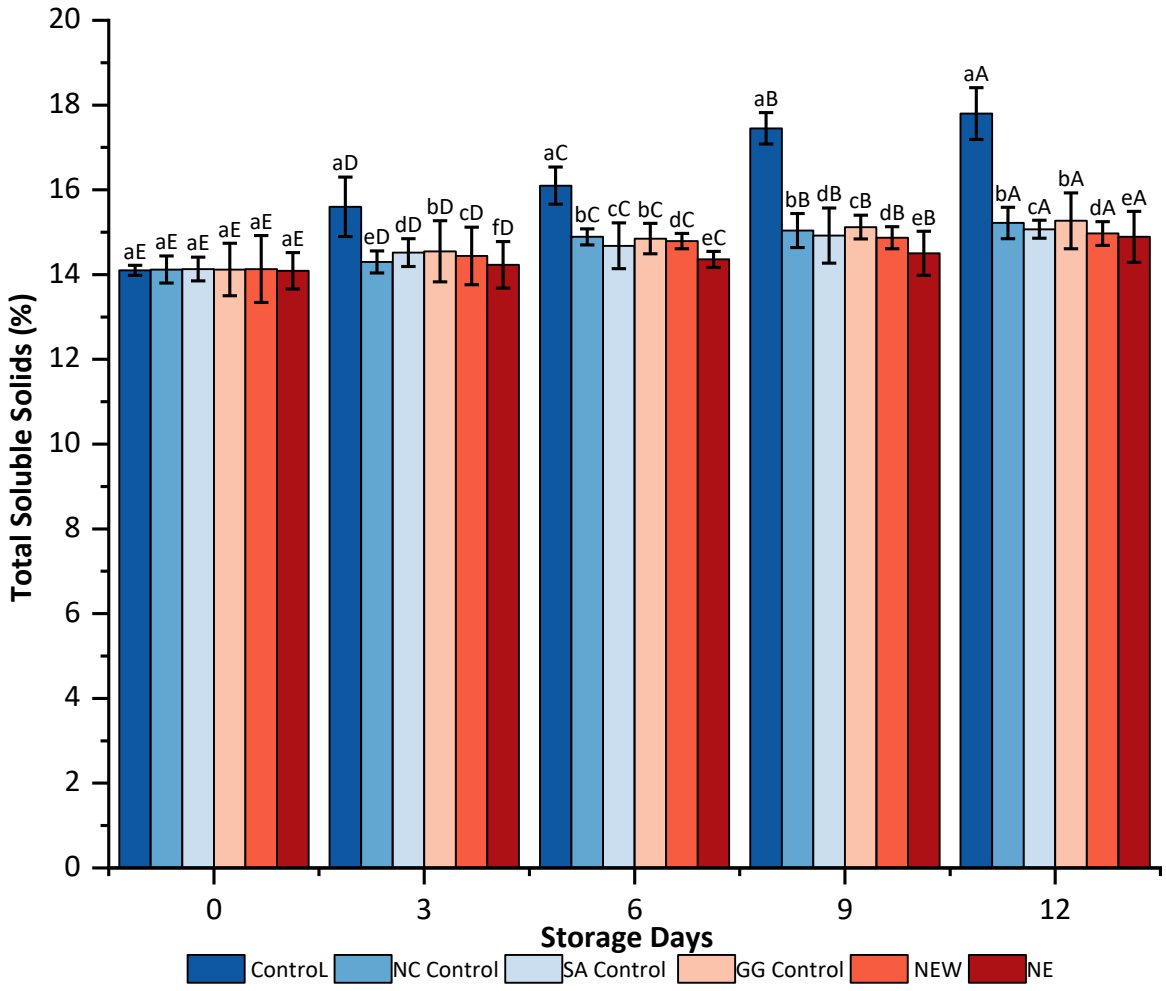

Fig. 4.99 Changes in Total Soluble Solids (%) of fresh-cut pear slices during storage under different packaging materials

Note: NC: Nanocellulose, SA: Sodium alginate, GG: Guar gum, NEW: Nanocellulose, sodium alginate, and guar gum without *Cucumis callosus* peel extract, and NE: Nanocellulose, sodium alginate, and guar gum with *Cucumis callosus* peel extract functional film. Different lowercase letters denote significant differences among treatments within the same storage day, while different uppercase letters denote significant differences within the same treatment across storage days ($p < 0.05$).

4.15.8 Total phenolic content (mg GAE kg^{-1})

Total phenolic content (TPC), expressed as mg gallic acid equivalents (mg GAE kg^{-1}) fresh weight, is a critical indicator of antioxidant potential, oxidative stability, and nutritional quality of fresh-cut fruits during storage showed in fig. 4.100 and 4.101. In the present investigation, uncoated samples exhibited a pronounced and statistically significant ($p < 0.05$) decline in TPC over the storage period showed in Tables 4.54 and 4.55. In cut apples, TPC decreased from

756.22 ± 14.36 mg GAE/kg at day 0 to 521.08 ± 11.92 mg GAE/kg by day 10, while cut pears showed a similar trend, declining from 742.33 ± 13.88 mg GAE kg^{-1} to 498.27 ± 10.74 mg GAE/kg. This substantial loss of phenolic compounds in uncoated samples can be mechanistically attributed to tissue disruption during cutting, which enhances oxygen diffusion and activates polyphenol oxidase (PPO), leading to enzymatic oxidation of phenolics into quinones and their subsequent polymerisation into brown pigments. Among the packaged treatments, nanocellulose (NC) films showed moderate protection against phenolic degradation, however, TPC retention remained significantly lower ($p < 0.05$) compared to other coated samples, with final values of 545.90 ± 12.18 mg GAE/kg in apples and 522.18 ± 11.46 mg GAE/kg in pears. This behaviour is likely associated with the hydrophilic nature and comparatively higher oxygen permeability of nanocellulose matrices, which permit continued oxidative reactions. In contrast, sodium alginate (SA) and guar gum (GG) films significantly ($p < 0.05$) enhanced TPC retention, maintaining values of 564.19 ± 10.92 to 568.90 ± 11.35 mg GAE/kg in apples and 538.60 ± 12.04 to 542.47 ± 10.88 mg GAE/kg in pears by day 10. The improved performance of these films is attributed to their denser polymer networks, which reduce oxygen ingress and suppress PPO-mediated phenolic oxidation. The composite film demonstrated further stabilisation of phenolic compounds, retaining 575.70 ± 9.84 mg GAE/kg in apples and 551.22 ± 10.15 mg GAE kg^{-1} in pears, indicating synergistic interactions among polymer constituents that enhanced barrier integrity and restricted oxidative degradation. Notably, the functional nanohydrogel (NE) film exhibited the highest TPC retention throughout storage, with final values of 594.86 ± 8.96 mg GAE kg^{-1} for apples and 568.40 ± 9.32 mg GAE/kg for pears, which were significantly higher ($p < 0.05$) than all other treatments. This superior preservation is attributed to the combined effects of enhanced oxygen-barrier properties, reduced enzymatic activity, and the presence of bioactive components with intrinsic antioxidant capacity, which collectively inhibited phenolic oxidation and maintained the nutritional and antioxidant quality of fresh-cut apples and pears during refrigerated storage.

Table 4.54 Total Phenolic Content (mg GAE kg^{-1}) of Packaged and Unpackaged Fresh-Cut Apples

Day	Control (mg GAE kg^{-1})	NC Control (mg GAE kg^{-1})	SA Control (mg GAE kg−1)	GG Control (mg GAE kg^{-1})	NEW Control (mg GAE kg^{-1})	NE Control (mg GAE kg^{-1})
0	756.22 ± 0.80^{cA}	760.40 ± 0.41^{cA}	762.51 ± 0.73^{bA}	764.83 ± 0.23^{bA}	766.42 ± 0.35^{abA}	768.10 ± 0.56^{aA}

3	698.12 ± 0.67^{eB}	712.81 ± 0.50^{dB}	725.32 ± 0.45^{cB}	738.80 ± 0.66^{bB}	752.31 ± 0.19^{aB}	756.51 ± 0.56^{aB}
6	634.81 ± 0.21^{eC}	650.22 ± 0.43^{dC}	657.16 ± 0.30^{cC}	660.77 ± 0.13^{cC}	666.10 ± 0.40^{bC}	670.88 ± 0.51^{aC}
9	580.66 ± 0.34^{eD}	600.56 ± 0.89^{dD}	639.22 ± 0.79^{cD}	644.45 ± 0.30^{cD}	650.74 ± 0.26^{bD}	655.36 ± 0.66^{aD}
12	521.08 ± 0.33^{eE}	545.90 ± 0.29^{dE}	564.19 ± 0.55^{cE}	568.90 ± 0.40^{cE}	575.70 ± 3.00^{bE}	594.86 ± 0.47^{aE}

Data are presented as mean ± SD (n = 3). Means within a column with different uppercase letters (A–E) and within a row with different lowercase letters (a–e) differ significantly ($p < 0.05$) on the same storage day.

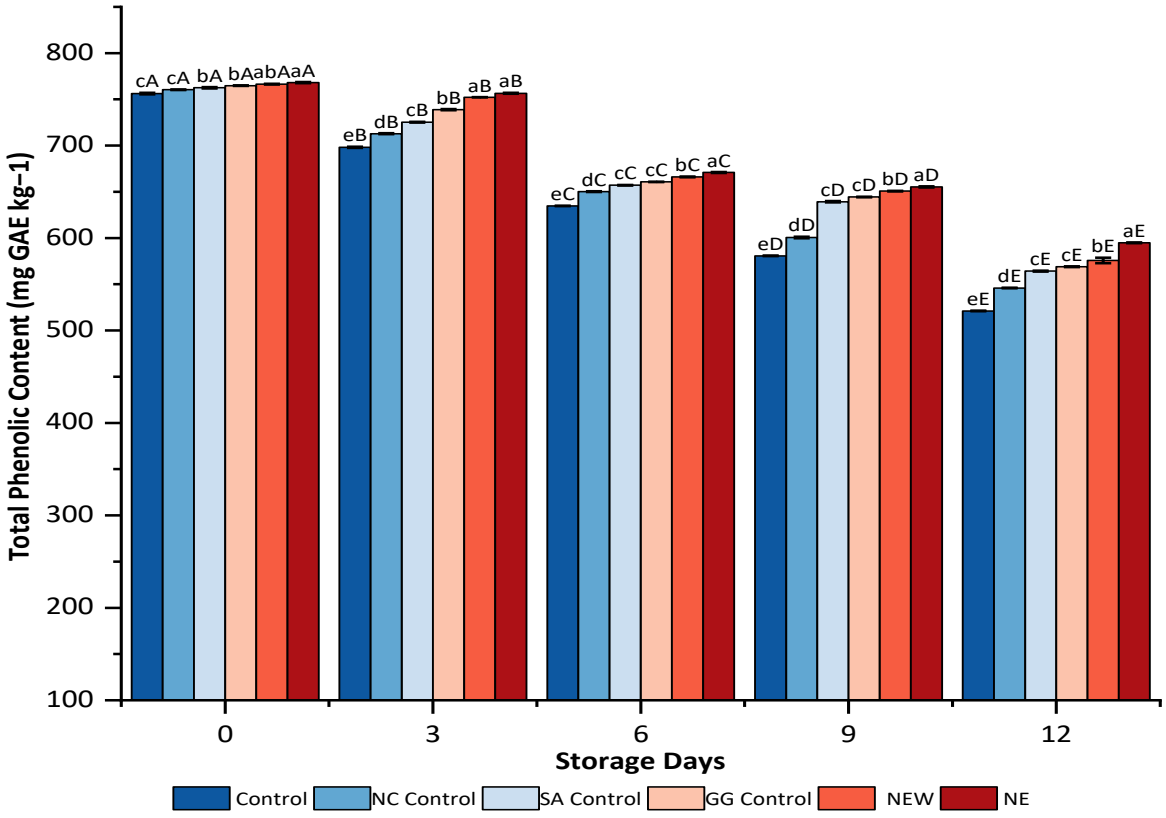

Fig. 4.100 Changes in Total Phenolic Content (mg GAE kg^{-1}) of fresh-cut apple slices during storage under different packaging materials

Note: NC: Nanocellulose, SA: Sodium alginate, GG: Guar gum, NEW: Nanocellulose, sodium alginate, and guar gum without *Cucumis callosus* peel extract, and NE: Nanocellulose, sodium alginate, and guar gum with *Cucumis callosus* peel extract functional film. Different lowercase letters denote significant differences among treatments within the same storage day, while different uppercase letters denote significant differences within the same treatment across storage days ($p < 0.05$).

Table 4.55 Total Phenolic Content (mg GAE kg^{-1}) of Packaged and Unpackaged Fresh-Cut pears

Day	Control (mg GAE kg^{-1})	NC Control (mg GAE kg^{-1})	SA Control (mg GAE kg−1)	GG Control (mg GAE kg^{-1})	NEW Control (mg GAE kg^{-1})	NE Control (mg GAE kg^{-1})
0	742.33 ± 0.14^{cA}	746.50 ± 0.36^{cA}	748.29 ± 0.55^{bA}	750.71 ± 0.17^{bA}	752.11 ± 0.21^{abA}	754.20 ± 0.39^{aA}
3	700.10 ± 0.21^{eB}	715.42 ± 0.62^{dB}	720.37 ± 0.91^{cB}	724.60 ± 0.44^{cB}	729.23 ± 0.55^{bB}	733.80 ± 0.81^{aB}
6	648.41 ± 0.38^{eC}	665.10 ± 0.15^{dC}	671.56 ± 0.30^{cC}	675.71 ± 0.51^{cC}	681.40 ± 0.32^{bC}	687.11 ± 0.83^{aC}
9	595.55 ± 0.67^{eD}	620.20 ± 0.27^{dD}	635.25 ± 0.81^{cD}	640.19 ± 0.29^{cD}	647.70 ± 0.55^{bD}	653.80 ± 0.31^{aD}
12	498.27 ± 0.16^{eE}	522.18 ± 0.65^{dE}	538.60 ± 0.26^{cE}	542.47 ± 0.73^{cE}	551.22 ± 0.45^{bE}	568.40 ± 0.29^{aE}

Data are presented as mean ± SD (n = 3). Means within a column with different uppercase letters (A–E) and within a row with different lowercase letters (a–e) differ significantly ($p < 0.05$) on the same storage day.

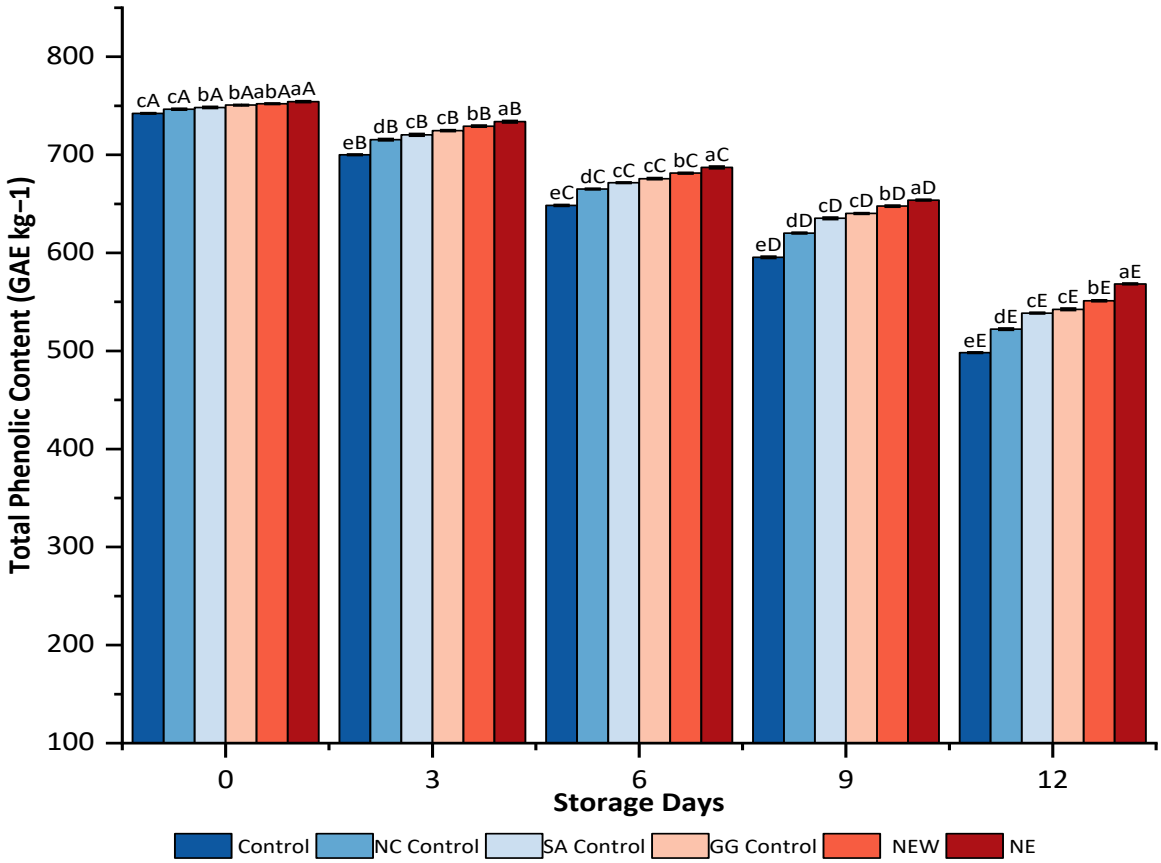

Fig. 4.101 Changes in Total Phenolic Content (mg GAE kg^{-1}) of fresh-cut pear slices during storage under different packaging materials

Note: NC: Nanocellulose, SA: Sodium alginate, GG: Guar gum, NEW: Nanocellulose, sodium alginate, and guar gum without *Cucumis callosus* peel extract, and NE: Nanocellulose, sodium alginate, and guar gum with *Cucumis callosus* peel extract functional film. Different lowercase letters denote significant differences among treatments within the same storage day, while different uppercase letters denote significant differences within the same treatment across storage days ($p < 0.05$).

4.15.9 Ascorbic acid (mg/100 g)

Ascorbic acid content declined progressively during storage in both fresh-cut apples and pears, as shown in the figure. 4.102 and 4.103, with the magnitude of loss being significantly influenced ($p < 0.05$) by packaging treatment and storage duration, as shown in Tables 4.56 and 4.57. On day 0, no significant differences ($p > 0.05$) were observed among uncoated and coated samples for either fruit, indicating comparable initial ascorbic acid levels before storage. As storage progressed, the uncoated samples exhibited a significantly greater reduction ($p < 0.05$) in ascorbic acid, decreasing to 5.30 mg/100 g in apples and 4.65 mg/100 g in pears by day 12, reflecting accelerated oxidative degradation under unrestricted oxygen exposure. Among the coated samples, nanocellulose-based films retained significantly lower ascorbic acid ($p < 0.05$) compared to composite and functional films, although values remained significantly higher than those of uncoated samples. In contrast, sodium alginate and guar gum films showed a non-significant difference ($p > 0.05$) between each other at corresponding storage intervals, indicating similar protective efficacy against ascorbic acid degradation. The composite film preserved significantly higher ascorbic acid levels ($p < 0.05$) than SA and GG films at later storage stages, demonstrating enhanced barrier performance. Notably, the functional film (NE) consistently maintained the highest ascorbic acid content, which was significantly higher ($p < 0.05$) than all other treatments from day 3 in both apples and pears. Apples retained significantly higher ascorbic acid ($p < 0.05$) than pears under comparable treatments, suggesting varietal and tissue-specific differences in antioxidant stability.

Table 4.56 Variation in Ascorbic Acid Content (mg/100 g) of Fresh-Cut Apples during Storage

Day	Control (mg/100 g)	NC Control (mg/100 g)	SA Control (mg/100 g)	GG Control (mg/100 g)	NEW Control (mg/100 g)	NE Control (mg/100 g)
0	9.83 ± 0.18^{aA}	9.90 ± 0.88^{aA}	9.92 ± 0.37^{aA}	9.95 ± 0.67^{aA}	9.97 ± 0.20^{aA}	9.99 ± 0.37^{aA}

3	8.55 ± 0.65^{fB}	8.80 ± 0.56^{eB}	9.01 ± 0.55^{dB}	9.10 ± 0.21^{cB}	9.22 ± 0.49^{bB}	9.33 ± 0.88^{aB}
6	7.30 ± 0.23^{fc}	7.70 ± 0.74^{ec}	7.96 ± 0.39^{dc}	8.12 ± 0.50^{cc}	8.29 ± 0.62^{bc}	8.49 ± 0.28^{ac}
9	6.20 ± 0.34^{fD}	6.60 ± 0.83^{eD}	6.89 ± 0.19^{dD}	7.06 ± 0.33^{cD}	7.29 ± 0.81^{bD}	7.49 ± 0.27^{aD}
12	5.30 ± 0.11^{fE}	5.80 ± 0.22^{eE}	6.12 ± 0.41^{dE}	6.28 ± 0.91^{cE}	6.51 ± 0.85^{bE}	6.71 ± 0.17^{aE}

Data are presented as mean ± SD (n = 3). Means within a column with different uppercase letters (A–E) and within a row with different lowercase letters (a–e) differ significantly ($p < 0.05$) on the same storage day.

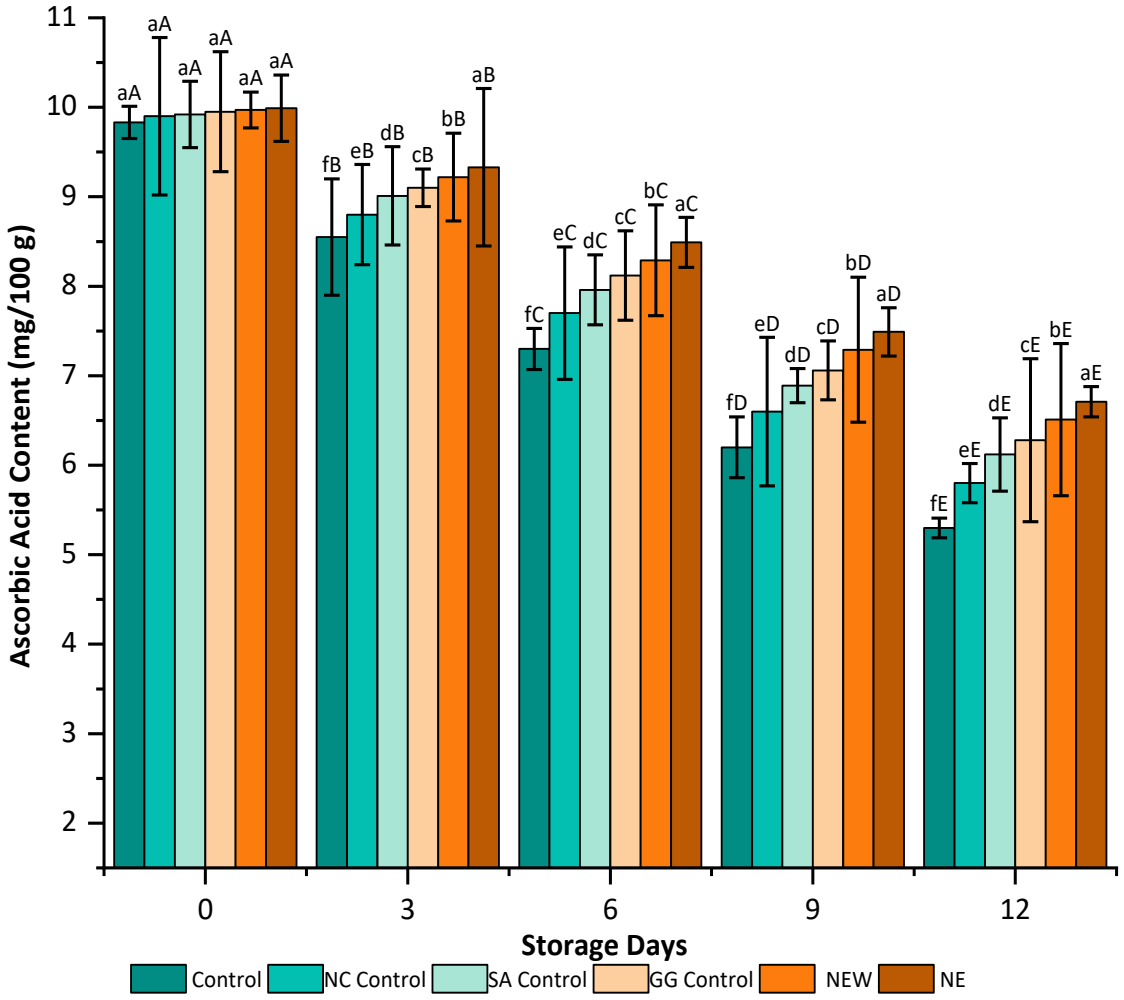

Fig. 4.102 Changes in Ascorbic Acid Content (mg/100 g) of fresh-cut apple slices during storage under different packaging materials

Note: NC: Nanocellulose, SA: Sodium alginate, GG: Guar gum, NEW: Nanocellulose, sodium alginate, and guar gum without *Cucumis callosus* peel extract, and NE: Nanocellulose, sodium alginate, and guar gum with *Cucumis callosus* peel extract functional film. Different lowercase

letters denote significant differences among treatments within the same storage day, while different uppercase letters denote significant differences within the same treatment across storage days ($p < 0.05$).

Table 4.57 Variation in Ascorbic Acid Content (mg/100 g) of Fresh-Cut pears during Storage

Day	Control (mg/100 g)	NC Control (mg/100 g)	SA (mg/100 g)	GG Control (mg/100 g)	NEW Control (mg/100 g)	NE Control (mg/100 g)
0	8.80 ± 0.25^{aA}	8.80 ± 0.35^{aA}	8.82 ± 0.87^{aA}	8.85 ± 0.22^{aA}	8.87 ± 0.15^{aA}	8.90 ± 0.30^{aA}
3	7.52 ± 0.54^{fB}	7.88 ± 0.84^{eB}	8.02 ± 0.77^{dB}	8.18 ± 0.65^{cB}	8.30 ± 0.32^{bB}	8.42 ± 0.41^{aB}
6	6.20 ± 0.42^{fc}	6.65 ± 029^{ec}	6.92 ± 0.68^{dc}	7.14 ± 0.14^{cc}	7.30 ± 0.37^{bc}	7.48 ± 0.29^{ac}
9	5.30 ± 0.21^{fD}	5.72 ± 0.32^{eD}	6.01 ± 0.90^{dD}	6.22 ± 0.51^{cD}	6.40 ± 0.88^{bD}	6.60 ± 0.16^{aD}
12	4.65 ± 0.19^{fE}	5.02 ± 0.11^{eE}	5.30 ± 0.61^{dE}	5.51 ± 0.72^{cE}	5.73 ± 0.13^{bE}	5.94 ± 0.85^{aE}

Results are expressed as mean ± SD (n = 3). Means within a column bearing different uppercase letters (A–E) and within a row bearing different lowercase letters (a–e) differ significantly ($p < 0.05$) on the same storage day.

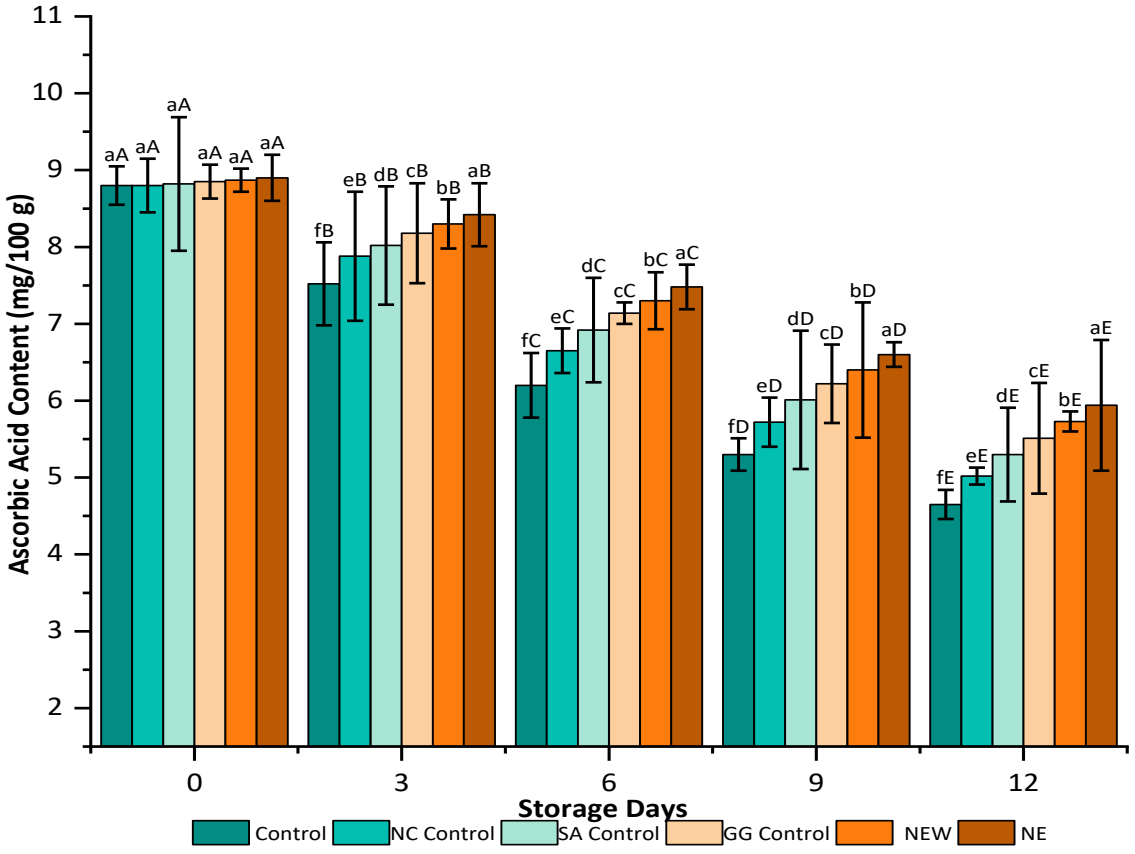

Fig. 4.103 Changes in Ascorbic Acid Content (mg/100 g) of fresh-cut pear slices during storage under different packaging materials

Note: NC: Nanocellulose, SA: Sodium alginate, GG: Guar gum, NEW: Nanocellulose, sodium alginate, and guar gum without *Cucumis callosus* peel extract, and NE: Nanocellulose, sodium alginate, and guar gum with *Cucumis callosus* peel extract functional film. Different lowercase letters denote significant differences among treatments within the same storage day, while different uppercase letters denote significant differences within the same treatment across storage days ($p < 0.05$).

4.15.10 Respiration rate (mg kg^{-1} h^{-1})

Respiration rate, expressed as mg kg^{-1} h^{-1}, is a critical physiological parameter reflecting metabolic activity, stress response, and senescence progression in fresh-cut fruits in fig. 4.104 and 4.105. As shown in Tables 4.58 and 4.59, both packaging treatment and storage duration significantly influenced ($p < 0.05$) the respiration rate of fresh-cut apples and pears. Among the treatments, unpackaged apple slices exhibited significantly ($p < 0.05$) higher respiration rates throughout storage, decreasing from 46.25 ± 0.31 mg kg^{-1} h^{-1} on day 0 to 43.65 ± 0.47 mg kg^{-1} h^{-1} by day 12. The consistently higher respiration and narrow SD values indicate elevated and uniform metabolic activity caused by unrestricted oxygen diffusion and cutting-induced physiological stress, which enhances mitochondrial respiration through increased tricarboxylic acid cycle and electron transport activity. In contrast, all packaged apple samples showed significantly lower respiration rates ($p < 0.05$) with comparatively low SD values, indicating stable metabolic regulation by the films. Notably, NE-coated apple slices exhibited the lowest respiration rate, declining to 40.50 ± 0.19 mg kg^{-1} h^{-1} by day 12, which was significantly ($p < 0.05$) lower than all other treatments. The superior performance of the functional NE film is attributed to its compact, semi-permeable structure, which restricts oxygen ingress, moderates internal carbon dioxide levels, and reduces ethylene-mediated metabolic stimulation, thereby suppressing stress-induced respiration. The NEW composite film (41.00 ± 0.26 mg kg^{-1} h^{-1}) and GG film (41.60 ± 0.28 mg kg^{-1} h^{-1}) showed intermediate respiration control, whereas NC-coated samples (42.80 ± 0.16 mg kg^{-1} h^{-1}) retained relatively higher respiration among the packaged treatments, possibly due to moderate oxygen permeability associated with the nanocellulose matrix. A similar trend was observed in fresh-cut pear slices, where unpackaged samples showed significantly ($p < 0.05$) higher respiration rates, decreasing from 44.74 ± 0.77 mg kg^{-1} h^{-1} on day 0 to 41.30 ± 0.18 mg kg^{-1} h^{-1} by day 12, reflecting accelerated substrate depletion and senescence under open storage conditions. In contrast, NE-coated pear slices recorded the lowest respiration rate (38.21 ± 0.21 mg kg^{-1} h^{-1}), which was significantly ($p <$

0.05) lower than all other treatments. The reduced respiration in packaged pear slices suggests effective regulation of gas exchange, reduced cellular dehydration, and delayed enzymatic turnover. Overall, the results that functional NE-based packaging provides the most effective control of respiratory metabolism, thereby enhancing physiological stability and extending the shelf life of fresh-cut apples and pears.

Table 4.58 Respiration rate (mg kg^{-1} h^{-1}) of packaged and unpackaged fresh-cut apple slices

Day	Control (mg kg^{-1} h^{-1})	NC Control (mg kg^{-1} h^{-1})	SA Control (mg kg^{-1} h^{-1})	GG Control (mg kg^{-1} h^{-1})	NEW Control (mg kg^{-1} h^{-1})	NE Control (mg kg^{-1} h^{-1})
0	46.50 ± 0.31^{aA}	46.38 ± 0.73^{aA}	45.88 ± 0.43^{bA}	45.20 ± 0.29^{cA}	45.05 ± 0.30^{cA}	45.90 ± 0.28^{bA}
3	45.10 ± 0.55^{aB}	44.70 ± 0.35^{bB}	44.30 ± 0.34^{bB}	43.59 ± 0.33^{cB}	43.31 ± 0.15^{cB}	43.61 ± 0.63^{cB}
6	44.30 ± 0.33^{aC}	43.68 ± 0.68^{bC}	43.10 ± 0.66^{bC}	42.48 ± 0.37^{cC}	42.60 ± 0.88^{cC}	41.55 ± 0.37^{dC}
9	43.85 ± 0.12^{aD}	43.34 ± 0.41^{bD}	42.43 ± 0.41^{cD}	41.77 ± 0.40^{dD}	41.56 ± 0.41^{dD}	40.25 ± 0.20^{eD}
12	43.65 ± 0.47^{aE}	42.80 ± 0.16^{bE}	42.21 ± 0.35^{cE}	41.55 ± 0.44^{dE}	41.10 ± 0.58^{dE}	40.13 ± 0.19^{eE}

Data are expressed as mean ± SD (n = 3). $^{(A-E)}$ Mean values show significant (p<0.05) differences within the same column, and $^{(a-e)}$ mean values within the row indicate significant (p<0.05) differences on the same storage day.

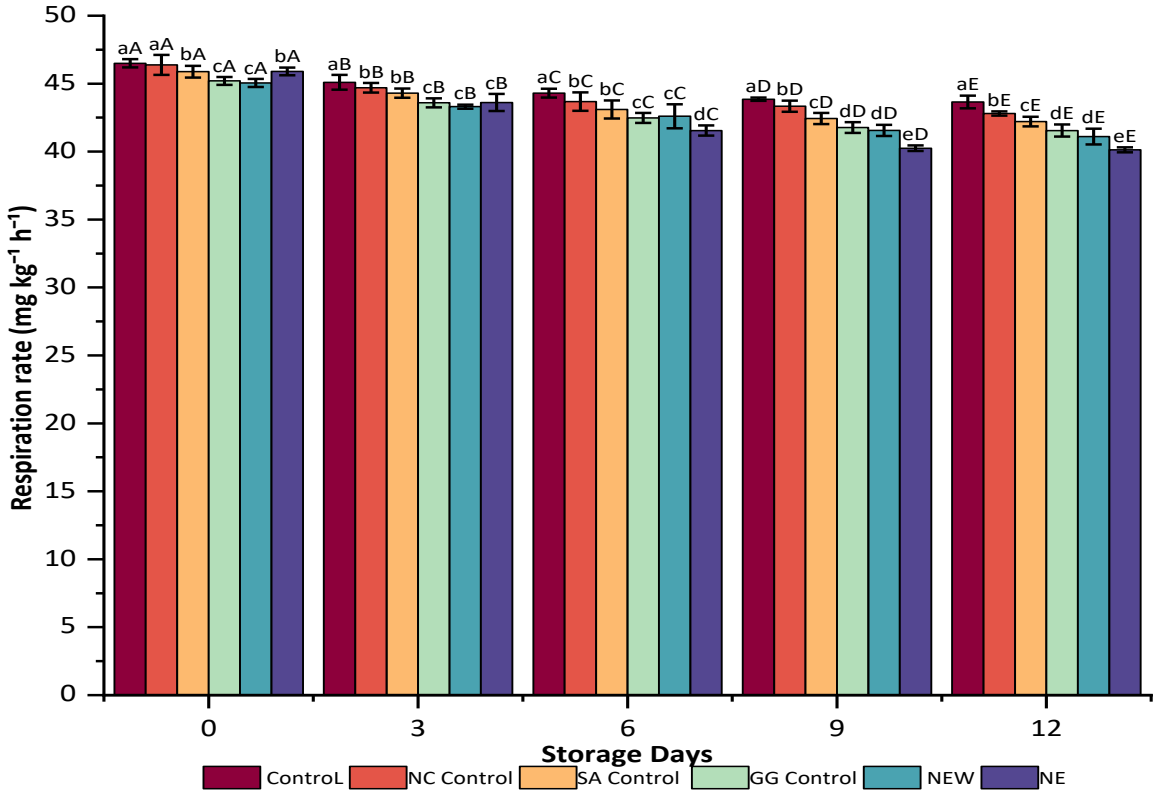

Fig. 4.104 Changes in Respiration rate (mg kg^{-1} h^{-1}) of fresh-cut apple slices during storage under different packaging materials

Note: NC: Nanocellulose, SA: Sodium alginate, GG: Guar gum, NEW: Nanocellulose, sodium alginate, and guar gum without *Cucumis callosus* peel extract, and NE: Nanocellulose, sodium alginate, and guar gum with *Cucumis callosus* peel extract functional film. Different lowercase letters denote significant differences among treatments within the same storage day, while different uppercase letters denote significant differences within the same treatment across storage days ($p < 0.05$).

Table 4.59 Respiration rate (mg kg^{-1} h^{-1}) of packaged and unpackaged fresh-cut pear slices

Day	Control (mg kg^{-1} h^{-1})	NC Control (mg kg^{-1} h^{-1})	SA Control (mg kg^{-1} h^{-1})	GG Control (mg kg^{-1} h^{-1})	NEW Control (mg kg^{-1} h^{-1})	NE Control (mg kg^{-1} h^{-1})
0	44.74 ± 0.77^{bA}	44.92 ± 0.27^{aA}	44.22 ± 0.40^{cA}	43.12 ± 0.50^{dA}	43.25 ± 0.89^{dA}	43.40 ± 0.21^{dA}
3	43.80 ± 0.35^{aB}	43.25 ± 0.81^{bB}	42.85 ± 0.89^{bB}	42.22 ± 0.58^{cB}	$41.75 \pm 0.17^{c}B$	41.26 ± 0.26^{cB}
6	42.33 ± 0.22^{aC}	41.87 ± 0.43^{bC}	41.34 ± 0.77^{bC}	40.05 ± 0.24^{cC}	40.63 ± 0.79^{cC}	39.40 ± 0.40^{dC}
9	41.81 ± 0.62^{aD}	41.15 ± 0.36^{bD}	40.75 ± 0.20^{bD}	39.58 ± 0.57^{cD}	39.80 ± 0.21^{cD}	38.85 ± 0.83^{dD}
12	41.30 ± 0.18^{aE}	40.62 ± 0.44^{bE}	39.20 ± 0.31^{cE}	39.20 ± 0.91^{cE}	38.51 ± 0.64^{dE}	38.21 ± 0.21^{dE}

Data are presented as mean ± SD (n = 3). Means within the same column marked with different uppercase letters (A–E) and within the same row marked with different lowercase letters (a–d) differ significantly ($p < 0.05$) on the same storage day.

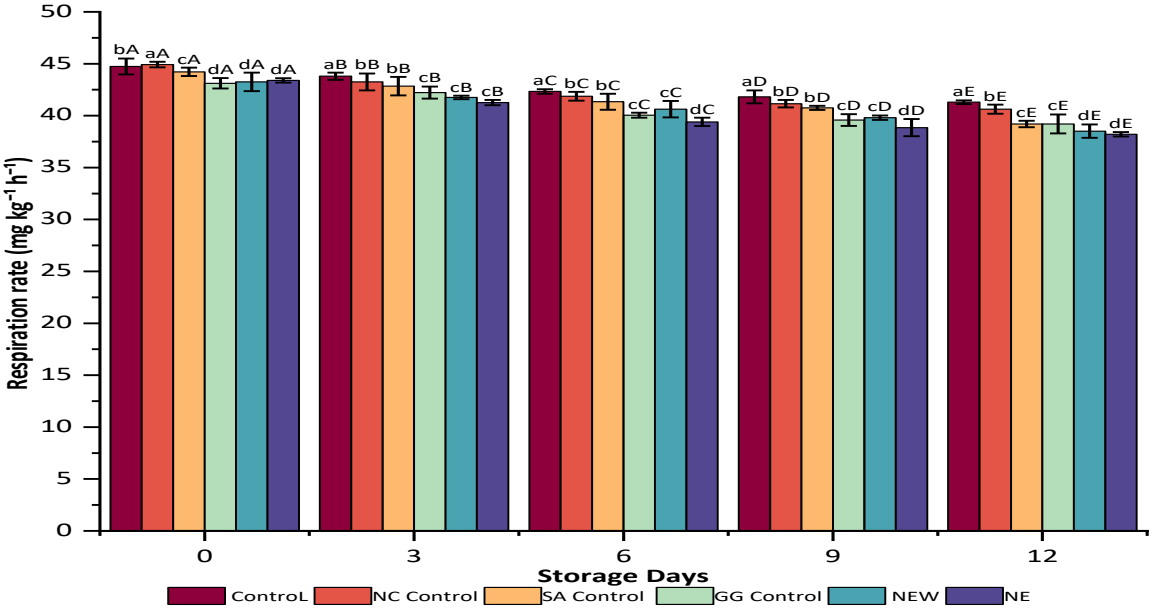

Fig. 4.105 Changes in Respiration rate (mg kg^{-1} h^{-1}) of fresh-cut pear slices during storage under different packaging materials

Note: NC: Nanocellulose, SA: Sodium alginate, GG: Guar gum, NEW: Nanocellulose, sodium alginate, and guar gum without *Cucumis callosus* peel extract, and NE: Nanocellulose, sodium alginate, and guar gum with *Cucumis callosus* peel extract functional film. Different lowercase letters denote significant differences among treatments within the same storage day, while different uppercase letters denote significant differences within the same treatment across storage days ($p < 0.05$).

4.15.11 Antioxidant activity (%)

Antioxidant activity (%), reflecting the capacity of fresh-cut fruits to scavenge reactive oxygen species and resist oxidative stress, was significantly influenced by both packaging treatment and storage duration ($p < 0.05$), as presented in Tables 4.60 and 4.61. In fresh-cut apples, unpackaged samples exhibited a marked and significant ($p < 0.05$) decline in antioxidant activity from 18.95 ± 0.28% at day 0 to 8.10 ± 0.20% by day 12, indicating rapid oxidative degradation of bioactive constituents under unrestricted oxygen exposure, as represented in fig. 4.106 and 4.107. This pronounced reduction is primarily associated with enhanced oxidation of phenolic compounds and ascorbic acid, induced by tissue disruption during cutting, increased respiration rate, and elevated free-radical generation during storage. In contrast, all packaged apple samples retained significantly ($p < 0.05$) higher antioxidant activity throughout the storage period. Among the treatments, NE-coated apple slices demonstrated the highest antioxidant retention, decreasing from 18.60 ± 0.61% to 11.53 ± 0.35%, followed by NEW (11.03 ± 0.21%) and GG (10.42 ± 0.50%), while NC (9.10 ± 0.44%) and SA (9.98 ± 0.19%) showed comparatively lower retention among the packaged samples. The superior antioxidant preservation observed in NE-treated apples is attributed to the functional emulsion-templated film enriched with peel extract, which effectively restricts oxygen diffusion while simultaneously contributing additional antioxidant compounds that mitigate oxidative stress. A comparable trend was observed in fresh-cut pear slices. Unpackaged pears showed a significant ($p < 0.05$) reduction in antioxidant activity from 16.33 ± 0.15% at day 0 to 7.85 ± 0.18% at day 12, reflecting oxidative depletion under open storage conditions. In contrast, packaged pear samples maintained significantly ($p < 0.05$) higher antioxidant activity across all storage intervals. The highest retention was recorded in NE-coated pears (13.85 ± 0.28% at day 12), followed by NEW (10.30 ± 0.70%), GG (9.70 ± 0.20%), SA (9.24 ± 0.35%), and NC (8.62 ± 0.83%) treatments. The reduced rate of antioxidant loss in packaged pears can be attributed to

restricted oxygen permeability, minimized cellular dehydration, and delayed oxidative reactions, which collectively contribute to the preservation of antioxidant compounds.

Table 4.60 Antioxidant activity (%) of Fresh-Cut Apples during Storage

Day	Control (%)	NC Control (%)	SA Control (%)	GG Control (%)	NEW Control (%)	NE Control (%)
0	18.95 ± 0.28^{aA}	18.10 ± 0.56^{dA}	18.21 ± 0.20^{cdA}	18.32 ± 0.31^{cA}	18.45 ± 0.27^{cA}	18.60 ± 0.61^{bA}
3	14.52 ± 0.91^{fB}	15.40 ± 0.33^{eB}	16.02 ± 0.25^{dB}	16.41 ± 0.64^{cB}	16.88 ± 0.78^{bB}	17.29 ± 0.28^{aB}
6	11.33 ± 0.12^{fC}	13.10 ± 0.27^{eC}	13.92 ± 0.78^{dC}	14.38 ± 0.47^{cC}	14.97 ± 0.44^{bC}	15.48 ± 0.31^{aC}
9	9.80 ± 0.52^{fD}	10.90 ± 0.69^{eD}	11.61 ± 0.83^{dD}	12.19 ± 0.90^{cD}	12.82 ± 0.32^{bD}	13.31 ± 0.22^{aD}
12	8.10 ± 0.20^{fE}	9.10 ± 0.44^{eE}	9.98 ± 0.19^{dE}	10.42 ± 0.50^{cE}	11.03 ± 0.21^{bE}	11.53 ± 0.35^{aE}

All values are expressed as mean ± SD (n = 3). Means within the same column with different uppercase letters (A–E) and within the same row with different lowercase letters (a–f) differ significantly ($p < 0.05$) on the same storage day.

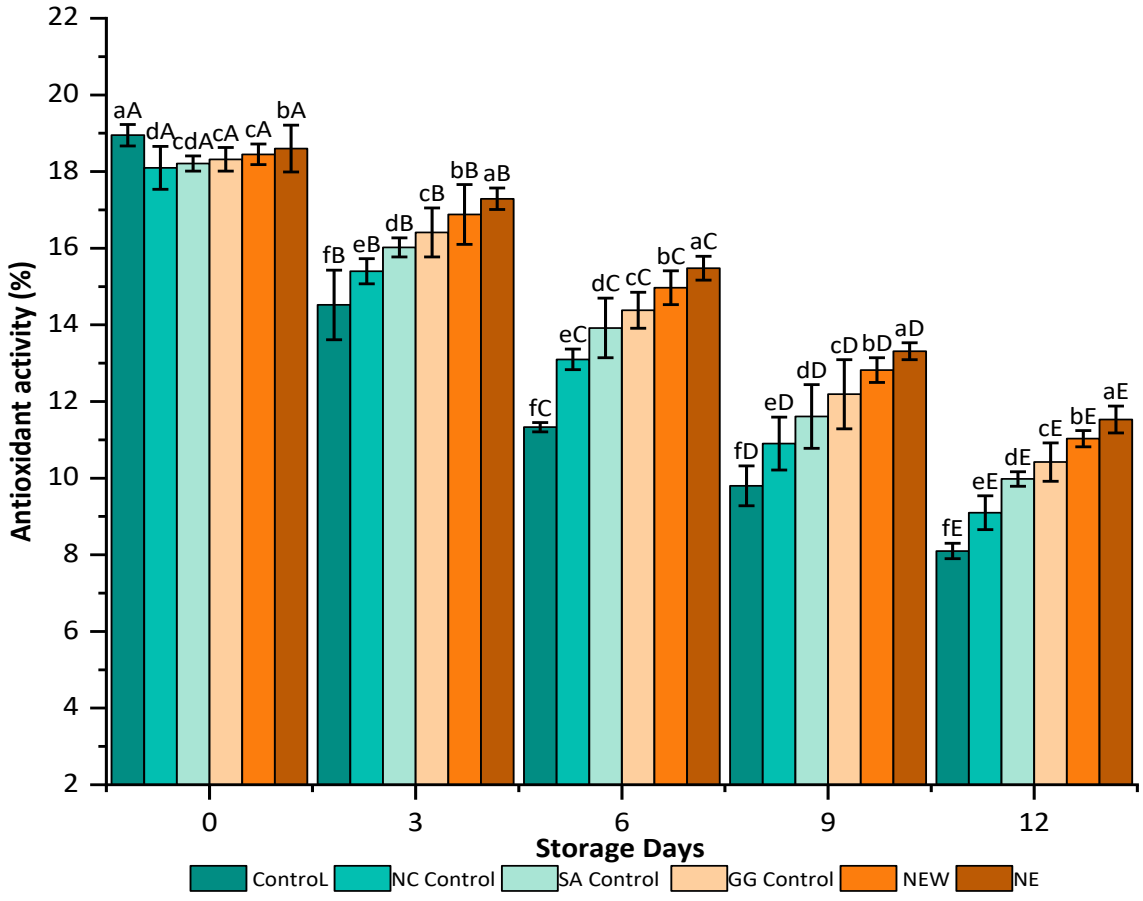

Fig. 4.106 Changes in Antioxidant activity (%) of fresh-cut apple slices during storage under different packaging materials

Note: NC: Nanocellulose, SA: Sodium alginate, GG: Guar gum, NEW: Nanocellulose, sodium alginate, and guar gum without *Cucumis callosus* peel extract, and NE: Nanocellulose, sodium alginate, and guar gum with *Cucumis callosus* peel extract functional film. Different lowercase letters denote significant differences among treatments within the same storage day, while different uppercase letters denote significant differences within the same treatment across storage days ($p < 0.05$).

Table 4.61 Antioxidant activity (%) of Fresh-Cut pears during Storage

Day	Control (%)	NC Control (%)	SA Control (%)	GG Control (%)	NEW Control (%)	NE Control (%)
0	16.33 ± 0.15^{deA}	16.92 ± 0.78^{dA}	17.21 ± 0.27^{bA}	17.12 ± 0.11^{cA}	17.25 ± 0.58^{bA}	16.67 ± 0.21^{aA}
3	13.80 ± 0.45^{fB}	14.25 ± 0.24^{eB}	14.85 ± 0.67^{dB}	15.22 ± 0.30^{cB}	15.75 ± 0.83^{bB}	15.20 ± 0.34^{aB}
6	11.35 ± 0.32^{fC}	12.15 ± 0.78^{eC}	12.70 ± 0.37^{dC}	13.05 ± 0.24^{cC}	13.65 ± 0.33^{bC}	14.25 ± 0.12^{aC}
9	9.66 ± 0.20^{fD}	10.55 ± 0.21^{eD}	10.75 ± 0.62^{dD}	11.22 ± 0.51^{cD}	11.84 ± 0.66^{bD}	12.40 ± 0.87^{aD}
12	7.85 ± 0.18^{fE}	8.62 ± 0.83^{eE}	9.24 ± 0.35^{dE}	9.70 ± 0.20^{cE}	10.30 ± 0.70^{bE}	13.85 ± 0.28^{aE}

All values are expressed as mean ± SD (n = 3). Means within the same column with different uppercase letters (A–E) and within the same row with different lowercase letters (a–f) differ significantly ($p < 0.05$) on the same storage day.

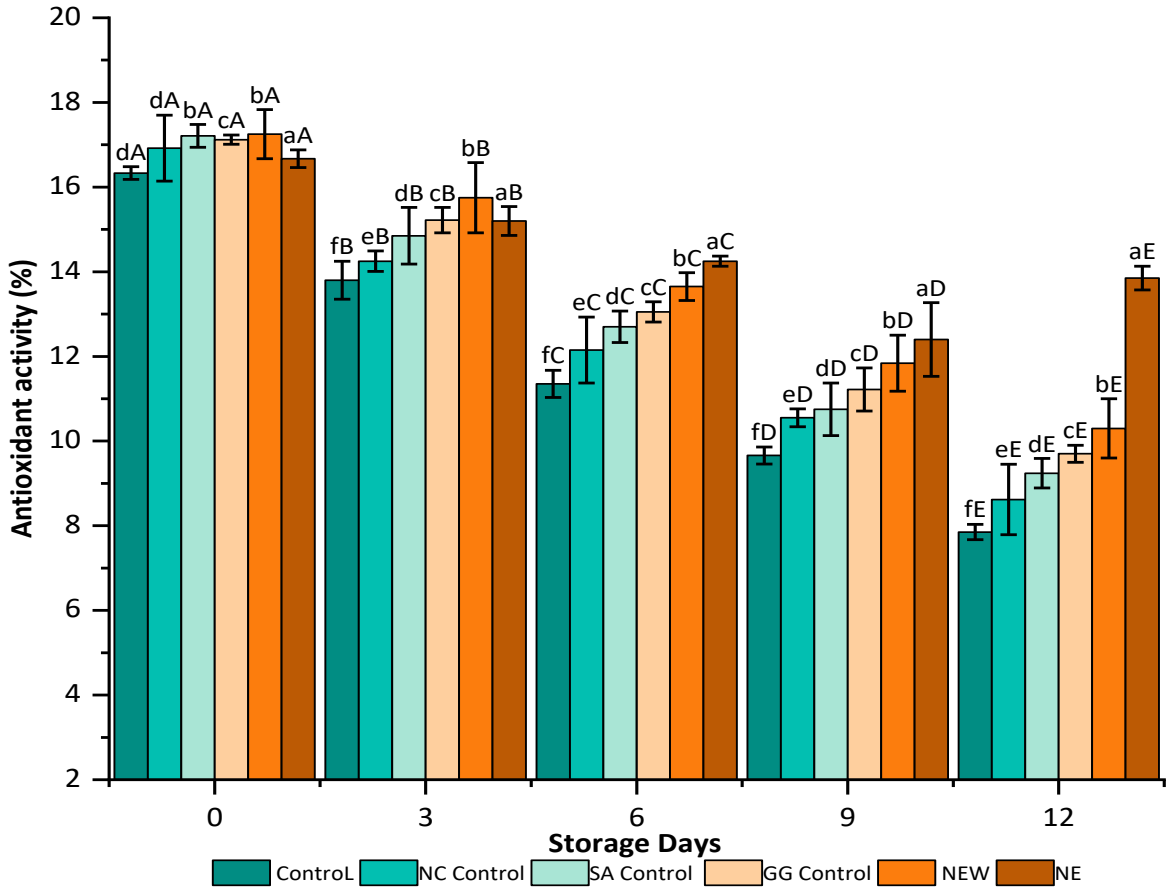

Fig. 4.107 Changes in Antioxidant activity (%) of fresh-cut pear slices during storage under different packaging materials

Note: NC: Nanocellulose, SA: Sodium alginate, GG: Guar gum, NEW: Nanocellulose, sodium alginate, and guar gum without *Cucumis callosus* peel extract, and NE: Nanocellulose, sodium alginate, and guar gum with *Cucumis callosus* peel extract functional film. Different lowercase letters denote significant differences among treatments within the same storage day, while different uppercase letters denote significant differences within the same treatment across storage days ($p < 0.05$).

4.15.12 Firmness (N)

Firmness is a critical quality attribute reflecting cell wall integrity, middle lamella stability, and textural acceptability of fresh-cut fruits during storage in fig. 4.108 and 4.109. In the present study, unpackaged samples exhibited a significantly greater reduction in firmness with increasing storage duration in both apples and pears ($p < 0.05$), as shown in Tables 4.58 and 4.59. On day 0, unpackaged apple and pear slices recorded firmness values of 62.39 N and 48.72 N, respectively, which gradually declined to 51.08 N in apples and 42.10 N in pears by day 12, as shown in Table. 4.62 and 4.63. The progressive softening observed from day 3 onwards in the control samples is primarily attributed to unrestricted moisture loss, elevated

respiration rate, and enhanced enzymatic degradation of cell-wall polysaccharides following tissue disruption. Among the packaged samples, all emulsion films significantly ($p < 0.05$) improved firmness retention compared to the unpackaged control throughout storage, as indicated by distinct lowercase superscripts within each storage day. At days 3 and 6, nanocellulose-coated samples exhibited moderate firmness retention in both fruits, however, a noticeable decline was evident by days 9 and 12, suggesting limited resistance to long-term moisture migration. In contrast, sodium alginate- and guar gum-based films significantly ($p < 0.05$) restricted firmness loss, maintaining higher firmness values from day 6 onwards, with final values of 58.90–59.25 N in apples and 48.15–48.95 N in pears on day 12. This improved textural stability is associated with their higher water-binding capacity and formation of continuous hydrocolloid networks that slow tissue softening. The NEW composite film further stabilised firmness during extended storage, showing comparatively smaller reductions between day 6 and day 12, thereby indicating synergistic interactions among polymeric constituents that enhanced film compactness and reduced enzymatic softening. Notably, NE-treated samples consistently exhibited the highest firmness at all storage intervals, retaining 59.80 N in apples and 50.20 N in pears by day 12, which were significantly ($p < 0.05$) higher than all other treatments on the same day. The superior firmness preservation from day 3 through day 12 in NE-coated samples is attributed to effective moisture retention, moderated gas exchange, and delayed enzymatic breakdown of pectic substances, thereby preserving cellular cohesion over time.

Table 4.62 Changes in Firmness (N) of Fresh-Cut Apples under Different Biodegradable Packaging Films

Day	Control (N)	NC Control (N)	SA Control (N)	GG Control (N)	NEW Control (N)	NE Control (N)
0	62.39 ± 0.49^{cA}	60.85 ± 0.61^{eA}	61.92 ± 0.45^{dA}	62.40 ± 0.39^{cA}	63.14 ± 0.52^{bA}	64.73 ± 0.44^{aA}
3	55.28 ± 0.42^{fB}	59.90 ± 0.48^{eB}	60.85 ± 0.55^{dB}	61.33 ± 0.40^{cB}	61.95 ± 0.46^{bB}	63.40 ± 0.36^{aB}
6	54.20 ± 0.46^{fC}	58.80 ± 0.53^{eC}	59.95 ± 0.47^{dC}	60.17 ± 0.41^{cC}	60.70 ± 0.49^{bC}	61.85 ± 0.34^{aC}
9	52.13 ± 0.35^{fD}	57.85 ± 0.50^{eD}	58.95 ± 0.43^{dD}	59.05 ± 0.38^{cD}	59.55 ± 0.45^{bD}	60.10 ± 0.29^{aD}
12	51.08 ± 0.32^{fE}	56.95 ± 0.48^{eE}	58.90 ± 0.52^{dE}	58.12 ± 0.37^{cE}	59.25 ± 0.41^{bE}	59.80 ± 0.33^{aE}

All values are expressed as mean ± SD (n = 3). Means within the same column with different uppercase letters (A–E) and within the same row with different lowercase letters (a–f) differ significantly ($p < 0.05$) on the same storage day.

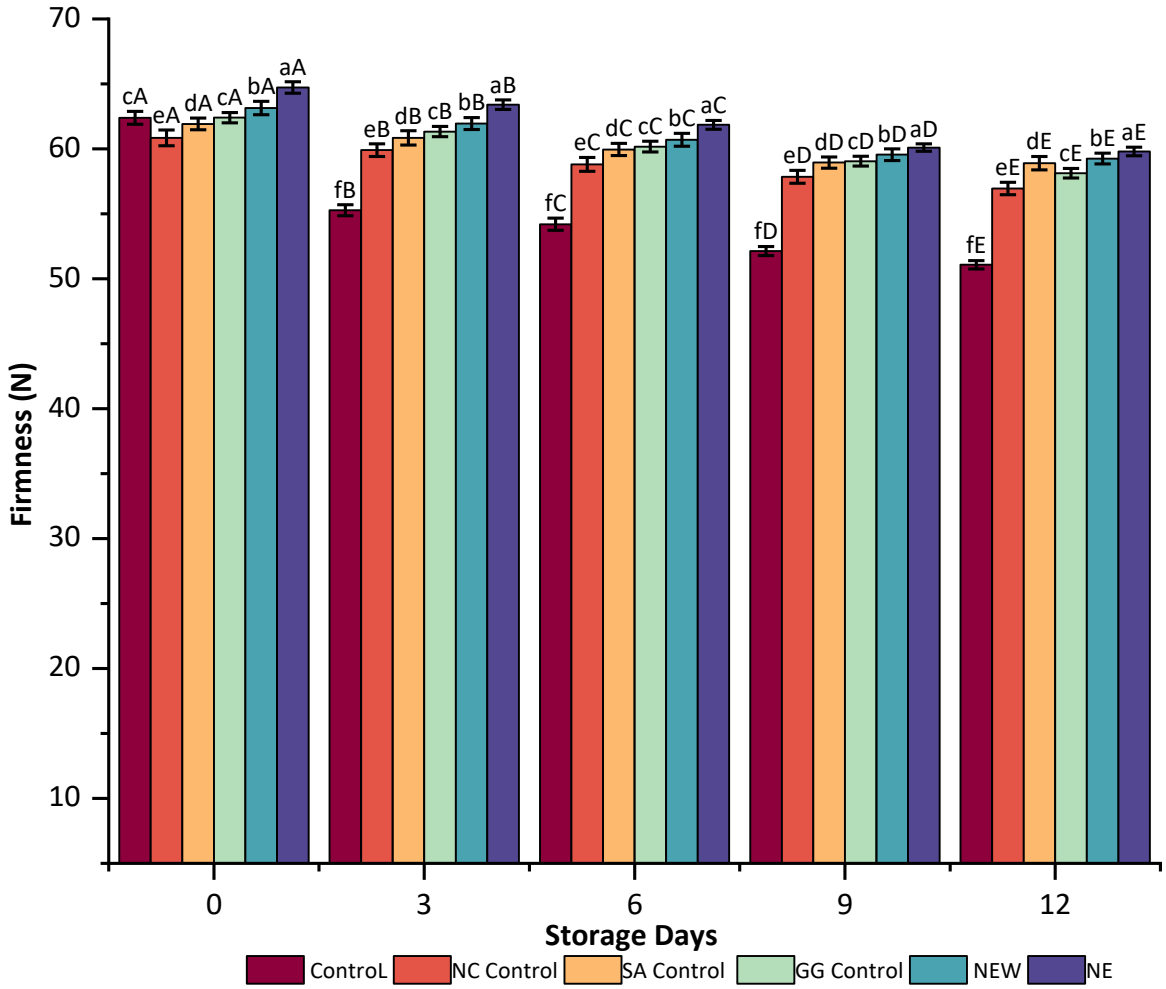

Fig. 4.108 Changes in Firmness (N) of fresh-cut apple slices during storage under different packaging materials

Note: NC: Nanocellulose, SA: Sodium alginate, GG: Guar gum, NEW: Nanocellulose, sodium alginate, and guar gum without *Cucumis callosus* peel extract, and NE: Nanocellulose, sodium alginate, and guar gum with *Cucumis callosus* peel extract functional film. Different lowercase letters denote significant differences among treatments within the same storage day, while different uppercase letters denote significant differences within the same treatment across storage days ($p < 0.05$).

Table 4.63 Changes in Firmness (N) of Fresh-Cut pears under Different Biodegradable Packaging Films

Day	Control (N)	NC Control (N)	SA Control (N)	GG Control (N)	NEW Control (N)	NE Control (N)
0	52.72 ± 0.44^{eA}	52.25 ± 0.32^{eA}	53.12 ± 0.23^{dA}	53.95 ± 0.19^{cA}	55.05 ± 0.55^{bA}	56.31 ± 0.38^{aA}
3	46.90 ± 0.41^{fB}	50.10 ± 0.66^{eB}	51.20 ± 0.83^{dB}	52.19 ± 0.77^{cB}	53.30 ± 0.32^{bB}	54.55 ± 0.30^{aB}

6	45.13 ± 0.54^{fC}	48.30 ± 0.40^{eC}	49.64 ± 0.63^{dC}	50.42 ± 0.31^{cC}	51.65 ± 0.29^{bC}	52.89 ± 0.79^{aC}
9	43.35 ± 0.35^{fD}	47.23 ± 0.66^{eD}	48.45 ± 0.46^{dD}	49.20 ± 0.72^{cD}	50.35 ± 0.30^{bD}	51.55 ± 0.25^{aD}
12	42.10 ± 0.15^{fE}	46.85 ± 0.34^{eE}	48.15 ± 0.20^{dE}	48.95 ± 0.89^{cE}	49.71 ± 0.91^{bE}	50.20 ± 0.81^{aE}

All values are expressed as mean ± SD (n = 3). Means within the same column with different uppercase letters (A–E) and within the same row with different lowercase letters (a–f) differ significantly ($p < 0.05$) on the same storage day.

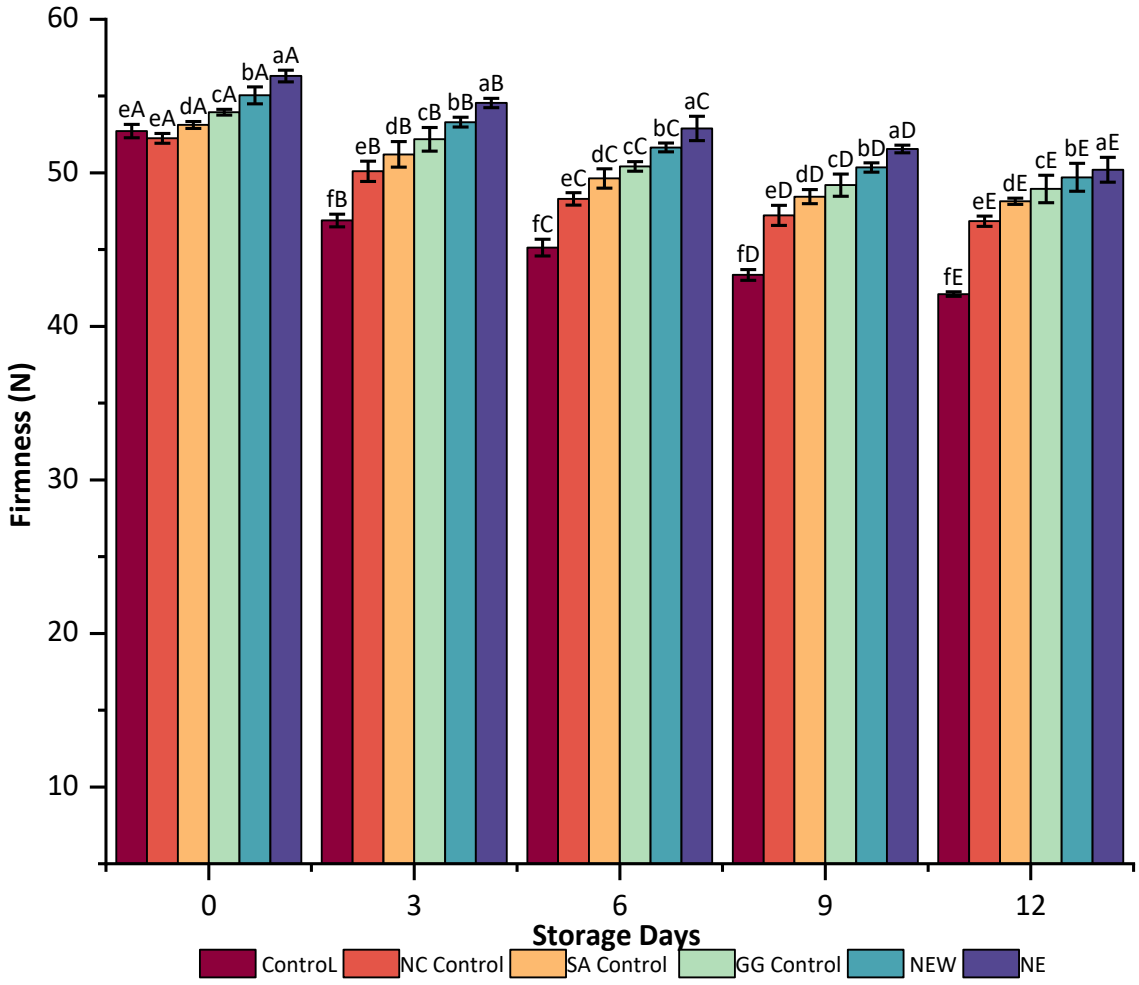

Fig. 4.109 Changes in Firmness (N) of fresh-cut pear slices during storage under different packaging materials

Note: NC: Nanocellulose, SA: Sodium alginate, GG: Guar gum, NEW: Nanocellulose, sodium alginate, and guar gum without *Cucumis callosus* peel extract, and NE: Nanocellulose, sodium alginate, and guar gum with *Cucumis callosus* peel extract functional film. Different lowercase letters denote significant differences among treatments within the same storage day, while

different uppercase letters denote significant differences within the same treatment across storage days ($p < 0.05$).

4.15.13 Titrable acidity (%)

Titratable acidity is a key biochemical quality parameter reflecting organic acid metabolism, respiratory intensity, and senescence-associated biochemical transformations in fresh-cut fruits during storage. In the present study, unpackaged samples exhibited a significantly ($p < 0.05$) higher increase in titratable acidity throughout the 0–12 day storage period in Tables 4.64 and 4.65, with TA in cut apples increasing from 0.22 ± 0.05% on day 0 to 0.42 ± 0.04% by day 12, and in cut pears from 0.18 ± 0.04% to 0.35 ± 0.05%, which was significantly ($p < 0.05$) higher than all packaged treatments fig. 4.110 and 4.111. This pronounced acid accumulation in Controls is attributed to unrestricted oxygen diffusion, elevated respiration rates, and enhanced tricarboxylic acid (TCA) cycle activity following tissue disruption, resulting in accelerated synthesis of organic acids such as malate and citrate. Among the control films, nanocellulose-based packaging resulted in significantly ($p < 0.05$) higher titratable acidity compared to other packaged treatments, with TA in apples increasing from 0.17 ± 0.04% to 0.32 ± 0.06%, and in pears from 0.17 ± 0.05% to 0.32 ± 0.06%. These values were significantly higher ($p < 0.05$) than those observed for SA, GG, NEW, and NE treatments, which may be attributed to the moderate gas permeability of nanocellulose matrices that permits sustained respiratory metabolism. In contrast, sodium alginate and guar gum films exhibited significantly ($p < 0.05$) lower titratable acidity than NC-coated samples. Specifically, TA increased from 0.24 ± 0.06% to 0.39 ± 0.05% (SA) and from 0.24 ± 0.05% to 0.40 ± 0.05% (GG) in apples, and from 0.18 ± 0.06% to 0.33 ± 0.05% (SA) and from 0.18 ± 0.05% to 0.34 ± 0.05% (GG) in pears. The NEW composite film further reduced titratable acidity, maintaining values of 0.21 ± 0.04% to 0.35 ± 0.04% in apples and 0.17 ± 0.03% to 0.30 ± 0.03% in pears, which were significantly ($p < 0.05$) lower than those of NC, SA, and GG treatments. Notably, the NE functional film exhibited the significantly ($p < 0.05$) lowest titratable acidity throughout the storage period, with TA increasing only from 0.19 ± 0.03% to 0.25 ± 0.03% in apples, and from 0.16 ± 0.03% to 0.28 ± 0.03% in pears, values that were significantly ($p < 0.05$) lower than all other treatments. This superior suppression of acid accumulation under NE treatment is attributed to effective oxygen barrier properties, reduced respiratory flux, delayed TCA cycle activity, and downregulation of enzymes involved in organic acid biosynthesis.

Table 4.64 Changes in Titratable Acidity (%) of Fresh-Cut Apples Stored under Different Packaging Conditions

Day	Control (%)	NC Control (%)	SA Control (%)	GG Control (%)	NEW Control (%)	NE Control (%)
0	0.22 ± 0.005^{aA}	0.17 ± 0.004^{aA}	0.24 ± 0.006^{aA}	0.24 ± 0.005^{aA}	0.21 ± 0.003^{bA}	0.19 ± 0.005^{cA}
3	0.28 ± 0.006^{aB}	0.23 ± 0.005^{aB}	0.29 ± 0.004^{aB}	0.30 ± 0.004^{aB}	0.24 ± 0.003^{bB}	0.21 ± 0.002^{cB}
6	0.33 ± 0.006^{aC}	0.26 ± 0.005^{aC}	0.32 ± 0.006^{aC}	0.33 ± 0.005^{aC}	0.27 ± 0.006^{bC}	0.23 ± 0.003^{cC}
9	0.38 ± 0.005^{aD}	0.30 ± 0.006^{a}D	0.36 ± 0.005^{aD}	0.37 ± 0.002^{aD}	0.31 ± 0.003^{bD}	0.24 ± 0.005^{cD}
12	0.42 ± 0.004^{aE}	0.32 ± 0.006^{aE}	0.39 ± 0.007^{aE}	0.40 ± 0.005^{aE}	0.35 ± 0.003^{bE}	0.25 ± 0.003^{cE}

All values are expressed as mean ± SD (n = 3). Means within the same column with different uppercase letters (A–E) and within the same row with different lowercase letters (a–f) differ significantly ($p < 0.05$) on the same storage day.

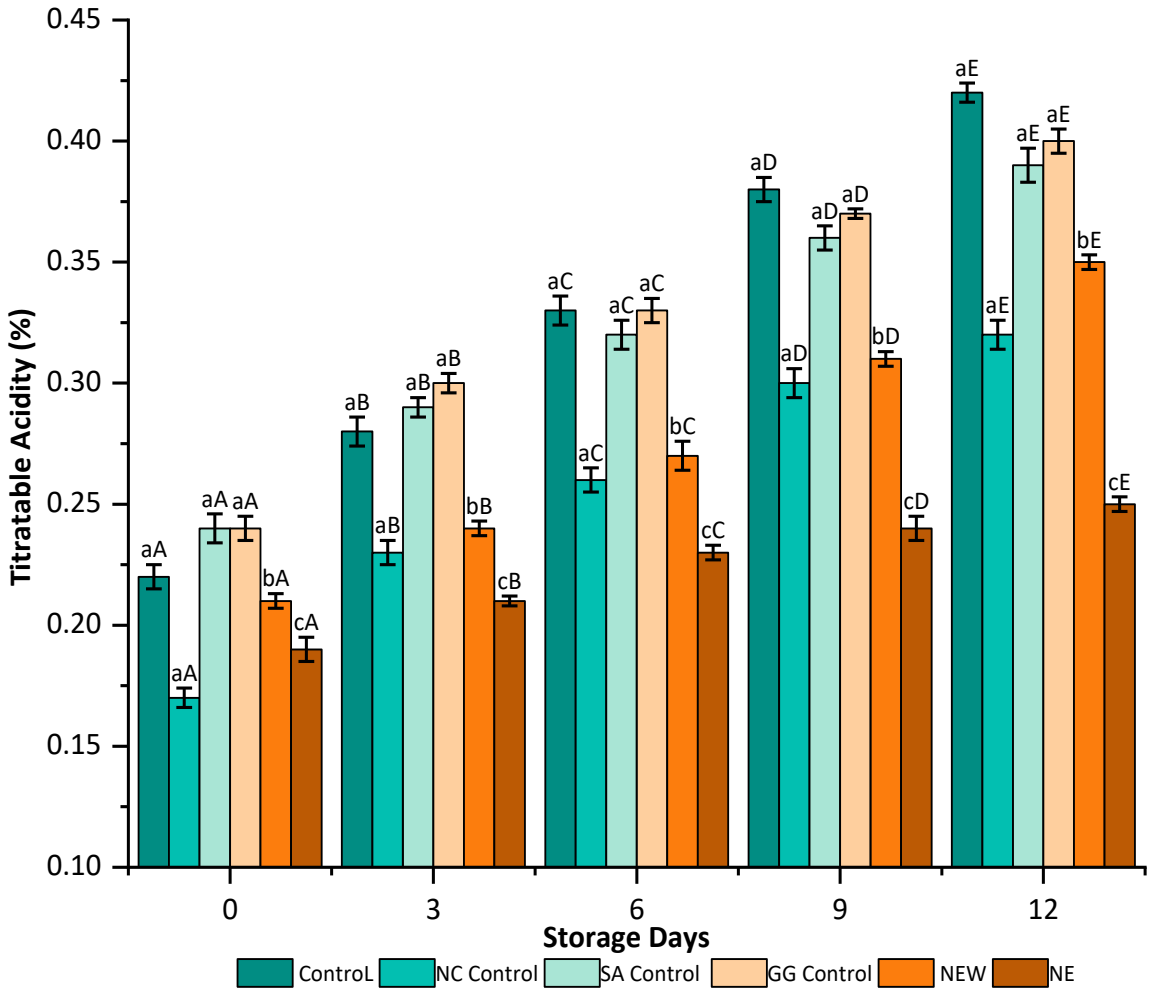

Fig. 4.110 Changes in Titratable Acidity (%) of fresh-cut apple slices during storage under different packaging materials

Note: NC: Nanocellulose, SA: Sodium alginate, GG: Guar gum, NEW: Nanocellulose, sodium alginate, and guar gum without *Cucumis callosus* peel extract, and NE: Nanocellulose, sodium alginate, and guar gum with *Cucumis callosus* peel extract functional film. Different lowercase letters denote significant differences among treatments within the same storage day, while different uppercase letters denote significant differences within the same treatment across storage days ($p < 0.05$).

Table 4.65 Changes in Titratable Acidity (%) of Fresh-Cut pears Stored under Different Packaging Conditions

Day	**Control (%)**	**NC Control (%)**	**SA Control (%)**	**GG Control (%)**	**NEW Control (%)**	**NE Control (%)**
0	0.18 ± 0.004^{aA}	0.17 ± 0.005^{aA}	0.18 ± 0.006^{aA}	0.18 ± 0.005^{aA}	0.17 ± 0.003^{bA}	0.16 ± 0.002^{cA}
3	0.23 ± 0.005^{aB}	0.22 ± 0.005^{aB}	0.23 ± 0.004^{aB}	0.24 ± 0.005^{aB}	0.21 ± 0.005^{bB}	0.20 ± 0.003^{cB}
6	0.28 ± 0.006^{aC}	0.26 ± 0.005^{aC}	0.27 ± 0.006^{ac}	0.28 ± 0.004^{aC}	0.24 ± 0.003^{bC}	0.23 ± 0.004^{cC}
9	0.32 ± 0.005^{aD}	0.29 ± 0.006^{aD}	0.30 ± 0.005^{aD}	0.31 ± 0.003^{aD}	0.27 ± 0.006^{bD}	0.25 ± 0.005^{cD}
12	0.35 ± 0.005^{aE}	0.32 ± 0.006^{aE}	0.33 ± 0.007^{aE}	0.34 ± 0.005^{aE}	0.30 ± 0.003^{bE}	0.28 ± 0.003^{cE}

All values are expressed as mean ± SD (n = 3). Means within the same column with different uppercase letters (A–E) and within the same row with different lowercase letters (a–f) differ significantly ($p < 0.05$) on the same storage day.

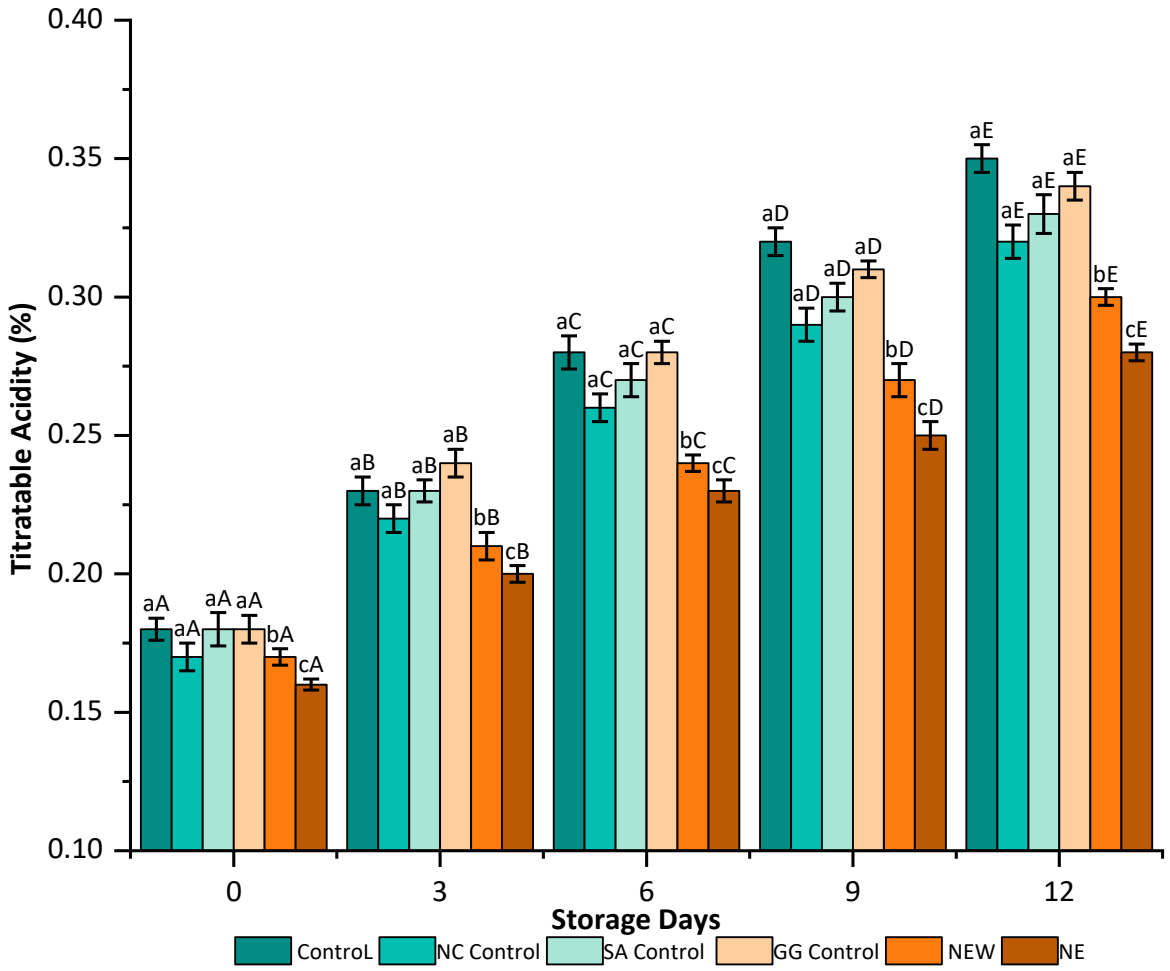

Fig. 4.111 Changes in Titratable Acidity (%) of fresh-cut pear slices during storage under different packaging materials

Note: NC: Nanocellulose, SA: Sodium alginate, GG: Guar gum, NEW: Nanocellulose, sodium alginate, and guar gum without *Cucumis callosus* peel extract, and NE: Nanocellulose, sodium alginate, and guar gum with *Cucumis callosus* peel extract functional film. Different lowercase letters denote significant differences among treatments within the same storage day, while different uppercase letters denote significant differences within the same treatment across storage days ($p < 0.05$).

Chapter 5 Summary and Conclusion

The increasing demand for sustainable materials and environmentally responsible food packaging systems necessitates innovative approaches that integrate biomass valorization with advanced material engineering. The present study established a scientifically validated biorefinery approach for converting *Cyamopsis tetragonoloba* guar straw and *Cucumis callosus* peel into high-value nanostructured biomaterials and functional biodegradable packaging systems. The study systematically covered the physicochemical characterization of raw biomass, optimization of cellulose and nanocellulose extraction, evaluation of bioactive potential, fabrication of composite and emulsion-templated films, and assessment of postharvest performance in fresh-cut apples and pears. Compositional analysis confirmed that guar straw is a lignocellulosic-rich agricultural residue containing substantial cellulose, hemicellulose, and lignin fractions, making it a suitable substrate for cellulose isolation. The material also exhibited favourable hydration and oil-binding capacities, supporting its potential application in polymeric and food-related systems.

Spectroscopic and morphological analyses verified the presence of characteristic cellulose functional groups and fibrous microstructure, while diffraction studies confirmed its semi-crystalline organization. Thermal characterization demonstrated adequate structural stability, indicating suitability for conversion into nanostructured reinforcing materials. Controlled alkaline pretreatment enabled effective delignification and cellulose purification, whereas subsequent acid hydrolysis produced nanocellulose with reduced particle dimensions and improved surface characteristics. Structural analyses further confirmed the preservation of β-glycosidic linkages and semi-crystalline architecture after nanoscale transformation.

The bioactive extract obtained from *Cucumis callosus* peel demonstrated antioxidant, antimicrobial, enzyme inhibitory, and cytotoxic activities. These functional properties were mainly associated with the presence of phenolic compounds, which contributed to free radical scavenging potential and biological activity. Thus, the selected agricultural residues served not only as structural sources for biomaterial development but also as reservoirs of functional phytochemicals suitable for active packaging applications.

Nanocellulose was incorporated into polysaccharide-based matrices to fabricate composite and emulsion-templated biodegradable films. The emulsion-templating approach promoted the development of a hierarchical polymer network with improved dispersion of nanocellulose and encapsulated bioactive constituents. Enhanced intermolecular hydrogen bonding, physical

entanglement, and improved matrix cohesion contributed to better mechanical performance, flexibility, and barrier properties. The reduction in water vapour transmission and improved structural compactness indicated that the developed films achieved a suitable balance between mechanical reinforcement and moisture regulation.

The functional films containing *Cucumis callosus* peel extract exhibited improved active performance due to synergistic interactions between the nanocellulose-reinforced matrix and bioactive compounds. Application studies on fresh-cut apples and pears showed that the developed films improved postharvest quality retention during refrigerated storage. The packaging system reduced moisture migration, limited oxygen permeability, suppressed enzymatic browning, and helped preserve tissue firmness. Antioxidant activity of the incorporated bioactives contributed to reduced oxidative deterioration, while antimicrobial effects helped retard microbial proliferation.

Mechanistically, the improved preservation performance can be attributed to the combined effects of structural reinforcement and active functionality. The nanocellulose-reinforced matrix increased diffusion tortuosity, thereby reducing oxygen and water vapour transmission. Simultaneously, the presence of phenolic compounds helped inhibit oxidative reactions and enzymatic pathways associated with fruit quality deterioration. The emulsion-templated architecture supported uniform distribution of active components and maintained film integrity during storage.

In conclusion, this study demonstrates an environmentally sustainable and scientifically rigorous strategy for transforming lignocellulosic agro-residues into nanocellulose-reinforced active biodegradable packaging materials. The integration of biomass processing, nanotechnology, material science, and postharvest physiology provides a validated platform for sustainable packaging innovation. The developed system shows strong potential for improving postharvest quality of perishable fruits while reducing dependence on synthetic polymer-based packaging materials. Overall, this work supports circular bioeconomy principles and provides a promising pathway for the development of high-performance active food packaging systems.

References

1. Aaliya, B., Sunooj, K. V., & Lackner, M. (2021). Biopolymer composites: A review. International Journal of Biobased Plastics, 3(1), 40–84.
2. Abdel-Hakim, A., & Mourad, R. M. (2023). Nanocellulose and its polymer composites: Preparation, characterization, and applications. Russian Chemical Reviews, 92(4).
3. Abdel-Halim, E. S., & Al-Deyab, S. S. (2011). Low temperature bleaching of cotton cellulose using peracetic acid. Carbohydrate Polymers, 86(2), 988–994.
4. Abdelhamid, H. N. (2026). Green and sustainable nanocellulose production. In Cellulose science and technology (pp. 15–27). Elsevier.
5. Abolore, R. S., Jaiswal, S., & Jaiswal, A. K. (2024). Green and sustainable pretreatment methods for cellulose extraction from lignocellulosic biomass and its applications: A review. Carbohydrate Polymer Technologies and Applications, 7, 100396.
6. Addagada, L., & Nair, A. M. (2025). Assessment of kinetics and thermodynamic parameters of Cocos nucifera using thermogravimetric analysis. Biomass Conversion and Biorefinery, 15(7), 10885–10895.
7. Adhikary, N. D., Bains, A., Tosif, M. M., Chawla, P., Ali, N., Ansari, M. A., & Goksen, G. (2024). Development of ternary polymeric film based on modified mango seed kernel starch, carboxymethyl cellulose, and gum acacia to extend the shelf-life of bun-bread. International Journal of Biological Macromolecules, 273, 132915.
8. Afrin, S., & Karim, Z. (2017). Isolation and surface modification of nanocellulose: Necessity of enzymes over chemicals. ChemBioEng Reviews, 4(5), 289–303.
9. Ahmed, A. Z., Satyam, S. M., Shetty, P., & D'Souza, M. R. (2021). Methyl gallate attenuates doxorubicin-induced cardiotoxicity in rats by suppressing oxidative stress. Scientifica, 2021, 6651359.
10. Ahmed, M. M., Nabi, M. H. B., Mia, M. S., Ahmad, I., & Zzaman, W. (2025). Valorization of plant-based agro-waste into sustainable food packaging materials: Current approaches and functional applications. Applied Food Research, 5, 101368.
11. Akashi, Y., Fukuda, N., Wako, T., Masuda, M., & Kato, K. (2002). Genetic variation and phylogenetic relationships in East and South Asian melons (Cucumis melo L.) based on the analysis of five isozymes. Euphytica, 125(3), 385–396.

12. Akram, F., ul Haq, I., Shah, F. I., Aqeel, A., Ahmed, Z., Mir, A. S., & Raja, S. I. (2022). Genus Thermotoga: A valuable home of multifunctional glycoside hydrolases (GHs) for industrial sustainability. Bioorganic Chemistry, 127, 105942.
13. Alemdar, A., & Sain, M. (2008). Biocomposites from wheat straw nanofibers: Morphology, thermal, and mechanical properties. Composites Science and Technology, 68(2), 557–565.
14. Alexandre, E. M. C., Lourenço, R. V., Bittante, A. M. Q. B., Moraes, I. C. F., & do Amaral Sobral, P. J. (2016). Gelatin-based films reinforced with montmorillonite and activated with nanoemulsion of ginger essential oil for food packaging applications. Food Packaging and Shelf Life, 10, 87–96.
15. Alfaro-Rodríguez, M. C., Prieto, P., García, M. C., Martín-Piñero, M. J., & Muñoz, J. (2022). Influence of nanoemulsion/gum ratio on droplet size distribution, rheology and physical stability of nanoemulgels containing inulin and omega-3 fatty acids. Journal of the Science of Food and Agriculture, 102(14), 6397–6403.
16. Ali, N. E. H. (2020). Agricultural waste management system (AWMS) in Malaysia. Open Access Journal of Waste Management & Xenobiotics, 3(2), 1–2.
17. Almashhadani, A. Q., Leh, C. P., Chan, S. Y., Lee, C. Y., & Goh, C. F. (2022). Nanocrystalline cellulose isolation via acid hydrolysis from non-woody biomass: Importance of hydrolysis parameters. Carbohydrate Polymers, 286, 119285.
18. Almeida, T., Karamysheva, A., Valente, B. F., Silva, J. M., Braz, M., Almeida, A., & Freire, C. S. (2023). Biobased ternary films of thermoplastic starch, bacterial nanocellulose and gallic acid for active food packaging. Food Hydrocolloids, 144, 108934.
19. Al-Mofty, S. E. D., Elghazawy, N. H., & Azzazy, H. M. (2023). A one-step facile process for extraction of cellulose from rice husk and its use for mechanical reinforcement of dental glass ionomer cement. RSC Sustainability, 1(7), 1743–1750.
20. Al-Rajabi, M. M., En, K. J., Mahmod, S. S., & Abdullah, M. F. (2024). Impact of alkali concentration in delignification treatment for cellulose extraction from rice straw. Jordanian Journal of Engineering & Chemical Industries, 7(3).
21. Altemimi, A., Ali, H. I., Al-HiIphy, A. R. S., Lightfoot, D. A., & Watson, D. G. (2018). Electric field applications on dried key lime juice quality with regression modeling. Journal of Food Processing and Preservation, 42(6), e13637.

22. Alzarieni, K. Z., Bani Amer, A. R., & Kenttämaa, H. I. (2025). Characterization of cellulosic fibers from the inflorescences of Echinops sphaerocephalus: An unexplored source of eco-friendly sustainable fibers. Journal of Natural Fibers, 22(1), 2546019.
23. Amândio, M. S., Rocha, J. M., & Xavier, A. M. (2023). Enzymatic hydrolysis strategies for cellulosic sugars production to obtain bioethanol from Eucalyptus globulus bark. Fermentation, 9(3), 241.
24. Amini, E., Valls, C., & Roncero, M. B. (2021). Ionic liquid-assisted bioconversion of lignocellulosic biomass for the development of value-added products. Journal of Cleaner Production, 326, 129275.
25. Anonymous. (2010). Baseline survey of nutritional status of tribals of Sirohi district of Rajasthan. Krishi Vigyan Kendra, Sirohi.
26. AOAC. (2010). Official methods of analysis of the Association of Official Analytical Chemists. AOAC International.
27. Araújo, D. J. C., Vilarinho, M. C. L. G., & Machado, A. V. (2019). Agroindustrial residues as cellulose source for food packaging applications. In Wastes: Solutions, treatments and opportunities III (pp. 217–223). CRC Press.
28. Arora, D. S., Sharma, R. K., & Chandra, P. (2011). Biodelignification of wheat straw and its effect on in vitro digestibility and antioxidant properties. International Biodeterioration & Biodegradation, 65(2), 352–358.
29. Arora, R., Kaur, M., & Gill, N. S. (2011). Antioxidant activity and pharmacological evaluation of Cucumis melo var. agrestis methanolic seed extract. Research Journal of Phytochemistry, 5(3), 146–155.
30. Attar, U. A., & Ghane, S. G. (2021). Proximate composition, ionomics, phytochemical, antioxidant, anti-diabetic and acetylcholinesterase inhibitory activity of Cucumis species from Western Ghats of India. Indian Journal of Pharmaceutical Sciences, 83(4), 741–749.
31. Ayllón-Parra, N., Castellari, M., Gou, P., & Ribas-Agustí, A. (2025). Cricket powder (Acheta domesticus) nutritional and techno-functional properties and effects of solid-state fermentation with Pleurotus ostreatus and Rhizopus oligosporus. Innovative Food Science & Emerging Technologies, 104066.
32. Azimi, B., Maleki, H., Gigante, V., Bagherzadeh, R., Mezzetta, A., Milazzo, M., & Danti, S. (2022). Cellulose-based fiber spinning processes using ionic liquids. Cellulose, 29(6), 3079–3129.

33. Bai, L., Xiang, W., Huan, S., & Rojas, O. J. (2018). Formulation and stabilization of concentrated edible oil-in-water emulsions based on electrostatic complexes of a food-grade cationic surfactant (ethyl lauroyl arginate) and cellulose nanocrystals. Biomacromolecules, 19(5), 1674–1685.
34. Bąk, A., & Podgórska, W. (2016). Interfacial and surface tensions of toluene/water and air/water systems with nonionic surfactants Tween 20 and Tween 80. Colloids and Surfaces A: Physicochemical and Engineering Aspects, 504, 414–425.
35. Bangar, S. P., Cao, Y., Kumar, M., Ravindran, R., Trif, M., Kumar, A., et al. (2023). Valorization of wheat straw in food packaging: A source of cellulose. International Journal of Biological Macromolecules, 235, 123276.
36. Bangar, S. P., Kajla, P., & Ghosh, T. (2023). Valorization of wheat straw in food packaging: A source of cellulose. International Journal of Biological Macromolecules, 227, 762–776.
37. Banvillet, G., Depres, G., Belgacem, N., & Bras, J. (2021). Alkaline treatment combined with enzymatic hydrolysis for efficient cellulose nanofibrils production. Carbohydrate Polymers, 255, 117383.
38. Baron, R. I., Chibac-Scutaru, A. L., Biliuta, G., & Coseri, S. (2025). Synergistic reinforcement: Harnessing nanocellulose for robust double network hydrogels. Cellulose Chemistry & Technology, 59.
39. Basu, B., Dutta, S., Rahaman, M., Dutta, S., Ansari, M. N., Prajapati, B. G., & Ghosh, S. (2025). Exploring the impact of polysaccharide-based nanoemulsions in drug delivery. Journal of Biomedical Materials Research Part B: Applied Biomaterials, 113(5), e35582.
40. Bayram, G., Denizli-Turan, S., & Erdem, R. (2021). A review on sustainable polymeric materials for food packaging applications. Food Packaging and Shelf Life, 29, 100726.
41. Begum, F., Chutia, H., Bora, M., Deb, P., & Mahanta, C. L. (2024). Characterization of coconut milk waste nanocellulose-based curcumin-enriched Pickering nanoemulsion and its application in a blended beverage of defatted coconut milk and pineapple juice. International Journal of Biological Macromolecules, 259, 129305.
42. Bhatt, R. K., Jukanti, A. K., & Roy, M. M. (2017). Cluster bean (Cyamopsis tetragonoloba (L.) Taub.), an important industrial arid legume: A review. Legume Research – An International Journal, 40(2), 207–214.
43. Bhattacharyya, P., Bhaduri, D., Adak, T., Munda, S., Satapathy, B. S., Dash, P. K., & Pathak, H. (2020). Characterization of rice straw from major cultivars for best

alternative industrial uses to reduce straw burning. Industrial Crops and Products, 143, 111919.

44. Bhrijavasi, G., Anusha, D. A. P. S., Mishra, K., & Chawla, R. (2024). Underutilized fruit crops in semi-arid climates: Challenges, innovations, and future prospects. International Journal of Advanced Biochemistry Research, 8, 488–496.
45. Bian, H., Yang, Y., Tu, P., & Chen, J. Y. (2022). Value-added utilization of wheat straw: From cellulose and cellulose nanofiber to all-cellulose nanocomposite film. Membranes, 12(5), 475.
46. Binnemans, K., & Jones, P. T. (2023). Ionic liquids and deep-eutectic solvents in extractive metallurgy: Mismatch between academic research and industrial applicability. Journal of Sustainable Metallurgy, 9(2), 423–438.
47. Bohra, P., Waman, A. A., Roy, T. K., & Shivashankara, K. S. (2020). Blood fruit (Haematocarpus validus (Miers.) Bakh. f. ex Forman): A novel source of natural food colourant. Journal of Food Science and Technology, 57, 381–389.
48. Branco, I. G., Sen, K., & Rinaldi, C. (2020). Effect of sodium alginate and different types of oil on the physical properties of ultrasound-assisted nanoemulsions. Chemical Engineering and Processing: Process Intensification, 153, 107942.
49. Camiletti, C., Rodríguez, M. S., Poli, A. L., & Baldini, M. (2023). Agro-industrial seed wastes as functional fillers in biopolymer packaging films. Journal of Polymers and the Environment, 31(3), 1251–1263.
50. Cao, Y., Zhang, Z., Liu, Y., & Wang, H. (2025). Recent advances in cellulose-based biodegradable packaging materials: Structure, property, and functionality. Food Packaging and Shelf Life, 37, 101258.
51. Carnaval, S., Pires, A. M., & de Souza, A. F. (2024). Biotechnological production of polyhydroxyalkanoates from agro-wastes: Toward circular bio-manufacturing. Bioresource Technology Reports, 25, 101651.
52. Carvalho, M. J., Costa, J. R., Pedrosa, S. S., Pintado, M., Oliveira, A. L., & Madureira, A. R. (2023). Sugarcane straw extracts: Production and purification by Amberlite XAD-2. Food and Bioproducts Processing, 140, 189–199.
53. Catarino, R. P. F., Mascareli, V. A. B., Leite da Costa, V. L., Pavanello, A. C. L., & Spinosa, W. A. (2025). Sustainability and influencing factors in bacterial cellulose production: A review of the impact of microorganisms, culture media, and cultivation methods. Food Technology and Biotechnology, 63(3), 332–350.

54. Ceaser, R., & Chimphango, A. F. (2021). Comparative analysis of physical and functional properties of cellulose nanofibers isolated from alkaline pre-treated wheat straw in optimized hydrochloric acid and enzymatic processes. International Journal of Biological Macromolecules, 171, 331–342.
55. Chaka, K. T. (2022). Extraction of cellulose nanocrystals from agricultural by-products: A review. Green Chemistry Letters and Reviews, 15(3), 582–597.
56. Chand, T., Bhandari, A., Kumawat, B. K., Basniwal, P., Sharma, S., & Verma, R. (2012). In vitro antioxidant activity of alcoholic extract of seed of Cucumis callosus (Rottl.) Cogn. American Journal of PharmTech Research, 2(3).
57. Chand, T., Bhandari, A., Kumawat, B. K., Sharma, A., Pareek, A., & Bansal, V. K. (2012). In vitro antioxidant activity of aqueous extract of seeds of Cucumis callosus (Rottl.) Cogn. Der Pharmacia Lettre, 4(3), 840–844.
58. Chang, S., et al. (2023). The characteristics of polysaccharide from Gracilaria chouae and its application in food packaging with carboxymethyl cellulose and lysozyme. Food Hydrocolloids, 135, 108109.
59. Chawla, P., Bhandari, L., Sadh, P. K., & Kaushik, R. (2017). Impact of solid-state fermentation (Aspergillus oryzae) on functional properties and mineral bioavailability of black-eyed pea (Vigna unguiculata) seed flour. Cereal Chemistry, 94(3), 437–442.
60. Chawla, P., Sridhar, K., Kumar, A., Sarangi, P. K., Bains, A., & Sharma, M. (2023). Production of nanocellulose from corn husk for the development of antimicrobial biodegradable packaging film. International Journal of Biological Macromolecules, 242, 124805.
61. Chen, Y., Wei, Q., Chen, Y., Feng, A., & Zhang, W. (2024). Enhancement of hydrogen bonds between proteins and polyphenols through magnetic field treatment: Structure, interfacial properties, and emulsifying properties. Food Research International, 192, 114822.
62. Cheng, L., Zhang, X., Hong, Y., Li, Z., Li, C., & Gu, Z. (2017). Characterisation of physicochemical and functional properties of soluble dietary fibre from potato pulp obtained by enzyme-assisted extraction. International Journal of Biological Macromolecules, 101, 1004–1011.
63. Chik, J. Y., Wan-Ibrahim, W. S. F. A., & Tamat, N. S. M. (2024). Extraction of cellulose from corn tassel using alkaline pretreatment and bleaching process. In BIO Web of Conferences (Vol. 131, p. 01004). EDP Sciences.

64. Choudhary, S. K., Patel, A. K., Chouhan, R., Ram, K., Ambawat, S., Shekhawat, S., & Shekhawat, N. S. (2024). Micropropagation, micromorphological evaluation and genetic homogeneity validation of Cucumis collosus (Rottl.) Cogn.: A wild progenitor of melon. Biocatalysis and Agricultural Biotechnology, 61, 103378.
65. Choudhary, S. S., Panigrahi, P. N., Dhara, S. K., Sahoo, M., Dan, A., Thakur, N., & Dey, S. (2023). Cucumis callosus (Rottl.) Cogn. fruit extract ameliorates calcium oxalate urolithiasis in ethylene glycol-induced hyperoxaluric rat model. Heliyon, 9(3), e14494.
66. Ci, Y., Chen, T., Li, F., Zou, X., & Tang, Y. (2023). Cellulose dissolution and regeneration behavior via DBU-levulinic acid solvents. International Journal of Biological Macromolecules, 252, 126548.
67. Cristofoli, A., Torres-León, C., Ramírez-Guzmán, N., & Ramírez, A. C. (2023). Circular bioeconomy for sustainable food packaging from agricultural residues. Food Hydrocolloids, 146, 108924.
68. Cristofoli, N. L., Lima, A. R., Tchonkouang, R. D., Quintino, A. C., & Vieira, M. C. (2023). Advances in the food packaging production from agri-food waste and by-products: Market trends for sustainable development. Sustainability, 15(7), 6153.
69. D'Ambrosio, S., Zaccariello, L., Sadiq, S., D'Albore, M., Battipaglia, G., D'Agostino, M., & Cimini, D. (2023). Grape stalk valorization: An efficient re-use of lignocellulosic biomass through hydrolysis and fermentation to produce lactic acid from Lactobacillus rhamnosus IMC501. Fermentation, 9(7), 616.
70. Das, P. P., Kalyani, P., Kumar, R., & Khandelwal, M. (2023). Cellulose-based natural nanofibers for fresh produce packaging: Current status, sustainability, and future outlook. Sustainable Food Technology, 1(4), 528–544.
71. de Farias, D. T., Labidi, J., Pedrazzi, C., Gatto, D. A., de Cademartori, P. H. G., Welter, C. A., & de Almeida, T. M. (2024). Acid-hydrolysis-assisted cellulose nanocrystal isolation from Acacia mearnsii de Wild. wood kraft pulp. Polymers, 16(23), 3371.
72. Deepika, S., & Kumari, A. (2024). Nutritional, shelf-life, and sensory evaluation of Cucumis callosus-based optimized syrup. Plant Foods for Human Nutrition, 79(1), 225–233.
73. Deepika, S., Kumari, A., Prajapati, P., Sarita, Kumar, S., Aluko, R. E., Singh, S., & Garg, M. (2023). Pharmacological and therapeutic potential of Cucumis callosus: A novel nutritional powerhouse for the management of non-communicable diseases. Plant Foods for Human Nutrition, 78(4), 630–642.

74. Deva, S. (2019). Preparation of land for upcoming season. Agriculture & Food: E-Newsletter, 21530, 180.
75. Dhara, A. K., Suba, V., Sen, T., Pal, S., & Chaudhuri, A. N. (2000). Preliminary studies on the anti-inflammatory and analgesic activity of the methanolic fraction of the root extract of Tragia involucrata Linn. Journal of Ethnopharmacology, 72(1–2), 265–268.
76. Dilucia, F., Lorusso, N., Tylewicz, U., & Ragni, L. (2020). Active packaging based on natural antioxidants and antimicrobial compounds derived from agro-industrial by-products. Food Packaging and Shelf Life, 26, 100600.
77. Dong, S., Bortner, M. J., & Roman, M. (2016). Analysis of the sulfuric acid hydrolysis of wood pulp for cellulose nanocrystal production: A central composite design study. Industrial Crops and Products, 93, 76–87.
78. Dong, X., Chen, L., Xu, D., Zhang, J., Hu, F., & Ping, Q. (2025). Green synthesis of citric acid-crosslinked ethanol lignin/carboxymethyl cellulose films for fresh-cut apple preservation. Industrial Crops and Products, 237, 122283.
79. Donkor, L., Kontoh, G., Yaya, A., Bediako, J. K., & Apalangya, V. (2023). Bio-based and sustainable food packaging systems: Relevance, challenges, and prospects. Applied Food Research, 3(2), 100356.
80. Dutta, D., & Sit, N. (2024). A comprehensive review on types and properties of biopolymers as sustainable bio-based alternatives for packaging. Food Biomacromolecules, 1(2), 58–87.
81. Dwivedi, N. K., Dhariwal, O. P., Gopala Krishnan, S., & Bhandari, D. C. (2010). Distribution and extent of diversity in Cucumis species in the Aravalli ranges of India. Genetic Resources and Crop Evolution, 57(3), 443–452.
82. Dzyubenko, N. I., Dzyubenko, E. A., Potokina, E. K., & Bulyntsev, S. V. (2017). Clusterbeans Cyamopsis tetragonoloba (L.) Taub.: Properties, use, plant genetic resources and expected introduction in Russia. Sel'skokhozyaistvennaya Biologiya (Agricultural Biology), 52(6), 1116–1128.
83. Dzyubenko, N. I., et al. (2017). Clusterbeans Cyamopsis tetragonoloba (L.) Taub: Properties, use, plant genetic resources and expected introduction in Russia. Sel'skokhozyaistvennaya Biologiya (Agricultural Biology), 52(6), 1116–1128.
84. Embuscado, M. E. (2014). Functionalizing carbohydrates for food applications: Texturizing and bioactive/flavor delivery systems. DEStech Publications.
85. Espinosa, E., Bascón-Villegas, I., Rosal, A., Pérez-Rodríguez, F., Chinga-Carrasco, G., & Rodríguez, A. (2019). PVA/(ligno)nanocellulose biocomposite films: Effect of

residual lignin content on structural, mechanical, barrier, and antioxidant properties. International Journal of Biological Macromolecules, 141, 197–206.

86. Etman, E. K., Abou-Elenin, E. I., & El-Monayer, I. (2014). Using a new protein source in feeding of ruminants: Effect of feeding different levels of guar korma as a source of protein on the productive performance of Egyptian buffaloes. Journal of Animal and Poultry Production, 5(12), 619–634.
87. Etxabide, A., Young, B., Bremer, P. J., & Kilmartin, P. A. (2022). Non-permanent primary food packaging materials assessment: Identification, migration, toxicity, and consumption of substances. Comprehensive Reviews in Food Science and Food Safety, 21(5), 4130–4145.
88. Eze, C. G., Nwankwo, C. E., Dey, S., Sundaramurthy, S., & Okeke, E. S. (2024). Food chain microplastics contamination and impact on human health: A review. Environmental Chemistry Letters, 22(4), 1889–1927.
89. Farshi, P., Tabibiazar, M., Ghorbani, M., Mohammadifar, M. A., Amirkhiz, M. B., & Hamishehkar, H. (2019). Whey protein isolate–guar gum stabilized cumin seed oil nanoemulsion. Food Bioscience, 28, 49–56.
90. Fialho, J., Moniz, P., Duarte, L. C., & Carvalheiro, F. (2023). Green fractionation approaches for the integrated upgrade of corn cobs. ChemEngineering, 7(2), 35.
91. Fotakis, G., & Timbrell, J. A. (2006). In vitro cytotoxicity assays: Comparison of LDH, neutral red, MTT and protein assay in hepatoma cell lines following exposure to cadmium chloride. Toxicology Letters, 160(2), 171–177.
92. Fotakis, G., & Timbrell, J. A. (2006). In vitro cytotoxicity assays: Comparison of LDH, neutral red, MTT, and protein assay in hepatoma cell lines following exposure to cadmium chloride. Toxicology Letters, 160(2), 171–177.
93. Gadekar, N. K., Raut, P. S., Bhagyashree, M., & Sanap, G. S. (2023). On Cucumis callocus. World Journal of Pharmaceutical Research, 12(5), 2109–2120.
94. Garavand, F., Cacciotti, I., Rehman, A., & Mohammadi, R. (2022). Recent advances in biopolymer-based active and intelligent packaging materials for food preservation. Trends in Food Science & Technology, 121, 234–252.
95. Gautam, R., et al. (2024). Breeding guar (Cyamopsis tetragonoloba (L.) Taub): A variety compendium of a multifaceted industrial crop for resource-constrained scenario in India. Industrial Crops and Products, 214, 118502.

96. Gautam, R., Verma, A. K., Dwivedi, S., & Jhang, T. (2024). Breeding guar (Cyamopsis tetragonoloba (L.) Taub.): A variety compendium of a multifaceted industrial crop for resource-constrained scenario in India. Industrial Crops and Products, 214, 118502.
97. Gautam, R., Verma, A. K., Dwivedi, S., & Jhang, T. (2024). Breeding guar (Cyamopsis tetragonoloba (L.) Taub.): A variety compendium of a multifaceted industrial crop for resource-constrained scenarios in India. Industrial Crops and Products, 214, 118502.
98. Geies, A., Abdelazim, M., Sayed, A. M., & Ibrahim, S. (2020). Thermal, morphological and cytotoxicity characterization of hardwood lignins isolated by in-situ sodium hydroxide–sodium bisulfate method. Natural Resources, 11(10), 427–438.
99. Geies, A., Abdelazim, M., Sayed, A. M., & Ibrahim, S. (2020). Thermal, morphological and cytotoxicity characterization of hardwood lignins isolated by in-situ sodium hydroxide–sodium bisulfate method. Natural Resources, 11(10), 427–438.Ghasemi, S.,
100. Espahbodi, A., Naqvi, M., Zare, Y., & Rhee, K. Y. (2025). Mechanical percolation in nanocellulose-filled composites: A model for the modulus of composites containing nanocellulose/interphase network. Cellulose, 1–14.
101. Ghatak, H. R. (2023). TGA–FT–IR analysis of evolution of oxygenated organics by isothermal low-temperature decomposition of rice straw hydrolysis residue. Iranian Journal of Chemistry and Chemical Engineering, 42(11).
102. Ghodki, B. M., Srihari, G., Dukare, A. S., Kannaujia, P. K., Kalnar, Y. B., & Vishwakarma, R. K. (2021). Potential utilization of guar straw and wood wool in controlling relative humidity and temperature of storage environment. Journal of Food Process Engineering, 44(2), e13618.
103. Ghodki, B. M., Srihari, G., Dukare, A. S., Kannaujia, P. K., Kalnar, Y. B., & Vishwakarma, R. K. (2021). Potential utilization of guar straw and wood wool in controlling relative humidity and temperature of storage environment. Journal of Food Process Engineering, 44(2), e13618.
104. Gill, N. S., Bajwa, J., Dhiman, K., Sharma, P., Sood, S., Sharma, P. D., & Bali, M. (2011). Evaluation of therapeutic potential of traditionally consumed Cucumis melo seeds.
105. Gojiya, D. K., & Vyas, D. M. (2015). Studies on effect of slice thickness and temperature on drying kinetics of Kothimbda (Cucumis callosus) and its storage. Journal of Food Processing and Technology, 6(1), 1–8.

106. Gojiya, D. K., & Vyas, D. M. (2015). Studies on the effect of slice thickness and temperature on drying kinetics of Kothimbda (Cucumis callosus) and its storage. Journal of Food Processing and Technology, 6(1).

107. Goulas, A. E., Riganakos, K. A., & Kontominas, M. G. (2004). Effect of ionizing radiation on physicochemical and mechanical properties of commercial monolayer and multilayer semirigid plastics packaging materials. Radiation Physics and Chemistry, 69(5), 411–417.

108. Goyal, M., & Sharma, S. K. (2009). Traditional wisdom and value addition prospects of arid foods of desert region of north-west India.

109. Guo, D., Shibuya, R., Akiba, C., Saji, S., Kondo, T., & Nakamura, J. (2016). Active sites of nitrogen-doped carbon materials for oxygen reduction reaction clarified using model catalysts. Science, 351(6271), 361–365.

110. Han, J., Ruiz-Garcia, L., Qian, J., & Yang, X. (2018). Food packaging: A comprehensive review and future trends. Comprehensive Reviews in Food Science and Food Safety, 17, 860–877.

111. Hasan, M. H., Hossain, S., Rahman, M. L., Rahman, G. S., Khan, M. A., & Al Mamun, M. A. (2025). Effect of hydrolysis agitation and suspension drying temperature on the synthesis of crystalline cellulose from jute fiber. Carbohydrate Polymer Technologies and Applications, 10, 100769.

112. Hasanin, M. S., et al. (2025). Bioactive preservative nano-packaging films based on food wastes of orange peels and shrimp for apple (Malus domestica var. Anna) fruit quality and storage. Bioresources and Bioprocessing, 12(1), 54.

113. Hassan, O. F., Dawoud, M. H., & Ibrahim, S. M. (2025). Selenium and iron oxide nanoparticles mitigate doxorubicin-induced cardiomyopathy in rats via Nox1/p53 pathway inhibition. Journal of Pharmacy and Pharmacology, 77(12), 1762–1776.

114. Hassanzadeh, H., Alizadeh, M., Hassanzadeh, R., & Ghanbarzadeh, B. (2022). Garlic essential oil-based nanoemulsion carrier: Release and stability kinetics of volatile components. Food Science & Nutrition, 10(5), 1613–1625.

115. He, X., Liu, D., & Jiang, L. (2020). Edible and biodegradable films from fruit and vegetable processing residues: A review. Food Chemistry, 330, 127230.

116. Hendriks, A. T. W. M., & Zeeman, G. (2009). Pretreatments to enhance the digestibility of lignocellulosic biomass. Bioresource Technology, 100(1), 10–18.

117. Hernandez, C. C., Ferreira, F. F., & Rosa, D. S. (2018). X-ray powder diffraction and other analyses of cellulose nanocrystals obtained from corn straw by chemical treatments. Carbohydrate Polymers, 193, 39–44.

118. Hernandez, C. C., Ferreira, F. F., & Rosa, D. S. (2018). X-ray powder diffraction and other analyses of cellulose nanocrystals obtained from corn straw by chemical treatments. Carbohydrate Polymers, 193, 39–44.

119. Hindi, J., Muralishwara, K., & Gurumurthy, B. M. (2025). Comparative analysis of physical, morphological, tensile and thermal stability characteristics of raw and alkali treated novel Tinospora cordifolia natural fiber. Scientific Reports, 15(1), 18596.

120. Hong, S. J., et al. (2025). Polyhydroxyalkanoates for sustainable food packaging: A comprehensive review on production, applications, and end-of-life scenarios for food packaging. Trends in Food Science & Technology, 105294.

121. Hong, S. Y., et al. (2021). A review of pears (Pyrus spp.), ancient functional food for modern times. BMC Complementary Medicine and Therapies, 21(1), 219.

122. Huang, K., & Wang, Y. (2025). Advances in bio-based smart food packaging for enhanced food safety. Trends in Food Science & Technology, 159, 104960.

123. Huang, S., Zou, S., & Wang, Y. (2023). Construction of compostable packaging with antibacterial property and improved performance using sprayed coatings of modified cellulose nanocrystals. Carbohydrate Polymers, 305, 120539.

124. Hung, O. N., Chan, C. K., Kan, C. W., & Yuen, C. W. M. (2017). An analysis of some physical and chemical properties of CO_2 laser-treated cotton-based fabrics. Cellulose, 24, 363–381.

125. Hung, O. N., Chan, C. K., Kan, C. W., & Yuen, C. W. M. (2017). An analysis of some physical and chemical properties of CO_2 laser-treated cotton-based fabrics. Cellulose, 24, 363–381.

126. Hussain, H., Truong, T., Bansal, N., & Bhandari, B. (2017). The effect of manipulating fat globule size on the stability and rheological properties of dairy creams. Food Biophysics, 12(1), 1–10.

127. Ibáñez, A., Garrido-Chamorro, S., Vasco-Cárdenas, M. F., & Barreiro, C. (2023). From lab to field: Biofertilizers in the 21st century. Horticulturae, 9(12), 1306.

128. Ibáñez, A., Garrido-Chamorro, S., Vasco-Cárdenas, M. F., & Barreiro, C. (2023). From lab to field: Biofertilizers in the 21st century. Horticulturae, 9(12), 1306.

129. Ibrahim, F., Moniruzzaman, M., Yusup, S., & Uemura, Y. (2015). Dissolution of cellulose with ionic liquid in pressurized cell. Journal of Molecular Liquids, 211, 370–372.

130. Ihtifazhuddin, M. I., Nursyam, H., & Ekawati, A. W. (2016). The influence of fermentation time on the physical and chemical composition of fermented soybean husk using Aspergillus niger on the quality of raw feed materials. Journal of Experimental Life Science, 6(1).

131. Ihtifazhuddin, M. I., Nursyam, H., & Ekawati, A. W. (2016). The influence of fermentation time on the physical and chemical composition of fermented soybean husk using Aspergillus niger on the quality of raw feed materials. Journal of Experimental Life Science, 6(1).

132. Inman, G., Nlebedim, I. C., & Prodius, D. (2022). Application of ionic liquids for the recycling and recovery of technologically critical and valuable metals. Energies, 15(2), 628.

133. Jaglan, P., Kaushik, D., Kumar, M., Kumar, A., Kaur, J., Oz, E., & Oz, F. (2023). Structural, thermal, techno-functional and chemical characterization of Moringa oleifera flower powder using FTIR, GC–MS, TGA, FESEM and EDX analysis. International Journal of Food Science and Technology, 58(11), 5992–6005.

134. Jaglan, P., Kaushik, D., Kumar, M., Kumar, A., Kaur, J., Oz, E., & Oz, F. (2023). Structural, thermal, techno-functional and chemical characterization of Moringa oleifera flower powder using FTIR, GC–MS, TGA, FESEM and EDX analysis. International Journal of Food Science and Technology, 58(11), 5992–6005.

135. Jiang, S., Liu, S., & Zhang, Y. (2020). Antimicrobial nanocomposite films reinforced with silver-doped cellulose nanofibers derived from corn stalks. Carbohydrate Polymers, 241, 116343.

136. John, K. J., Scariah, S., Nissar, V. A., Latha, M., Gopalakrishnan, S., Yadav, S. R., & Bhat, K. V. (2013). On the occurrence, distribution, taxonomy and genepool relationship of Cucumis callosus (Rottler) Cogn., the wild progenitor of Cucumis melo L. from India. Genetic Resources and Crop Evolution, 60(3), 1037–1046.

137. Kamalesh, T., Kumar, P. S., Hemavathy, R. V., & Rangasamy, G. (2023). A critical review on sustainable cellulose materials and their multifaceted applications. Industrial Crops and Products, 203, 117221.

138. Kamboj, R., Sadh, P. K., Khan, M. R., Bains, A., & Goksen, G. (2025). Development of antimicrobial eugenol-infused biodegradable nanocellulose/gum

arabic/sodium alginate film: A comprehensive study on mechanical and techno-functional characteristics. Food Bioscience, 107856.

139. Kapoor, M., Sharma, C., Kaur, N., Kaur, G., Kaur, R., Batra, K., & Rani, J. (2020). Phyto-pharmacological aspects of Cucumis melo var. agrestis: A systematic review. Pharmacognosy Reviews, 14(27), 74–80.

140. Karpiesiuk, K., Kozera, W., Daszkiewicz, T., Lipiński, K., Kaliniewicz, J., Okorski, A., & Matusevičius, P. (2023). The effect of dietary supplementation with guar (Cyamopsis tetragonoloba) meal protein on the quality and chemical composition of pig carcasses. Annals of Animal Science, 23(4), 1095–1104.

141. Karpiesiuk, K., Kozera, W., Daszkiewicz, T., Lipiński, K., Kaliniewicz, J., Okorski, A., & Matusevičius, P. (2023). The effect of dietary supplementation with guar (Cyamopsis tetragonoloba) meal protein on the quality and chemical composition of pig carcasses. Annals of Animal Science, 23(4), 1095–1104.

142. Kasle, P., Bains, A., Goksen, G., Dhull, S. B., Ali, N., Nagarik, R., & Chawla, P. (2025). Exploring the properties of carboxymethyl cellulose blended with other polymeric compounds for the formulation of biodegradable packaging films and edible coatings: A review. Comprehensive Reviews in Food Science and Food Safety, 24(4), e70215.

143. Katiyar, S. K., Singh, T., Prasad, R., Sun, Q., & Vaid, M. (2012). Epigenetic alterations in ultraviolet radiation-induced skin carcinogenesis: Interaction of bioactive dietary components on epigenetic targets. Photochemistry and Photobiology, 88(5), 1066–1074.

144. Kaur, J., Borah, A., Chutia, H., & Gupta, P. (2024). Extraction, modification, and characterization of native litchi seed (Litchi chinensis Sonn.) starch. Journal of the Science of Food and Agriculture, 104(1), 215–224.

145. Kawamura, K., Qi, F., & Kobayashi, J. (2018). Potential relationship between the biological effects of low-dose irradiation and mitochondrial ROS production. Journal of Radiation Research, 59(Suppl. 2), ii91–ii97.

146. Khanra, R., Dewanjee, S., Dua, T. K., & Bhattacharjee, N. (2017). Taraxerol, a pentacyclic triterpene from Abroma augusta leaf, attenuates acute inflammation via inhibition of NF-κB signaling. Biomedicine & Pharmacotherapy, 88, 918–923.

147. Klunklin, W., Hinmo, S., Thipchai, P., & Rachtanapun, P. (2023). Effect of bleaching processes on physicochemical and functional properties of cellulose and carboxymethyl cellulose from young and mature coconut coir. Polymers, 15(16), 3376.

148. Knez, M., Ranic, M., Gurinovic, M., Glibetic, M., Savic, J., Mattas, K., & Yercan, M. (2023). Causes and conditions for reduced cultivation and consumption of underutilized crops: Is there a solution? Sustainability, 15(4), 3076.

149. Kohajdová, Z., Karovičová, J., & Jurasová, M. (2013). Influence of grapefruit dietary fibre rich powder on the rheological characteristics of wheat flour dough and on biscuit quality. Acta Alimentaria, 42(1), 91–101.

150. Kossalbayev, B. D., Belkozhayev, A. M., Abaildayev, A., Kadirshe, D. K., Tastambek, K. T., Kurmanbek, A., & Toleutay, G. (2025). Biodegradable packaging from agricultural wastes: A comprehensive review of processing techniques, material properties, and future prospects. Polymers, 17(16), 2224.

151. Kshash, B. H., Mijwel, A. K., & Sabri, Z. N. (2023). The economic feasibility of cultivating local cucumbers (Cucumis melo var. flexuosus) in plastic house. Euphrates Journal of Agricultural Science, 15(2).

152. Kumar, M., Guleria, S., Chawla, P., Khan, A., Modi, V. K., Kumar, N., & Kaushik, R. (2020). Anti-obesity efficacy of selected high altitude Himalayan herbs: In vitro studies. Journal of Food Science and Technology, 57, 3081–3090.

153. Kumar, M., Guleria, S., Chawla, P., Khan, A., Modi, V. K., Kumar, N., & Kaushik, R. (2020). Anti-obesity efficacy of selected high-altitude Himalayan herbs: In vitro studies. Journal of Food Science and Technology, 57, 3081–3090.

154. Kumar, M., Kapoor, S., Dhumal, S., Tkaczewska, J., Changan, S., Saurabh, V., et al. (2022). Guava (Psidium guajava L.) seed: A low-volume, high-value byproduct for human health and the food industry. Food Chemistry, 132694.

155. Kumar, M., Kaushik, D., Kaur, J., Proestos, C., Oz, F., Oz, E., & Ritika, R. (2022). A critical review on obesity: Herbal approach, bioactive compounds, and their mechanism. Applied Sciences, 12(16), 8342.

156. Kumar, M., Kaushik, D., Kaur, J., Proestos, C., Oz, F., Oz, E., & Ritika, R. (2022). A critical review on obesity: Herbal approach, bioactive compounds, and their mechanism. Applied Sciences, 12(16), 8342.

157. Kumar, M., Kaushik, D., Kumar, A., Gupta, P., Proestos, C., Oz, E., & Oz, F. (2023). Green synthesis of copper nanoparticles from Nigella sativa seed extract and evaluation of their antibacterial and anti-obesity activity. International Journal of Food Science and Technology, 58(6), 2883–2892.

158. Kumar, M., Kaushik, D., Kumar, A., Gupta, P., Proestos, C., Oz, E., & Oz, F. (2023). Green synthesis of copper nanoparticles from Nigella sativa seed extract and

evaluation of their antibacterial and anti-obesity activity. International Journal of Food Science and Technology, 58(6), 2883–2892.

159. Kumar, M., Saurabh, V., Tomar, M., Hasan, M., Changan, S., Sasi, M., et al. (2021). Mango (Mangifera indica L.) leaves: Nutritional composition, phytochemical profile, and health-promoting bioactivities. Antioxidants, 10(2), 299.

160. Kumar, R. S., Kar, B., Dolai, N., Bala, A., & Haldar, P. K. (2012). Evaluation of antihyperglycemic and antioxidant properties of Streblus asper Lour against streptozotocin-induced diabetes in rats. Asian Pacific Journal of Tropical Disease, 2(2), 139–143.

161. Kumar, R., Arora, V., Ram, V., Bhandari, A., & Vyas, P. (2015). Hypoglycemic and hypolipidemic effect of allopolyherbal formulations in streptozotocin-induced diabetes mellitus in rats. International Journal of Diabetes Mellitus, 3(1), 45–50.

162. Kumar, S., Mukherjee, A., & Katiyar, V. (Eds.). (2024). Agro-waste derived biopolymers and biocomposites: Innovations and sustainability in food packaging. John Wiley & Sons.

163. Kumari, M., & Chattopadhyay, S. (2023). Evaluation of the performance of rice husk and rice straw as potential matrix to obtain the best lipase immobilized system: Creating wealth from wastes. Preparative Biochemistry & Biotechnology, 53(7), 763–772.

164. Kumari, M., & Chattopadhyay, S. (2023). Evaluation of the performance of rice husk and rice straw as potential matrices to obtain the best lipase immobilized system: Creating wealth from wastes. Preparative Biochemistry & Biotechnology, 53(7), 763–772.

165. Kuna, A., Sowmya, M., Sahoo, M. R., Mayengbam, P. D., Dasgupta, M., & Sreedhar, M. (2018). Value addition and sensory evaluation of products made from underutilized Kachai lemon (Citrus jambhiri Lush.). Journal of Pharmacognosy and Phytochemistry, 7(5), 3032–3036.

166. Kusuma, H. S., Sabita, A., Putri, N. A., Azliza, N., Illiyanasafa, N., Darmokoesoemo, H., & Kurniawan, T. A. (2024). Waste to wealth: Polyhydroxyalkanoates (PHA) production from food waste for a sustainable packaging paradigm. Food Chemistry: Molecular Sciences, 9, 100225.

167. La Rubia, I., Torres, M., Domínguez, J. M., & Rodríguez, A. (2024). Sustainable extraction of microcrystalline cellulose from cotton and sunflower stalks for biodegradable film reinforcement. Industrial Crops & Products, 210, 116268.

168. Lackner, M., & Besharati, M. (2025). Agricultural waste: Challenges and solutions—A review. Waste, 3(2), 18.

169. Lau, A. Y., & Sarbon, N. M. (2022). Effect of glycerol concentrations on the mechanical and physical properties of chicken skin gelatin–tapioca starch composite films. Food Research, 6(4), 428–436.

170. Leal Filho, W., et al. (2025). Policy gaps and opportunities in bio-based plastics: Implications for sustainable food packaging. Foods, 14(11), 1955.

171. Lee, H. V., Hamid, S. B. A., & Zain, S. K. (2014). Conversion of lignocellulosic biomass to nanocellulose: Structure and chemical process. The Scientific World Journal, 2014, 631013.

172. Li, H., Zhang, H., Xiong, L., Chen, X., Wang, C., Huang, C., & Chen, X. (2019). Isolation of cellulose from wheat straw and its utilization for the preparation of carboxymethyl cellulose. Fibers and Polymers, 20(5), 975–981.

173. Li, J. H., Li, M. J., Li, W. L., Li, X. Y., Ma, Y. B., Tan, X., & Ma, X. R. (2024). Leguminous industrial crop guar (Cyamopsis tetragonoloba): The chromosome-level reference genome de novo assembly. Industrial Crops and Products, 216, 118748.

174. Li, J. H., Li, M. J., Li, W. L., Li, X. Y., Ma, Y. B., Tan, X., & Ma, X. R. (2024). Leguminous industrial crop guar (Cyamopsis tetragonoloba): The chromosome-level reference genome de novo assembly. Industrial Crops and Products, 216, 118748.

175. Li, J., Zha, Y. N., Wang, H. M., Tian, J. N., & Hou, Q. X. (2025). Advances in lignin chemistry during pulping and bleaching. Industrial Crops and Products, 229, 121004.

176. Liu, J., Zhang, Y., Liu, J., Zhang, H., Gong, L., Li, Z., & Wang, Z. (2024). Effect of non-covalently bound polyphenols on the structural and functional properties of wheat germ protein. Food Hydrocolloids, 149, 109534.

177. Liu, J., Zhang, Y., Liu, J., Zhang, H., Gong, L., Li, Z., & Wang, Z. (2024). Effect of non-covalently bound polyphenols on the structural and functional properties of wheat germ protein. Food Hydrocolloids, 149, 109534.

178. Liu, R. H. (2003). Health benefits of fruit and vegetables are from additive and synergistic combinations of phytochemicals. The American Journal of Clinical Nutrition, 78(3), 517S–520S.

179. Liu, T., et al. (2024). Preparation, physicochemical and biological evaluation of chitosan–Pleurotus ostreatus polysaccharides active films for food packaging. International Journal of Biological Macromolecules, 254, 127470.

180. Liu, X., Yan, X., Bi, J., Liu, J., Zhou, M., Wu, X., & Chen, Q. (2018). Determination of phenolic compounds and antioxidant activities from peel, flesh, and seed of guava (Psidium guajava L.). Electrophoresis, 39(13), 1654–1662.

181. Liu, Y., Nie, Y., Lu, X., Zhang, X., He, H., Pan, F., & Zhang, S. (2019). Cascade utilization of lignocellulosic biomass to high-value products. Green Chemistry, 21(13), 3499–3535.

182. Lu, Y., He, Q., Fan, G., Cheng, Q., & Song, G. (2021). Extraction and modification of hemicellulose from lignocellulosic biomass: A review. Green Processing and Synthesis, 10(1), 779–804.

183. Luo, Z., Li, G., Du, Y., Yi, J., Hu, X., & Jiang, Y. (2024). Enhancing fresh-cut apple preservation: Impact of slightly acidic electrolyzed water and chitosan–apple essence microencapsulation coating on browning and flavor. Foods, 13(10), 1585.

184. Ma, X., & Cao, S. (2025). Structures, properties, and fabrication of cellulose-based natural biopolymer materials.

185. Macha, M. A., Zargar, S. M., Bhat, A. A., & Uddin, S. (Eds.). (2025). Neglected and underutilized crops: Unveiling potential for cancer drug discovery.

186. Maeda, N., Sakkayawong, N., & Singkhonrat, J. (2025). Fabrication of Pickering double emulsions loaded with curcumin ionic liquids stabilized by cellulose nanocrystals, sodium alginate and lecithin. Colloid and Polymer Science, 1–16.

187. Magalhães, S., Fernandes, C., Pedrosa, J. F., Alves, L., Medronho, B., Ferreira, P. J., & Rasteiro, M. D. G. (2023). Eco-friendly methods for extraction and modification of cellulose: An overview. Polymers, 15(14), 3138.

188. Mahajan, A., Singh, I., & Arora, N. (2023). An integrated multi-criteria decision-making framework for the selection of sustainable biodegradable polymer for food packaging applications. Environment, Development and Sustainability.

189. Mahmood, A. M. (2024). Potential impact of non-conventional protein resources Cyamopsis tetragonoloba (guar meal) in lamb's diet.

190. Mahmood, A. M. (2024). Potential impact of non-conventional protein resources Cyamopsis tetragonoloba (guar meal) in lamb's diet.

191. Mahmood, K., et al. (2023). Enhancing the functional properties of fish gelatin mats by dual encapsulation of essential oils in β-cyclodextrins/fish gelatin matrix via coaxial electrospinning. Food Hydrocolloids, 137, 108324.

192. Mangal, R., Wen, Y. H., Choudhury, S., & Archer, L. A. (2016). Multiscale dynamics of polymers in particle-rich nanocomposites. Macromolecules, 49(14), 5202–5212.

193. Mann, S., Chaudhary, I., & Gupta, R. K. (2013). Value addition scenario of arid foods of desert area and evaluation of their nutritional and phytochemical potential. International Journal of Pharmacy & Life Sciences, 4(1).

194. Mao, X., Auer, D. L., Buchalla, W., Hiller, K. A., Maisch, T., Hellwig, E., & Cieplik, F. (2020). Cetylpyridinium chloride: Mechanism of action, antimicrobial efficacy in biofilms, and potential risks of resistance. Antimicrobial Agents and Chemotherapy, 64(8).

195. Mao, X., Auer, D. L., Buchalla, W., Hiller, K. A., Maisch, T., Hellwig, E., & Cieplik, F. (2020). Cetylpyridinium chloride: Mechanism of action, antimicrobial efficacy in biofilms, and potential risks of resistance. Antimicrobial Agents and Chemotherapy, 64(8).

196. Marchetti, A., Grumi, M., Salvatori, G., Marcoaldi, C., Nguemna, L. T., Basar, A. O., & Prieto López, C. (2024). Developing bioplastics from agro-industrial wastes for applications in food packaging.

197. Mazumder, M. A. J., Quraishi, M. A., Al-Ahmed, A., & Wiley, J. (Eds.). (2022). Polymeric corrosion inhibitors for greening the chemical and petrochemical industry. Wiley-VCH.

198. Mazumder, M. A. J., Quraishi, M. A., Al-Ahmed, A., & Wiley, J. (Eds.). (2022). Polymeric corrosion inhibitors for greening the chemical and petrochemical industry. Wiley-VCH.

199. McHugh, T. H., & Senesi, E. (2000). Apple wraps: A novel method to improve the quality and extend the shelf life of fresh-cut apples. Journal of Food Science, 65(3), 480–485.

200. Meena, S. R., Singh, R. S., Sharma, B. D., & Singh, D. (2016). Most favourite traditional cucurbitaceous vegetables and their utilization pattern in Thar desert of western Rajasthan, India.

201. Meghwal, P. R., Singh, A., & Singh, D. (2022). Underutilized fruits and vegetables in hot arid regions of India: Status and prospects. Agricultural Reviews, 43(1).

202. Méndez, D. A., et al. (2023). Sustainable bioactive pectin-based films to improve fruit safety via a circular economy approach. Food Hydrocolloids, 137, 108327.

203. Meng, X., Liu, F., Xiao, Y., Cao, J., Wang, M., & Duan, X. (2019). Alterations in physicochemical and functional properties of buckwheat straw insoluble dietary fiber by alkaline hydrogen peroxide treatment. Food Chemistry: X, 3, 100029.

204. Meng, X., Liu, F., Xiao, Y., Cao, J., Wang, M., & Duan, X. (2019). Alterations in physicochemical and functional properties of buckwheat straw insoluble dietary fiber by alkaline hydrogen peroxide treatment. Food Chemistry: X, 3, 100029.

205. Miao, C., Mirvakili, M. N., & Hamad, W. Y. (2022). A rheological investigation of oil-in-water Pickering emulsions stabilized by cellulose nanocrystals. Journal of Colloid and Interface Science, 608, 2820–2829.

206. Mieles-Gómez, L., Quintana, S. E., & García-Zapateiro, L. A. (2023). Ultrasound-assisted extraction of mango (Mangifera indica) kernel starch: Chemical, techno-functional, and pasting properties. Gels, 9(2), 136.

207. Mikus, M., & Galus, S. (2022). Biopolymers from agriculture waste and by-products. In Biopolymers: Recent updates, challenges and opportunities (pp. 111–128). Springer.

208. Mirigian, S., & Schweizer, K. S. (2015). Dynamical theory of segmental relaxation and emergent elasticity in supercooled polymer melts. Macromolecules, 48(6), 1901–1913.

209. Mitharwal, S., Kumar, A., Chauhan, K., & Taneja, N. K. (2022). Nutritional, phytochemical composition and potential health benefits of taro (Colocasia esculenta L.) leaves: A review. Food Chemistry, 383, 132406.

210. Modenbach, A. A., & Nokes, S. E. (2014). Effects of sodium hydroxide pretreatment on structural components of biomass. Transactions of the ASABE, 57(4), 1187–1198.

211. Moe, S. T., Janga, K. K., Hertzberg, T., Hägg, M. B., Øyaas, K., & Dyrset, N. (2012). Saccharification of lignocellulosic biomass for biofuel and biorefinery applications: A renaissance for concentrated acid hydrolysis. Energy Procedia, 20, 50–58.

212. Mohammed, M. A., Basirun, W. J., Abd Rahman, N. M., Shalauddin, M., & Salleh, N. M. (2022). The effect of acid hydrolysis parameters on the properties of nanocellulose extracted from almond shells. Journal of Natural Fibers, 19(16), 14102–14114.

213. Mohammed, M. T., Al-Qaisi, T. S., Jabbar, A. A., Raouf, M. M., Ismail, P. A., Mothana, R. A., & Awad, M. (2025). Prophylactic effects of rhamnetin flavonoid on

indomethacin-induced gastric ulceration by modulating HSP70/Bax, SOD/MDA and TNF-α/IL-10. Clinical and Experimental Pharmacology and Physiology, 52(4), e70029.

214. Mohan, P., Yusof, N. M., Thomas, S., & Rahman, A. (2024). Ultrasound–alkali-assisted isolation of cellulose from coconut shells. BioResources, 19(4), 787.

215. Mohd Zaini, N. A., Azizan, N. A. Z., Abd Rahim, M. H., Jamaludin, A. A., Raposo, A., Raseetha, S., & Wan-Mohtar, W. A. A. Q. I. (2023). A narrative action on the battle against hunger using mushroom, peanut, and soybean-based wastes. Frontiers in Public Health, 11, 1175509.

216. Morcillo-Martín, R., Espinosa, E., Rabasco-Vílchez, L., Sanchez, L. M., de Haro, J., & Rodríguez, A. (2022). Cellulose nanofiber-based aerogels from wheat straw: Influence of surface load and lignin content on their properties and dye removal capacity. Biomolecules, 12(2), 232.

217. Moreira, L. R. S., & Filho, E. X. F. (2016). Insights into the mechanism of enzymatic hydrolysis of xylan. Applied Microbiology and Biotechnology, 100(12), 5205–5214.

218. Mujtaba, M., Fraceto, L. F., Fazeli, M., Mukherjee, S., Savassa, S. M., de Medeiros, G. A., & Vilaplana, F. (2023). Lignocellulosic biomass from agricultural waste to the circular economy: A review with focus on biofuels, biocomposites and bioplastics. Journal of Cleaner Production, 402, 136815.

219. Mujtaba, M., Fraceto, L. F., Fazeli, M., Mukherjee, S., Savassa, S. M., de Medeiros, G. A., & Vilaplana, F. (2023). Lignocellulosic biomass from agricultural waste to the circular economy: A review with focus on biofuels, biocomposites and bioplastics. Journal of Cleaner Production, 402, 136815.

220. Mukherjee, P. K., Singha, S., Kar, A., Chanda, J., Banerjee, S., Dasgupta, B., et al. (2022). Therapeutic importance of Cucurbitaceae: A medicinally important family. Journal of Ethnopharmacology, 282, 114599.

221. Mukherjee, P., Pal, S., & Sivaprakasam, S. (2024). Process parameter controls for efficient enzymatic hydrolysis of cellulosic biomass. In Handbook of biorefinery research and technology (pp. 1–29). Springer.

222. Mutlu, N., Kurtuldu, F., Nowicka, A., Liverani, L., Galusek, D., & Boccaccini, A. R. (2025). Morphology and topography of chitosan–Zn complex/PEO fiber mats influence cell viability and attachment. International Journal of Biological Macromolecules, 143394.

223. Nabi, M. H. B., Ahmed, M. M., Zzaman, W., & Mia, M. S. (2025). Bio-based active food-packaging films incorporated with plant-derived essential oils: Functional performance and shelf-life extension. Journal of Applied Packaging Science, 12(1), 35–49.

224. Nahak, B. K., Preetam, S., Sharma, D., Shukla, S. K., Syväjärvi, M., Toncu, D. C., & Tiwari, A. (2022). Advancements in net-zero pertinency of lignocellulosic biomass for climate neutral energy production. Renewable and Sustainable Energy Reviews, 161, 112393.

225. Nandal, U., & Bhardwaj, R. L. (2014). The role of underutilized fruits in nutritional and economic security of tribals: A review. Critical Reviews in Food Science and Nutrition, 54(7), 880–890.

226. Naser, A. Z., Deiab, I., & Darras, B. M. (2021). Poly(lactic acid) (PLA) and polyhydroxyalkanoates (PHAs), green alternatives to petroleum-based plastics: A review. RSC Advances, 11(28), 17151–17196.

227. Nazar, M., Tian, J., Wang, X., Wang, S., Khan, N. A., Cheng, Y., & Ding, C. (2025). Biological delignification and anaerobic fermentation of wheat straw: A promising approach for sustainable utilization of crop straw bioresources. Industrial Crops and Products, 227, 120839.

228. Nazar, M., Tian, J., Wang, X., Wang, S., Khan, N. A., Cheng, Y., & Ding, C. (2025). Biological delignification and anaerobic fermentation of wheat straw: A promising approach for sustainable utilization of crop straw bioresources. Industrial Crops and Products, 227, 120839.

229. Ngwabebhoh, F. A., Erdagi, S. I., & Yildiz, U. (2018). Pickering emulsions stabilized nanocellulosic-based nanoparticles for coumarin and curcumin nanoencapsulations: In vitro release, anticancer, and antimicrobial activities. Carbohydrate Polymers, 201, 317–328.

230. Nuruddin, M., Hosur, M., Uddin, M. J., Baah, D., & Jeelani, S. (2016). A novel approach for extracting cellulose nanofibers from lignocellulosic biomass by ball milling combined with chemical treatment. Journal of Applied Polymer Science, 133(9).

231. Olawade, D. B., Akinpelu, A. E., & Olatunji, S. O. (2024). Agro-waste utilization for eco-friendly packaging materials: Advances and perspectives. Environmental Technology & Innovation, 34, 103125.

232. Olivito, F., Jagdale, P., & Oza, G. (2023). Direct production of furfural from fructose catalyzed by iron(III) sulfate using a simple distillation apparatus. ACS Sustainable Chemistry & Engineering, 11(50), 17595–17599.

233. Oliyaei, N., Moosavi-Nasab, M., & Tanideh, N. (2022). WITHDRAWN: Preparation of fucoxanthin nanoemulsion stabilized by natural emulsifiers: Fucoidan, sodium caseinate, and gum Arabic. Heliyon.

234. Omar, J. A., Zaazaa, A., Sheqwarah, M., Shanab, B. A., Qaisi, W., & Abdallah, J. (2021). Effects of guar (Cyamopsis tetragonoloba) residues on the performance and nutrients digestibility in finishing Awassi lambs. Open Journal of Animal Sciences, 11(1), 96.

235. Omar, J. A., Zaazaa, A., Sheqwarah, M., Shanab, B. A., Qaisi, W., & Abdallah, J. (2021). Effects of guar (Cyamopsis tetragonoloba) residues on the performance and nutrient digestibility in finishing Awassi lambs. Open Journal of Animal Sciences, 11(1), 96.

236. Othman, S. H., Ahmad, K., Nor, N. M., & Amin, K. N. (2020). Banana pseudostem fiber reinforced starch-based biodegradable films for food packaging applications. Food Packaging and Shelf Life, 24, 100469.

237. Oun, A. A., & Rhim, J. W. (2016). Isolation of cellulose nanocrystals from grain straws and their use for the preparation of carboxymethyl cellulose-based nanocomposite films. Carbohydrate Polymers, 150, 187–200.

238. Oyedeji, S., Patel, N., Krishnamurthy, R., & Fatoba, P. O. (2024). Agricultural wastes to value-added products: Economic and environmental perspectives for waste conversion. In Biowaste to value-added products: Economics and technologies (pp. 215–248).

239. Panda, S. P., Jena, B. R., Kalyani, G., & Panigrahy, U. P. (2018). Overexpressed CYP450 mediated apoptosis evaluates cytotoxicity and teratotoxicity of Cucumis callosus. Oriental Pharmacy and Experimental Medicine, 18(4), 365–375.

240. Panda, S., Chakraborty, M., Majumder, P., Mazumder, S., Das, S., & Haldar, P. K. (2016). Antidiabetic, antioxidant and anti-hyperlipidaemic activity of Cucumis callosus in streptozotocin-induced diabetic rats. International Journal of Pharmaceutical Sciences and Research, 7(5), 1978.

241. Patil, N. D., Thakur, S., Bains, A., Kaur, S., Ali, N., Arora, R., … Chawla, P. (2024). Exploration of *Calocybe indica* mushroom phenolic acid–kidney bean protein

complex: Functional properties, amino acid profiles, in-vitro digestibility, and application in vegan product development. *Food Chem.*, 460, 140401.

242. Papadopoulou, E. L., Kosmidou, T., & Kourkoumelis, N. (2019). Agro-waste-derived proteins and phenolic compounds for reinforcement of biopolymer packaging. Journal of Cleaner Production, 236, 117609.

243. Parthasarathy, V. A., & Sambandam, C. N. (2005). Taxonomy of Cucumis callosus (Rottl.) Cogn., the wild melon of India. Cucurbits Genetic Cooperative Report, 3, 66–67.

244. Patel, A. R. (2025). Management of agri-food wastes via novel biotechnological methods: Emerging trends and technological advances. In Biotechnological approaches for sustainable environment management (p. 351).

245. Patel, S., & Rauf, A. (2017). Edible seeds from Cucurbitaceae family as potential functional foods: Immense promises, few concerns. Biomedicine & Pharmacotherapy, 91, 330–337.

246. Pathak, R., Chandra, P., & Sachan, N. (2025). Unravelling peptic ulcers: Comprehensive insights into etiology, diagnosis, screening techniques, and treatment. Current Pharmaceutical Design, 31(26), 2065–2084.

247. Pedersen, M., & Meyer, A. S. (2010). Lignocellulose pretreatment severity: Relating pH to biomatrix opening. New Biotechnology, 27(6), 739–750.

248. Pei, W., Yu, Y., Wang, P., Zheng, L., Lan, K., Jin, Y., & Huang, C. (2024). Research trends of bio-application of major components in lignocellulosic biomass (cellulose, hemicellulose, and lignin) in orthopedics fields based on bibliometric analysis: A review. International Journal of Biological Macromolecules, 267, 131505.

249. Permata, D. A., Kasim, A., & Asben, Y. A. (2021). Delignification of lignocellulosic biomass. World Journal of Advanced Research and Reviews, 12(2), 462–469.

250. Pessarakli, M. (Ed.). (2016). Handbook of cucurbits: Growth, cultural practices, and physiology. CRC Press.

251. Phaniendra, A., Jestadi, D. B., & Periyasamy, L. (2015). Free radicals: Properties, sources, targets, and their implication in various diseases. Indian Journal of Clinical Biochemistry, 30(1), 11–26.

252. Pourdarbani, R., Sabzi, S., Rohban, M. H., Garcia-Mateos, G., Paliwal, J., & Molina-Martinez, J. M. (2022). Using metaheuristic algorithms to improve the

estimation of acidity in Fuji apples using NIR spectroscopy. Ain Shams Engineering Journal, 13(6), 101776.

253. Prajapati, K. V., Sheth, N. R., & Dudhrejiya, A. V. (2017). Antidiabetic activity of chloroform fraction of methanolic extract of fruits of Cucumis callosus Cogn. Pharma Science Monitor, 8(2).

254. Qi, W., Qi, W., Xiong, D., & Long, M. (2022). Quercetin: Its antioxidant mechanism, antibacterial properties and potential application in prevention and control of toxipathy. Molecules, 27(19), 6545.

255. Quideau, S., Deffieux, D., Douat-Casassus, C., & Pouységu, L. (2011). Plant polyphenols: Chemical properties, biological activities, and synthesis. Angewandte Chemie International Edition, 50(3), 586–621.

256. Rahman, M. M., Jahan, M. S., Islam, M. M., & Susan, M. A. B. H. (2024). Dissolution of cellulose in imidazolium-based double salt ionic liquids. International Journal of Biological Macromolecules, 267, 131331.

257. Rahmani, F., Sodaeizadeh, H., Yazdani-Biouki, R., Hakimzadeh-Ardakani, M. A., & Aliabadi, K. K. (2024). Effect of bio-priming on morphological, physiological and essential oil of chamomile (Matricaria chamomilla L.) under salinity stress. South African Journal of Botany, 167, 630–642.

258. Rajendran, S., Al-Samydai, A., Palani, G., Trilaksana, H., Sathish, T., Giri, J., & Nasri, F. (2025). Replacement of petroleum-based products with plant-based materials: Green and sustainable energy—A review. Engineering Reports, 7(4), e70108.

259. Ramírez-Estrada, A., Mena-Cervantes, V. Y., Elizalde-Martínez, I., Pineda-Flores, G., & Hernández-Altamirano, R. (2024). Chemical pretreatment of corncob for the selective dissolution of hemicellulose and lignin: Influence of pretreatment on the chemical, morphological and thermal features. Biofuels, 15(1), 89–103.

260. Ramírez-Estrada, A., Mena-Cervantes, V. Y., Mederos-Nieto, F. S., Pineda-Flores, G., & Hernández-Altamirano, R. (2022). Assessment and classification of lignocellulosic biomass recalcitrance by principal components analysis based on thermogravimetry and infrared spectroscopy. International Journal of Environmental Science and Technology, 19(4), 2529–2544.

261. Ramyashree, S., Jain, S. K., Kumar, N., Jain, S. S. L., Kumar, A., & Singh, P. K. (2024). Effect of different pretreatments and air temperatures on drying characteristics of Kachri (Cucumis callosus) dried in a heat pump dryer. Environment and Ecology, 42(1), 20–26.

262. Rani, R., Kaushik, D., Babagil, G. E., Proestos, C., Brennan, C., Oz, F., & Kumar, M. (2025). Exploring the deciphering properties of Cyamopsis tetragonoloba: Its food application, feasibility, and future aspects. International Journal of Food Science and Technology, vvae098.

263. Rani, R., Kaushik, D., Babagil, G. E., Proestos, C., Brennan, C., Oz, F., & Kumar, M. (2025). Exploring the deciphering properties of Cyamopsis tetragonoloba: Its food application, feasibility, and future aspects. International Journal of Food Science and Technology, vvae098.

264. Rašeta, M., Mišković, J., Kebert, M., Berežni, S., Krstić, S., Gojgić-Cvijović, G., & Karaman, M. (2025). Mycochemical profiles and bioactivities of Fistulina hepatica and Volvopluteus gloiocephalus from Serbia: Antioxidant, enzyme inhibition, and cytotoxic potentials. Food Bioscience, 66, 106221.

265. Rašeta, M., Mišković, J., Kebert, M., Berežni, S., Krstić, S., Gojgić-Cvijović, G., & Karaman, M. (2025). Mycochemical profiles and bioactivities of Fistulina hepatica and Volvopluteus gloiocephalus from Serbia: Antioxidant, enzyme inhibition, and cytotoxic potentials. Food Bioscience, 66, 106221.

266. Ravera, F., Santini, E., Liggieri, L., Cristofolini, L., & Orsi, D. (2025). Emulsions and interfacial properties. In Emulsions (pp. 109–137). CRC Press.

267. Razali, S. M., & Kasim, K. F. (2022). Assessment of natural cellulosic powder from pepper pericarp waste (Piper nigrum L.) after alkalization and bleaching treatment: Effect of alkali concentration and treatment cycle. Sains Malaysiana, 51(4), 1061–1074.

268. Razzaq, S., Shahid, S., Farooq, R., Noreen, S., Perveen, S., & Bilal, M. (2024). Sustainable bioconversion of agricultural waste substrates into poly(3-hydroxyhexanoate) (mcl-PHA) by Cupriavidus necator DSM 428. Biomass Conversion and Biorefinery, 14(8), 9429–9439.

269. Reddy, N., Jiang, Q., & Yang, Y. (2018). Cross-linking of natural polymers for improved water-resistance of biopolymer films. Carbohydrate Polymers, 197, 479–486.

270. Riaz, S., Maan, A. A., Butt, M. S., & Khan, M. K. I. (2024). Valorization of agricultural residues in the development of biodegradable active packaging films. Industrial Crops and Products, 215, 118587.

271. Ribeiro, S., Almeida, R., Batista, L., Lima, J., Sarinho, A., Nascimento, A., & Lisboa, H. (2024). Investigation of guar gum and xanthan gum influence on essential thyme oil emulsion properties and encapsulation release using modeling tools. Foods, 13(6), 816.

272. Rigueto, C. V. T., et al. (2022). Gelatin films from wastes: A review of production, characterization, and application trends in food preservation and agriculture. Food Research International, 162, 112114.

273. Robles-Sánchez, R. M., Rojas-Graü, M. A., Odriozola-Serrano, I., González-Aguilar, G., & Martin-Belloso, O. (2013). Influence of alginate-based edible coating as carrier of antibrowning agents on bioactive compounds and antioxidant activity in fresh-cut Kent mangoes. LWT – Food Science and Technology, 50(1), 240–246.

274. Sabet, M. (2025). Exploring biodegradable polymer composites for sustainable packaging: A review on properties, manufacturing techniques, and environmental impacts. Iranian Polymer Journal, 34(1), 123–142.

275. Saleem, M. (2022). Possibility of utilizing agriculture biomass as a renewable and sustainable future energy source. Heliyon, 8(2).

276. Samadia, D. K., Haldhar, S. M., Ram, H., Verma, A. K., & Gurjar, P. S. (2024). Kachri melon (a non-dessert form of Cucumis melo): Diversity, germplasm utilization and varietal development under hot arid climate. Journal of Agriculture and Ecology, 18, 14–27.

277. Sánchez, O., Sierra, R., & Alméciga-Díaz, C. J. (2011). Delignification process of agro-industrial wastes: An alternative to obtain fermentable carbohydrates for producing fuel. In Alternative fuel (p. 7).

278. Sarkhel, S., Kaur, S., Das, R., Sharma, A., Kheto, A., Saha, D., & Kumar, Y. (2025). Antimicrobial active packaging with biopolymers and natural extracts: Sustainable solutions and technological challenges. Sustainable Food Technology.

279. Saupi, F. A. C., Yusof, N. S. M., Rajagopal, V., & Rahman, N. M. M. A. (2025). Comparative analysis of nanocellulose extraction from Cocos nucifera shell by ultrasonication versus acid hydrolysis for methylene blue dye removal. Iranian Polymer Journal, 1–24.

280. Segers, B., Nimmegeers, P., Spiller, M., Tofani, G., Jasiukaitytė-Grojzdek, E., Dace, E., & Billen, P. (2024). Lignocellulosic biomass valorisation: A review of feedstocks, processes, and potential value chains and their implications for decision-making. RSC Sustainability, 2(12), 3730–3749.

281. Selvam, T., Zainal Abidin, S. Z., & Abd Rahman, N. M. M. (2025). Transforming biomass into batteries: Harnessing cellulose and nanocellulose for a sustainable energy storage future. International Journal of Materials Research.

282. Serrano-Martínez, V. M., Pérez-Aguilar, H., Carbonell-Blasco, M. P., García-García, A., Arán-Ais, F., & Orgilés-Calpena, E. (2025). Effect of acid hydrolysis conditions on the extraction of cellulose nanocrystals. Polymers, 17(10), 1313.

283. Shafie, M. H., Yusof, R., Samsudin, D., & Gan, C. Y. (2020). Averrhoa bilimbi pectin-based edible films: Effects of the linearity and branching of the pectin on the physicochemical, mechanical, and barrier properties of the films. International Journal of Biological Macromolecules, 163, 1276–1282.

284. Shahbazi, P., Behzad, T., & Heidarian, P. (2017). Isolation of cellulose nanofibers from poplar wood and wheat straw: Optimization of bleaching step parameters in a chemo-mechanical process by experimental design. Wood Science and Technology, 51(5), 1173–1187.

285. Shakir, M., & Sadaqat, H. A. (2020). A review on guar (Cyamopsis tetragonoloba L.): A cash crop. International Research Journal of Pharmacy, 11(4), 1–7.

286. Shakir, M., & Sadaqat, H. A. (2020). A review on guar (Cyamopsis tetragonoloba L.): A cash crop. International Research Journal of Pharmacy, 11(4), 1–7.

287. Shanmuka, S. M., Mamilla, R. S., & N, V. (2025). Experimental investigation on post processing of additively manufactured surgical steel by viscoelastic abrasive finishing. In International Mechanical Engineering Congress and Exposition–India (Vol. 89138, p. V001T01A053). American Society of Mechanical Engineers.

288. Sharif, F., Muhammad, N., & Zafar, T. (2020). Cellulose-based biomaterials: Benefits and challenges. In Biofibers and biopolymers for biocomposites: Synthesis, characterization and properties (pp. 229–246). Springer.

289. Sharma, A., Kumar, A. A., Mohanty, B., & Khanam, S. (2023). Synthesis, characterization and thermo-kinetic analysis of sawdust biochar for adsorbent and combustion drives. Bioresource Technology Reports, 22, 101485.

290. Sharma, A., Kumar, A. A., Mohanty, B., & Khanam, S. (2023). Synthesis, characterization and thermo-kinetic analysis of sawdust biochar for adsorbent and combustion drives. Bioresource Technology Reports, 22, 101485.

291. Sharma, P., Sharma, S., Ramakrishna, G., Srivastava, H., & Gaikwad, K. (2021). A comprehensive review on leguminous galactomannans: Structural analysis, functional properties, biosynthesis process and industrial applications. Critical Reviews in Food Science and Nutrition, 62(2), 443–465.

292. Shashikant, M., Bains, A., Chawla, P., Sharma, M., Kaushik, R., Kandi, S., & Kuhad, R. C. (2022). In vitro antimicrobial and anti-inflammatory activity of modified

solvent evaporated ethanolic extract of Calocybe indica: GC–MS and HPLC characterization. International Journal of Food Microbiology, 376, 109741.

293. Shashikant, M., Bains, A., Chawla, P., Sharma, M., Kaushik, R., Kandi, S., & Kuhad, R. C. (2022). In vitro antimicrobial and anti-inflammatory activity of modified solvent evaporated ethanolic extract of Calocybe indica: GC–MS and HPLC characterization. International Journal of Food Microbiology, 376, 109741.

294. Shen, Y., Seidi, F., Ahmad, M., Liu, Y., Saeb, M. R., Akbari, A., & Xiao, H. (2023). Recent advances in functional cellulose-based films with antimicrobial and antioxidant properties for food packaging. Journal of Agricultural and Food Chemistry, 71(44), 16469–16487.

295. Shlush, E., & Davidovich-Pinhas, M. (2022). Bioplastics for food packaging. Trends in Food Science & Technology, 125, 66–80.

296. Showkat, S., Anjum, N., Ayaz, Q., Mustafa, S., Malik, A. R., Beigh, M. A., & Wani, S. M. (2025). Enhancing shelf life of plum fruit by chitosan-based nanoemulsion coating incorporated with ginger essential oil. Applied Food Research, 5(1), 100768.

297. Singh, R., Das, R., Sangwan, S., Rohatgi, B., Khanam, R., Peera, S. P. G., & Misra, S. (2021). Utilisation of agro-industrial waste for sustainable green production: A review. Environmental Sustainability, 4(4), 619–636.

298. Singh, S., Verma, R., & Sharma, H. (2024). Exploring the therapeutic potential and bioactive compounds in Pyrus species. Pharmacological Research – Modern Chinese Medicine, 10, 100342.

299. Singh, Y., Sharma, S., Kumar, U., Sihag, P., Balyan, P., Singh, K. P., & Dhankher, O. P. (2024). Strategies for economic utilization of rice straw residues into value-added by-products and prevention of environmental pollution. Science of the Total Environment, 906, 167714.

300. Singh, Y., Sharma, S., Kumar, U., Sihag, P., Balyan, P., Singh, K. P., & Dhankher, O. P. (2024). Strategies for economic utilization of rice straw residues into value-added by-products and prevention of environmental pollution. Science of the Total Environment, 906, 167714.

301. Smit, R. (2019). Postharvest phytosanitary disinfestation strategies using thermal and atmospheric stress: Commodity and insect tolerances (Doctoral dissertation, Stellenbosch University).

302. Soam, P. S., Singh, T., Vijayvergia, R., & Jayabaskaran, C. (2013). Liquid chromatography–mass spectrophotometry based profile of bioactive compounds of Cucumis callosus. European Journal of Experimental Biology, 316–326.

303. Sodaeizadeh, H., Karimian, A. A., Jafari, S. H., & Arani, A. M. (2024). A preliminary study on heavy metal monitoring in soil and guar (Cyamopsis tetragonoloba) biomass amended with sewage sludge. Environmental Monitoring and Assessment, 196(2), 201.

304. Sodaeizadeh, H., Karimian, A. A., Jafari, S. H., & Arani, A. M. (2024). A preliminary study on heavy metal monitoring in soil and guar (Cyamopsis tetragonoloba) biomass amended with sewage sludge. Environmental Monitoring and Assessment, 196(2), 201.

305. Sood, A., Kaur, P., & Gupta, R. (2012). Phytochemical screening and antimicrobial assay of various seed extracts of Cucurbitaceae family. International Journal of Applied Biology and Pharmaceutical Technology, 3, 401–409.

306. Spasojević, L., et al. (2019). Edible water barrier films prepared from aqueous dispersions of zein nanoparticles. LWT – Food Science and Technology, 109, 350–358.

307. Srikanth, R., Reddy, C. H. S., Siddartha, G., Ramaiah, M. J., & Uppuluri, K. B. (2015). Review on production, characterization and applications of microbial levan. Carbohydrate Polymers, 120, 102–114.

308. Srikanth, R., Reddy, C. H. S., Siddartha, G., Ramaiah, M. J., & Uppuluri, K. B. (2015). Review on production, characterization and applications of microbial levan. Carbohydrate Polymers, 120, 102–114.

309. Sümbül, A., Uzun, A., Yaman, M., Tunç, Y., Khadivi, A., & Keçe, Y. M. (2025). Antioxidant capacity, biochemical composition, and mineral composition of leaves in two apple species (Malus domestica Borkh. and M. kirghisorum). BMC Plant Biology, 25(1), 297.

310. Sun, R., Lawther, J. M., & Banks, W. B. (1996). Fractional and structural characterization of wheat straw hemicelluloses. Carbohydrate Polymers, 29(4), 325–331.

311. Sun, R., Lawther, J. M., & Banks, W. B. (1996). Fractional and structural characterization of wheat straw hemicelluloses. Carbohydrate Polymers, 29(4), 325–331.

312. Sun, Z. Y., Tang, Y. Q., Iwanaga, T., Sho, T., & Kida, K. (2011). Production of fuel ethanol from bamboo by concentrated sulfuric acid hydrolysis followed by continuous ethanol fermentation. Bioresource Technology, 102(23), 10929–10935.

313. Szabó, L., Milotskyi, R., Sharma, G., & Takahashi, K. (2023). Cellulose processing in ionic liquids from a materials science perspective: Turning a versatile biopolymer into the cornerstone of our sustainable future. Green Chemistry, 25(14), 5338–5389.

314. Taherdanak, M., & Zilouei, H. (2014). Improving biogas production from wheat plant using alkaline pretreatment. Fuel, 115, 714–719.

315. Tahmouzi, S., Meftahizadeh, H., Eyshi, S., Mahmoudzadeh, A., Alizadeh, B., Mollakhalili-Meybodi, N., & Hatami, M. (2023). Application of guar (Cyamopsis tetragonoloba L.) gum in food technologies: A review of properties and mechanisms of action. Food Science & Nutrition, 11(9), 4869–4897.

316. Tak, Y., Samota, M. K., Meena, N. K., Kaur, G., Jain, M. C., Kumar, R., et al. (2024). Underutilized fruit lasoda (Cordia myxa L.): Review on bioactive compounds, antioxidant potentiality and applications in health bioactivities and food. Fitoterapia, 105898.

317. Tanaka, K., Nishitani, A., Akashi, Y., Sakata, Y., Nishida, H., Yoshino, H., & Kato, K. (2007). Molecular characterization of South and East Asian melon (Cucumis melo L.) and the origin of Group Conomon var. makuwa and var. conomon revealed by RAPD analysis. Euphytica, 153(1), 233–247.

318. Tanwar, R., Panghal, A., Kumari, A., & Chhikara, N. (2023). Effect of finger millet on nutritional, rheological, cooking and pasting profile of Asian noodles. Journal of Food Chemistry and Nanotechnology, 9, S647–S652.

319. Tanwar, R., Panghal, A., Kumari, A., & Chhikara, N. (2023). Effect of finger millet on nutritional, rheological, cooking and pasting profile of Asian noodles. Journal of Food Chemistry and Nanotechnology, 9, S647–S652.

320. Teacă, C. A., & Tanasă, F. (2020). Wood surface modification: Classic and modern approaches in wood chemical treatment by esterification reactions. Coatings, 10(7), 629.

321. Teixé-Roig, J., Oms-Oliu, G., Odriozola-Serrano, I., & Martín-Belloso, O. (2022). Enhancing the gastrointestinal stability of curcumin by using sodium alginate-based nanoemulsions containing natural emulsifiers. International Journal of Molecular Sciences, 24(1), 498.

322. Teo, S. H., Chee, C. Y., Fahmi, M. Z., Wibawa Sakti, S. C., & Lee, H. V. (2022). Review of functional aspects of nanocellulose-based Pickering emulsifier for non-toxic applications and its colloid stabilization mechanism. Molecules, 27(21), 7170.

323. Teymoory, P., Driscoll, S. B., Zhao, J., & Shen, C. (2025). Impact of salt and fillers on the rheological properties of polymer composites. Polymer Composites, 46(8), 6998–7011.

324. Tijani, A. T., Ayodele, T., Liadi, M., Sarker, N. C., & Hammed, A. (2024). Mechanical and thermal characteristics of films from glycerol mixed emulsified carnauba wax/polyvinyl alcohol. Polymers, 16(21), 3024.

325. Toop, T. A., Ward, S., Oldfield, T., Hull, M., Kirby, M. E., & Theodorou, M. K. (2017). AgroCycle – Developing a circular economy in agriculture. Energy Procedia, 123, 76–80.

326. Torres-León, C., Ramírez-Guzmán, N., López, J. A., & Ramírez, A. C. (2018). Agro-industrial fruit wastes as sources of pectin and starch for sustainable packaging. Food Hydrocolloids, 81, 320–329.

327. Tosif, M. M., Bains, A., Sridhar, K., Inbaraj, B. S., Ali, N., Dikkala, P. K., & Sharma, M. (2024). Fabrication and characterization of taro (Colocasia esculenta) mucilage-based nanohydrogel for shelf-life extension of fresh-cut apples. Gels, 10(2), 95.

328. Tosif, M. M., Rehman, M. Z., Kaushik, R., Nagraik, R., & Bains, A. (2025). Cordia dichotoma fruit nanomucilage and beetroot anthocyanin-infused nanoemulsion: A functional and antimicrobial strategy for post-harvest management of tomato. Food Bioscience, 65, 106054.

329. Tramutola, A., Lanzillotta, C., Perluigi, M., & Butterfield, D. A. (2017). Oxidative stress, protein modification, and Alzheimer disease. Brain Research Bulletin, 133, 88–96.

330. Tripathi, P., & Swain, S. N. (2016). In vitro antioxidant and free radical scavenging activity of Alpinia calcarata in Andaman Islands. Plant Archives, 16, 685–694.

331. Tursi, A., & Olivito, F. (2021). Biomass conversion: General information, chemistry, and processes. In Advances in bioenergy and microfluidic applications (pp. 3–39). Elsevier.

332. Uzun, A., Koçyiğit, Ş., & Yılmaz, K. U. (2023). Determination of tolerance to scab disease in apple genotypes of Malus kirghisorum species using molecular markers. Journal of Erciyes Agriculture and Animal Science, 6(2), 74–78.

333. Uzun, A., Turgunbaev, K., Abdullaev, A., Pınar, H., Ozongun, S., Muratbekkızı, A., Badyrov, M., Ilbas, A. İ., Gürcan, K., & Kaymak, S. (2019). Genetic diversity in apple accessions belonging to different species collected from natural populations of Tianshan Mountains, South-West Kyrgyzstan. Erwerbs-Obstbau, 61(4), 363–371.

334. Vaghasiya, S., & Ishnava, K. (2024). Biological activity and phytochemical analysis of Cucumis callosus (Rottl.) Cogn.: An underutilized vegetable.

335. Valle, C., Voss, M., Calcio Gaudino, E., Forte, C., Cravotto, G., & Tabasso, S. (2024). Harnessing agri-food waste as a source of biopolymers for agriculture. Applied Sciences, 14(10), 4089.

336. Van Meerloo, J., Kaspers, G. J., & Cloos, J. (2011). Cell sensitivity assays: The MTT assay. In Cancer cell culture: Methods and protocols (pp. 237–245).

337. Van Meerloo, J., Kaspers, G. J., & Cloos, J. (2011). Cell sensitivity assays: The MTT assay. In Cancer cell culture: Methods and protocols (pp. 237–245).

338. Varadharajan, R., Rajalingam, D., & Palani, S. (2016). GC–MS/MS analysis and cardioprotective potential of Cucumis callosus on doxorubicin-induced cardiotoxicity in rats. International Journal of Pharmacy and Pharmaceutical Sciences, 8(9), 239–245.

339. Varghese, S., John, E. M., & Thomas, S. (2023). Plant-based lignocellulosic fibers for biodegradable composites and packaging materials. Composites Part B: Engineering, 255, 110614.

340. Verma, J., Rathore, D. S., Agarwal, S., & Tripathi, V. (2015). Effects of Citrullus colocynthis and Cucumis callosus extract on blood glucose levels in alloxan-induced diabetic rats. SGVU International Journal of Environmental Science and Technology, 1(1), 50–56.

341. Vincent, S., & Kandasubramanian, B. (2021). Cellulose nanocrystals from agricultural resources: Extraction and functionalisation. European Polymer Journal, 160, 110789.

342. Vishwakarma, V. K., Gupta, J. K., & Upadhyay, P. K. (2017). Pharmacological importance of Cucumis melo L.: An overview. Asian Journal of Pharmaceutical and Clinical Research, 8–12.

343. Vonnie, J. M., Rovina, K., Azhar, R. A., Huda, N., Erna, K. H., Felicia, W. X. L., & Halid, N. F. A. (2022). Development and characterization of biodegradable film derived from eggshell and cornstarch. Journal of Functional Biomaterials, 13(2), 67.

344. Wada, M., Yoshimura, A., & Amano, Y. (2018). U.S. Patent No. 9,951,192. U.S. Patent and Trademark Office.

345. Waghmare, P., Xu, N., Waghmare, P., Liu, G., Qu, Y., Li, X., & Zhao, J. (2023). Production and characterization of cellulose nanocrystals from eucalyptus dissolving pulp using endoglucanases from Myceliophthora thermophila. International Journal of Molecular Sciences, 24(13), 10676.

346. Wang, J., & Delavar, M. A. (2023). Techno-economic analysis of phytoremediation: A strategic rethinking. Science of the Total Environment, 902, 165949.

347. Wang, J., & Delavar, M. A. (2023). Techno-economic analysis of phytoremediation: A strategic rethinking. Science of the Total Environment, 902, 165949.

348. Wang, T., & Zhao, Y. (2021). Optimization of bleaching process for cellulose extraction from apple and kale pomace and evaluation of their potentials as film-forming materials. Carbohydrate Polymers, 253, 117225.

349. Wang, Y., Wang, Z., Li, S., Ma, J., Dai, X., & Lu, J. (2024). Deciphering JAK/STAT signaling pathway: A multifaceted approach to tumorigenesis, progression and therapeutic interventions. International Immunopharmacology, 131, 111846.

350. Wang, Y., Zhang, J., Wang, D., Wang, X., Zhang, F., Chang, D., & Wang, X. (2023). Effects of cellulose nanofibrils treatment on antioxidant properties and aroma of fresh-cut apples. Food Chemistry, 415, 135797.

351. Wan-Mohtar, W. A. A. Q. I., Khalid, N. I., Rahim, M. H. A., Luthfi, A. A. I., Zaini, N. S. M., Din, N. A. S., & Mohd Zaini, N. A. (2023). Underutilized Malaysian agro-industrial wastes as sustainable carbon sources for lactic acid production. Fermentation, 9(10), 905.

352. Winuprasith, T., & Suphantharika, M. (2015). Properties and stability of oil-in-water emulsions stabilized by microfibrillated cellulose from mangosteen rind. Food Hydrocolloids, 43, 690–699.

353. Wohlert, M., Benselfelt, T., Wågberg, L., Furó, I., Berglund, L. A., & Wohlert, J. (2022). Cellulose and the role of hydrogen bonds: Not in charge of everything. Cellulose, 29(1), 1–23.

354. Woldie, W. A., Shibeshi, N. T., & Kuffi, K. D. (2025). Optimization of cellulose nanocrystals extraction from teff straw using acid hydrolysis followed by ultrasound sonication. Carbohydrate Polymer Technologies and Applications, 9, 100707.

355. Wu, H., Wang, C., Mao, H., Wen, Y., Zheng, C., Zhang, W., & Yi, S. (2025). Value-added bio-products extracted from straw utilized as carriers for pesticide delivery: Innovative repurposing of agricultural waste. Industrial Crops and Products, 223, 120294.

356. Wu, H., Wang, C., Mao, H., Wen, Y., Zheng, C., Zhang, W., & Yi, S. (2025). Value-added bio-products extracted from straw utilized as carriers for pesticide delivery: Innovative repurposing of agricultural waste. Industrial Crops and Products, 223, 120294.

357. Wu, J., et al. (2018). Diversification and independent domestication of Asian and European pears. Genome Biology, 19(1), 77.

358. Xiao, R., Yang, W., Cong, X., Dong, K., Xu, J., Wang, D., & Yang, X. (2020). Thermogravimetric analysis and reaction kinetics of lignocellulosic biomass pyrolysis. Energy, 201, 117537.

359. Xiao, R., Yang, W., Cong, X., Dong, K., Xu, J., Wang, D., & Yang, X. (2020). Thermogravimetric analysis and reaction kinetics of lignocellulosic biomass pyrolysis. Energy, 201, 117537.

360. Xiong, Y., Zhang, Z., Wang, X., Liu, B., & Lin, J. (2014). Hydrolysis of cellulose in ionic liquids catalyzed by a magnetically recoverable solid acid catalyst. Chemical Engineering Journal, 235, 349–355.

361. Xu, H., et al. (2023). Development and characterization of active starch-based films incorporating graphene/polydopamine/Cu^{2+} nanocomposite fillers. Carbohydrate Polymers, 305, 120498.

362. Xu, J. B., Prayag, G., & Song, H. (2022). The effects of consumer brand authenticity, brand image, and age on brand loyalty in time-honored restaurants: Findings from SEM and fsQCA. International Journal of Hospitality Management, 107, 103340.

363. Xu, J. B., Prayag, G., & Song, H. (2022). The effects of consumer brand authenticity, brand image, and age on brand loyalty in time-honored restaurants: Findings from SEM and fsQCA. International Journal of Hospitality Management, 107, 103340.

364. Xu, T., Chen, L., Chen, J., & Assem, S. (2025). Evolution in functional groups of agricultural straw during pyrolysis at elevated temperature: In situ synchrotron radiation infrared spectroscopy. Bioresource Technology, 133125.

365. Xue, H., Zhang, Y., Zhao, Z., Gao, H., Bao, W., Li, J., & He, Q. (2025). A review: Sources, preparation, and application of nanocellulose. Journal of Polymer Materials, 42(2).

366. Yao, X., Li, G., Bai, Q., Xu, H., & Lü, C. (2013). Taraxerol inhibits LPS-induced inflammatory responses through suppression of TAK1 and Akt activation. International Immunopharmacology, 15(2), 316–324.

367. Yashwant, A. S., Kashyap, P., & Goksen, G. (2023). Recent advances in the improvement of protein-based edible films through non-thermal and thermal techniques. Food Bioscience, 55, 103032.

368. Yildirim-Yalcin, M., Tornuk, F., & Toker, O. S. (2022). Recent advances in the improvement of carboxymethyl cellulose-based edible films. Trends in Food Science & Technology, 129, 179–193.

369. Yin, Y., & Woo, M. W. (2024). Transitioning of petroleum-based plastic food packaging to sustainable bio-based alternatives. Sustainable Food Technology, 2(3), 548–566.

370. Zalasiewicz, J., Gabbott, S., & Waters, C. N. (2019). Plastic waste: How plastics have become part of the Earth's geological cycle. In Waste (pp. 443–452). Academic Press.

371. Zhang, H., & Li, G. (2025). Microbial strategies for enhancing nickel nanoparticle detoxification in plants to mitigate heavy metal stress. Phyton, 94(5).

372. Zhang, H., & Li, G. (2025). Microbial strategies for enhancing nickel nanoparticle detoxification in plants to mitigate heavy metal stress. Phyton, 94(5).

373. Zhang, H., Zhao, B., Wei, H., Zeng, H., Sheng, D., & Zhang, Y. (2022). Cucurbitacin B controls M2 macrophage polarization to suppress metastasis via targeting JAK-2/STAT3 signalling pathway in colorectal cancer. Journal of Ethnopharmacology, 287, 114915.

374. Zhang, Z., O'Hara, I. M., & Doherty, W. O. (2012). Pretreatment of sugarcane bagasse by acid-catalysed process in aqueous ionic liquid solutions. Bioresource Technology, 120, 149–156.

375. Zhao, X., Chen, J., Chen, F., Wang, X., Zhu, Q., & Ao, Q. (2013). Surface characterization of corn stalk superfine powder studied by FTIR and XRD. Colloids and Surfaces B: Biointerfaces, 104, 207–212.

376. Zhao, X., Cheng, K., & Liu, D. (2009). Organosolv pretreatment of lignocellulosic biomass for enzymatic hydrolysis. Applied Microbiology and Biotechnology, 82(5), 815–827.

377. Zhao, X., Li, S., Wu, R., & Liu, D. (2017). Organosolv fractionating pretreatment of lignocellulosic biomass for efficient enzymatic saccharification: Chemistry, kinetics, and substrate structures. Biofuels, Bioproducts and Biorefining, 11(3), 567–590.

378. Zheng, Y., Pan, Z., & Zhang, R. (2009). Overview of biomass pretreatment for cellulosic ethanol production. International Journal of Agricultural and Biological Engineering, 2(3), 51–68.

379. Zhong, C., Wang, C., Huang, F., Jia, H., & Wei, P. (2013). Wheat straw cellulose dissolution and isolation by tetra-n-butylammonium hydroxide. Carbohydrate Polymers, 94(1), 38–45.

380. Zhou, G., Li, M.-C., Wang, F., Liu, C., & Mei, C. (2022). 3D printing of cellulose nanofiber monoliths for thermal insulation and energy storage applications. Additive Manufacturing, 59, 103124.

Plagiarism Report

Final Thesis 12208549

ORIGINALITY REPORT

9%	4%	9%	1%
SIMILARITY INDEX	INTERNET SOURCES	PUBLICATIONS	STUDENT PAPERS

Exclude quotes	On	Exclude matches	< 14 words
Exclude bibliography	On		

Environmental Technology & Innovation 40 (2025) 104569

Contents lists available at ScienceDirect

Environmental Technology & Innovation

journal homepage: www.elsevier.com/locate/eti

Polyphenol-rich extract from *Cyamopsis tetragonoloba* straw: Characterization, bioactivity, cytotoxicity, and anti-obesity potential

Ritu Rani [a], Deepika Kaushik [b], Fatih Oz [c,d,e,**], Graciela Dolores Avila-Quezada [f], Elsayed Fathi Abd_Allah [g], Abeer Hashem [h], Mukul Kumar [a,*]

[a] Department of Food Technology and Nutrition, Lovely Professional University, Phagwara, Punjab 144411, India
[b] Department of Biotechnology, Faculty of Applied Sciences and Biotechnology, Shoolini University, Solan, HP 173229, India
[c] Department of Food Engineering, Faculty of Agriculture, Ataturk University, Erzurum 25240, Turkiye
[d] Kyrgyz-Turkish Manas University, Engineering Faculty, Department of Food Engineering, Bishkek 720038, Kyrgyzstan
[e] East Anatolian High Technology Research and Application Center (DAYTAM), Ataturk University, Erzurum 25240, Turkiye
[f] Facultad de Ciencias Agrotecnológicas, Universidad Autónoma de Chihuahua, Chihuahua, Chihuahua 31350, Mexico
[g] Department of Plant Production, College of Food Science and Agriculture, King Saud University, P.O. Box. 2460, Riyadh 11451, Saudi Arabia
[h] Department of Botany and Microbiology, College of Science, King Saud University, P.O. Box. 2455, Riyadh 11451, Saudi Arabia

ARTICLE INFO

Keywords:
Amylase
Guar straw
Obesity
Lipase
Waste valorisation
Cytotoxicity

ABSTRACT

India annually generates over 683 million tonnes of agricultural waste, with *Cyamopsis tetragonoloba* straw representing an unexplored lignocellulosic byproduct possessing significant biotechnological potential. This study aims to evaluate the phytochemical, functional, and bioactive properties of *Cyamopsis tetragonoloba* straw, whereas phytochemical profiling showed the presence of polyphenolic compounds such as cinnamic acid, chlorogenic acid, caffeic acid, and vanillic acid. Proximate composition of straw was moisture (4.43 %), fat (0.30 %), protein (4.89 %), ash (2.16 %), and fiber (39.65 %) content. Moreover, the straw exhibits techno-functional properties, including a density of 0.34 g/cm^3, a tapped density of 0.58 g/cm^3, a water-holding capacity of 5.08 g/g, and an oil absorption capacity of 4.85 g/g. Antioxidant potential was confirmed through DPPH radical scavenging activity (3.83 mg QE/g), total phenolic content (4.15 mg GAE/g), and total flavonoid content (3.83 mg QE/g). Furthermore, Fourier-transform infrared (FTIR) spectroscopy identified characteristic functional groups linked to bioactive constituents. Antimicrobial assays demonstrated a concentration-dependent inhibitory effect, with significant ($p < 0.05$) activity observed at different concentrations of 50 and 100 μL/mL. Additionally, cytotoxicity analysis shows the highest inhibitory effects at a concentration of 50 μL/mL of straw extract. It also showed significantly ($p < 0.05$) higher amylase (90.99 %) and lipase inhibition activity (71.86 %). Overall, it exhibits promising potential as a sustainable source of bioactive compounds with potential applications in the nutraceutical, pharmaceutical,

* Corresponding author.
** Corresponding author at: Department of Food Engineering, Faculty of Agriculture, Ataturk University, Erzurum 25240, Turkiye.
E-mail addresses: ritufoodtechlpu@gmail.com (R. Rani), dk4275388@gmail.com (D. Kaushik), fatihoz@atauni.edu.tr, fatih.oz@manas.edu.kg (F. Oz), gdavila@uach.mx (G.D. Avila-Quezada), eabdallah@ksu.edu.sa (E.F. Abd_Allah), habeer@ksu.edu.sa (A. Hashem), mukulkolish@gmail.com (M. Kumar).

https://doi.org/10.1016/j.eti.2025.104569
Received 24 July 2025; Received in revised form 22 September 2025; Accepted 13 October 2025
Available online 17 October 2025
2352-1864/© 2025 The Author(s). Published by Elsevier B.V. This is an open access article under the CC BY license (http://creativecommons.org/licenses/by/4.0/).

International Journal of Food Science and Technology, 2025, 60(1), vvae098
https://doi.org/10.1093/ijfood/vvae098
Advance access publication 8 January 2025
Review

Exploring the deciphering properties of *Cyamopsis tetragonoloba*: its food application, feasibility, and future aspects

Ritu Rani[1], Deepika Kaushik[2], Gülçin Emel Babagil[3], Charalampos Proestos[4], Charles Brennan[5,6], Fatih Oz[7,8,*], and Mukul Kumar[1,*]

[1]Department of Food Technology and Nutrition, Lovely Professional University, Phagwara, India
[2]Faculty of Applied Sciences and Biotechnology, Department of Biotechnology, Shoolini University, Solan, India
[3]Food and Feed Department, Republic of Türkiye Ministry of Agriculture and Forestry Erzurum Directorate of Provincial Agriculture and Forestry, Erzurum, Türkiye
[4]Laboratory of Food Chemistry, Department of Chemistry, School of Sciences, National and Kapodistrian University of Athens, Athens, Greece
[5]School of Science, RMIT University, Melbourne, Australia
[6]Department of Food Science, Riddet Institute, Palmerston North, New Zealand
[7]Department of Food Engineering, Agriculture Faculty, Ataturk University, Erzurum, Turkiye
[8]East Anatolian High Technology Research and Application Center (DAYTAM), Ataturk University, 25240, Erzurum, Türkiye

*Corresponding authors: Department of Food Technology and Nutrition, Lovely Professional University, Phagwara 144411, Punjab, India.
Email: mukulkolish@gmail.com; Department of Food Engineering, Agriculture Faculty, Ataturk University, Erzurum 25240, Türkiye.
Email: fatihoz@atauni.edu.tr

Abstract

Cyamopsis tetragonoloba belongs to the Fabaceae family and is an erect, drought-resistant, coarse-textured, annual legume. This species serves as a valuable source of nutrition for both livestock and humans. The purpose of this review is to explore the nutritional profile of *C. tetragonoloba*, highlighting its richness in dietary fibre, proteins, and essential minerals, alongside its bioactive compounds, such as flavonoids and polysaccharides, which demonstrate antioxidant, anticancer, and antidiabetic properties and its applications. The potential of *C. tetragonoloba* in developing biodegradable packaging materials is also explored, highlighting its ability to enhance mechanical properties and food product storage stability, making it a viable alternative to petrochemical-based plastics. Additionally, this review addresses *C. tetragonoloba* cultivation's environmental impact and sustainability, emphasising the importance of efficient byproduct valorization, pharma industry, and its role in circular economy practices. Key challenges and future research directions include improving processing technologies, exploring novel applications for *C. tetragonoloba*-based materials, and enhancing *C. tetragonoloba* cultivation and utilisation for environmental and economic sustainability.

Keywords: bioactivity, nutritional profile, food application, pharmaceutical, packaging

Downloaded from https://academic.oup.com/ijfst/article/60/1/vvae098/7943402 by guest on 02 September 2025

Received: 3 November 2024. **Accepted:** 13 December 2024
© The Author(s) 2025. Published by Oxford University Press on behalf of Institute of Food Science and Technology.
This is an Open Access article distributed under the terms of the Creative Commons Attribution License (https://creativecommons.org/licenses/by/4.0/), which permits unrestricted reuse, distribution, and reproduction in any medium, provided the original work is properly cited.

Check for updates

Wiley
Journal of Food Processing and Preservation
Volume 2026, Article ID 1620988, 14 pages
https://doi.org/10.1155/jfpp/1620988

WILEY

Review Article

Bioactivity and Vital Application of Underutilized *Cucumis callosus* Fruit: An Overview on the Present Status and Its Potential Utilization

Ritu Rani,[1] Aarti Bains,[2] Mukul Kumar,[1] Sanju Bala Dhull,[3] Agnieszka Najda,[4] Rupak Nagraik,[5] and Prince Chawla[1]

[1]*Department of Food Technology and Nutrition, Lovely Professional University, Phagwara, Punjab, India*
[2]*School of Health Sciences and Technology, University of Petroleum and Energy Studies, Dehradun, Uttarakhand, India*
[3]*Department of Food Science and Technology, Chaudhary Devi Lal University, Sirsa, Haryana, India*
[4]*Department of Vegetable and Herbal Crops, University of Life Sciences in Lublin, Lublin, Poland*
[5]*Department of Biotechnology, Graphic Era (Deemed to be University), Dehradun, India*

Correspondence should be addressed to Sanju Bala Dhull; sanjudhull_fst@cdlu.ac.in
and Prince Chawla; princefoodtech@gmail.com

Received 6 February 2025; Revised 6 October 2025; Accepted 13 November 2025

Academic Editor: Valentina Prosapio

Copyright © 2026 Ritu Rani et al. Journal of Food Processing and Preservation published by John Wiley & Sons Ltd. This is an open access article under the terms of the Creative Commons Attribution License, which permits use, distribution and reproduction in any medium, provided the original work is properly cited.

Unexplored fruits and vegetables reveal a reservoir of potential, offering an excellent source of numerous biologically active and nutritional components. *Cucumis callosus* is one of the underutilized fruits from the Cucurbitaceae family, which presents promising yet underexplored potential for food and pharmaceutical applications. Hence, this review explores current knowledge on the bioactive properties and potential utilizations of *Cucumis callosus*, highlighting its phytochemical constituents, nutritional profile, and therapeutic benefits. *Cucumis callosus* exhibits significant antioxidant, antimicrobial, and anti-inflammatory activities due to the abundance of essential vitamins, minerals, and bioactive compounds such as flavonoids, phenolics, and saponins. These properties signify its effective utilization in developing functional foods, nutraceuticals, and pharmaceuticals aimed at combating oxidative stress, microbial infections, and inflammatory conditions. Furthermore, its traditional medicinal applications describe its relevance in ethnomedicine, where it has been used for treating various ailments, including diabetes, gastrointestinal disorders, and skin diseases. Despite its evident potential, the commercial utilization and comprehensive scientific investigation of *Cucumis callosus* remain limited. This review also reveals for intensified research efforts to explore the mechanistic pathways of its bioactive compounds and their health benefits. Hence, by bridging the gap between traditional knowledge and recent scientific research, *Cucumis callosus* could emerge as a valuable resource in promoting health and wellness in society.

Keywords: bioactivity; *Cucumis callosus*; harvesting; nutritional profile; therapeutic properties

Summary

- *Cucumis callosus* is a horticultural crop that grows in dry places with low relative humidity levels.
- The biochemical assessment of *Cucumis callosus* reveals a well-balanced proximate composition with high protein content.
- Bioactive compounds strengthen the immune system, lowering blood cholesterol levels and the risk of intestinal tumors.

1. Introduction

The Cucurbitaceae family has been extensively explored by researchers and industries for its nutritional richness and potential therapeutic properties [1]. However, numerous

Rani et al.
CABI Reviews (2025) 20:1, 0049
https://doi.org/10.1079/cabireviews.2025.0049

CABI Reviews

REVIEW

Unveiling the approach of campesterol: Its application and circular bio-economy

Ritu Rani[1], Deepika Kaushik[2]*, Ashwani Kumar[3], Prasad Rasane[1], Emel Oz[4], Vishal Kumar[1], Kalpana Patra[1], Fatih Oz[4,5,6], Charalampos Proestos[7] and Mukul Kumar[1]*

Affiliations: [1]Department of Food Technology and Nutrition, Lovely Professional University, Phagwara, 144411, Punjab, India
[2]Department of Biotechnology, Faculty of Applied Science and Biotechnology, Shoolini University, Solan, 173229, Himachal Pradesh, India
[3]Institute of Food Technology, Bundelkhand University, Jhansi, 284127, India
[4]Department of Food Engineering, Faculty of Agriculture, Ataturk University, Erzurum 25240, Turkiye
[5]Engineering Faculty, Department of Food Engineering, Kyrgyz-Turkish Manas University, Bishkek, 720038, Kyrgyzstan
[6]East Anatolian High Technology Research and Application Center (DAYTAM), Ataturk University, Erzurum, 25240, Türkiye
[7]Laboratory of Food Chemistry, Department of Chemistry, School of Sciences, National and Kapodistrian University of Athens Zogafou, Athens, 15784, Greece

Abstract

Campesterol is a naturally occurring phytosterol found in the plant cell membranes, and it shows medicinal uses in nutraceuticals and pharmaceuticals due to its strong biological activities, such as antioxidant, anti-inflammatory, and anticancer properties. Several extraction methods exist, *i.e.* docking, chromatographic, gas chromatography-mass spectrometry, subcritical fluid extraction, cold-pressed, Soxhlet, mechanical shaking, silica solid-phase and microwave-assisted; however, silica solid-phase extraction method is a highly efficient approach for isolating campesterol from plant cells. Campesterol is also used for enhancing the nutritional value and functional qualities of food such as margarine, dairy products, including milk, yoghurt, and cheese, salad dressings and beverages like soy milk, almond milk, peanut milk, and oat milk. It also plays an important role in cosmetics products (moisturizing lotions, lipsticks, and shampoos) and biomaterials (gelatin, chitin, silk sericin, chitosan, and alginate). Valorization of underutilized horticultural crops (green and yellow vegetables, nuts, seeds, legumes, fruits, and grains) and fruit waste peel, pulp, and seed as a source of campesterol directly shows impact on circular bio-economy. This review focuses on campsterol's bioactivity, extraction, and sustainable applications in food and pharma industries.

Keywords: bioactivity, campesterol, therapeutic properties, food, valorization

Introduction

Phytosterols are naturally occurring bioactive compounds found in plants, structurally characterized by a tetracyclic core, and more than 250 phytosterols have been reported in dietary sources, which are present in legumes, nuts, cereals, vegetables and their oils, fruits, and fats. The most common phytosterols found in plants are campesterol, β-sitosterol and stigmasterol. Campesterol is a sterol with a four-ring core structure, as shown in Fig. 1. Therefore, it also shows several health benefits such as cholesterol-lowering effects and potential anticarcinogenic properties, and physiological functions in plants (Choi *et al*., 2007). Campesterol plays a vital role in maintaining membrane dynamics and serves as a precursor for specialized metabolites, including the phytohormone brassinosteroids (Xu *et al*., 2023; Valitova *et al*., 2024; Wang *et al*., 2024). Canola and maize oils contain the highest concentrations of campesterol; however, it is present in many other plant sources, including oil seeds and herbaceous plants, as well as the waste from industrial softwood and hardwood processing. Due to their structural similarity, campesterol and cholesterol are competitively absorbed in the human intestine, influencing intestinal cells and proteins, and affecting lipid metabolism, including cholesterol synthesis, esterification, and lipoprotein (Nazir *et al*., 2023). Recent studies have shown that campesterol exhibits anticancer properties, particularly by inhibiting the metastasis of ovarian cancer, leukaemia, and hepatocellular carcinoma cells (Bae *et al*., 2021). Epidemiological studies have revealed that a daily consumption of 10 mg of campesterol decreases cancer risk by 13%, demonstrating an inverse relationship between its intake levels and cancer risk (Chuu *et al*., 2007; O'Callaghan *et al*., 2013). Grains (barley, buckwheat, maize, millet, quinoa, rye, and spelt), legumes (butter beans, chick peas, kidney beans, lentils, and peas-marrowfat), fruits (orange, mango, bananas, pomegranates etc.), and vegetables (pea, broccoli, scallion, carrot, cabbage, etc.) are a major source of campesterol, and these crops, utilized in Ayurvedic

*Corresponding Authors: Mukul Kumar; Deepika Kaushik. Email: mukulkolish@gmail.com; dk4275388@gmail.com

Submitted: 13 May 2025. Accepted: 10 June 2025. Published: 02 July 2025

© CAB International 2025

CABI

SSAFNS
Recent Trends in Smart and Sustainable Agriculture for Food and Nutritional Security

SCHOOL OF AGRICULTURE

ThinkBIG

NAAC GRADE A++

Certificate No. 349542

Certificate of Merit

This is to certify that **Mr./Ms./Dr. Ritu Rani** of **Lovely Professional University, Punjab** stood **Third** in **Oral Presentation** on **Optimization of cellulose extraction process from cyamopsis tetragonoloba by using response surface methodology** in the **International Conference on Recent Trends in Smart and Sustainable Agriculture for Food and Nutritional Security (SSAFNS)** held from **27th September, 2024** to **28th September, 2024** organized by ***School of Agriculture***, Lovely Faculty of Technology and Sciences, at Lovely Professional University, Punjab.

Date of Issue : 28-09-2024
Place : Phagwara (Punjab), India

Prepared by
(Administrative Officer-Records)

Joint Organizing Secretary/HOS
School of Agriculture

Head of Faculty
LPU

dhanuka

ELSEVIER Scopus

SCHOOL OF
AGRICULTURE

NAAC GRADE A++

Certificate No. 435288

Certificate of Merit

This is to certify that **Ms. Ritu Rani** of **Lovely Professional University, Punjab** stood **First** in the Oral Presentation on "**Optimization of Acid Hydrolysis Parameters for Efficient Extraction of Nanocellulose from Cyamopsis tetragonoloba Straw"** in the **International Conference on Recent Trends in Smart and Sustainable Agriculture for Food and Nutritional Security (SSAFNS 2025)** held from **November 27, 2025,** to **November 28, 2025** organized by School of Agriculture at Lovely Professional University, Phagwara, Punjab.

Date of Issue: 15-01-2026
Place: Phagwara, Punjab, India

Prepared by
(Administrative Officer-Records)

Organizing Secretary
School of Agriculture

Head of School
School of Agriculture

ICEFB-2024

सत्यमेव जयते
पृथ्वी विज्ञान मंत्रालय
Ministry of Earth Sciences

International Conference on Global Challenges in Environment, Food and Biotechnology for Sustainable Development

Certificate

This is certified that Prof./Dr./Mr./Ms. Ritu rani from Lovely Professional University, Phagwara, Punjab participated/presented a paper (oral/poster) entitled Valorizing Cyamopsis tetragonoloba Waste for packaging material: Exploring its biological activity and sustainable applications. during International Conference on Global Challenges in Environment, Food and Biotechnology for Sustainable Development (ICEFB-2024) organized by Faculty of Environmental and Bio Sciences & Technology, GJUST, Hisar held during February 21-23, 2024.

Prof. Asha Gupta	Prof. Rajesh Lohchab	Prof. Manish Kumar	Prof. Anil Kumar
Convener	Co-convener	Co-convener	Co-convener